NASA Conference Publication 2340

13th Space Simulation Conference

The Payload – Testing for Success

Proceedings of a symposium held at
Sheraton Twin Towers, Orlando, Florida
October 8-11, 1984

NASA

NASA Conference Publication 2340

13th Space Simulation Conference

The Payload – Testing for Success

Sponsored by
National Aeronautics and Space Administration
Institute of Environmental Sciences
The American Institute for Aeronautics and Astronautics
The American Society for Testing and Materials

Proceedings of a symposium held at
Sheraton Twin Towers, Orlando, Florida
October 8-11, 1984

NASA
National Aeronautics
and Space Administration

Scientific and Technical
Information Branch

1984

PREFACE

The Thirteenth Space Simulation Conference, held at the Sheraton Twin Towers, Orlando, Florida, October 8-11, 1984 was sponsored by the Institute of Environmental Sciences and supported by the National Aeronautics and Space Administration, the American Institute of Aeronautics and Astronautics, and the American Society for Testing and Materials. These conferences have brought together engineers and scientists of diverse disciplines with the common interests of space simulation, its applications and solutions of complex problems that are encountered.

This conference was favored with a wide variety of papers concerning facilities, testing and contamination control. Our featured speaker was Francis J. Logan, Deputy Project Manager, Solar Maximum Repair Mission, who spoke of the problems and successes of retrieving and repairing an orbiting spacecraft utilizing the Shuttle. This endeavor was a historic first for the space program. The meeting was concluded with a trip to the Kennedy Space Center to see the Shuttle complex and other points of interest.

I wish to acknowledge the splendid effort of the many people who made this meeting successful. Robert P. Parrish, Jr., Martin Marietta Corp., Technical Program Chairman and his committee gave us a well rounded, informative program; Joseph L. Stecher, NASA GSFC, as Publications Chairman assembled these proceedings; John D. Campbell, Perkin Elmer Corp., was extremely helpful in his capacity as the IES Meeting Manager; and Betty Peterson, IES Executive Director, and Janet A. Ehman, IES Deputy Executive Director, did their usual excellent efforts in all administrative areas.

R. T. Hollingsworth
General Chairman

COMMITTEES FOR

13TH SPACE SIMULATION CONFERENCE

MEETING MANAGEMENT COMMITTEE

General Chairman:	Russell T. Hollingsworth, NASA Goddard Space Flight Center
Technical Program:	Robert P. Parrish, Jr., Martin Marietta Corporation
IES Meeting Manager:	John D. Campbell, Perkin-Elmer Corporation
Publication Chairman	Joseph L. Stecher III, NASA Goddard Space Flight Center
Facilities Chairman:	James E. Easley, Micro Filtrations Inc.
IES Deputy Executive Director:	Janet A. Ehmann, Institute of Environmental Sciences
IES Executive Director:	Betty Peterson, Institute of Environmental Sciences

TECHNICAL PROGRAM COMMITTEE

Ernest Oddo, The Aerospace Corporation
Steven W. Liu, TRW
Ward F. Petrie, Perkin-Elmer Corporation
Raymond Kruger, NASA Goddard Space Flight Center
John Harrell, Jet Propulsion Laboratory
David G. Billingsley, Lyndon B. Johnson Space Center
Raymond Rempt, Martin Marietta Aerospace
Eugene N. Borson, The Aerospace Corporation

JOINT POLICY COMMITTEE

IES

John D. Campbell, Perkin-Elmer Corp.
George Frankel, Grumman Aerospace

ASTM

Eugene N. Borson, Aerospace Corp.
Charles H. Duncan, NASA-GSFC

AIAA

David G. Billingsley, NASA Johnson Space Center
Albert R. Lunde, The Boeing Company

CONTENTS

Section Page

SESSION III: SPECIAL TOPICS

Chairmen: Eugene Borson, The Aerospace Corporation

George F. Wright, Sandia National Laboratories

PANEL: SIMULATION OF UPPER ATMOSPHERE OXYGEN

Section Page

SESSION IV: MEASUREMENTS AND TECHNIQUES

Chairmen: Steve Liu, TRW

Emile S. J. Wang, McDonnell Aircraft Co.

SESSION V: SOLAR MAX MISSION

Chairmen: David G. Billingsley, NASA Johnson Space Center

Richard Hartenbaum, RCA

SESSION VI: MEASUREMENTS AND TECHNIQUES

Chairmen: Ward Petrie and A. Westfall, Perkin-Elmer Corporation

DEVELOPMENT OF A THERMAL ENVIRONMENT SIMULATOR FOR LARGE TEST ARTICLES IN A VACUUM

Hal B. Storrs
Martin Marietta Aerospace

ABSTRACT

Most of the thermal balance testing done at the Space Simulation Laboratory of Martin Marietta Aerospace has used the 16′ diameter solar simulator in the 29′ x 65′ vacuum chamber. With the development of the shuttle, test articles which are too large to fit in the solar beam are becoming commonplace. To be able to test those articles, a new technique was required. The thermal environment could be simulated by varying the effective sink temperature about the test article. The accuracy of this simulation depends upon the spectral emissivity/absorptivity, the number and size of the control zones, the temperature of each zone, and the geometry of the enclosure. Cost and control complexity also enter into the problem. The idea of a very large number of zones closely conforming to the surface of the test article quickly become prohibitive due to expense and control problems. Likewise, a two zone, low price enclosure would not have the fidelity required for thermal balance testing. Martin Marietta has concepted a simulator that, for a reasonable cost, will be able to simulate the thermal balance environment for most large test articles in the future.

INTRODUCTION

The need to perform thermal balance and thermal vacuum testing of space articles and satellites is the driving force behind most thermal vacuum chambers. These tests have two different approaches.

Thermal balance testing is performed to prove the analysis and thermal model of the test article. This involves subjecting the test article to a predetermined environment and comparing the actual response to the response predicted by the computer model.

Thermal vacuum testing, on the other hand, is used to qualify or accept a working craft. This involves driving the test article to temperature extremes beyond the normal expected levels.

Martin Marietta has used two different systems in its large space chamber to perform these tests. A 16′ diameter solar simulator, gimbal, and LN_2 shroud have been used for thermal balance testing. For thermal vacuum testing, a combination of IR lamp cages, temperature controlled shroud, and heaters on the test article have been used.

These systems have worked well on all past test articles. However, with the shuttle operational and the increasing complexity of space articles, we could forsee test articles being too large and complex to test with the existing hardware. Thus, a new system was needed; a system large and versatile enough to handle shuttle-sized items.

Size, configuration, and capabilities of this new simulator had to be determined.

REQUIREMENTS

To start, some basics on potential test article size had to be determined. The space shuttle has simplified this problem because most satellites and space probes are being designed to fit in its cargo bay. The shuttle cargo bay is 15 feet in diameter by 60 feet in length.

Our large space chamber has internal clear dimensions of 24 feet in diameter and up to 53 feet in height. Thus it was feasible to aim for a simulator that would utilize the existing chamber and handle most articles that would fit in the shuttle cargo bay.

The thermal capabilities were almost as easy to determine. Only a small number of space probes will be sent beyond earth orbit and of these only those going to Venus, Mercury, or to orbits that approach the sun will see more than one solar constant. The majority of space hardware will operate either from the shuttle cargo bay or in orbit about the earth. This meant that if the simulator could present any part of the test article with the range from the cold black sink of space to over one solar constant of heat it could simulate all but a very few of the environments that will be encountered by space articles.

PRACTICAL LIMITATIONS

These basic requirements left many options for the design of the simulator. Some of the options could easily be eliminated. Any design utilizing an enlarged solar simulator was out for two reasons:

a) the existing solar simulator was already as large as the chamber could practically accommodate, and

b) simulation of the conditions in the cargo bay or planet albedos would still require additional equipment.

This left enclosing the test article in a zoned enclosure as the best approach. A two zone enclosure would be simple and inexpensive but would be too limited to simulated multiple heat sources or a rotating space craft. The other extreme of many very small zones conforming to the surface of the test article would give good simulations, but would be too complex and expensive to be practical. Between these two extremes would be a compromise that would produce an adequate simulation, but yet be simple enough to control and reasonable in cost.

To keep the distance from a zone to the test article small, the inside clearance of the simulator was set at 16 feet. In most cases, this will minimize the effect on the test article of adjacent control zones. This also means that any solar panels, antennas, or booms that extend from the test article will have to either extend through the simulator enclosure or be left off of the test article. This was considered a minimal sacrifice, since most appendages could not be completely deployed in the chamber, and since the thermal effect of an appendage can easily be simulated by a heater at the interface point.

The height of the enclosure was set at 36 feet. A design requirement was that less than the full 36 feet could be used for short test articles and that the height could be increased if needed in

the future. Limiting the height meant that the collimating mirror for the solar simulator would not have to be removed to install the thermal environment simulator in the chamber.

The next question was, "Into how many thermal zones should this enclosure be divided?" After examining many possible configurations, a division into six rings of eight zones each and four zones on each end was selected (see figure 1). This gave a total of 56 control zones, each approximately 6′ x 6′ in size (the end zones are closer to 8′ x 8′). Several factors made this configuration desirable. Fifty-six zones was considered reasonable for real time analysis and control modification during tests. The octagon shape would also allow simulation of sunlight/shadow and cargo bay conditions. An added point was that the computer model of the shuttle used at Martin for thermal analysis divided the cargo bay into five longitudinal zones so the simulation could have finer fidelity that the math analysis.

INDIVIDUAL ZONES

The remaining question was, "What would each individual zone look like?" Two different approaches for solving this problem give different designs for the zones.

If the simulator is thought of as a thermal sink, then the environment is achieved by controlling the temperature of the zones. This approach leads to a design involving high emissivity thermal panels where the panel temperature is controlled using a heat exchange fluid and heaters.

On the other hand, if the simulator is thought of as a thermal source, then the environment is achieved by controlling the heat flux from each zone. This approach leads to a design involving a cold shroud to prevent background radiation and infrared lamps or heaters to generate the desired flux levels.

Either approach will work to simulate an environment but both have technical problems. In the case of the sink panels, the large mass involved make transition between hot and cold conditions slow and the large amount of fluid lines, valves, and heat exchangers makes control complex and the risk of leakage high. In the case of the heat flux sources, achieving uniformity and an accurate measurement of the heat flux is very difficult.

Since neither approach had a clear advantage over the other, the simulator zones were specified in terms of both. Each zone would be controllable from $-250°$ to $+300°$ F with an emissivity of .9 or greater, or each zone would be controllable from a heat flux of 3 to 515 BTU/sq. ft./hr. Transition from one extreme to the other was set at 2 hours for both methods. Error tolerance, accuracy of control, and uniformity were specified in both degrees F and in BTU/sq. ft./hr. and designed to conform to MIL. STD. 810 c.

CONTROL SYSTEM

Control of the simulator would involve monitoring a minimum of 56 measurements and simultaneously adjusting inputs to each of the 56 zones. To allow this to be done efficiently, a computerized control system with manual backup was specified. This system would be primarily

for control of the simulator, but to prevent possible future needs from being ignored, it would also have expansion capabilities for additional monitoring and control functions.

CHARACTERISTICS

These, then are the basics of the thermal environment simulator as specified by Martin Marietta:

1) A 16 foot octagon enclosure, 36 feet high and divided into 56 independent thermal control zones.

2) Each zone be capable of either $-250°$ F to $+300°$ F with an emissivity of greater than .9 or 3 to 515 BTU/sq. ft./hr.

3) Transition from one extreme to the other in two hours or less.

4) Operation of the simulator by a computerized control system.

PROPOSALS

A request for proposal was released and four companies responded. Three companies proposed using flat panels with nitrogen gas as a heat exchanger medium. The fourth company (High Vacuum Equipment Corporation) proposed a hybrid system using heated louvers and the existing LN_2 shroud. This proposal was chosen as the best design and HVEC is in the process of building this simulator.

CONCEPT

The hybrid system overcomes many of the drawbacks of both the sink panels and of the radiant sources by being able to act like both. At the high temperature/high heat flux condition, the closed louvers have the uniformity and analytical simplicity of a flat panel. Opening the louvers can create the cold/low heat flux conditions without the complexity and risk of leakage associated with a fluid system. By changing the louver positions, rapid changes in conditions can be made. For example, fully opening the louvers can reduce the heat flux by as much as 90% with no change in louver temperature. Thus, simulations of entering a shadow can be more accurately made. Since the open louvers will radiate approximately 90% of their heat in 36 minutes, and the heaters will be capable of a 500° F change in about 30 minutes, changes from one extreme to the other will be about four times as fast as specified.

Variations in uniformity will occur with the louvers open, but this will only happen at the cold/low heat flux condition or during rapid transitions when these variations can be tolerated.

Several configurations for the louvers were tried before the design was finalized. The original concept had the louvers all rotating the same direction like venetian blinds (figure 2a). Since the front of the louvers would be black and the back bright, the panel would be asymmetrical when

open and would still present a hot black surface to objects off to one side. The second try moved the louvers like bifold doors (figure 2b). This was much better thermally as it opened a much larger area to objects off to the side but mechanical difficulties made the louvers likely to jam. The final design has every other louver rotating clockwise and the rest rotating counterclockwise (figure 2c). This design maintains symmetry and since an object to the side sees the back (bright) side of half the louvers the effective sink temperature is lower.

CONTROL AND CALIBRATION

To control the simulator, a computer will be used to monitor the temperature of the louvers and control the louver position and heater power. Stepper motors will drive the louvers and SCR's will be used to regulate the heater power.

The sequence of operation will start with the requirements from the thermal engineers. The form will be either heat flux or temperatures desired on the various areas of the test article. The simulator will have to be programmed to generate these conditions.

A program for the control computer to model the simulator is being developed. Through an iterative process it will generate a matrix of louver temperature and position needed to satisfy the test requirements. To obtain the actual heat flux output of each zone as a function of louver temperature and angle, the interior of the simulator will be scanned with calibrated radiometers for various conditions. The correction factors generated in this calibration will be incorporated into the computer model.

The control computer is capable of multiple task operation. This will allow the model program to run even while the simulator is in operation so quick response to new test requirements will be possible.

SUMMARY

Because of the growing size and complexity of new satellites and space articles, a larger and versatile thermal simulator was needed for the large vacuum chamber at Martin Marietta. To satisfy this need, the High Vacuum Equipment Corporation is building a 56 zone, computer controlled, thermal enclosure for MMDA. By a combination of cold from the existing chamber liquid nitrogen shroud and heat from the louvers, each zone will be able to simulate conditions from the cold black of space to 1.2 solar constants of heat. Using advanced computer modeling and control techniques along with extensive calibration, the thermal environment simulator will be able to produce almost any environment required to test present and future space articles.

I would like to thank Wayne Pollard of HVEC and Neal Harmon of MMDA for assisting in the preparation of this paper.

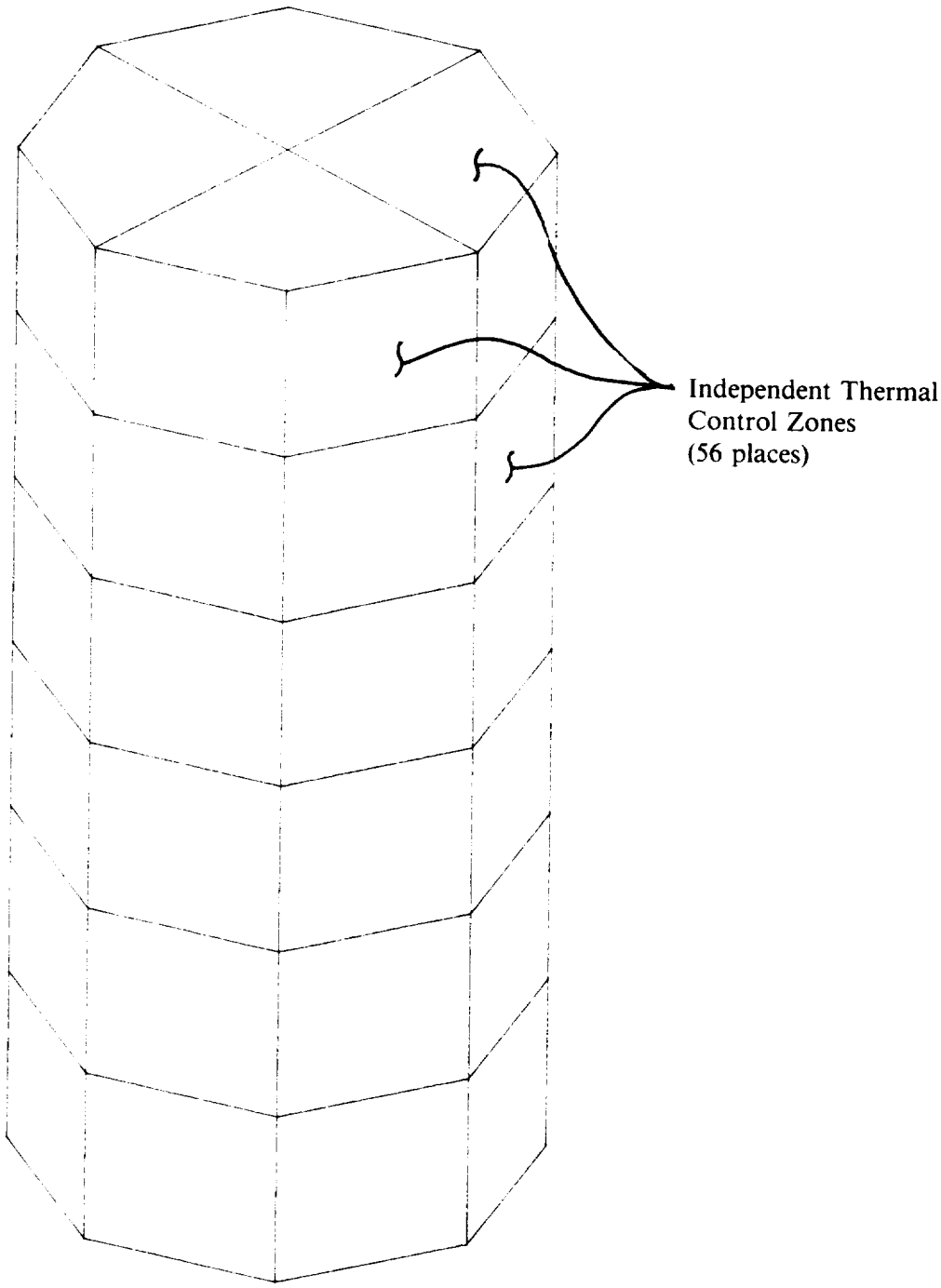

Figure 1 - Thermal Environment Simulator Configuration

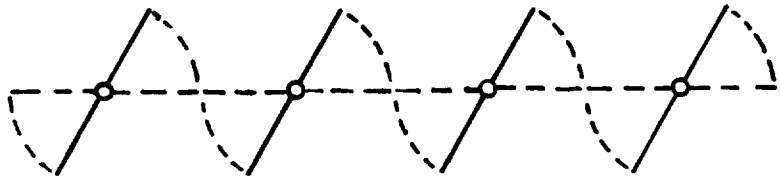

Figure 2a - Asymmetrically Rotating Louvers

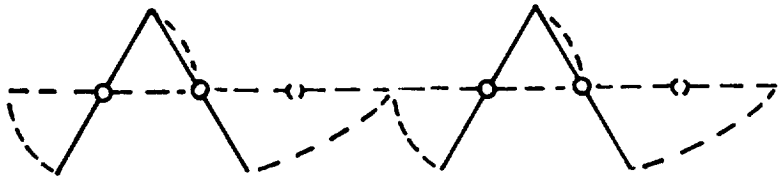

Figure 2b - Bifold Louvers

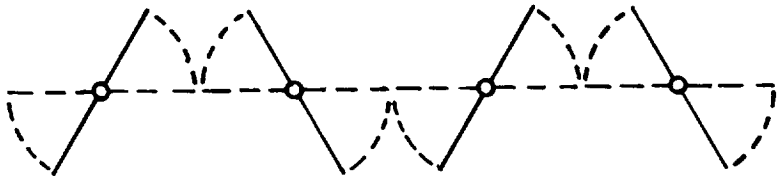

Figure 2c - Symmetrically Rotating Louvers

INNOVATIVE METHOD FOR THE THERMAL CYCLING OF LARGE SPACECRAFT SYSTEMS

Carlos H. Steimer, Section Head
Avery D. Hale, Section Head

TRW Space & Technology Group

ABSTRACT

TRW has implemented the use of low-cost, off-the-shelf, prefabricated enclosures for spacecraft system thermal cycling applications. The enclosures are erected in the satellite integration areas without disturbing the test article, electrical test set, or RF interfaces. They are assembled using metal clad, modular urethane panels. These panels are self-supporting, and are locked and sealed to each other on assembly. Penetrations for interconnecting cables, coaxial and waveguide services; and temperature conditioning inlet and outlet ducts are easily incorporated where required. The subject paper describes the facility and discusses its advantages and intrinsic benefits.

INTRODUCTION

Industry experience, including TRW history, indicated that thermal (temperature) cycling was the most cost effective method of detecting workmanship defects in spacecraft/payload systems. The evolution of MIL-STD 1540 recognized this by specifying extended thermal cycling tests at the system or segment level in addition to those required at the compartment/unit level. Shuttle launched payloads have grown to a size which exceeds TRW's fixed environmental test facility envelopes.

A large, relatively inexpensive, temporary, and reusable thermal cycling facility was thus proposed which could provide several advantages:

- Capability of erecting the facility, as required, in the area where spacecrafts are assembled and tested
- Permanent/dedicated floor area would not be required
- Reduced schedule, costs and risks associated with the transporting, installation, hook-up and checkout of the spacecraft at a remote general purpose environmental test chamber
- Lightweight, reusable, portable, and easily stored
- Could be relatively inexpensive when compared to the cost of a permanent facility

TRW has successfully implemented such facilities. It is believed that the aerospace industry, in general, would benefit from TRW's experience.

BACKGROUND

MIL-STD 1540 has always specified thermal cycling tests at the component/unit level. As the reliability of this type of testing insofar as detecting defects became more evident, revisions of MIL-STD 1540 responded with more stringent thermal cycling requirements. To the areospace industry, by virtue of the quantity of units being produced, these requirements dictated the use of small, economical and reusable chambers. This in itself, provided for the growth of the environmental chamber manufacturer industry that exists today. Many aerospace companies have also built small, temporary chambers in-house, using many different construction methods and materials. If the volume of units is not large, this provides a low-cost alternative to capital acquisition of vendor provided chambers.

Now, with MIL-STD 1540 specifying thermal cycling at the system or segment level, larger chambers are needed. With payload sizes increasing due to the Shuttle, still larger chambers will be needed. Disadvantages associated with such chambers are evident, i.e., large capital cost, requirement for fixed floor space, inflexibility and facility schedule conflicts.

ALTERNATIVE APPROACHES

Could a temporary thermal cycling facility be erected in the satellite integration area without disturbing the test article or test set configuration?

TRW undertook an in-house study to answer this question. The need was present. Already existant were two Shuttle payload contracts that would require a thermal cycling facility exceeding available envelopes. One alternative was to purchase a turn-key permanent facility, designed and built by one of the environmental chamber manufacturers. This alternative, however, did not meet the self-imposed criteria established by the above question. (Not to speak of its associated acquisition cost estimated at approximately $1.2M.) The study objectives were scoped to: first, predict the feasibility, effectiveness and costs of incorporating small enclosure construction methods for a large thermal cycling chamber application; and second, determine the viability of using an inflatable fabric enclosure, similar to mobile shelters or radomes, as a thermal cycling chamber and estimate the associated costs.

For the purposes of the study, the facility requirements were simple:

- Reusable, portable and storable
- Temporary enclosure erected over test article
- Size: 32 feet long x 24 feet wide x 20 feet high
- Conditioning medium: Air or GN_2
- Temperature range: -20°F to +140°F
- Temperature change rate: 2°F/minute (maximum)

The study thoroughly evaluated three (3) selected rigid and reusable small enclosure construction approaches in addition to the inflatable fabric enclosure concept (alternatives). Advantages and disadvantages of each alternative, relative to the requirements specified, were identified. Also determined were the overall coefficient of heat transfer for each of the wall construction methods. This information was used to estimate wall transmission losses in order to size and cost the temperature conditioning equipment required for each of the alternatives.

SELECTED ALTERNATIVE

The results of the study showed that an enclosure utilizing modular, prefabricated, metal clad urethane panels was preferred for a large temporary thermal cycling chamber application. This alternative not only best fulfilled the identified requirements, but also provided the most attractive cost of approximately $100K, since the panels were available off-the-shelf from a walk-in cooler and refrigerated building manufacturer. Recurring costs per test for total chamber assembly/disassembly were estimated at $12K. Overall coefficient of heat transfer was .03 BTU/Hr-Ft^2-ΔT°F (interior at -20°F, exterior at +70°F). With this enclosure configuration, attainable temperature range was -50°F to +150°F. Other benefits associated with this alternative included:

- Total external assembly and disassembly
- Self-supporting panels
- Locking mechanism integral to panel assembly
- Enclosure can readily be made smaller or larger (with purchase of additional panels)
- Panel construction
  - 100% foamed in-place rigid urethane
  - 97% homogeneous
  - Choice of exterior metal skins (aluminum or stainless steel)

The study also recommended the use of GN_2 as the conditioning medium as opposed to dehumidified air. The use of the latter was a "soft requirement" in order to allow for access to the chamber for troubleshooting purposes during test. The costs of a mechanical refrigeration and filtering system, in conjunction with "ante-room" construction costs were sufficiently prohibitive when compared to recirculating LN_2/GN_2 heat exchanger systems.

Several programmatic concerns surfaced after the study was completed. To best resolve these concerns, a proto-type facility utilizing the suggested enclosure method was built. If the concerns were resolved and the facility operation verified, it would be used for an in-house project already in its integration and test phase.

FACILITY DESCRIPTION

The thermal test enclosure used during the verification tests is a free-standing 13½' x 19½' x 12' room shown in the diagram of Figure 1 and Figure 2. All panels have a stucco embossed aluminum exterior finish, a 20 gauge polished stainless steel interior finish, with four (4) inches of polyurethane foam between the metal sheets. Cam locking devices are integral to each of the panels and in this case, are operated from the interior of the enclosure. Hole covers for the cam locking penetrations are provided by the manufacturer. As shown in Figure 3, the floor panels of the chamber are covered with 3/8" aluminum diamond thread plate for load distribution purposes. The enclosure is equipped with over and under pressure relief ports which are sized to relieve at 0.75 inches of water pressure. Two personnel access doors are included, which can be opened from either the inside or outside, and contain heated viewing windows. Pressure relief port and door edges are equipped with thermostatically controlled heaters to maintain them at 70°F when the chamber is cycled to cold temperatures.

The GN_2 distribution and recovery is through 8 inch diameter x 10 feet long, vertical (acid etched aluminum) ducts, which are located at diagonal corners within the enclosure. Ducts are equipped with 1 inch x 8 inch vertical slots, at 90° angles, which create turbulence and prevent laminar flow between the discharge and return ducts. Ducts are shown in Figure 3.

A 0.5 micron high flow filter is situated between the TCU and the chamber discharge duct. A 1500 CFM LN_2/GN_2 temperature controller with 12 KW heaters supply the conditioned recirculated GN_2.

Pressure and dew point instrumentation are attached to sample station penetrations, which are permanently installed ¼ inch stainless steel tubes.

Waveguide and semi-rigid coaxial test cable penetrations can be permanently installed feedthroughs as shown in Figures 1 and 4. Removable test cabling access can also be incorporated by installing ports similar to the type utilized for inlet and outlet distribution ducts. In this case, ports are sealed after cabling is installed.

PROGRAMMATIC CONCERNS AND RESOLUTIONS

SAFETY

Concern: Large quantities of GN_2 will be used around untrained personnel. How will personnel be protected while working in the general area?

The areas adjacent to the chamber are safeguarded by O_2 monitors. The monitors have both a visual and audible alarm. The internal alarm's audio tone and visual light were considered inadequate. The alarm circuit was modified to drive an external portable alarm system with a more intense audible tone and a larger visual light.

The O_2 monitors are installed in place at the time of chamber assembly. Placement is governed by procedure and verified by Quality Assurance.

Concern: How will personnel be protected against accidental entry into an inadequately ventilated chamber?

A double "lock bar" system is installed. Installation and removal is by mutual approval of chamber operations and the hardware test conductors. Nitrogen is not transported to the integration area until the lock bar is in place and locked. After transport of nitrogen to the integration area, no one is allowed into the chamber until the chamber is certified safe.

Safe certification entails isolation of the chamber's nitrogen transport lines. Chamber operations and hardware test conductors authorize unlocking the lock bar. After lock bar removal, an O_2 monitor is placed adjacent to the door. All personnel except chamber operators are evacuated from the area around the chamber. The door is opened and the interior of the chamber is purged with air for a minimum of 30 minutes or until the indicated O_2 content is $>19.5\%$. Entry is not permitted until the interior of the chamber is probed for O_2 adequacy. During the probing operation, personnel wearing rebreathing equipment, are standing by. Probing activity is governed by procedure with Quality Assurance surveillance.

Concern: During assembly of the chamber, what safeguards will be used to protect the test (flight) hardware?

The panel manufacturer was contacted to instruct personnel on the proper method of handling the panels. The manufacturer made recommendations for panel storage, protection of sealing surfaces and for installation of lifting devices.

A procedure was developed to safely assemble the chamber around the test hardware. Its most significant features are in the use of personnel. During the crane lifting operation, a minimum of two persons handle each panel. Present are a crane operator, an operations director, a Quality Assurance person and a buffer. The buffer's only job is to place himself between any vertical panel being installed and the test hardware. If at any time hardware is jeopardized, the buffer moves the panel in a direction

away from the test hardware. The top of the chamber is assembled starting at one end of the erected walls. One top end panel is located and then locked in place. Each succeeding panel is transported over the in-place roof panel(s). This method is designed to minimize the activity above the test hardware. All activities are governed by procedure with Quality Assurance surveillance.

CLEANLINESS DURING CHAMBER OPERATION

Concern: Will operation of the chamber contribute to-, stay at the same level-, or reduce particulate contamination?

The facility was assembled with the chamber, temperature conditioning equipment, filter, ducting and instrumentation. Interior surfaces of the chamber were cleaned by conventional methods to remove particulate contamination. A particulate count was obtained and the chamber TCU system activated. After the first 24 hour period, the particulate count had dropped by approximately 15%. After 72 hours, by approximately 25%. The chamber was operated for four (4) more days and the particulate count continued to decrease.

TEMPERATURE UNIFORMITY

Concern: What level of temperature uniformity can be expected in this type of facility?

A temperature uniformity test was conducted. With a 2.5 KW live load, the chamber was cycled to both high and low temperature extremes and allowed to stabilize. Temperature data obtained showed that the worst-case distribution was within 6°F.

DRYNESS - PRECIPITATION - CONDENSATION

Concern: What are the risks of precipitation on the hardware or the interior of semi-sealed boxes (units)?

To preclude moisture condensation on exposed surfaces, procedural constraints would be implemented during the test conduct. All test hardware and chamber temperatures would be maintained a minimum of 10°F warmer than the measured chamber GN_2 dew point temperature throughout all phases of the test.

Previous tests at TRW on simulated units (boxes) inside of a temperature enclosure have shown that they will aspirate as the enclosure temperature is cycled between a high and low temperature. Also the units will assimilate the surrounding environment after controlled cycling to a lower temperature on each successive cycle. As back-up for previous information, witness units were installed during the verification test and the first two hardware tests. The witness units verified the earlier tests and their use has now been discontinued.

Concern: What precautions are to be taken if a TCU (temperature conditioning unit) fails when the test hardware temperature is lower than the integration area's local dew point?

A catastrophic failure recovery plan was proposed and then a test was conducted to verify the viability of the plan. Major points of the plan were:

- LN_2 systems transfer pump which supplies the GN_2 generator is connected to an automatic emergency power generator. This insures an adequate supply of LN_2 to convert to GN_2 at all times.
- Chamber operational procedures require a minimum of 15 CFM positive pressure purge of GN_2 at all times during a test. This purge would initiate recovery, if a facility power or TCU failure would occur.

For the test, a simulated mass was installed in the chamber to represent the test article. The temperature of the mass model was reduced to 20°F below the flight hardware cold acceptance temperature and the TCU was disabled. A 15 CFM atmospheric, ambient temperature, positive pressure, GN_2 purge was initiated. Temperature data for the mass model (passive), and chamber interior was obtained and recorded as was the chamber environment GN_2 dew point temperature. At all times the chamber dew point remained well below the afore mentioned 10°F constraint, between dew point and hardware temperature.

TCU RELIABILITY

Concern: How reliable is the TCU operation over a sustained period of time?

TRW has designed, built, modified, maintained and operated the type of TCU utilized for approximately 20 years. The longest continuous operation was documented at 1,000 hours (a forty day test without a shut-down).

Other precautionary measures utilized are: knowledgeable inspections of the TCU to pinpoint any necessary mechanical adjustment or parts replacement; pretest operational checkouts to minimize the risk of failure or to identify any potentially hidden problems; and a periodic bearing lubrication program, during a prolonged test, to minimize bearing failure.

PANEL SEAL DETERIORATION OR DAMAGE

Concern: What are the risks of seal deterioration or damage during assembly, disassembly or storage?

The panel manufacturer was consulted and recommendations were implemented. Careful handling of the panels (no dragging, no scuffing, no setting tongues on hard surfaces) during assembly and disassembly will assure repeatable seals. Storing the panels width-wise on the groove side of the panel will protect the exposed tongue edges and insure that the

panels will resist warpage. When the floor is left in place, a positive protective device is installed over the groove seat to protect the floor sealing surfaces. Recommendations given appeared to be common sense, but like the man said, "Education is acquired, but common sense is a God given gift". Therefore, handling and storage operations are governed by procedure. If a seal is damaged, it can be repaired either by the manufacturer or the user.

ADVANTAGES/BENEFITS

With the implementation of these types of facilities, several advantages and benefits were realized and should be identified. They result from the inherent ability to erect the thermal cycling enclosure in the satellite integration area with the test article in place. They are broadly divided into technical and programmatic.

TECHNICAL

After the test article is assembled, checkout at ambient temperature completed and functional baseline data obtained, the thermal cycling test can be initiated immediately. These is no need to break interconnects to the test sets and reconfigure/reverify at the facility. Data at temperature is directly correlatable to ambient baselines and the risks involved with the reconfiguration are eliminated.

PROGRAMMATIC

There are always risks involved in transporting the test article and test sets to and from the facility. These are well in hand by the procedures utilized and safety controls exercised. If the moves are not necessary, however, the risks are eliminated.

The project is allowed to dictate its own schedule. Conflicts with other projects at a general purpose facility are eliminated.

In-line project schedule time is saved by avoiding the move to the facility from the integration area and eliminating the need for reconfiguration and reverification. This can result in up to a two week schedule savings.

CONCLUSIONS

An innovative method for the thermal cycling of large spacecraft systems has been described. Programmatic concerns associated with this method were addressed and successfully resolved during the implementation phase. The advantages and benefits associated with the method were recognized immediately by the various project offices. Currently, four (4) such facilities are in operation at TRW, with near term plans for two (2) more. It is believed that the industry will also be receptive to such thermal cycling facilities that do not require large capital acquisition costs.

YES, YOU CAN bring your facility to the test article.

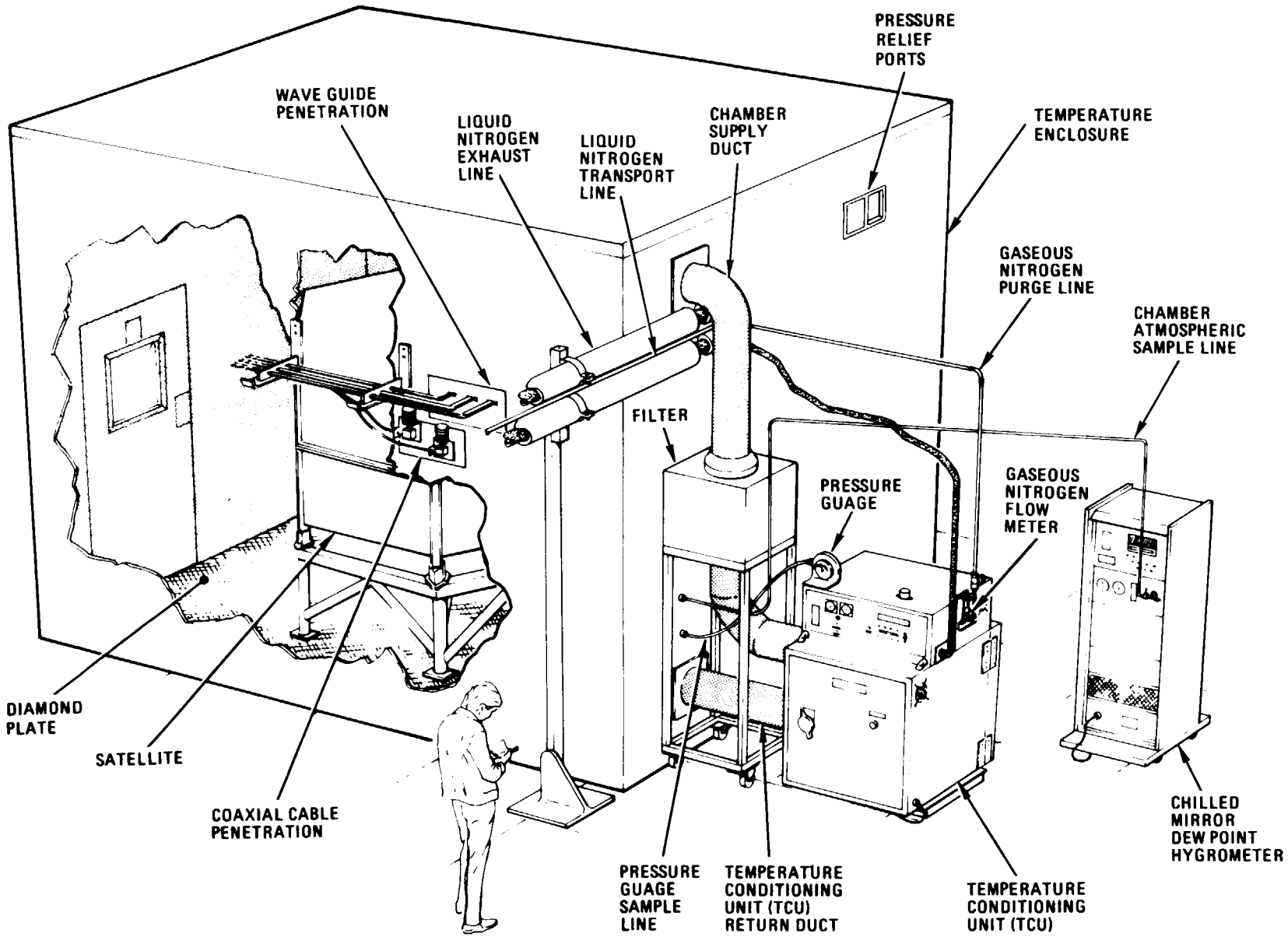

Figure 1 - Large Temporary Thermal Cycling Facility

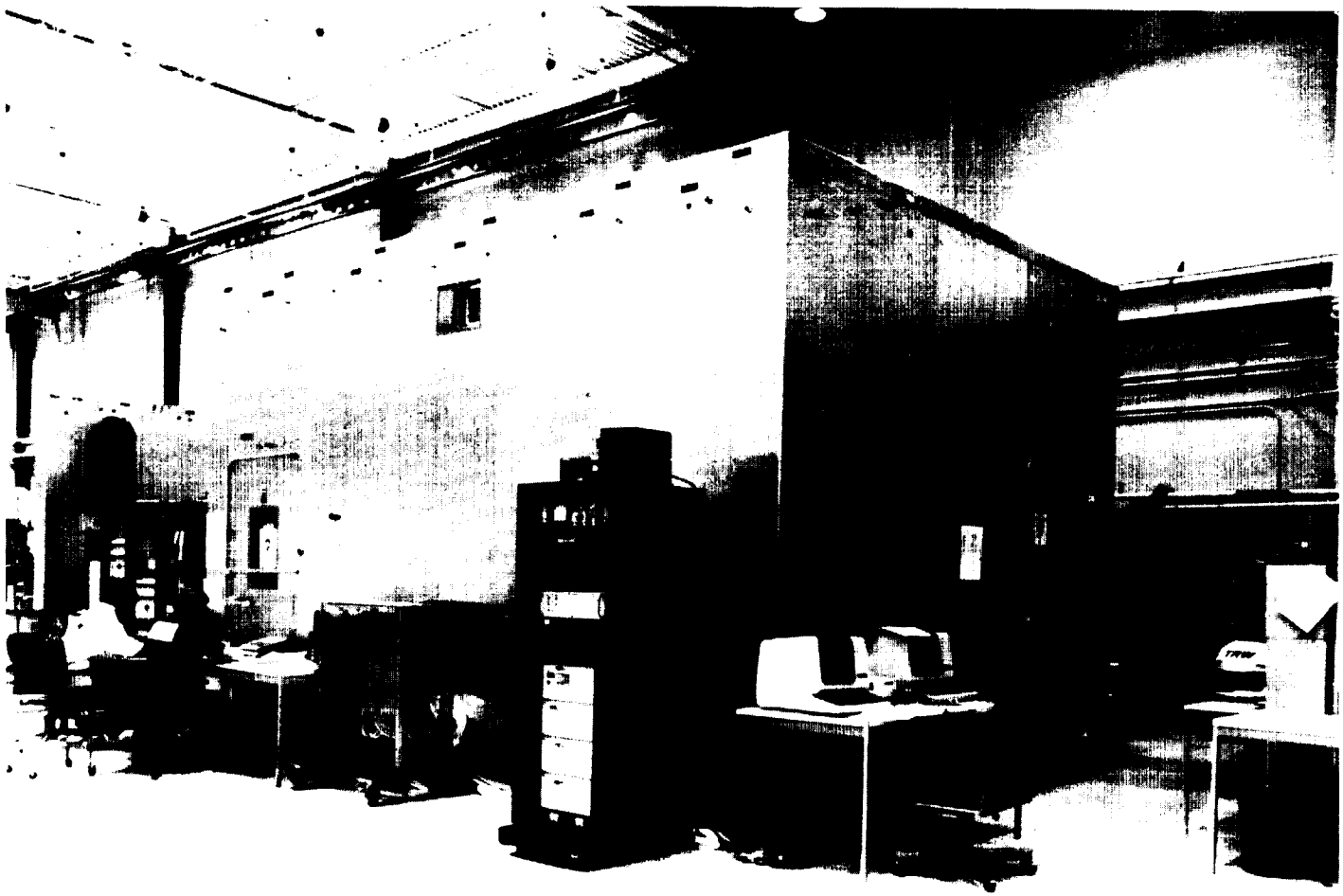

Figure 2 - Operational Large Temporary Thermal Cycling Facility

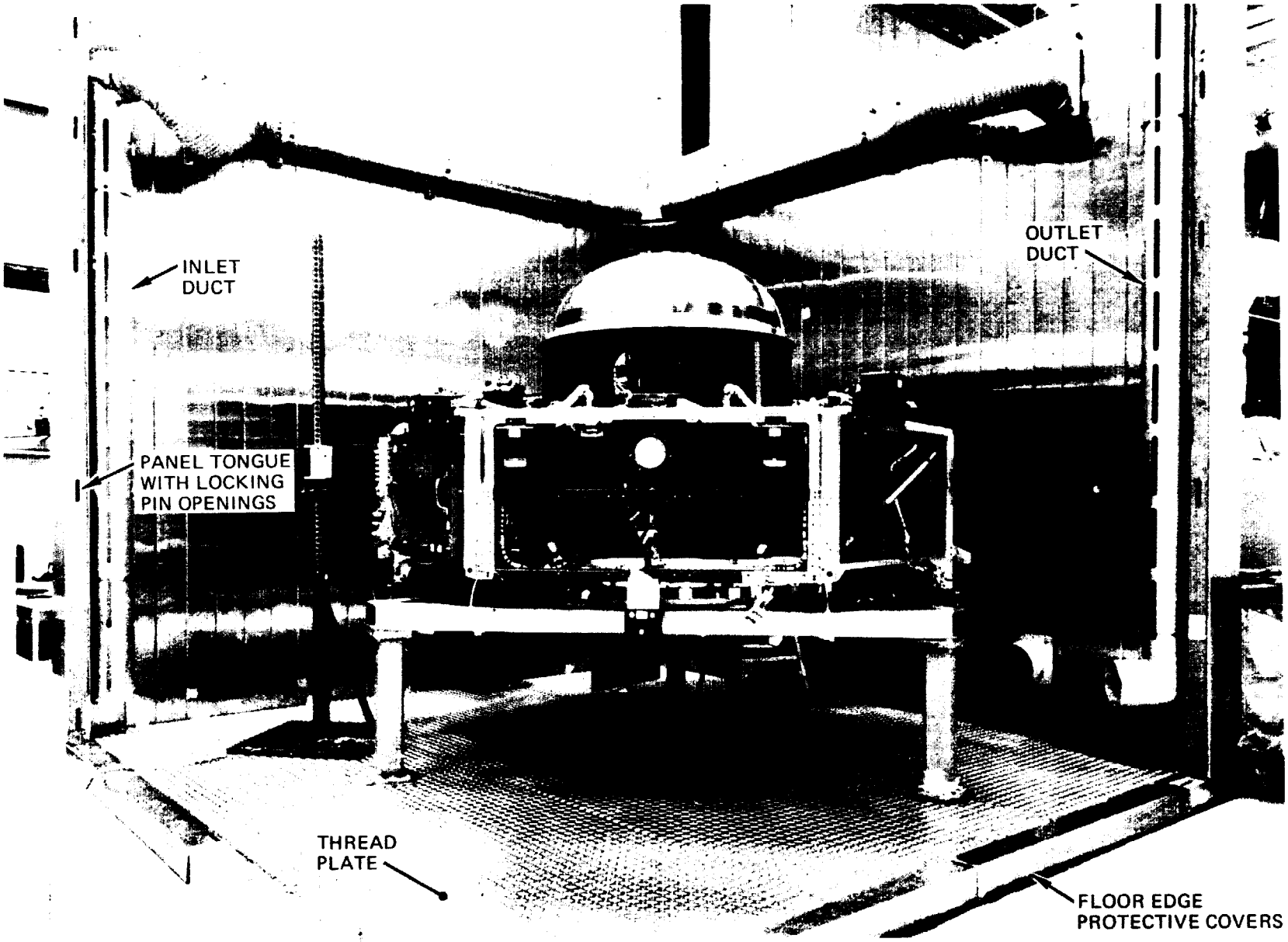

Figure 3 - GN_2 Distribution/Recovery System

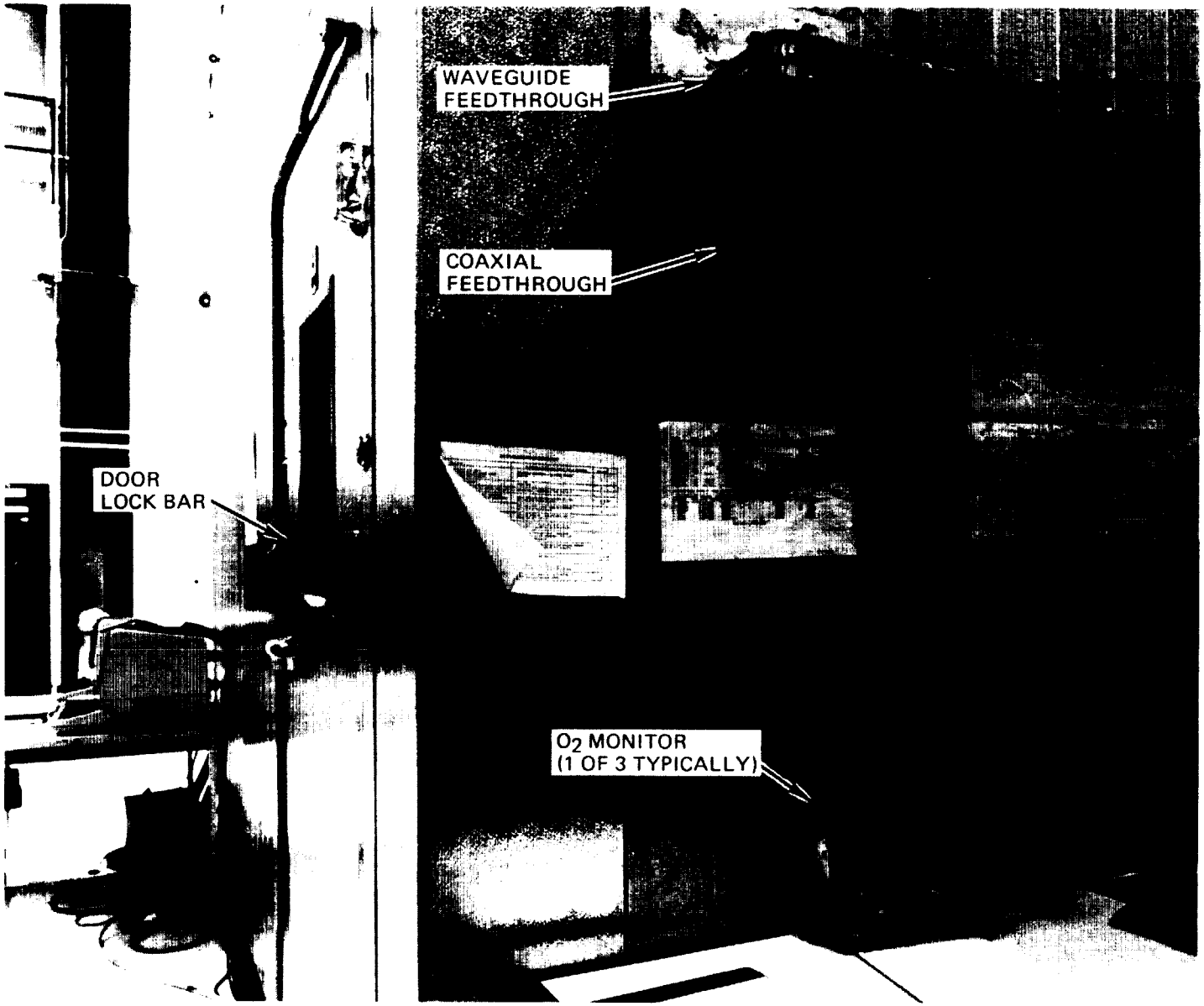

Figure 4 - Waveguide and Coaxial Cable Feedthroughs

SPACE SIMULATION TESTING

OF THE

EARTH RADIATION BUDGET SATELLITE

Edward Magette and Derrin Smith
Ball Aerospace Systems Division

ABSTRACT

The Earth Radiation Budget Satellite (ERBS) is a low-inclination, orbiting satellite that is a part of the NASA Earth Radiation Budget Experiment Research Program. The purpose of this research program is to increase our knowledge of the earth radiation budget components and dynamics. This derived data will be a key to understanding the interactions of this energy cycle, which influences our climate. The ERBS will be launched via the Space Shuttle in October 1984.

The satellite package was subjected to space simulation testing at Ball Aerospace Systems Division in March/April 1984. The size of the spacecraft dictated that the testing be conducted in the new BRUTUS Thermal Vacuum Facility. BRUTUS is approximately 20 ft by 20 ft cylindrical and is cryogenically evacuated. Capable of hard vacuum to 10E-08 torr and thermal extremes from -200 degrees Celsius to +150 degrees Celsius, the BRUTUS chamber can be programmed to provide a variety of environmental conditions. Computer aided control (CAC), quartz crystal microbalance (QCM), and residual gas analysis (RGA) monitoring were combined with rigid contamination control procedures to protect the flight hardware from anomalous and potentially destructive out-of-scope test environments.

INTRODUCTION

Ball Aerospace Systems Division in Boulder, Colorado was the prime contractor on the Earth Radiation Budget Satellite (Figure 1). All of the facilities required for design, production, integration and test are located at the Colorado industrial site. Of particular interest is the Space Simulation Laboratory, which provided environmental test support for a variety of project operations. A synopsis of the spacecraft mission, and details of several aspects of the ERBS test program, will be presented herein.

The Space Simulation Laboratory was called upon to provide test services at three distinct levels of project production and integration. During the early production phase of the program, minor components and sub-assemblies were vacuum processed at high temperature to cure potting epoxies, outgas non-volatile residues and generally clean the hardware prior to the next level of assembly.

Thermal vacuum environments were provided for the qualification and

acceptance testing of sub-system components, such as antenna assemblies and electronics boxes. The Stratospheric Aerosol and Gas Experiment II (SAGE II), one of three scientific instruments that were integrated onto the spacecraft bus, also received a full complement of these types of tests.

At the end of the assembly phase of the ERBS program, which included integration of the Earth Radiation Budget Experiment (ERBE) dual-instrument package and the SAGE II, thermal balance and thermal vacuum spacecraft testing was conducted in the Space Simulation Laboratory. These tests included simulation of deployment and initialization, as well as complete functional testing of the satellite payload.

ERBS TEST CONFIGURATION AND MISSION

The Earth Radiation Budget Satellite, with its three-instrument payload, is one of a series of satellites and instruments that will be gathering data on the earth radiation budget. The scientific observations are expected to enhance our knowledge of the thermal equilibrium that exists between the Earth, the Sun, and space. It is a widely accepted hypothesis that one key to constructing valid climatological models is to first obtain a blue-print of the earth radiation budget.

The Stratospheric Aerosol and Gas Experiment II (SAGE II) is the heaviest of the instruments at 33.6 kg (74.1 lbs). It is a sun-scanning radiometer with seven channels of silicon photo-diode detectors. Aerosol concentrations, known to scatter and reflect solar radiation, will be measured in the atmosphere from 10 km to 150 km altitude. Concentrations of nitrogen dioxide and other trace gas constituents will also be mapped in this atmospheric region. Spectral measurements will be in the range of 0.385 um to 1.020 um. Peak power consumption of the SAGE II instrument is 45 W, with an orbital average consumption of only 14 W.

The Earth Radiation Budget Experiment (ERBE) payload consists of a non-scanner (ERBE-NS) and a scanner (ERBE-S). These actinometers will measure radiant activity in the range of 0.20 to 50 um. ERBE-NS has four cavity radiometer detectors for Earth viewing which are mounted on an elevation gimbal. The fifth cavity radiometer detector is fixed in elevation, but may be rotated in azimuth. This fifth detector is for solar viewing and measurement of the solar constant. Power consumption of the ERBE-NS is rated at an orbital average of 22 W.

The ERBE-S will use three radiometric thermistor bolometers to provide three channel measurement capability in the 0.20 um to 50 um range. The instrument weighs 29 kg (63.9 lbs) with an orbital average power consumption of 28 W. In order to provide continuous cross-track scanning, the detectors are mounted on a scanhead assembly. A total of eight detection channels are provided by ERBE-NS and ERBE-S.

With a minimum proposed mission life of one year, the spacecraft bus must

survive the orbital environment while providing continuous operational support to the three on-board instruments. Thermal protection, power requirements, orbital guidance, and other functions must be accomplished. Thermal balance testing in the large BRUTUS facility (Figure 2) confirmed the validity of the ERBS spacecraft thermal model. Additional space simulation testing was necessary to verify system integrity in the extreme thermal vacuum environment of the 610 km orbit. This altitude was necessarily attained in predetermined stages.

The Space Shuttle Orbiter will be launched into a 350 km circular orbit, and at T + 8.5 hours the remote manipulator system (RMS) will release the ERBS. At approximately T + 20 hours a mono-propellant hydrazine motor will be activated. The programmed firing sequence will raise the 2,250 kg (4,960 lbs) satellite to the prescribed orbital altitude.

TEST CONTAMINATION REQUIREMENTS

Thermal protection for the instruments is provided by a combination of passive and active heaters, louvers, surface finishes, and multilayer insulation (MLI). Protection against contaminant degradation of the detectors was an elusive problem, particularly due to the large MLI surface areas as a source of non-volatile residues (NVR). Cleanliness could only be ensured by implementing thorough materials and handling procedures early in the program. This provided the impetus for a rigorous vacuum baking process commencing early in the production stages.

CHAMBER BACKGROUND

The small vacuum facilities were used for production support. A solution of 50/50 iso-alcohol and 1,1,1 trichloroethane was used to solvent scrub the chambers, followed by a non-abrasive solvent rinse. Contamination plates with dimensions of one-square-foot were carefully cleaned by the BASD Materials and Processes Laboratory and installed in each vacuum chamber. A high-temperature vacuum bake-out, typically at +125 degrees Celsius and less than 10E-06 torr pressure, would then be conducted for twenty-four hours. At the conclusion of the bake-out, a solvent rinse-test would be performed on the contamination sample plate. Residues could then be weighed and spectroscopically analyzed to determine the background contamination of each vacuum chamber.

PRODUCTION COMPONENTS CONTAMINATION MEASUREMENTS

As components for the SAGE-II instrument or the ERBS spacecraft were manufactured, they would be solvent cleaned and processed in a vacuum chamber with a known cleanliness level. Comparison of contamination data before and after each production bake-out verified the cleanliness of the component prior to integration into the next level assembly. Although the specification would allow up to .5 milligram of non-volatile residues (NVR) per square foot, this

procedure provided rinse results consistently at or below .15 milligram per square foot.

SUBASSEMBLIES CONTAMINATION MEASUREMENTS

When larger subassemblies arrived for qualification and acceptance testing in thermal vacuum, this same contamination control procedure was continued. Residual gas analysis (RGA) with a mass spectrometer was added to provide detailed information on outgassing trace constituents. Mylar and kapton materials, to be used for constructing the multilayer insulation (MLI) and spacecraft covers, were similarly processed either before or after pattern cutting.

CHAMBER EVACUATION AND SPACECRAFT CONTAMINATION MEASUREMENTS

All of this attention to cleanliness contributed to the success of the final spacecraft thermal vacuum testing. In the absence of a volume of outgassing contaminants, the specified vacuum level was quickly attained in the cryogenically evacuated chamber. The longest stage of the chamber pump-down was the mechanical "roughing" process. Chamber pressure was reduced from 650 torr (altitude atmosphere) to 26 microns in 3.5 hours. Vacuum improved from 26 microns to 7.5 X 10E-05 torr within five minutes of high-vacuum valve actuation. Less than six hours after initiation of the pumping sequence, a vacuum of 10E-06 torr had been achieved.

Cleanliness levels were continuously sampled by a RGA unit and a quartz crystal microbalance (QCM). The most substantial outgassing species recorded were water, hydrocarbons, carbon dioxide, air, argon, and silicones. Potential contaminants of concern were: aliphatic and aromatic hydrocarbons, silicones, and phthalate esters (recorded separately from hydrocarbons). The partial pressures of these potential contaminants were low enough to be considered not hazardous to the spacecraft or instrument detectors. The final ambient temperature RGA scan recorded partial pressures as follows:

Hydrocarbon	1.4 X 10E-08 torr (expressed in Nitrogen equivalents)
Silicones	3.1 X 10E-09 torr
Phthalates	1.1 X 10E-09 torr

Of the four NVR contamination plates in the facility during thermal vacuum and thermal balance testing, the highest measured level was less than 35% of the specified contamination tolerance. Apparently the contamination control procedures, implemented at all levels of hardware assembly and integration, were successful.

SPECIAL TEST REQUIREMENTS

Functional tests on the ERBS Observatory during thermal vacuum and thermal

balance testing included checkout of the Orbit Adjust Propulsion System (OAPS). The simulated OAPS firing would release quantities of gas into the chamber, and this prospect generated some concerns.

The BRUTUS Chamber thermal shrouds would be in a liquid nitrogen flooded configuration. A loss of chamber vacuum to the 10E-03 or 10E-04 torr range could cause the multilayer insulation (MLI) to lose its effectiveness and possibly cool the spacecraft to below allowable limits. Another possibility included degradation of the cryopumps to a degree that high vacuum operation could not be maintained or expediently recovered.

Prior to conducting an experimental OAPS simulation, with the chamber in a clean, dry and empty configuration, thruster gas flow rates and chamber pumping speeds were calculated. The OAPS parameters were as follows:

Two spherical, 30 inch diameter tanks (on-board gas source)

Load Pressure of 30 psig

Flow rate of 15 scc per second per valve

Maximum of six valves (thrusters) flowing gas at one time

Test Gas composed of 90% Nitrogen and 10% Argon

Based upon the chamber volume and cryopump pumping speeds, with six thrusters flowing gas for an extended period the chamber pressure would rise to about 8 X 10E-04 torr. The chamber pressure would recover rapidly at the termination of the gas flow. This determination was made using pumping speeds applying in a chamber pressure of 10E-05 torr and below.

The trial run was conducted with a gas flow into the chamber equal to the maximum flow anticipated during OAPS simulation with the ERBS Observatory. A calibrated leak was installed in a feedthru port with a variable leak adjustment. The test gas was 90/10 Nitrogen/Argon, as it would be with the obervatory in the chamber. Duration of leak exposure would be limited to ten seconds at first until several samples had been made. Finally, the leak would be left open for an extended period to verify that chamber pumping speeds were adequate to handle the additional gas load.

Although chamber pressures did briefly exceed the 10E-05 range, the pumps proved to be capable of sustaining high vacuum operations. The cryopumps are able to adsorb thousands of standard liters before requiring regeneration, so total OAPS tank volume could be accommodated. This volume was estimated to be about 1,500 standard liters, and would not increase the pump temperatures enough to cause them to cease pumping effectively.

Residual gas analysis could not accurately measure the argon leak rate of the OAPS. During the actual spacecraft testing the thermal shrouds were in a liquid nitrogen flooded configuration. This cryopumping action of the shrouds, combined with the continuous pump operation, prevented significant

RGA data. The chamber vacuum was recorded at 4.5 X 10E-05 torr within two seconds of the OAPS activation, having increased from a level of 5.0 X 10E-07 torr.

THERMAL CYCLING REQUIREMENTS

In many respects, this was the simplest aspect of the thermal balance and thermal vacuum testing. The BRUTUS thermal shroud was flooded with liquid nitrogen, and maintained at approximately -200 degrees Celsius or maximum cold. All other temperature adjustment was accomplished by the ERBS on-board thermal control sub-system.

Active heaters enabled the test support crew to simulate the "Hot Case" or the maximum predicted in-flight external absorbed energy fluxes. The maximum level of internal power dissipation was thus established. Similarly, the "Cold Case" provided the minimum predicted in-flight external absorbed energy fluxes, and the minimum internal power dissipation was determined.

The spacecraft was allowed to soak for a minimum of forty hours at each of these thermal extremes, or at least until thermal equilibrium was established. Three transitions from the cold extreme to the hot extreme, and three such transitions from hot to cold were conducted. As a rule, the instrument hot temperatures did not exceed +45 degrees Celsius, and the cold temperatures did not exceed -35 degrees Celsius. A typical thermal cycle is shown in Figure 3. In the case of more exposed components, such as ESSA Antenna, temperatures could range from +60 degrees Celsius (Hot) to -40 degrees Celsius (Cold).

On-board thermistors provided temperature data to a hard copy recorder. Type T copper-constantan thermocouples provided additional thermal information to assist in chamber operation and to map the thermal vacuum support fixture. Sensors were mounted either with a cured epoxy stake or with vacuum compatible tape, depending upon the application of the temperature sensor (permanent or test-only).

CONCLUDING REMARKS

The unique challenges of space simulation testing in support of a large spacecraft program are easily managed, provided that input from the laboratory personnel begins early in the program. Contamination and handling procedures, if established at the component production stages, will significantly enhance the final space simulation test effort. Test programs are a multidisciplinary effort, and must be approached accordingly.

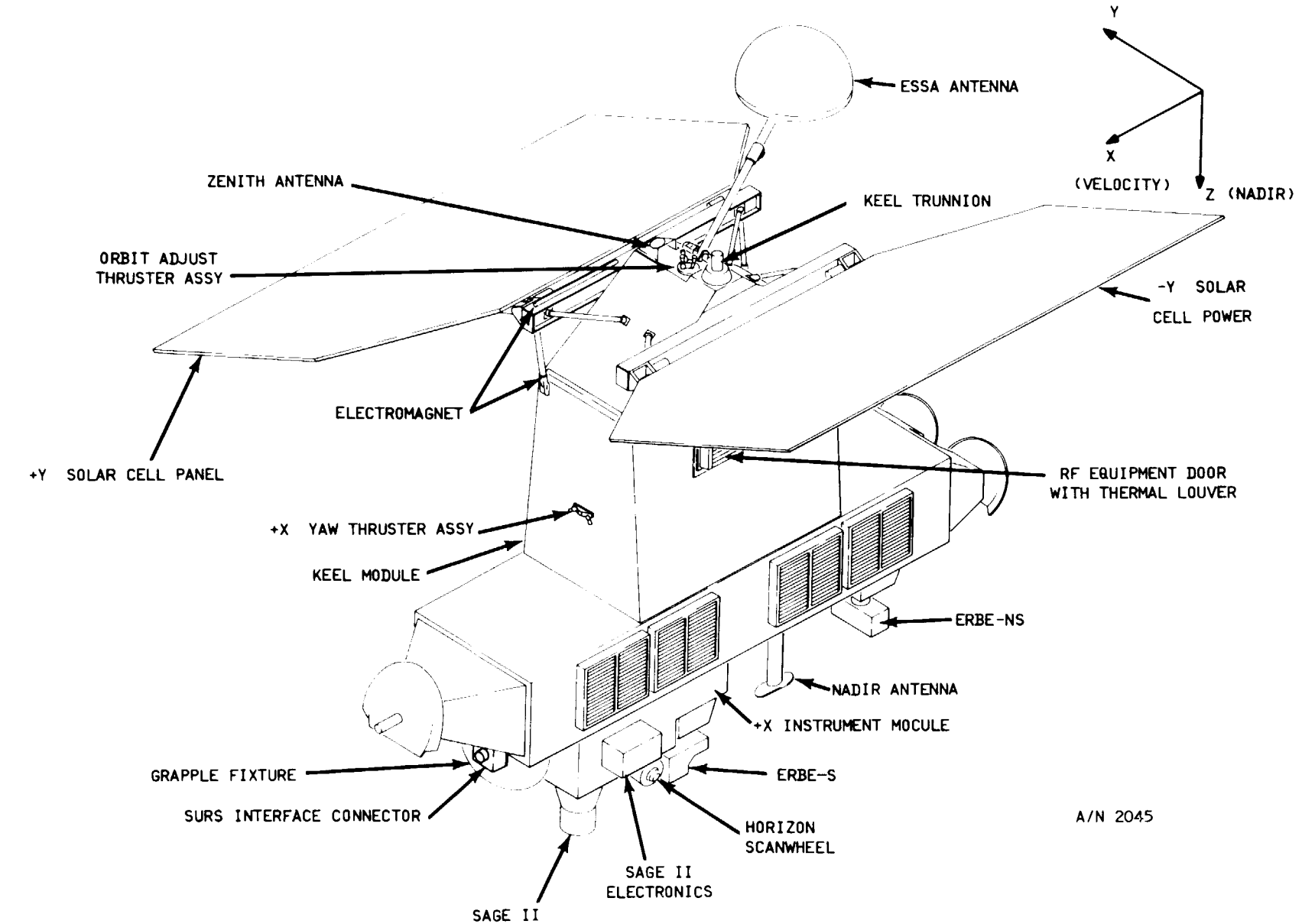

Figure 1 - ERBS Configuration, On-Orbit

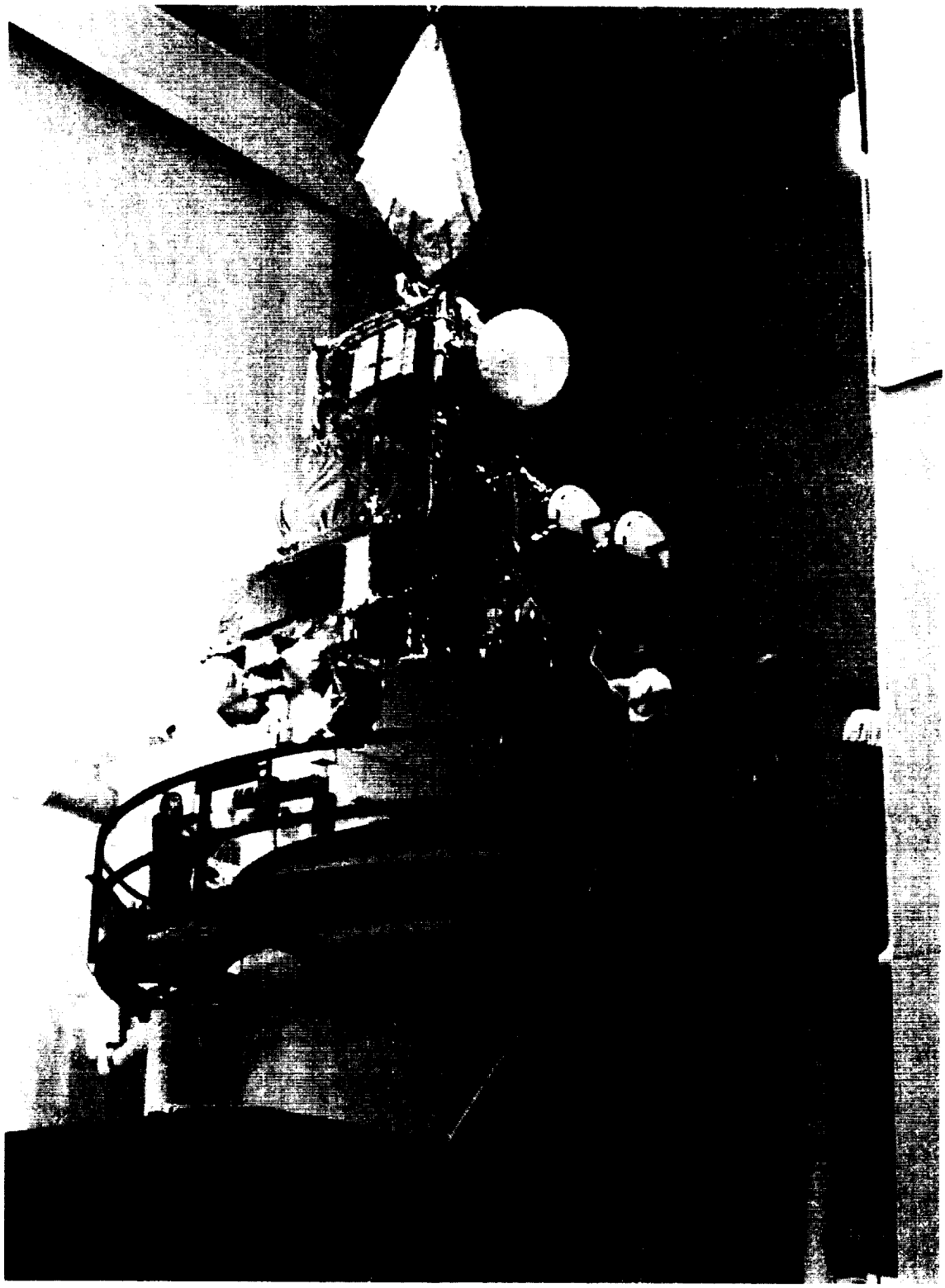

Figure 2 - Loading ERBS Into Brutus

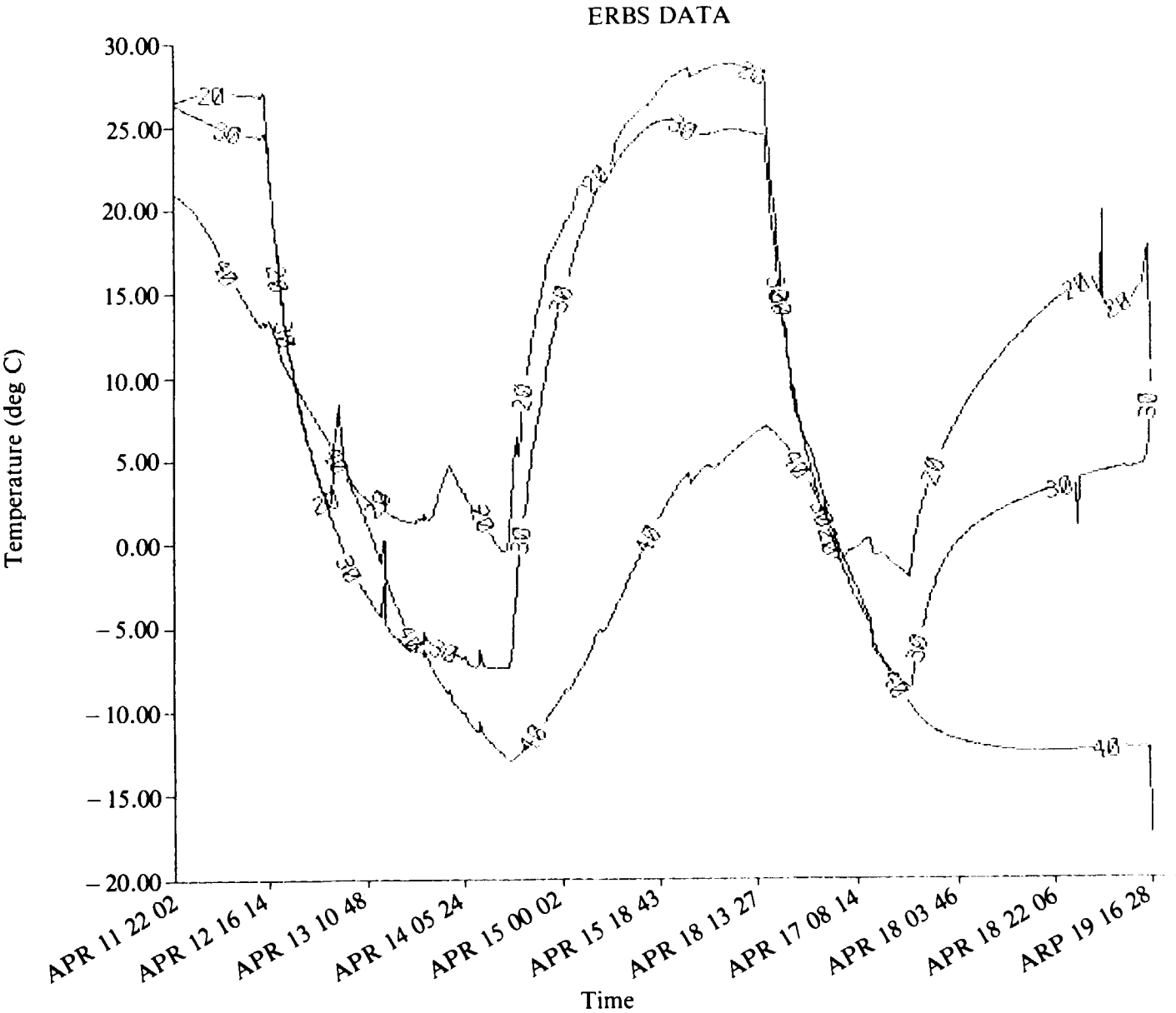

Figure 3 - Typical Thermal Cycle

MAIN CHARACTERISTICS OF THE LARGE SPACE SIMULATOR (LSS) AT ESA/ESTEC

Peter W. Brinkmann
European Space Research and Technology Centre ESA/ESTEC
Noordwijk, The Netherlands

ABSTRACT

The European Space Agency (ESA) has started the implementation of a Large Space Simulator at its European Space Research and Technology Centre (ESTEC) located at Noordwijk, The Netherlands. After its completion in early 1986 this facility will enable mechanical and thermal tests on large satellites. The chamber will be equipped with a collimated solar beam of 6 Meter diameter. In addition Infrared equipment is available as alternative or complementary source of thermal radiation. Also controlled variation of shroud temperatures can be utilised for thermal testing or temperature cycling of hardware. The "Design and Definition Phase" of the project has been successfully completed by the end of 1983. The paper presents the basic concept and major design aspects of this facility. At the time of the conference, the large chamber is already under construction on site.

INTRODUCTION

The existing European Space Simulation facilities are no longer compatible with the test requirements on future ARIANE or Shuttle payloads, due to limitation in size and due to restrictions in the associated infrastructure. ESA has therefore decided to modify its 10 meter Dynamic Test Chamber (DTC) at ESTEC and to convert it into a Solar Simulation Facility with a beam diameter of 6 meters. This modification is under way and the test chamber will become operational in 1986. This facility is the first large solar simulation facility, to have been built for about 15 years. Hence concept and specifications contain new elements reflecting the experience gained in the meantime and the new requirements of space projects. Furthermore, it is obvious that up-to-date control and data-handling equipment will be implemented.

The configuration of the Large Space Simulator (LSS) is illustrated in figure 1. The vertical "Main Chamber" (existing DTC) and the horizontal "Auxiliary Chamber" are interfaced by a nozzle with a diameter of 8 meters. Main chamber and nozzle will be equipped with a shroud lining the

complete chamber surface, while the shroud elements in the Auxiliary Chamber have the form of light baffles.

The Collimation Mirror, consisting of 121 hexagenal segments, is suspended from the rear stiffening ring of the Auxiliary chamber. A spout provides the interface between the vacuum chamber and the lamp-house. The lamp-house contains 19 lamp modules, collection optics and transfer optics and provides a protective environment for all optical elements.

The test articles can be mounted on a vibration-free support platform (if required via a motion simulator) or suspended from support lugs in the upper part of the Main Chamber.

CONSTRAINTS

The implementation of the Large Space Simultor is part of a general extension of the European Test Facilities. Consequently the design of the facility has to take account of existing facilities and infrastructure. Thus the existing 10 meter diameter DTC will become the "Main Chamber" of the new LSS. This will help to keep the overall costs of the project to a minimum.

On the other hand, the re-use of the existing vessel creates conflicts with test plans of various existing Space Programmes, for which the DTC is an indispensable facility. Moreover, the implementation plan of the LSS is constrained by the requirement of future programmes, which need a Large European Solar Simulator as from 1986 at the latest.

It goes without saying that the budget limitations are severe, which is illustrated by the fact that the contingency for the four project phases, "Design and Definition", "Procurement and Manufacturing", "Transport and Installation", and "Acceptance" is only about 3% of the overall value of the LSS procurement contracts.

FACILITY CONCEPT AND PRIMARY DESIGN ASPECTS

The main characteristics of the Large Space Simulator are listed in table 1. In the subsequent context it is not intended to give a detailed description of design and performance of the Large Space Simulator. It is intended that those details will be reported in the future and particularly, when actual performance data become available. The present paper limits itself to the presentation of the basic concept and major design aspects.

THE CONCEPT

Multi-Purpose-Facility

Although the existing 10 meter Dynamic Test Chamber (DTC) will be converted into a solar simulation facility, it is intended to maintain its present special features and capabilities:

- A special structure serves as a platform for test articles isolated from chamber and building motions. The mechanical vibration level is less than 0.005 g. This permits the execution of dynamic tests under vacuum such as deployments, separations, dynamic balancing, spin performance, determination of M.O.I., etc. Machines for physical property measurement in vacuum are available.

- Large infrared test rig and control equipment is available and has already been very successfully used in the DTC primarily for test on large solar arrays (e. . Intelsat V and VI, see ref.: 2).

In addition to solar simulation and mechanical tests, it will be possible to perform Vacuum Temperature Cycling Tests (VTC) by controlling the shroud temperature with a GN_2 circulation system.

The flexibility provided by the new facility, which will serve for a variety of tests and simulations, is reflected in its name: Large Space Simulator (LSS).

Link to other Test Facilities

The Large Space Simulator is part of a series of facilities forming a Test Centre at ESTEC, which makes it possible to perform a full series of environmental tests at the ESTEC site. Integration and test areas are located in one building complex, so specimens can be transferred from one test-location to another with minimum requirements for reconfiguration or packing.

All facilities are "under one roof" and specimens can be transported by overhead cranes. The present configuration is illustrated in Figure 2. It is intended to complement the test centre along the same lines with further facilities such as an acoustic chamber, antenna test facility, etc. Check-out areas, data handling systems, meeting rooms and offices for test crews are located in the same building, and this will help to ensure fast and efficient operations, and facilitate communications.

Horizontal Beam

Vertical beam configurations have been selected in the past for the solar simulation facilities with a collimated solar beam of similar size (e.g. JPL, Martin Marietta, G.E.). The shape of the vacuum vessel for vertical beam facilities can be cylindrical and the light sources can be

operated in a vertical or "close-to-vertical" position. The required building area is relatively small.

In spite of the above indicated advantages a horizontal beam has been specified for the LSS for the following reasons:

- The implementation of heat-pipes has become standard practice primarily for telecommunication satellites on geostationary orbit. These heatpipes provide the required heat transfer from high dissipating units to the radiators mounted on the "North" and "South" panels of the satellite. In a horizontal beam the heat-pipes can usually be operated despite the earth gravity field, because the heat pipe arrangement between North and South walls of the test article can be adjusted to the required horizontal level. This means that satellites can be functionally tested including actual heat-pipe operations.

- The horizontal beam provides a chamber configuration, which supports the possibility for "Top-Loading" of the test facility by means of an X-Y-crane. Hence the loading procedures are simple, complex handling equipment is not required. The loading operations can be performed quickly and safely without special effort.

PRIMARY DESIGN ASPECTS

Stability of solar beam

The stability of the solar radiation in the reference volume is the most essential performance parameter of a solar simulation facility. This includes the reproducibility of the intensity pattern during test as compared with the pattern verified during the previous calibration under ambient conditions. Deficiencies in the local intensity distribution, and mismatches of the spectral distribution are less critical and can be taken into account relatively easily, as long as these effects are known and do not vary with time. The stability requirements for the LSS are therefore rather stringent and enjoy priority over other performance characteristics (see Table 1). The requirements have therefore affected lay-out and design of the LSS, leading to the following solutions:

a) Support of optical elements and test article

The test specimen is fixed to the ground via a special support structure. This structure is isolated from the vacuum chamber by means of specially designed bellows, which prevents the transfer of mechanical loads from the vacuum vessel or the building structure to the test article.

Similarly, the lamp array and transfer optics are fixed to the ground, thus ensuring that test article and radiation source will maintain their relative positions independently of chamber deformations or

vibrations (e.g. during pump-down). The chamber window and collimation mirror are the only optical elements that are supported by the vacuum vessel.

Movements of the window are uncritical from an optical point of view. Nevertheless, the shapes of the spout (Chamber-Window-Interface) and associated stiffeners have been selected in such a way that axial and lateral window displacements during a load cycle (depressurisation / repressurisation) are small, so that the window diameter can be kept to a minimum. Calculations indicate that axial and lateral displacements will be less than 1 mm.

With respect to the collimation mirror, the possibility was considered (as an option) of isolating the mirror support from the auxiliary chamber, if predicted chamber movements should have an unacceptable impact on the stability requirements. In the ase ine n ept, however, the mirror is supported from a special bridge structure between the rear stiffening ring of the "Auxiliary Chamber" and the end-dome. A sliding support eliminates the influence of end-dome deformations.

The displacements of the mirror support point during a pressure cycle are less than 1 mm, which eans that a separate suspension of the mirror is not required. The suspension concept of specimen and optics is illustrated in Figure 3.

b) Temperature control of collimation mirror

On the one hand the stability of the collimated beam requires proper supports of the optical elements, but on the other hand it is also dependent on a stable shape of the mirror surface. The temperatures of both the mirror support structure and the mirror segments themseleves are actively controlled by a GN_2 system. In calibration as well as in solar simulation mode the temperature levels can be maintained at ambient temperature within a tolerance of ± 2 degrees. Deformation of support structure and/or mirror elements are negligible under these conditions.

The mirror can be heated up to 120°C for decontamination purposes. During this operation the temperature differences on the support structure can reach 15 degrees. Even under these extreme circumstances the calculated misalignment of individual mirror segments will be in the order of ½ arc minute, which is well within the overall alignment requirements for the segment mirror. No measurable impact on the distribution pattern is therefore expected in the test volume. Calculated deflections of the mirror under extreme temperature conditions are illustrated in Figure 4.

Intensity distribution

The definition of reference plane and test volume of the LSS are illustrated in Figure 5. The required intensity distribution has been specified more stringently in the front end of the test volume. In this part the uniformity is expected to be better than ± 4%, whereas the allowance for the overall test volume is ± 6%. The distribution is to be determined with a sensor size not larger than 4 cm^2.

This specification is based on the fact that in most test applications the conditions in the front end of the beam are more important than the aft end, which is usually shadowed anyway.

Extensive analysis has been performed on the optical system. This analysis is based on actual design parameters and makes it possible to identify the influences of manufacturing and installation on alignment tolerances. According to these calculations the intensity distribution in the test volume will be within specification. Table 2 shows the list of the software, which has been used so far for the analysis of the optical system.

Spheric transfer optics with circular lens shapes will result in a beam cross section in the reference plane which is elliptical. This effect is dependent on the "entrance angle", i.e. the angle between the axis of the projection optics and the axis of the collimated beam. It becomes larger with increasing entrance angles.

Based on the geometry of the LSS with an entrance angle of 29 degrees, the beam diameter varies from 6 m to 6.45 m, with circular field-lenses. This beam deformation has been corrected by implementing field and projection lenses with elliptical edge-shape. This avoids radiation losses beyond the specified test volume.

Growth potential

At its completion the facility will be equipped with 20kW xenon lamps, which will provide an intensity of approximately 1.6 kW/m^2 in the reference plane. This intensity level is achieved without filtering and without taking into consideration losses due to degradation of optical elements. The design of the Sun Simulator and all associated supplies (power supplies, cooling equipment, etc.) is compatible with the operation with 30 kW xenon lamps. This contingency provides possibilities for the implementation of optical filters at a later stage or for the operation at elevated intensities.

Fast operations

The duration of pre- and post-test activities as well as for maintenance is considerably longer than the time required for actual test operations. In fact, it is these activities in the first instance that

limit the number of tests, that can be performed per year. The effort and time required for these activities have a considerable impact on the overall cost of the tests. This aspect has been taken into consideration in the design of the LSS. A few examples are given below.

- The shrouds in the "Main chamber" are removable. To facilitate fast mounting and dismounting, these shrouds are split up into the following four elements:
  bottom shroud;
  lower cylinder;
  upper cylinder;
  top shroud.
  Each element is self-supporting and can be removed in one piece by means of the overhead crane.

- In contrast to standard practice, the shroud elements in the auxiliary chamber do not line the walls of the vessel. As can be seen in Figure 6 these shrouds are designed as light baffles. This lay-out provides the following advantages:
  a) Free access to the chamber walls for surface cleaning.
  b) Free access to suspension points and rails on, or along, the chamber walls.
  c) Free access to both sides of chamber flanges, and crane-access into the chamber via the top flanges.
  All items support maintenance and repair activities within the auxiliary chamber and in particular on the the cryo-pump or the collimation mirror, which are both located in the auxiliary chamber. Furthermore, the baffle-design requires less material, which reduces not only the investment costs but also the LN_2 consumption during the cool-down of the facility.

- Each of the LSS subsystems is monitored and controlled via a PLC (Programmable Logic Control). Analog housekeeping data are independently recorded, evaluated, and presented to the operators via a dedicated computer. This computer is interfacing with the PLC's as well.
  The overall monitoring and control concept is illustrated in Figures 7a and 7b. The system provides the following possibilities:
  a) Interlocks and automatic sequences are programmable.
  b) Identification and recording of housekeeping data and status signals.
  c) Early warning capabilities and alarm event communication.
  d) Subsystem mimic presentations.
  e) Computer aided problem investigation.
  f) Computer aided test reporting.
  These features will provide high flexibility in adjusting subsystem operations to different test requirements. Trouble shooting can be done with low manpower effort and fault identification can be established within short periods. Individual assemblies (e.g. High Pressure Water Cooling, Lamp-House GN_2 Cooling, etc.) can be isolated

from the Central Control Room and can be operated separately from Local Panels. Higher-level interlocks are not in operation in this mode. This enables repair and maintenance on individual assemblies without blocking the availability of other assemblies or subsystems.

CONCLUSIONS

The LSS complements the ESA test centre at Noordwijk for tests on large payloads. The facility concept takes into consideration experience and recent trends for test requirements and will allow dynamic, infrared, VTC and solar simulation tests in the same test chamber. The design incorporates prerequisites for efficient and fast operations, as well as stable and reliable facility performance.

Subsystem monitoring and control are based on state-of-the-art technology and provide flexibility with respect to experimenters' requirements. Computer aided reporting on facility performance will provide without delay a rather complete and detailed documentaion of parameters and conditions during test activities, not only for the benefit of operations and maintenance but also in support of efficient and quick test analysis of the experiments.

REFERENCES

1. Classen E., May 1984, New Integration and Test Facilities at ESTEC, ESA-bulletin no. 38, May 1984.

2. Bonnot P., Brinkmann P.W., June 1982, Large Infrared Test Rig for Vacuum Temperature Cycling Tests in the ESTEC "DTC", ESA SP-173, June 1982.

TABLE 1: LARGE SPACE SIMULATOR MAIN CHARACTERISTICS

SUBSYSTEM	CONFIGURATION	SPECIFICATION
1. CHAMBER	o Auxiliary Chamber	Horizontal cone/cylinder diam.: 11.6 m (max) length: 14.0 m
	o Main Test Chamber	Vertical cylinder diam.: 10 m height: 15 m
	o Material	AISI 304 SS - Polished $\varepsilon < 0.2$
	o Removable Top Lid	diam.: 10 m
	o Sliding Side Door	diam.: 5 m
	o Hinged Side Door	diam.: 2 m
	o Volume	$\sim$ 2200 m^3
	o Specimen Support Structure (Mechanically de-coupled from chamber)	Dimension: 3.2 x 3.2 m Mechanical noise: < 0.005 g
	o 3 suspension brackets in upper part of Main Test Chamber	Pitch: 120° Max load: 25000 N each
	o 30 ports with shroud openings	Diameter 250 mm

TABLE 1: LARGE SPACE SIMULATOR MAIN CHARACTERISTICS

SUBSYSTEM	CONFIGURATION	SPECIFICATION
2. SHROUDS AND NITROGEN EQUIPMENT (SNSE)	o Shroud Surface Area	approx. 615 m^2
	o Material	approx. 190000 N
	o Surfaces facing test volume are painted with black paint	Paint type: Chemglaze Z306 Emissivity: ≥ 0.90 $\alpha_s \geq 0.95$
	o Remaining surfaces polished	Emissivity: ≤ 0.2
	o Baffle (disc) shrouds in Auxiliary Chamber (C2)	Optically tight viewed from test volume
	o Shroud lining in Main Test Chamber (C1) (4 sections removable)	clear diameter: 9.5 m overall height: 10.0 m
	o Modes of operation	C1: Cool down; LN_2; VTC; Warm-up C2: Cool down; LN_2; Warm-up
	o LN_2 mode	Surface temperature: $\leq$ 100 K Temp. distribution: $\leq$ 5 degrees Max heat load: 170 KW Operational pressure of LN_2 circuit: 8 - 12 bar Calculated LN_2 consumption: $\sim$ 4 m^3/h

TABLE 1: LARGE SPACE SIMULATOR MAIN CHARACTERISTICS

SUBSYSTEM	CONFIGURATION	SPECIFICATION
SNSE (cont.)	o VTC mode	Surface temperatures: 173K ÷ 373K Temp. distribution: ± 5 degrees (stationary condition) Max heat load 10 KW Operational pressure 1.5 bar Calculated LN_2 consumption 2.0 m^3/h
3. VACUUM PUMP	o 2 multivane pumps	2500 m^3/h each Pressure range: 1013 to 1.3 mbar
	o 3 roots pumps	3000 m^3/h each Pressure range: 26 to 7×10^{-2} mbar
	o 4 turbo molecular pumps	2000 l/sec each
	o 1 LHe cryo-pump	400000 l/sec for N_2
	o 1 LN_2 cryopanel	surface: 14 m^2 temp: $\leq$ 80°K
	o Expected working pressure in test volume	3×10^{-6} mbar

TABLE 1: LARGE SPACE SIMULATOR MAIN CHARACTERISTICS

SUBSYSTEM	CONFIGURATION	SPECIFICATION
4. SUN SIMULATOR (SUSI)	o Specified test volume	diameter 6 m length 5 m
	o Collimation (half) angle	$< 2°$
	o Intensity level with 19 x 20 KW Xenon lamps at nominal lamp power of 20 KW	1.61 KW/m^2 (unfiltered)
	o Intensity distribution (measured by sensor of 2 x 2 cm)	a) front end of test volume $< \pm 4\%$ b) overall test volume $< \pm 6\%$ (see figure 5)
	o Stability	$<$ ±0.5% of the adjusted level
	o Reproducibility of intensity levels	$<$ ±0.5%
	o Reproducibility of intensity distribution pattern	$<$ ±1% during a duration of 400 hours of operation
	o Number of lamps	19
	o Type of lamps	High Pressure Xenon 20 KW or 30 KW

TABLE 1: LARGE SPACE SIMULATOR MAIN CHARACTERISTICS

SUBSYSTEM	CONFIGURATION	SPECIFICATION
SUSI (cont.)	o Collimation mirror with 121 hexagonal segments	Temperature-controlled structure and segments with GN_2 Segments $AlSiO_2$-coated Heatable for contamination protection or decontamination up to 120°C
	o Transfer optics	Integrator with 55 field and projection lenses, MgF_2-coated
	o Chamber window	diameter: 1080 mm thickness: 80 mm material: HERASIL MgF_2-coated

TABLE 2: LIST OF COMPUTER PROGRAMS USED FOR THE SUN SIMULATOR OF THE ESTEC LSS FACILITY

PROGRAM	DESCRIPTION
1. JPL VRR: + subroutins	Calculation and optimisation of the intensity distribution in the test plane. Influence of the aberration caused by the off axis angle and the mirror shape.
2. COLLAR + subroutins	Calculation and optimisation of the collimation angle. Calculation of key points of the ray trace.
3. COLMIR: + subroutins	Calculations for the segmented mirror: o Position of the segments o Gaps in between o Coordinates and length of the centerbolts and adjustment screws
4. COLDI: - subroutins	Calculation and plot of the collector shape.
5. COLBER: + subroutins	calculation and optimisation of the intensity distribution in the integrator pupil.

PROGRAM	DESCRIPTION
6. PL BOG	Calculation and plot of the arc distribution.
7. PL VRTE	Plot of the intensity distribution in the integrator plane.
8. PL WIRK	Calculation and plot of the efficiency lsb
9. BOG NUZ	Calculation of the arc utilisation.
10. INTEGR	Calculation of the integration quality of the integrator.
11. EXT	Raytracing program for off-axis systems (for optimisation of the integrator i.e. field and projection lenses)

NOTE: Programs 1 through 10 available at IABG, West-Germany;
program 11 available at Carl Zeiss, West-Germany

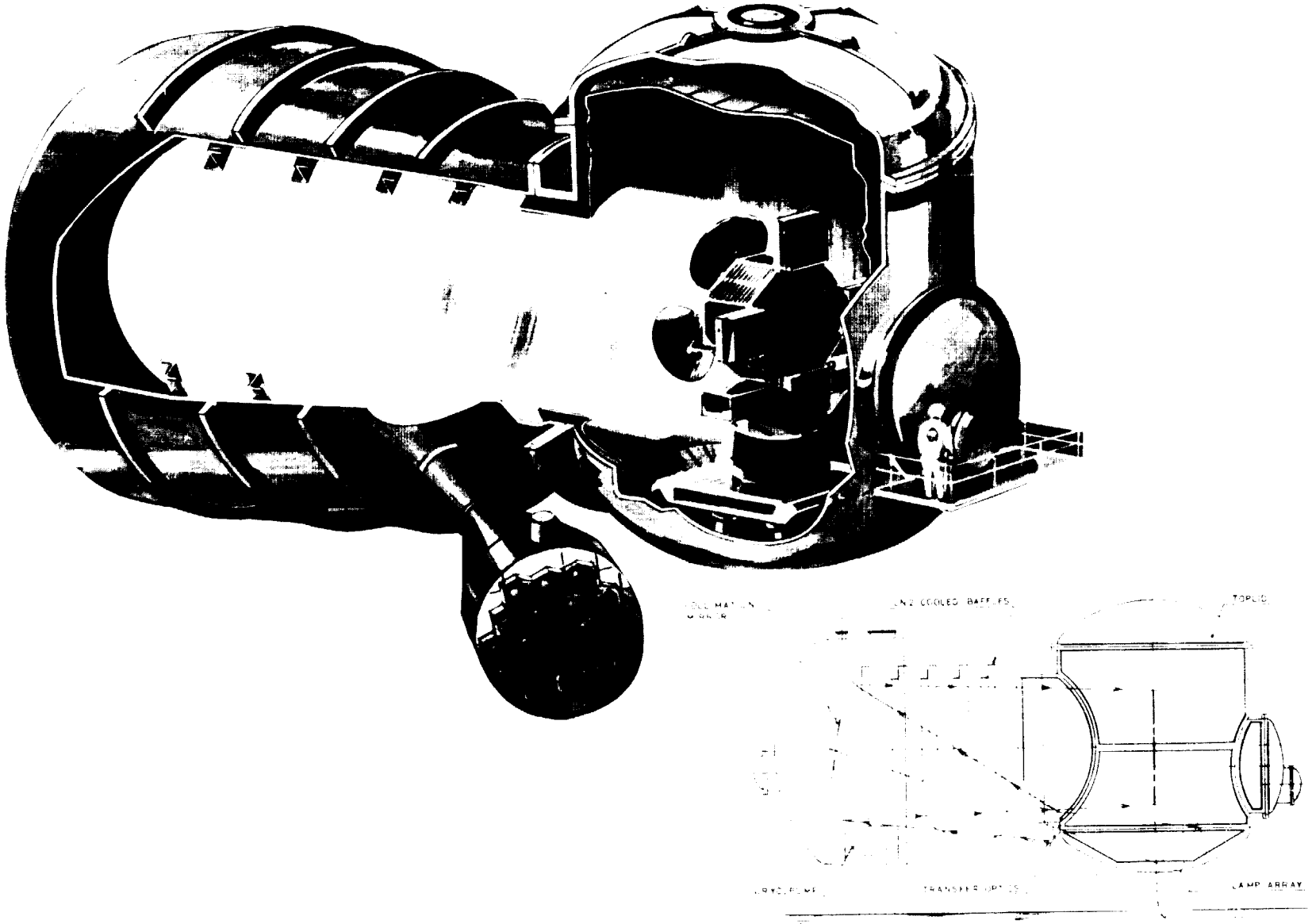

Figure 1 - Schematic and Artist's Impression of the Large Space Simulator (LSS) at ESTEC

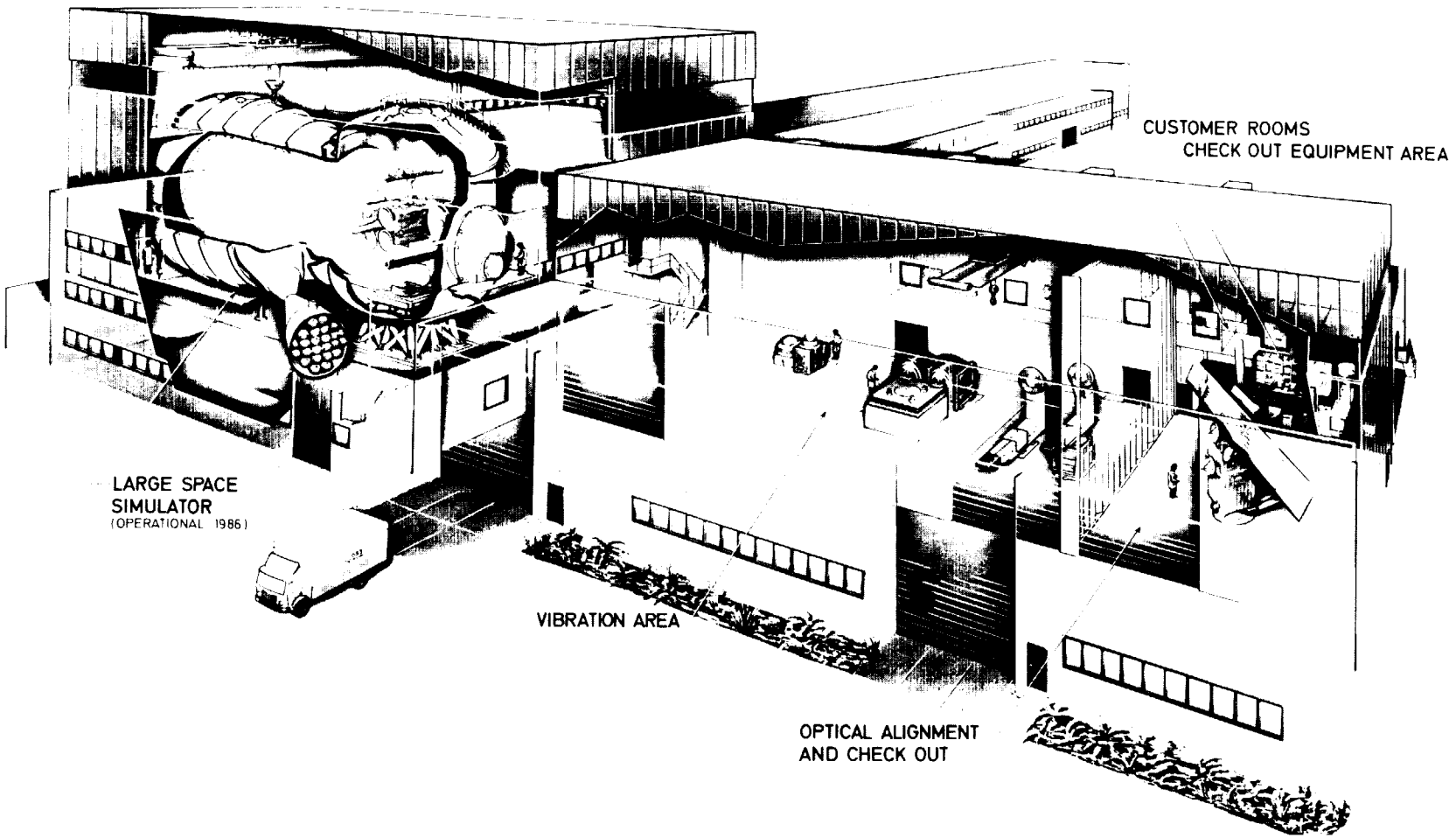

Figure 2 - Large Integration and Test Facilities

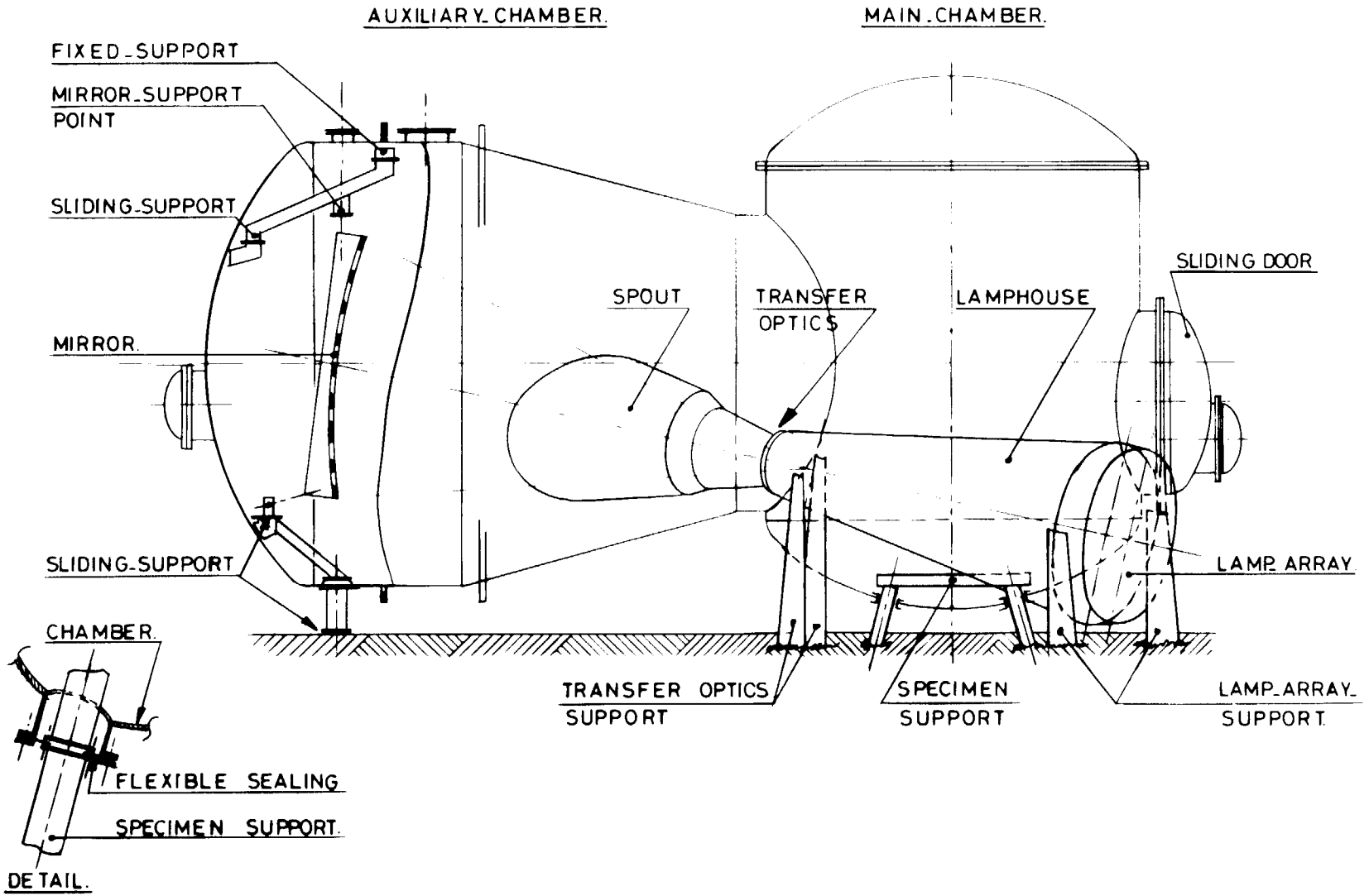

Figure 3 - Concept of Suspension for Specimen and Optics

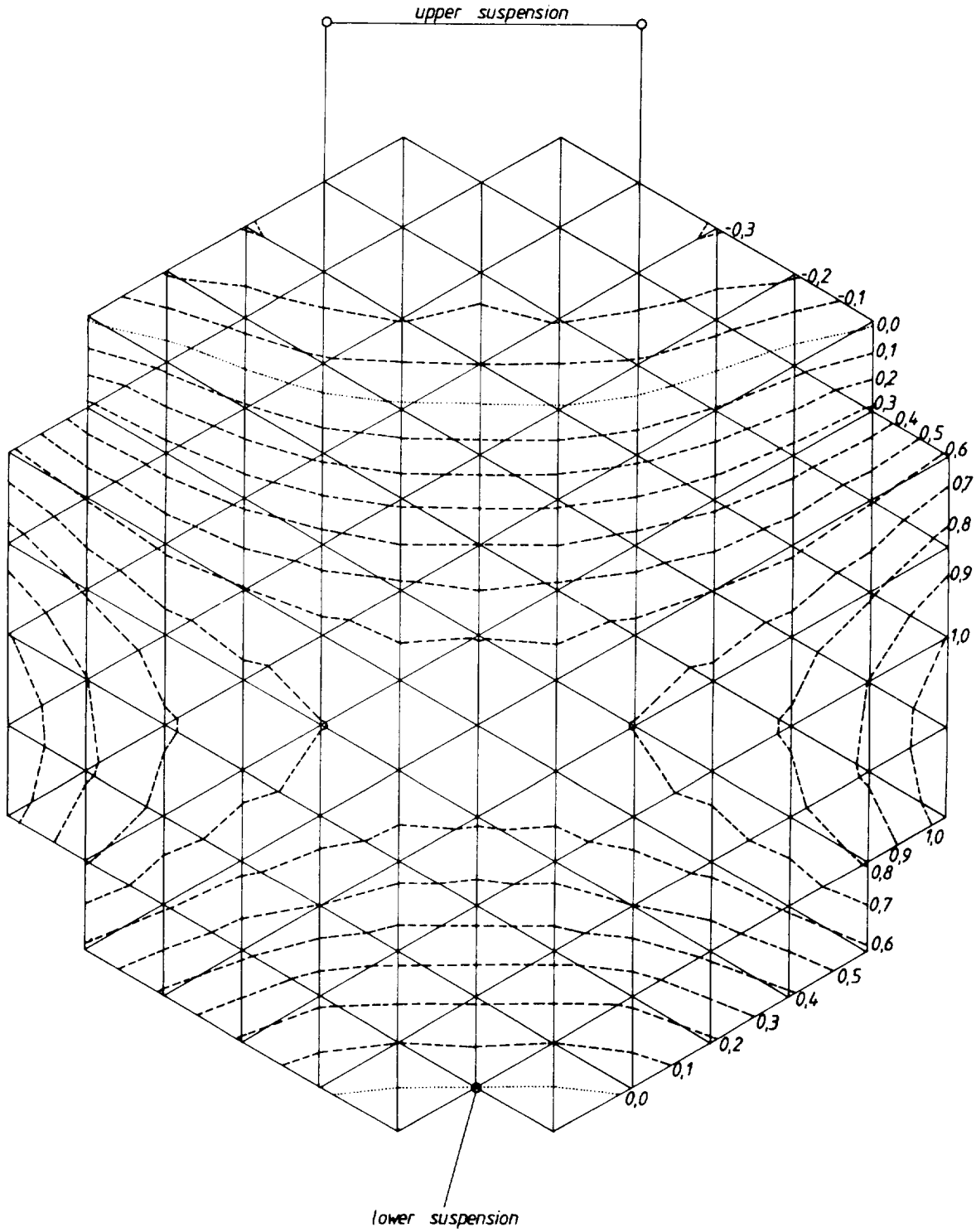

Figure 4 - Collimation Mirror Structure Deformation
Vertical beams cooled to 15 kelvin below temperature of cross-bracings. Mirror suspension points at intersections of grid. Lines of equal displacement parallel to the optical axis. Dimensions in mm.

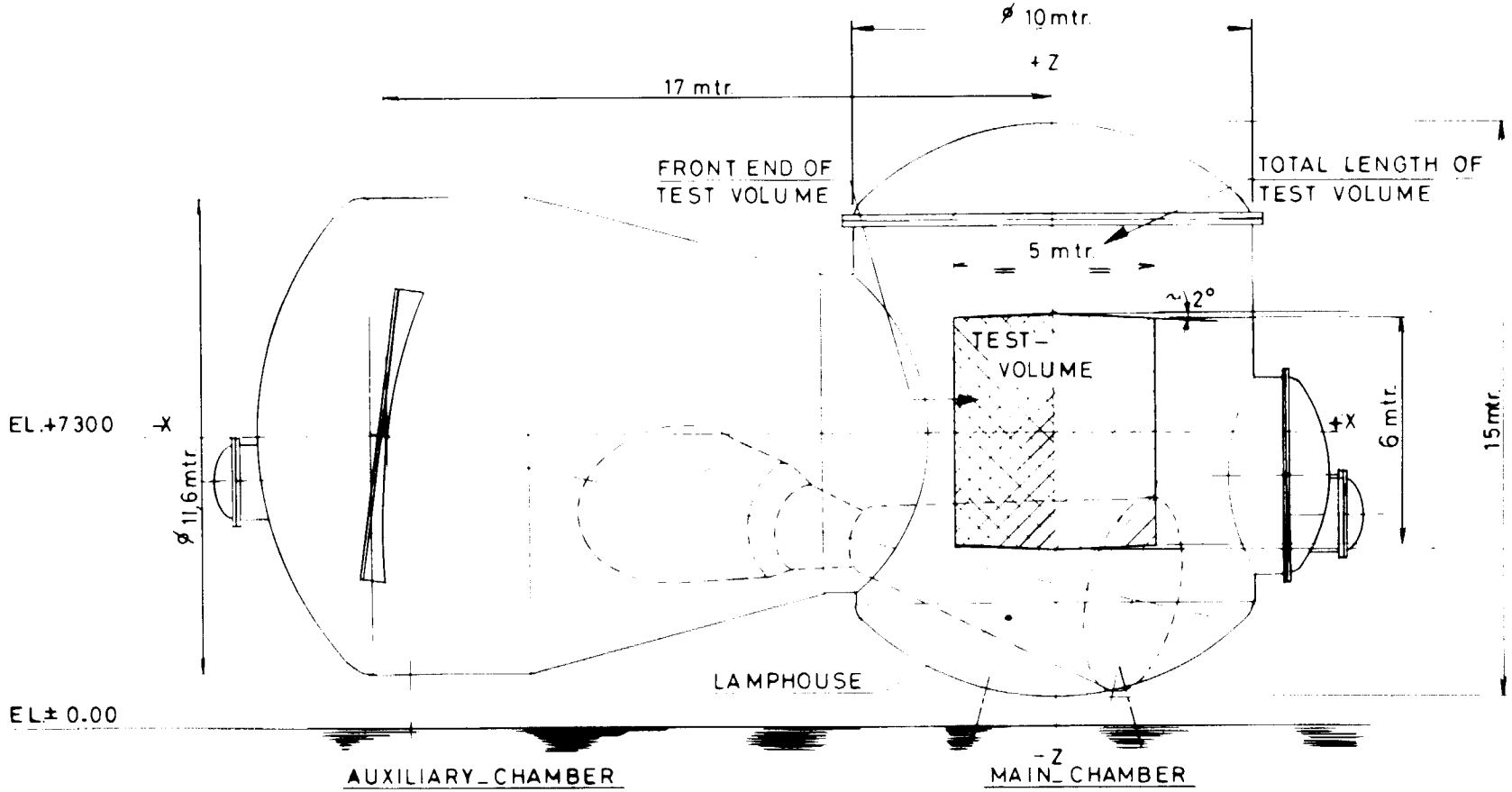

Figure 5 - Definition of Test Volume for Solar Radiation

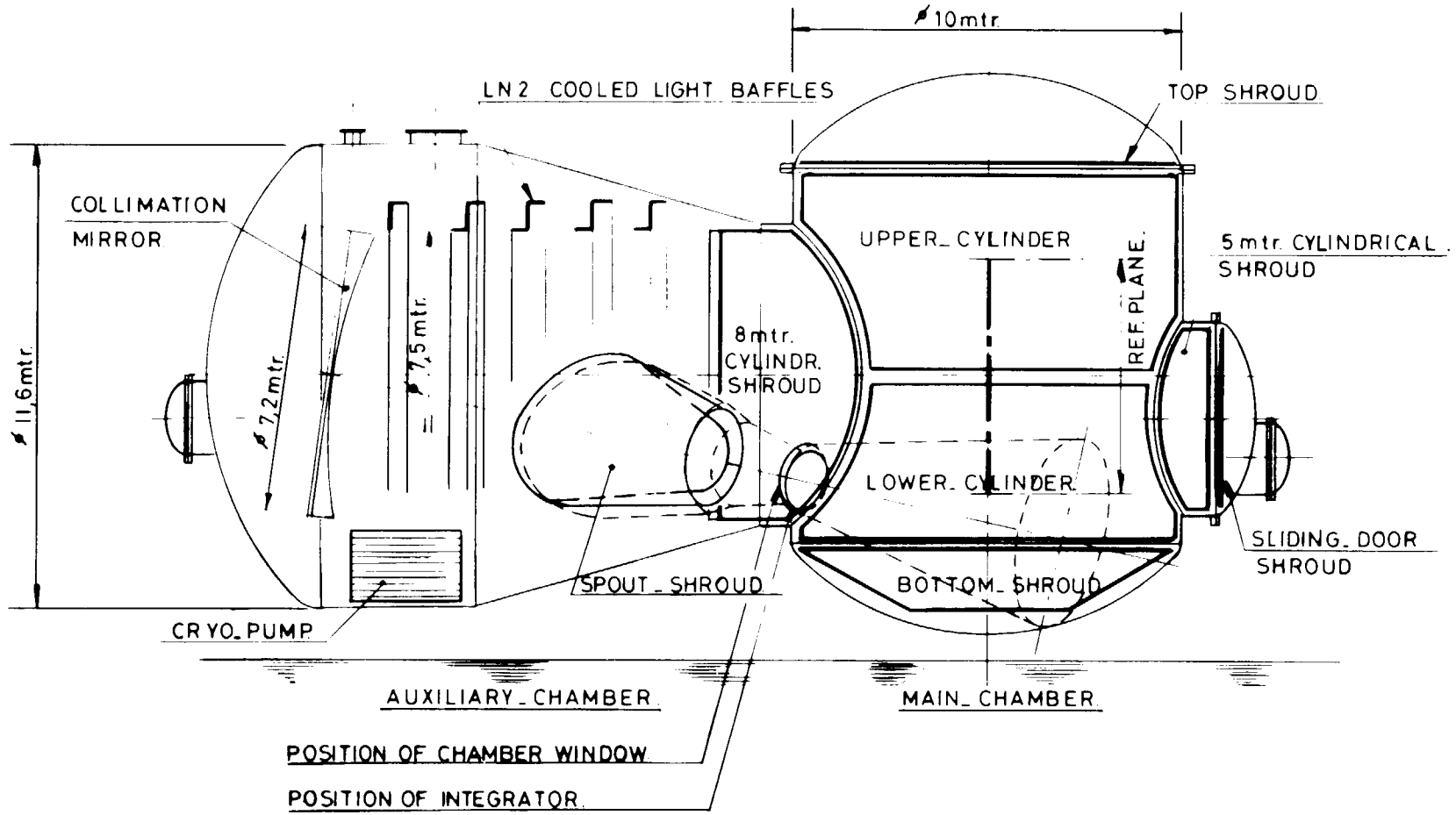

Figure 6 - Layout of Shroud Elements

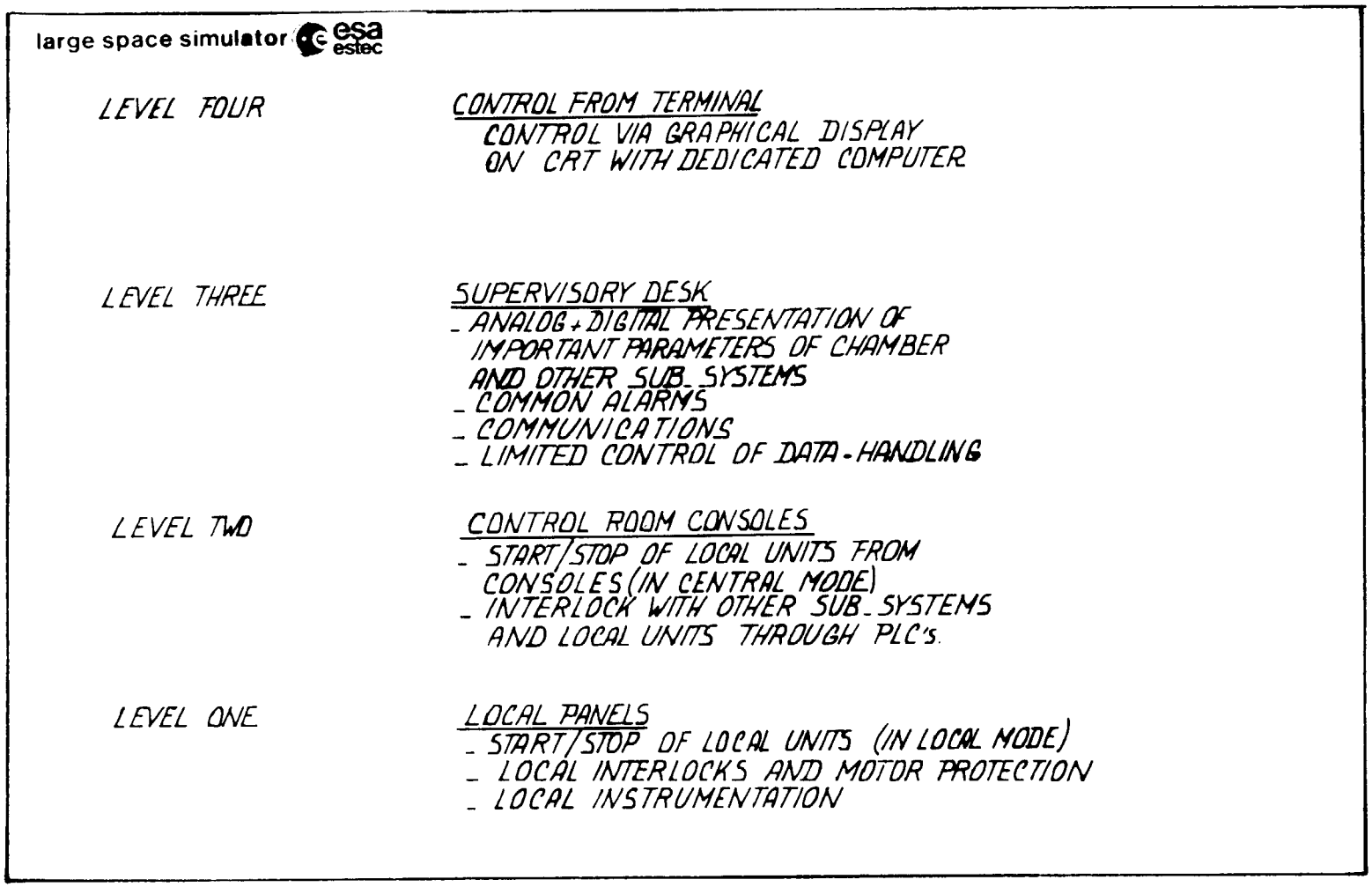

Figure 7a - LSS Control Concept

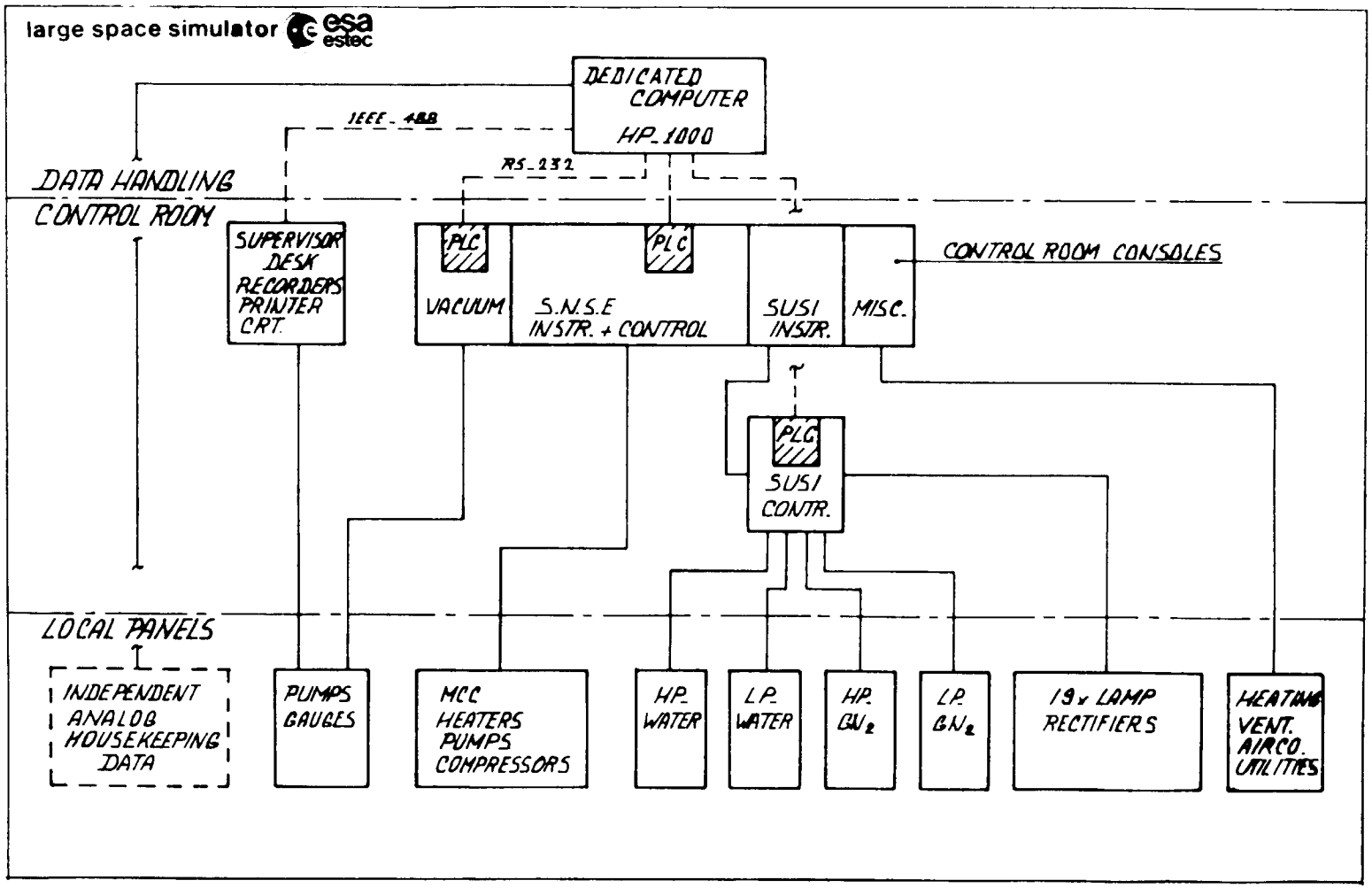

Figure 7b - Block Diagram LSS Control

SIMULTANEOUS THERMAL-VACUUM TESTING OF GPS DRIVES FOR NAVSTAR

By Thomas G. Brown, Ball Aerospace Systems Division

ABSTRACT

High technology sub-contracts for such state-of-the-art programs as NavStar can present special challenges in the space simulation test arena. It is often necessary to modify existing environmental facilities and equipment in order to achieve the condition required by the newest test specifications. Not only are safe and highly accurate control systems necessary, but the concern of volume test support must often be addressed.

INTRODUCTION

The solar array drive assemblies for the Global Positioning Satellite (GPS) are being built and tested by Ball Aerospace Systems Division. Schedule requirements and production volume dictated the need to perform thermal-vacuum acceptance testing on at least two complete units simultaneously. The dollar value represented by two test beds and two flight units operating in the same vacuum facility was an immediate concern. The safety of the flight hardware was of primary importance.

Simultaneous space simulation testing of two complete drive packages required only minor modification to the high vacuum pump stack. Specific attention was given to upgrading system safeties for high-vacuum operation. Major modifications were designed and implemented for the thermal control system and supporting subsystems. The automated thermal control system and test-bed hardware are of primary interest from a "unique facility" standpoint.

Preliminary testing without flight hardware installed in the test beds helped determine if the electrical and liquid nitrogen delivery systems were capable of supporting these space simulation tests. The "prove-in" testing also provided, from a computer control standpoint, valuable information on the interaction between controllers, thermal fixtures, and mock-up flight hardware. We were thus able to ascertain the corrective action necessary to compensate for this interaction.

Thermal interaction of the two test systems was relatively minor. The small amount of interaction that did exist was removed when we placed shrouds around the drives and electronics box. These shrouds effectively isolated the two test units from each other.

TEST DESCRIPTION

The tests are performed on the components that keep the satellite solar panels pointed toward the sun. The components consist of 1 control electronics box, 2 drive motors and 2 sun sensors or eyes.

The tests are conducted in our medium sized 48 inch diameter diffusion pumped vacuum chamber. This chamber was a good fit for the test fixturing that was required. We also had elec-

trical facilities already available at this chamber. The liquid nitrogen delivery system was upgraded with vacuum jacketed tubing and foam insulated tubing up to the point where the lines encountered the control valves.

The vacuum system was in good operating condition and the only modification that was necessary was an emergency shut-down system that would close the high-vacuum valve in the event of a major system malfunction.

The procedure for conducting this test was to first subject the unit to a hard vacuum condition. The pressure had to be reduced to less than 1 x 10-5 torr.

After preliminary hardware tests are performed at ambient temperature, the units are subjected to 300 hours of thermal cycles. The extremes of these cycles were determined by the individual components. The drive motors and the control electronics box are subjected to temperatures from -20 degrees Celcius to $+61$ degrees Celsius. Because of their placement on the spacecraft, the sun sensors are subjected to a wider range of temperatures. Their temperature range is from -24 degrees Celsius to $+85$ degrees Celsius.

The transition rates are based on the response of the drive units and the control electronics. The rate of change of these units was set at 3 degrees Celsius per minute during both cooling and heating cycles. The sun sensors were required to make their transitions during the same time frame as the drives and control electronics. This resulted in a slightly higher per minute temperature change for the sun sensors.

THERMAL CYCLING OF DRIVE MOTORS AND CONTROL ELECTRONICS

We used relatively well known bimodal control techniques to thermally cycle the drive motors and the control electronics units.

The thermal baseplates consisted of a heavy copper 8 inch diameter ring for mounting each of the drive motors and a thick 8 inch by 8 inch aluminum plate for mounting the control electronics box.

Heating elements were inserted through the thickness of the rings along the inner and outer circumference in a symmetrical manner. A groove was machined under the heating elements and tubing was inserted for liquid nitrogen cooling tubes.

The heating elements in the control electronics box base plate were placed in a horizontal position with the cooling tubes alternating with the heating elements.

The heaters were operated by time proportioned zero crossing triac circuits. These circuits were used because of almost noiseless turn-off. The triac circuits are controlled by a linear 0 to 5 volt signal that is sent from the temperature controllers.

Cooling was controlled with special stainless steel electro-pneumatic cryogenic valves. Electro-pneumatically operated valves have been found to be more trouble free than purely electrically

operated valves. The initial cost of the electro-pneumatic valves is considerably higher than conventional electric valves but this cost has proved to be negligible in the long run. This is due to the extreme reliability factor present in the electro-pneumatic valves. This reliability factor must also be considered when the safety of the test article is of utmost concern.

Thermal data from the baseplates came from two thermocouples that were peened into the surface of each baseplate. One thermocouple was used as a control, and as such was connected directly to the temperature controller. The other thermocouple was used strictly for alarm and monitoring purposes. We have found it to be good practice to use separate and independent thermocouples for control and alarm.

THERMAL CYCLING OF SUN SENSORS

Controlling the sun sensors or eyes presented a challenge. Since the eyes are mounted on top of the drive motors and must rotate, it was difficult to place a temperature sensor on them. Since there were several slip rings in the drive motors that were not used to communicate with the eyes, they became our means of getting the temperature sensor data. Since the temperature data must go through the slip rings, it was not possible to use thermocouples as was used on the drive motors and control electronics box.

Sensing the temperature of the eyes was achieved using four wire one hundred ohm platinum probes. The output of these probes was conditioned through linear bridges to give a one milli-volt per degree Celsius output. This output went to a controller which in turn supplied the necessary heating action to keep the temperature at the specified level.

The heaters were mounted in a small block of aluminum that the sun sensors are mounted on. The power for the heaters comes from a special DC power circuit. DC powers was used rather than the time proportioned AC because of the susceptibility of noise pick-up in the surrounding circuitry of the sun sensors. The power was passed to the heaters through a set of slip rings as the heaters had to rotate with the sun and temperature sensors.

Cooling was accomplished in a purely radiative manner. A shroud was placed around the eyes and cooled to -150 degrees Celsius whenever it was necessary for the eyes to transition cold. The shroud was cooled with liquid nitrogen, again using the same type of electro-pneumatic valves as used on the drives and electronics box.

Since the sun sensors already have shrouds around them, there was no thermal interaction between the systems and no further action was required to isolate them.

SETTING AND MONITORING THE TEMPERATURE CONTROLLERS

As stated previously, the tests consisted of many temperature cycles from -20 degrees Celsius to $+85$ degrees Celsius for the sun sensors and from -24 degrees Celsius to $+61$ degrees Celsius for the drive motors and control electronics boxes.

A microprocessor system was set up to allow constant communications with the controllers. The microprocessor system allowed us to send temperature profile data to the controller and receive data on the present state of the controller.

Since the microprocessor was monitoring the controllers constantly, it was possible to get a real time picture of what was happening inside the vacuum chamber.

Because of the necessity to test two complete drive systems simultaneously, the microprocessor system was used to coordinate the cycling of the two systems. The microprocessor system staggered the cycling of the two systems so that both systems were not going hot or cold at the same time. This staggering prevented overloading of the electrical and liquid nitrogen delivery lines.

The microprocessor system not only communicated with the controllers, but also with the system operators via a video terminal. From this video terminal, the operator could watch the temperature transitions and the stable plateaus to see if the controllers were doing their jobs correctly. If any problems were encountered, the operator could gain manual control of the system and take any action he or she deemed necessary.

ALARM AND EMERGENCY SHUTDOWN SYSTEMS

Probably the single most important subsystem in the test console is the alarm and emergency shutdown circuits.

The thermal control system was designed to use only two power feeds. One was the 110 VAC power that was fed from our emergency power buss. This emergency power is supplied from an on premises generator if there is a loss of commercial power. The other power feed was a three phase 208 VAC circuit. This line was not on emergency power and was not powered during a commercial power failure. The 208 VAC line was used to provide the power for the heaters and the liquid nitrogen control valves.

The reason that the 110 VAC power came off of the emergency power buss was so that we would get power back to the monitoring system immediately. This was necessary because we would need to know what the temperatures were doing during the loss of heating and cooling power. This would not be as critical if the units were at the hot point in the thermal cycles because the thermal losses from the units under test to the chamber walls would probably prevent the units from over heating. However, the same is not true if the units are at the coldest part of their thermal cycle. Liquid nitrogen may be left in the cooling tubes of the drive motor base plates or the control electronics base plate, also the shrouds around the sun sensors have been cooled to minus 150 degrees Celsius. The trapped nitrogen could cause the temperatures to drop far below the survivable temperature range of the components.

In order to help remove any possible trapped liquid nitrogen, a special circuit was installed that would start an immediate purge of the liquid nitrogen lines with gaseous nitrogen. This purge is initiated with the loss of power on the 208 VAC circuit. Power for this purge circuit comes from a non-interruptable power supply. This special power supply was used in case of the unlikely event that emergency power did not come on during a commercial power failure.

Another method of triggering this purge is via the operators console. There is a large red panic button located on this panel. Its purpose is to shut off the power to the heaters and valves if there should arise some type of catastrophic failure. The button would also cause the high vacuum valve on the vacuum chamber to close.

For normal failures, there is a more conventional alarm system. There is a separate alarm circuit for each of the base plates and sun sensors. If any circuit detects an out of specification hot or cold condition, a audible signal is produced and either the heating or cooling is cut to that particular circuit. Full functionality can not be returned to that circuit until the operator has acknowledged the failure.

CONCLUSION

With the coming of the space shuttle, space hardware is leaving the realm of one of a kind components and entering the world of volume production. With this transformatoin comes the necessity for equipment and techniques that can be used for long periods of time with relatively little down time. For most of these jobs, the same hardware that has been used for many years is adequate, however, new emphasis must be placed on safety hardware. Some of the test specifications for the new generation of space hardware are difficult to achieve and require computer control and monitoring. The hardware is now commonly available to perform these difficult tests.

Using good planning techniques combined with modern technologies, the volume production and testing of space flight hardware can be accomplished economically and with a high degree of safety.

THE SCEPTRE FACILITY: IMPROVED SIMULATION OF THE SPACE ENVIRONMENT THROUGH THE APPLICATION OF ADVANCED TECHNOLOGY*

John D. Ruley

University of Dayton Research Institute
Dayton, Ohio

ABSTRACT

SCEPTRE (Space Combined Effects Primary Test Research Equipment) is the Air Force Materials Laboratory's primary device for performance testing of spacecraft thermal control materials. It has been undergoing a major upgrade in the last two years aimed at making it capable of simulating the synergistic effects of vacuum, ultraviolet radiation, and electron radiation. In the course of this work, a number of advances have been made in the areas of computer data processing, solar simulation, and the analysis of test results.

INTRODUCTION

The extraterrestrial environment is a hostile one for many candidate spacecraft materials. At the Air Force Wright Aeronautical Laboratories, Materials Laboratory (AFWAL/ML) a Space Combined Effects Primary Test Research Equipment (SCEPTRE) system has been developed to provide simulation of the environment, and evaluation of its effects on spacecraft materials. This paper will outline this development, and the advances which have accompanied it.

Ground-based simulation of the orbital environment is necessary in order to predict the performance of potential spacecraft materials. Figure 1 presents solar absorbtance data on several thermal control materials from the ML-101 satellite. In each case (particularly so for the S-13G) a significant increase is indicated, which could result in thermal imbalance and mission failure. In order to avoid such failure, facilities such as SCEPTRE are needed to provide accurate data on material performance. This problem is becoming increasingly serious as longer mission times become common, and will be especially important for the proposed space station project.

The major environmental factors affecting spacecraft material performance are illustrated in Figure 2. Those marked by an asterisk (*) are simulated by SCEPTRE. These factors are:

(1) Surface contamination: This is primarily a result of the relatively dirty nature of existing spacecraft particularly on manned missions.

* This research was performed under U.S. Air Force Contract No. F33615-82-C-5039, Air Force Wright Aeronautical Laboratories, Materials Laboratory, Wright-Patterson AFB, Ohio 45433

Thruster exhaust, waste dumping, etc., produce a contaminant cloud in orbit with the vehicle. Some of these contaminants condense out with various effects on the material. This problem is the focus of a major Air Force study (Ref. 1) and a simulation of it is not attempted in SCEPTRE at this time.

(2) Photon Radiation: This includes the solar ultraviolet (UV), as well as x-ray and gamma-ray radiation. The solar ultraviolet is generally considered to be one of the most significant environmental factors for thermal control and is provided for by SCEPTRE's Advanced Technology Solar Simulator (ATSS).

(3) Low Energy Charged Particles: Electrons and protons in the kilovolt energy range have a major effect on material performance. SCEPTRE simulates the solar electrons by a Bi-Energetic Electron Flood System (BEEFS). Proton simulation is not now incorporated, but is planned to be added at a later date.

(4) High Energy Charged Particles: This includes solar-flare particles (megavolt protons and electrons), and cosmic rays. As these particles have their major effect in the material substrate, they are not simulated by SCEPTRE.

(5) Spacecraft Structure Temperature: The operating temperature of a material has a major effect on the rate at which radiation induced damage occurs. In general it appears that elevated temperatures have an accelerating effect on the degradation (Ref. 2). At present, this is simulated by a water-cooled sample holder to keep the samples at room temperature. A planned modification will provide for individual thermoelectric coolers for each sample.

In addition to these factors, the basic space environment must be considered: it is an extremely hard vacuum (10^{-8} to 10^{-12} torr). Past testing in which samples have been exposed to air during measurement has been adversely affected by oxygen recombination in some samples (Ref. 3). In order to avoid this problem, all testing and measurement is performed at an operating pressure in the micro-torr range.

Simulating the environment is not enough. To be useful, a space simulation facility must also provide for measurement of the environmental effects on the test materials. As SCEPTRE is intended primarily to test thermal control and optical materials, these measurements are performed by an in-situ spectrophotometer system. Additionally, a variety of auxiliary instrumentation is used to monitor the environment in the vacuum chamber. Once the raw data is collected it must be reduced and analyzed. In SCEPTRE these functions are performed electronically by the facility computer system, which is coupled to the instrumentation.

The remainder of this paper details each of the SCEPTRE subsystems, with particular attention to those which are unique.

DESCRIPTION OF SCEPTRE

SCEPTRE is made up of four major subsystems:

Vacuum and Control Subsystem:

This consists of an 18" diameter vacuum chamber, a turbomolecular pump, mechanical backing pump, associated instrumentation, and the main system controls. It is capable of sustaining a vacuum level of better than 5×10^{-6} torr for more than 1000 hours. The instrumentation includes a 0-500 amu quadrupole mass spectrometer and quartz-crystal microbalance (QCM) for outgassing measurement, a hot-cathode ion gauge, two thermocouple vacuum gauges, three thermocouples for temperature measurement (two inside the chamber for measurement of sample temperatures, one outside), a calibrated solar cell for qualitative measurement of the solar simulator output, and a modified Faraday cup for electron flux measurement.

Connection of the mass spectrometer to the facility computer provides an advance in outgassing determination. During a test run, the mass spectrometer may be continuously swept with the computer recording any significant (greater than 10% peak change) in the mass spectrum. This permits identification of when outgassing begins, and estimation of its extent. By combining this with QCM data, a first-order determination of the outgassing rate may be made. Figure 3 is a typical spectrum from the mass spectrometer under normal conditions.

Ionizing Radiation Subsystem:

This includes the Advanced Technology Solar Simulator (ATSS) and Bi-Energetic Electron Flood System (BEEFS). The ATSS is a locally designed adaptation of a Spectrolab X-25 solar simulator providing approximately a 100% increase in available flux with the same lamps previously used. It provides 3-5 equivalent ultraviolet suns (EUVS) over the target area, with a close match to the solar irradiance spectrum. This was accomplished by completely redesigning the X-25 optical system, incorporating all-reflective, aspheric optics of a type not available until quite recently. The ATSS optical design is presented in Figure 4, and the ATSS spectrum along with the exoatmospheric solar spectrum (Ref. 4) is presented in Figure 5.

The electron gun system consists of two Kimball EFG-11 flood guns adapted for computer control, and provides up to 10^{10} electrons/sec at 0-20 keV from each gun. In the past, electron simulation has generally been performed with a single monoenergetic electron beam, but recent testing has indicated that this may be inaccurate (Ref. 5). BEEFS addresses this problem by using two flood beams, with a resultant electron spectra estimated in Figure 6. The computer control permits beam modulation to improve the time-averaged uniformity of electron exposure over the samples, and can also be used to provide for cycling of the beam energies and intensities.

Optical Measurement Subsystem:

This is the heart of SCEPTRE. It consists of two instruments: a Beckman Acta M-IV spectrophotometer modified so that the detectors reside in the vacuum chamber, and a spectroradiometer which was constructed in-house.

The spectrophotometer measures light reflected from the samples in the region 2000 - 26,000 Angstroms, from which absorbtance can be calculated, and total solar absorbtance inferred. To increase accuracy beyond the instruments inherent noise limits (± 2%), repetitive scanning is used, and an average of several spectra is eventually produced - with an accuracy on the order of ± 0.1%. In order to provide for this averaging to be performed in minimum time, the spectrophotometer is connected to the facility computer which automatically records and averages the spectral data as the instrument is scanned.

The radiometer measures the light produced by the solar simulator in the 2000 - 12,000 Angstrom range. It was constructed from a used monochromator, a silicon photodiode, and some mirrors. Data recording is computer controlled, as with the spectrophotometer.

Facility Computer Subsystem:

A Digital Equipment Corp. LSI-11/23 minicomputer is used to store and report the instrument data. It also serves as the operator's log book, and as a terminal to the Materials Laboratory computer, which is used for data analysis. Additionally, it is being adapted to provide for automatic monitoring of facility instrumentation during a test, without operator intervention.

Unfortunately, connecting the computer to the instruments is, by itself, not enough to produce anything more than a form of digital data recording. To extract the best performance from the system, specialized software had to be provided. Two general-purpose programs are used with the computer: Research Analyst (RA) and the Macro Interpretive Spectral Translator (MIST), both of which were designed by the author.

RA is the program used to control acquisition of instrument data. Essentially, it provides a "user friendly" front end which not only performs the data collection, but also provides the operator with step-by-step instructions for controlling the instrument (in general, SCEPTRE's instrumentation was not originally intended for computer control). This tends to minimize human error, and allows data to be accurately recorded in a very brief time. The data is then transmitted to the AFWAL/ML PRIME 850 computer for analysis.

MIST is the analysis program on the PRIME 850. It provides a relatively simple way for the operator or analyst to perform analysis on the data generated by SCEPTRE's instrumentation. This is accomplished by coupling a relatively sophisticated mathematical analysis library with a graphic display, so that the operator can see what the computer is doing. This technique is

particularly useful in the analysis of optical data, where tedious point-by-point integration techniques, which would take a human being hours to perform, can be accomplished in minutes.

Figure 7 is an example of the MIST data screen. Here the solar spectral irradiance is being integrated to give the solar constant. It should be noted that the integration steps have been exaggerated for this figure. In a normal MIST integration, the steps would be so small that the curve would appear completely filled in.

The effect of coupling the facility instrumentation to the computers, with the MIST and RA software, has been to drastically reduce the time required to perform analysis on optical data. For example, generation of a solar absorbtance figure - one number - from a spectrophotometer chart takes about one hour by hand, if mechanical aids are utilized. With MIST this takes just a few seconds. Additionally, the hand calculated data is at best, accurate to only two decimal places while the computer calculated data is accurate to three. Thus data reduction and analysis is greatly speeded up, with no loss in accuracy.

In SCEPTRE, the speed increase has been used to accomplish something unheard of in large-scale simulation work: same day data analysis. That is, fully reduced data is produced on the same day that the measurements are taken. This permits the operator to make immediate judgements affecting the test in a way which would otherwise be impossible - for example, if the solar absorbtance has ceased to change the test can be terminated; or if a new absorbtion band is appearing in a material, additional measurements may be taken. Without the computer, the data could not be analyzed until the run was complete.

The computer also provides for some new approaches to data display. Most readers are probably familiar with display formats such as Figures 8 and 9, representing pre- and post-test reflectances, and change in solar absorbtance, respectively. The computer permits new formats for the same data, such as Figure 10, a three-dimensional plot of absorbtance as a function of time and wavelength. Incidentally, all three of these figures are from an early test run on 0.1 mil anodized aluminum at low intensity U.V. exposure.

CONCLUSION

This paper has described major developments in the SCEPTRE facility, with particular emphasis on modifications now in progress. These modifications are now in an advanced development state, and installation should be completed late this summer.

REFERENCES

1. Proceedings of the USAF/NASA International Spacecraft Contamination Conference, Capt. J. M. Jemiola, ed., NASA CP-2039, Washington, D.C. (1978).

2. R. L. Olson, L. A. McKellor, and J. V. Stewart, "The Effects of Ultraviolet Radiation on Low α_s/ϵ Surfaces," Lockheed Missiles & Space Co., Palo Alto, CA, Paper #42, NASA SP-55, Symposium on Thermal Radiation of Solids, Washington, D.C. (1965).

3. H. T. Macmillan, A. T. Slensky, and L. A. McKellar, "Measurements During Ultraviolet Irradiation in Vacuum," AIAA Thermophysics Specialist Conference, Monterey, CA (1965).

4. The Solar Constant and the Solar Spectrum Measured from a Research Aircraft, NASA TR R-351, Matthew P. Thekaekara, ed., Goddard Space Flight Center, Washington, D.C. (1970).

5. M. Treadaway, R. Leadon, C. Mallon, T. Flanagan, R. Denson, and E. Wenoss, "Dielectric Discharge Characteristics in a two-electron simulation environment," JAYCOR Co. Paper #1, NASA CP-2182, Space Charging Technology-1980, Washington, D.C. (1981).

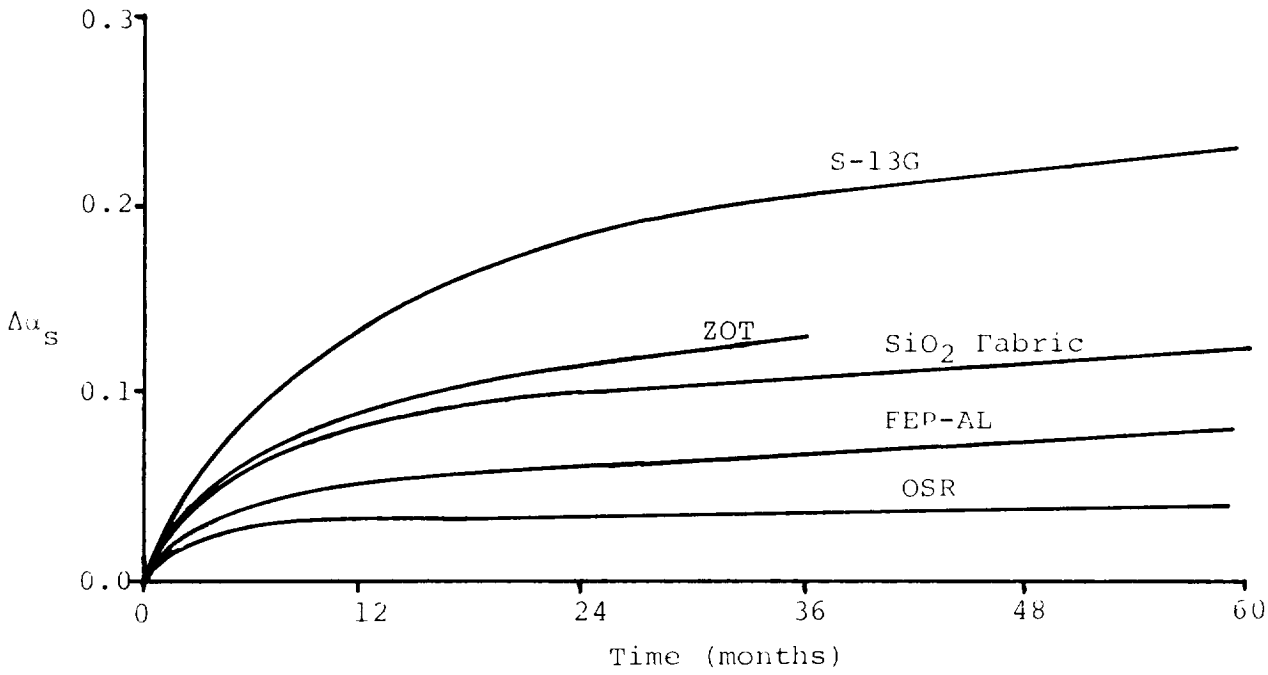

Figure 1 - Solar-Induced Degradation of Thermal Control Materials

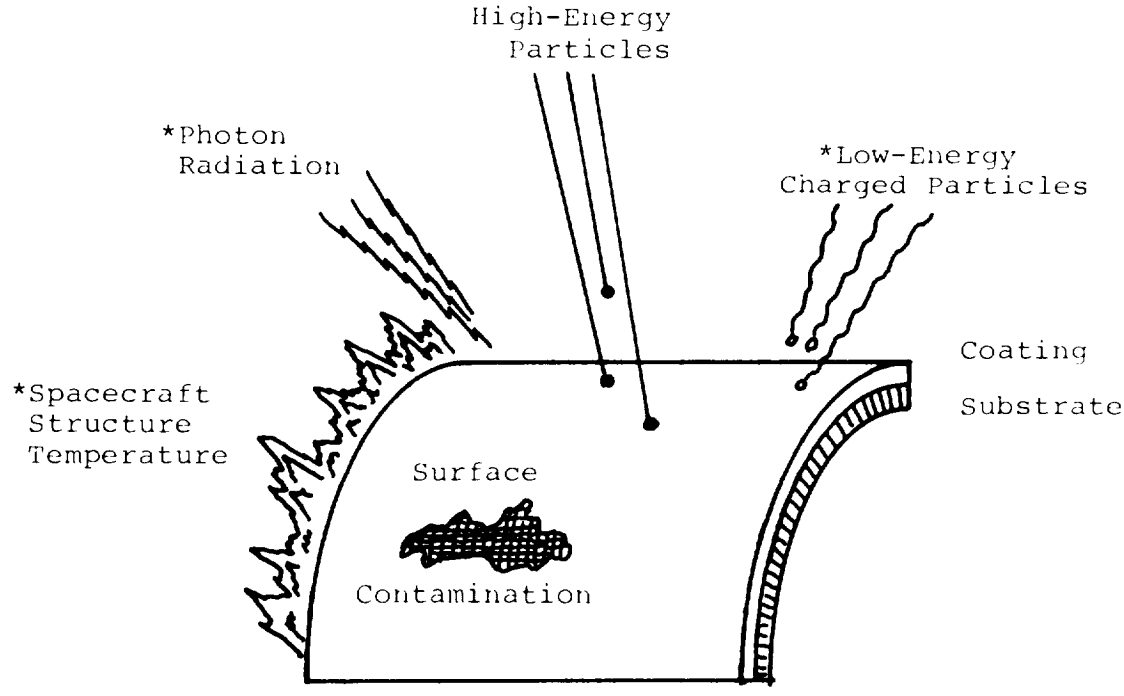

Figure 2 - Spacecraft Coating Environmental Factors

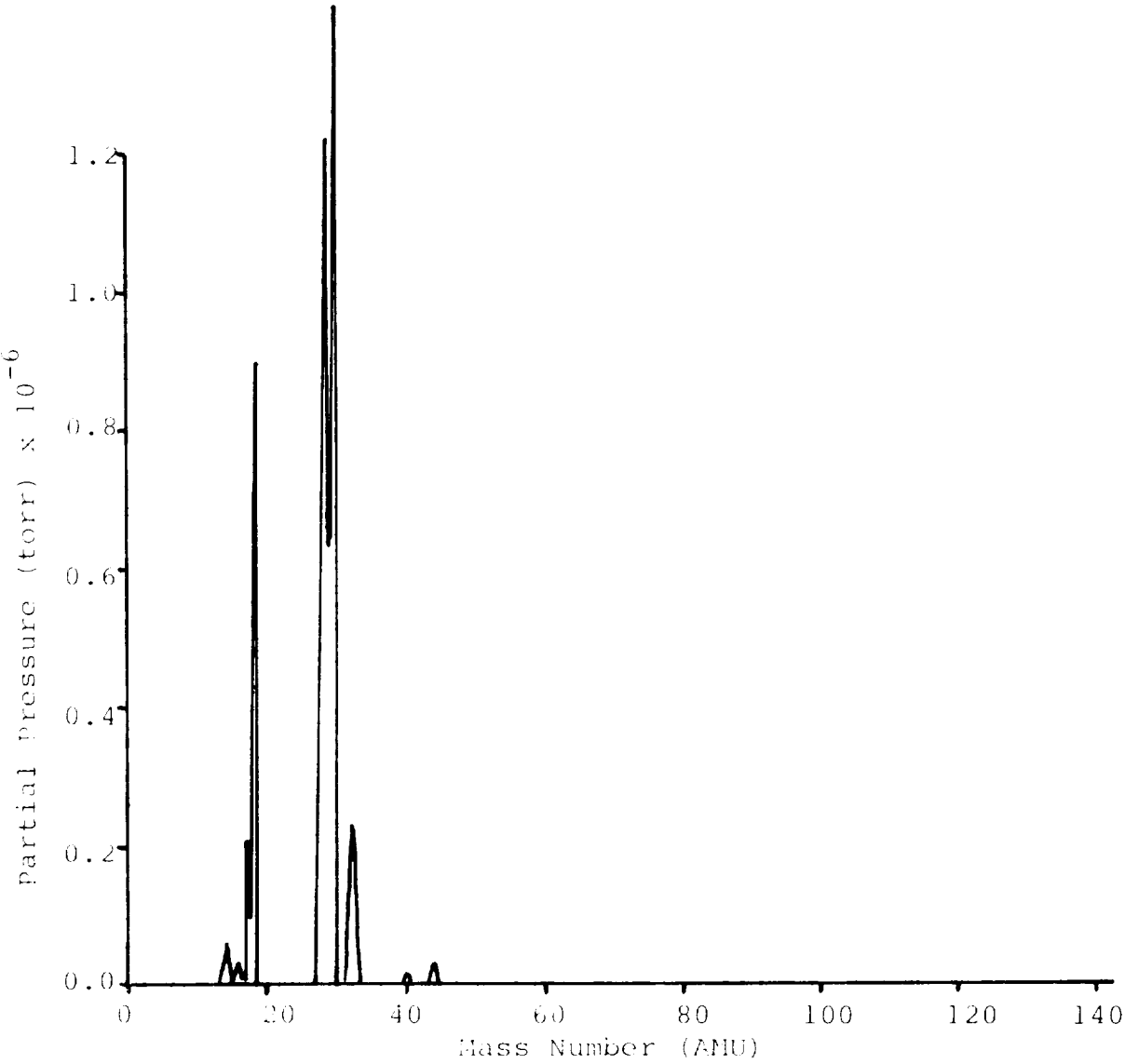

Figure 3 - SCEPTRE Mass Spectrum

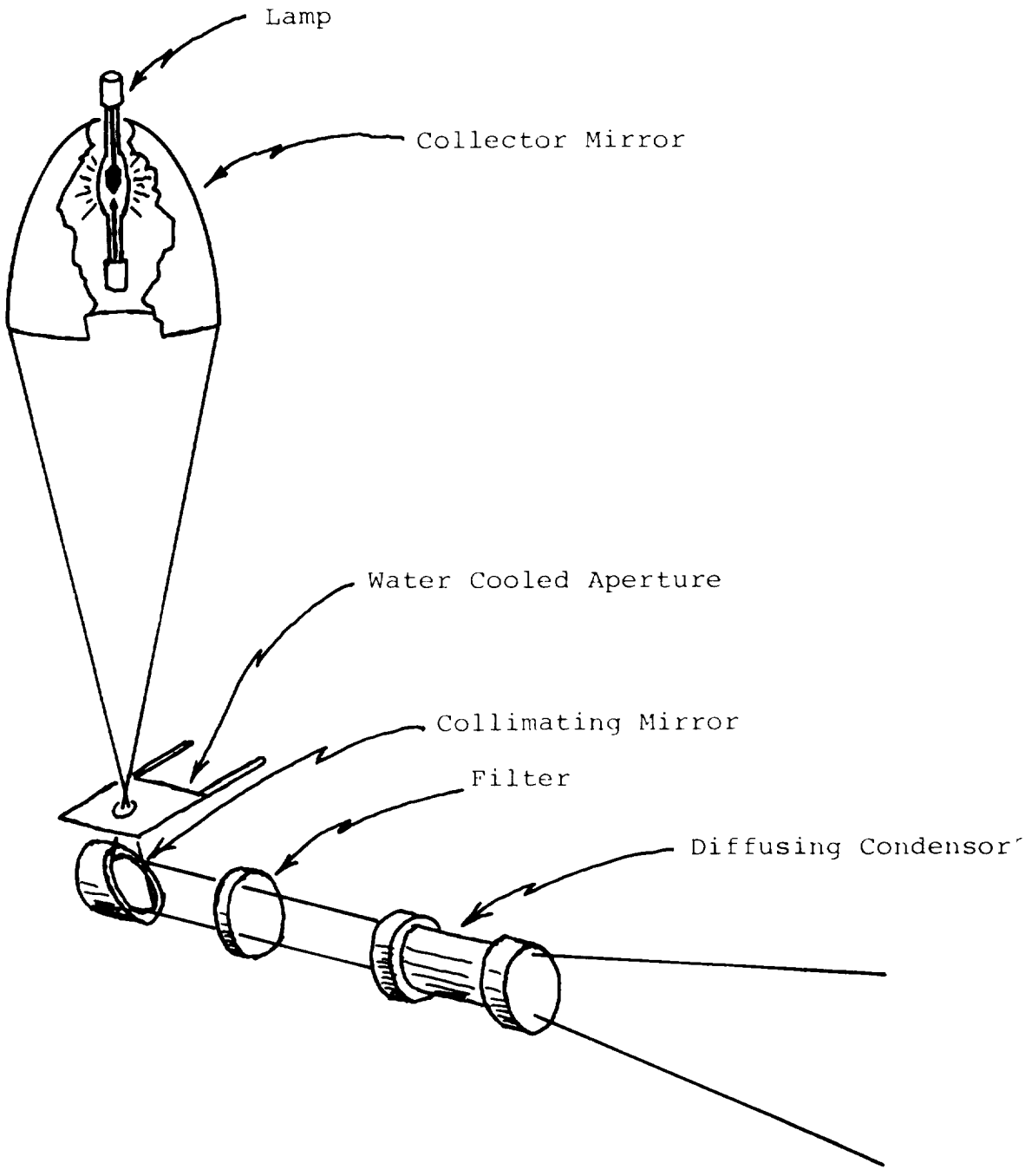

Figure 4 - ATSS Optical Path

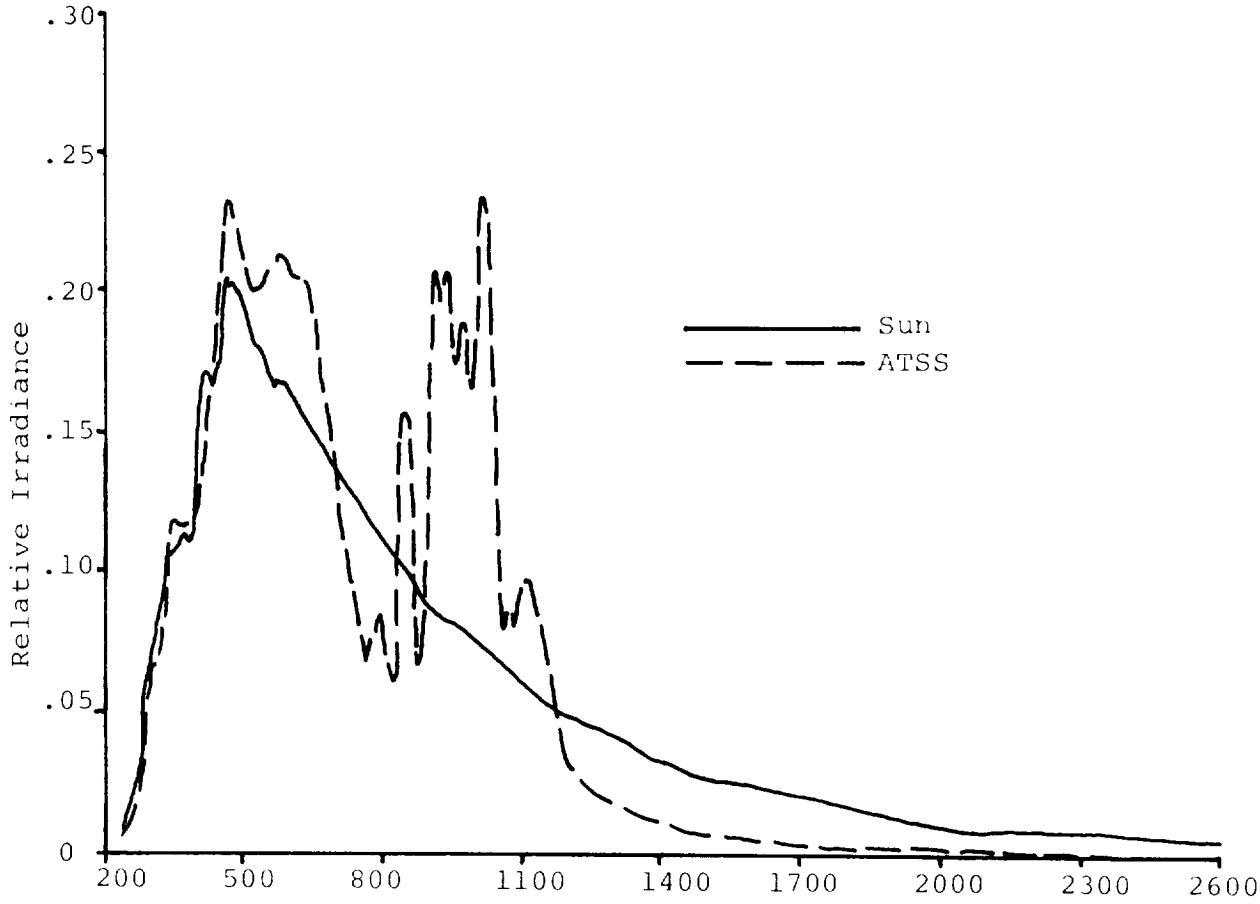

Figure 5 - Optical Spectra

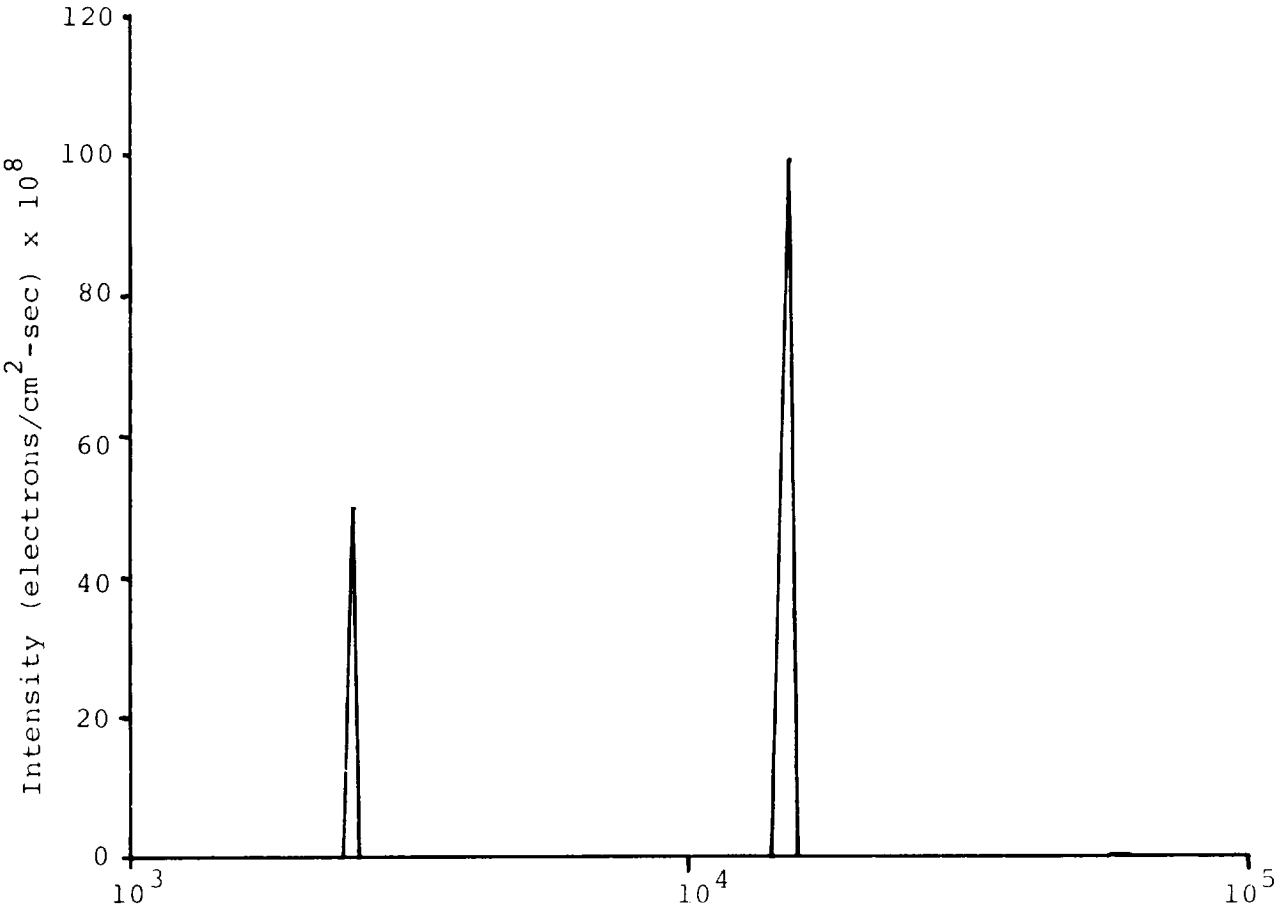

Figure 6 - BEEFS Spectrum (estimated)

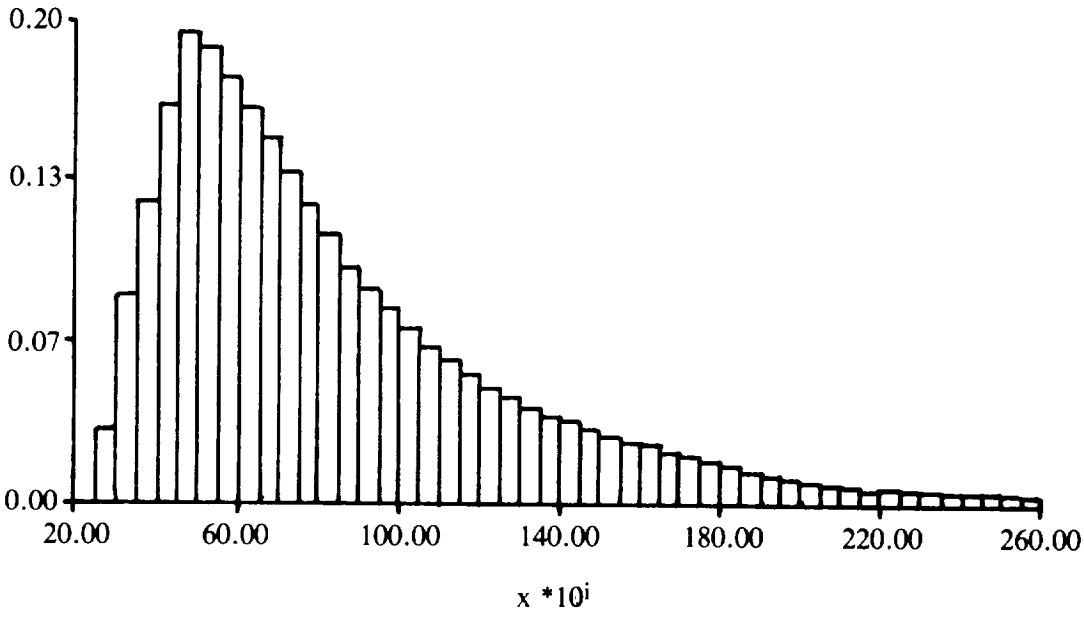

>135.100

>IRAD.Solar Integrate Print

Figure 7 - MIST Data Screen

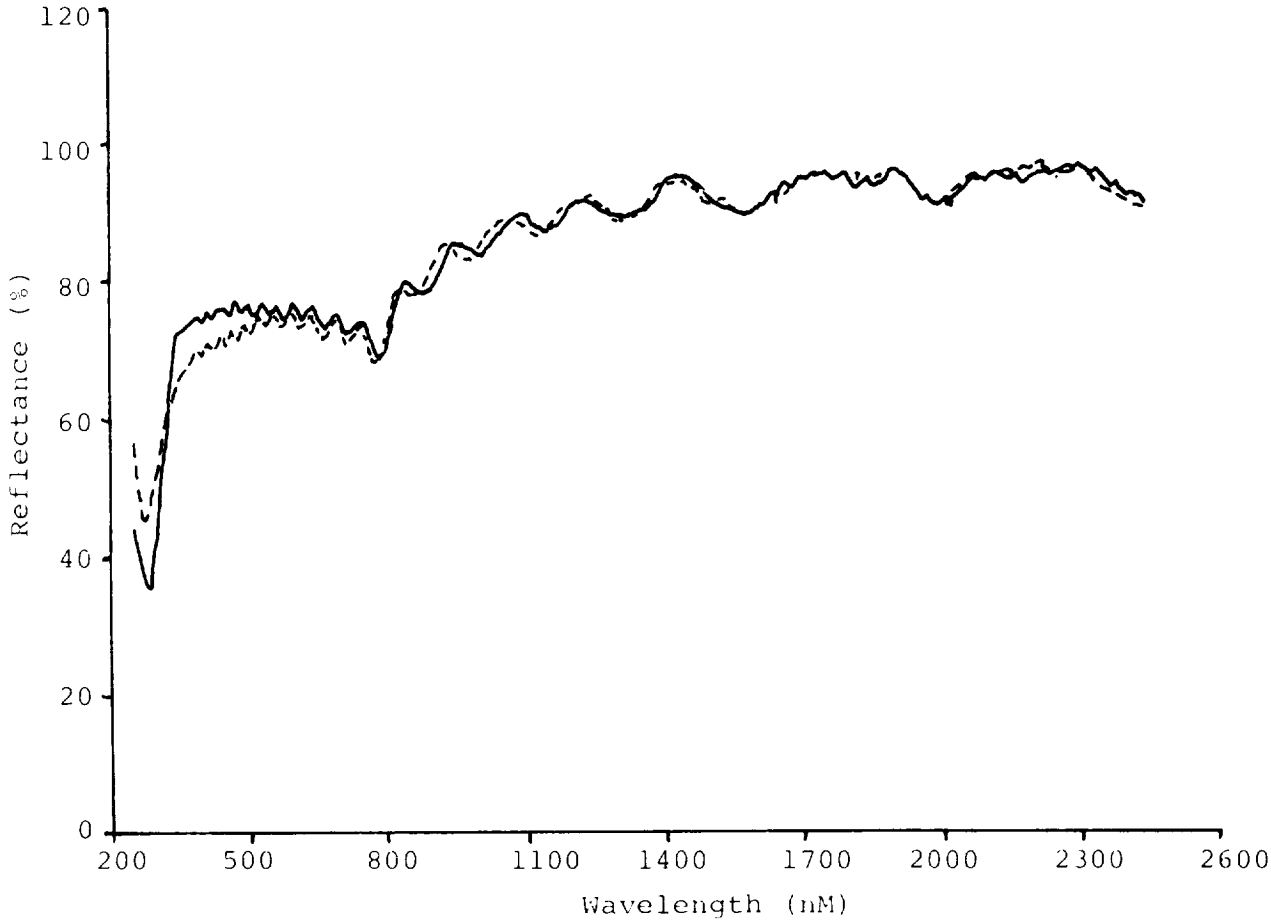

Figure 8 - Change in Spectroreflectance

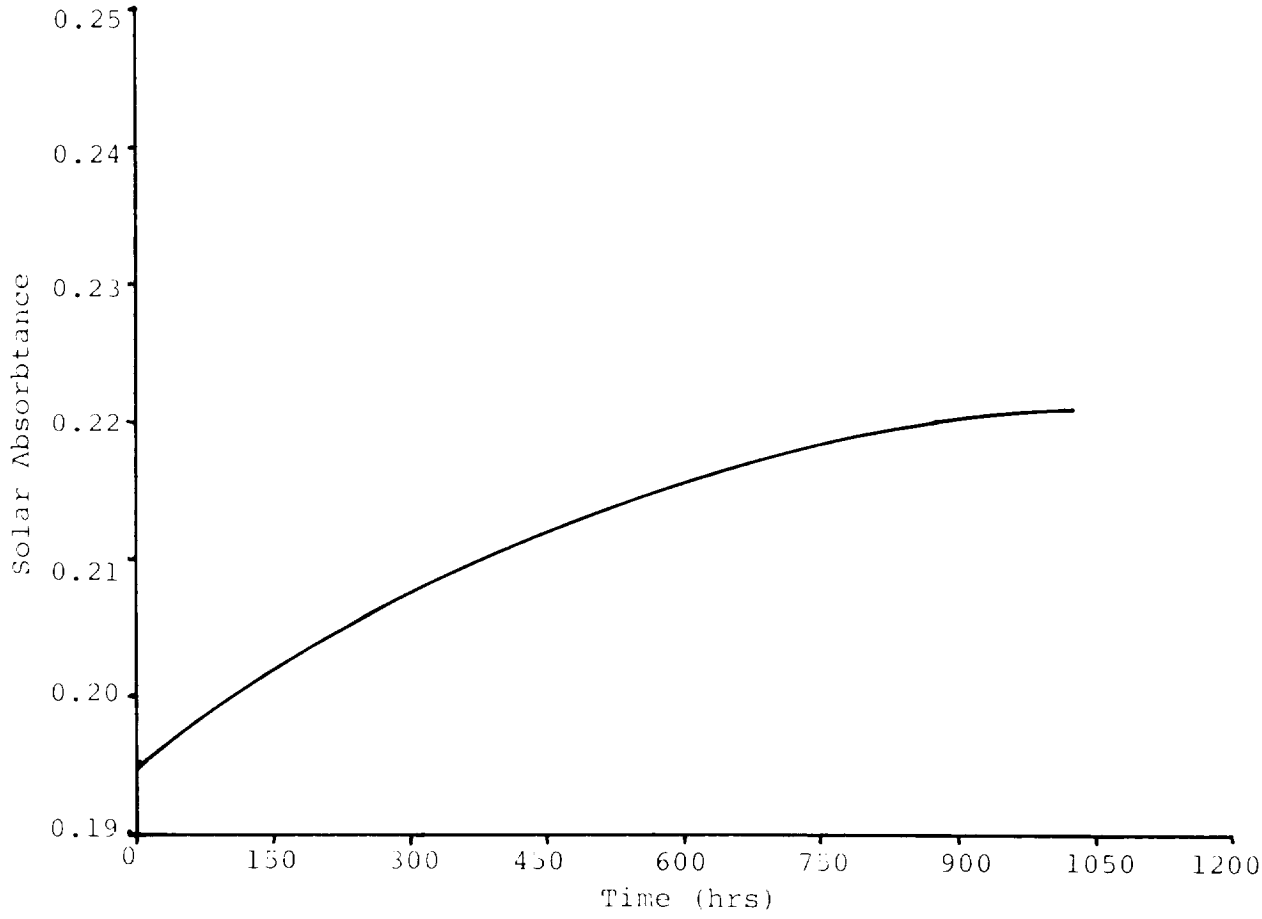

Figure 9 - Change in Solar Absorbtance

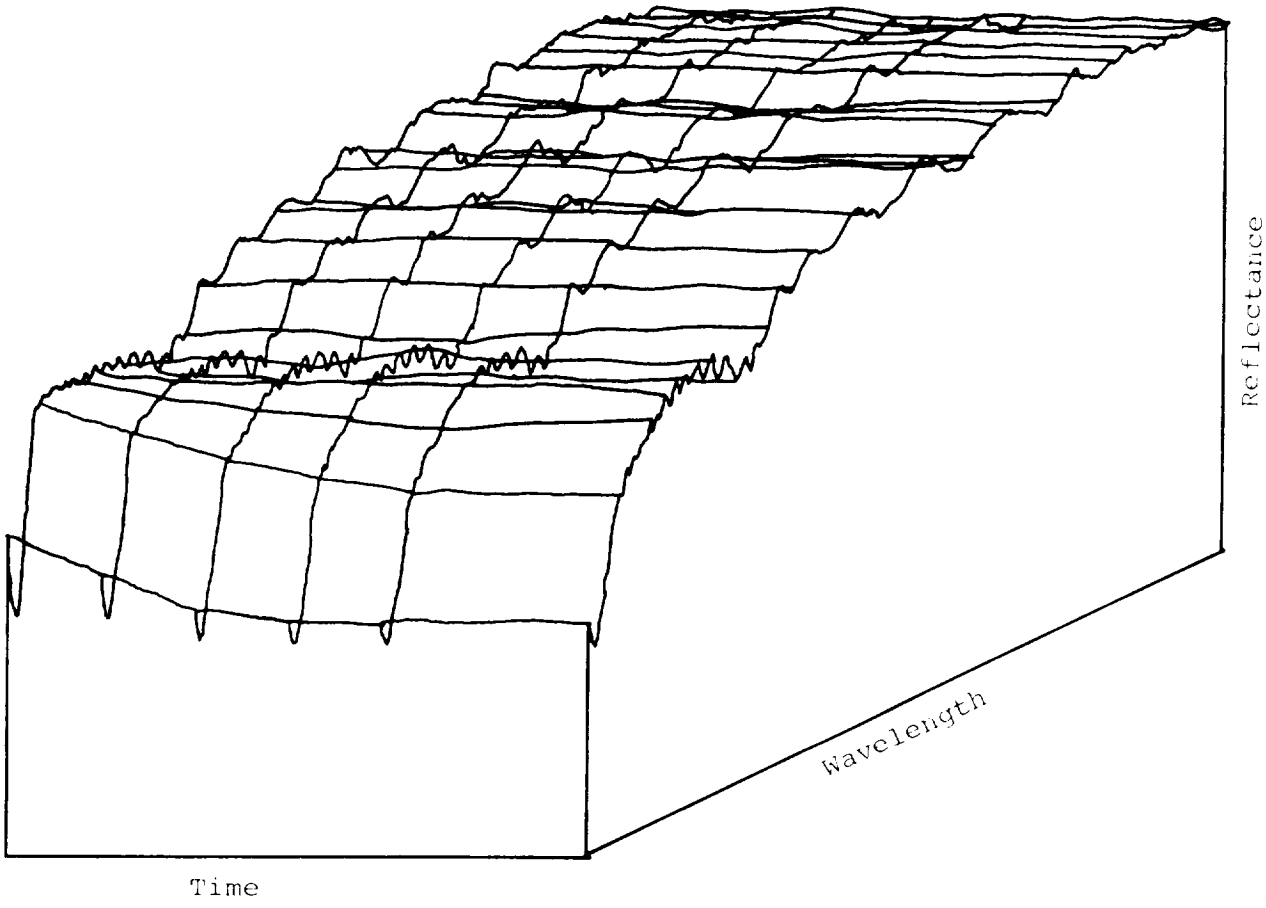

Figure 10 - 3-D Plot of Spectral Reflectance vs. Time

STANDARDIZATION IN SOFTWARE CONVERSION OF (ROM) ESTIMATING

Glen H. Roat
Martin Marietta Denver Aerospace

ABSTRACT

Technical problems and their solutions comprise by far the majority of work involved in space simulation engineering. But space simulation is a business, a business where a service is provided to a customer for a fee. These customers are becoming more cost conscious in these days of tighter budgets and more stringent schedules. Fixed price contracts with schedule award fees are becoming more and more prevalent. Accurate estimation of these jobs is critical to maintain costs within limits and to predict realistic contract schedule dates. Computerized estimating may hold the answer to these new problems, though up to now computerized estimating has been complex, expensive, and geared to the business world, not to technical people. The objective of this effort was to provide a simple program on a desk top computer capable of providing a Rough Order of Magnitude (ROM) estimate in a short time. This program is not intended to provide a highly detailed breakdown of costs to a customer, but to provide a number which can be used as a rough estimate on short notice. With more debugging and fine tuning, a more detailed estimate can be made.

INTRODUCTION

Problem; a potential customer calls wanting to know a rough figure on the cost to perform a five day thermal vacuum test on his black box. He needs the number in thirty minutes to give to his boss.

His question actually poses two problem areas. The first is his lack of information about his test article and environmental constraints and the second is his time limit for the estimate. This occurs frequently in the Martin Marietta Corporation Space Simulation Laboratory (SSL). Most often the potential customer simply does not know the right questions to ask and, unaware of the difficulty of making an accurate estimate even with sufficient information, he does not allow enough time for the estimator. The problem can be compounded by an estimator that does not gather sufficient information from the customer before making the estimate.

Asking the proper questions of the customer and calculating the estimated cost in a limited amount of time are both performed well by a computer. The questions the computer asks and the estimated cost it calculates are at least highly consistent.

The questions that are asked in the program are taken from SSL's estimate sheet. The sheet has been used for many years to aid engineers in asking customers the questions pertinent to thermal vacuum tests. The sheet has been revised and updated many times during its years of use and is complete in identifying tasks associated with testing in the MMC SSL vacuum chambers and

thermal chambers. This made the job of identifying thermal vacuum tasks for the computer to address much easier.

The job of establishing a method of calculating task hours was the more difficult one. Many tasks require subjective thinking on the part of the estimator, an ability not possessed by a computer. Therefore, a general rule has to be made, one that a computer can apply. The rule uses a difficulty based on the size of the chamber used and the complexity of the test article configuration. Each size category of chamber that SSL uses is assigned a difficulty level to a task relating to chamber size. The assigned number is the number of men needed to run the chamber per shift, the equation was derived by trial and error. Configuration complexity is determined as the questions are answered by the customer. For example, when thermal plates are used the computer asks:

"Enter the statement number that describes the thermal plate that is required." The choices are:

1. Ready made, standard cold plate.

2. Standard cold plate with intricate mounting.

3. Thermal plate controlled with heater tape.

4. Custom designed heating and cooling loop.

The statements are in order of difficulty from 1 - the easiest, to 4 - the most complex. The statement number chosen is then used in an equation to determine the hours required to design, build, install, and leak check the thermal plate. As the attached example shows, this type of question is asked more than once in the program.

Once the computer program has completed the questionaire and numbers representing manhours required for each task are either assigned or calculated, totals are then calculated. The totals are separated into two groups; non-recurring figures, such as procedures and fixtures, and recurring figures such as the test itself. Since this program is a ROM estimate, the individual categories such as procedures and test are not broken down in the totals section.

Finally, time function consumables are calculated using a cost per hour as specified by MMC for each piece of equipment. This multiplied by the length of time the equipment is used produces a total cost for use of the equipment. Time function consumables include such things as chamber pumps, solar lamps and liquid nitrogen. Solar simulation is of particular interest as its cost for a long-term test can be very high.

CONCLUSIONS

Since the program was first written it has been tested by inputting information known about tests that have been completed in SSL and comparing

the computer generated figures against those actually recorded. Though individual numbers were not pinpoint accurate, the totals derived by the program were all within 20% of the actual figures used and most tests were within 10%. Appendix A shows a sample of such a test. More work can be done on the program to help provide a higher degree of accuracy to the individual tasks so that true estimating can be accomplished with it. For now the program is checked against actual estimates and used to give quick ROM estimates as it was intended.

APPENDIX A

The following is an example of the program questions, operator response, and computer print of final copy on plotter. The example is a 120 hour test in the 6 x 15 chamber with requirements as follows:

A) Requirements

1. Environment Temps: -70 to 140^{o}F
2. Thermal Plate Temp: -40 to 104^{o}F
3. SSL Will Install 30 T/C's
4. IR Required: 4,000 w/m^{2}, 2 ft^{2} Area
5. Solar Required (3ft Dia): 15 Hours Operation
6. No Shadow Shield
7. Two (2) Thermal Plates Both Custom Design
8. Mount Off Chamber Floor
9. Three (3) MicRIcon Loops
10. No Mech Actuation

B) Computer Program (On succeeding pages, the computer program shall be typed in two (2) columns.)

SSL ROM Program, answer all questions in deg F, W/M^{2} and NA if not applicable.

```
I.  Test Conditions
    A) Which Chamber Or Cold Box
    ?
    6X15
    B) Vacuum Required (Y Or N)
    ?
    Y
    C) Hours at Vacuum
    ?
    120
    D) Environment Temps (High,Low)
    ?
    140,-70
```

```
E) Thermal Plate Temperature
(High,Low)
?
104,-40
F) Will SSL Install The T/C's
(Y Or N)
?
Y
   1. Number Of T/C's Needed
?
30
G) IR Required (Y Or N)
?
Y
   1. Heat Flux Required (W/M2)
?
4000
   2. Area To Be Lighted (Ft2)
?
2
   3. Hours Of IR Operation
?
120
H) Solar Required (Y Or N)
?
Y
   1. Power Needed In Solar
Constants
?
1.0
   2. Diameter Of Article To Be
Lighted
?
3
   3. Hours Of Solar Operation
?
15
   4. Is A Shadow Shield
Required
?
No
 I) How Many Thermal Plates Are
Needed
?
2
Plate Number              1
  A. Enter The Statement Number
That Describes The Thermal Plate
That Is Required
  1. Ready Made, Standard Cold
Plate
  2. Standard Cold Plate With
Intricate Mounting
  3. Thermal Plate Controlled
With Heater Tape
  4. Custom Designed Heating And
Cooling Loop
?
4
Plate Number        2
  A. Enter The Statement Number
That Describes The Thermal Plate
That Is Required
  1. Ready Made, Standard Cold
Plate
  2. Standard Cold Plate With
Intricate Mounting
  3. Thermal Plate Controlled
With Heater Tape
  4. Custom Designed Heating And
Cooling Loop
?
4
 J) Enter The Statement Number
 That Describes The Test Article
 Mounting Fixture
   1. None
   2. Suspension
   3. Mount On Cold Plate
   4. Support Off Chamber Floor
   5. Support Off Gimbal
 ?
 4
K) If A Micricon Is To Be Used Enter
 The Number Of Loops, If Not,
 Enter 0
 ?
 3
L) Is Mechanical Actuation Needed
 Inside The Chamber (Y Or N)
 ?
 N
 I. Non Recurring
  A. Eng Mhrs =          136.5
  B. Tech Mhrs =         168
 II. Recurring Totals
  A. Eng Mhrs =          177.6
  B. Tech Mhrs =         470.4
 III. TFC's
  A. Chamber =           540
  B. Infrared =          10.8
  C. Solar =             847.35
```

IV. Liquid Nitrogen
  A. Gallons = 36000
  B. LN2 Dollars = 9000
 V. Total Eng Mhrs = 314.1
VI. Total Tech Mhrs = 638.4
VII. Total TFC & LN2 = 10398.15
VIII. Material = $3849

FATIGUE INDUCED CRACKING IN ALUMINUM LN_2 SHROUD OF 39 FOOT VACUUM CHAMBER

Arthur A. Edwards

Ford Aerospace and Communications Corporation

Western Development Laboratory Division

Palo Alto, California

INTRODUCTION

ABSTRACT

Fourteen years after completion of Ford's 39-foot space simulation chamber, leaks began to appear in its LN_2 shroud. Although the shroud had been tight since its acceptance, cracks appeared in 1983 in some of the field welds of the one inch tubes which interconnect the LN_2 panels. The resulting leaks were large enough to prevent pump down to high vacuum and could be heard easily when the chamber was at ambient conditions. New cracks appeared during each thermal cycle making it impossible to utilize the chamber for thermal vacuum testing.

FACILITY DESCRIPTION

Ford's space simulation facility was built in the late 1960's by CVI Corp. and PDM Corp. It is a 39-foot diameter sphere (See Figure 1) constructed of 304 stainless steel, and is pumped to high vacuum by 20 K cryogenic pumps. The cold body of outer space is simulated by an aluminum shroud (See Figure 2) which completely surrounds the 30-foot diameter work space. Liquid nitrogen is circulated through the shroud at 100 psig pressure to provide low temperature simulation. The extruded shroud panels are made of 1100 aluminum and the interconnection tubing is made from 3003-H14 aluminum. The shroud is loosely suspended and interconnected to allow the panels to move during thermal cycling without restraint as shown in Figure 3.

PROBLEM

During 1983, leaks began to appear in the LN_2 shroud, and by November achieving high vacuum was impossible. As a consequence, thermal vacuum testing of the Intelsat V spacecraft was halted while all efforts were made to identify and solve the problem. It is interesting to note that all of the leaks were caused by cracks in the aluminum tubing that interconnects the shroud panels (See Figure 4). The cracks typically appeared in the heat-affected zone adjacent to welds made in the field and usually occurred during the cool down cycle.

HISTORY

Discussion with several aerospace companies revealed that others had experienced similar problems. It was learned that most of the companies whose chambers had developed leaks in their shrouds had decided that it was technically and economically more feasible to replace the entire shroud than to attempt to repair it. There seemed to be no agreement regarding the mechanism of the tube failure, nor was anyone optimistic about finding an economical solution to the problem. There was general agreement however that the replacement of Ford's LN_2 shroud would cost approximately $1 million.

INVESTIGATION

In its effort to find a solution to the problem, Ford hired Aptech Engineering Services of Palo Alto to perform an engineering evaluation and make appropriate recommendations. Although Aptech had no previous experience with vacuum/cryogenic facilities, they had performed failure analysis and engineering evaluations of nuclear reactor and fossil fired boiler facilities with emphasis on metallurgy, stress analysis, weld failures and fatigue cracking. The first task was the identification of a plan to effect whatever repair or replacement would be necessary to return the shroud to its normal operating condition.

PLAN

The plan was separated into two phases. The object of the first phase was to return the facility to operation as rapidly as possible, and the object of the second was to identify and accomplish a permanent solution so that future testing could be planned with a high degree of reliability. Before either phase could be accomplished, information was needed which would help to describe the mechanics of the tubing failure. It was necessary to acquire more data regarding the movement of the shroud and thermal gradients within the components as well as a sample of the cracked tubing.

DATA GATHERING

Data describing the thermal gradients along and between panels would have been difficult to obtain without the installation of thermocouples at various points along the LN_2 path. This was possible but expensive to accomplish and unnecessary since calculations could predict with sufficient accuracy overall pressure and temperature excursions during cool down. The measurement of relative panel movement was accomplished with a scratch measuring device designed by Ford and shown in Figure 5. The device was attached to two adjacent panels in seven locations and measured the relative movements between the two panels during cool down by leaving a permanent mark on the carbon coated surface. The sample of a cracked weld was obtained by the removal of a tube section around a crack as shown in Figure 6. The sample was examined in Aptech's lab and was the basis for most of the metallurgical and stress related conclusions reached.

RESULTS OF INVESTIGATION

METALLURGICAL EXAMINATION

A low magnification macrograph of the polished and etched cross section of the sample crack is shown in Figure 7 and shows the cracks and weld fusion line clearly. Note the reverse curvatures and changes in thickness along the cross section and the localized necking at the main crack location. These features are indicative of incipient plastic collapse which would make quantitative analysis of the operative stresses and strains nearly impossible. Although the crack appears to be located far from the weld tip in this picture, it is deceptive because the crack actually started at the tip of a protruding portion of a weld scallop and grew tangent to the curvature at the tip. Photomicrographic analysis revealed that the major crack was characterized by a blunt crack tip, and a wide opening at the surface with occasional branching, all of which are indicative of large deformation in a ductile material. A micro-hardness survey taken along most of the sample length showed a softening of the aluminum in the heat affected zone (HAZ) of the weld. This would tend to concentrate strain even in the absence of geometric factors and cause a local hardening where the cyclic deformation actually occurred. The peak hardness was unquestionably at the strain field associated with the main crack.

Observation of the opened crack surface in the scanning electron microscope revealed elliptical marks that document the step-wise advance of the crack from the outside to the inside of the tube wall (Figure 8). Each mark represents a position at which the crack arrested; thus the distance between marks is a measure of crack front movement with each deformation cycle. In other words, the leaks in the tubing are the result of crack initiations and growth by a low-cycle fatigue process. Note that the crack arrest lines are not the same as high cycle fatigue striations. Here, each cycle consists of a striation and a region of ductile tearing (Figure 9).

RELATIVE PANEL MOVEMENT

Seven scratch gauges were installed in representative locations around the shroud so that the relative movement of typical panels could be recorded. After completion of a pump-down and thermal cycle the gauges were removed and analyzed as shown in Figure 10. All gauges clearly showed the nonlinear behavior of the relative motion of the two ends of the U-bend, and some showed that the motion did not start and end in the same spot. These observations support the conclusion that the motion tended to be in a "slip stick" manner which made analytical modeling extremely difficult. The motion appeared to be nearly horizontal on the gauges located on upper U-bends while those on the lower U-bends indicated some vertical motion of greater magnitude. Because of the relatively small sample size, it is possible that displacements larger than the 1/2 inch horizontal and 3/8 inch vertical actually seen existed at other locations in the chamber. However, it will be shown that the maximum calculated motion compares favorably with the values measured.

CALCULATIONS

Steady State Analysis

Calculations showed that it is possible for the panels to move as much as 0.45 inch for a typical excursion from ambient to cryogenic temperatures. Thus it appears that there was good agreement between predicted and measured displacements between adjacent panels. The next step in the analysis was to predict the stress levels in the U-bend welds and compare the life predictions based on these stresses with the actual history of the chamber. For a 1/2-inch deflection, the nominal bending stress on the tube in the region of the field weld was 30.0 klb/in^2 and 22.9 klb/in^2 in the elbow, including stress intensification effects due to internal pressure. The geometry of the weld was such that a stress concentration existed at the weld. Conservatively estimating the stress concentration factor for the weld to be 2.5, the concentrated stress at the weld was 75.2 klb/in^2. However, the material yield strength is only 21 klb/in^2. As a result, significant plastic deformation occurred, the peak stress was limited to about 22 klb/in^2, and the amount of plastic strain was estimated to be about 0.022. Because the peak stress was due to a combination of stress concentration and a bending stress field, the peak stress was high enough that the tube should have failed by plastic collapse. In fact, several of the tubes were observed to contain signs of plastic collapse. Because the system was loaded by displacement control, the onset of plastic collapse supplied compliance to the system, resulting in a drop-off in loading, and therefore, total collapse of the tube did not occur. The local plastic strain, however, might well have induced a low cycle fatigue failure. In comparing the available data on cyclic life versus stress range of 3003 aluminum it can be seen that the 22 klb/in^2 peak stress exceeded the low cycle fatigue strength given. Because the material cyclically softened it experienced progressive plastic flow

(racheting) which led to failure in a relatively low number of cycles (i.e., less than 100).

Transient Analysis

Cool Down--Four modes (or phases) of heat transfer occur during panel cool-down from ambient to cryogenic temperature.

Phase I is that of forced gas convection. The nitrogen gas is bled through the cryopanel tubing under its own tank pressure. The cyropanel temperature is high enough so the flow is almost entirely cool nitrogen gas. During Phase I, the heat transfer coefficient used in calculations is based upon forced convection alone.

Phase II is film boiling. This phase occurs as the cyropanel temperature begins to approach the temperature of liquid nitrogen (approximately at 130°F temperature difference). In this phase, conditions permit the nitrogen to be in liquid form in the center of the cyropanel tubing and gaseous form at the tube inner surface. A thin nitrogen gas film exists between the liquid nitrogen and the metal of the tube. The heat transfer coefficient during Phase II is based upon this liquid/gas combination.

Phase III is nucleate boiling combined with forced liquid convection. This phase occurs when the temperature difference between the cryopanel and the liquid nitrogen reaches about 60°F. Some of the liquid nitrogen then comes in direct contact with the metal wall of the tube. There are still bubbles of nitrogen gas at the wall-liquid nitrogen interface. Due to the flow of liquid nitrogen in contact with the tube interior wall, forced liquid convection exists in addition to nucleate boiling. A computer run of the simulations indicates that the greatest rate of temperature change occurs during Phase III.

Phase IV is entirely forced-liquid convection heat transfer. The temperature difference between the tube wall and the liquid nitrogen is not great enough to produce any gaseous nitrogen.

Comparison of the measured and simulated shroud temperature showed that there is reasonable agreement between the two. The simulation predicted a higher rate of temperature change than the thermocouple data indicated in the region of rapid temperature change, thus making the computer model conservative for these purposes.

All thermocouple data indicated that there is a higher rate of temperature change during cool-down than during warm-up.

Summary of Heat Transfer Calculations

The greatest rate of temperature change during a complete thermal cycle occurred during Phase III of panel cool-down (nucleate boiling

combines with forced liquid convection). The greatest temperature change during any period was 35°R. Therefore, the maximum temperature difference between any two adjacent panels was about 35°R.

The upper bound estimate of the peak transient temperature difference between the inlet of one cyropanel and the exit of the subsequent cyropanel was 70°R. Applying the same boundary conditions that were used in the steady state analysis, the maximum possible deformation of the U-bend would be 0.080 inch. Analysis indicated that this resulted in a peak stress of 16 klb/in^2 at the weld, which was below the aluminum's strength. Thus, there is no analytical evidence to support a conclusion that the cracking phenomenon was due to transient thermal events.

CONCLUSIONS

Based on this analysis, it can be postulated that the cracking was due to a low cycle fatigue mechanism which was driven by the thermal strain associated with the steady state temperature cycling (+70 to -320°F). The resulting thermal strains are sufficiently large to cause significant plastic strain during each cycle. Because the material cyclically softened, it suffered progressive plastic flow during each cycle resulting in a racheting-type failure. There is no analytical evidence that the rate of cool-down or warm-up had any significant effect on the fatigue failures.

The steady state and transient analysis provide a strong indication of the sources of relative motion leading to the imposition of strain on the U-bend connections between adjacent panels. Since the source was most likely the steady state temperature difference between ambient and the liquid nitrogen temperature, the strain arising from metal contraction must be accomodated in such a way so as not to cause failure of a component pressure boundary by repeated strain (or the resultant stress). Attaching the U-bend to the cyropanel with a fillet weld constitutes a strain concentrator at the weld joint. Mitigation of the effects of the strain can best be accomplished by increasing the ability of the U-bend to accept the strain without consequential failure.

Of particular importance is the fact that the characteristics of the crack sample strongly suggested that the cracks started on the outside surface of the tube. Thus, crack detection by visual methods such as dye-penetrant inspection is eminently reasonable. Although a network of small cracks was also found on the inside surface of the tube, it could be concluded from their number and from metallographic evidence that these cracks were not the main threat to system integrity.

Following are the salient points from metallurgical investigation:

- The through-crack and some secondary cracks originated on the outside surface of the piping connector, at the toe of the weld.

- The through-crack advanced from outside to inside of the tube in discrete steps.

- Each discrete advance of the fatigue crack was associated with a cool-down and heat-up (test) cycle of the space-simulation chamber.

- The low-cycle fatigue process observed here was characterized by unusually large deformations (strains).

IMPLICATIONS OF THE METALLURGICAL OBSERVATION

Spacing between crack arrest lines were measured on photographs from which the following can be summarized:

- Spacings between adjacent crack arrest lines did not change systematically with location on the fracture surface; i.e., for all intents and purposes the fatigue crack advanced uniformly per cycle. This is characteristic of displacement (or strain) controlled fatigue, since under stress control, one would expect the spacing to increase as the crack grew through the section.

- The frequency of occurrence of crack-arrest spacings peaked fairly sharply at the spacing intervals 0.0015 inch. Thus, for a wall thickness of 0.050 inch, the total number of crack arrests (or cycles) to generate a through-wall crack is 31 for the most frequent spacing, or 33 for the average of the spacing range.

It has been estimated that the chamber has experienced between 75 and 125 thermal cycles, or tests. About one hundred cycles will be assumed for simplicity. If crack propagation across the wall thickness takes about thirty cycles, then crack initiation must be accomplished in about seventy cycles. Two other investigations agreed closely on the number of cycles experienced before crack initiation occurred in aluminum alloys subject to low-cycle strain-controlled fatigue. For initiation in 70 cycles (140 reversals), approximately 0.02 plastic strain amplitude (0.04 plastic strain range) is required in alloy 1350-H17, which is similar to the 3003-H14 in the piping connectors.

Although the estimate of 0.02 plastic strain amplitude for crack initiation in 70 cycles is large, it is consistent with the appearance of the sample in Figure 7. In addition, cyclic strain was also estimated from the stress analysis. In order to convert from virtual stress to local strain, it was necessary to extrapolate beyond the stress-strain range and the results must be regarded as only qualitative. Nevertheless, the estimate of 0.022 strain is of the right order of magnitude.

One other comment may be worthwhile concerning cyclic deformation of these aluminum piping connectors. Tubes have cracked at the toes of the welds joining the U-bends to the cyropanels. In other words, the cracks were initiated in the HAZ of the tubes, and it may be asked if the fatigue analysis has accounted for that fact adequately. It is a fact that most aluminum alloys have similar resistance to strain (displacement) controlled fatigue within 50 to 500 cycles. Thus, the softened HAZ in 3003-H14 tubes will deform before the surrounding material, and thereby concentrate the strain. The cyclic life at that local strain, however, would be little different from the life of a specimen of bulk material cycled at that same strain.

The main feature about this situation is that strain concentrations do, in fact, occur by virtue of geometric and material property factors. Therefore, mitigative actions must be directed at reducing the stress and strains at the failure locations to values consistent with the forseeable cyclic life of the space simulation chamber. In other words, adequate not infinite life is required.

CORRECTIVE ACTION

PHASE ONE

In order to return the chamber to operation, a plan was initiated that would allow the identification of potential crack areas and effect repairs before leaks appear. To locate cracks, a dye-penetrant test procedure was developed, and Ford personnel were trained in the process.

The dye-penetrant technique was chosen for this application due to its inherent reliability in locating small surface defects and its relatively low cost. Quantitatively analyzing the probability of detecting fatigue cracks in aluminum as a function of flaw size/surface finish with loading and NDE technique indicates that the probability of finding surface fatigue cracks using penetrant inspection is large for cracks that are deeper than 0.035 inch and/or longer than 0.15. Since the thickness of the tube is 0.050 inch, it can be assumed that fatigue cracks which initiate from the outside surface of the tube should be detected with 0.015 inch of tube thickness remaining. Since the striation spacings (depth of the fatigue crack advancement per cycle) were found to range from 1 to 4 mils, it can be assumed that after a tube has been inspected, 3 to 15 thermal cycles can be applied without causing the tube to leak.

All field welds were dye-checked and nine cracks were discovered in various stages of development. The cracks were ground out and rewelded, and cool-down cycles were run to verify that all leaks were repaired and the potential for future leaks reduced. The technique worked for the first stage solution and allowed the thermal vacuum testing to continue with little or no delay.

It should be remembered that this repair scheme does not remove all of the fatigue damaged material but only that material near the major cracking. Local weld repair of cracked regions will not result in significant improvements in future reliability since fatigue initiation will be very rapid in the nearby damaged material not removed during repair. Probability calculations indicated that no more than three thermal cycles should be run between dye check tests on the tubing. Perhaps the most efficient technique would be to check one-third of the shroud welds between each test on those U-bends which are not replaced.

PHASE TWO

The analysis performed indicated that the cracks were the result of large movements between LN_2 Panels causing stress concentration in the heat affected zone of the jumper tube welds. Mitigation of the effects of the strain could best be accomplished by increasing the ability of the U-bend to accept the strain without consequential failure.

Ideally, a rubber hose joint capable of taking the pressure load while retaining its flexibility at a low temperature ($-320^{o}F$) would solve the problem. However, it is impossible to find an elastomer that does not become brittle and is easy to join to the aluminum cryopanels with a leak-tight fitting. Metallic flexible hoses using corrugated metal bellows have been successfully used, but the most common material that has been used at cryogenic temperatures is stainless steel. The flexibility and ability to accept displacement in three axes (most strain in two axes with a small component in the third axis) is available but the problem of making a leak-tight connection to the aluminum piping remains.

During this investigation, the principal known suppliers of flexible hose connections were contacted; none offered an "off-the-shelf" item that would satisfy the specified requirements. Those that were available still required some development and qualification testing. No doubt the vendor who develops a weldable, flexible, leak-tight aluminum hose connection will have a large market.

A mitigative design which increases flexibility and provides a leak-tight, welded connection can be made from a single turn loop tubing connector using a stronger, weldable aluminum alloy such as 6061-T6 (Figure 11). In order to assess the integrity of this potential fix, a steady state analysis of this design was performed and the results are summarized below.

Assuming that a single loop with the maximum possible diameter (13 inches) is used, and the ends are displaced by 1/2 inch, the maximum stress would occur at Point A in Figure 11. At this point, the peak bending stress is 20.9 klb/in^2, compared with 20.3 klb/in^2 and 20.6 klb/in^2 at Points B and C, respectively. The peak nominal stress is lower than for the U-bend, and it occurs in a region away from welds or

other geometric stress concentrations. The high cyclic stress within the loop itself (Points A and B) can be accommodated by using material such as aluminum alloy 6061-T6 for the loop. Compared with the 25 klb/in^2 yield strength at -320°F of 3003-H14 or 9 klb/in^2 yield strength (-320°F) of 3003-0, alloy 6061-T6 has a yield strength of 40 klb/in^2 at room temperature which increases to 47 klb/in^2 at -320°F. The cyclic properties are correspondingly improved. The 5 x 10^8 cycle limit for 6016-T6 in reversed bending at room temperature is 14 klb/in^2 compared to 9 klb/in^2 for 3003-H14.

However, because of possible interferences, the welded connection to the extrusion cannot be made at Point C, consequently a short riser must be used, which causes an increase in moment (and therefore stress) at the location of the weld. Assuming that the weld is made at the top of the extrusion, approximately 7 inches below Point C, the nominal stress at the weld is 22 klb/in^2. Again assuming a stress concentration factor for a butt weld of 2.5, this design results in a peak stress of 55.4 klb/in^2, which means that there will be some plastic deformation along with the possibility of low cycle fatigue. This risk can be minimized by using a socket weld, which causes the largest part of the stress concentration to be on the stronger 6061-T6 material.

Another simple solution can be accomplished by replacing the U-bends with new U-bends that have longer risers. This can be done with the same material or a stronger material such as 6061-T6. With a few exceptions, there is sufficient clearance that the risers on the U-bends could be extended by about 12 inches on upper U-bends and 14 inches on lower U-bends. Assuming that the transition weld is made at the extrusion interface and the U-bend risers are as long as possible without interference from the shell, the peak (concentrated) stress can be reduced from 125 klb/in^2 to 32.4 klb/in^2 at upper and 27.8 klb/in^2 for lower U-bends.

Similarly, the riser could be lengthened for the expansion loops. With the longest possible risers, the peak stress is reduced from 55.4 klb/in^2 to 31.2 klb/in^2 at upper loops and 22.5 klb/in^2 at lower loops. It should be noted that in all these cases, the peak stresses exceed the endurance limit of the 6061 material. Therefore, none of these designs can be considered "infinite life" fixes, but there will be a substantial improvement in life over the existing design.

PANEL SUPPORT SYSTEM

Inspection of the panel connection devices around the shroud (Figure 3) indicated that they are only marginally successful. It seems to be inherent in the design of the system that the joints will not move at equal rates during cool-down or warm-up. Due to unequal friction coefficient, some joints will absorb all of the movement while others will not move, resulting in a "slip-stick" condition. There is a question

whether the panel support system contributes to the stress load on the tubes. If the answer to this question is yes, it would be unwise to modify the U-bends without modifying the support system as well.

COURSE OF ACTION

Although the expanded U-joint made from 6060-T6 aluminum would improve the stress concentration at the weld, it is not a permanent solution. In fact, none of the potential solutions would guarantee that the jumpers would never crack again. Consequently the solution implemented should consider the economic and schedule implications of the chamber operations.

Obviously it is not necessary to replace the entire LN_2 shroud in order to return the chamber to operation. In fact a new shroud of the same design would probably begin to crack and leak after experiencing 50 to 100 thermal cycles as did the original shroud. The question is which solution or combination of possible actions could provide the highest probability of success at the lowest cost with the least impact on scheduled operations.

After careful evaluation of all of the alternatives, the following plan was implemented:

- Dye-penetrant check all field welds and weld those suspected of cracking. (Note, nine cracks, were found and welded.)

- Dye-penetrant check one-third of all field welds before each chamber pump down.

Since dye-penetrant checking accomplishes nothing toward the long term prevention of fatigue cracking, it was decided to effect the modification proposed by Aptech. However, modifications of the U-bends has several disadvantages:

- Cutting the tubes could contaminate the inside of the chamber and the inside of the tube.

- Welding the new U-bends in place of the removed sections could result in more leaks possibly caused by porous welds, holes, cracks or stress concentration.

- The replacement of the jumpers would remove the chamber from scheduled vacuum testing for a long period of time.

- Because no leaks have shown up since the initial dye check, it is possible that the first group of leaks was caused by special factors which do not apply to remaining field welds. Consequently replacement of the jumpers might not be necessary.

Consideration of all of these factors along with Ford's contract obligations and Aptech's proposed solutions resulted in a course of action which basically agrees with their primary recommendation. Since there will be a 6-month period of little or no vacuum testing in the later part of 1984, all of the field welded U-bends will be removed and replaced at that time with new ones. The replacement U-bends will be made of 6061-T6 aluminum and will be a loop design as shown in Figure 11. Necessary steps will be taken to protect the chamber from contamination and all welds will be dye and leak checked.

No change will be and in the panel interconnecting system (Figure 3). Although it is possible that the existing connections are contributing to the tubing failure, it is also possible that a new design could make the situation worse. It would be desirable to have a perfect connection which would allow panels to move freely during cool-down without sticking. Although the existing system is far from perfect, it will be retained in its present configuration.

DISCUSSION

The dye-penetrant checking that was accomplished during Phase I proved to be effective and returned the chamber to operation in a few days. It is interesting to note that no new cracks which have been discovered in the shroud since the initial nine were repaired. It can be argued that the cracks which showed up during 1983 were a delayed result of faulty fabrication techniques, bad material, or especially high strain concentration and that no other cracks are likely to appear in the near future. Unfortunately, Ford cannot afford to gamble on this situation. The cost of a satellite test delayed because of a leaking shroud is far greater than the expense of effecting a relatively permanent repair. Consequently, the decision was made to effect a repair as recommended by Aptech.

FUTURE IMPLICATIONS

The results of this investigation have implications for the design and construction of future LN_2 shrouds. The following points should be considered by contractors and users when designing and installing cryogenic shrouds in vacuum chambers.

- A thorough analysis should be made of the fatigue chacteristics, stress concentration, and strain induced loading on the U-bend and other critical tube locations throughout the shroud. This analysis should be done for the tubes at both ambient and cryogenic temperatures since shroud movement can occur at either. On top of this analysis, a large safety factor should be added to the final design to account for unknown or unusual movements and stresses.

- The panel support system should be carefully designed to allow even movement between panels during cool-down and warm-up. The system should allow this movement without sticking or concentrating strain.

- Work should be done to develop a practical aluminum bellows for use in vacuum/cryogenic environments.

- The shroud should be designed to prevent the use of tube jumpers as hand or foot supports for people climbing around in the chamber.

- Extreme care should be taken in the selection and training of welders who weld aluminum tubes in the field.

- Shroud field welds should be dye-penetrant checked periodically throughout the life of the chamber as a continuing preventive maintenance procedure.

Much has been learned about the design and construction of large space simulation chambers over the past 20 years. Some of the lessons have been learned as the result of material and equipment failures and malfunctions. LN_2 shrouds are an important part of many vacuum chambers large and small, and their continued functioning is essential to the chambers' successful operation. Experience now indicates that it is possible to identify and solve some types of shroud fatigue failures before they become serious.

Unfortunately, Ford's experience is not unusual. The analysis presented here implies that many, if not all, of the aluminum LN_2 shrouds now in use may be in various stages of fatigue failure. The probability is high that fatigue cracks are working through the aluminum tubing in heat-affected zones of some field welds. The cracks may not be apparent yet, but after the shroud has experienced a certain number of thermal cycles these cracks will work through the material and become serious leaks. Fortunately, appropriate planning, analysis, and checking can, with a relatively small expenditure of money, help to avoid large and unexpected shroud failures and keep the chamber operational as long as it is needed.

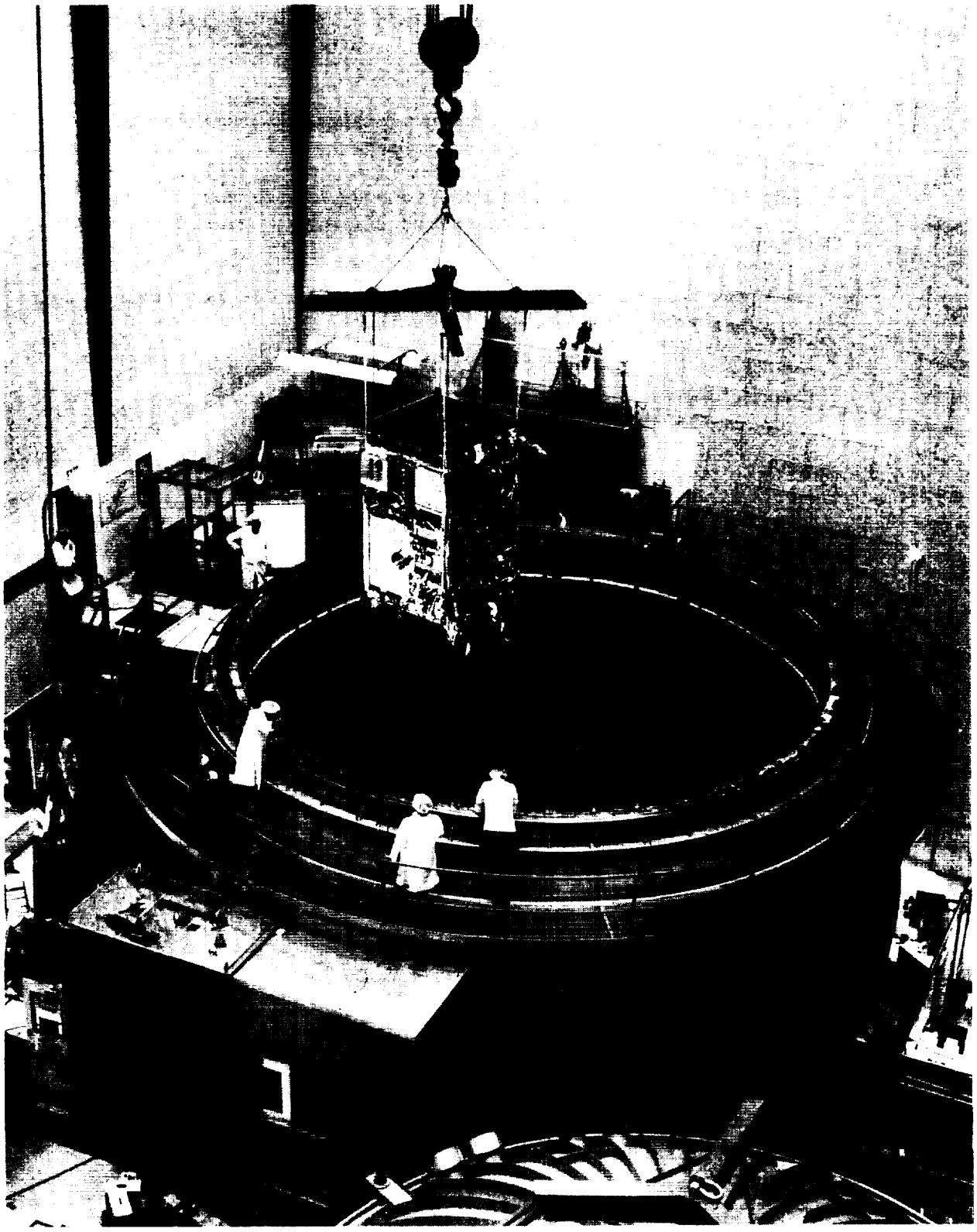

Figure 1 - 39′ Spherical Space Chamber

Figure 2 - LN_2 Shroud

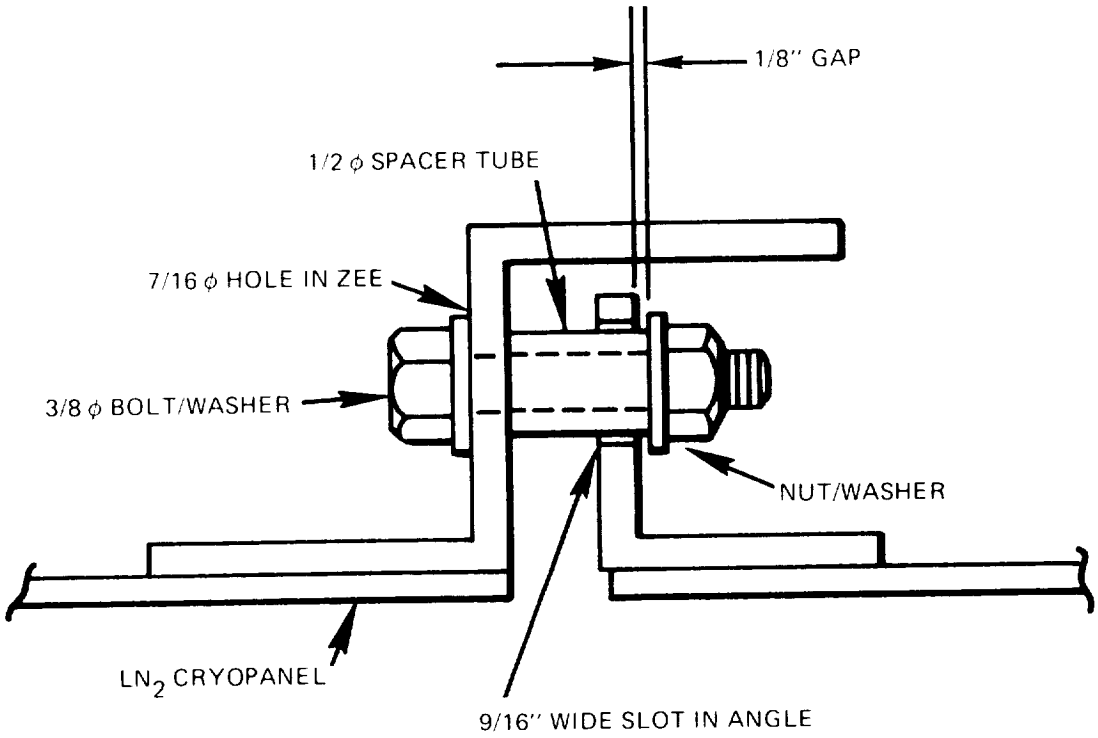

Figure 3 - LN_2 Panel Vertical Suspension System

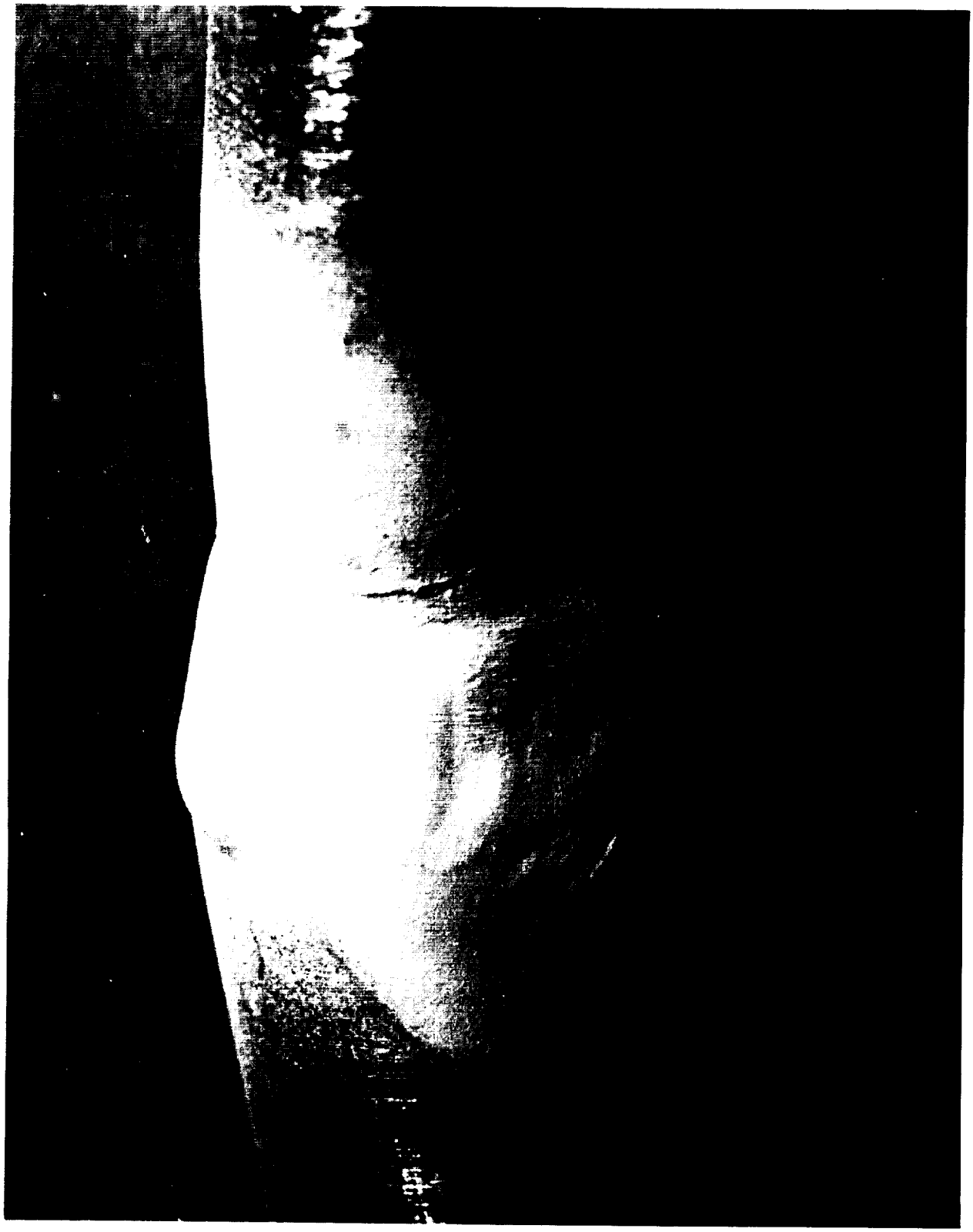

Figure 4 - Typical Cracked Tube

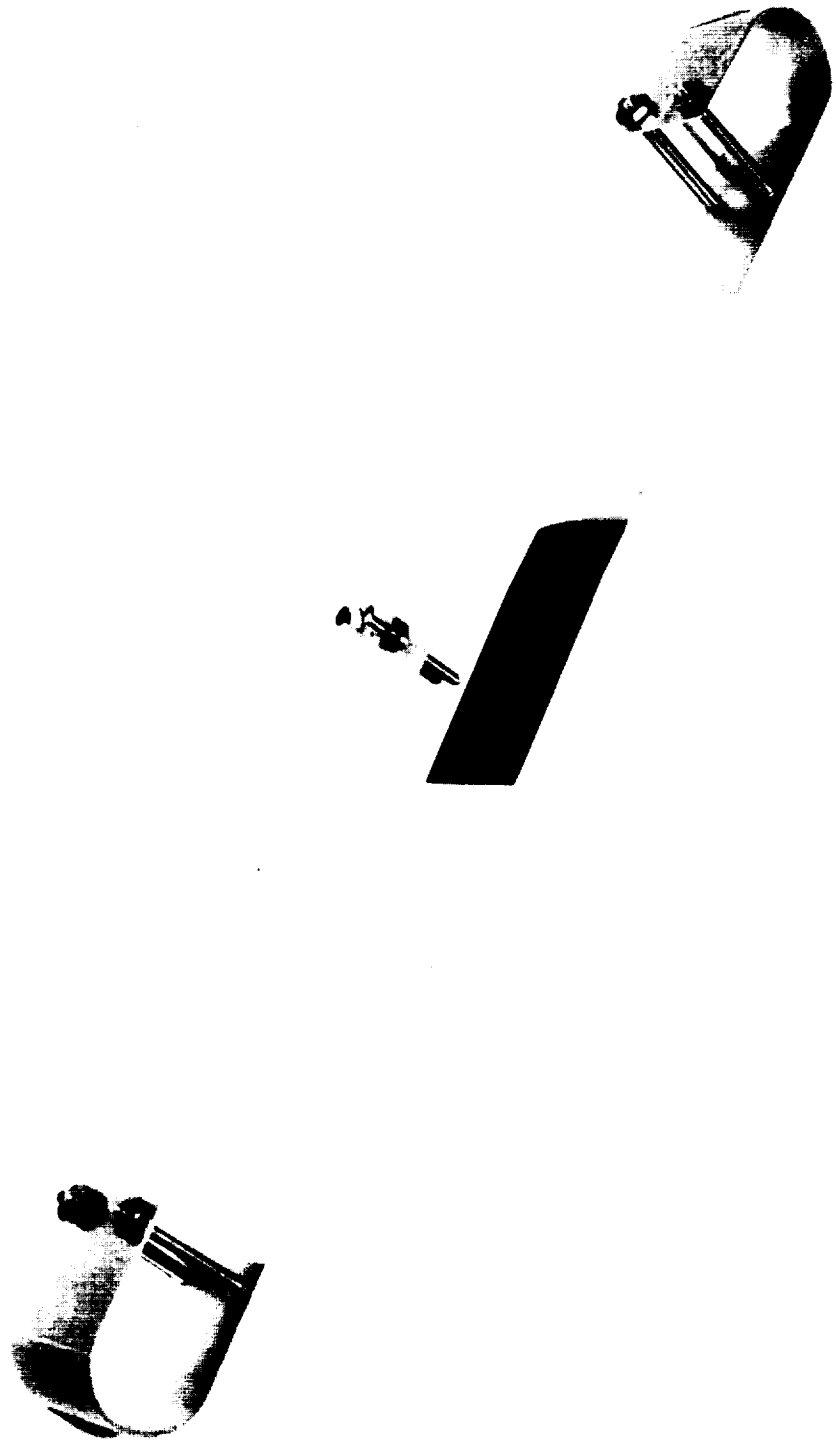

Figure 5 - Scratch Marker

Figure 6 - Cracked Tube Sample

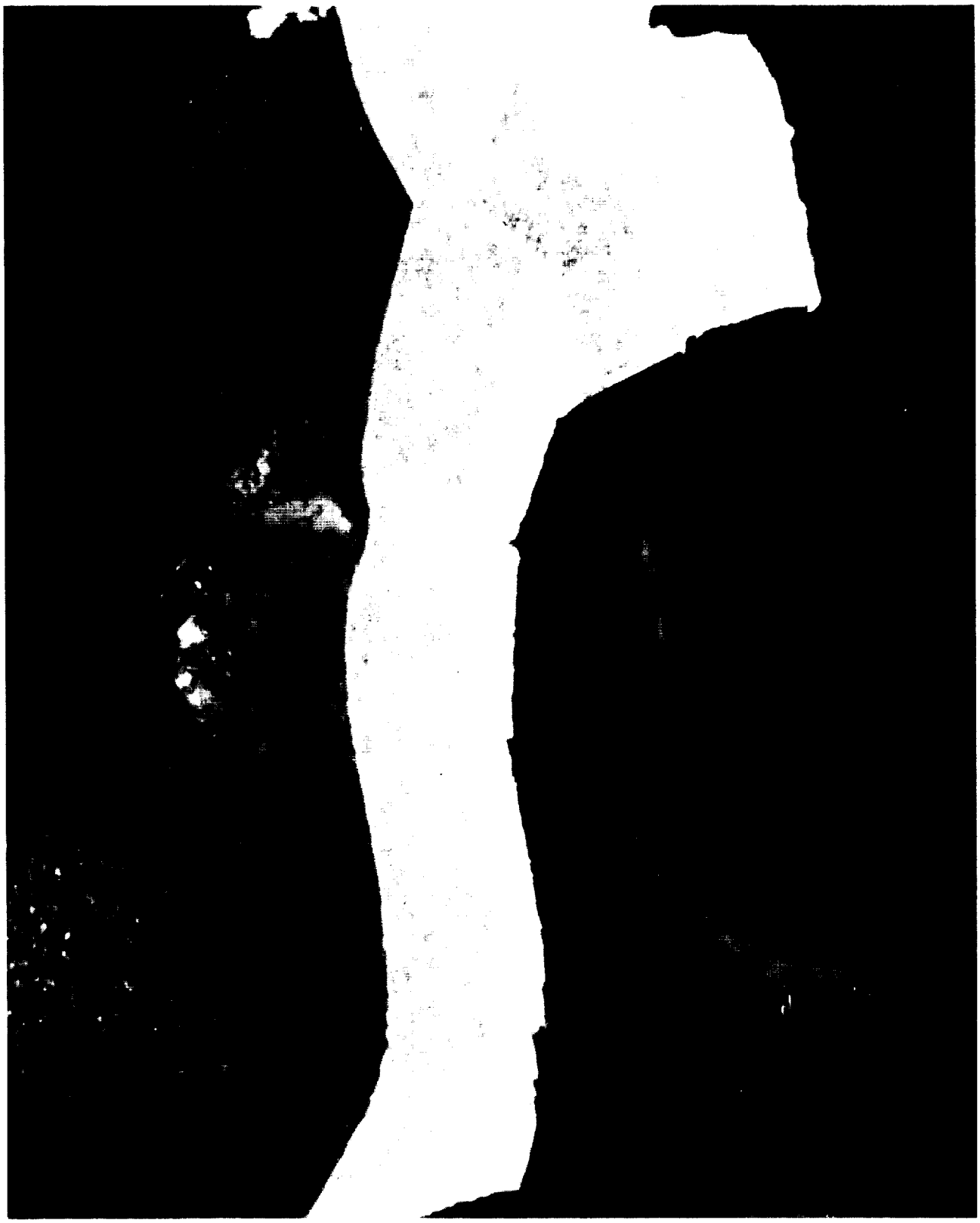

Figure 7 - Metallurgical Cross Section of Weld Showing Cracks

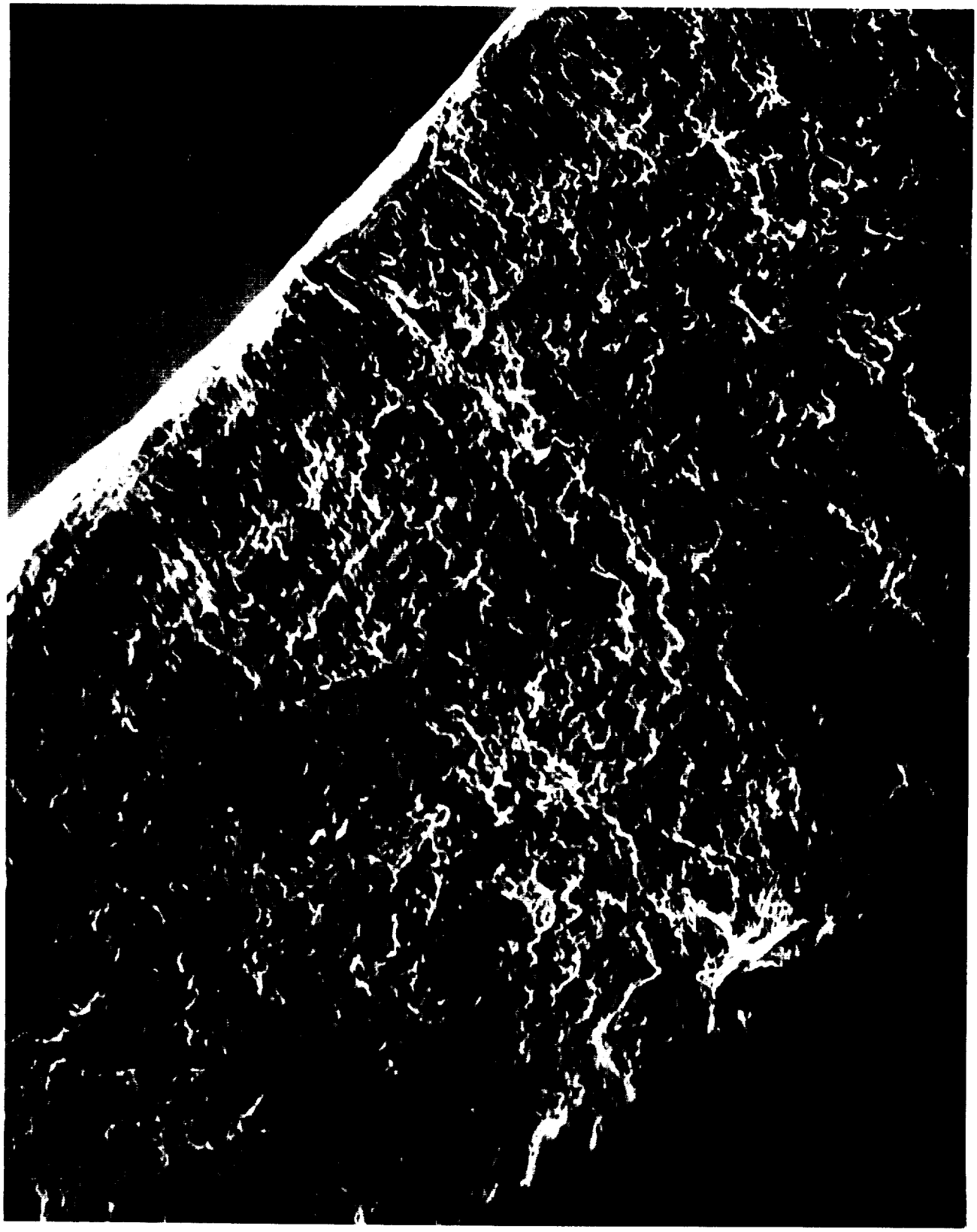

Figure 8 - 60X Magnification of Fracture Surface

Figure 9 - 1000X Magnification of Fracture Surface

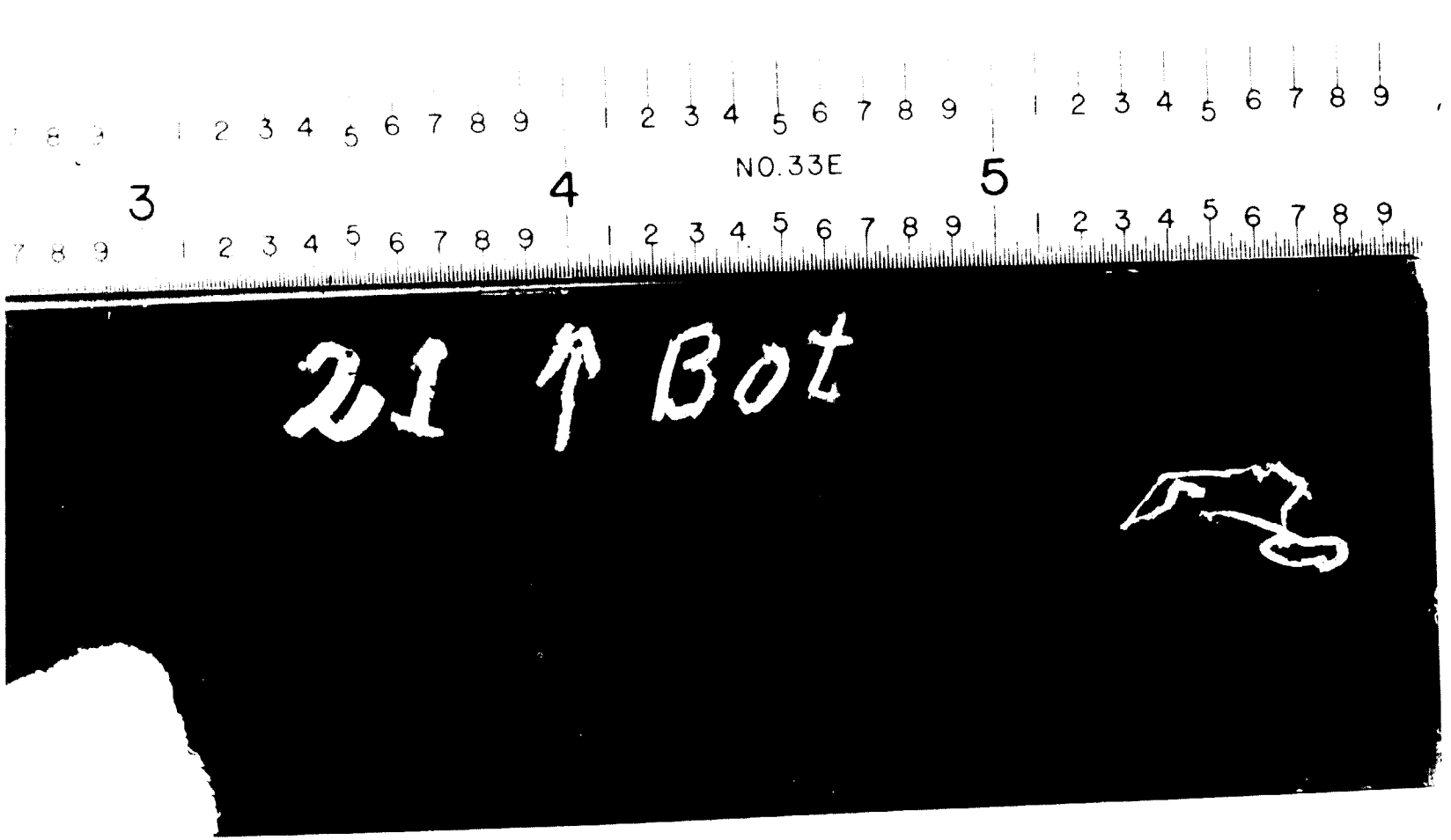

Figure 10 - Scratch Gage Marking Showing Movement Between Panels 21 and 22 (Lower)

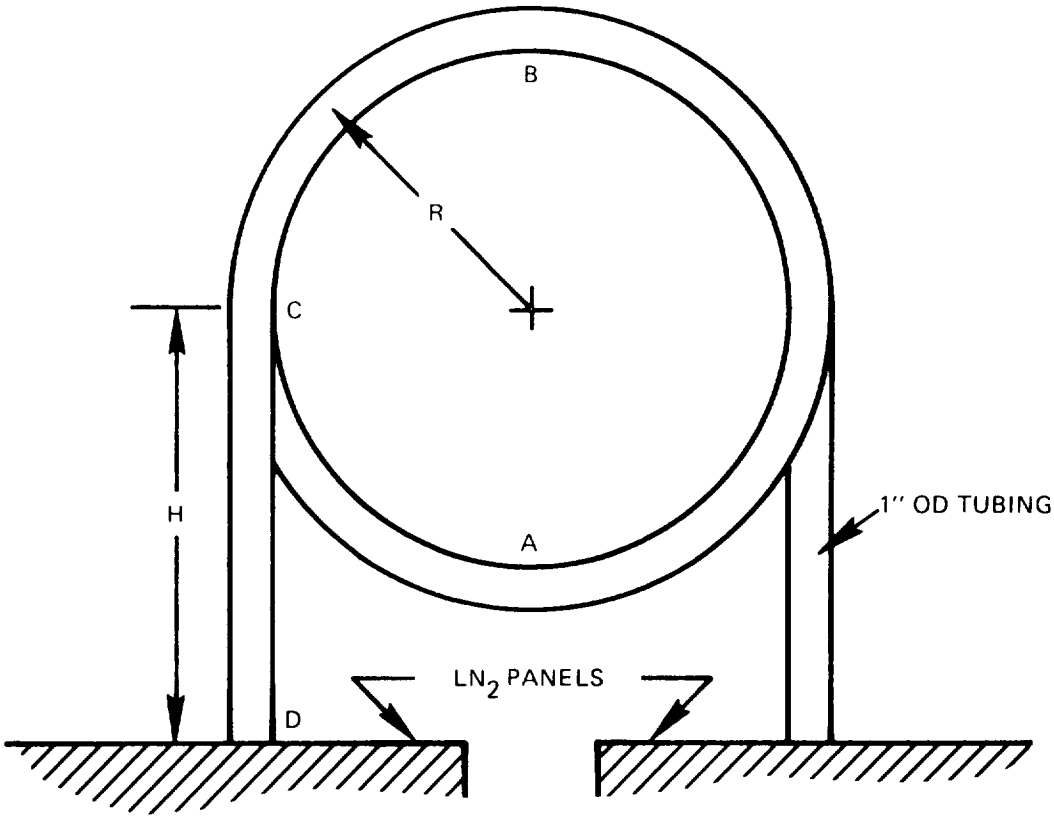

Figure 11 - Expansion Loop U-Bend

SPACE SHUTTLE REACTION CONTROL SUBSYSTEM

PROPELLANT TANK MASKED SCREEN TEST

John B. Henderson
Propulsion and Power Division
Engineering Directorate
Johnson Space Center

During final development testing of the Space Shuttle Reaction Control Subsystem propellant tanks, a problem with pressure transients in the system was uncovered. Due to the nature of the tanks, performance tests to determine the impact of the transients on the expulsion efficiency of the tanks could not directly simulate the actual conditions which would be present in a low-gravity environment. However, by "masking" or covering various segments of the propellant acquisition device, a good simulation of a low-gravity environment was achieved in ground testing.

INTRODUCTION

The Space Shuttle Reaction Control Subsystem (RCS) has to perform under many different conditions. It is active for attitude control and translation from just after main engine cut-off until Mach 1.0 during entry. While it is active, liquid propellants, nitrogen tetroxide and monomethylhydrazine, need to be delivered to any of the 38 RCS primary thrusters delivering 870 pounds of thrust each for attitude control and translation. Because most of the propellant is required during the low-gravity portion of mission, an expulsion device must be used to separate the propellant from the pressurant gas.

In previous spacecraft, a Teflon membrane was used to physically separate the propellant and pressurant. However, Teflon membranes rupture after relatively few expulsion cycles, and therefore would be unsuitable for the 100-mission life requirement on the Shuttle RCS. No elastomeric membranes sufficiently compatible with the RCS propellants to assure a 10-year life have been developed. For these reasons, and because of its weight advantage over the bellows-type tank, a screen propellant acquisition device was chosen to supply gas-free liquid outflow (figure 1.)

SCREEN ACQUISITION DEVICE

The screen acquisition device used in the Space Shuttle RCS propellant tank consists of rectangular cross-section channels which are covered with a finely woven stainless steel mesh. When this mesh or screen is wetted by the liquid propellant, the surface tension of the liquid forms a barrier to the pressurant gas. The strength of this barrier is finite, and the pressure differential at which gas will be forced through the liquid barrier is called the bubble point. When the bubble point is exceeded, the screen is said to "breakdown", in other words, to transfer gas. However, as long as the pres-

sure differential is less than the bubble point, gas cannot penetrate the surface tension barrier and only the liquid will be pulled through into the channels. Therefore, the goal in designing a screen tank is to minimize the pressure loss while maximizing the amount of propellant expelled. The pressure loss is made up of two major components--the flow losses due to viscous loss, such as turning loss, entrance loss, etc., and the hydrostatic head loss (figure 2). The latter is a function of the acceleration to which the tank is subjected. The flow losses depend on puddle size and liquid flow rate. For a given flow rate, as the volume of propellant decreases, the screen surface area in contact with the puddle decreases; thus, the velocity through the screen must be greater, and therefore, the pressure differential must increase. The greatest flow losses occur with the smallest puddle in contact with the smallest amount of screen. The expulsion efficiency is defined as the smallest percentage of the loaded propellant which has been expelled from the tank when the pressure differential (the flow and hydrostatic head losses combined) equals the bubble point of the screen. Because the tank is designed to work primarily in a low-gravity environment, the hydrostatic head term in this environment is small. However, any ground system testing has to be performed in a one-g environment, where the hydrostatic head term quickly becomes the dominant term. Therefore, the performance in a low-gravity environment of a large surface tension acquisition device cannot be directly determined or demonstrated in ground testing.

RCS PROPELLANT TANKS

In order to certify the RCS propellant tanks for flight, it was necessary to develop sophisticated mathematical models which characterized the on-orbit performance of the tank. These math models were correlated using ground tests of subassemblies in which flow losses of each device were measured.

However, in early 1980, testing at the system level uncovered a serious deficiency in the math models. Because of the nature of the RCS, combinations of thrusters can be fired simultaneously at any time and for almost any duration. System level testing revealed hydraulic pressure transients, associated with concurrent start-up of several thrusters, of such a magnitude as to cause screen breakdown with high propellant residuals. This transient pressure drop had not been considered in previous analyses. Because of these transients, gas could be fed out to the thrusters and perhaps cause a thruster to misfire and be deselected during a critical mission phase.

To try to quantify the severity of the transients on the tank performance, an intensive effort was initiated to develop an advanced transient-pressure math model. This was correlated with data from a test tank in one-g using Freon 113 as a referee fluid and simulated thruster valves. A more detailed model validation plan was then developed using a test tank which was specially instrumented with high-response pressure transducers in the critical locations. This tank was placed in a system and various combinations of thruster firings were performed. These tests were run in various attitudes and, because of the large hydrostatic head-pressure loss, with a large resi-

dual puddle. This test data was compared to the math model predictions for ground tests and then the math model was used to determine the on-orbit performance of the tank. Based on these predictions, the digital autopilot of the Space Shuttle was constrained to fire only three thrusters simultaneously from any of the RCS systems, and the expulsion efficiency was severely decreased.

This analysis also indicated that a minor redesign of the acquisition system could alleviate most of the transient-pressure concerns. This redesign could not be incorporated in the already installed OV-102 (Columbia) tanks. However, the OV-099 (Challenger) tanks were modified to the new configuration. To certify the performance on the new design, it was necessary to validate the revised math model. However, instead of repeating the original performance test, a new test program was devised.

In order to simulate the flow conditions in a nearly depleted tank which is in a low-gravity environment, a small hydrostatic head and a small screen area for liquid to flow into the channels are required. To achieve this simulation, the screen channels could be wrapped or masked, leaving only a small area of screen in the predicted worst-case location uncovered. With the tank almost completely filled, the hydrostatic head term is small and, because the flow area into the screen channels is small, the flow losses are maximized. Thus, low-gravity conditions are simulated (figure 3).

RCS PROPELLANT MASKED SCREEN TEST

In order to implement this new test program, a great deal of development work was required. The masking material had many requirements which had to be met. First, it had to be compatible with the propellant in which it was being used. From test data and analysis, it was determined that the transient-pressure problem was greatest in the oxidizer tank. Unfortunately, there are very few flexible materials which will retain their physical properties after exposure to the oxidizer, nitrogen tetroxide. Secondly, the masking material could not interfere with the dynamics of the transient pressure. It had been found that, because the screen is not rigid during a transient, the screen will flex and tend to damp out the transient. The masking material, therefore, could not change the amount of flexing or the phasing of the flexing.

Besides these two requirements, the masking material had to seal the channels from the liquid. Obviously, the purpose of the masking is to limit the flow area into the channels and, to correctly simulate the low-gravity residual, a large amount of leakage into the channels would lead to errors in the test results.

Lastly, and perhaps most importantly, in those areas in which the masking extended into the pressurant gas, the masking material could not cause any degradation of the screen bubble point. Because a portion of the test program was to continue pulsing until gas was ingested into the channels (until the hydrostatic head became great enough that the combination of transient pressure and hydrostatic head exceeded the bubble point), if the

bubble point was degraded because of the masking material, gas would be ingested into the channels at a lower pressure differential that would be the case during flight. To satisfy all of these requirements, only one material seemed promising, Teflon. To determine whether it was suitable for a masked screen test, preliminary testing was performed. Six layers of Teflon tape of various dimensions were carefully wrapped around a single channel, and then exposed to oxidizer for an extended period of time. During this soak period, leakage across the tape was found to be small. Also, the compliance, or amount of flexing of the screen, was determined.

The idea which up until now was being developed at JSC, was then proposed to the contractor, and additional tests were performed. The effect of the masking on transients were found to be minimal, and the tape had no effect on the screen bubble point. Based on these test results in which the tape successfully met all of the requirements, the decision was made to mask an acquisition device and perform a test at the White Sands Test Facility in an RCS test system. This fluid system is identical to a Space Shuttle aft RCS system. In this test article system, the actual fluid dynamics which a tank would be exposed to in flight could be simulated.

The propellant acquisition system was masked such that the remaining flow area was slightly greater than the predicted flow area necessary to cause breakdown of the screens with five thrusters pulsing (figures 4 and 5). High response transducers were placed in the channels at various locations to monitor the severity of the transients. High point bleeds were installed in the acquisition device so that breakdown of the screens could be detected and the amount of gas ingested into the channels measured. The tank was then installed in the test article and the test was run.

A test series consisted of a steady-state firing, depleting the propellant level down to a desired liquid height (hydrostatic head) and then a series of pulse firings, until breakdown of the screen occurs as indicated by gas in the high point bleeds. Several test series were run with from three to seven thrusters pulsing, along with combinations of steady-state and pulsing thrusters (figure 6). The data collected indicates that the mathematical models used to predict performance of the RCS propellant tanks were slightly conservative and were adequate for the certification of the tanks.

CONCLUSIONS

A test was performed at White Sands Test Facility to determine, in a one-g environment, the performance of the screen acquisition deviced used in the Space Shuttle RCS. By masking the screen channels with Teflon tape, the flow losses within the device could be maximized and the hydrostatic head minimized, such that a low-gravity environment was simulated. Using this technique, mathematical models, which were used to predict tank performance under any set of conditions, were validated. Based on these results, the predicted expulsion efficiency of the tanks was increased, thereby making more propellant available for use during a mission, and the capability exists to revise the digital autopilot to command more thrusters simultaneously.

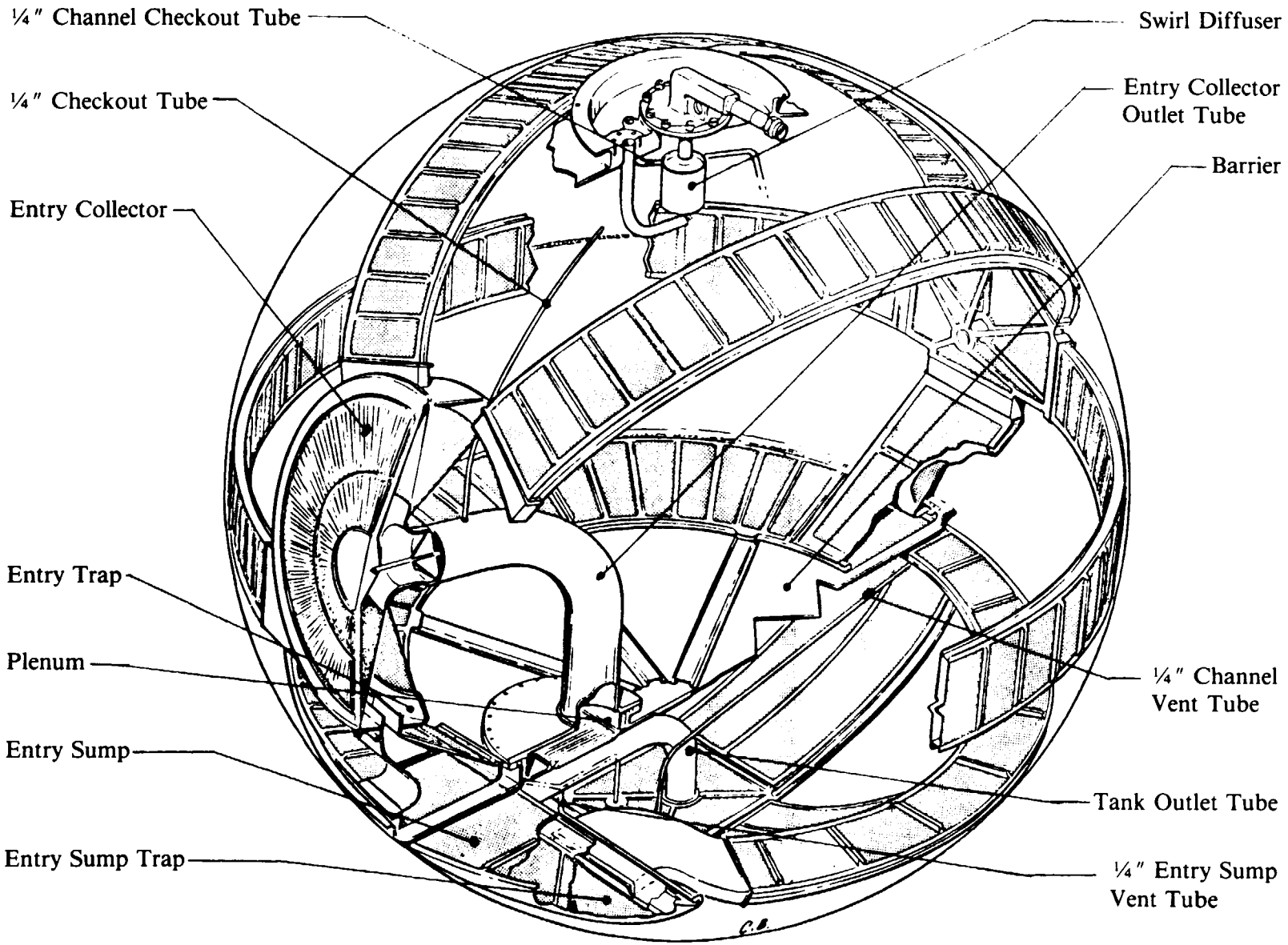

Figure 1 - Shuttle RCS Tank - AFT Configuration

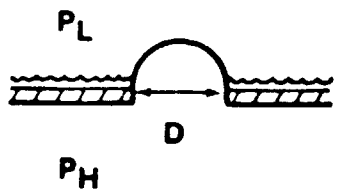

$$\Delta P \frac{\pi D^2}{4} = \delta \pi D$$

$$\Delta P_{MAX} = \frac{4\delta}{D} = \text{B.P.}$$

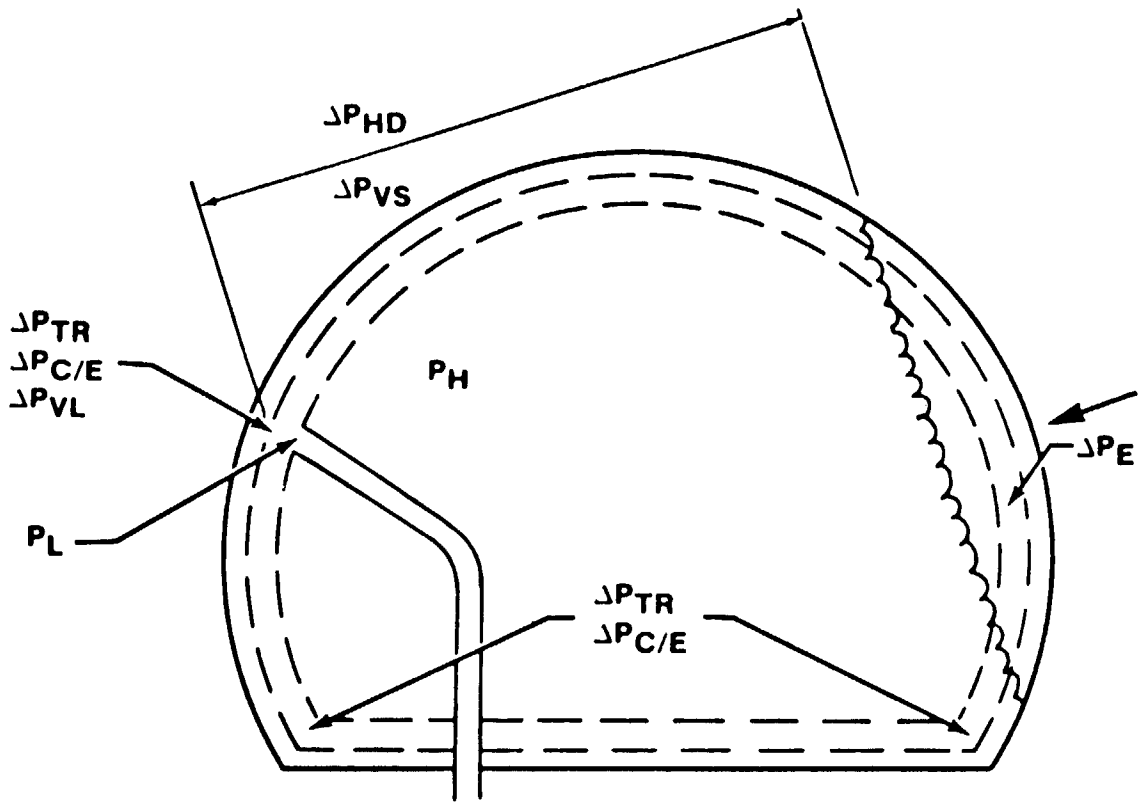

$\Delta P_{MAX} = P_H - P_L$

$\Delta P_{MAX} = \Sigma(\Delta P_{HD} + \Delta P_{VS} + \Delta P_{TR} + \Delta P_{C/E} + \Delta P_{VL} + \Delta P_E)$

$\Delta P_{MAX} < \text{B.P.}$, GAS-FREE PROPELLANT

$\Delta P_{MAX} = \text{B.P.}$, BREAKDOWN

BUBBLE POINT IS THAT ΔP REQUIRED TO FORCE GAS THROUGH THE WETTED SCREEN.

ΔP_{HD} = HEAD LOSS

ΔP_{VS} = VISCOUS LOSSES

$\Delta P_{C/E}$ = CONTRACTION/EXPANSION LOSSES

ΔP_{TR} = TURNING LOSSES

ΔP_{VL} = VELOCITY LOSS

ΔP_E = ENTRANCE LOSS

Figure 2 - Tank Pressure Losses

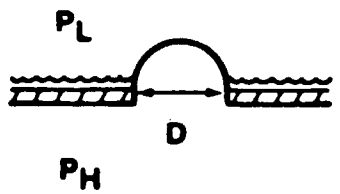

$$\Delta P \frac{\pi D^2}{4} = \delta \pi D$$

$$\Delta P_{MAX} = \frac{4\delta}{D} = \text{B.P.}$$

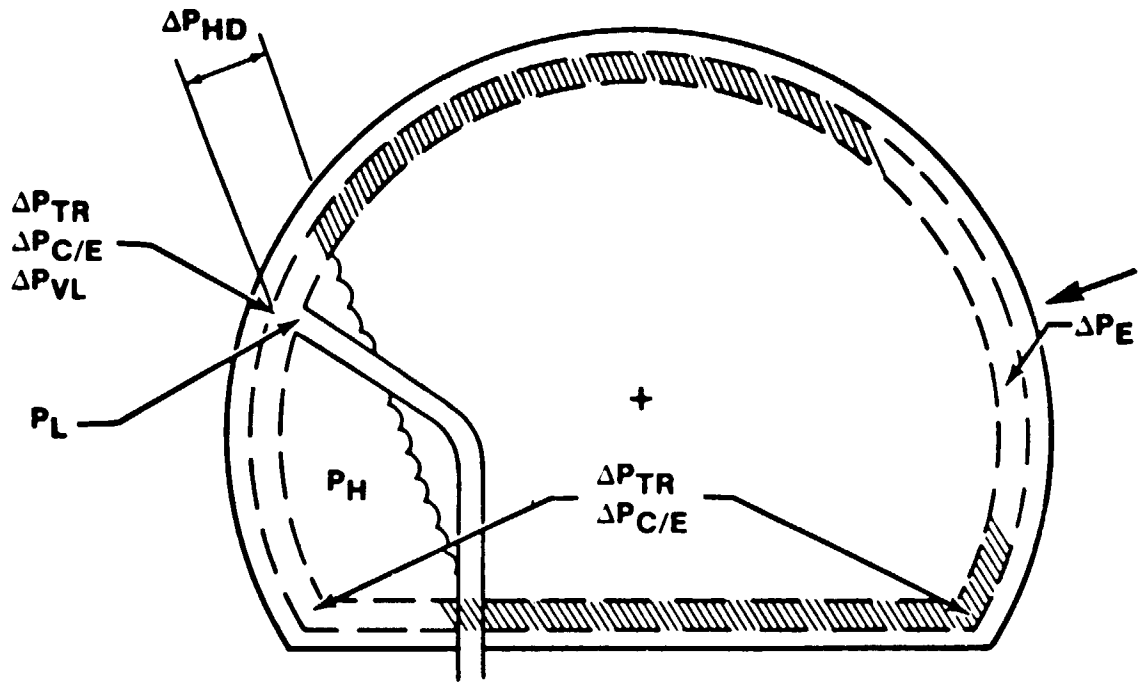

$\Delta P_{MAX} = P_H - P_L$

$\Delta P_{MAX} = \Sigma(\Delta P_{HD} + \Delta P_{VS} + \Delta P_{TR} + \Delta P_{C/E} + \Delta P_{VL} + \Delta P_E)$

$\Delta P_{MAX} < \text{B.P.}$, GAS-FREE PROPELLANT

$\Delta P_{MAX} = \text{B.P.}$, BREAKDOWN

BUBBLE POINT IS THAT ΔP REQUIRED TO FORCE GAS THROUGH THE WETTED SCREEN.

ΔP_{HD} = HEAD LOSS

ΔP_{VS} = VISCOUS LOSSES

$\Delta P_{C/E}$ = CONTRACTION/EXPANSION LOSSES

ΔP_{TR} = TURNING LOSSES

ΔP_{VL} = VELOCITY LOSS

ΔP_E = ENTRANCE LOSS

Figure 3 - Pressure Drops With Masked Screen

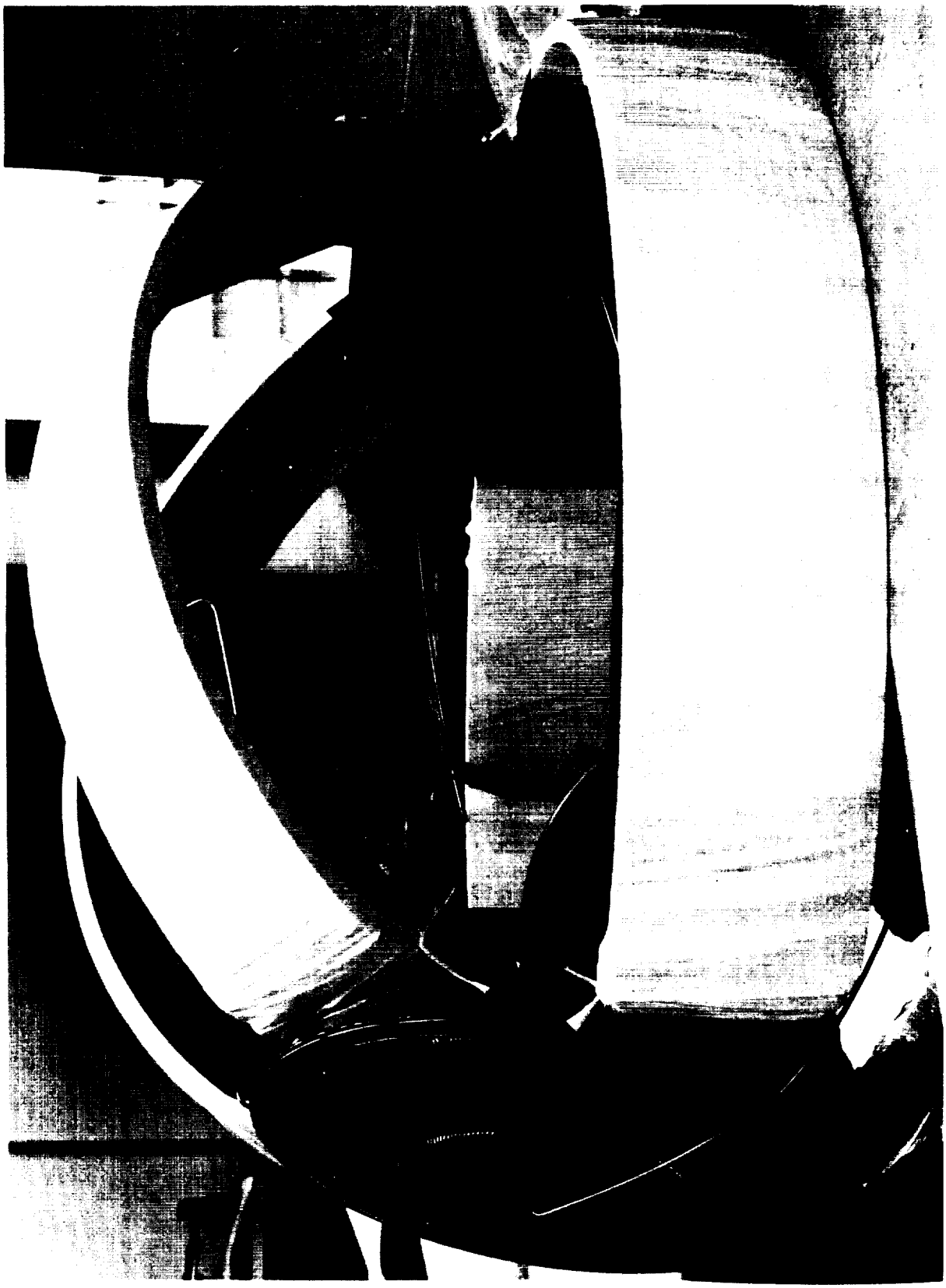

Figure 4

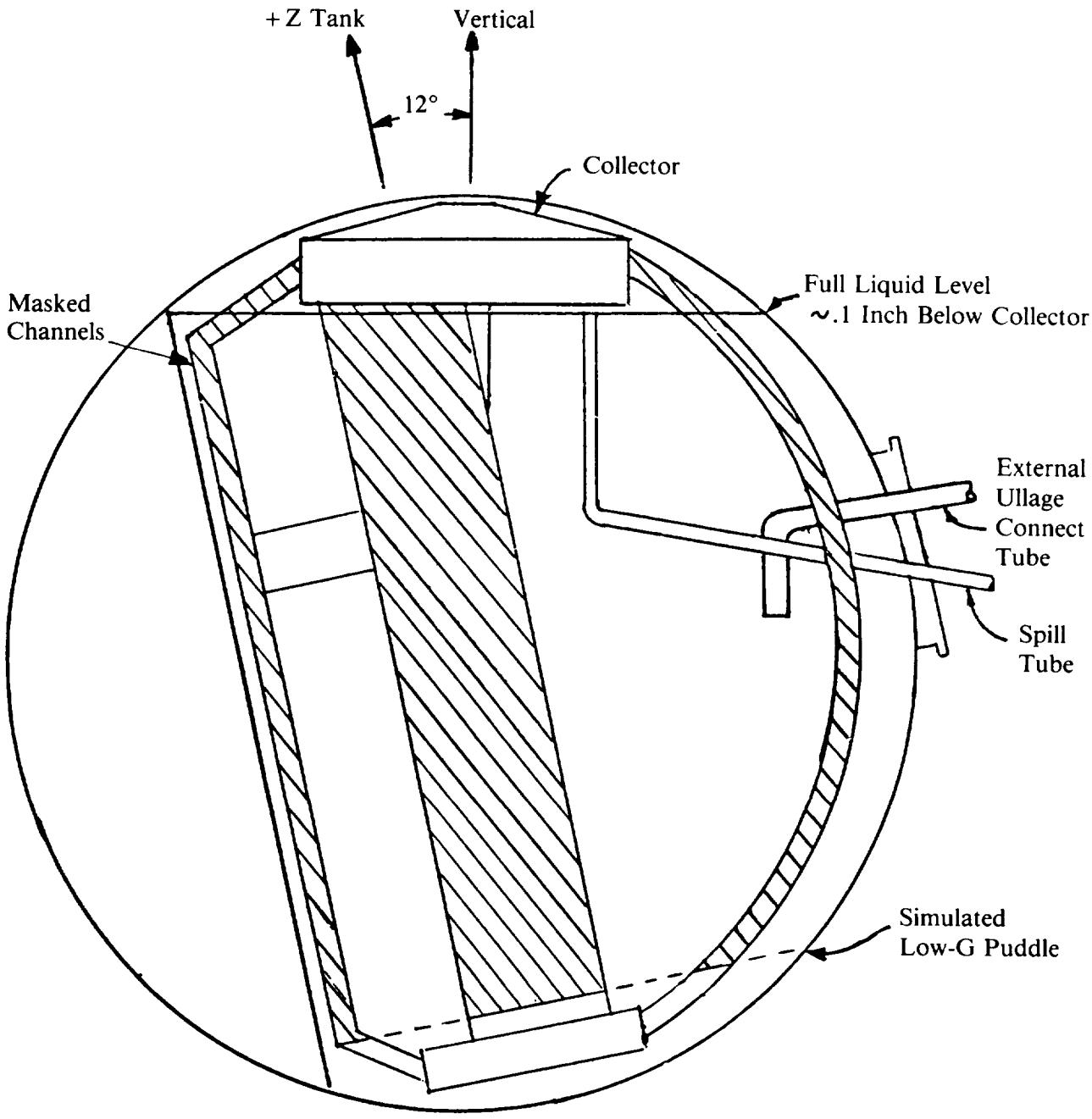
+Z Tank
Vertical
12°
Collector
Full Liquid Level
~.1 Inch Below Collector
Masked
Channels
External
Ullage
Connect
Tube
Spill
Tube
Simulated
Low-G Puddle

Figure 5.

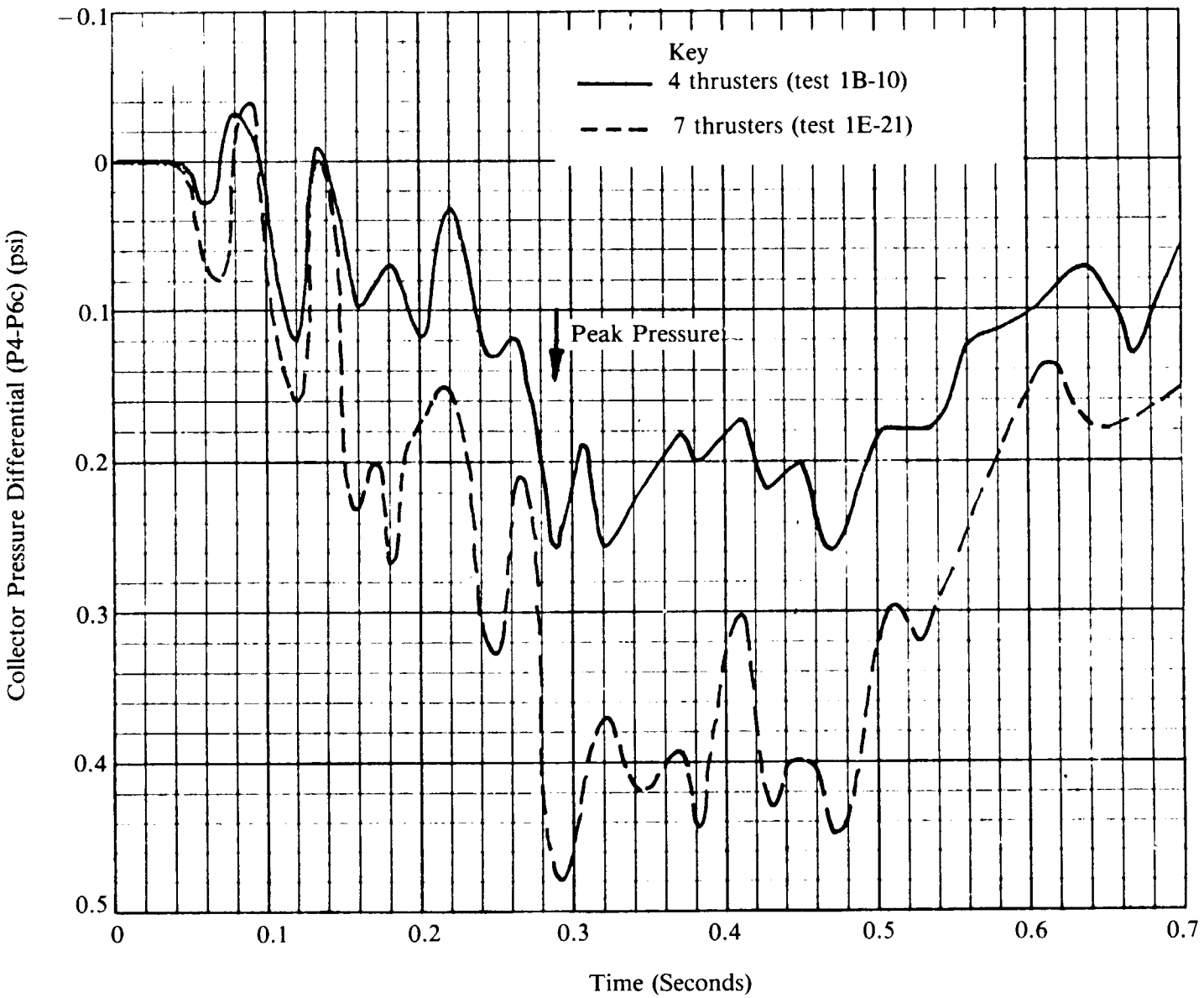
Key
4 thrusters (test 1B-10)
7 thrusters (test 1E-21)
Peak Pressure
Collector Pressure Differential (P4-P6c) (psi)
Time (Seconds)
-0.1
0
0.1
0.2
0.3
0.4
0.5
0
0.1
0.2
0.3
0.4
0.5
0.6
0.7

Figure 6.

GROUND TEST CHALLENGES IN THE DEVELOPMENT OF THE SPACE SHUTTLE ORBITER AUXILIARY POWER UNIT

Norman H. Chaffee, Renee' J. Lance, and Dwayne P. Weary
NASA-Johnson Space Center

ABSTRACT

A conventional aircraft hydraulic system design approach was selected to provide fluid power for the Space Shuttle Orbiter. Developing the power unit, known as the Auxiliary Power Unit (APU), to drive the hydraulic pumps presented a major technological challenge. A small, high speed turbine drive unit powered by catalytically decomposed hydrazine and operating in the pulse mode was selected to meet the requirement. Because of limitations of vendor test facilities, significant portions of the development, flight qualification, and postflight anomaly testing of the Orbiter APU were accomplished at the Johnson Space Center (JSC) test facilities. This paper discusses the unique requirements of attitude, gravity forces, pressure profiles, and thermal environments which had to be satisfied by the APU, and presents the unique test facility and simulation techniques employed to meet the ground test requirements. In particular, the development of the zero-g lubrication system, the development of necessary APU thermal control techniques, the accomplishment of integrated systems tests, and the postflight investigation of the APU lube oil cooler behavior are discussed.

INTRODUCTION

The JSC maintains extensive engineering and development laboratory and test facilities to support its mission in the areas of technology, development, qualification, flight support, and anomaly investigation testing. The Thermochemical Test Area (TTA), operated by the Propulsion and Power Division (PPD), is part of that capability and has provided significant support to all United States' manned spacecraft programs in the areas of propulsion, power and pyrotechnics systems.

This paper focuses on some of the unique and challenging elements of the Orbiter APU ground test program which were performed at the TTA. Emphasis is placed on the development and utilization of innovative test facilities, techniques and procedures in accomplishing the tests rather than on a detailed, analytical interpretation of engineering test results.

This paper also serves to show the utility of the TTA engineering test facilities throughout the entire life cycle of a program, including initial

technology evaluation, concept feasibility testing, development, qualification, flight support, problem investigation, and product improvement testing.

APU REQUIREMENTS AND DESCRIPTION

Unlike other systems on the Orbiter, there was no precedent in earlier manned spacecraft for a hydraulic system nor for the power unit to drive the hydraulic pumps. The only prototype power units available were aircraft auxiliary power units, which were not required to operate in the severe environments of a spacecraft or to have the life of an Orbiter unit. The approach selected to meet the fluid power requirements for the Orbiter program was to use a conventional 3000 psia hydraulic system and thereby to establish conventional aircraft hydraulic system technology as the foundation of the Orbiter system. This approach minimized the technology development requirements except for the power supply unit. During the ascent, descent, and landing phases of an Orbiter mission, reliance is placed on the Orbiter hydraulic system for critical flight control functions. A simplified functional schematic of an Orbiter hydraulic system and identification of the key control functions it performs is shown in figure 1. Hydraulic system flow demands of up to 69 gallons per minute may be required during the mission.

Because of the criticality of these control functions, developing a reliable and safe power supply unit to drive the hydraulic pumps presented a major challenge for the Orbiter program. The conceptual approach selected for the unit was to use a small, high speed, low inertia monopropellant-fueled turbine power unit to drive a conventional aircraft-type hydraulic pump. Although a misnomer, the power unit was labeled an APU because of its similarity to aircraft auxiliary power units, traditionally called APU's. Here, in the name, much of the similarity ends. The stringent requirements imposed on the Orbiter APU quickly made this machine different from any existing aircraft APU. The Orbiter APU's are required to operate in severe temperature, pressure and acceleration environments. The units are required to operate for approximately 92 minutes during each mission at output power levels from 8 to 148 horsepower. A minimum of two restarts is required for each mission. In addition, with appropriate repair and refurbishment, the APU's are to meet a 100-mission life requirement. Key APU design requirements are summarized in Table 1.

The Orbiter has three completely redundant APU systems and three hydraulic systems. The APU's, including their fuel systems, are isolated from each other. Pressure-actuated switching valves are provided between the hydraulic systems so that in case of a failure in a single APU or hydraulic system, the remaining two systems can provide the hydraulic load. The APU's are hydrazine fueled, turbine driven and restartable. Power is delivered to the hydraulic pump through a lubricated, zero-g, all attitude gearbox. The units have a thermal control system to prevent both freezing of the fuel during periods of low temperature environmental exposure, and overheating during heat soakback following operation and shutdown. An electronic controller

provides all of the functions to checkout key APU status parameters before launch, to control the APU during operation (startup, speed control, shutdown, redundancy management), and to provide thermal control. A functional schematic of the APU system is shown in figure 2. Figure 3 shows the APU configuration. The three APU systems are mounted in the upper aft section of the Orbiter fuselage, behind the payload bay and below the vertical tail. The three APU's themselves are mounted on the aft face of the major structural bulkhead which separates the payload bay from the aft compartment.

Monopropellant-grade hydrazine fuel (MIL-P-26536) is supplied from the diaphragm fuel tank to the inlet of the fuel pump at pressures ranging from 80 psia to 370 psia. The fuel pump increases the pressure to approximately 1500 psia. The high-pressure fuel is directed through the gas generator valve module (GGVM) to the gas generator (GG). The GG catalytically decomposes the fuel into gas at a temperature of 1700°F and at a nominal pressure of 1260 psia; the gas is then directed through a two-stage, supersonic reentry turbine. After work is extracted by the turbine, the gas is used to cool the gas generator by flowing over it before exiting the APU.

Once turbine operating speed is achieved, it is controlled within ± 8 percent by the GGVM, the electronic controller, and speed sensors. Three redundant speed sensors mounted at the turbine shaft provide the electronic controller with pulsed speed signals. The primary nominal turbine operating speed is 74,000 rpm. If the primary speed control mode fails, a secondary speed control mode of 81,000 rpm is activated automatically. This secondary mode may also be selected manually in the event the APU is required to have greater load-carrying capacity. Should the secondary speed control mode fail, a backup (part of the primary circuit) control mode of 83,000 rpm is activated automatically. If both primary and secondary control modes are inoperative, automatic shutdown occurs at 93,000 rpm.

The power from the turbine shaft is transmitted to the hydraulic pump, the fuel pump, and the lubrication pump through the gearbox. The gearbox design uses piston accumulators that function as variable-capacity oil reservoirs and gearcase walls that closely conform to the gears. These features enable the lubrication system to function in any attitude and in zero g.

The hydraulic power units which operate the nozzle gimbal actuators of the Space Shuttle solid rocket boosters are similar to the Orbiter APU's. Both types of units are supplied by the Sundstrand Corporation.

THERMOCHEMICAL TEST AREA DESCRIPTION AND CAPABILITIES

The Thermochemical Test Area was designed and built as an element of JSC's engineering and development laboratories. It is located on 115 acres in the northwest corner of JSC and is managed and operated by the Thermochemical Test Branch (TTB) of the Propulsion and Power Division. The TTA has

been operational since 1964 and has primarily been utilized in solving problems for subsystems for which the Propulsion and Power Division has technical responsibility. It has provided significant support to all U.S. Manned Space Programs. For the Space Shuttle Program, this support has included the Orbital Maneuvering System, Main Propulsion System, Reaction Control System, Auxiliary Power Unit System, Hydraulic System, Cryogenic System, Fuel Cell System, Pyrotechnics, and Batteries.

The TTA is comprised of five independent test facilities, each with unique test capabilities. In addition, the TTA has supporting laboratories for electrical and mechanical systems/equipment fabrication, chemical analysis, system cleaning and assembly, instrumentation calibration, and data acquisition/reduction. The dedicated facilities and support laboratories provide a quick response investigative capability that the Propulsion and Power Division utilizes to scope a problem and examine potential solutions. A limited number of qualification programs have been accomplished when a contractor does not have the facility capability or when there are other compelling reasons. The TTB also conducts test programs on the JSC "O-G" aircraft stationed at nearby Ellington Air Force Base.

Most active APU systems testing was accomplished at the Propulsion Test Facility (building 353). This facility has the capability for both sea level and altitude testing of the APU system. A 20 ft. diameter subssystems altitude test chamber was used for APU and integrated systems testing. This chamber is a rugged vacuum test chamber built to contain explosive reactions should they occur. Two pumping systems serve the chamber. One is a mechanical pumping system capable of maintaining the environment at 170,000 ft simulated altitude for systems testing at very limited mass injection rates. The other is a three-stage steam ejection system capable of maintaining 110,000 - 130,000 ft altitude during "normal" pulse mode testing of the APU. Portable thermal enclosures and panels within the chamber can provide local thermal environments ranging from -65°F to +300°F.

Other test chambers in the TTA provided thermal vacuum test capability for non-firing APU tests. Thermal environments in these chambers can vary from -320°F to +300°F at vacuum levels of 10^{-6} torr.

SCOPE OF JSC ACTIVITIES IN APU DEVELOPMENT

The Propulsion and Power Division has always used the TTA aggressively to carry out extensive technology efforts, to provide independent assessment of hardware and systems, and to provide quick problem resolution response to the program offices in the assigned areas of propulsion and power systems. TTA is a mandatory tool for personnel training, for maintenance and expansion of staff skills and experience, and for effective management of industrial development programs. This philosophy was applied avidly during the Orbiter APU development program.

Early Space Shuttle Orbiter studies focused extensively on an integrated cryogenic oxygen/hydrogen system for the orbital maneuvering, reaction control, and auxiliary power unit systems. A program of analyses and hardware testing conducted at TTA and at similar facilities at the Marshall Space Flight Center and the Lewis Research Center led to the conclusion that technological maturity, system complexity and projected costs of the O_2/H_2 system were not compatible with the Shuttle Program. This finding, although a "negative" one, was a very positive program input and undoubtedly saved the Shuttle Program millions of dollars of extra development cost and the associated schedule delays. JSC TTA test programs in cryogenic valves, flow control devices, ignition systems, and combustor technology were important inputs to this decision.

When hydrazine-powered turbine drive units came into consideration for the Orbiter APU application, JSC had extensive hydrazine system and combustor experience but limited turbine experience. Two applicable hardware units existed in the technology base--the Concorde Supersonic Transport emergency power unit, and the Spartan Missile APU. Both of these units were smaller than the Orbiter application in power rating (approximately 45 horsepower) and were intended for very limited operation. The Concorde unit operated at 110,000 rpm while the Spartan unit was a 70,000 rpm device. Both units were procured and tested extensively at TTA in 1973. The testing evaluated both thermal and catalytic gas generators; it evaluated both pulse modulation and flow modulation speed control approaches; and it assessed performance, response to load changes, and thermal characteristics of the units. Both units were driving conventional aircraft-type hydraulic pumps. Testing was performed at both sea level and simulated altitude conditions in the TTA subsystems test chamber. Special provisions for ducting the exhaust gases were employed in the chamber and a special lube oil cooling system and a variable hydraulic system load bank had to be designed and fabricated for these programs. These special facility accommodations were the first of successively more complex test support systems required for APU testing. The Concorde unit ran successfully for over 50 hours and the Spartan unit ran for 17 hours--much beyond the intended life of either unit.

As a result of the Concorde and Spartan APU tests, it was determined that a hydrazine APU was technologically feasible at an acceptable risk level. Subsequently, the Orbiter Program did commit to the hydrazine APU concept. A short time later, another decision was made to reduce system redundancy from four 50 percent APU systems to three systems. The TTA ability to undertake these tests independently, quickly, and with reasonable test condition fidelity, supplied "hard" information at an appropriate time and was an important factor in the program decisions.

As soon as the program commitment to the hydrazine APU was made and a supplier selected, JSC made arrangements to procure an APU for inhouse test and evaluation. The original intent was to carry out independent assessments of hardware characteristics and performance, to evaluate the "zero-g" lubrication system, to characterize APU thermal behavior, and to test the APU at altitude in conjunction with a high fidelity hydraulic system. These tests

were to provide the JSC technical staff with extensive knowledge of the hardware, but were not to be part of the formal qualification process.

The scope of the JSC testing expanded greatly beyond these initial expectations and since early 1976 when TTA received the first APU prototype hardware, TTA has hardly been without at least one active APU related test program. An early recognition of an inadequacy of vendor altitude test capability forced JSC/TTA into a much more active and formal test role. The vendor was able to provide only limited altitude test capability and it was determined that the postfiring thermal "soakback" behavior of the APU at sea level or low altitude conditions was different and less severe than behavior at high vacuum conditions (because of induced convection, free convection, and degraded insulation performance at low altitude conditions). An early explosive APU gas generator failure under "hot restart" conditions at altitude led to extensive involvement of JSC/TTA in the thermal aspects of the APU development program, including performance of portions of the formal qualification program. The TTA subsystem chamber and its excellent altitude test capability were important aspects of the subsequent development program.

The extensive hardware expertise and test proficiency acquired early by the JSC staff, coupled with an increasing workload of APU-related development problems, and the capability of the TTA test systems, led to major involvement of the TTA facilities in all aspects of the APU development, qualification and flight program, including the following areas:

1. Fuel tank

    a. Life tests
    b. Diaphragm evaluation tests
    c. Diaphragm permeation and bubble growth tests

2. System filter (life tests)

3. Fuel pump

    a. Thermal soakback
    b. Bubble growth
    c. Cooling
    d. Gear material selection

4. Valve module

    a. Thermal soakback
    b. Bubble growth
    c. Cooling
    d. Adiabatic detonation characteristics

5. Gas generator

    a. Life
    b. Cooling

6. Thermal control

    a. Heater sizing
    b. Failure case characterization

7. Gearbox

    a. Pressurization system
    b. Accumulator design
    c. Zero-g performance

8. Lube Oil (response to hydrazine contamination)

9. System testing

    a. Mission duty cycles
    b. Integrated tests (with hydraulics and cooling systems)

10. Flight support (postflight anomaly investigations)

11. Product improvement

    a. Improvd APU
    b. Long life gas generator

The following sections will discuss selected TTA tests which were of particular importance to the APU development program and which required substantial test facility innovation.

ZERO-G GEARBOX TESTING

The APU gearbox is designed to reduce the speed of the 74,000 rpm turbine wheel to the 3900 rpm drive speed of the hydraulic pump while transferring as much as 148 horsepower. The gearbox lube pump and the hydrazine fuel pump are also driven through the gearing. The gearbox operates with a "dry sump," minimizing heat generation and churning of the lube oil, and does not depend on gravity for lube pump suction head. The lubricant is MIL-L-23699B lubricating oil, a synthetic base aircraft engine lubricant. The function of the gearbox lubrication system is to provide lubrication to the gears and bearings and to remove heat from the gearbox. The lubrication system consists of a lube pump, external heat exchanger (water boiler), filter, accumulators, relief valve, lube jets (orifices), internal lube oil passages, a scavenging system, and emergency repressurization system as shown in figure 4.

A mixture of lube oil and nitrogen pressurant is pumped from the gearbox by a positive displacement eccentric rotor pump to the external water boiler. The oil/gas mix is returned to the gearbox through a filter to the flow-through type accumulators. The function of the accumulators is to compensate for thermal expansion of the oil and maintain a relatively constant gas volume in the gearbox. The oil is then routed to the lube jets to lubricate and cool the bearings and gears. The oil is finally returned to the pump by the scavenge system. The scavenge system utilizes the gears to centrifugally pump oil to the close-tolerance, shaped collector manifolds at the outer diameter of the gears which direct oil to the pump inlet. A magnetic particle collector/detector is positioned upstream of the lube pump suction. The gearbox is sealed at the turbine, hydraulic pump, and fuel pump drive splines with carbon face seals, spring loaded to contain internal pressure.

The key requirements for the gearbox lube system include operating in the launch attitude (at accelerations up to 3 g's) and entry attitude, as well as under zero-g conditions, while providing reliable lubrication/cooling to the gears and bearings.

Concern was expressed within the program office, as well as by outside advisory groups, as to a methodology for demonstrating gearbox lube system adequacy. Specific concerns as to the ability of the APU gearbox and lube system to function satisfactorily for all Orbiter requirements are as follows:

1. Oil quantity effects.

2. Gearbox pressure effects.

3. Ability of the scavenge system to operate in all attitudes and in varying "g" environments.

4. Ability to initiate lube oil flow in adverse environments including high and low "g" fields, and for varying oil quantities and gearbox pressures.

5. Ability to maintain adequate cooling to all critical areas under all environments.

6. Effects of head pressure on the lube pump.

7. Ability of the accumulators to function satisfactorily under all required environments.

To address these concerns, a special two-phase test program was devised in 1977. The first test phase involved an extensive parametric ground test program to evaluate the effects of all key parameters. The second test phase involved verification tests aboard the JSC zero-g KC-135 aircraft.

For these tests, only the gearbox was utilized; a complete APU was unnecessary. For the ground test phase, a special double gimbal test fixture was designed to mount the gearbox test article. With this mounting fixture, the gearbox could be oriented in any of six attitudes (referenced to Orbiter position): belly down (level flight), belly up, nose down, nose up (launch), left bank (left wing down), or right bank (right wing down). The gearbox was driven by a 3000 psi hydraulic motor which was powered by a hydraulic pump operated by a 440 VAC three-phase electric motor. An external water cooled lube oil heat exchanger was provided. Tools and procedures for servicing lube oil into the gearbox and for verifying void volume were developed for this test. The test system was mounted in a special high altitude test chamber.

The ground test phase evaluated three different accumulator concepts (elastomeric diaphragm; no accumulator; piston accumulator) at a variety of void volumes and gearbox pressures, and at sea level and vacuum conditions for all six gearbox attitudes. It was found that the elastomeric diaphragm accumulator was unsatisfactory due to material degradation. The need for a gearbox pressurization system was identified to keep gearbox pressures above approximately four psia to maintain adequate lube oil flow. No significant effect of gearbox attitude was seen.

To verify the apparent insensitivity of the lube system to attitude/acceleration, the test system was placed aboard the JSC KC-135 zero-g aircraft for test. The piston accumulator was used. For the aircraft test, the gearbox was driven by a conventional aircraft hydraulic pump powered by a 115 VAC 400 Hertz electric motor using KC-135 power. A closed water cooling system was designed using a fan-driven air/water heat exchanger to cool the lube oil. Three flights were made, each with a different void volume in the gearbox (1000 cc, 1400 cc, and 2000 cc). For each void volume, the gearbox was successively oriented in each of the six attitudes and then five aircraft parabolas were flown for each attitude. In each case, the gearbox flow was started during the zero-g portion of the first parabola and then was allowed to run during the remaining four parabolas. Thus, for each void volume and attitude (18 separate conditions), a zero-g start and four subsequent cycles of high-g (aircraft pull-out and climb), zero-g (top of parabola), and low-g (aircraft dive) were accumulated. Gearbox/lube system performance was nominal and no effect of varying attitude or acceleration forces was seen. As a result of these tests, this issue was resolved.

APU THERMAL CHARACTERIZATION

A major portion of the APU work accomplished at TTA was focused on characterizing APU thermal behavior and resolving thermal problems. It has previously been noted that the TTA facilities were well suited to thermal testing because the entire APU, while firing, could be maintained in a high altitude environment. The vendor did not possess this capability.

Early in the program a failure of an APU (gas generator) occurred at the vendor's facility during an APU hot restart test (simulating abort-once-around conditions where an Orbiter ascent problem forces entry during the first orbital period). Subsequently, in investigating this behavior under altitude test conditions at TTA, another gas generator explosive failure occurred. It was determined that gas generator soakback temperatures following APU shutdown at altitude conditions remained high (no free convection cooling), and that attempted restarts before the gas generator internal injector temperature fell to the 415°F range could result in explosions of the incoming hydrazine in the injector. Natural cooling of the gas generator at altitude conditions required approximately two and a half hours, which was incompatible with mission hot restart requirements. It was determined that additional gas generator cooling was required. Static and conductive techniques were found to be inadequate and a forced water cooling technique was investigated at TTA.

Small capillary coils were fabricated and soldered into the internal central cavity of the gas generator. Water was passed through these capillary coils in a gas generator which had been heated to 1000° - 1200°F in an oven. This technique was effective but still required greater than ten minutes to reduce gas generator temperature below 450°F. Both water and ammonia coolant flows were evaluated. The most successful technique involved the direct spray of a capillary stream of water into the central gas generator cavity. This provided an immediate, rapid evaporative cooling effect to the gas generator and achieved acceptable temperatures within a few minutes with the expenditure of approximately one pound of water. The steam created was vented external to the gas generator. This concept was implemented for the flight APU's and a gas generator water cooling system was added to the vehicle which can be operated by crew command and provides a 210 second spray of water into the gas generator central cavity to achieve temperatures for safe restart. Since APU operational circuits in the controller make it possible for the gas generator cooling flow to be commanded when the gas generator is not at high temperatures, a special test was run simulating this case to insure that the gas generator would not be overcooled and that ice would not be formed and block the cavity. This test was successful.

During APU testing focused on the hot restart problem at TTA, it was found that large vapor bubbles were being formed in the fuel system as a result of high thermal soakback temperatures of the fuel pump and control valve. Excessive dwell time at temperatures above 200°F (as high as 300°F) were causing fuel decomposition and bubble formation. It was shown that the bubble size was directly proportional to dwell time at the higher temperatures. The gas bubbles caused slow startup transients, even leading to APU underspeed shutdowns when operating speed of the turbine was not reached in the specified time. Of much more serious consequence was a control valve explosive failure due to the adiabatic compression and detonation of a hot fuel vapor bubble in the valve during hot restart testing.

This valve explosion led to an extensive series of APU tests at TTA to characterize the parameters of vapor bubble formation. Additional water

cooling systems were developed for both the control valve and fuel pump. The APU cooling locations are shown in figure 5. The valve and pump cooling systems consisted of water spray plates, mounted on the valve and between the pump and the APU structure, which contained small spray orifices to spray coolant water directly on the components. The evaporative cooling effect of the water controlled the component temperature. The pump plate also acted to inhibit/intercept soakback heat flow into the pump. Subsequent tests verified the performance of the cooling systems and verified the acceptability of a 200°F upper thermal limit for the control valve and fuel pump. A single water system valve controls spray to both the APU control valve and fuel pump.

This cooling scheme was adopted for the flight APU and a second, separate water system was installed on the vehicle which applies pulsing water spray to both the control valve and fuel pump to limit their soakback temperatures to 200°F when the APU is shut down. The water spray is controlled thermostatically. The coolant spray is not performed after landing because the evaporative cooling effect is not strong at sea level pressure conditions.

Formal qualification testing of the APU water cooling systems was performed at TTA.

Extensive preparation of test facility systems was required to carry out both the development and qualification tests. Among the special facility equipment and test techniques required for these tests were the following:

1. A high fidelity hydraulic load system was provided which matched vehicle thermal mass and inertia characteristics and pressure drop characteristics. The simulated hydraulic system contained a number of actual flight components. A series of hydraulic load valves was provided to enable various flow demand situations. For many tests involving mission duty cycle simulations the load valves were automatically programmed to provide a time sequenced simulation of ascent, on-orbit, and entry hydraulic loads.

2. A high fidelity lubrication system external loop was provided, often including a flight configuration water spray boiler (WSB) which provides APU lube cooling and hydraulic fluid cooling on the Orbiter. The lube system mass and thermal inertia matched that of the Orbiter. Lube oil flow was monitored in a sight glass via closed circuit TV during tests.

3. A lubrication system oil servicing tool was developed and provided to achieve and verify the correct oil volume/void volume in the gearbox.

4. A high fidelity fuel storage and feed system was provided, including a flight fuel tank, flight filter, and a geometrically high fidelity plumbing system. Also, a special tool and procedure for measuring fuel system bubbles was developed and provided.

5. Separate thermal enclosures for the APU and for the WSB and hydraulic system were provided. These enclosures surrounded the test hardware, were

painted with black thermal control paint, and contained coils to permit the circulation of a thermal conditioning fluid. The enclosures could be independently controlled over the temperature range -65°F to +220°F. Time phased thermal profiles could also be performed. For example, when performing an ascent simulation the temperature of the APU enclosure was increased over a 20-minute time period from 75°F to 125°F, held at 125°F for two hours, and then returned to 75°F for the remainder of the mission simulation test. The facility thermal control systems were very flexible and offered a great deal of capability.

6. Mission simulation testing involved the simulation of sea level start and operation, ascent, shutdown, on-orbit checkout, shutdown, and entry and landing. Some mission duty cycle tests covered a 5-day period and included simulation of high ascent and entry temperatures as well as low (-65°F) on-orbit cold soak temperatures. Of particular interest is the performance of ascent and entry pressure profiles. Ascent and entry pressure profiles are shown in figures 6 and 7. For ascent simulation, a pressure of 0.089 psia (the triple point of water) is reached in 108 seconds.

To perform an ascent pressure profile the subsystem test chamber was closed, evacuated, and back-filled with nitrogen to provide a safe chamber environment for the venting of APU exhaust into the chamber (the mixing of APU exhaust gases--N_2, H_2, NH_3--would provide an explosive mixture with air). The APU was started, sea level pressure maintained, and at the appropriate time the isolation valve between the chamber and the steam ejector system was regulated to produce the ascent profile of figure 6.

For mission duty cycle tests requiring long non-operating APU periods, the steam ejector system was valved off and shut down, and chamber altitude was maintained by mechanical pumps.

The descent pressure profiles of figure 7 were produced by adjusting and closing the chamber isolation valve to the steam system, and then in-bleeding nitrogen to reach sea level pressures. After the APU was shut down at sea level pressures and soakback data were obtained, the chamber was evacuated and backfilled with air for test personnel entry.

One other important aspect of APU thermal testing which was accomplished at TTA was the development and verification of the APU thermal control system. In early altitude tests at TTA, it was found that the gas generator and fuel system heaters would maintain APU temperatures within acceptable ranges over the entire environmental range (including a 50-hour cold soak at -65°F environmental temperature) for the voltage range of 23-32 VDC. The response of the APU temperatures to heater "off" failure at -65°F environmental temperatures, and to heater "on" failure at 150°F environmental temperature and 32 VDC was determined. These tests were performed in the subsystem chamber at simulated altitudes of 130,000 feet. It was found that the heaters were oversized and that control set points were higher than they needed to be. It

was also found that the heater "on" failure case allowed very little time for crew corrective action before unacceptable temperatures of 300°F in the fuel system were reached.

In later tests of a non-operating APU performed in a different high altitude (10^{-6} torr) thermal test chamber with deionized water simulating the fuel data were obtained to permit resizing of the APU heaters. New heater sizes were identified by varying the voltage to the existing heaters until a 50 percent duty cycle was obtained at cold soak conditions. These new heater power levels were then verified adequate over the complete environmental range, and all failure cases were rerun. The heater failed "on" case at 32 VDC allowed 47 minutes for crew problem detection and corrective action.

It should be noted that an improved APU being developed under JSC contract has recently been tested at TTA and has successfully demonstrated the new heater sizes as well as passively controlled fuel valve and fuel pump temperatures (e.g., the water cooling system was eliminated for these components).

INTEGRATED SYSTEM TESTS

Because of the capability of the TTA facilities, a number of integrated system tests were performed at TTA. These included specific tests to verify the compatibility of the APU with the separately developed WSB. The APU lube pump actually pumps a slurry-type mixture of oil and nitrogen. The WSB was not developed with the frothy mix. Also, the APU lube system tends to suffer the formation of wax from leakage of turbine exhaust and hydrazine fuel into the lube system. It was not known whether the wax would contaminate the WSB and inhibit heat transfer. Extensive full-up APU/WSB testing was accomplished at altitude and under mission duty cycle conditions using the facility features discussed in th previous section. It was found that the APU and WSB performed satisfactorily together.

An important series of integrated tests were performed following early Shuttle flights when the APU lube oil cooling during ascent was inadequate for one APU, forcing premature shutdown of the APU. Subsequent testing at TTA investigated this problem, and even included the use of the "problem" APU and WSB which were removed from the Orbiter for the test. In general, it was found that the exhaust orifice of the WSB was too large (1.25" diameter) and permitted pressures to occur in the WSB at the end of ascent which were below the triple point of water. This allowed the incoming water to freeze rather than to spray on the lube oil and hydraulic oil cooling tubes. The ice blocked the water spray valve nozzles in the WSB and prevented cooling. A smaller WSB exhaust orifice was installed (0.80" diameter) which maintained an adequate pressure in the WSB.

During these tests, a special test rig was developed to allow the WSB to be rotated during mission duty cycle testing from the launch attitude

initially, to an upside down attitude (water draining) simulating zero-g, to the entry attitude. The test set-up for this test is shown in the subsystem test chamber in figure 8.

SUMMARY

The JSC in-house APU test programs conducted at TTA as a part of the development, qualification and flight problem investigation for the Orbiter APU system have produced significant and unique results. These results have served to solve or prevent critical problems, provide operational flexibility and confidence in the hardware, and provide test data and design options that significantly reduced development, qualification, and problem resolution costs.

Table I. - ORBITER APU DESIGN REQUIREMENTS

Power Level	
Nominal	134 Horsepower
Maximum	148 Horsepower
Mission Operating Time	
Nominal Mission	92 minutes
Abort Once Around	120 minutes
Tanked Fuel	350 pounds
Operating Time (between scheduled maintenance)	20 hours
Starts Per Mission	
Minimum	2
Maximum	5
Environmental Temperatures	
Prelaunch (minimum)	0°F
On-orbit (minimum)	-65°F
Entry (maximum)	225°F
Acceleration	
Boost	3.3 g
On-orbit	-0-
Landing	1.5 g
Pressure	
Prelaunch, Postlaunch	14.7 psia
On-orbit	Space vacuum

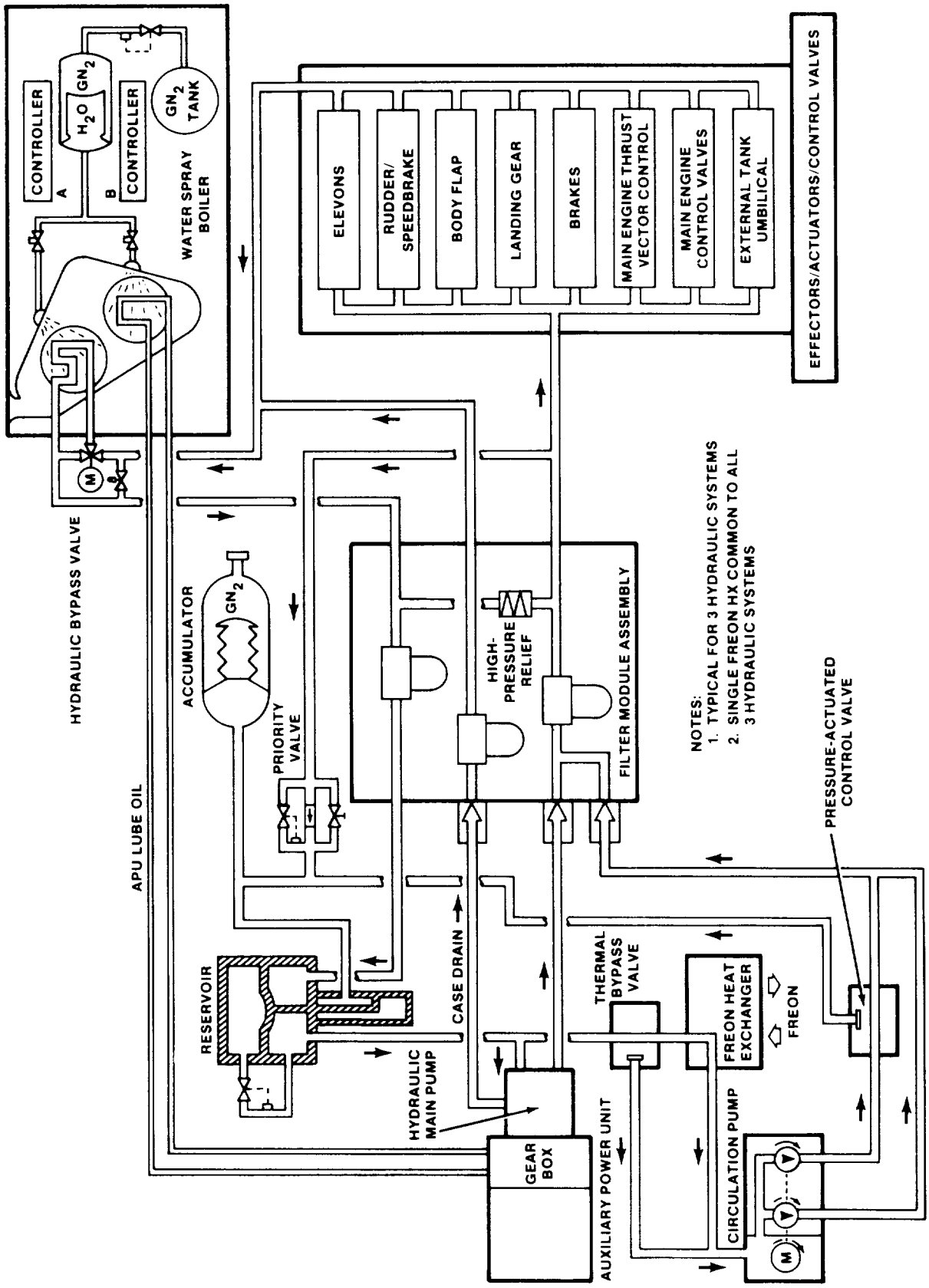

Figure 1 - Orbiter Hydraulic System Schematic

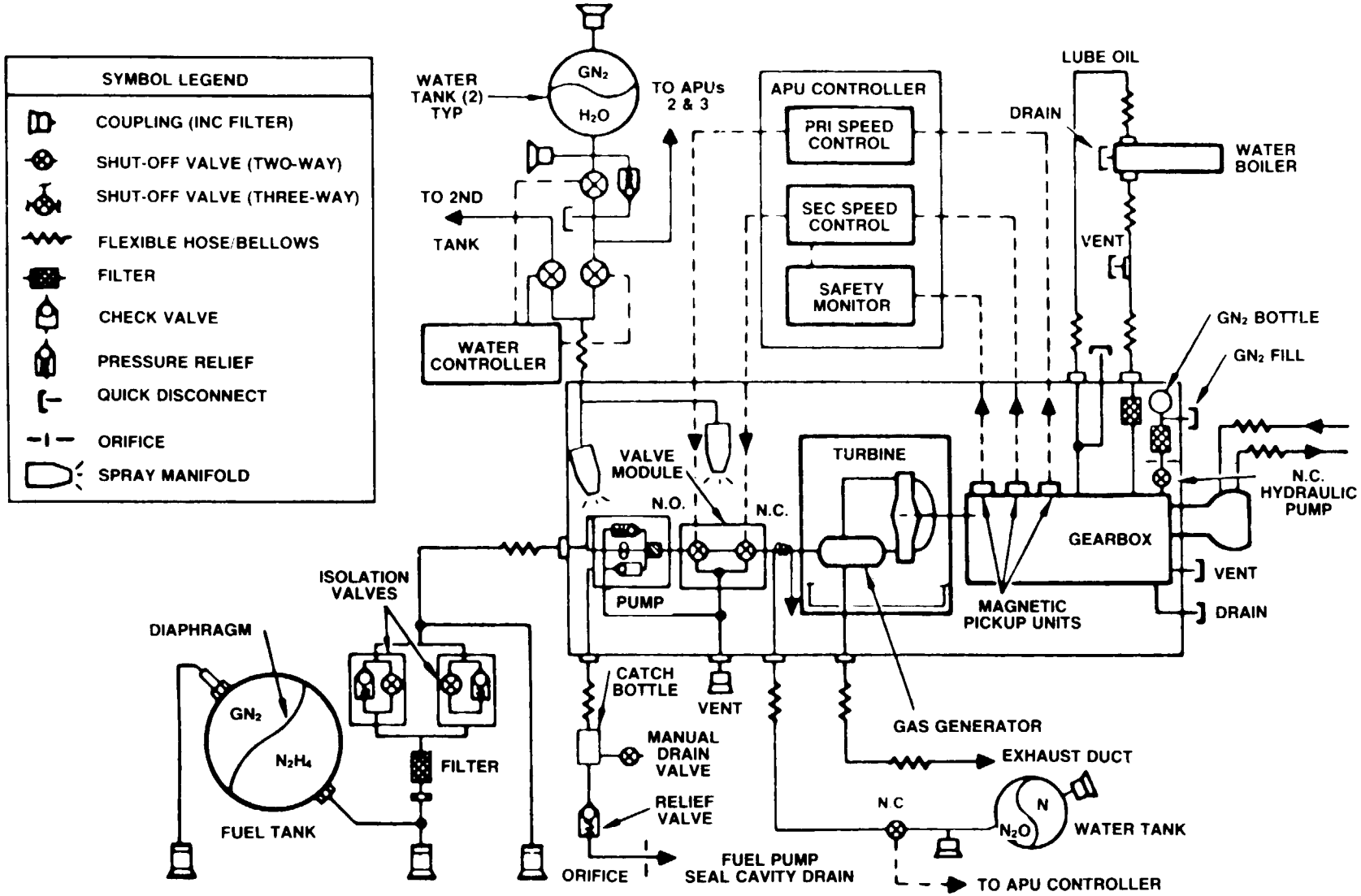

Figure 2 - Auxiliary Power Unit Subsystem Schematic

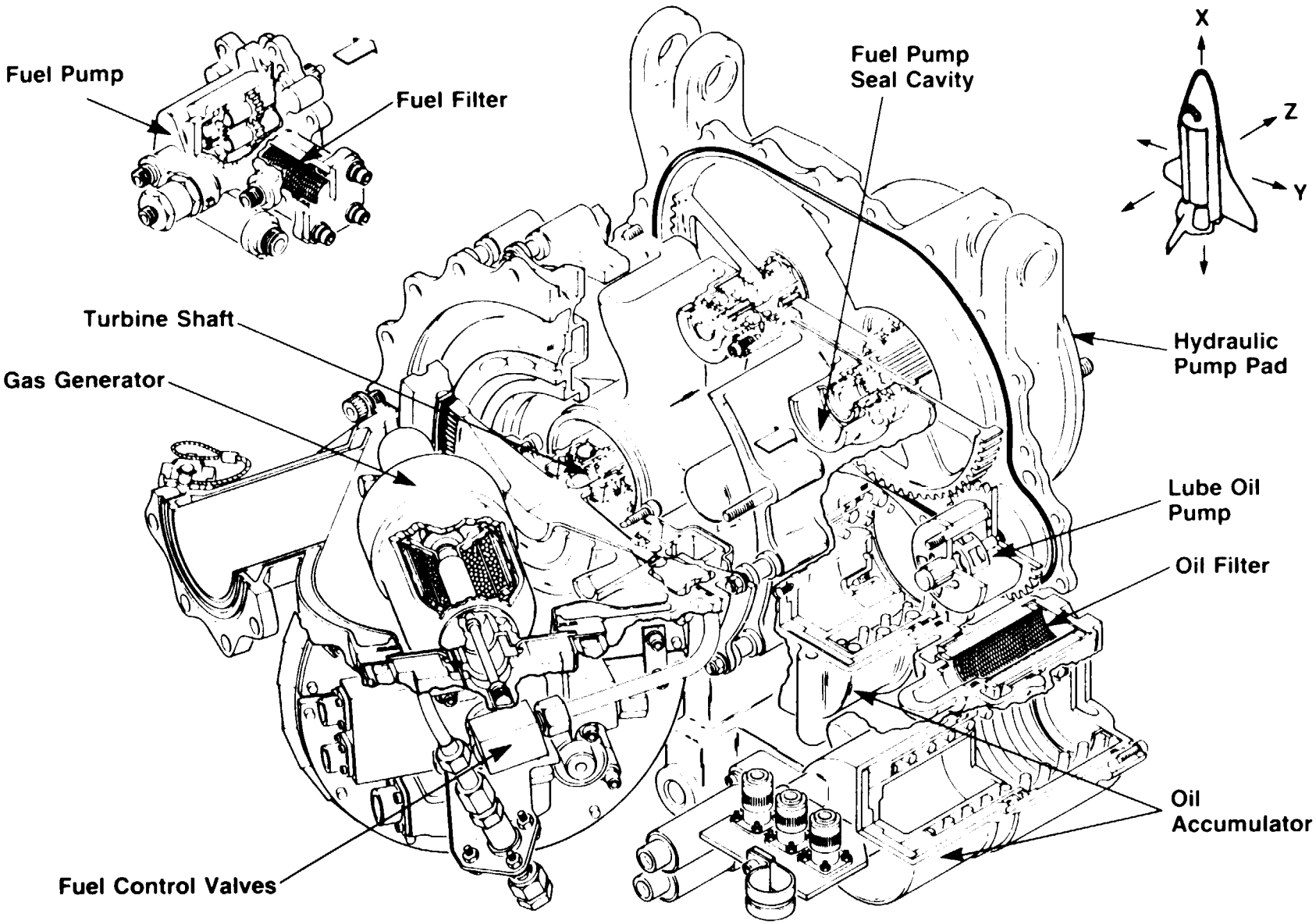

Figure 3 - Auxiliary Power Unit

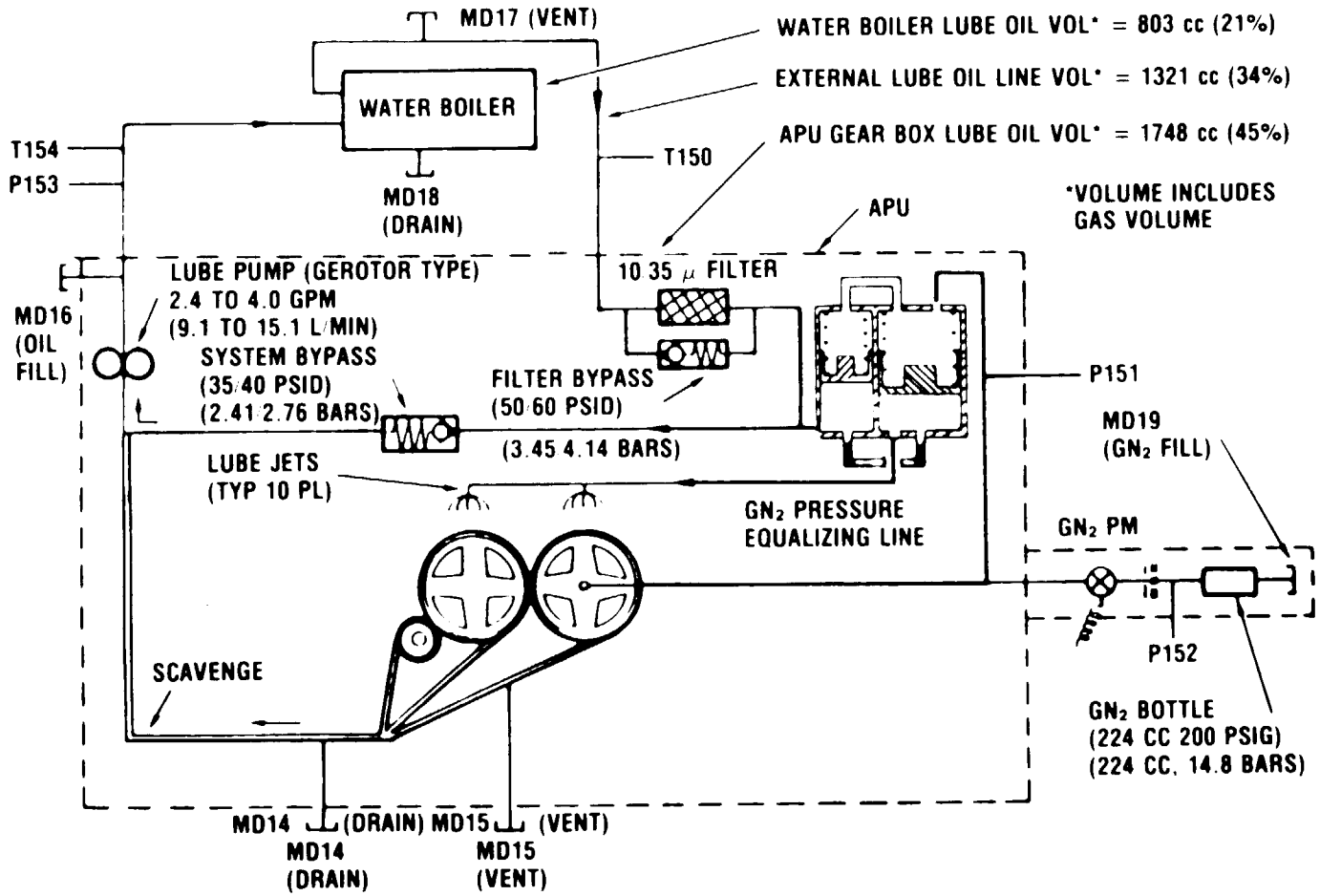

Figure 4 - APU Lubrication System

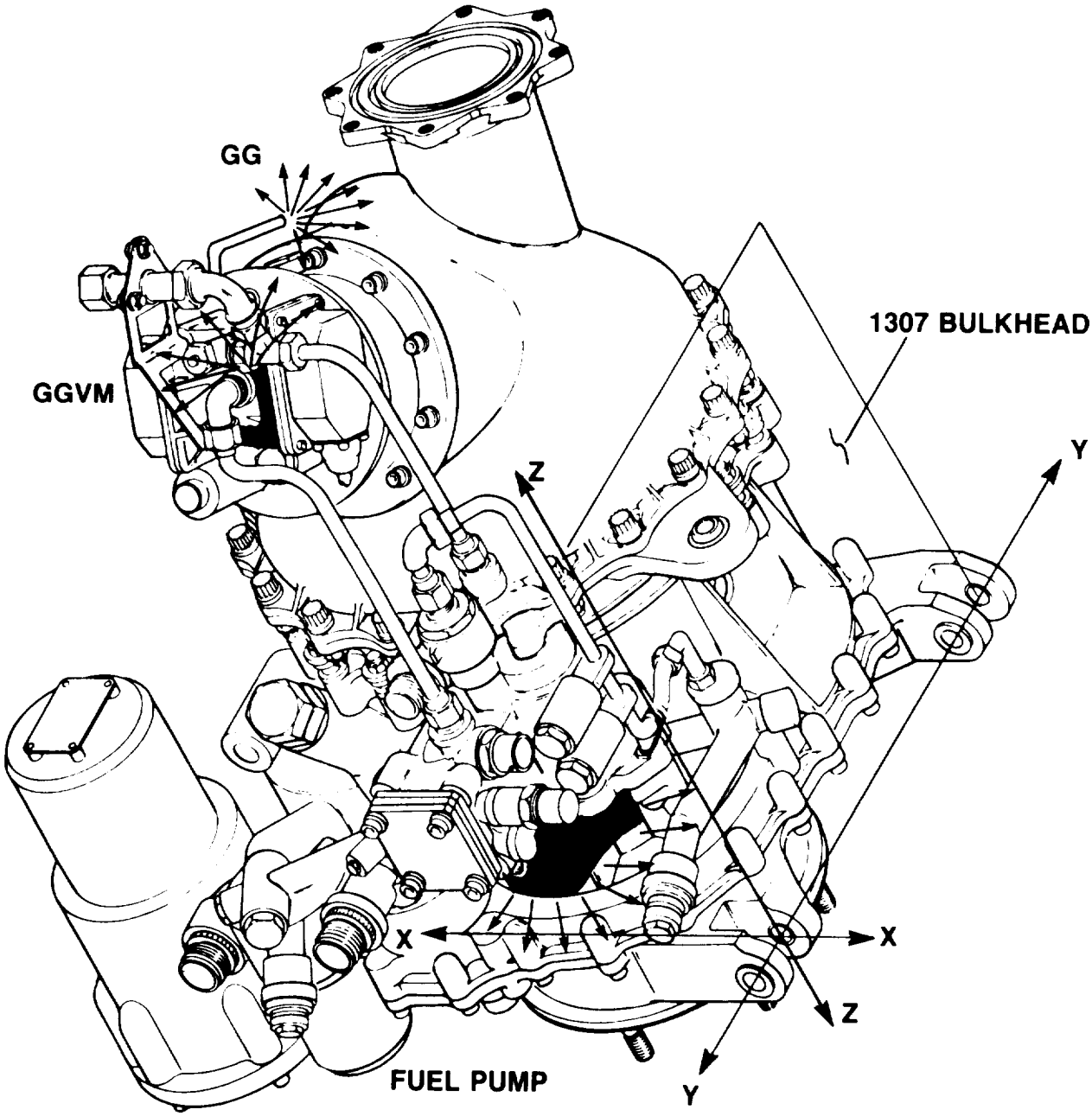

Figure 5 - Orbiter APU Cooling Regions

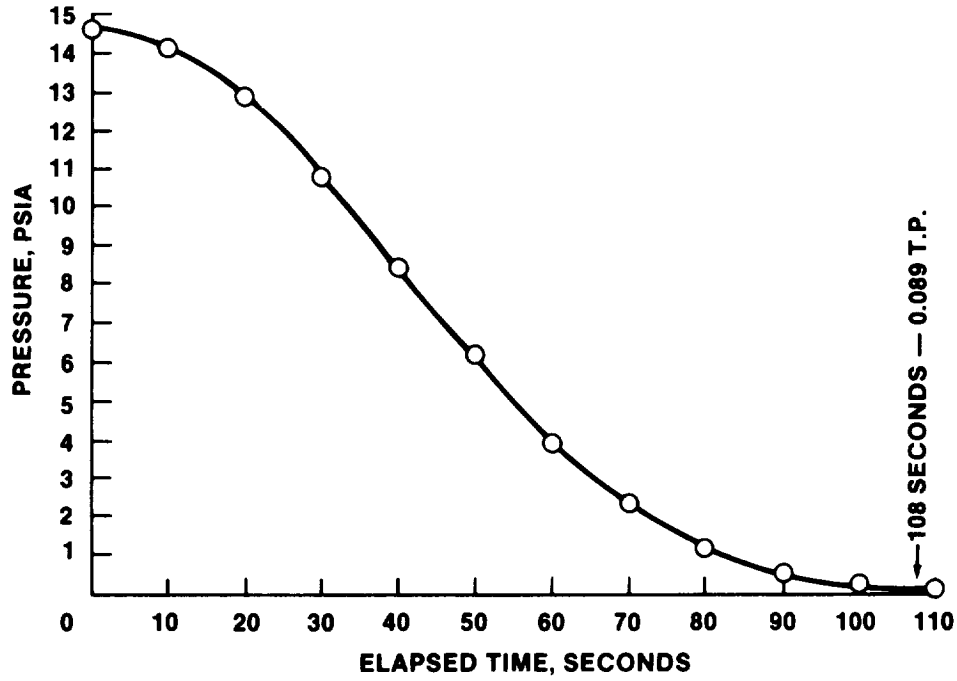

Figure 6 - Simulated Ascent Pressure Profile
(Shows pressure decreasing from 14.7 psia to near zero over 110 second period)

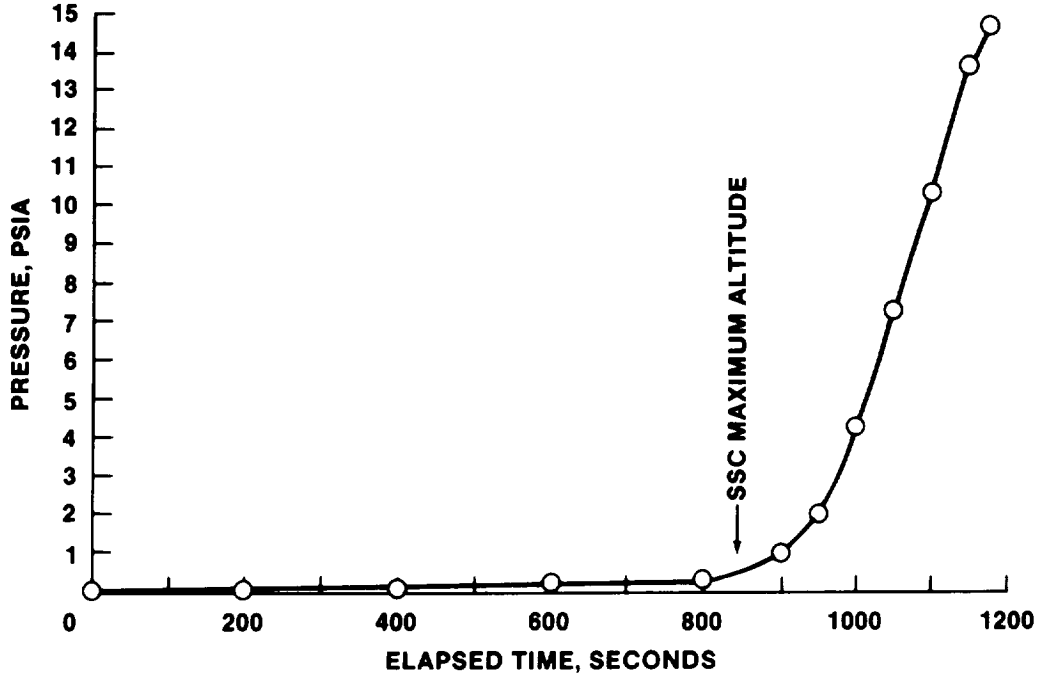

Figure 7 - Simulated Descent Pressure Profile
(Shows pressure increasing from near zero to 14.7 psia over a 1200 second period)

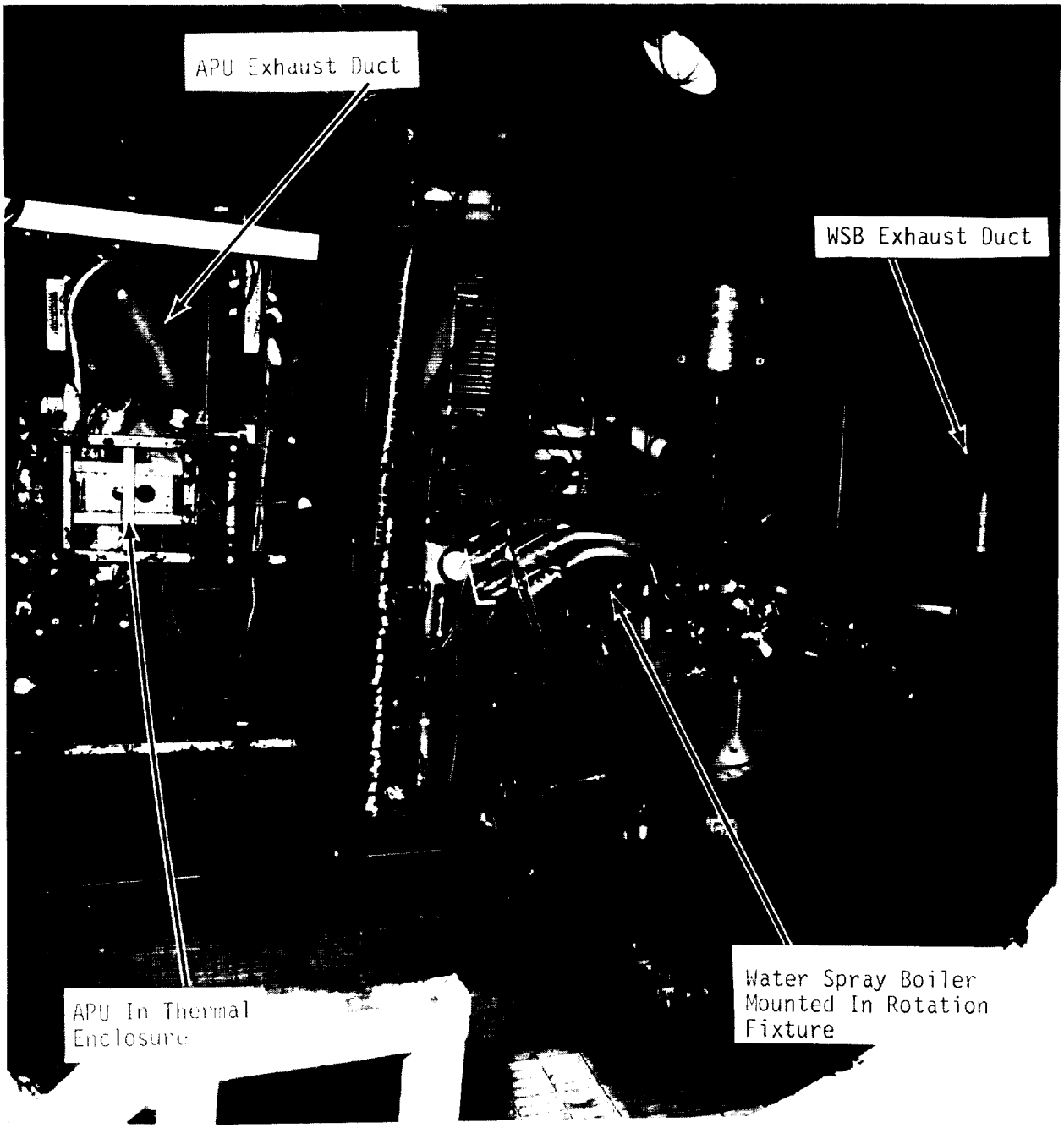

Figure 8 - Integrated APU/WSB Test Set-up

INTRODUCTION TO:
SIMULATION OF UPPER ATMOSPHERE OXYGEN

SATELLITE EXPOSURE TO ATOMIC OXYGEN IN LOW EARTH ORBIT

Daniel R. Peplinski and Graham S. Arnold
Chemistry and Physics Laboratory

Eugene N. Borson
Materials Sciences Laboratory

The Aerospace Corporation
El Segundo, CA 90245

ABSTRACT

A brief review of atmospheric composition in low Earth orbit is presented. The flux of ambient atomic oxygen incident on a surface orbiting in this environment is described. Estimates are presented of the fluence of atomic oxygen to which satellite surfaces in various orbits are exposed.

INTRODUCTION

Experience on unmanned spacecraft and Shuttle flights has shown that atmospheric interactions with spacecraft surfaces in low Earth orbit can have significant effects on the performance of components.[1-7] Oxidation of the materials and the formation of volatile products results in mass loss. The formation of new, stable compounds on surfaces may also affect some functional properties.

Flight experiments located in the Shuttle Orbiter payload bay have provided worthwhile data, but such experiments are difficult to implement and control.

Laboratory experiments have not been able to simulate all the important aspects of the oxygen-surface interactions but have the opportunity to apply diagnostic techniques that cannot, practically, be included in a flight experiment.

The objective of this paper is to provide an introduction to the papers on simulation, that follow, by describing the environment encountered by spacecraft in low Earth orbits.

ATMOSPHERIC COMPOSITION

Figure 1 shows the atmospheric composition as a function of altitude over the range of altitudes commonly considered to comprise low Earth orbit (LEO).[8] One can see that in the range of 200-700 km, the predominant species is atomic oxygen, and at altitudes above and below this range, it remains a significant constituent.

The Earth's upper atmosphere is not a simple function of altitude, as one might infer from Figure 1. It varies in composition, density, and temperature with, among other things, solar activity, variations in the Earth's magnetic field, latitude, local time, and season.[9] The composition shown in Figure 1 is an average one. Figure 2 shows the way in which the oxygen atom density varies with solar activity, which is the variable with the largest impact on the thermospheric composition.[8, 9] The variation between "low" and "high" solar activity conditions takes place on a roughly eleven year cycle, although the exact period and amplitude of an approaching maximum or minimum are quite uncertain.

ATOMIC OXYGEN FLUX IN LEO

The atomic oxygen density in LEO is not particularly high. Even at Shuttle altitudes, the 10^9 cm^{-3} density corresponds to the density of residual gas in a room temperature vacuum chamber at 10^{-7} torr, conditions which are generally considered to be "high vacuum". However, the high velocity of satellites in LEO causes the flux of atomic oxygen on an exposed spacecraft surface to be quite high, indeed. This conversion from (static) density to flux, assuming a nominal velcity of 8 km s^{-1}, is shown on the upper abscissa of Figure 2. The flux of 10^{15} $cm^{-2}s^{-1}$ encountered at Shuttle altitudes is generally considered to be approximately "monolayer" coverage each second.

The ambient temperature of the atmosphere is not particularly high, ranging roughly from 1000-1500 K.[8, 9] Again though, the satellite velocity transforms this relatively familiar (at least to the laboratory) environment into a scarcely investigated one. A relative velocity of 8 km s^{-1} between a solid surface and an oxygen atom corresponds to a translational energy of 510 kJ $mole^{-1}$ (5.3 eV, 8.5 x 10^{-12} erg, 122 kcal $mole^{-1}$). This is equivalent to placing a solid (at the satellite's temperature) in a gas of atomic oxygen at 4.8 x 10^4 K. The types of chemistry which occur in such a non-equilibrium system at such extremes of "temperature" are not well understood.

The fact that the atmosphere has a finite temperature has two (at least) effects on the nature of the interaction between it and an orbiting spacecraft. It introduces a spread in the (normal) impact energy and in the angle of impact. A temperature of 1000 K implies an average thermal O atom velocity of about 1.1 km s^{-1}. Thus, the range in collision energy of atmospheric oxygen with an 8 km s^{-1} spacecraft is approximately 370-670 kJ $mole^{-1}$ (3.9-7.0 eV). Figure 3 shows a plot of the distribution of angles of impact for the case of a surface at 7.7 km s^{-1}, normal to the velocity vector, intercepting a gas of atomic oxygen at 1000 K.[10] One can see that the effective width of this distribution is approximately 15 degrees.

EXPOSURE IN TYPICAL ORBITS

The interaction of a spacecraft surface at orbital velocities with the ambient atmosphere in LEO presents a regime of gas surface chemistry which heretofore has been the subject of little investigation because of the difficulties inherent in reproducing these conditions in the laboratory. Figure 4 shows that this is not an inherently uninteresting regime. In this figure are plotted the orbits (apogee-perigee) of US satellite launches into low Earth orbit over the past few years. NASA, USAF, and unidentified US vehicles into all orbits are listed in the references indicated on the figure.[11, 12, 13] These launches into LEO represent over 40% of all US launches listed in these sources over the period surveyed.

The best initial indicator of the magnitude of an effect of atmospheric bombardment of some particular spacecraft material is the fluence (integrated flux) of atomic oxygen that the vehicle might encounter during the period of interest. Of course, the fluence which any given surface on an orbiting spacecraft will encounter is a tedious function of the satellite's orbit, its orientation, and the exact time at which it flies. However, it is possible to provide some upper bounds on the fluence received for some "typical" conditions. Table 1 shows the fluence incident on a surface normal to the velocity vector for high, average, and low solar activities for four orbital cases: one year on orbit at 830 km (450 n.mi.), five days or five hours at 260 km (140 n.mi.), or 70 minutes in an 150 x 175 km (80 x 95 n.mi.) parking orbit. These fluences were computed by taking straightforward averages of the densities quoted in reference 8 assuming the surface normal always to be pointed along the velocity vector.

A slightly different way to examine the magnitude of atmospheric oxygen bombardment of a surface is to estimate the time, T_{CR}, required (in the particular orbit of interest) for some fluence to accrue on a satellite surface. Tables 2, 3, and 4 show the results of such an estimate for eight different orbits, under three different assumptions of solar activity, in which the fluence of interest was 4.8×10^{21} cm^{-2}. Also shown in these tables are the numbers of orbits, Z, required for that fluence to accrete. These estimates are plotted in Figures 5 and 6.

REFERENCES

1. Leger, L. J.; Spiker, I. K.; Kuminecz, J. F.; Ballentine, T. J.; and Visentine, J. T., "STS-5 LEO Effects Experiment: Background, Description, and Thin Film Results", AIAA Paper #83-2631-CP, Nov. 1983.

2. Leger, L. J.; Visentine, J. T.; and Kuminecz, J. F.; "Low Earth Orbit Atomic Oxygen Effects on Surfaces", AIAA Paper #84-0548, Jan. 1984.

3. Whitaker, A., "Leo Effects on Spacraft Materials", AIAA Paper #83-2632-CP, Nov. 1983.

4. Fraundorf, P.; Lindstrom, D.; Pailer, N.; Sandford, S.; Swan, P.; Walker, R.; and Zinner, E., "Erosion of Mylar and Protection by Thin Metal Films", AIAA Paper #83-2636, Nov. 1983.

5. Park, J. J.; Gull, T. R.; Herzig, H.; and Toft, A. R., "Effects of Atomic Oxygen on Paint and Optical Coatings", AIAA Paper #83-2635CP, Nov. 1983.

6. Peterson, P. N.; Linton, R. C.; and Miller, E. R., "Results of Apparent Atomic Oxygen Reactions on Ag, C, and Os Exposed During the Shuttle STS-4 Orbits", Geophysical Research Letters, Vol. 10, July 1983, pp. 569-571.

7. Arnold, G. S.; Peplinski, D. R.; and Herm, R. R., "A Facility for the Simulation of Low Orbit Atmospheric Oxygen Atom Bombardment", ATR-82(8443)-1, The Aerospace Corporation, El Segundo, CA, 1 July 1982.

8. Hedin, A. E.: Tables of Thermospheric Temperature, Density and Composition Derived from Satellite and Ground Based Measurements. Laboratory of Planetary Atmospheres, Goddard Space Flight Center. Volumes 2, 2, and 3. January, 1979.

9. Hedin, A. E.; Salah, J. E., Evans, J. V.; Reber, C. A.; Newton, G. P.; Spencer, H. W.; Kayser, D. C.; Alcayde, D.; Bauer, P.; Cogger, L.; and McClure, J. P.: A Global Thermospheric Model Based on Mass Spectrometer and Incoherent Scatter Data 1, N_2 Density and Temperature. J. Geophys Res., Vol. 82, 1977, pp. 2139-2147.
and
Hedin, A. E.; Reber, C. A.; Newton, G. P.; Spencer, N. W.; Brinton, H. C.; Mazer, H. G.; and Pottes, W. E.: A Global Thermospheric Model Based on Mass Spectrometer and Incoherent Scatter Data MSIS 2, Composition, J. Geophys. Res., Vol. 82, 1977, pp. 2148-2156.

10. Herm, R. R. and Johnson, B. R., Chemistry and Physics Laboratory, The Aerospace Corporation, El Segundo, CA., to be published.

11. Sherman, M. W., (ed.): The TRW Space Log, Electronics and Defense Sector of TRW, 1 Space Park Way, Redondo Beach, CA, 1983.

12. King-Hele, D. G.; Pilkington, J. A.; Walker, D.M.C.; Hiller, H.; and Winterbottom, A. N.: The RAE Table of Earth Satellites 1957-1982, John Wiley and Sons, New York, 1983.

13. Office of Public Affairs, NASA Goddard Space Flight Center, Satellite Situation Report, NASA/GSFC, Greenbelt, Md., Vol. 23, 1983 (published bi-monthly).

Table 1. ATOMIC OXYGEN FLUENCES FOR VARIOUS ORBITS[a]

Altitude (km/n.mi.)	Period	Fluence (cm^{-2}) Low Solar Activity	Standard Atmosphere	High Solar Activity
830/450	1 year	3.3×10^{16}	3.3×10^{18}	3.3×10^{20}
260/140	5 hours	9.6×10^{18}	1.9×10^{19}	2.3×10^{19}
	5 days	2.3×10^{20}	4.3×10^{20}	5.6×10^{20}
150 x 175/ 80 x 95	70 min.	3.3×10^{19}	3.0×10^{19}	3.7×10^{19}

a. Surface normal to the velocity vector for duration of exposure.

Times Required for A Fluence of 4.8×10^{21} cm^{-2} to Accrue
Table 2. Results for the High Solar Activity Case.

Orbit Type	Altitude (km/n.mi.)	T_{CR} (days)	Z (No. of Orbits)
Circular, equatorial	185/100	9.2×10^{0}	1.5×10^{2}
	290/155	5.2×10^{1}	8.4×10^{2}
	320/200	1.6×10^{2}	2.5×10^{3}
	800/432	2.9×10^{4}	4.2×10^{5}
Circular, polar	185/100	9.9×10^{0}	1.6×10^{2}
	290/155	5.6×10^{1}	9.0×10^{2}
	320/200	1.7×10^{2}	2.7×10^{3}
	800/432	3.4×10^{4}	4.9×10^{5}

Table 3. Results for the "Average" Solar Activity Case.

Orbit Type	Altitude (km/n.mi.)	T_{CR} (days)	Z (No. of Orbits)
Circular, equatorial	185/100	1.0×10^{1}	1.7×10^{2}
	290/155	7.3×10^{1}	1.2×10^{3}
	320/200	2.7×10^{2}	4.3×10^{3}
	800/432	1.3×10^{5}	1.8×10^{6}
Circular, polar	185/100	1.1×10^{1}	1.9×10^{2}
	290/155	7.9×10^{1}	1.3×10^{3}
	320/200	2.9×10^{2}	4.5×10^{3}
	800/432	1.3×10^{5}	1.8×10^{6}

Table 4. Results for the Low Solar Activity Case.

Orbit Type	Altitude (km/n.mi.)	T_{CR} (days)	Z (No. of Orbits)
Circular, equatorial	185/100	1.3×10^{1}	2.2×10^{2}
	290/155	1.7×10^{2}	2.8×10^{3}
	320/200	1.0×10^{3}	1.6×10^{4}
	800/432	3.7×10^{6}	5.4×10^{7}
Circular, polar	185/100	1.4×10^{1}	2.3×10^{2}
	290/155	1.8×10^{2}	2.8×10^{3}
	320/200	9.8×10^{2}	1.5×10^{4}
	800/432	3.7×10^{6}	5.4×10^{7}

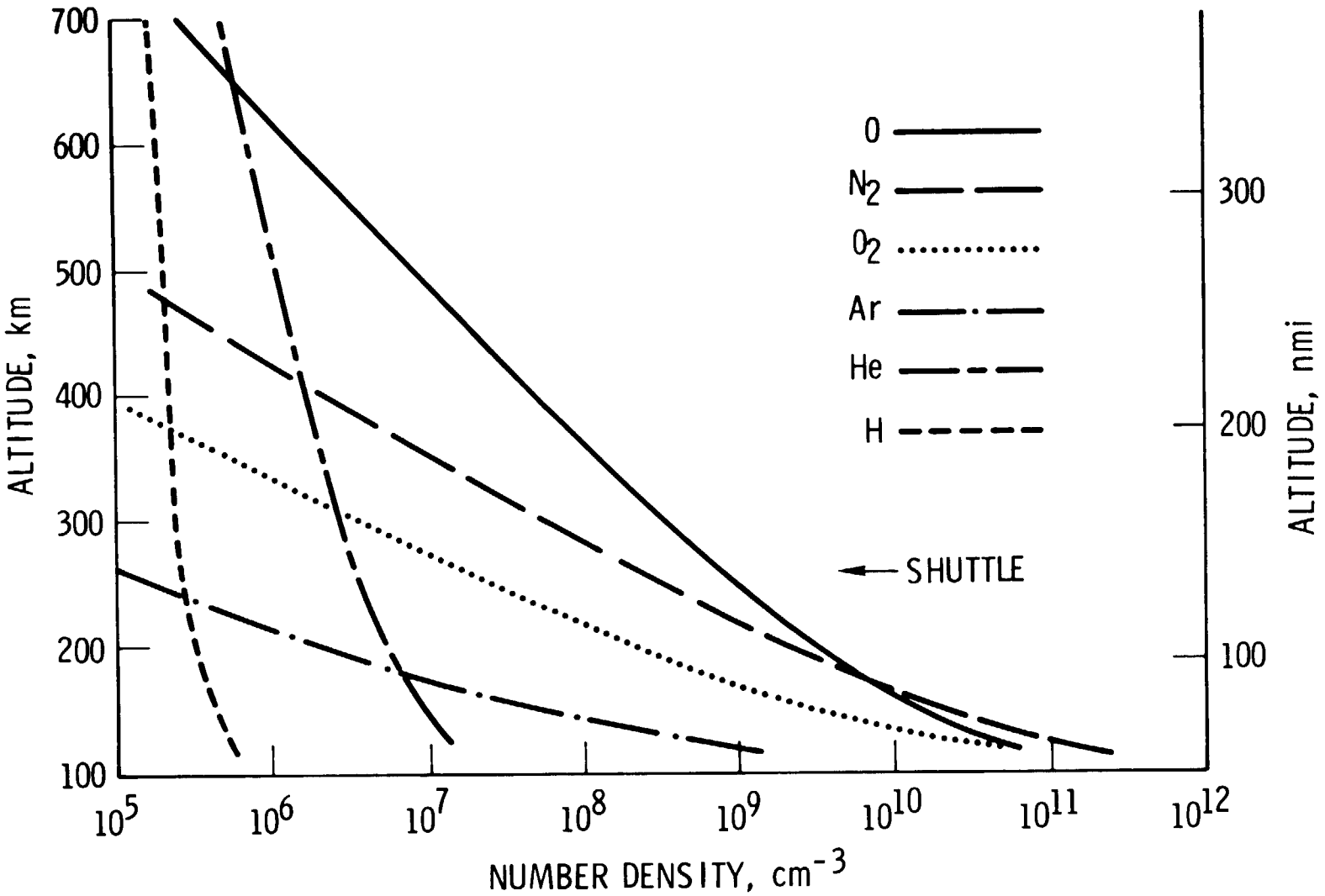

Figure 1 - Atmospheric composition in low Earth orbit

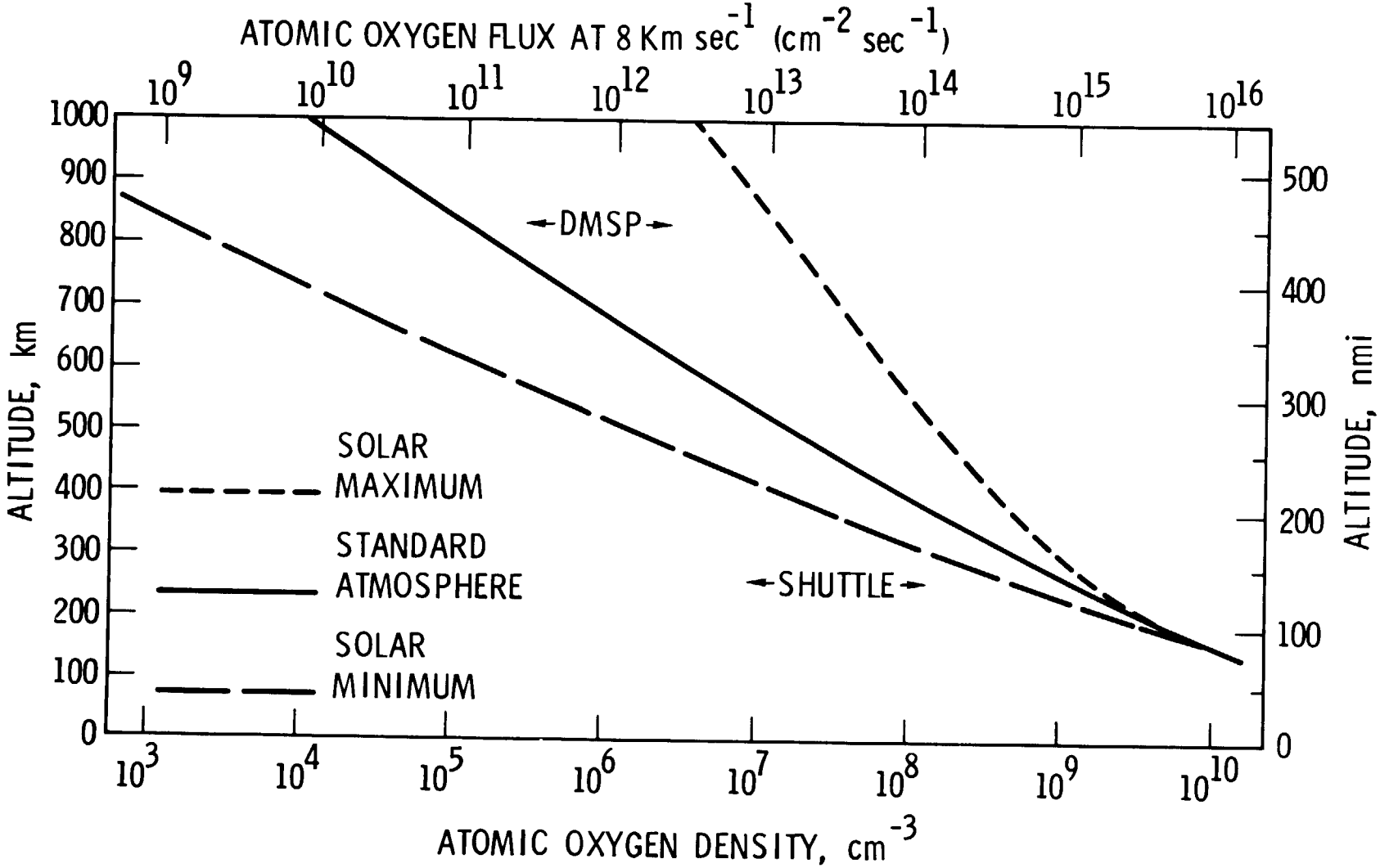

Figure 2 - Atmospheric atomic oxygen density in low Earth orbit

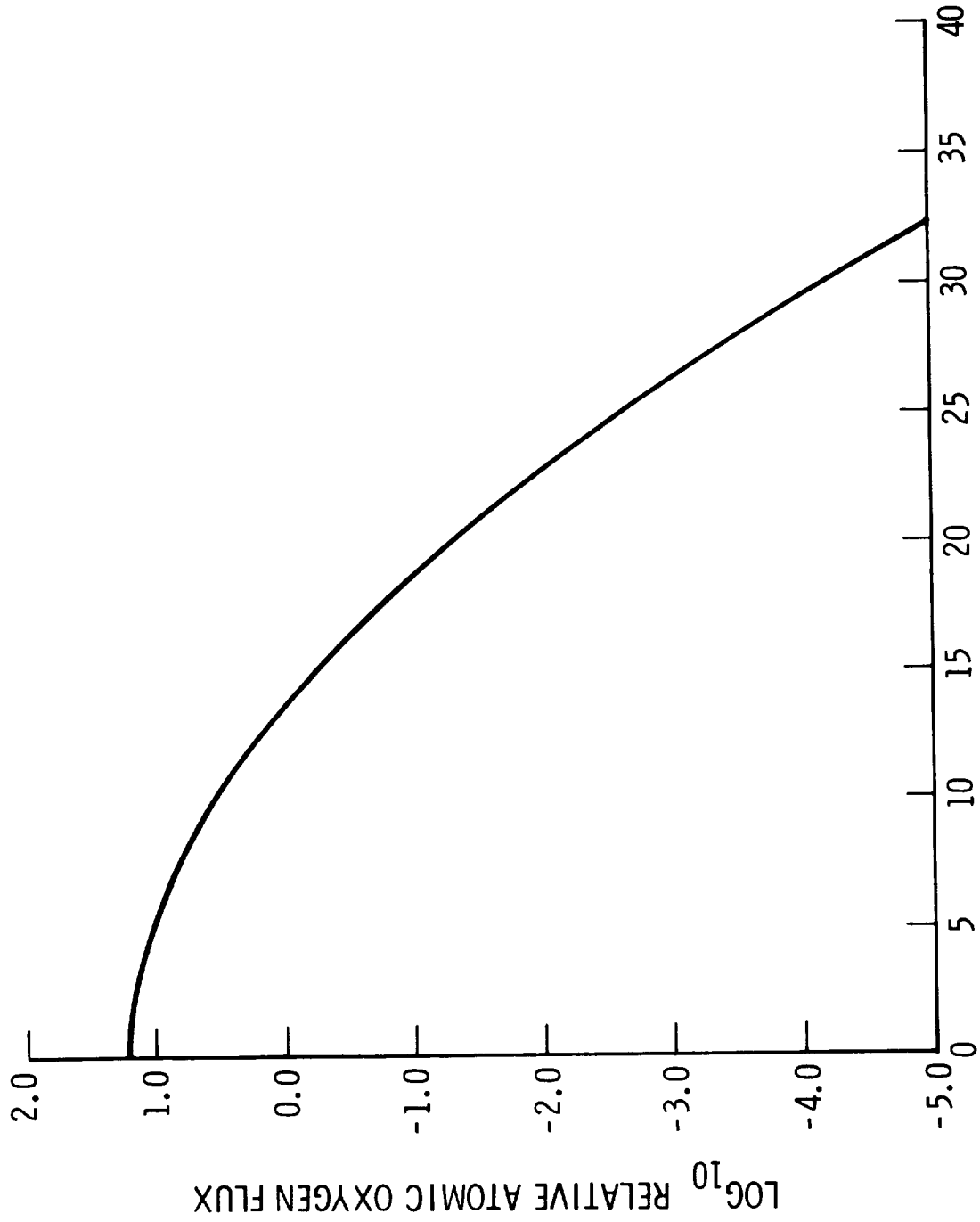

Figure 3 - Distribution of impact angles of atomic oxygen on a surface normal to the velocity vector in low Earth orbit

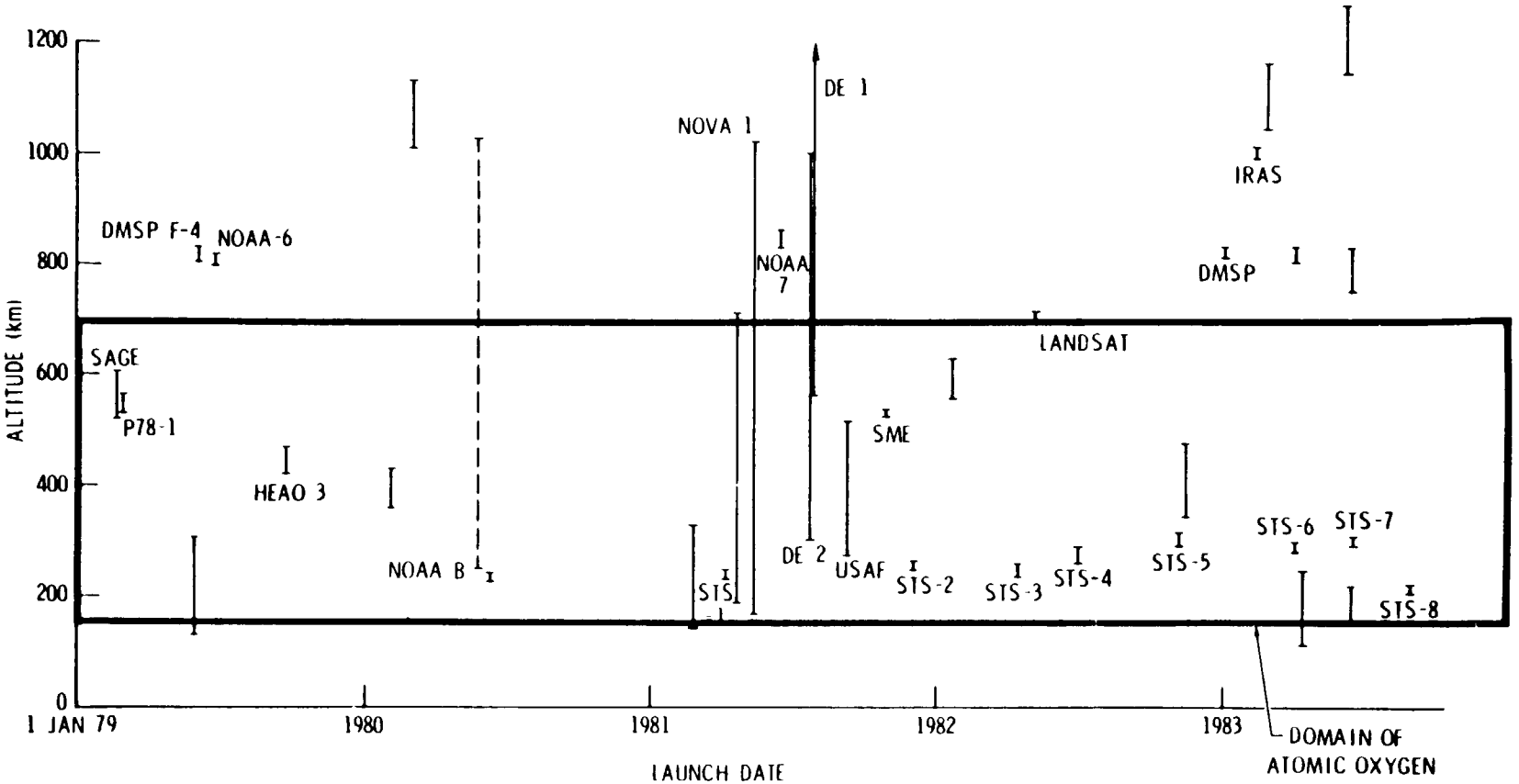

SOURCES: TRW SPACE LOG
R.A.E. TABLE OF EARTH SATELLITES
GODDARD SATELLITE SITUATION REPORT

Figure 4 - U.S. launches to low Earth orbit

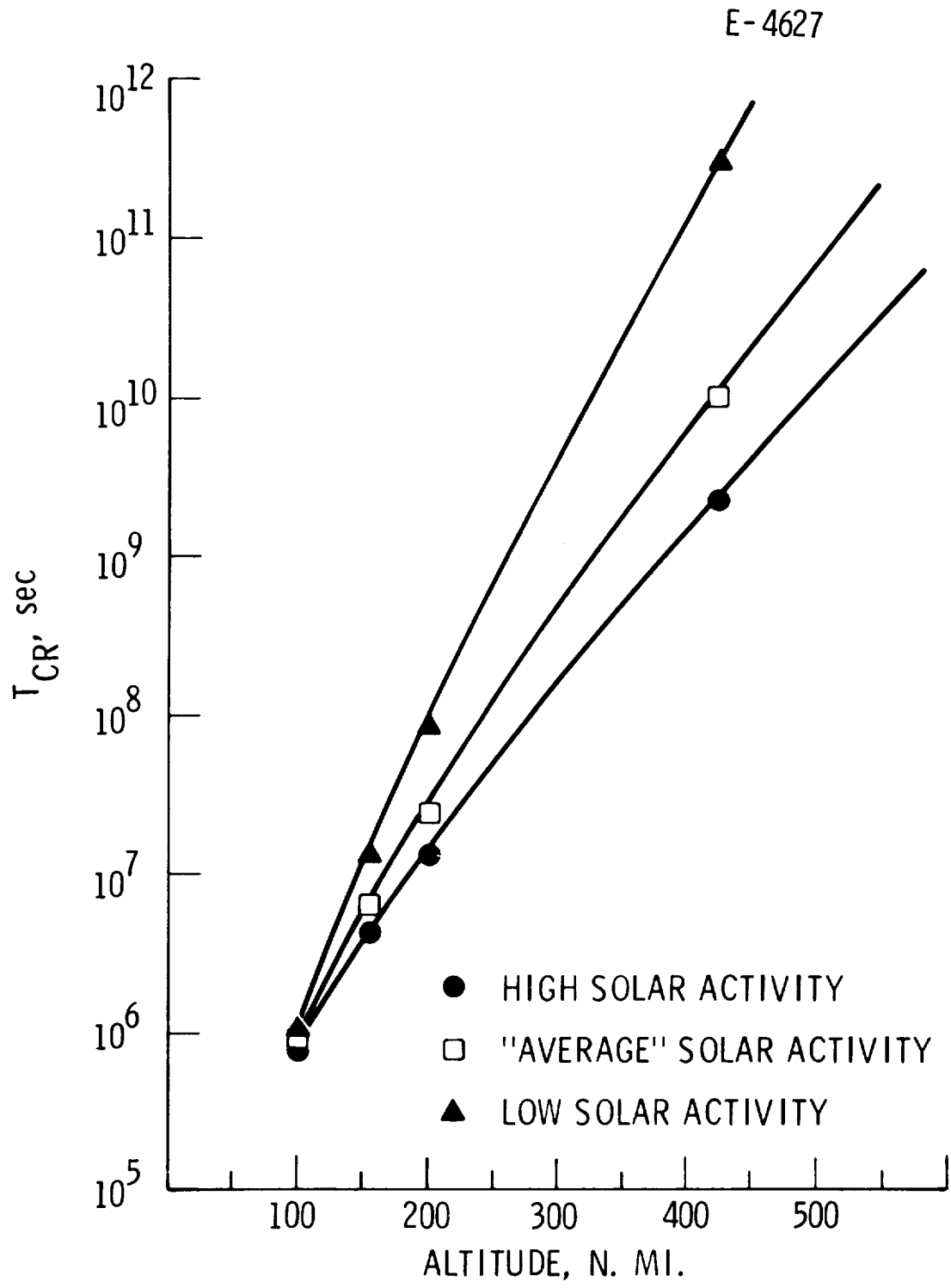

Figure 5 - Time to accrue a fluence of atomic oxygen of 4.8×10^{21} cm^{-2} in various (nominally) equatorial circular orbits. (Points connected to aid the eye.)

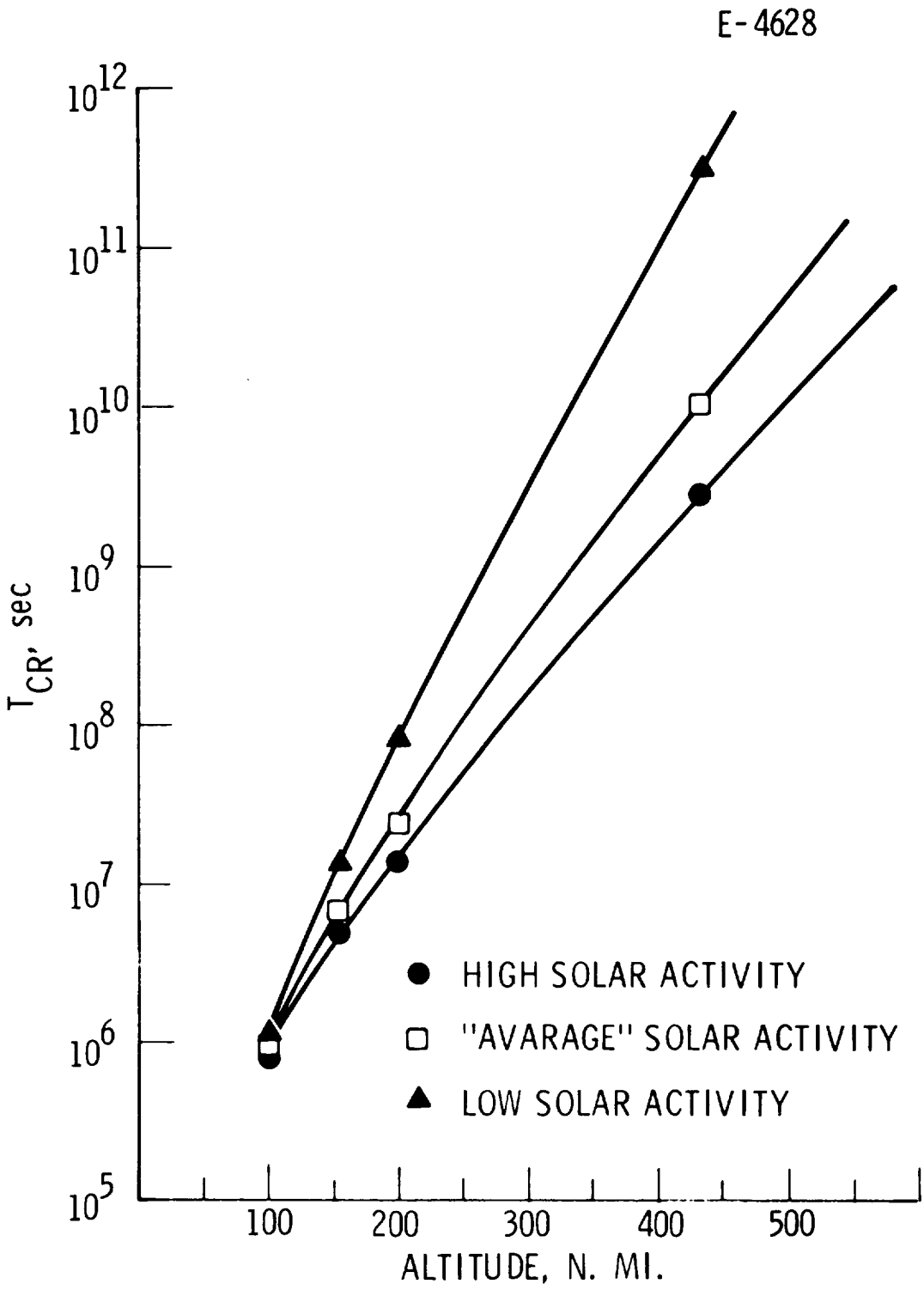

Figure 6 - Time to accrue a fluence of atomic oxygen of 4.8×10^{21} cm^{-2} in various circular polar orbits. (Points connected to aid the eye.)

HYPERVELOCITY SUPERSONIC NOZZLE BEAM SOURCE OF ATOMIC OXYGEN[≠]

A. Freedman, W. Unkel[*], J. Silver, and C. Kolb
Aerodyne Research, Inc.
45 Manning Rd, Billerica, MA 01821

ABSTRACT

A hypervelocity source of atomic oxygen has been developed. Dissociation of molecular oxygen is accomplished by injection into a flow of helium and/or argon which has been heated in a commercial plasma torch. Atomic velocities of up to 4 kms^{-1} have been produced; recent improvements offer the possibility of even higher velocities. This source has been utilized in studies of translational-to-vibrational energy transfer in carbon dioxide and in an investigation of the "shuttle glow" effect.

INTRODUCTION

Space-based facilities face an unexpectedly hostile environment at orbital altitudes (between 100 and 400 km) due to chemical interaction with atomic oxygen at the high velocities of orbiting spacecraft (up to 8 kms^{-1}). Recent shuttle-based experiments indicate substantial degradation and erosion of various materials which face into the "atmospheric wind". This effect could have profound implications for both the effective life and utility of satellites and space station systems. A further ramification is that surface degradation apparently produces direct optical interferences as well as molecular off-gassing which can lead to significant contamination of space-based optical instrumentation.

Recent work at the Air Force Geophysics Laboratory has resulted in the first continuous high flux atomic oxygen source which produces an atomic beam approaching orbital velocities. The source derives from the work of Knuth and co-workers,[1] who developed an electrical arc discharge source which produced very high energy (up to 21 eV) beams of rare gases. Bickes, et al.[2] later developed a similar source for producing nitrogen atoms by blending molecular nitrogen into the rare gas flow. In both cases, however, significant production of excited state species was found. Moreover, a significant drawback in using these sources with oxygen is the rapid corrosion of the metal electrodes. We solved these problems by introducing oxygen as a minor constituent downstream of the discharge region. By providing a long channel before the beam is formed, most metastable and ionic species are quenched. If sufficient time is available, the resulting species distribution approaches that of high

[≠]Work supported by Subcontract 83-046 from Utah State University.

[*]Permanent address: Dept. of Mechanical Engineering, Massachusetts Institute of Technology, Cambridge, Massachusetts

temperature equilibrium (~ 3000 - 4000 K), while the supersonic expansion provides for a narrow velocity distribution.

EXPERIMENTAL

The atomic oxygen source[3] consists of two parts, a commercial DC plasma torch (TAFA Corporation) and a beam-forming nozzle section constructed of OHFC copper. The torch is used to provide a source of high temperature inert gas at atmospheric pressure. The arc operates in a "non-transferred mode", meaning that the gas is heated as it passes through the discharge, which is contained entirely within the body of the torch. As illustrated in Figure 1, the oxygen is admixed 2 cm downstream of the discharge region through an inlet originally intended for introduction of powder for spray deposition. The inlet diameter was reduced to 0.04 cm so that it provides rapid mixing of the oxygen with the carrier gas. The gas then flows down a 4 cm (0.80 cm diameter) channel in the nozzle section before encountering a chamber through which virtually all of the gas is exhausted. A small fraction flows through a 0.0125 cm diameter hole into the vacuum chamber, forming the molecular beam. The design of the nozzle section is such that it has no internal O-rings and the water-cooling and gas channels are completely separated.

RESULTS AND DISCUSSION

This source has been used to study the excitation cross sections of the (001) vibrational mode of CO_2 by collision with atomic oxygen.[4] Upper limits for this system have been set at 0.03Å^2 at relative velocities of 3.85 kms^{-1} in an experiment utilizing crossed molecular beams and detection of collision induced infrared fluorescence. The source has also been used in an attempt to simulate visible emission attributed to space shuttle atmosphere interactions (shuttle glow). When a shuttle tile was bombarded with 4 kms^{-1} oxygen atoms, no radiation attributable to this interaction was detected.

Recent efforts have centered on improving the performance of the source by improving its durability and increasing the beam velocity to near orbital velocities (up to 8 kms^{-1}). The first problem has been solved by increasing water flow velocities through the redesigned front nozzle and mixing channel sections. This improved cooling capacity allows the use of much higher power settings (up to 18 kW) and decreased carrier gas flow (at a considerable savings in gas usage). This allows the production of much higher temperatures in the carrier gas (~ 5000 K) which should lead to higher oxygen dissociation yields and beam velocities.

REFERENCES

1. D.H. Winicur and E.L. Knuth, J. Chem. Phys. 46, 4318 (1967); W.S. Young, W.E. Rodgers and E.L. Knuth, Rev. Sci. Instrum. 40, 1346 (1969); W.S. Yong and E.L. Knuth, Entropie 30, 25 (1969); D.H. Winicur, E.L. Knuth, and W.E. Rodgers, Entropie 30, 154 (1969).

2. R.W. Bickes, K.R. Newton, J.M. Herrmann, and R.B. Bernstein, J. Chem. Phys. 64, 3648 (1976).

3. J. Silver, A. Freedman, C. Kolb, A. Rahbee and C. Dolan, Rev. Sci. Instrum. 53, 1714 (1982).

4. A. Freedman, A. Rahbee, J. Silver and A. Stanton, AFGL, TR-83-0078 (1983).

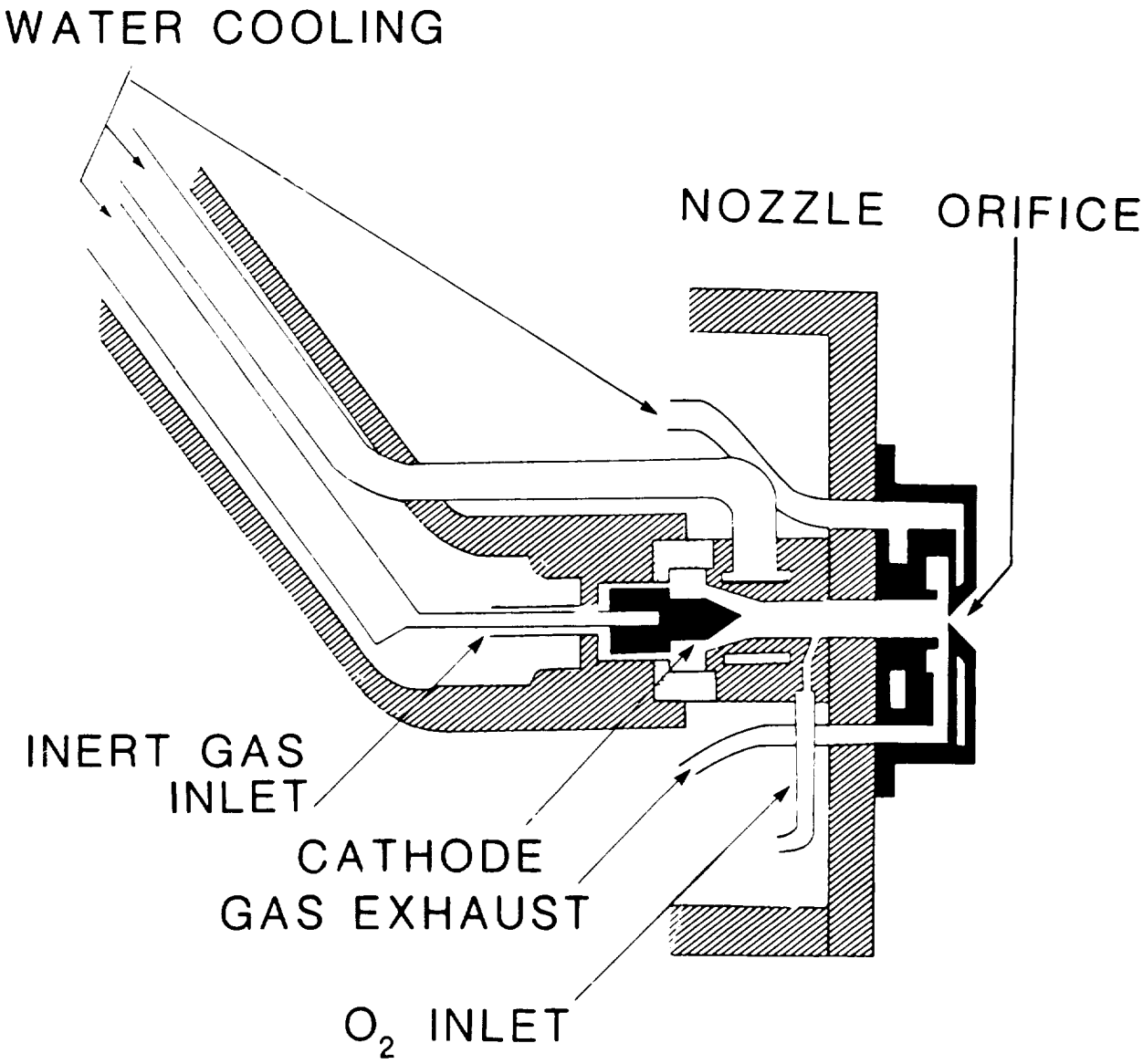

Figure 1 - Schematic of Hypervelocity Atomic Oxygen Beam Source

A FACILITY FOR INVESTIGATING INTERACTIONS OF ENERGETIC ATOMIC OXYGEN WITH SOLIDS[a]

Graham S. Arnold and Daniel R. Peplinski

Chemistry and Physics Laboratory
The Aerospace Corporation
El Segundo, California, 90245

ABSTRACT

A facility for the investigation of the interactions of energetic atomic oxygen with solids is described. The facility is comprised of a four-chambered, differentially pumped molecular beam apparatus which can be equipped with one of a variety of sources of atomic oxygen. The primary source is a DC arc-heated supersonic nozzle source which produces a flux of atomic oxygen in excess of 10^{15} cm^{-2} sec^{-1} at the target, at a velocity of 3.5 km sec^{-1}. Results of applications of this facility to the study of the reactions of atomic oxygen with carbon and polyimide films are briefly reviewed and compared to data obtained on various flights of the Space Shuttle.

INTRODUCTION

As the period for which satellite missions are required to function increases, so also the importance of the long term effects of exposure of spacecraft materials to the upper atmosphere increases. The advent of the Shuttle Orbiter, operating at relatively low altitudes, and plans for a permanent, manned space station in low Earth orbit (LEO) place further importance upon the action of atmospheric species because of the relatively high atmospheric density in LEO.

A spacecraft in the altitude range of 200-700 km experiences bombardment by an atmosphere whose primary constituent is neutral atomic oxygen.[1] Although the ambient gas temperature is only on the order of 1000 K, the 8 km sec^{-1} velocity of the spacecraft causes the oxygen atoms to strike satellite surfaces at a relative kinetic energy of 500 kJ $mole^{-1}$ (5 ev). At Shuttle altitudes, the atomic oxygen density is on the order of 10^{9} cm^{-3}, which corresponds to a flux of about 10^{15} cm^{-2} sec^{-1}. These conditions present a regime of gas-surface chemistry which has been the subject of very little experimental investigation because of the difficulties inherent in reproducing them in the laboratory. A variety of effects observed on NASA and USAF

a. This work was sponsored by the Aerospace Sponsored Research Program.

spacecraft have been ascribed to the action of the ambient atmosphere. These include material erosion,[2,3] optics degradation,[4] and luminescence.[5,6]

This paper describes a facility assembled specifically for the investigation of the interactions of energetic atomic oxygen with solid surfaces. The major elements of this facility, which are described below, are the four-chambered differentially pumped molecular beam apparatus, the provisions for mounting and interrogating solid samples, and the DC arc-heated supersonic atomic beam source. Results of experimental work using this facility which demonstrate its utility in performing its appointed task are briefly presented along with indications of planned and recommended future work.

FACILITY DESCRIPTION

VACUUM SYSTEM

Figure 1 shows a schematic representation of the molecular beam apparatus. The vacuum system is comprised of four differentially pumped stainless steel chambers.

The first three chambers are 0.46 m^3 boxes equipped with Viton or Buna-N "O-ring" seals. The first chamber, or source chamber is pumped by an unbaffled 8000 l sec^{-1} oil diffusion pump (Varian model VHS-400). The second and third chambers are pumped by Consolidated Vacuum Corporation 10 inch oil diffusion pumps, each equipped with a Mount Vernon Research Co. liquid nitrogen cooled trap and a Vacuum Research Manufacturing Co. electropneumatically actuated, viton-sealed gate valve. The pump fluid for the first two chambers is Dow Corning 704 silicone diffusion pump oil, while in the third chamber the hydrocarbon oil Monsanto Santovac 5 is used. The approximate pumping speed of the 10 inch pump-baffle-valve stacks is 1500 l sec^{-1}.

The diffusion pump on the first chamber is backed by two pumps in parallel: a Stokes Model 1731 Mechanical Booster Pump (24 l sec^{-1} mechanical, 243 l sec^{-1} blower) and a Leybold-Heraeus blower model WAU-500 (160 l sec^{-1}) backed by a Balzers DU090 (26 l sec^{-1}) two stage mechanical pump. The forelines on chambers 2 and 3 are pumped by one Sargeant-Welch 1397 (8.4 l sec^{-1}).

In the most frequently used configuration, the aperture connecting chambers 1 and 2 is a Beam Dynamics, Inc. model 2 nickel skimmer of 0.9 mm diameter. Chambers 2 and 3 are connected via a 4.8 mm diameter circular orifice. Using these apertures, pressures with the dc arc-heated beam source (see below) in operation are 7×10^{-2}, 7×10^{-4}, and 5×10^{-5} Pascal in chambers 1, 2, and 3, respectively.

The fourth chamber is a cylindrical clean chamber utilizing crushed metal seals. It is recessed into chamber 3 to reduce the total length of the

facility (as measured from the source). This chamber is equipped with a high vacuum gate valve (Huntington model GVAP-600) and 570 l sec^{-1} turbomolecular pump (Balzers model TPU 510). The turbomolecular pump is used in preference to more conventional UHV pumping technology because of the large helium load which this chamber must bear.

SAMPLE AND ANALYSIS SYSTEMS

The facility is equipped with a quadrupole mass spectrometer (Extranuclear Laboratories, Inc.) comprised of a crossed beam electron-impact ionizer, a quadrupole mass filter with 17 mm diameter rods, and a Johnston MM-1 particle multiplier. The mass spectrometer has been used so far only for beam source characterization (see below).

When solid samples are to be bombarded, they may be mounted either in chamber 2, when it is desirable to maximize the available beam flux on target, or in chamber 4 when sample cleanliness is the paramount concern. A liquid nitrogen cooled shroud surrounds samples in chamber 2 to inhibit contamination. The beam is typically collimated to subtend a circular spot of approximately 7 mm in diameter when samples are mounted in this shroud, however spots as large as 17 mm are possible. A three-axis-plus-rotation precision manipulator is provided for mounting solid samples. Active temperature control on the range of 300-450 K is typical.

The only <u>in situ</u> diagnostics currently available in this facility are optical. Transmission measurements of samples mounted in either location are possible. Figure 2 shows a schematic representation of the optical path for transmission measurements in chamber 4. Ultra-violet transmission has been used to measure the rate of oxidation of carbon by high velocity atomic oxygen[7] and infrared transmission has been used to measure the effect of atomic oxygen on clean and contaminated infrared optics.[4]

ATOMIC OXYGEN SOURCES

The primary beam source used in this facility is a DC arc-heated supersonic nozzle source which relies on a modified, commercially available plasma torch. The design, testing, and development of this source have been an important part of this program.

A schematic view of the arc-heated source is shown in Figure 3. A more detailed scale view of the gas flow path in the source is shown in Figure 4. The modifications to the commercial device include attachments for a water-cooled nozzle, through which the atomic beam expands into the vacuum system, a high pressure oxygen injector, and exhaust channels to dispose of excess torch gas. A similar source has been described in the literature.[8]

The torch operates in the non-transferred mode, i.e., the electric arc is confined within the torch. A plasma is formed in helium (flowing at a nominal rate of 2 1-atm sec^{-1}, 265 scfh) by a DC arc, dissipating in total

approximately 16 kW. A small amount of O_2 (nominally 2% of the total gas flow) is injected downstream of the arc, where it is thermally dissociated into oxygen atoms by the hot helium. The high source temperature and isentropic expansion into the vacuum system produce a supersonic beam of high velocity.[9] Typical beam source operating conditions and performance specifications are summarized in Table I.

Beam composition, ($He/O_2/O$), intensity, and velocity distribution are measured by the quadrupole mass spectrometer. The fractional dissociation of O_2 in the beam is calculated from relative mass peak heights by the formula of Miller and Patch:[10]

$$y = \frac{N_O}{N_{O_2}} = P_d \left(\frac{\sigma_{O_2}}{\sigma_O}\right) \left(\frac{1}{\eta} \frac{S_O}{S_{O_2}} - 1\right) \tag{1}$$

where N_O/N_{O_2} is the inferred number density ratio of O to O_2, P_d is the probability of dissociative ionization, σ_{O_2}/σ_O the ratio of electron impact ionization cross sections, S_O/S_{O_2} is the ratio of mass spectrometer signals of O and O_2 with the torch on, and η is that ratio with the torch off. The per cent dissociation is given by:

$$\%D = 100\ y/(y + 2) \tag{2}$$

The degree to which the molecular oxygen is dissociated depends on torch operating conditions. Figure 5 shows a plot of percent dissociation as a function of total torch power, for several different nozzle diameters.

With the aid of the known temperature dependence of the equilibrium constant[11] for the reaction

$$1/2\ O_2 \overset{K_p}{\rightleftharpoons} O \tag{3}$$

one can convert the observed fractional dissociation of oxygen into one effective temperature for the source. Figure 6 shows that this temperature depends very nearly linearly on the nozzle diameter. This suggests that performance of the source, as measured by fractional dissociation (and very probably velocity), is limited by heat losses or catalytic surface reactions within the nozzle. The suggestion exists in these data that significant improvements in performance may be made by increasing the nozzle diameter. However, the nozzle diameter of 0.22 mm used routinely in this facility is essentially the largest consistent with the pumping speed of the first chamber.

For most conceivable applications of this facility, it is necessary to know the absolute flux of atomic oxygen in the beam. This quantity is measured by calibrating the response of the mass spectrometer to molecular

oxygen. A nearly effusive, room temperature beam source, for which it is possible to calculate reliably the flux and velocity distribution,[12] is used for this calibration. Comparison of the mass spectrometer signals obtained using this source with those obtained by adding to the mass spectrometer chamber a static pressure of O_2, measured by a Bayard-Alpert ionization gauge, provides a means for rapidly recalibrating the mass spectrometer to O_2 before each experimental run.

Since a mass spectrometer equipped with an electron impact ionization source is a number density detector, this calibration allows one to convert an observed mass spectrometer signal for O_2 in the beam to an absolute effective number density or "beam pressure." The number density of O_2 is then converted to a flux by multiplying it by the nominal beam velocity.

Figure 7 shows a plot of the most probable beam velocity (for helium) measured by time-of-flight, as a function of total power dissipated by the torch, when the source gas consists of the routinely used helium/oxygen mixture. The O_2 and O velocities are only slightly less than the helium velocity. Thus a nominal velocity of 3.5 km sec^{-1}, which corresponds to a translational energy of approximately 100 kJ $mole^{-1}$ (1 eV), is used to calculate the beam flux.

Finally, the atomic oxygen flux is obtained by multiplying the calculated O_2 flux by the fractional abundance of O in the beam (see Equation 1). Typical O atom fluxes are on the order of 10^{15} to 10^{16} cm^{-2} sec^{-1} for a target mounted in the cryoshroud located in chamber 2 (see Figure 1) and approximately one tenth that for mounting in the clean chamber. The absolute value of the atomic oxygen flux is subject to an uncertainty estimated to be ±50% owing predominantly to systematic uncertainty in the calibration of the mass spectrometer. Reduction of these "error bars" would be a straightforward, but extremely tedious, process.

The beam source is in essence a windowless, atmospheric pressure helium arc lamp. Thus it produces light as well as an atomic beam. Since the beam is comprised of neutral atoms and molecules, separation of the beam from the light can only be effected readily by a mechanical chopper. A two segment slotted disk velocity selector of 40% nominal transparency has been designed for this facility.[13] The role of this device is not to prepare a beam of narrow velocity distribution, but merely to block species, such a photons, travelling at velocities in excess of the selected velocity. Since the selector has only two disks, it naturally has an infinite number of low velocity side bands. This device has not heretofore been used for experiments performed in this facility.

Two other beam sources for producing atomic oxygen are available for use in this facility: a microwave discharge source[4] and a resistively-heated thermal dissociation source[14] for which iridium or rhenium source tubes with a variety of orifice diameters are available. Both sources are capable of producing substantial fluxes of atomic oxygen, but at velocities on the order

of 1 km sec^{-1}. These lower velocity sources are needed to gain a more complete understanding of the kinetics of the reactions of atomic oxygen with solids. (See Recommendations section.)

FACILITY APPLICATIONS

REACTION OF ATOMIC OXYGEN WITH SOLIDS

This facility has been used to investigate the rate of reaction of atomic oxygen with two types of carbon[7,15] and with Kapton film, a polyimide material manufactured by E.I. duPont de Nemours & Co., Inc.[16] The results of these investigations are summarized very briefly below.

Carbon

Figure 8 shows an Arrhenius plot (in carbon surface temperature) of the probability of reaction of atomic oxygen with carbon including data from ground-based measurements and flight experiments and other observations from various flights of the Space Shuttle. The reaction probability plotted is defined as the probability that an oxygen atom impact will remove a carbon atom from the surface, regardless of its final state of aggregation. (For a detailed discussion of these data the reader should consult reference 7 and works cited therein.)

The open circles and open triangle represent the results of measurements performed in this facility. The dashed line labelled "Park" is a fit to several laboratory measurements of the rate of reaction of atomic oxygen with various forms of carbon, under more-or-less thermal conditions.[17] The other data include limits on the reaction probability inferred[7] from removal of carbon surfaces on the STS-3 Plasma Diagnostics Package[a] and on the STS-4 Marshall Space Flight Center Induced Environment Contamination Monitor passive sample array,[18] a probability calculated from the observed thickness loss of vitreous carbon included on the STS-5 Evaluation of Oxygen Interaction with Materials (EOIM) passive sample array,[15] and the reaction probability calculated from the observed rate of mass loss from an amorphous carbon coated temperature controlled quartz crystal microbalance on the Goddard Space Flight Center's Contamination Monitor Package flown as a "Get-Away Special" on STS-8.[b]

---

a. G. B. Murphy, University of Iowa, Department of Physics and Astronomy, Iowa City, IA, private communication.

b. J. J. Triolo, NASA/Goddard Space Flight Center, Greenbelt, MD, private communication.

These data lead one to the conclusion that the rate of reaction of atomic oxygen with carbon, at collision energies of up to 100 kJ $mole^{-1}$ (1 eV), does not depend strongly on the translational energy of impact. Indeed when one compares laboratory and flight data for similar samples of carbon, the evidence that rates occurring on-orbit are significantly different from the thermal rate of reaction of O atoms with carbon is not strong. However, the results of Gregory and Peters (not shown on Figure 7), who infer probabilities in excess of 0.1 from STS-8 EOIM results, militate against drawing an unambiguous conclusion in this matter.[a] Comparable laboratory data for carbon identical to that of Peters and Gregory are not available.

Kapton

Table II shows a comparison between the average probabilities for the reaction of atomic oxygen with Kapton measured in this facility[16] and inferred from the STS-5 and STS-8 EOIM experiments.[2,3] In this case, the reaction probability is conventionally defined as the thickness of material removed divided by the fluence of atomic oxygen incident on the sample.

The agreement between the laboratory and flight results is quite good in comparison to the uncertainties in the various data. This relatively good agreement suggests that there is not a great dependence on O atom impact energy of the average efficiency of the reaction of atomic oxygen with Kapton over a range of impact energy from 1 to 5 eV. However, these reaction rates are substantially greater than those one might infer from measurements of the rate of atomic oxygen with polymers in a room temperature gas containing atomic oxygen.[16,19] Further experimentation is required before one can understand this discrepancy.

FUTURE APPLICATIONS/RECOMMENDATIONS

In the immediate future, application of this facility will be directed toward two goals. The first is the development of a compact sensor specifically sensitive to the flux of atomic oxygen incident on a surface which is suitable for use in active experiments to investigate the effects of the LEO environment on spacecraft materials. The second is the investigation of the transfer of momentum and energy in high velocity collisions of atomic oxygen with solids. These latter experiments have as their eventual objective increasing the understanding of aerodynamic drag on a satellite in LEO where a large fraction of gas-solid collisions are potentially reactive. In such a collision, the relationship between energy and momentum imparted to the spacecraft is not straightforward.

---

a. J. C. Gregory, Chemistry Department, The University of Alabama at Huntsville, private communication.

The potential applications of ground-based experimental facilities to the investigations of atmospheric effects in LEO are myriad. However, we wish to point out a class of investigations which are both particularly amenable to ground-based studies and deserving of paramount concern: investigations to reveal the detailed kinetics of the erosion of organic polymers by ambient atomic oxygen in LEO. Such an understanding is required to provide for quantitative predictions of the useful lifetimes of materials in different orbits from and for longer durations than Shuttle sorties, for which the only reliable flight data exist. An additional benefit of gaining an understanding of the kinetic details of these reactions may be in indication of reliable means for studying the effects of O atoms on materials which are less costly, less time-consuming, and more flexible than the atomic beam technique used in this facility.

Questions raised, and not answered by currently available flight and laboratory data include:

1. What is the dependence of the rate of oxygen atom reactions with organic solids on the energy (velocity) with which the oxygen atom strikes the solid?

2. What is the dependence of the apparent rate of reaction on the flux of atomic oxygen incident on the solids?

3. What is the dependence of the instantaneous rate of reaction on the fluence of atomic oxygen which has struck the solid?

4. What are the volatile products of the reactions of atomic oxygen with commonly used spacecraft materials?

REFERENCES

1. Hedin, A. E.; Reber, C. A.; Newton, G. P., Spencer, N.W.; Brinton, H. C.; Mayr, H. G.; and Potter, W. E.: A Global Thermospheric Model Based on Mass Spectrometer and Incoherent Scatter Data MSIS 2: Composition. J. Geophys. Res., Vol. 82, June 1977, pp. 2148-2156.

2. Leger, L. J.; Spiker, I. K.; Kuminecz, J. F.; Ballentine, T. J.; and Visentine, J. T.: STS Flight 5 LEO Effects Experiments: Background Description and Thin Film Results. AIAA Shuttle Environment and Operations Meeting, Washington, D. C., AIAA paper #83-2631-CP, 31 October-2 November, 1983.

3. Leger, L. J.; Visentine, J. T.; and Kuminecz, J. F.: Low Earth Orbit Atomic Oxygen Effects on Surfaces. AIAA 22nd Aerospace Sciences Meeting, Reno NV, AIAA paper 84-0548, January, 1984.

4. Arnold, G. S.; Peplinski, D. R.; and Herm R. R.: Atmospheric Effects in Low Earth Orbit and the DMSP ESA Offset Anomaly. SD-TR-82-81, The Aerospace Corporation, El Segundo, CA, 20 September, 1982.

5. Banks, P. M.; Williamson, P. R.; and Raitt, W. J.: Space Shuttle Glow Observations. Geophys, Res. Lett., Vol. 10, No. 2 , February 1983, pp. 118-121.

6. Yee, J. H.; Abreu, V. J.: Visible Glow Induced By Spacecraft-Environment Interaction. Geophys. Res. Lett., Vol. 10, No. 2, February 1983, pp. 126-129.

7. Arnold, G. S.; and Peplinski, D. R.: Reactions of High Velocity Atomic Oxygen with Carbon. AIAA 22nd Aerospace Sciences Meeting, Reno, NV, AIAA paper #84-0549, January, 1984.

8. Silver, J. A.; Freedman, A.; Kolb, C. E.; Rahbee, A.; and Dolan, C. P.: Supersonic Nozzle Beam Source of Atomic Oxygen Produced by Electric Discharge Heating. Rev. Sci. Instrum., Vol. 53, No. 11, November 1982, pp. 1714-1718.

9. Fluendy, M. A. D.; and Lawley, K. P.: Chemical Applications of Molecular Beam Scattering, Chapman and Hall, London, 1973, pp. 72-79.

10. Miller, D. R.; and Patch, D. F.: Design and Analysis of a High Intensity Fast Oxygen Atom Source. Rev. Sci. Instrum., Vol. 53, No. 40, December 1969, pp. 1566-1569.

11. Stull, D. R.; and Prophet, H.: JANAF Thermochemical Tables, Nat. Stand. Ref. Data. Ser., Nat. Bur. Stand. (U.S.), No. 37, June 1971.

12. Anderson, J. B.; and Fenn, J. B.: Velocity Distributions in Molecular Beams from Nozzle Sources. Phys. Fluids, Vol. 5, No. 5, May 1965, pp. 780-787.

13. Fluendy, M. A. D.; and Lawley, K. P.: op. cit., pp. 97-104.

14. Henderson, W. R.; Fite, W. L.; and Brackmann, R. T.: Dissociative Attachment of Electrons to Hot Oxygen. Phys. Rev., Vol. 183, No. 1, July 1969, pp. 157-166.

15. Arnold, G. S.; and Peplinski, D. R.: Reaction of Atomic Oxygen with Vitreous Carbon: Laboratory and STS-5 Data Comparisons. AIAA Journal, accepted for publication.

16. Arnold, G. S.; and Peplinski, D. R.: Reaction of Atomic Oxygen with Polyimide Films. AIAA Journal, submitted for publication.

17. Park, C.: Effect of Atomic Oxygen on Graphite Ablation. AIAA Journal, Vol. 14, No. 11, November 1976, pp. 1640-1642.

18. Peters, P. N.; Linton, R. C.; and Miller, E. R.: Results of Apparent Atomic Oxygen Reactions on Ag, C, and Os Exposed During the Shuttle STS-4 Orbits. Geophys. Res. Lett., Vol. 10, No. 7, July 1983, pp. 569-571.

19. Hansen, R. H.; Pascale, J. V.; De Benedicitis, T.; and Rentzepis, P. M.: Effect of Atomic Oxygen on Polymers, J. Poly. Sci. A, Vol. 3, June 1965, pp. 2205-2214.

TABLE I. TYPICAL BEAM SOURCE CHARACTERISTICS

Feed Gas	$He:O_2/98:2$
Flow Rate	265 SCFH (2 l-atm sec^{-1})
Power Dissipated	16 kW
O flux on target[a]	5.0×10^{15} cm^{-2} sec^{-1}
O_2 flux on target[a]	7.5×10^{15} cm^{-2} sec^{-1}
Beam Velocity (oxygen atoms)	3.5 km sec^{-1}

a Target mounted in chamber 2, see Figure 1.

TABLE II. COMPARISON OF LABORATORY AND FLIGHT MEASUREMENTS OF THE AVERAGE PROBABILITIES FOR THE REACTION OF ATOMIC OXYGEN WITH KAPTON

Kapton Temperature kelvin	Reaction Probability 10^{-24} cm^3/O atom		
	Laboratory[a]	STS-5[b]	STS-8[c]
300	2.1 ± 1.1 1.7 ± 0.9	2.3 ± 0.9	--
338	1.4 ± 0.9	2.0 ± 0.8	3.0 ± 1.2
393	1.5 ± 0.9	2.1 ± 0.9	2.9 ± 1.2

a. See reference 16.

b. See Table 3 of reference 2. Nominal uncertainty is ±40%.

c. See Table 5 of reference 3. Nominal uncertainty is ±40%.

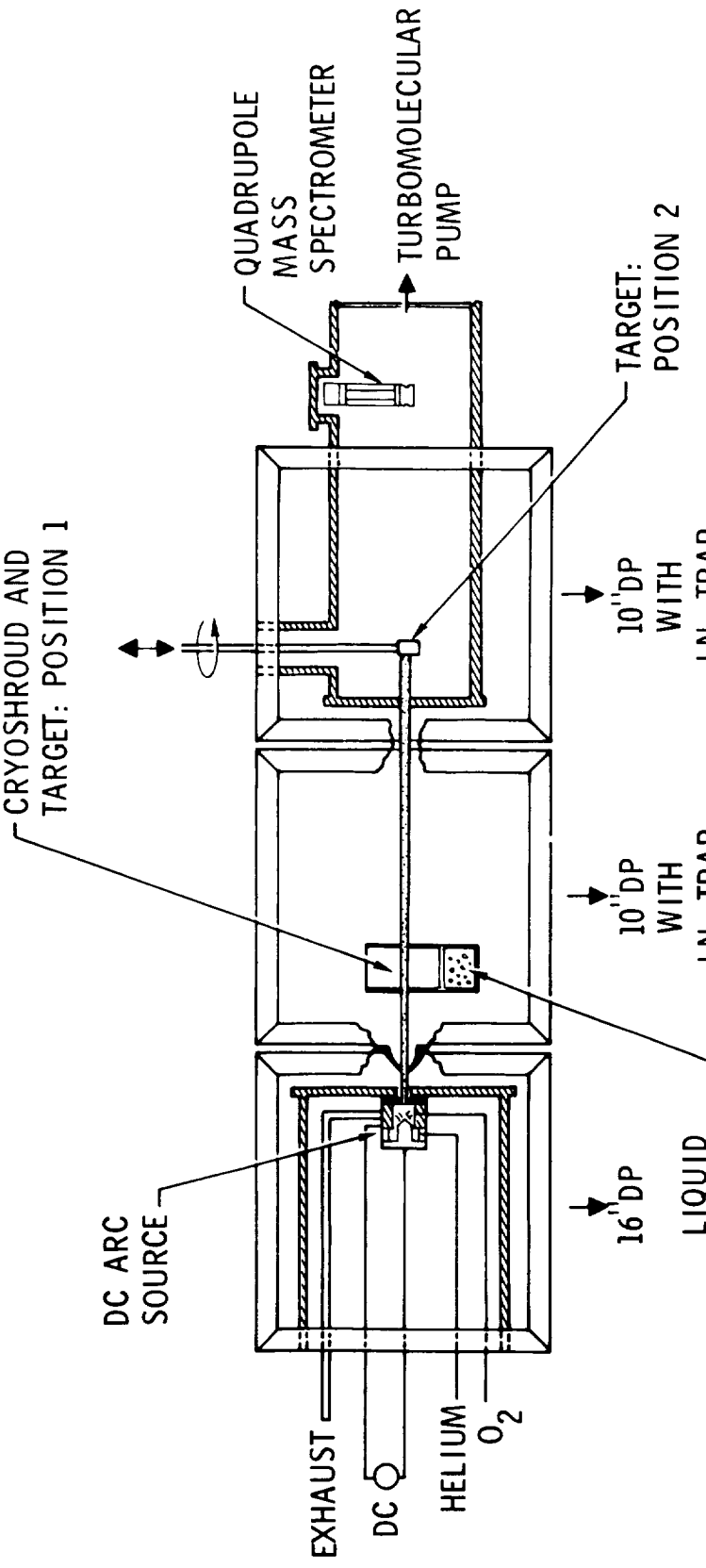

Figure 1 - Schematic representation of the high energy oxygen atom surface chemistry facility

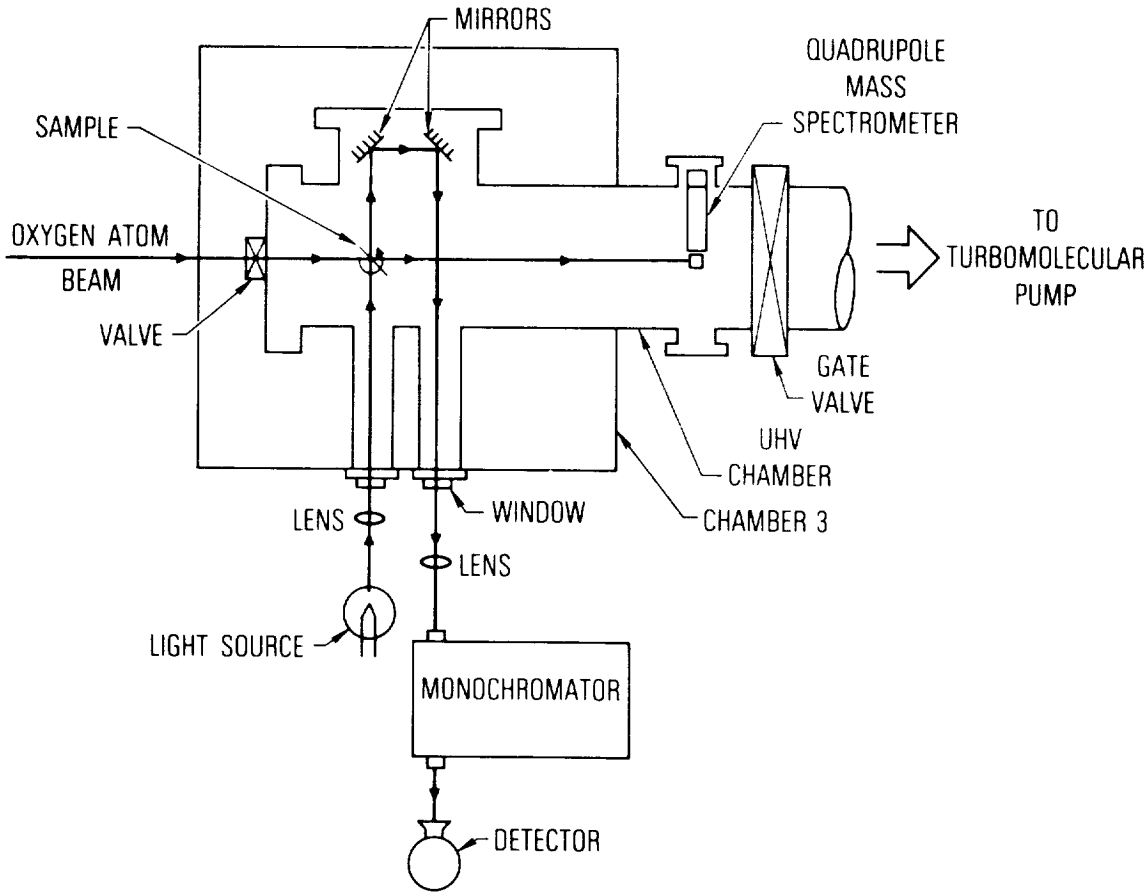

Figure 2 - Schematic representation of the fourth (clean) chamber showing path for in situ optical transmission measurements

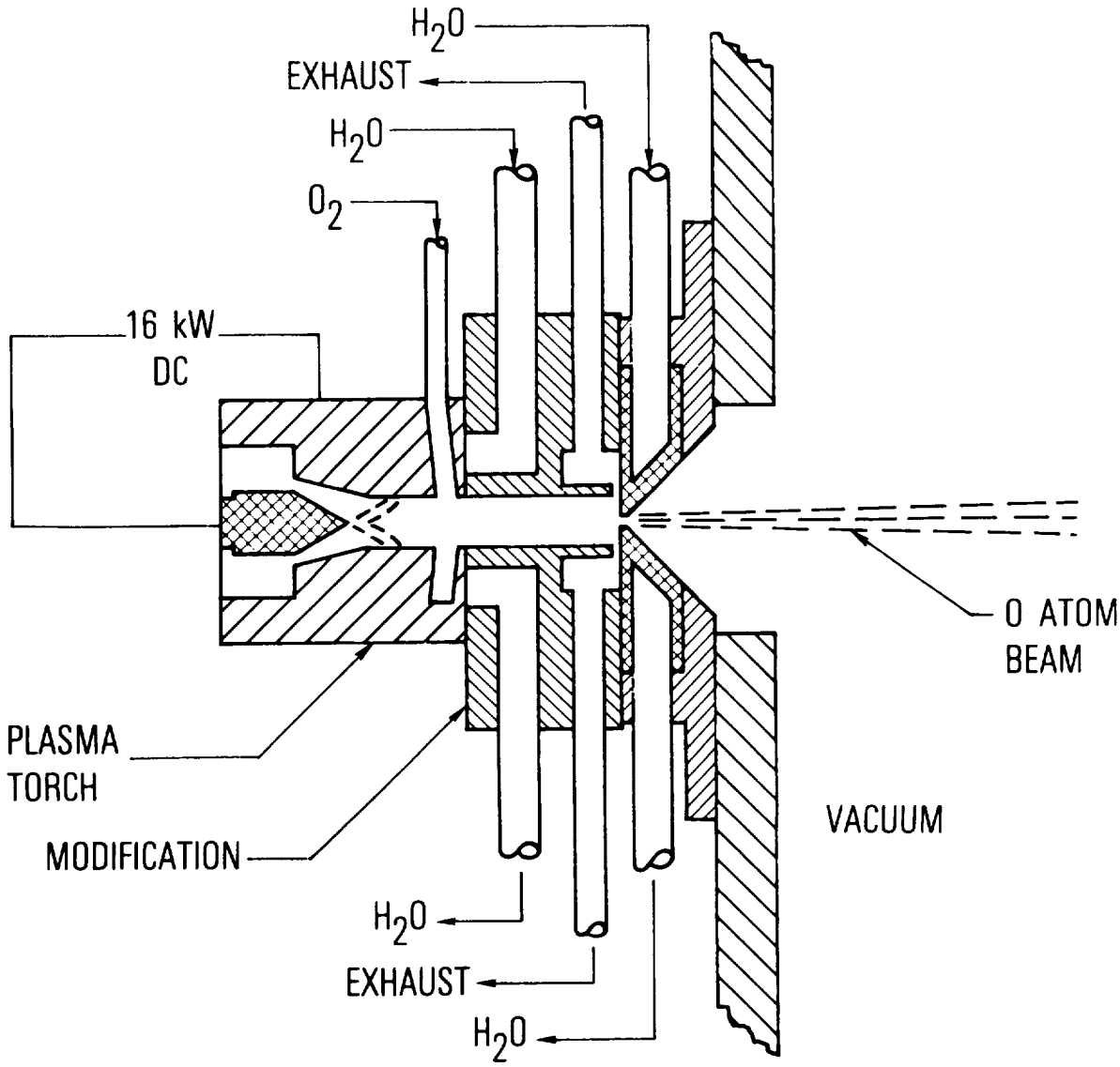

Figure 3 - Schematic representation of the dc arc-heated atomic beam source

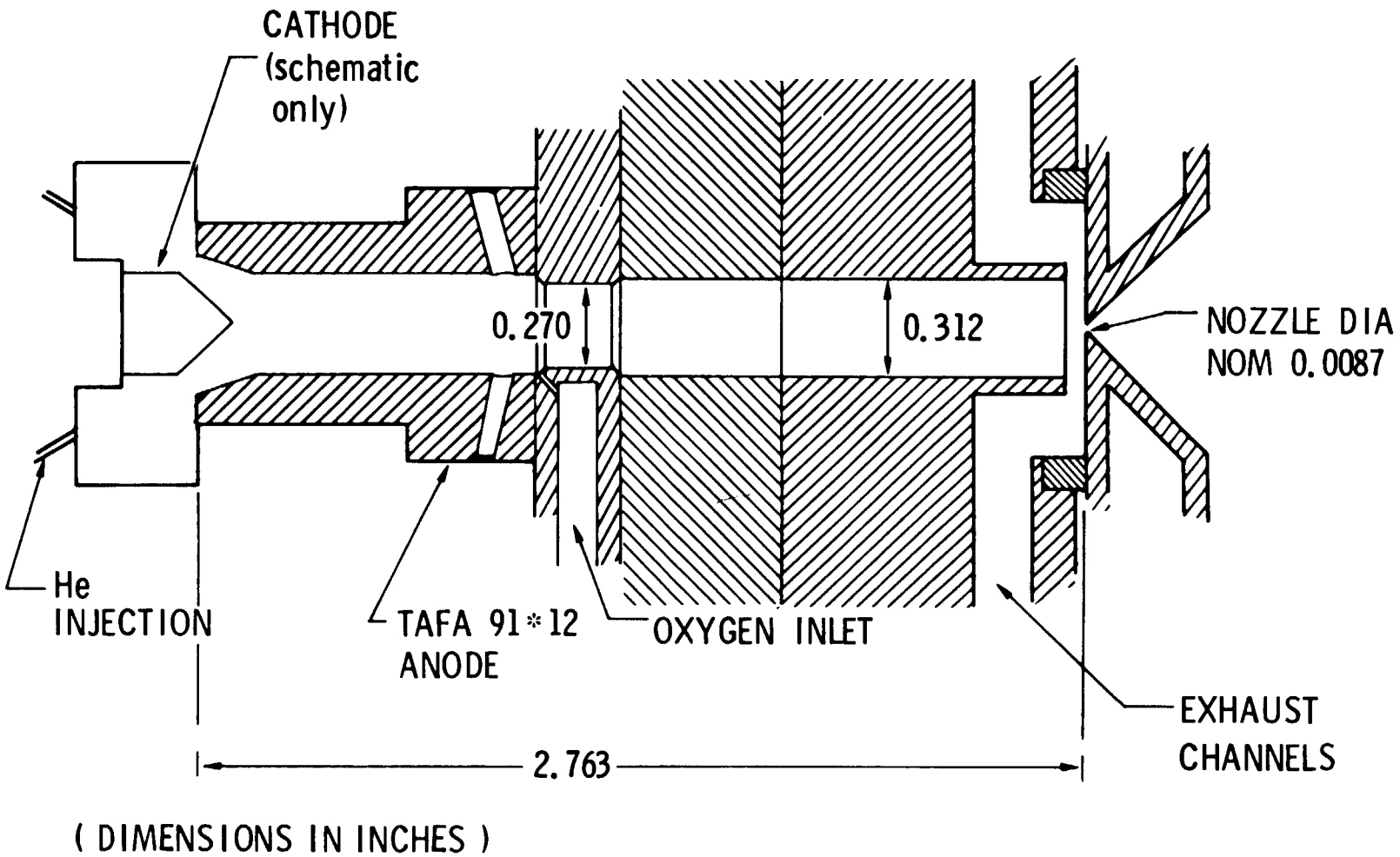

Figure 4 - Detailed view of the gas flow path in the dc arc-heated atomic beam source

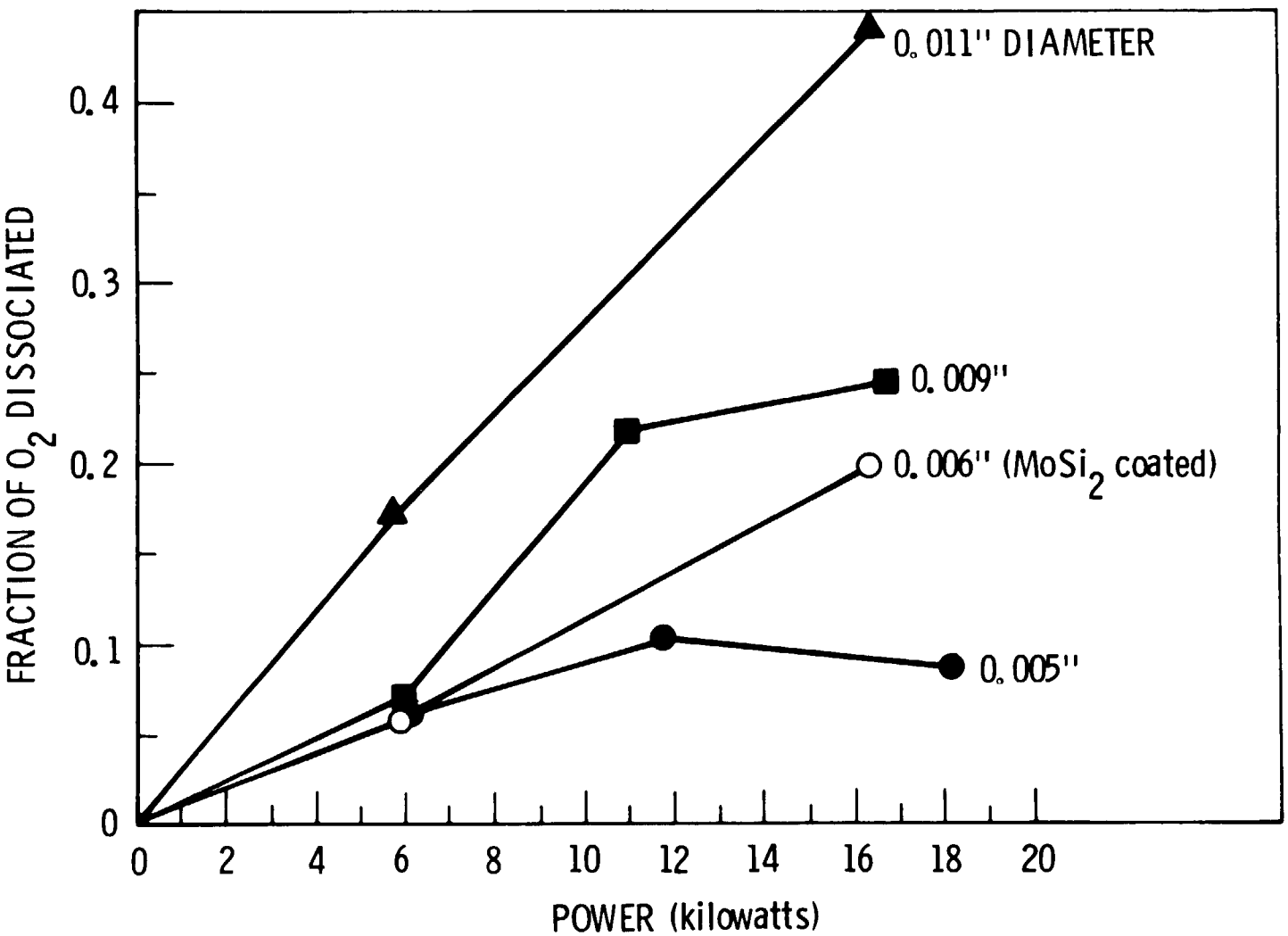

Figure 5 - Apparent fractional dissociation of O_2 in the atomic beam as a function of total power dissipated by the source for several nozzle diameters. (Points connected to aid the eye.) Note: 1 mil = 0.0254 mm.

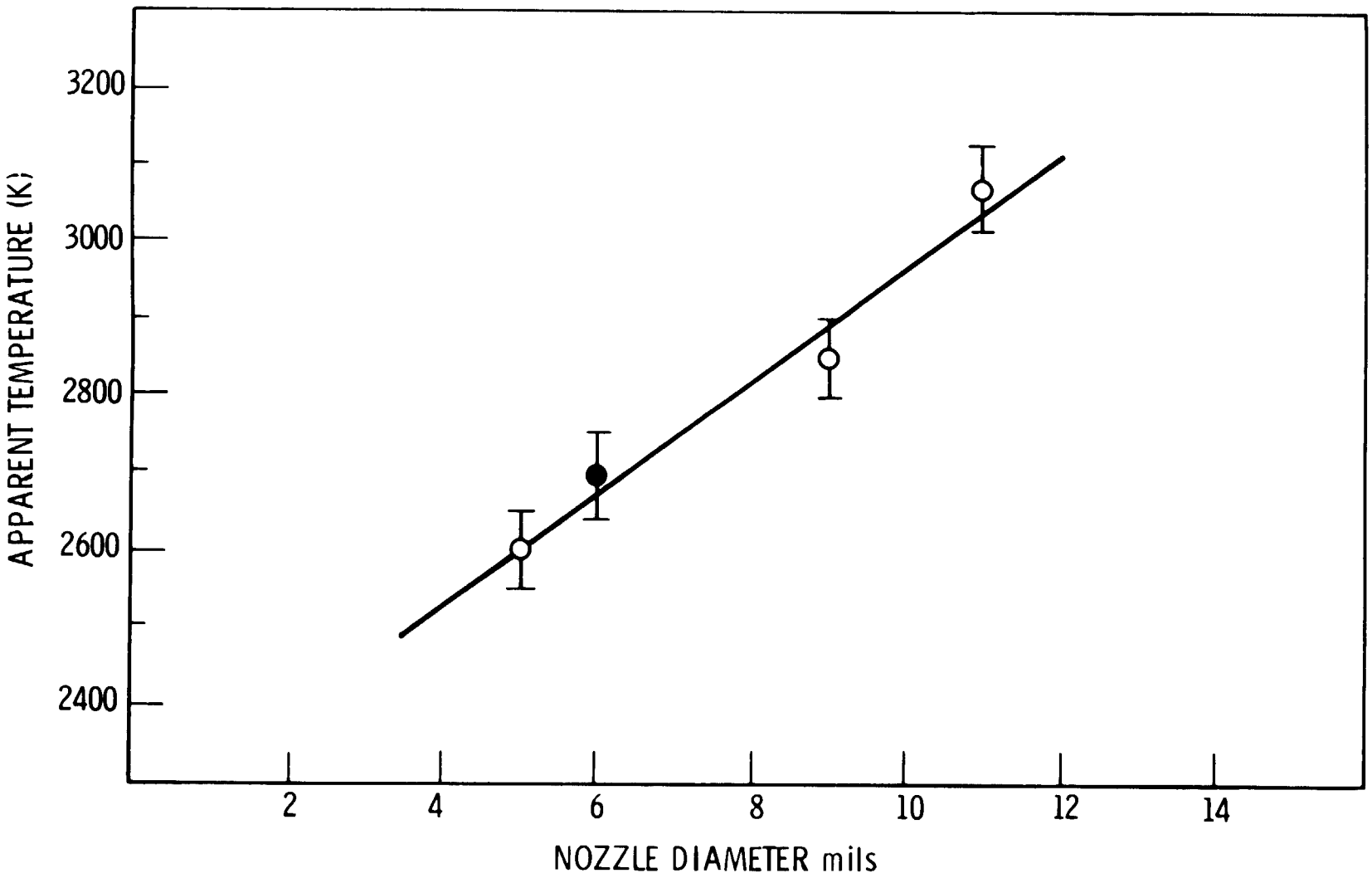

Figure 6 - Apparent oxygen temperature inferred from fractional dissociation of O_2 as a function of nozzle diameter. Straight line is a least squares fit of the form: $T/1000 = 2.23 + 7.4 \times 10^{-2} \times$ diameter (mils).

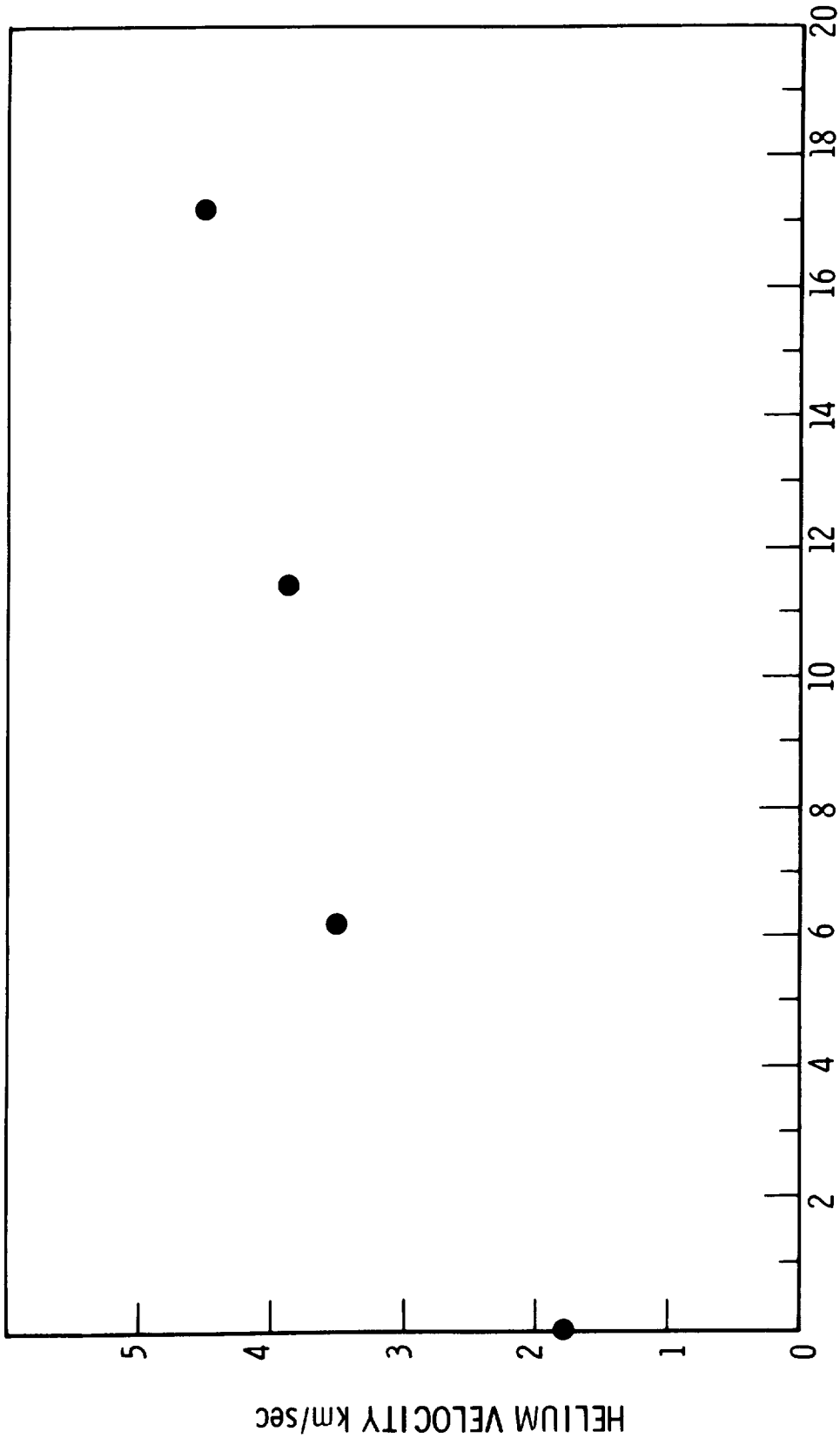

Figure 7 - Most probable helium velocity as a function of total power dissipated by the source

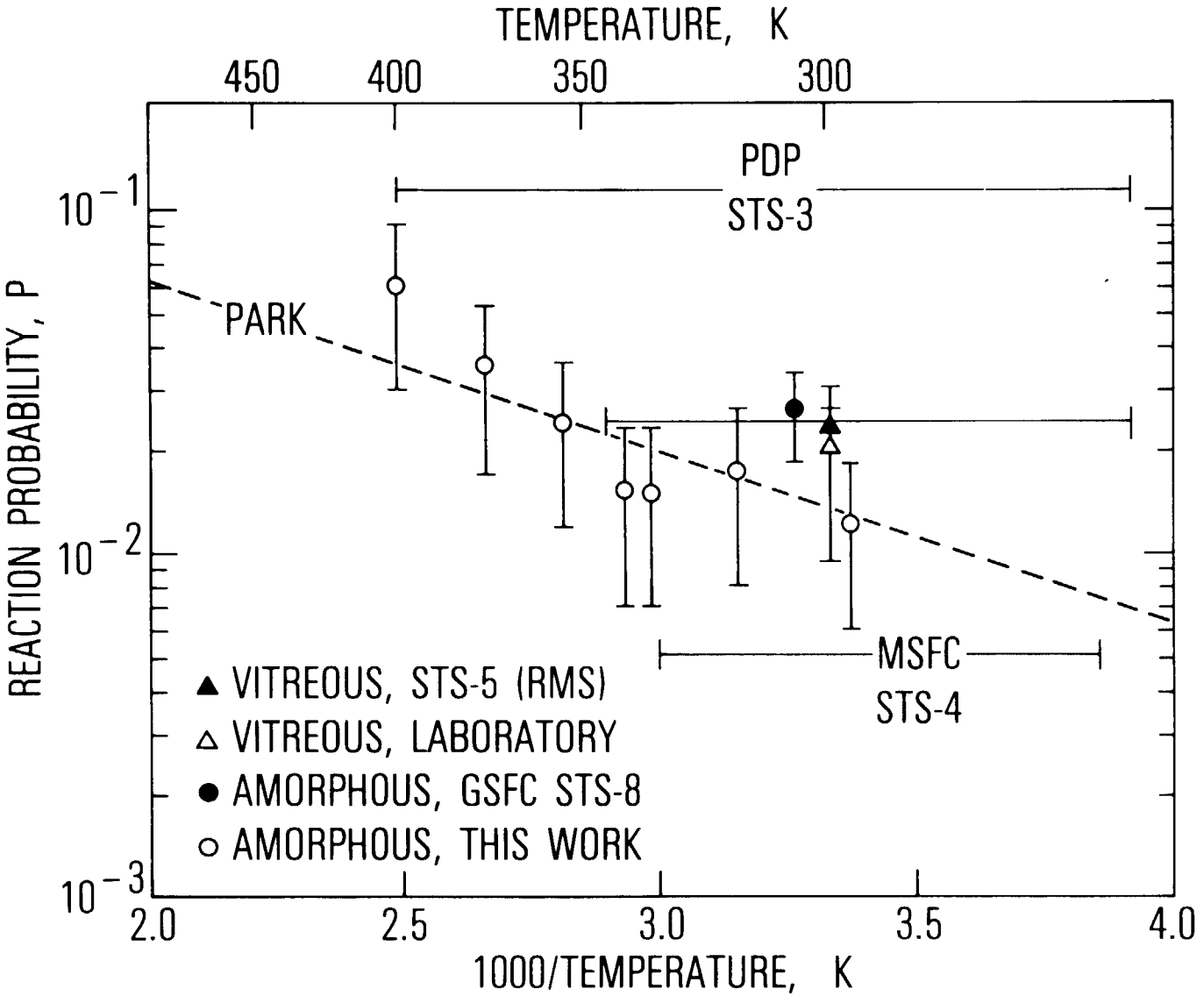

Figure 8 - Arrhenius plot (in carbon surface temperature) of the probability of the reaction of atomic oxygen with carbon. Various laboratory and flight data are shown (See text)

AN ATOMIC OXYGEN FACILITY FOR STUDYING POLYMER MATERIALS FOR SPACECRAFT APPLICATIONS

R. C. Tennyson, J. B. French, L. J. Kok and J. Kleiman
University of Toronto
Institute for Aerospace Studies

D. G. Zimcik
Communications Research Centre
(Canada)

ABSTRACT

A nozzle beam facility utilizing microwave discharge on a helium carrier gas seeded with oxygen to produce atomic oxygen fluxes of the order of 10^{15} atoms/cm^2-sec is described in this report. In addition, limited test results obtained from exposing a graphite/epoxy composite and Kapton (H) film are presented in terms of mass loss measurements and changes in surface morphology.

INTRODUCTION

An orbiting satellite can be regarded as a body in free molecular flow. One generally characterizes this domain in terms of the Knudsen number (Kn) (i.e., the ratio of the mean free path of a gas/characteristic dimension of the body) which, for the upper atmosphere, is very large. The lower boundary of the free molecular flow region is usually taken at Kn > 10, which is true for all altitudes greater than 125 km (ref. 1). In this regime, the probability of gas-gas collisions is small. One can refer to fig. 1 to see the dominant atmospheric constituent concentrations as a function of altitude. For example, it is of interest to note that at 200 km, the orbital velocity is 7.78×10^5 cm/sec and the mean free path for nitrogen corresponds to 7×10^4 cm. Taking the atmospheric density to be about 2×10^9/cm^3 at 200 km, the mean free path is about 700m. Thus Kn = 700 for a body of 1m dimension (ref. 1). For satellite-gas collision studies, this orbital velocity corresponds to impact gas energies of 0.34, 4.40 and 5.03 electron volts (eV) for hydrogen, nitrogen and oxygen atoms, respectively (ref. 1).

Many satellites orbit at altitudes ranging from 125 km - 600 km where atomic oxygen is the most active and dominant species interacting with the

---

Financial support was provided by the Communications Research Centre, Shirley Bay, Ottawa, under Contract No. OST83-00245.

surface of the vehicle. With the advent of the Space Transportation System flights (i.e., Space Shuttle), one has now been presented with the opportunity to witness the effects of gas-surface interactions on a variety of spacecraft materials. For example, materials housed in the shuttle's payload bay have been exposed to an atomic oxygen flux estimated to be in the range of 10^{14} to 10^{15} atoms/cm^2/sec. These materials include Teflon-coated Beta fabric and Kapton (primary constituents of thermal insulation blankets), various thermal and identification paints, and various graphite/epoxy structural members (refs. 2, 3). Some physical observations to-date include: Kapton exhibited a colour change from its inherent gold to a milky yellow; the paints showed what appeared to be rapid aging, as they were easily removed by lightly wiping the surface. Mass loss for the Kapton was determine to be 4.3 to 4.7 percent and was evident on over 35 percent of all the thermal insulation blankets (refs. 2, 3). Areas behind supporting members or brackets (with respect to the velocity vector) were protected from the effects, as evidenced by strong shadow patterns on the painted surfaces. The backside of the exposed surfaces showed little change. For further details and information on the effects of atomic oxygen on a variety of materials flown on STS missions (3 to 8), one should refer to ref. 3.

Based on STS test data and the observaions noted above, a need clearly exists to simulate the environmental conditions to study this phenomnenon. From a design viewpoint, it is essential to qualify materials for spacecraft applications subject not only to atomic oxygen bombardment, but other radiation effects and synergisms that may occur as well.

SYMBOLS

a	local speed of sound
A	area
C_p	specific heat at constant pressure
C_v	specific heat at constant volume
I	molecular flux per solid angle (molecules/steradian/sec)
K	degrees Kelvin
Kn	Knudsen number
m	mass
M_f	freezing Mach number
n	number density
N_{AV}	Avogadro's number, 6.02×10^{23}/mole

P	pressure
R	universal gas constant, 8.314×10^3 J/kilomole/K
T	temperature
u	molecular weight of gas
V	velocity
x	distance from the orifice
γ_{LV}	surface tension at liquid-vapour interface
γ_{SL}	surface tension at solid-liquid interface
γ_{SV}	surface tension at solid-vapour interface
σ_{EX}	total flux from orifice (molecules/sec)
σ_t	flux per unit area (atoms/cm^2-sec)
Ω_t	solid angle from nozzle to target
λ	mean free path
γ	ratio of specific heats, C_p/C_v
θ	polar angle with orifice exit as centre

NOZZLE BEAM GENERATION SYSTEMS

INTRODUCTION

There are two main types of molecular beams used for continuous high density particle flow simulation; the classical effusive beam and the nozzle beam systems (refs. 4, 5). The effusive beam is simply formed by particles effusing through a slit or orifice from a low pressure stagnation source into a vacuum system (fig. 2). The mean velocity from such a beam is a strong function of the throat temperature and can thus be calculated from the source equilibrium Maxwellian distribution (ref. 6). The nozzle beam, on the other hand, has molecules emanating from a stagnation source, which undergo a free jet expansion at the nozzle exit into the vacuum chamber, where the flow is essentially in the free molecular flow regime. The beam is accelerated as it expands and the molecules' vibrational, translational and rotational motions are converted to translational energy along the axis of the nozzle (ref. 4). The higher the pressure, the more complete is the conversion to translational energy.

One advantage of a nozzle beam is that the velocity distribution is smaller (when compared to the bulk beam velocity) than that for an effusive beam. Higher fluxes can also be realized as well as a higher terminal velocity in the final beam. The method of 'seeding' the beam can further increase the velocity of the molecular beam. This involves using a lighter gas, such as He, as a carrier gas with a small percentage of the heavier gas of interest, O_2 in this case. The lighter gas' higher terminal velocity for a given source temperature, T_o, is given by

$$(1/2)\ mV^2 = (3/2)\ T_o R/N_{av} \qquad (1)$$

The fast moving carrier gas will, however, accelerate the heavier gas by collisions, and if no slip occurs, speeds close to the terminal velocity of the lighter gas can be realized.

The latter beam system with the seeding technique was employed using a facility configuration developed by Lam (ref. 7). A heated beam can also increse the velocity but no ohmic heating was incorporated in this design due to its additional complexities, as experienced by Lam with thoria cavities (ref. 4).

EXPERIMENTAL APPARATUS

The experimental apparatus utilized by Lam (ref. 7) involving the generation of a high-velocity mono-energetic nozzle beam containing atomic oxygen was employed as shown in figs. 3-8. Microwave power discharge on a helium carrier gas seeded with 8% oxygen flowing through a quartz tube provided a partially dissociated oxygen flux into a vacuum chamber containing a sample target. There are two major advantages associated with the microwave method of producing atomic oxygen. Firstly, since no intermittent electrode discharges are present, one obtains a "clean", uncontaminated beam containing a constant supply of atomic oxygen (ref. 7). Secondly, after ionization of the gas by the microwave discharge, dissociation occurs at relatively low temperatures (850 ~ 1000 K) and thus the nozzle can be made from quartz. This provides a clean and stable surface which is very inefficient for recombining gas radicals (ref. 7). One should note that this method of dissociation by glow-discharge does introduce excited species which are retained in the beam, as contrasted with the thermal dissociation process which maintains all of the gas atoms in the ground state electronically (ref. 4). However, to create atomic oxygen by thermal dissociation requires very high temperatures (up to 3000 K) to overcome the 5.12 eV chemical bond of molecular oxygen (see Lam, ref. 4). On the other hand, higher dissociation values (~55%) and beam velocities (~3.8 km/sec) can be achieved using this approach (ref. 4), compared to the microwave discharge method.

The facility employed in this investigation utilized a Microtron 200 microwave power geneator unit (fig. 4) operating at a frequency of 2450 MHz (12.5 cm) with a rated power from 20 to 200 watts. A Tesla coil was used to initiate the microwave-induced plasma in the tunable cavity. The cavity was tuned so that the reflected power to the microwave generating unit was

minimized. This state corresponds to the maximum efficiency of the process and is characterized by the glow discharge in the tuning cavity (fig. 5). It should be emphasized, however, that the continuous wave magnetron can only withstand 75 watts reflected power for a short period or 40 watts continuously. Since long term exposure tests were required (i.e., operating periods of several weeks continuous running), the maximum power setting was maintained at 30 watts. Thus if the microwave plasma was accidentally extinguished, the maximum reflected power would not exceed the 40 watts limit.

The test chamber consisted of a Quick-fit Visible Flow vacuum vessel (fig. 6) fitted with a Balzers pumping system. The pumping occurred in two stages; the first handled by a roughing pump, the second by a diffusion pump. The former obtained pressures to 40 millitorr whereas the latter two-stage, water trap diffusion pump could attain a pressure of 4.0×10^{-5} torr with the beam in operation. Pressure readings were obtained through a Granville-Phillips ionization gauge fitted to the upper arm of the vacuum vessel.

Opposite to the entry port of the gas beam, an Aero Vac Vacuum Analyzer (fig. 7) was fitted, enabling the scanning of the mass spectrum to identify residual gases. Since the ionizer of this mass spectrometer faced directly into the beam flux, it would ionize only the background gases if the beam was blocked or "flagged", or a combination of the beam and background gases in the "unflagged" configuration. The ionization spectrometer can be calibrated for various pressure ranges from 10^{-4} to 10^{-10} torr. Scanning over the mass spectrum range (70-12 amu) can be done automatically or manually. The latter allows the spectrometer to be set to monitor one element during various phases of the nozzle beam operation.

The flow of gas was controlled by a series of regulator valves (fig. 8) with a constant mass flow rate being set by a Nupro needle valve. At this point the pressure was measured using a Wallace & Tiernan absolute pressure gauge.

ESTIMATION OF ATOMIC OXYGEN FLUX

It is difficult to measure the degree of oxygen dissociation achieved in the cavity itself (unless optical spectroscopy is available and carefully calibrated). Since the primary requirement for these tests is to know the actual beam fluxes of atomic and molecular oxygen, it was appropriate to start by using the available residual gas analyser, mounted on the opposite chamber wall so that its open ion source could be exposed to the atomic beam.

It should be emphasized that it is by now well-documented that microwave discharges operating under the conditions used in these tests typically produce dissociation fractions of the order of 1% ~ 5%. The addition of about 1% H_2O to the input gas can, however, increase the dissociation up to 20% (ref. 7). Based on Lam's experiments using a similar facility (ref. 7), it is estimated that the dissociation fraction is approximately 3%.

Although the beam facility is not capable of achieving the orbital energy level for atomic oxygen, it can provide the desired flux. Based on the free jet parameters and sample location, one can estimate the beam flux, as outlined in the Appendix.

Calculations show that the oxygen flux increases exponentially with increasing percentage of O_2 in the mixture (fig. 9). This would indicate that the optimum would be to use an all-oxygen gas mixture, although the beam velocity would decrease as described earlier. On the other hand, the lower the percentage of O_2 in the mixture, the higher the degree of dissociation and hence the lower the residual undissociated species content. In terms of sample placement, it can be seen (fig. 10) that the atomic oxygen flux falls off with distance squared. From these considerations, a low percentage mixture and location of the sample at the nozzle orifice would seem optimal. This, however, is not necessarily the case due to the formation of a bow shock wave which can reduce the flux impinging on the sample.

The initial experiments described in this report were conducted with the sample located 3 cm from the orifice. It should be noted that the flux is not constant over the sample area, but varies according to (ref. 8);

$$n(x,\theta) = 0.643\ n_0[\cos^2(1.1510]\cdot(x/R_0)^{-2} \qquad (2)$$

where θ is the polar angle coordinate with the orifice exit as centre. The corresponding variaion in flux density is shown in fig. 11.

Calculations performed in the Appendix estimate the incident atomic oxygen flux at $\sim 10^{15}$ atoms/cm^2-sec at the beam centre. Other characteristics of the beam are: Mach No: 1.9, and Energy: 0.14 eV. It should be noted that the flux level probably represents an over-estimate due to the presence of a bow shock. Future experiments will involve locating the sample about 30 cm from the orifice. Although the flux will decrease according to fig. 10, it is intended to determine if indeed the presence of the shock wave had a significant effect on reducing the incident beam flux on the target.

EFFECTS OF ATOMIC OXYGEN ON SAMPLES

SAMPLE EXPOSURE

Two types of samples were exposed to the atomic oxygen beam: Kapton, a polypyromelitimide manufactured by DuPont, and Hercules ASI/3501-6 graphite/epoxy composite. The Kapton was used mainly as a calibration sample, since data on the effects of atomic oxygen had already been documented by Leger (refs. 2, 3). Throughout the duration of the exposure, mass spectrographs were taken to determine the constituents being released from the sample by the oxidation and/or impact process. Immediately after exposure, the mass loss was determined for each of the samples. The surface activation energy was then measured to provide an indication of surface changes. Scanning electron

microscope images were also obtained to determine changes in surface morphology.

MASS SPECTROGRAPHS

After the initial pump-down of the vacuum vessel, a mass spectrograph was taken as a control (fig. 12). The elements shown largely result from residual amounts of gas from the atmosphere, although the hydrocarbon peaks are associated with the silicone oil used in the roughing pump. Once this pump is turned off, upon activation of the diffusion pump the presence of these hydrocarbons became imperceptible as testing proceeded.

Graphite Sample

The sample, once installed, was subjected to the atomic oxygen beam. Of concern was whether there was a detectable difference between having the atomic oxygen interacting with the sample as compared to having the carrier gas impinging on the surface. A mass spectrograph (fig. 13) was taken with the microwave generator on and off during the initial exposure tests on a graphite/epoxy sample. The purpose was to separate out the effects of the carrier gas mixture and that of atomic oxygen. As can be seen in fig. 13, increases in the levels of the hydrocarbons occurred when atomic oxygen was present, accompanied by the appearance of ethane (C_2H_6) and the C_2H_5 radical. In addition, increases in the H_2O and OH peaks probably resulted from the combination of O and O_2 with radical H atoms released in the reaction of atomic oxygen with the sample. As testing progressed, the levels of these latter peaks decreased, as can be seen in fig. 14. This spectrograph, taken just prior to sample removal after 265 hours of exposure, exhibits a marked increase in the methane peak (CH_4). Thus it would appear that there is an increased rate of reaction with time of atomic oxygen with the graphite/epoxy material. Furthermore, a mass spectrograph (fig. 15) taken at the same time only with the atomic oxygen source off, indicates the presence of the same CH_4 peak, but the CO_2, CH_3, C_2H_6 and C peaks have disappeared. The lingering methane peak probably demonstrates a continued reaction producing this outgassing product, even though the oxygen source has been terminated. With time, the methane peak was observed to subside.

Kapton Sample

A similar set of spectrographs was performed while the Kapton was being exposed (figs. 16 and 17). Hydrocarbon reaction products were also released when Kapton was bombarded with atomic oxygen but their number was less numerous. Only carbon, ethane, carbon monoxide and methane were released. The peak of the methane was much larger initially than that for the graphite/epoxy, although it also remained as an outgassing product once the atomic oxygen beam was extinguished (fig. 17).

MASS LOSS MEASUREMENTS

Table 1 summarizes the samples tested, their dimensions, exposure times and masses. Both the control samples and targets were weighed using a microbalance (sensitive to $\pm 1 \times 10^{-6}$ gm) before and after exposure. The major difficulty in assessing mass loss due to atomic oxygen impingement is the uncertainty associated with the target beam area and the net surface area subject to outgassing. As a result, two models were used to estimate probable mass losses:

(a) the target is assumed to outgas over its full surface area;

(b) the target is assumed to outgas over its full surface area less 1 cm^2 associated with the atomic oxygen beam.

A summary of these calculated % mass losses and mass loss rates due to vacuum alone and atomic oxygen is contained in Table 2. Note that the control samples provide the vacuum baseline data. From Table 2 it is evident that neither model predicts a mass loss for Kapton, even though a change in surface morphology has occurred (as described later). On the other hand, if one assumes for example that the target area facing the beam does not outgas , then indeed one arrives at a % mass loss of 0.023 and a mass loss rate/unit area of $\sim 1.12 \times 10^{-10}$ gms/cm^2-sec. Clearly more effort must be directed towards ascertaining the correct outgassing model for targets subject to molecular beam impingement.

SURFACE ACTIVATION ENERGIES

After removal, the samples were kept in a moisture-free container to prevent re-absorption of water vapour from the atmosphere which could possibly change the surface characteristics of the sample. The surface activation energy can be inferred by measuring the contact angle between a drop of fluid and the surface of a sample. The fluid used to determine the contact angle was distilled water, which tends to give the best results over a wide range of differing materials (ref. 9).

The procedure involved placing a drop of liquid on the sample and determining the angle between the surface of the sample and a line tangent to the drop at the bubble-surface interface. The equipment for the 'drop test' is composed of a horizontal platform on which the sample is mounted. A micro-pippette is used to dispense the drop onto the surface, after which a telescope with a protractor eyepiece can be used to determine the contact angle. An illumination source is provided so that the droplet-surface interface can be easily discerned. Parallax can be eliminated if the telescope is mounted on a track that allows two dgrees of freedom (ref. 10). A summary of the contact angles measured is found in Table 3.

From Young's equation:

$$\gamma_{SV} - \gamma_{SL} = \gamma_{LV} \cos\theta \qquad (3)$$

$$\gamma_{SL} = \frac{[[(\gamma_{SV})^2 + (\gamma_{SL})]^2]^{1/2}}{1 - 0.015(\gamma_{SV} \times \gamma_{LV})^{1/2}} \qquad (4)$$

Taking γ_{LV} = 72.5 mJ/m^2 for room temperature conditions, the surface tension of the interface (γ_{SL}) can then be calculated (Table 3). Since there is a marked change in surface tension, a change in surface energy is inferred, and hence a change in the characteristic morphology of the sample due to atomic oxygen exposure has occurred.

SCANNING ELECTRON MICROSCOPE STUDY

To detect surface morphology changes, an SEM was employed. The graphite/epoxy was analyzed directly due to its conductivity. However, the Kapton, being essentially an insulator, required a gold film to be deposited on its surface before being scanned. The SEM provided flat images as well as modulated ones that produced a 'contour map' of the area being observed. It was this latter feature that was very useful in studying the Kapton surface.

Graphite/Epoxy Sample

An unexposed, unprepared section of graphite/epoxy composite material (fig. 18) clearly shows the carbon fibres, approximately 10 microns in diameter, covered with epoxy. The target sample was polished so that a 'planar' surface could be obtained, thus providing better depth-of-field resolution for the SEM (fig. 19). After approximately 265 hours of exposure to atomic oxygen, the sample was removed and images were taken of the exposed region (fig. 20). It is evident in comparing the exposed and unexposed regions that the atomic oxygen reacted primarily with the epoxy and essentially removed the top layer down to the graphite fibres. Fibre breakage in the exposed areas was also observed to be more pronounced than in unexposed areas.

Kapton (H) Sample

The SEM images of Kapton revealed a much different morphology than the graphite/epoxy material. For example, consider first the control sample (figs. 21, 22) as viewed in the normal and Y-modulated SEM modes. In the direct 'picture mode' of operation (fig. 21), one sees a few lines and isolated dark and 'light' spots. However, in the modulated mode images (fig. 22), the lines correspond to ridges (probably associated with surface scratches on the Kapton film), with the dark and light spots depicting depressions and hills, respectively. Two other modulated views showing similar surface features on the control sample are shown in figs. 23 and 24.

When one examines the target sample after exposure to approximately 187 hours of atomic oxygen, one finds regions of intense dark spots (figs. 25, 27) which, when viewed in the modulated mode, clearly depict large depressions (figs. 26, 28). These areas are quite different from the depressions observed

on the control sample and exhibit 'pitting' characteristics. It would appear that the atomic oxygen has reacted with the Kapton to produce this change in surface morphology.

CONCLUDING REMARKS

An atomic oxygen nozzle beam facility has been assembled capable of providing a beam flux of about 10^{15} atoms/cm^2-sec at an energy level of ~0.14 eV. Although the system is providing dissociation fractions around 1% ~ 5%, the upper limit can be significantly increased (up to 20%) by the addition of ~1% H_2O to the input gas. Furthermore, higher energy levels can probably be attained by reducing the vacuum state below the current operating level of $\sim 10^{-5}$ torr.

Test results to date clearly show a change in surface morphology for graphite/epoxy and Kapton materials exposed to a total atomic oxygen fluence of $\sim 10^{21}$ atoms/cm^2 and 7×10^{20} atoms/cm^2, respectively. Note however that these fluence levels are probably too high, since the influence of the bow shock has not been considered in terms of reducing the incident beam flux on the target. Mass loss measurements based on these limited results were obtained only for graphite/epoxy (approximately 0.13% with a mass loss rate/unit area of $\sim 6 \times 10^{-10}$ gms/cm^2-sec). Insufficient exposure time for the Kapton film produced no significant mass loss and thus repeat testing is necessary.

REFERENCES

1. Jackson, D. P.: A Theory of Gas-Surface Interactions at Setellite Velocities. UTIAS Tech. Note No. 134, Nov. 1968.

2. Leger, L. J.: Oxygen Atom Reaction with Shuttle Materials at Orbital Altitudes. NASA TM 58246, L.B.J. Space Center, Houston, Texas, 1982.

3. Leger, L. J.; Visentine, J. T.; and Kuminecz, J. F.: Low Earth Orbit Atomic Oxygen Effects on Surfaces. proc. AIAA 22nd Aerospace Sciences Meeting, Paper No. 84-0548, Reno, Nevada, U.S.A., Jan. 1984.

4. Lam, Kalvin.: A Hypersonic Atomic Oxygen Molecular Beam Source. Doctoral Thesis, Institute for Aerospace Studies, University of Toronto, Canada, 1976.

5. French, J. B.: Molecular Beams for Rarefied Gasdynamic Research. AGARDograph 112, NATO, 1966.

6. Sears, F.; and Salinger, G.: Thermodynamics, Kinetic Theory and Statistical Thermodynamics (3rd Edition). Addison-Wesley Publishing Co., Don Mills, Canada, 1975.

7. Lam, Kalvin.: Development of a Nozzle Beam Containing Atomic Oxygen. UTIAS Technical Note No. 153, University of Toronto, Canada, 1970.

8. Ashkenas, H.; and Sherman, F. S.: In Rarefied Gas Dynamics, Ed. J. H. de Leeuw, VII, Academic Press, New York, 1966.

9. Neumann, A. W.; and Good, R. J.: Techniques of Measuring Contact Angles. Surface and Colloid Science (Vol. 11): Experimental Methods. Plenum Press, New York, 1979.

10. Hansen, R. H.; Pascale, J. V.; et al: Effect of Atomic Oxygen on Polymers. Journal of Polymer Science, Vol. 3, 1965, pp. 2205-2214.

APPENDIX: MODEL CALCULATIONS OF FREE-JET EXPANSION CHARACTERISTICS

Model calculations concerning the free-jet expansion of the nozzle beam in the test chamber are presented below:

(1) Total flux of molecules, σ_{ex}, issued out of source tube orifice per unit time.

$$\sigma_{ex} = [2/(\gamma+1)^{(\gamma+1)/2(\gamma-1)} n_o a_o A_o$$

where

$$a_o = (\gamma R T_o/u)^{1/2}$$

The apparent ratio of the specific heats, γ, is:

$$\gamma = (0.92 \times C_{p_{He}} + 0.08 \times C_{p_{O_2}})/(0.92 \times C_{v_{He}} + 0.08 \times C_{v_{O_2}})$$

for a 92% He and 8% O_2 mixture.

Given that,

$C_{p_{He}} = 2.50$ R, $C_{v_{He}} = 1.51$ R, $C_{p_{O_2}} = 3.53$ R, $C_{v_{O_2}} = 2.52$ R

then $\gamma = 1.627$ and

$R_s = R/u$

$= 8.3143 \times 10^3$ Nm kilomole^{-1}K^{-1}/(4×0.92 + 32×0.08)kg/kmole

$= 1.3324 \times 10^3$J

with $T_o = 293$ K, $a_o = (1.627 \times 1.3324 \times 10^3 \times 293)^{1/2} = 796.97$ m/sec,

$n_o = N(273/T_o)(P_o/760)$

which for P_o = 1.9 torr, $n_o = 2.35\times10^{16}$ molecules/cc

For an orifice diameter, D_o, of .06096 cm (24/1000"), $A_o = 2.9186\times10^{-3}cm^2$. Therefore, $\sigma_{ex} = 8.766\times10^{18}$ molecules/sec.

(2) Total molecular flux impinging on the sample per unit time per unit area.

$$I_{ex} = 0.6276\ \sigma_{ex} \text{ molecules/steradian/sec}$$

$$= 5.50\times10^{18} \text{ molecules/steradian/sec}$$

The solid angle, Ω_t, from the nozzle subtended by a 1 cm^2 target area 3 cm from the orifice is given by: $\Omega_t = 1/3^2 = .111$ steradians

Thus, $\sigma_t = .111\ I_{ex} = 6.11\times10^{17}$ molecules/cm^2/sec. Now, only 8% of these molecules are O_2 of which approximately 3% splits into 2-O atoms. Hence

$$\sigma_{t_O} = \sigma_{t_{O_2}} \times\alpha\times2 = 6.11\times10^{17}\times0.08\times0.03\times2$$

$$= 2.93\times10^{15} \text{ atoms/}cm^2\text{/sec}$$

(3) The energy of the impinging atomic oxygen atoms can be calculated if a no-slip condition is assumed between the He and oxygen atoms. That is to say, all particles take on the sonic velocity of the He gas.

The freezing Mach number is given by: $M_f = 1.18\ K_{no}^{-(\gamma-1)/\gamma}$

$$\text{but } K_{no} = \lambda_o/D_o,\ \lambda_o = 1/(n_o\times d^2\times\pi\times2^{1/2})$$

where d is the average molecular diameter:

$$d = 2(1.1\times10^{-8}\times0.92 + 1.9\times10^{-8}\times0.08)$$

$$= 2.328\times10^{-8}cm$$

$$\text{Thus } \lambda_o = 1/56.58 \text{ cm};\ K_{no} = 0.2899, \text{ giving } M_f = 1.898.$$

$$v = M_f a_o[1 + (\gamma-1)/2M_f^2]^{-1/2}$$

$$= 1.203\times10^3 \text{ m/sec}$$

$$a_{o_{He}} = (\gamma RT_o/u)^{1/2} = 1008.17 \text{ m/sec}$$

Hence, $V_{He} = 1.3135\times10^5$ cm/sec. Since $E = \frac{1}{2}\ mV^2$ then

$$E_o = \frac{1}{2}\ [15.994\times1.66\times10^{-27}\times(1.3135\times10^3)^2]$$

$$= 2.29\times10^{-20} \text{ J}$$
$$= 0.143 \text{ eV}$$

TABLE 1. DESCRIPTION OF MATERIALS TESTED IN ATOMIC OXYGEN BEAM FACILITY (3 CM FROM ORIFICE)

Samples		Exposure Time (hrs) Vacuum (10^{-5} torr)	Exposure Time (hrs) Atomic* Oxygen	Area (cm^2)	Initial Weight (gms)	Final Weight (gms)
Graphite/Epoxy Hercules AS1/3501-6 (0.318 mm thick)	Control	1152.30	-	9.74	.431902	.430355
	Target	See * below	264.47	9.74	.480055	.477724
Kapton H (0.127 mm thick)	Control	798.25	-	22.44	.391665	.390825
	Target	See * below	187.41	17.82	.326570	.325876

*Targets were subjected to same vacuum duration as control samples, but ~1 cm^2 area exposed to atomic oxygen on one face for duration noted: flux $\approx 10^{15}$ atoms/cm^2-sec; energy ≈0.14 eV.

TABLE 2. SUMMARY OF MASS LOSS RESULTS*

Material	Model**	% Mass Loss Vacuum	% Mass Loss Atomic Oxygen	Mass Loss Rate/Unit Area (gms/cm^2-sec) Vacuum	Mass Loss Rate/Unit Area (gms/cm^2-sec) Atomic Oxygen
Graphite/Epoxy Hercules AS1/3501-6	a	.358	.127	3.83×10^{-11}	6.42×10^{-10}
	b	.354	.132	3.83×10^{-11}	6.64×10^{-10}
Kapton H	a	.214	-	1.30×10^{-11}	-
	b	.213	-	1.30×10^{-11}	-

*The data presented are based on an estimated flux of ~10^{15} atoms/cm^2-sec and energy level ≈0.14 eV. The fluence ≈10^{21} and 7×10^{20} atoms/cm^2 for graphite/epoxy and Kapton, respectively.
**See secion 4.3 for model descriptions.

TABLE 3. CONTACT ANGLE AND SURFACE TENSION VALUES

Samples		Angle (degrees)	Tension (mJ/m^2)
Graphite/Epoxy Hercules ASI/3501	Exposed	40.00	3.167
		41.25	3.497
		40.00	3.167
		42.50	3.847
		40.67	3.340
	Avg.	40.88	3.404
	Unexposed	48.33	5.744
		46.33	5.045
		48.00	5.624
		47.67	5.505
	Avg.	47.58	5.480
Kapton	Exposed	52.00	7.159
		51.00	6.756
		54.00	8.002
		52.33	7.434
	Avg.	52.33	7.338
	Unexposed	44.33	4.396
		46.00	4.933
		45.56	4.823
		44.33	4.396
	Avg.	45.08	4.637

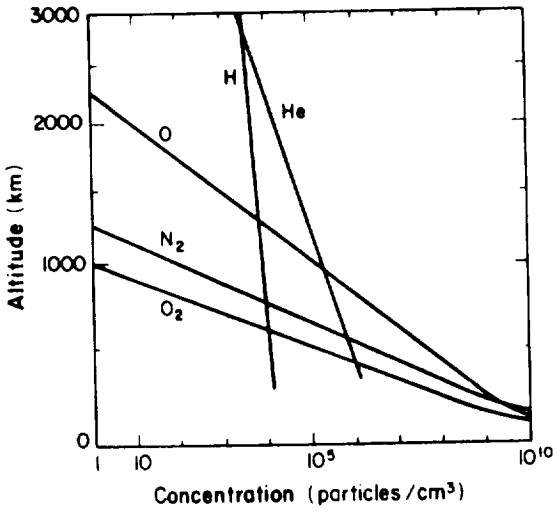

Figure 1 - Concentration of Atmospheric Constituents (Ref. 5)

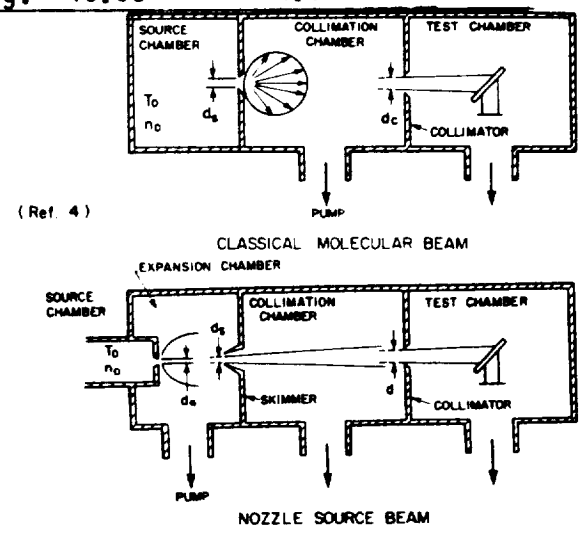

Figure 2 - Two Systems for Molecular Beam Generation

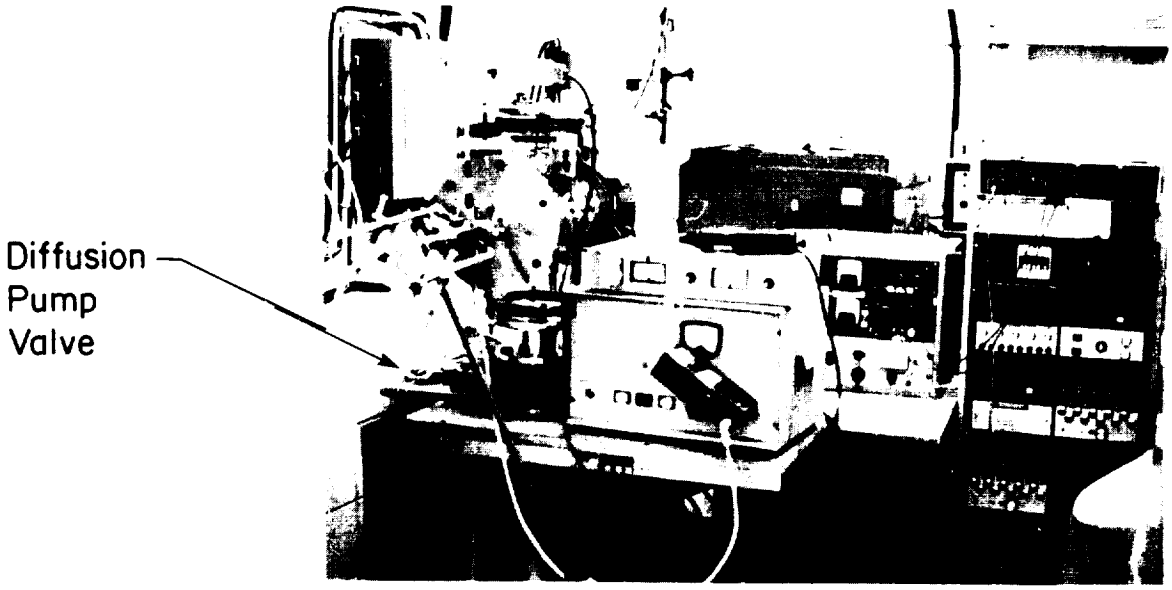

Figure 3

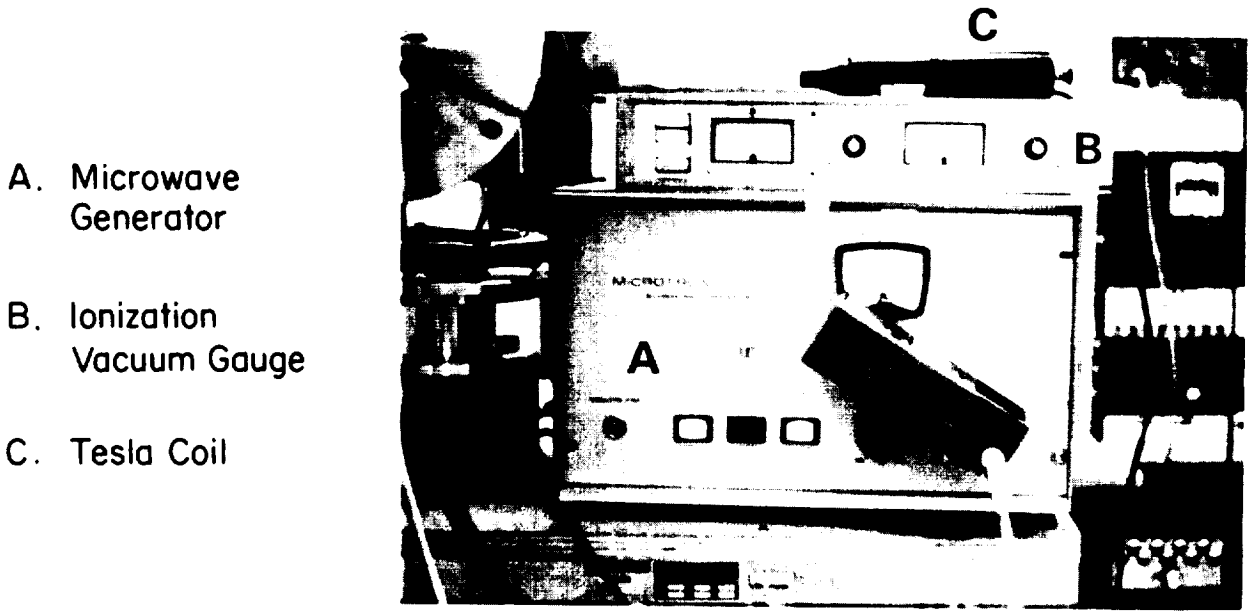

Figure 4

A. Cooling Air Tube

B. Tuning Cavity

C. Roughing Pump Valve

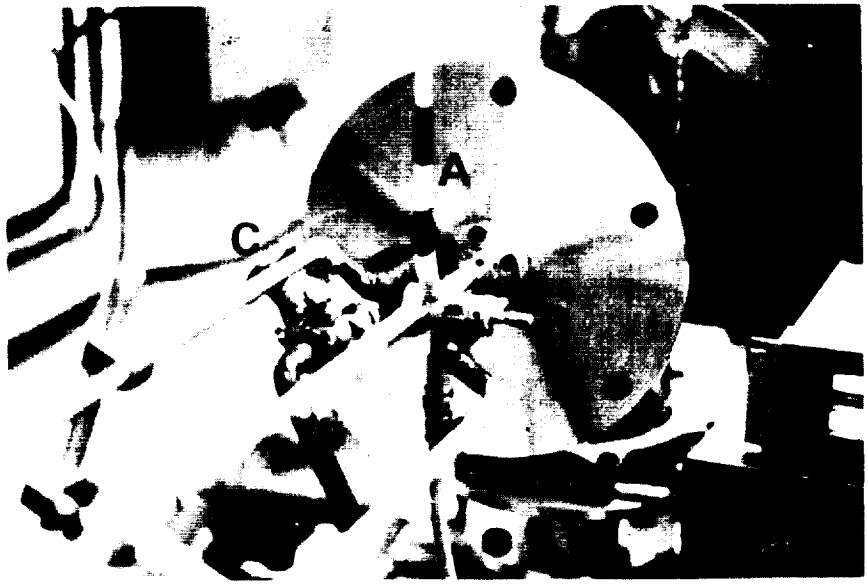

Figure 5

D. Ionization Coil Pick-up

E. Vacuum Vessel

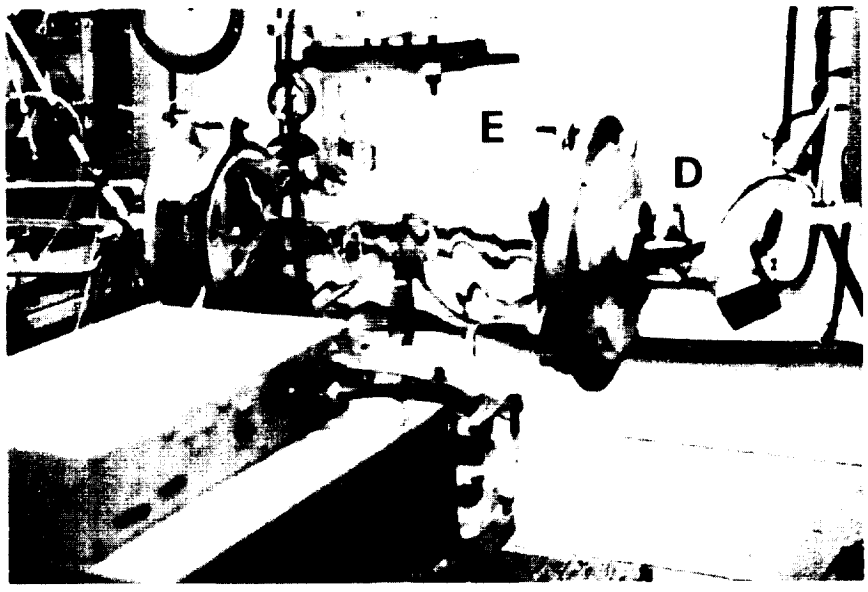

Figure 6

Mass
Spectrometer
Unit

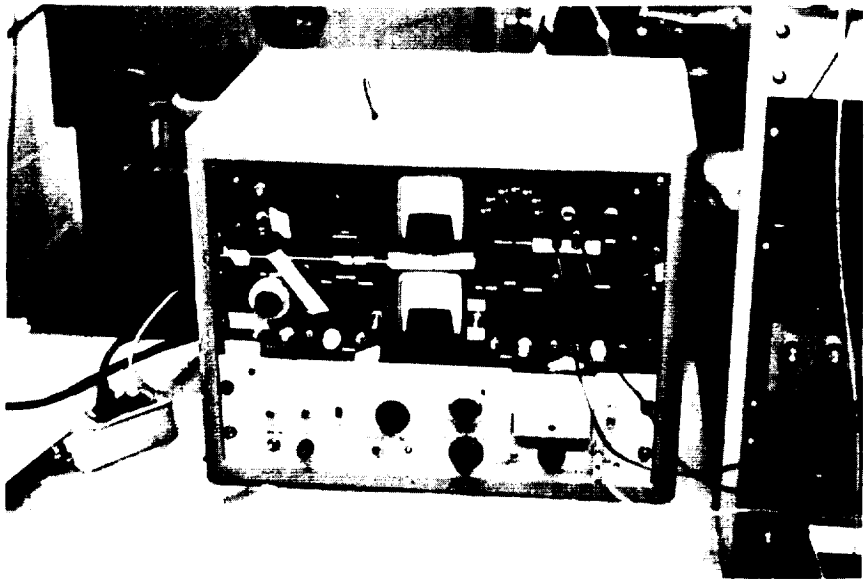

Figure 7

A. Cooling Air Valve

B. Needle Valve

C. Venting Valve

D. Manometer Valve

E. Feed Valve

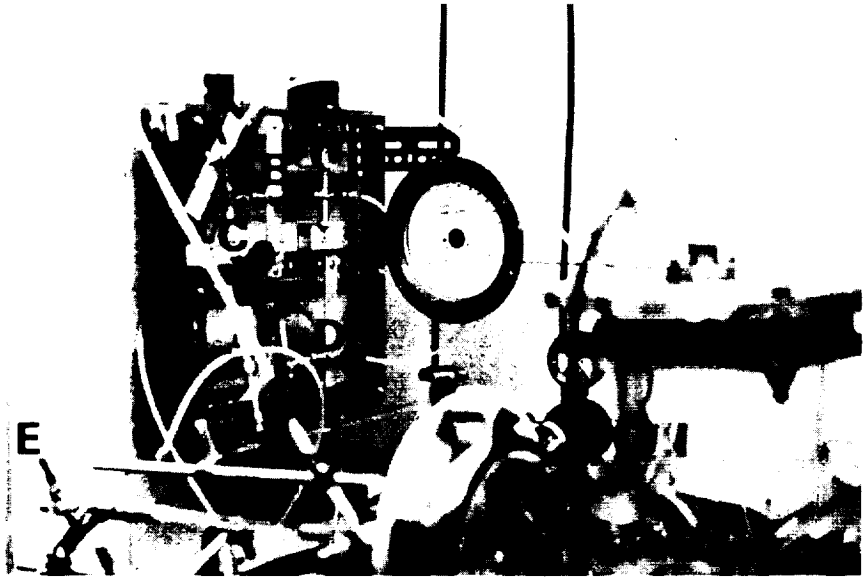

Figure 8

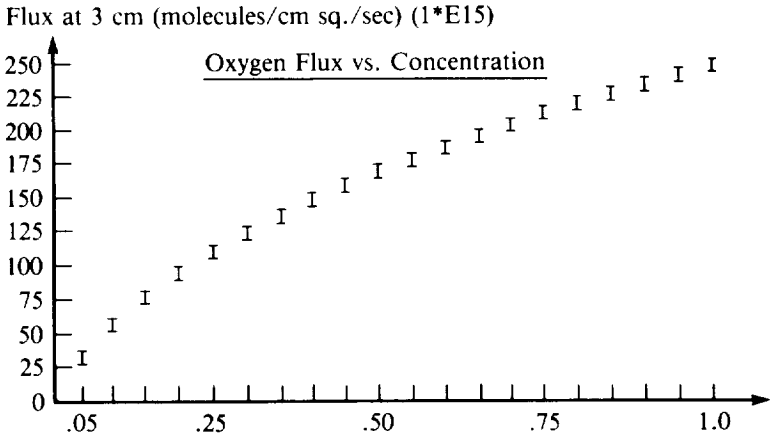

Figure 9 - Fraction of 02 in Mixture

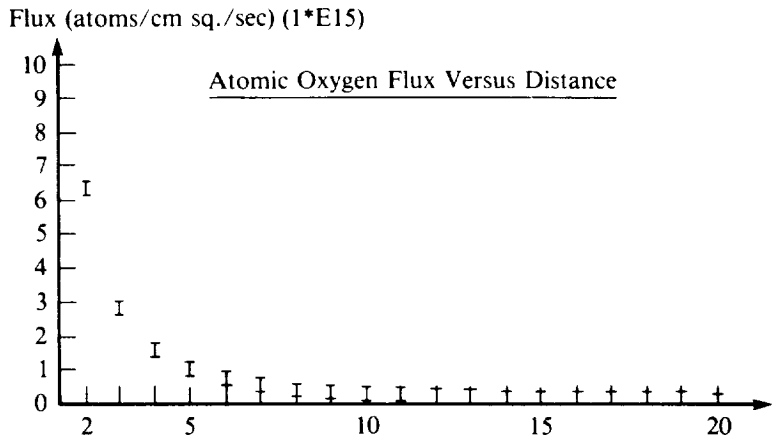

Figure 10 - Distance From Orifice (CM)

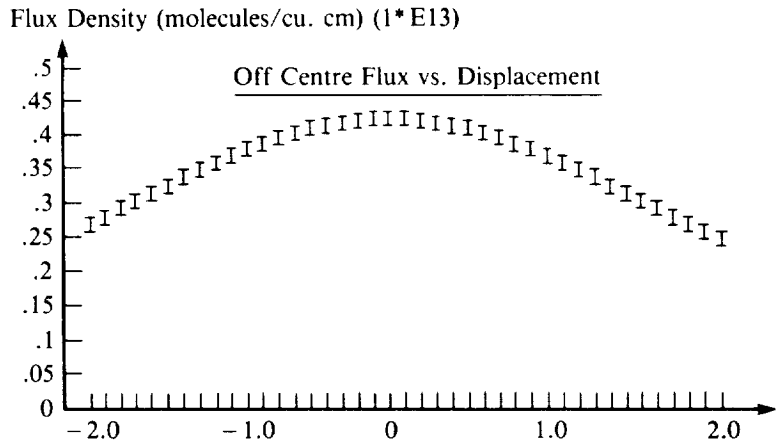

Figure 11 - Off-Centre Displacement (CM)

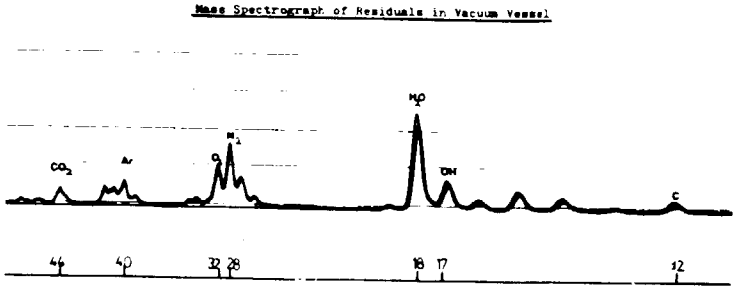

Figure 12

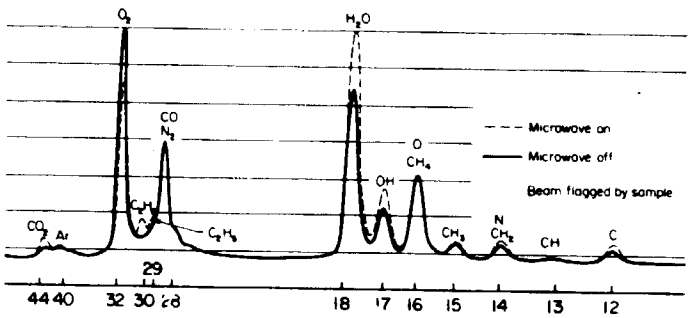

Figure 13 - Graphite/Epoxy: Mass Spectrograph

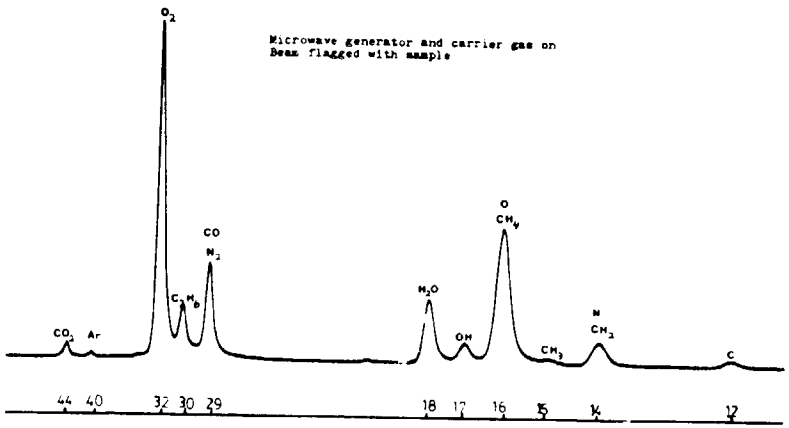

Figure 14 - Graphite/Epoxy: Mass Spectrograph

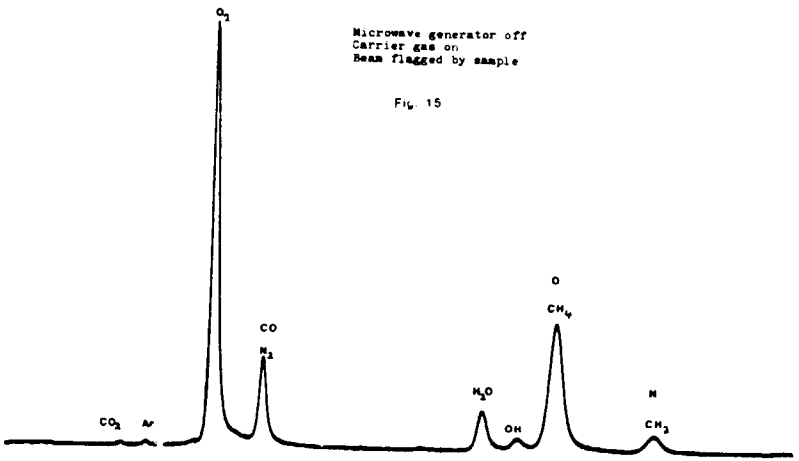

Figure 15 - Graphite/Epoxy: Mass Spectrograph

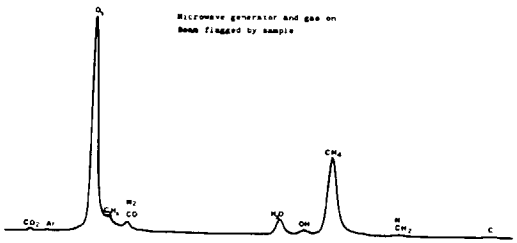

Figure 16 - Kapton: Mass Spectrograph

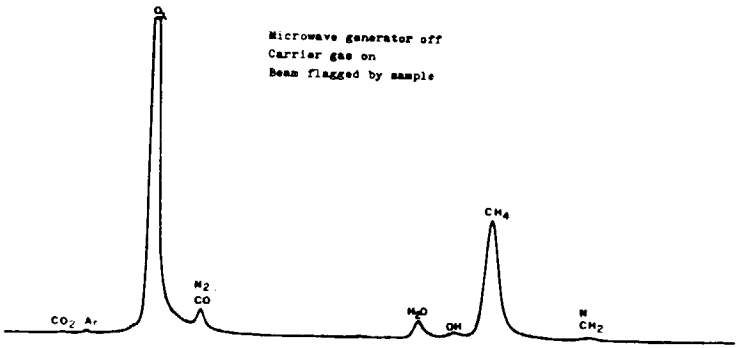

Figure 17 - Kapton: Mass Spectrograph

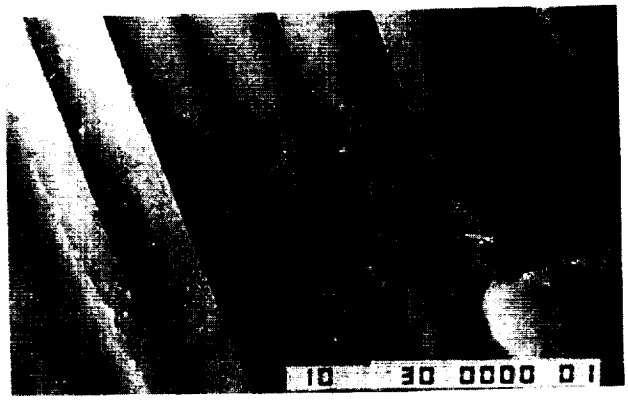

Figure 18 - SEM Photograph of Unprepared, Unexposed, Graphite/Epoxy Sample (1500 X)

Figure 19 - SEM Photograph of Prepared, Unexposed Graphite/Epoxy Sample (1000 X)

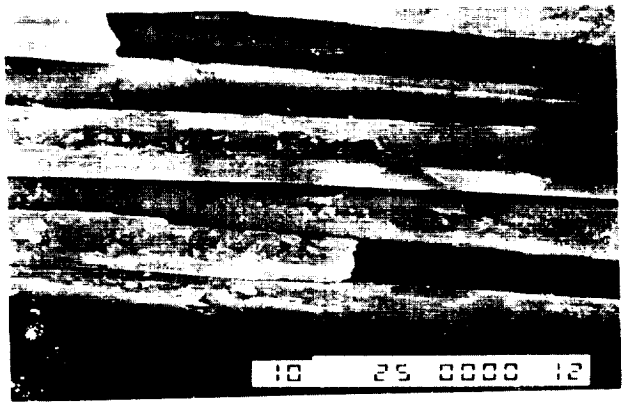

Figure 20 - SEM Photograph of Prepared, Exposed Graphite/Epoxy Sample (1000 X)

Figure 21 - SEM (Normal) Photograph of Unexposed Kapton Control Sample (100 X)

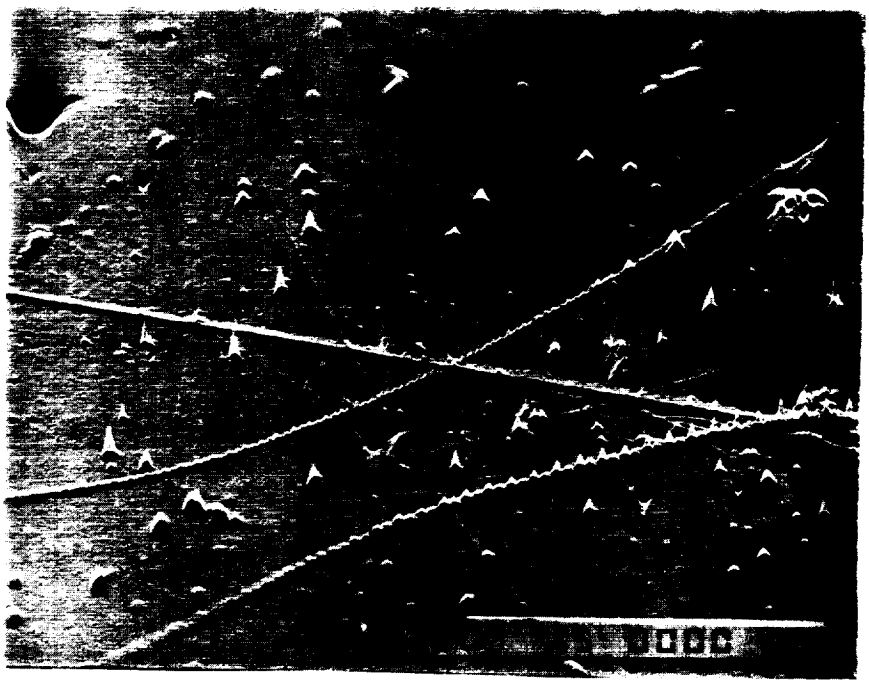

Figure 22 - SEM Y-Modulation Photograph of Unexposed Kapton Control Sample (100 X)

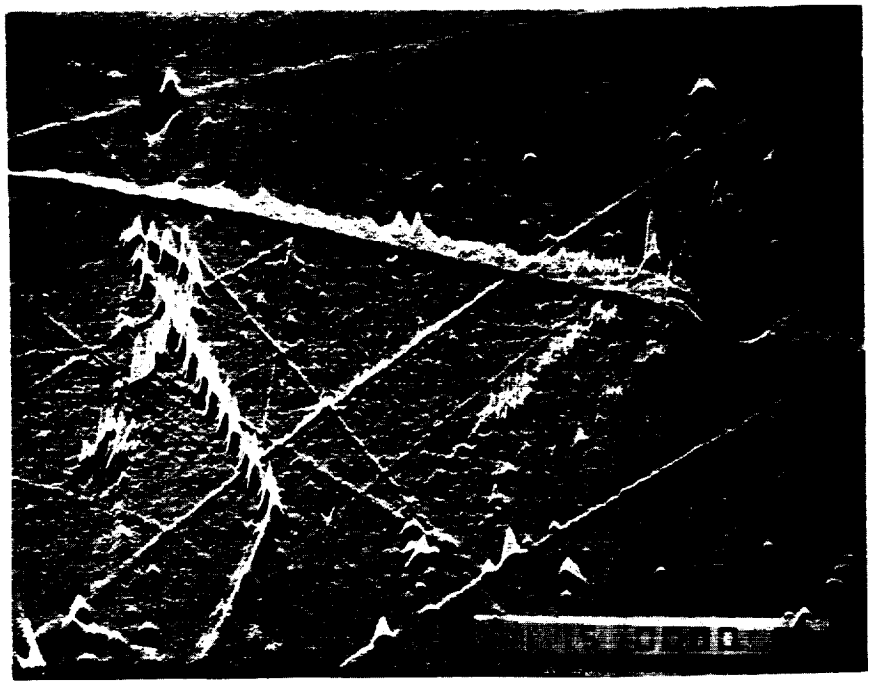

Figure 23 - SEM Y-Modulation Photograph of Unexposed Kapton Control Sample (100 X)

Figure 24 - SEM Y-Modulation Photograph of Unexposed Kapton Control Sample (100 X)

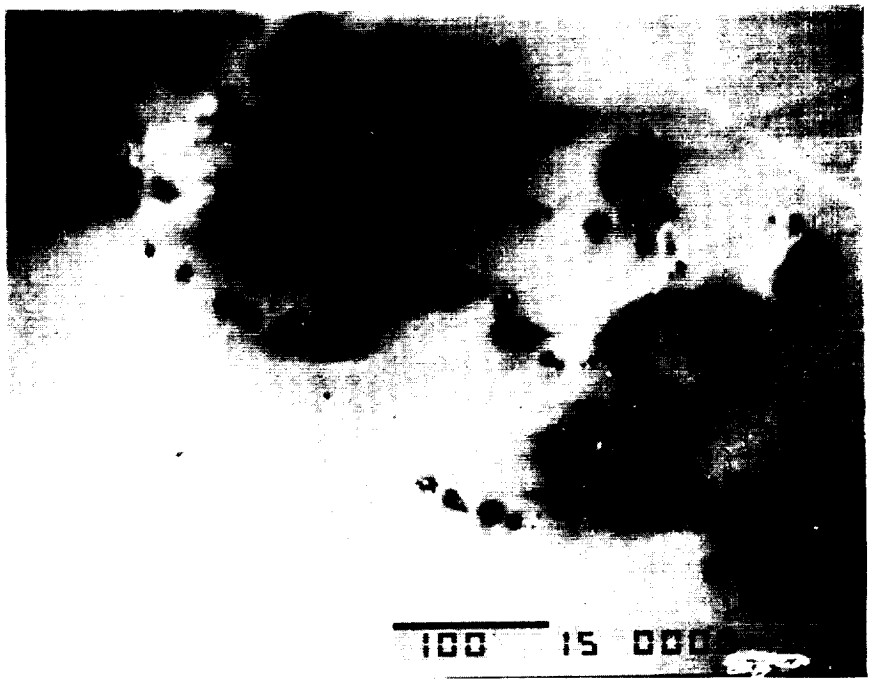

Figure 25 - SEM (Normal) Photograph of Exposed Kapton Sample (200 X)

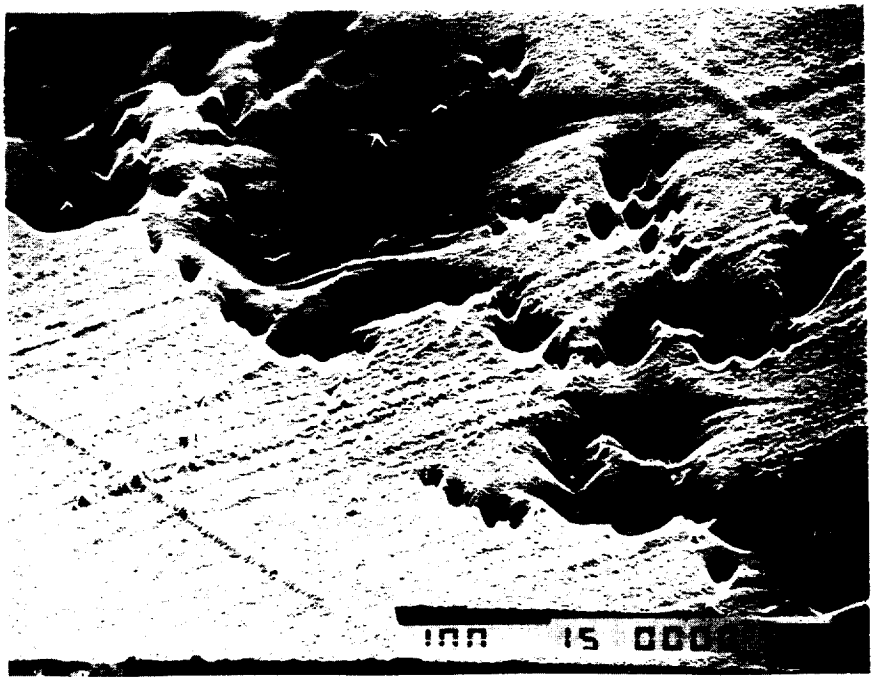

Figure 26 - SEM Y-Modulation Photograph of Exposed Kapton Sample (200 X)

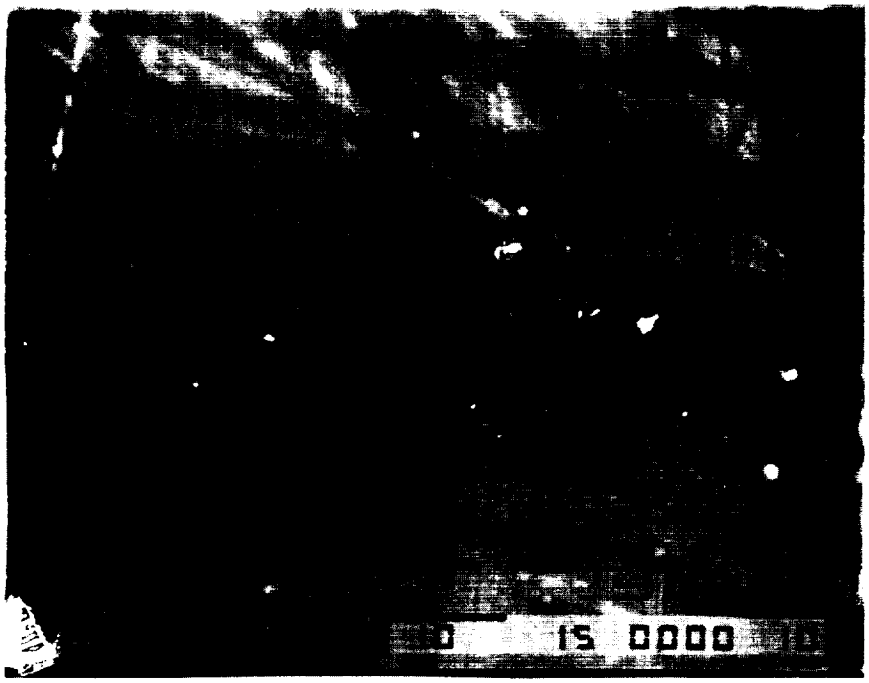

Figure 27 - SEM (Normal) Photograph of Exposed Kapton Sample (1500 X)

Figure 28 - SEM Y-Modulation Photograph of Exposed Kapton Sample (1500 X)

A LOW EARTH ORBIT MOLECULAR BEAM SPACE SIMULATION FACILITY

JON B. CROSS

LOS ALAMOS NATIONAL LABORATORY

CHM-2

ABSTRACT

A brief synopsis of the low earth orbit (LEO) satellite environment is presented including neutral and ionic species. Two ground based atomic and molecular beam instruments are described which are capable of simulating the interaction of space craft surfaces with the LEO environment and detecting the results of these interactions. The first detects mass spectrometrically low level fluxes of reactively and nonreactively surface scattered species as a function of scattering angle and velocity while the second UHV molecular beam, laser induced fluorescence apparatus is capable of measuring chemiluminescence produced by either gas phase or gas-surface interactions. A number of proposed experiments will be described.

INTRODUCTION

The low earth orbit (LEO) environment has been extensively studied over the past ten years and we are now

seeing an intensive investigation of the low earth orbit satellite (LEOS) environment (ref. 1) which is formed by the introduction of contaminant species into LEO by vehicle outgasing and the interaction of vehicle surfaces with the LEO environment at orbital velocities resulting in gas-surface collision energies of 5eV for oxygen atoms and 9.3eV for N_2 molecules. At an altitude of 300km the primary neutral constituents (ref. 2) are N_2 and O-atoms with number densities of approximately $10^8/cm^3$ and $5x10^8/cm^3$ respectively with a local temperature of 1000K while at 200km altitude the concentrations are roughly an order of magnitude higher with O_2 molecules having an equal concentration as O-atoms. Experiments on STS-3 (ref. 1) have shown a substantial perturbation of the natural LEO environment by the space shuttle creating a local low earth orbit satellite (LEOS) environment which interacts with shuttle surfaces. The following observations were made: plasma densities an order of magnitude higher than in the LEO environment, energetic (20-100eV) electron fluxes up to $10^{14}/cm^2$-s, ion fluxes with energies up to 30eV and densities of $10^4/cm^3$ for NO^+, $6x10^3/cm^3$ for O_2^+, and $5x10^5/cm^3$ for O^+-atoms at a altitude of 300km, a gas density up to $3x10^{11}/cm^3$ near surfaces facing the ram direction, and glow phenomena and plasma density increasing during thruster operations and daytime ram conditions. Extensive etching of surfaces exposed to LEOS environment has been observed (ref. 3, 4) and correlated with O-atom number density. The etching is most evident on those surfaces exposed in the ram direction (as high as 0.1 micron/orbit for kapton) but etching two to three times less has also been observed on shaded surfaces indicating that

thermal reflected O-atoms are also quite reactive. In order to simulate and investigate the mechanism of space craft etching (ref. 3, 4) and glow (ref. 5) gas phase reactants and products need to be identified and characterized as to their angular and velocity distributions as well as their internal state distributions while products remaining on the surface need to be identified. It is evident from these observations that simulation of the low earth orbit satellite (LEOS) environment must entail not only investigations of gas-surface interactions but also ion, electron-surface (ref. 6) and gas-gas and gas-plasma interactions and simulation facilities which simultaneously incorporate sources of these reactants along with surface and gas phase detectors need to be developed.

ENVIRONMENT SIMULATION AND INTERACTION STUDIES

Figures 1 and 2 depict some of the apparatus available at Los Alamos which are capable of 1) simulating the LEOS environment, 2) characterizing surface reactants and products, and 3) detecting gas phase reaction products and chemiluminescence produced by gas phase or surface plasma excited species. The first apparatus, designated as the Los Alamos Molecular Beam Dynamics Apparatus (ref. 7) (LAMBDA, Fig. 1) and patterned from the design of Lee (ref. 8) and coworkers, can be configured either for gas phase crossed molecular beam studies or gas-surface beam investigations. Figure 1 depicts LAMBDA configured for gas-surface studies and shows the extensive differential pumping present on both the mass spectrometer detector (3 stages) and gas beam source

(4 stages). The advantages of this apparatus are: 1) high pumping speed, 2) excellent isolation of both the high intensity beam source (4 stages of differential pumping) and electron bombardment detector (3 stages of differential pumping) from the test specimen, 3) high detection efficiency of electron bombardment ionizer-quadrupole mass filter combination (10^{-4}), 4) angular scan capability of detector from -10 deg to 120 deg, 5) capability to perform time of flight analysis of scattered species over the angular range using high transmission cross correlation techniques (ref. 9), 6) capability of performing either crossed molecular beam scattering experiments or molecular beam-surface scattering experiments using a crystal manipulator which takes the place of one of the gas beams, 7) the capability of introducing photon or ion beams for simulation of plasma interactions, and 8) the capability of performing Auger analysis on the test specimen surfaces. The primary disadvantage for gas-surface experiments is the inability to obtain UHV operation in the low 10^{-10} torr range though the apparatus routinely obtains 2×10^{-8} torr when running gas phase experiments and when using the liquid nitrogen cryoliner the apparatus will operate in the high 10^{-9} torr range. A slotted disk velocity selector (ref. 10) can be added to the beam source in order to create a dark source though the beam intensity would be decreased roughly an order of magnitude.

The second apparatus designated the molecular beam-fluorescence detection apparatus shown in figure 2 was designed for molecular beam scattering experiments on well characterized surfaces held in a UHV environment (10^{-10} torr)

and using laser induced fluorescence (LIF) for detection of the scattered species (ref. 11). The apparatus has three stages of differential pumping on the beam source; a cryoliner, ion-titanium sublimation and turbomolecular pumps on the bakeable UHV chamber along with Leed, Auger and LIF detection capability; and a bakeable differential pumping stage between the sample and nozzle beam source which can house a slotted disk velocity selector. The primary advantages of the system are 1) UHV capability and strict control of contaminant gases, 2) the capability of detecting fluorescence processes, and 3) the capability of performing insitu surface analytical procedures on the sample using Leed and Auger equipment. The primary disadvantages are relatively long path length from the beam source to the sample (50cm as opposed to 8cm on LAMBDA), fewer differential pumping stages on the beam source, and lack of a angular resolved mass spectrometer detector.

A number of low energy beam sources are on hand as well as a high temperature graphite source (ref. 12) for producing high velocity molecular and atomic beams. A thermal energy oxygen atom source employing discharge techniques (ref. 13) is being constructed for use in investigations of thermal O-atom etching of surfaces. The beam sources are interchangeable between the two apparatus and any source developed in the future would also be interchangeable thus increasing the number of options for experiments. In other words experiments involving particle identification and measurements of translational velocity distributions would be performed on LAMBDA and at a later time fluorescence

experiments would be performed with the same beam source on the UHV apparatus. In many cases a dark beam source will be needed, i.e. a source which is not a source of photons itself and this would again be accomplished through the use of a slotted disk velocity analyser.

PROPOSED EXPERIMENTS

We will first study thermal O-atom etching to gain a basic insight into the mechanism of reflected O-atom interactions with space craft surfaces. Gas phase reaction products will be identified mass spectrometrically and their recoil velocity and angular distributions will be measured while reaction products remaining on the surface will be identified using Auger analysis. Though we do not at present have the hardware to introduce ions or electrons on to the surface, this capability would be added to study the effects of plasma interaction on etching rates and dynamics. The results of these experiments, i.e. product identify, angular and recoil velocity distributions, and surface reaction products, can be used in contamination modeling (ref. 14) of reflected O-atom etching of space craft surfaces operating in low earth orbit as well as for the development of a fundamental understanding of the etching mechanism. Further experiments investigating the glow phenomena (ref. 5) associated with space craft in low earth orbit as well as O-atom etching of ram exposed surfaces requires the use of a high translational energy (5eV) O-atom source. Our effort to develop such a source using cw CO_2 laser sustained discharge techniques will be discussed at the meeting.

REFERENCES

1. S. Shawhan and G. Murphy, "Plasma Diagnostic Package Assessment of the STS-3 Orbiter Environment and System for Science", AIAA paper #83-0253 (1983).

2. E. S. Oran, D. F. Strobel, K. Mauersberger, J. Geophy. Res., 83, 4877 (1978).

3. P. N. Peters, R. Clinton and E. R. Miller, Geophy. Res. Lett., 10, 569 (1983).

4. L. J. Leger, J. T. Visentine and J. F. Kuminecz, "Low Earth Orbit Atomic Oxygen Effects on Surfaces", AIAA-8-0548, Presented AIAA 22nd Aerospace Sciences Meeting 1984.

5. P. M. Banks, P. R. Williamson and W. J. Raitt, Geophy. Res. Lett., 10, 118 (1983).

6. K. Papadopoulos, "The Space Shuttle Environment As Evidence of Critical Ionization Phenomena", Active Experiments in Space Symposium at Alpbach 24-28 May 1983, pp 227-244.

7. D. S. Bomse, J. B. Cross and J. J. Valentini, J. Chem. Phys., 78, 7175 (1983).

8. Y. T. Lee, J. D. McDonald, P. R. Lebreton and D. R. Herschbach, Rev. Sci. Instr., 40, 1402 (1969); G. H. Kwei (unpublished work).

9. V. L. Hirschy and J. P. Aldridge, Rev. Sci. Instr., 42, 381 (1971).

10. J. L. Kinsey, Rev. Sci. Instr., 37, 61 (1966).

11. Jon B. Cross and Jonathan B. Lurie, Chem. Phys. Lett., 100, 174 (1983).

12. James J. Valentini, Michael J. Coggiola and Yuan T. Lee, Rev. Sci. Instr., 48, 58 (1977).

13. Steven J. Sibener, Richard J. Buss, Cheuk Yiu Ng and Yuan T. Lee, Rev. Sci. Instr., 51, 167 (1980).

14. Ray O. Rantanen, "Space Craft Contamination Modeling", AIAA #77-739, AIAA 12th Thermophysics Conference, Albuquerque, NM, June 27, 1977.

FIGURE CAPTIONS

1. Los Alamos Molecular Beam Apparatus (LAMBDA). This figure shows the central portion of the instrument including the molecular beam source, the crystal manipulator-molecular beam intersection zone and a portion of the moveable detector. The detector is a electron bombardment ionizer-quadrupole mass spectrometer suspended from the rotatable lid of the main vacuum chamber. Two different apertures can be used at the entrance to the detector. The smaller aperture is circular with a 0.15 mm diameter and is set in place when the detector is positioned to monitor the direct beam while the larger is rectangular, 3 mm wide by 3 mm high, and is used to detect reaction products scattered from the test surface. Also shown is a time of flight chopping wheel which contains a series of slots forming a pseudorandom sequence which allows for 50% transmission efficiency and time of flight measurements by cross correlating the data with the sequence. Pumping on the scattering chamber is accomplished with a liquid nitrogen cryoliner, turbomolecular pump and a closed cycle gaseous helium cryopump. Pressures of 10^{-8} to 10^{-9} torr are obtained in the scattering chamber. Not shown in the figure is Auger surface analysis equipment located in the crystal manipulator housing for identifying surface adsorbed species. This apparatus will be used for investigations of space craft surface etching by O-atoms.

2. Molecular Beam Laser Induced Fluorescence Apparatus. This figure shows a detailed view of the central components which consist of a nozzle chamber, a differential pumping chamber containing flags, choppers and a slotted disk velocity selector, and a UHV (10^{-10} torr) chamber containing a cryoshroud, crystal manipulator, surface analysis equipment consisting of Leed and Auger units, and provision for collecting fluorescence light and introducing laser or other photon sources of light. This apparatus would be used primarily for investigations of O-atom damage to optical surfaces and investigations of surface-plasma glow phenomena observed on space craft surfaces.

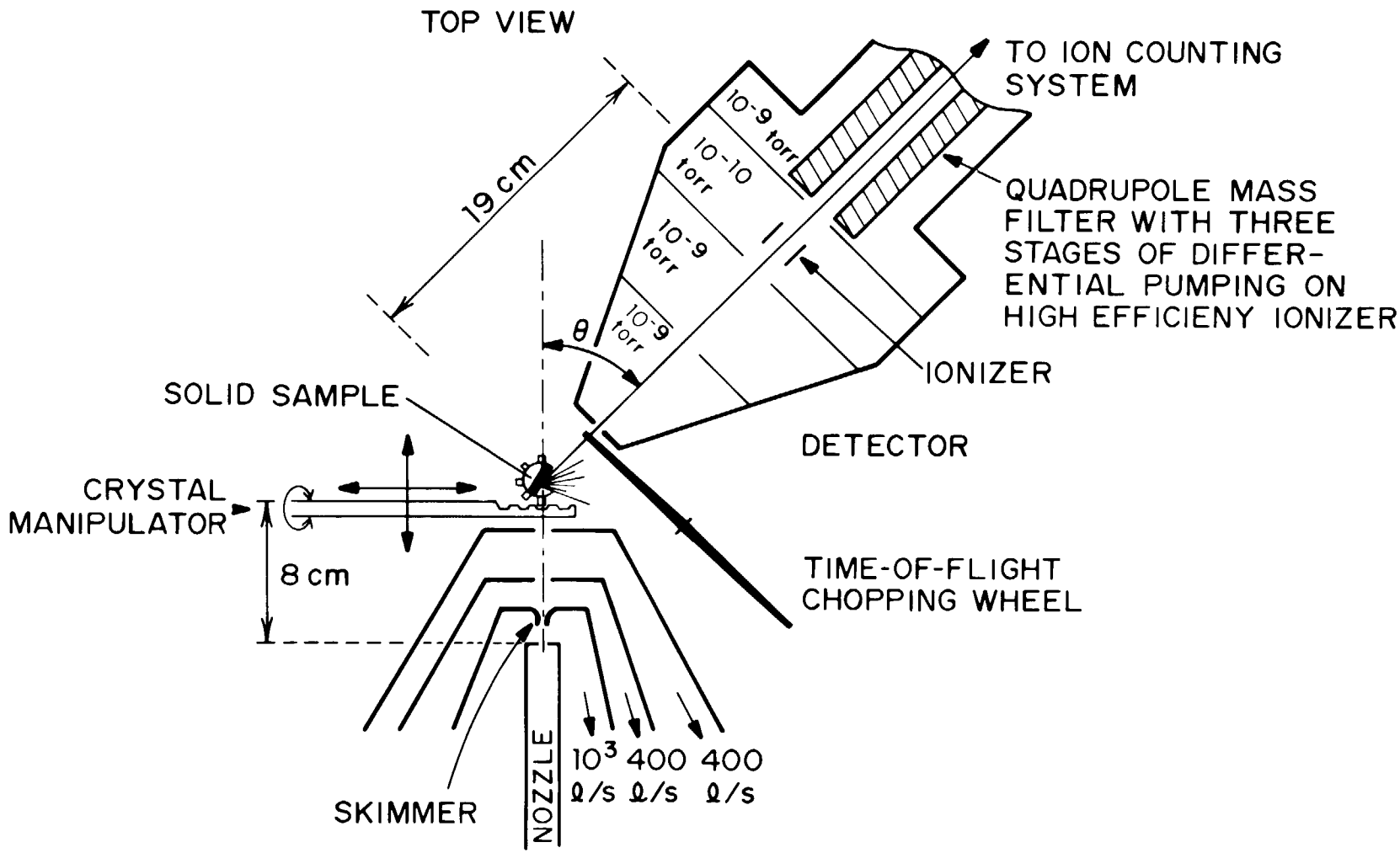
TOP VIEW
TO ION COUNTING SYSTEM
19 cm
10-9 torr
10-10 torr
10-9 torr
10-9 torr
θ
QUADRUPOLE MASS FILTER WITH THREE STAGES OF DIFFERENTIAL PUMPING ON HIGH EFFICIENY IONIZER
IONIZER
SOLID SAMPLE
DETECTOR
CRYSTAL MANIPULATOR
8 cm
TIME-OF-FLIGHT CHOPPING WHEEL
SKIMMER
NOZZLE
10³ ℓ/s
400 ℓ/s
400 ℓ/s

Figure 1

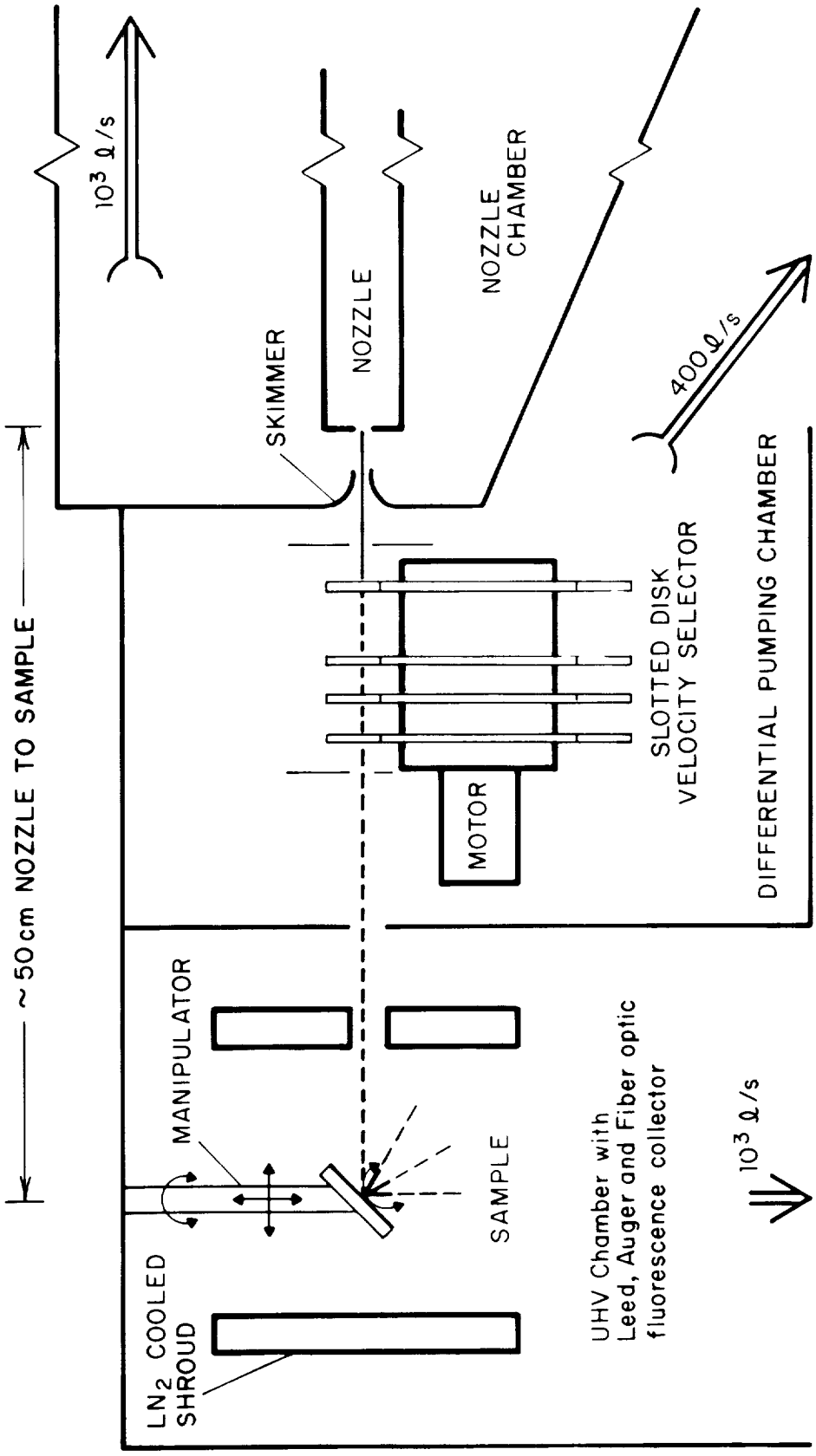
~ 50 cm NOZZLE TO SAMPLE
10^3 ℓ/s
SKIMMER
NOZZLE
NOZZLE CHAMBER
400 ℓ/s
SLOTTED DISK VELOCITY SELECTOR
MOTOR
DIFFERENTIAL PUMPING CHAMBER
MANIPULATOR
SAMPLE
LN_2 COOLED SHROUD
UHV Chamber with Leed, Auger and Fiber optic fluorescence collector
10^3 ℓ/s

Figure 2

THE ENERGY DEPENDENCE AND SURFACE MORPHOLOGY OF KAPTON* DEGRADATION UNDER ATOMIC OXYGEN BOMBARDMENT

Dale C. Ferguson
Lewis Research Center

ABSTRACT

Data from laboratory simulations and from samples returned from STS-8 are used to derive the energy dependence of the mass loss rate of Kapton under atomic oxygen bombardment and to discuss the development of surface structure and its effect on erosion rates. It is concluded that all the laboratory data from discharge and flow tubes and from accelerated beams, along with the orbital data from STS-3 through STS-8, can be accommodated by a rate of mass loss that varies with impact energy normal to the surface. It is hypothesized that increases of mass loss rate with exposure time may be due to trapping of the incoming atoms by the surface structure which develops.

INTRODUCTION

Kapton, a polyimide with wide applications in space technology, undergoes weight loss and surface degradation in low earth orbit. The changes comprise a loss of mass from the surface, a change of surface appearance from a glossy yellow transparency to a milky translucence, and surface roughening on micron length scales. These changes, first noted on early Space Shuttle flights (ref. 1), have important implications for extended operations in low earth orbit (LEO) such as the Space Station. It has been verified (ref. 2) that the cause of the degradation is chemical interaction with the atomic oxygen of the residual atmosphere, impacting the spacecraft surfaces at the spacecraft velocity.

The atomic oxygen in LEO impacts surfaces with an energy of approximately 5 eV (1 eV = 1.6×10^{-19} J). Previous laboratory simulations have attained energies of about 1 eV. In this paper are reported investigations at energies up to 800 eV, which may allow evaluation of the energy dependence of the reaction. In addition, the role of the surface structure in influencing the reaction rates will be discussed.

THE EXPERIMENT

Figure 1 is a schematic drawing of the experimental setup. For the results reported here, a tunable microwave resonant cavity (ref. 2) was used to dissociate and ionize technical grade oxygen gas. The gas was leaked into a glass container within the microwave cavity, and after ionization, was accelerated electrostatically to impact on samples of Kapton. The experiment was done in a horizontal cylindrical vacuum tank, measuring about 1 meter in radius and 4 meters in length.

*Kapton is a registered trade name of E.I. du Pont de Nemours & Co., Inc.

Tank pressures during beam operation were maintained by diffusion pumps at about 10^{-4} torr, compared to about 10^{-6} torr with the beam off (1 torr = 7.5×10^{-3} Pa).

The microwave cavity used a maximum of 100 W of 2450 MHz radiation. The cavity body was biased to a voltage of around +800 V and the accelerating grid was biased to about −200 V. The ion beam produced was about 5 cm in diameter, diverging as it streamed toward the samples. A typical oxygen flow rate was about 25 SCCM (4.2×10^{-7} m^3/s).

The Kapton samples were supported by a strip heater with attached thermocouples. Source to sample distance was about 10 cm for some trials and 23 cm for others. The samples analyzed in this paper were within 5 cm of the axial beam center. The plasma mean free path was always longer than the source to sample distance. Deceleration of the beam was attempted for some samples by biasing the aluminum backing of the samples with retarding potentials of up to +1000 V. The heater strip was insulated from the samples by 2 layers of 1 mil Kapton tape and from the tank wall by a fiberglass mounting beam (1 mil = 2.5×10^{-3} cm).

A retarding potential analyzer (RPA) which could be swung into and out of the beam was used to determine the beam current density. Typical RPA currents were 185 μA which, divided by the RPA collecting area of 13.4 cm^2, gives an average central beam current density of about 14 $\mu A/cm^2$. Spectroscopic analysis of the beam, done with a 0.5 meter Jarrel-Ash spectrometer with 0.1 Å resolution (1 Å = 10^{-8} cm), showed that the beam consisted predominantly of atomic oxygen ions, with neutral atomic oxygen as an added constituent.

No attempt was made to neutralize the beam, since in low energy sputtering studies (ref. 3), it has been established that charge exchange occurs very rapidly, before the momentum exchange necessary for the chemical reactions investigated in this and other papers could occur. Supporting this contention, no degradation of the Kapton exposed only to the thermal oxygen flux in the tank occurred, even though the thermal flux on the samples was orders of magnitude greater than the beam flux. Furthermore, runs made using argon gas instead of oxygen showed no degradation beyond that expected from sputtering alone, even though argon ions should be highly chemically reactive. One may be confident that the simulation reported here using oxygen ions is chemically similar to those using atomic oxygen and to the situation in LEO.

Table I gives the parameters of the studies reported here. Fluxes were calculated from RPA currents and estimated beam divergences, and total fluence from fluxes and exposure times. Table II gives the derived reaction rates for two of the trials along with the method. In a previous paper (ref. 2), it was supposed that the ambient oxygen reacted with the Kapton under the influence of the ion beam energy, to explain the exceedingly high reaction rates obtained. This ad hoc assumption neglects the difficulties found with maintaining electrical contact with the samples in the chamber. After the second run of table II, it was found that the backing on the ½ mil sample had completely lost electrical contact, explaining arcing which had been observed during the run between it and the adjacent sample. It must be assumed that the impact energy in the runs with attempted back biasing is unknown. Therefore, only the data of 11/24/82 will be used in the analysis of this paper, because no attempt was made to alter the impact energy.

Reported here also are the reuslts of a flight experiment on STS-8. Lewis Research Center was allocated 13 slots for samples on a controlled attitude Space Shuttle flight. Full results and a complete description of the experiment will be given elsewhere. For the purposes of this paper, a short

description is given here. Samples of Kapton and other materials were exposed to the ram influx of atomic oxygen in the Shuttle payload bay at an altitude of 120 nautical miles (222 km) for a total of 41.17 hours. Weight and other measurements were made before and after the flight. A mass loss determination was made from the before and after weighings, correcting for water absorption by using control samples. The major uncertainty in the mass loss rate determined from these samples was in the estimate of the total atomic oxygen fluence, which had to be derived from atmospheric models. For these data, the fluence was assumed to be 3.50×10^{20} atoms/cm^2. Samples of aluminum backed uncoated Kapton showed a mass loss rate of 4.29×10^{-24} g/atom, or about 2.60 amu/atom $+/-30\%$ (1 amu $= 1.66 \times 10^{-24}$ g).

THE ENERGY DEPENDENCE OF THE MASS LOSS RATE

Because of uncertainties in correcting for the attitude of the Shuttle Orbiter in flights STS-3 through STS-5, data on mass loss rates from those flights will be discussed later. First, the mass loss rate dependence on energy will be determined for flights and simulations in which the atomic oxygen impacted normal to the surface or in a statistically completely random fashion.

For the lowest energies, mass loss rates found in plasma ashers and other rf discharges and flow tubes will be used. Although it is commonly assumed (ref. 1 and 4) that the atomic oxygen produced in such discharges is at room temperature, it clearly cannot be. Busch and Vickers (ref. 5) found that in low pressure (~ 1 torr) microwave discharges in argon, the spectroscopic temperatures were always around 4000K. Although it might be argued that these were not kinetic temperatures, and that they were measured inside the discharge itself, not downstream in a flow tube away from the discharge, they may be taken to indicate that temperatures in the discharge may be high. In a closer approximation to the studies done on atomic oxygen degradation rates, Brake and Kerber (ref. 6) modelled the chemical kinetics in atomic oxygen flow tubes away from the microwave discharge source. They found that kinetic temperatures in the discharge were always greater than about 1000K and that the temperatures did not change in the flow tube downstream from the source. Thus, 1000K, may be a minimum value of the temperature in an oxygen flow tube or discharge, and 4000K a maximum. In such a discharge, Hansen et al (ref. 7) give a mass loss rate of 4.1×10^{-7} g/cm^2 and quote a flowrate of about 4 SCCM and number densities of 10^{14} to 10^{15} atoms/cm^3. While the error implied by the range of number densities is large, a lower limit to their mass loss rate per atom can be found by assuming that all the incoming gas was dissociated and that it all reacted with the polymer sample. A flow rate of 4 SCCM corresponds to 1.7×10^{18} molecules/s. If they are all dissociated, there will be 3.4×10^{18} atoms/s produced. Combined with the total mass loss rate quoted as 1.19×10^{-4} g/min one can find a mass loss rate of 5.8×10^{-25} g/atom, or 0.35 amu/atom. This would put the oxygen density somewhere near the lower value of 10^{14} /cm^3.

One can calculate the temperature in the discharge by assuming that the gas is in local thermodynamic equilibrium. Then, the ratio of the numbers of dissociated atoms to the number of molecules will be a function of the temperature. From the above considerations one can estimate the atomic oxygen density to be about 10^{14}/cm^3. From the ideal gas law at a temperature of 1700K, the number density at a pressure of 1 torr is about 4×10^{15}/cm^3. Finally, from the dissociation equation (ref. 8),

$$\log(N_A/N_B/N_{AB}) = 20.2735 + 1.5 \log m_{AB} + 1.5 \log T - 5040\ (D/T)$$

$$+ \log(U_A U_B/Q_{AB}), \qquad (1)$$

where N_A, N_B, and N_{AB} are the number densities of the dissociated species and the molecule, respectively, m_{AB} is the mass of the molecule in amu, T is the temperature in Kelvins, D is the dissociation energy in eV, U_A and U_B are the atomic partition functions, and Q_{AB} is the molecular partition function, one may find that the temperature is indeed near 1700K. Taking 1700K to be the temperature in the discharge yields a mean atomic kinetic energy of 0.23 eV, and a mean impact energy normal to the surface of 0.08 eV.

For the high energy datum, the mass loss rate of the run of 11/24/82 reported here will be used. The impact energy was about 800V and the mass loss rate was 169 amu/ion. This corresponds to a loss of about ten to thirteen atoms per impact, a rate which may be due to loss of large polymer chain fragments. Such a high mass loss rate is much higher than sputtering loss rates, and consistent with the negligible loss seen in the Lewis trials with argon bombarded samples at similar energies and fluences.

At intermediate energies, the orbital mass loss rate will be used, reported here on the basis of STS-8 results as 2.60 amu/atom at an energy of 5 eV, and the atomic oxygen beam rates found by Arnold and Peplinski (ref. 4). Their beam, operated at an energy of about 1 eV, yielded a mass loss rate of about 1.5 amu/atom +/−50%, with the major source of error being the calibration of a mass spectrometer used for beam flux determination.

The experimental data are shown in figure 2. Here it can be seen that all these measurements may be appropriated by an energy dependence of the form

$$R = A\,E^n, \qquad (2)$$

where R is the mass loss rate in amu/atom, E is the impact energy in eV, and A and n are constants. For these data, a least squares fit to the logarithms yields A = 1.5, and n = 0.68, with a correlation coefficient of 0.990, significant at more than the 99% level. Such a high correlation, over four orders of magnitude in energy, is impressive even considering the enormous error bars on the rate measurements. From attempts to fit lines through the error bars in figure 2, the true value of n is estimated to lie between 0.5 and 0.8.

Other reported values not included on figure 2 are worthy of mention, and demand explanation. Leger (ref. 9), for instance, gives mass loss rates from the STS-3 thru STS-5 flights which vary from 1.2 to 2.5 amu/atom. Even throwing out the lowest value as unexplained experimental error, there are still values which are lower than the STS-8 value by as much as 30%. An explanation for the lower values on STS-3 thru STS-5 may lie in a dependence not only on the impact energy, but on the energy normal to the surface. The attitude of the Shuttle was not controlled to keep the incoming flux normal to the surface on the earlier flights, but it was controlled on STS-8. In fact, there were samples on STS-8 which were held at a fixed angle to the velocity vector and which may shed some light on the dependence of the mass loss rate on impact angle. Leger (ref. 9) gives the results of measurements done on samples which were held at an angle of 42° to the velocity vector. He finds that the mass loss rate for these samples was only 59% to 68% as great

as for the samples normal to the velocity, even though the fluence was about 74% as high. Making the assumption that the mass loss rate depends on the impact energy normal to the surface raised to some power, one can calculate what that power law must be. If

$$R = B\,Ep^{n}\,, \tag{3}$$

where Ep is the energy perpendicular to the surface, then the angular dependence of the mass loss will be

$$R \propto \cos^{(1+n/2)}\theta, \tag{4}$$

where θ is the impact angle relative to the normal. Using the above values for the ratio of the mass loss rate to that at the normal, one can calculate n to be in the range

$$0.60 < n < 1.55. \tag{5}$$

Interestingly enough, the value of the exponent in the energy dependence found earlier for normal (or controlled) impact was $n = 0.68$. Thus, the off-axis mass loss rates can be explained if the mass loss is determined by the impact energy normal to the surface.

This may be a reason by the mass loss rates were lower on the other STS flights than on STS-8. In addition to the fluence being lower because of the orientation of the Shuttle Orbiter, the actual mass loss rate may have been lowered by the non-normal oxygen atom incidence.

A word is in order here about the form of the energy dependence which has been derived in this paper. Arnold and Peplinski (ref. 4) fit a function of the form

$$R = A \exp(-E_a/E) \tag{6}$$

to the three low energy points in figure 2, apparently by analogy to reactions occurring thermally. Here E_a is an "activation energy" for the reaction. However, there is no theoretical justification for a dependence of this form. In thermal reactions, the exponential term in this "Arrhenius" relation is to account for the fraction of atoms or molecules with energies above the activation energy, assuming a Boltzmann distribution. In the atomic oxygen beam case, no thermal distribution exists. Most of the reacting atoms in the incoming beam are at or near the beam energy, and so no activation energy is relevent to their energy. There may be an activation energy related to the temperature of the surface, but this has little to do with the energy of the incoming atoms. Despite the familiar form of the above equation, there is no justification for it. The same is true of the energy dependence derived in this paper. Only the high energy data reported herein give evidence to support any specific energy dependence.

Thus, it appears that the mass loss rate for Kapton undergoing atomic oxygen bombardment may be of the form

$$R = A\,E^{n}, \tag{7}$$

where A is about 1.5 and n is about 0.68, E is the impact energy in eV normal to the surface and R is in amu/atom.

THE DEVELOPMENT OF SURFACE MORPHOLOGY UNDER ATOMIC OXYGEN BOMBARDMENT

An important feature of Kapton degradation under atomic oxygen bombardment is the development of surface morphology on micron length scale. As has already been shown (ref. 2 and 10), this surface morphology may be responsible for the change in optical properties of the material. As will be discussed here, the surface morphology may also affect the mass loss rate.

In figure 3 may be seen the surface structure of pristine Kapton under the scanning electron microscope (SEM). The surface is relatively smooth, even at a magnification of 10,000x. This SEM photo is of the edge of a Kapton sample flown on STS-8, and protected from the incoming ram flow by a metal aperture. In contrast, figure 4 shows the center of the Kapton disk, after more than 41 hours of ram oxygen exposure. Here it can be seen that the Kapton surface is covered by a grasslike or carpetlike texture. In figure 5 is shown an area which was partly covered (on the extreme right) by the metal aperture and partly exposed to the direct ram flow (on the left). Also of interest here is an area where there has been some other surface damage. Where the tweezers used to handle the sample have touched the surface, the fibers lie down. In ref. 2 it was hypothesized that the Kapton surface properties returned to normal wherever this smoothing had occurred.

Similar structures appear on the Kapton surface under oxygen ion bombardment in the laboratory. In figure 6 is shown a Kapton surface after the bombardment which produced the mass loss discussed in the preceding section of this paper. Although the structures produced are not identical to those seen in orbit, the similarity is striking. Furthermore, samples returned from orbit on STS-2 and STS-3 show structure which is not identical to that from STS-8. It is conjectured here that the differences seen in surface structure are due more to the directionality of the incoming beam than to differences between the flights and laboratory simulations. On STS flight 2 for instance (ref. 11), where the ram flow came in first from one direction and then from another, the tall, grasslike features are not so evident, but are replaced by a frothy texture.

The direction of the ram flow is important in determining the surface structure. Figure 7 shows the structure which developed in the laboratory simulation when the beam was tangential to the surface. This occurred at the edge of the sample holder, where the Kapton tape sample was wrapped around the sample holder. Here it can be seen that the structures themselves become tangential to the surface, taking on the directionality of the beam itself.

A clue to how the structures develop comes from figure 8. This SEM of a Kapton surface bombarded by oxygen ions (by Beatrice Santos of Langley Research Center at the same facility and energy used for the bombardment of the sample shown in figures 6 and 7 reported here) was under bombardment for only 1 hour, compared to the four hour exposure of figure 6. One can see here that the structure has not yet fully developed. The Kapton surface has been etched away by the directional ion beam, but over most of the surface the original surface level may be seen as a plateau. Clearly, the erosion rate is not constant over the surface, but is much higher in some places, where full fledged valleys have been carved out. The erosion must first occur at weak spots on the surface, or at surface peculiarities. Mass loss must be higher at these places, perhaps by trapping of the incoming beam by the structures already formed. Further erosion occurs preferentially at these sites and in the beam direction. If the beam were to randomly change direction after the formation of these sites, one can imagine that the spots of maximum erosion would become

bubbles carved out of the Kapton matrix. This would account for the frothy appearance seen in SEM photos of some of the STS-2 and STS-3 samples (Leger, ref. 1 and 9). Also, the increase in reaction rate with time* seen in some laboratory studies might be due to trapping of the incoming oxygen in the valleys of the structure after they have had time to fully develop.

If the changes in optical properties of Kapton are due to the surface structure which develops, one might expect that the optical properties would not change after the structure was fully developed. Figure 8 shows that this stage is not reached until well after the structures reach their full depth, for the depth develops before much of the surface has been significantly eroded. Therefore calculations which assume the surface is optically eroded when the depth of the structures becomes of the order of one quarter wavelength might be in error. It would be most interesting to see how the optical properties of Kapton change with time during oxygen atom bombardment.

Simulations of LEO oxygen atom bombardment are continuing at Lewis Research Center, with the aim of accurately determining impact energies during beam retardation and on determining the chemistry and physics of the material degradation.

*Leger L.J., private communication, 1984.

REFERENCES

1. Leger, L.J.: Oxygen Atom Reaction With Shuttle Materials at Orbital Altitudes. NASA TM-58246, 1982.

2. Ferguson, D.C.: Laboratory Degradation of Kapton in a Low Energy Oxygen Ion Beam. NASA TM-83530, 1983.

3. Hagstrum, H.D.: Low Energy De-Excitation and Neutralization Processes Near Surfaces. Inelastic Ion-Surface Collisions, N.H. Tolk, J.C. Tully, W. Heiland, ed., Academic Press, 1977, pp. 1-25.

4. Arnold, G.S.; and Peplinski, D.R.: Reaction of Atomic Oxygen with Polyimide Films. AIAA Journal, submitted for publication June 11, 1984.

5. Busch, K.W.; and Vickers, T.J.: Fundamental Properties Characterizing Low-Pressure Microwave-Induced Plasmas as Excitation Sources for Spectroanalytical Chemistry, Spectrochimica Acta, 28B, 1973, pp. 85-104.

6. Brake, M.L.; and Kerber, R.L.: A Comparison of a Theoretical Model of an O_2 Plasma to an Experimental Investigation. IEEE International Conference on Plasma Science, 1982.

7. Hansen, R.H.; Pascale, J.V.; de Benedictis, T.; and Rentzepis, P.M.: Effect of Atomic Oxygen on Polymers. J. Polymer Science, Part A, Vol. 3, 1965, pp. 2205-2214.

8. Allen, C.W.: Astrophysical Quantities, 3rd. ed., Athlone Press, 1973, p. 47.

9. Leger, L.J.: STS-8 Atomic Oxygen Experiment Results Summary. Atomic Oxygen Working Group Meeting, NASA Hdqtrs, Washington, D.C., Jan. 23-24, 1984.

10. Banks, B.A.; Mirtich, M.J.; Ruthledge, S.K.; and Swec, D.M.: Sputtered Coatings for Protection of Spacecraft Polymers. NASA TM-83706, 1984.

11. Leger, L.J.; Ehlers, H.K.F.; Jacobs, S.; and Miller, E.: Space Shuttle Preliminary Contamination Assessment from STS-1 and STS-2. Proc. of 12th Space Simulation Conference, NASA CP-2229, 1982, p. 297.

TABLE I. - PARAMETERS OF LABORATORY STUDIES

Date	Thickness, mils	Material	Ion	Flux, $cm^{-2}s^{-1}$	Fluence, cm^{-2}	Ion energy, eV
11/24/82	1	Kapton tape	O^+	$6\text{-}12\times10^{14}$	1.3×10^{18}	800
12/08/82	1/2, 1, 3, and 5	Al backed Kapton	O^+	$2\text{-}3\times10^{13}$	2.1×10^{17}	0-50
12/09/82	1/2, 1, 3, and 5	Al backed Kapton	O^+	$2\text{-}3\times10^{13}$	2.4×10^{17}	< 30 ?
12/22/82	1/2, 1, 3, and 5	Al backed Kapton	A^+	$3\text{-}4\times10^{13}$	5.2×10^{17}	1065

TABLE II. - DERIVED ION BEAM REACTION RATES

Date	Ion	O^+ fluence, cm^{-2}	Rate, g/O^+ ion	Method
11/24/82	O^+	1.3×10^{18}	$> 2.8\times10^{-22}$	Total loss of 1 mil
12/09/82	O^+	2.4×10^{17}	$> 5\times10^{-22}$	SEM photos

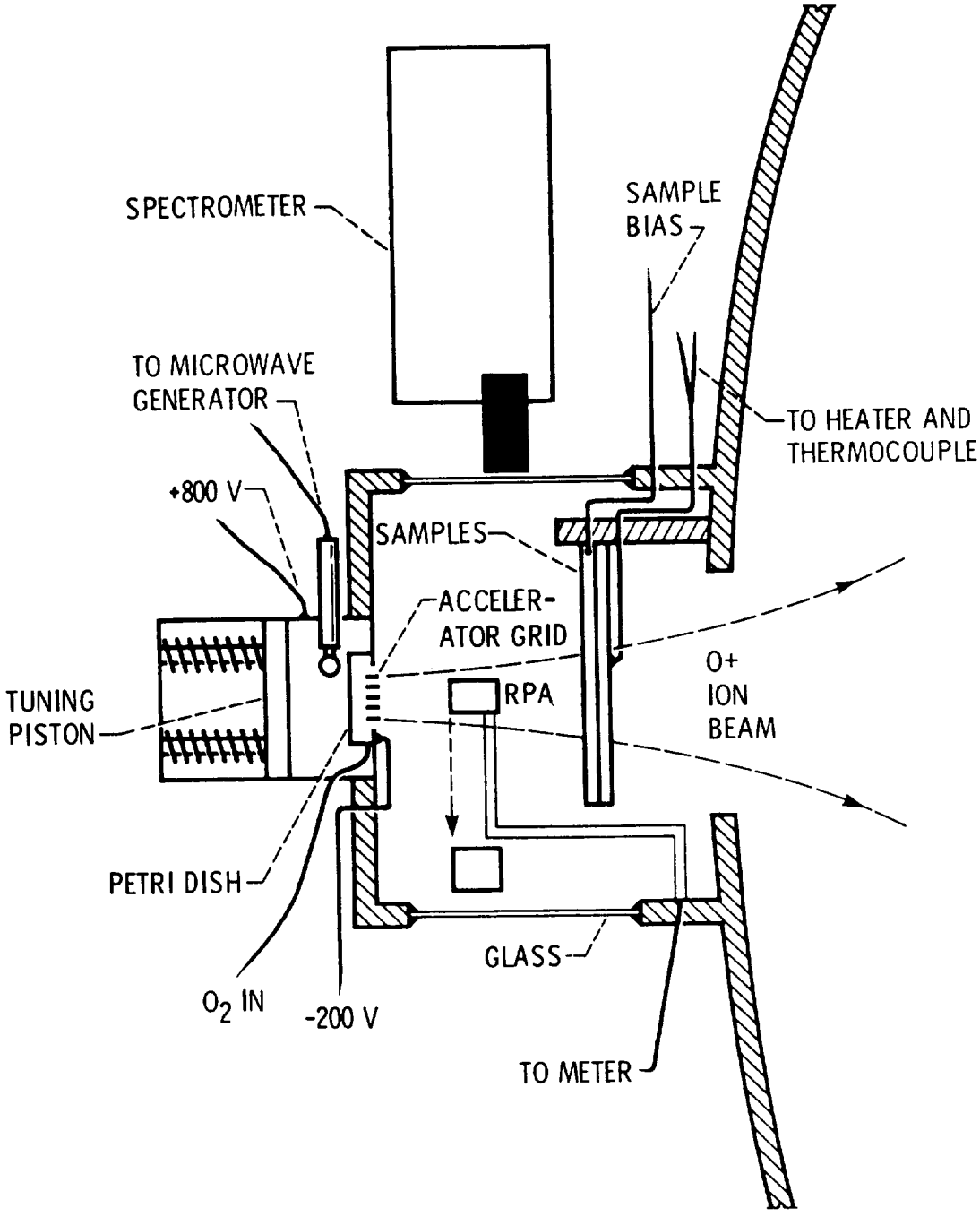

Figure 1 - The laboratory experimental setup.

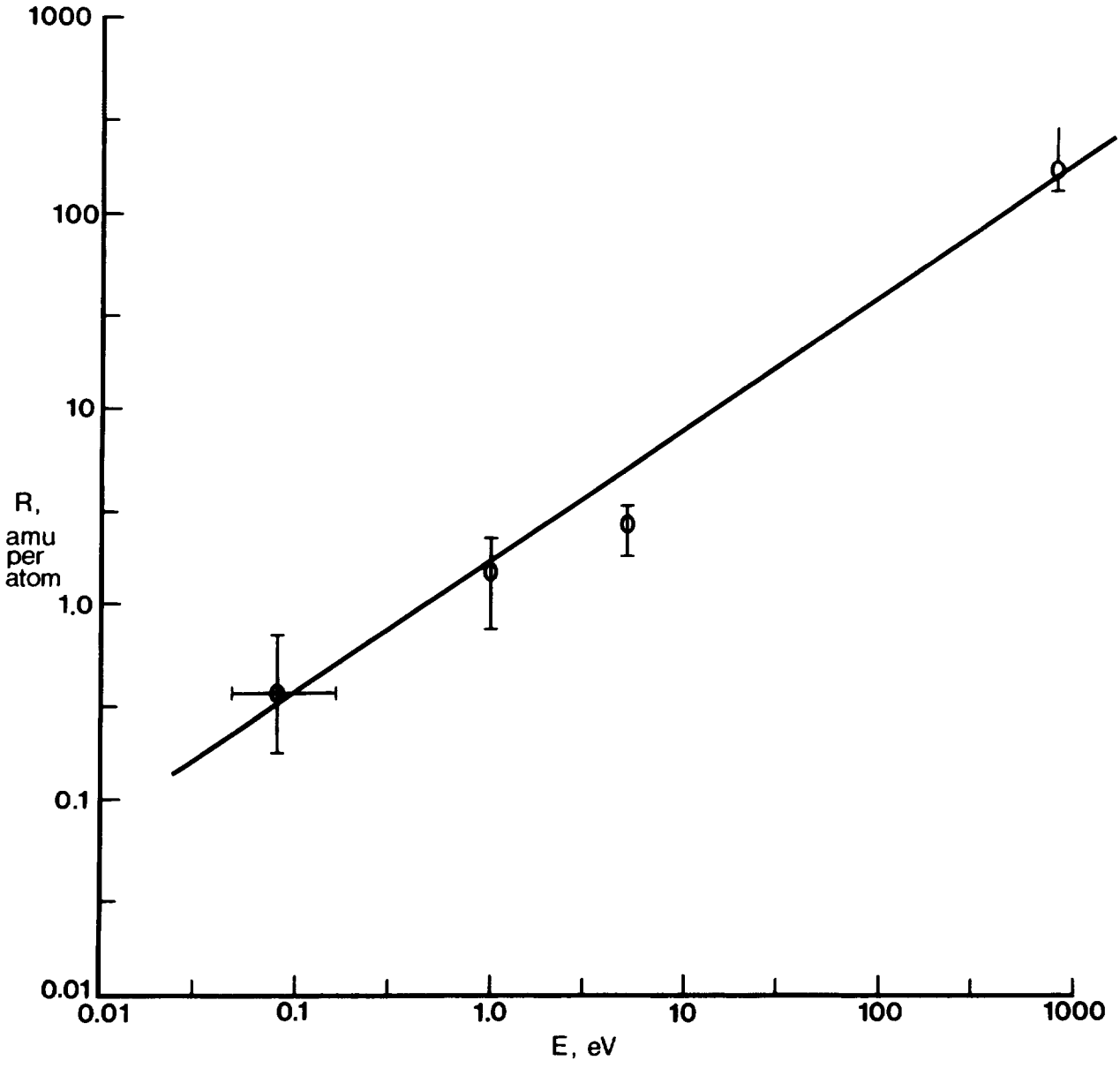

Figure 2 - A logarithmic plot of mass loss rate versus impact energy normal to the surface.

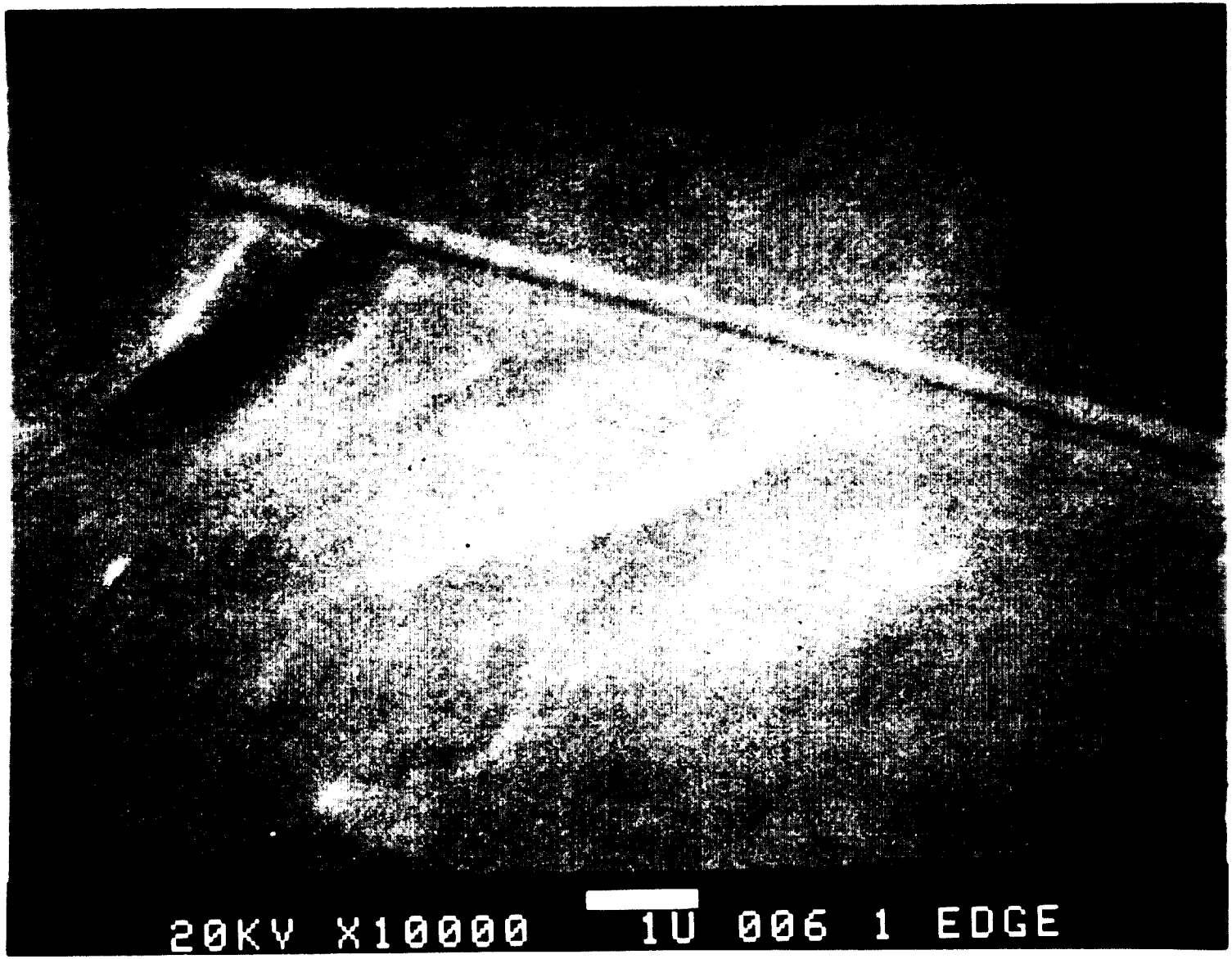

Figure 3 - Pristine Kapton at a magnification of 10,000x. Flown covered on STS-8.

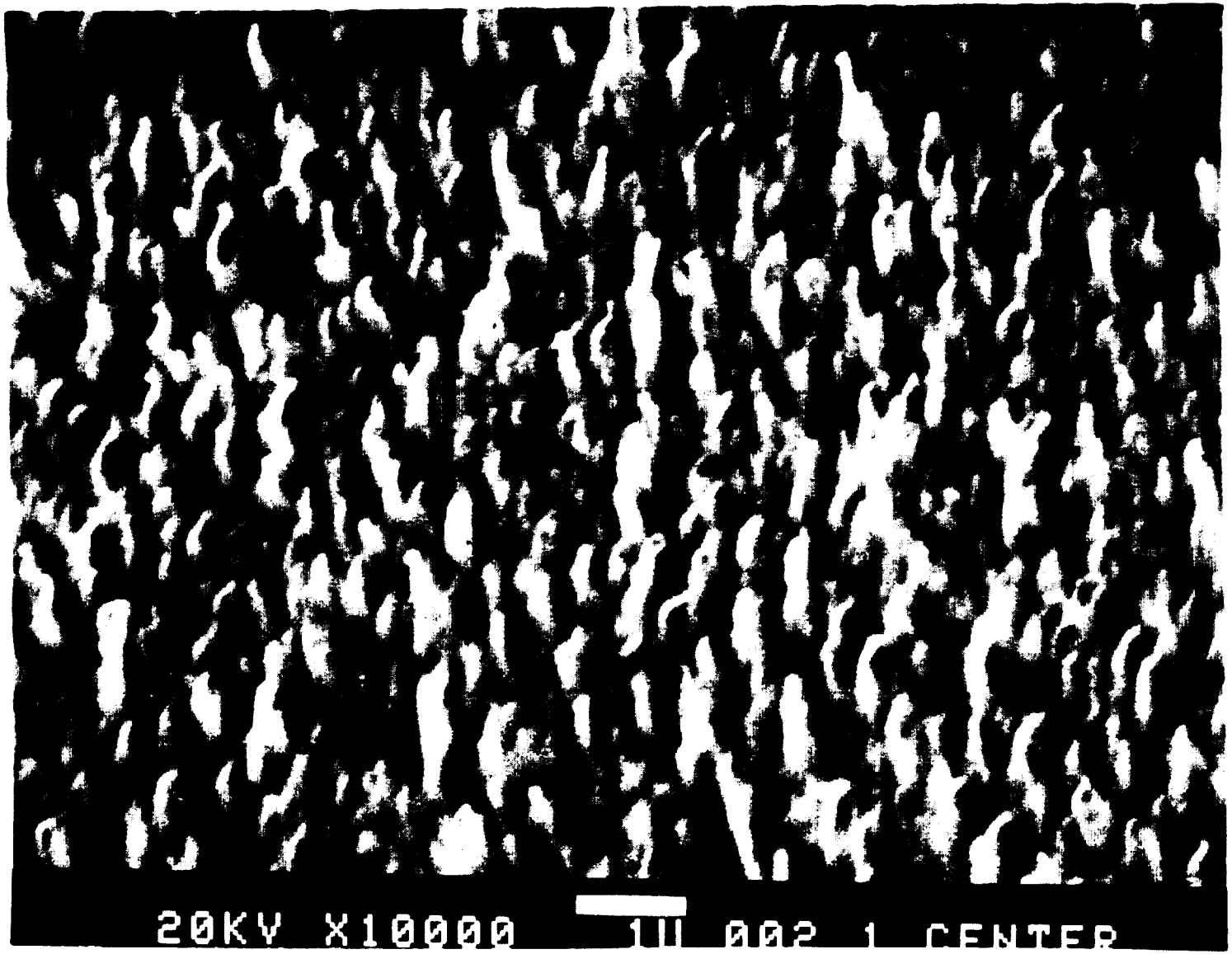

Figure 4 - Kapton subjected to 41 hours exposure to atomic oxygen at an altitude of 120 nautical miles on STS-8.

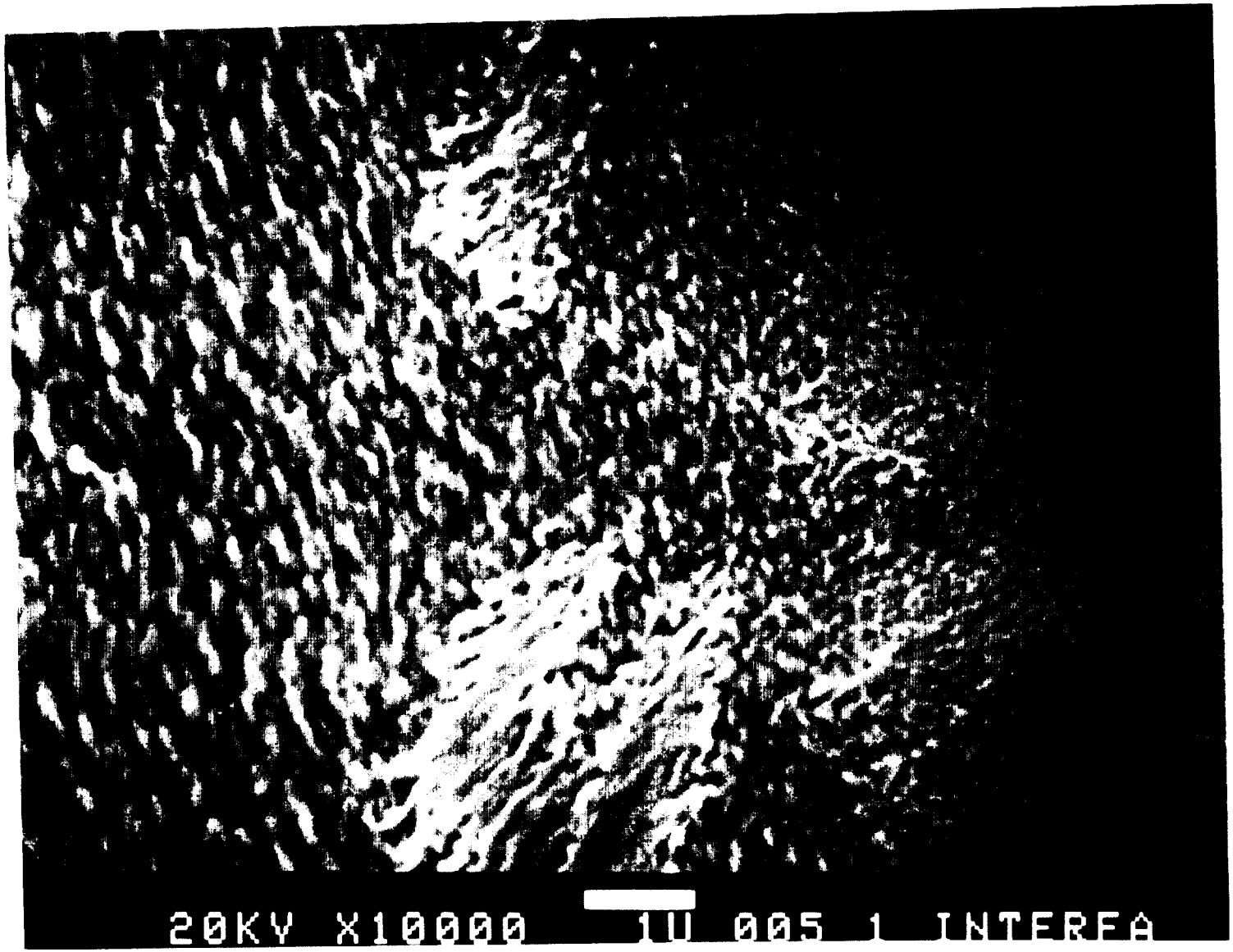

Figure 5 - The transition region between exposure and no exposure on the sample of figures 3 and 4. Other surface damage evident.

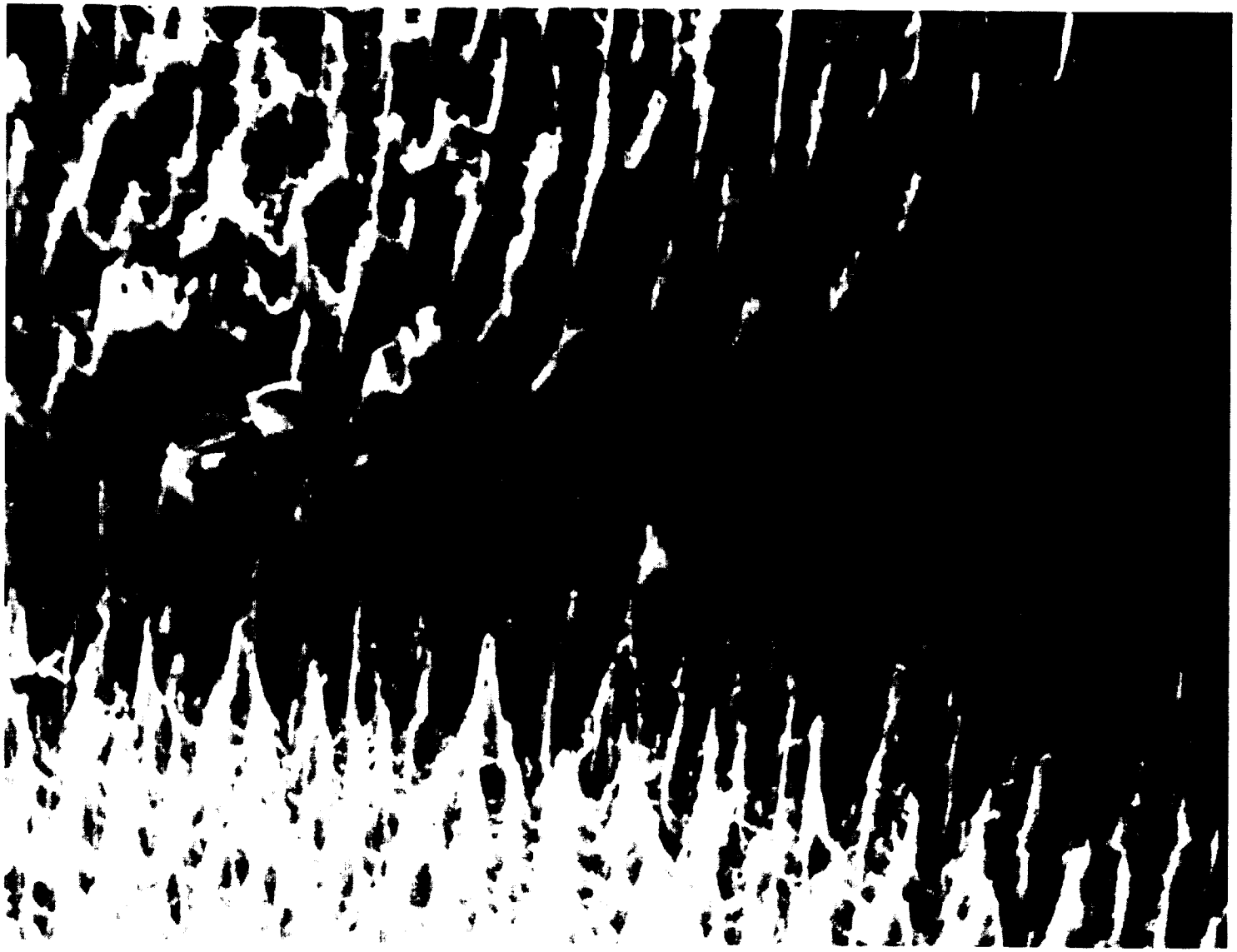

Figure 6 - Sample exposed to oxygen ion beam normal to the surface in laboratory simulation. Magnification same as for figures 3 through 5. Four hour oxygen beam exposure.

Figure 7 - Sample exposed tangentially to oxygen ion beam in laboratory simulation.

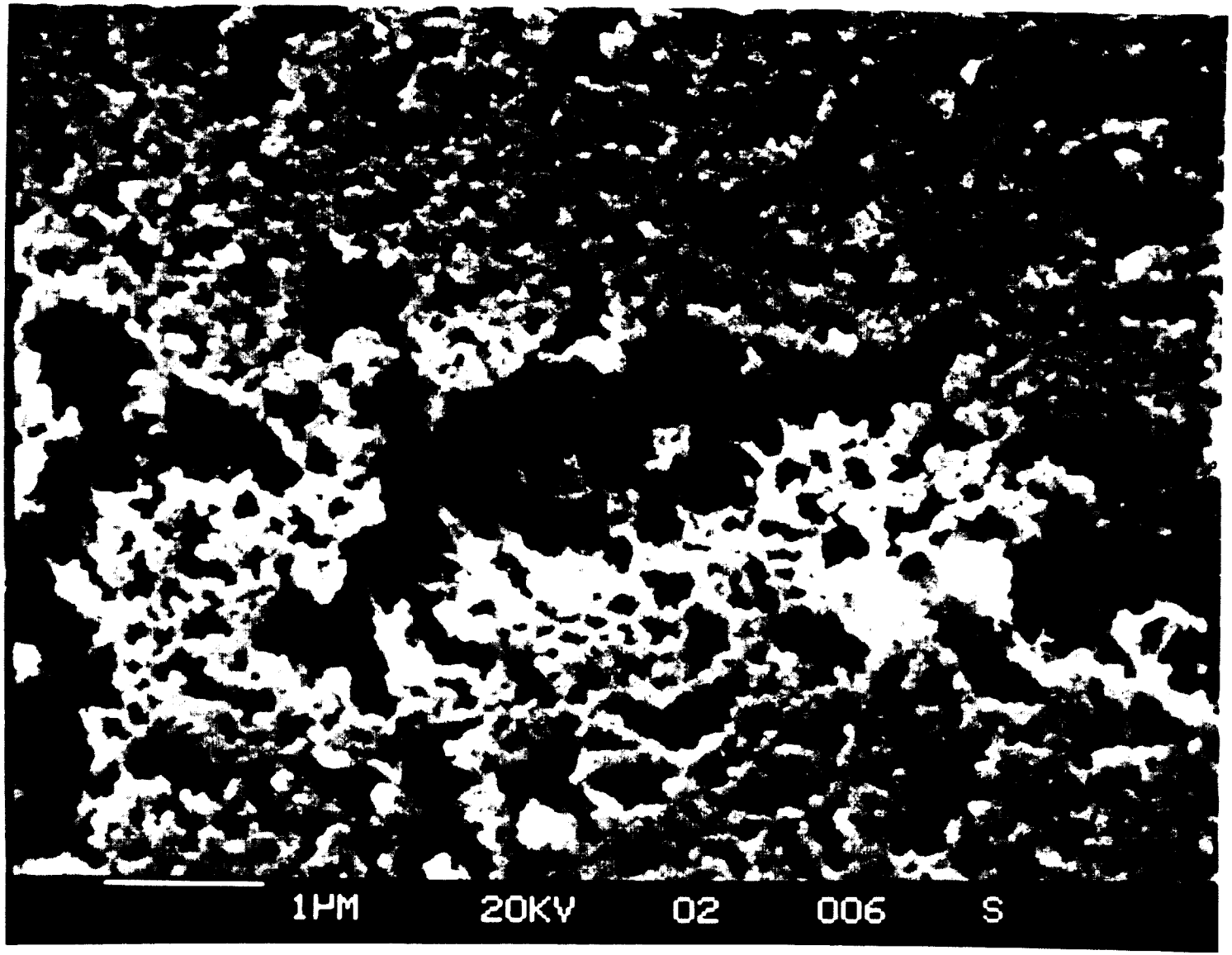

Figure 8 - Sample exposed to oxygen beam normal to the surface in laboratory simulation.
One hour oxygen exposure. Kindly furnished by Beatrice Santos of Langley Research Center.

ATOMIC BEAM SYSTEM FOR LABORATORY SIMULATION OF UPPER ATMOSPHERIC OXYGEN ATOM IMPACT ON STS SURFACES

P. Mahadevan
Aerophysics Laboratory
The Aerospace Corporation
El Segundo, California

ABSTRACT

An atomic beam apparatus capable of producing a collimated beam of O atoms or other atmospheric species at the STS impact velocity of 8 km/s is described.

INTRODUCTION

Exposure of polymer films and optical coatings, to the 8 km/s oxygen atom flux at STS altitudes is known to cause material degradation. (ref. 1,2) Each STS payload brings new materials and requirements which may impose new degradation problems for future STS missions. Pre-flight O-atom exposure testing of these materials will be necessary. A requirement for prior STS flight checkout will be both expensive and difficult to schedule. In addition, only gross effects are measured by this process and then only for limited exposure times and geometric orientation.

For future spacecraft and sensor applications a more detailed analysis of these effects would be desirable. As the number of these materials and the number of impingement variables increase, performing meaningful experiments on orbit becomes more demanding on the STS missions.

A cost effective solution to this problem would be to develop a test simulator capable of reproducing the observed effects in the laboratory. This simulation system must possess sufficient measurement sensitivity and experimental flexibility to impose the desired environmental conditions upon the samples and evaluate the degree of degradation as quickly as possible. One approach to developing this capability would be to use a beam with the desired O-atom flux at STS velocities so that integrated O-atom impacts can be achieved in real time. With this objective, a simulation facility, using atomic beam techniques, is under development at the Aerophysics Laboratory.

TECHNICAL APPROACH

We have adopted the conventional ion beam charge transfer neutralization approach to produce a projectile beam of fast oxygen atoms for atmospheric simulation. This approach was decided on after an extensive comparative evaluation of other alternatives. The prime considerations favoring this approach are:

- The ability to vary the velocity of the impacting species at will over a wide range on either side of the optimum required value of 8 km/s.

- Sample irradiation can be made with species other than O-atoms, such as O_2, N, or N_2.

APPARATUS

The apparatus configuration is basically the same as that of a system used earlier for low energy charge transfer cross section measurements. (ref. 3) In these experiments, ion beams of the noble gases were produced in an electron bombardment ion source, (ref. 4) mass selected with a magnetic sector mass spectrometer at a kinetic energy of a few hundred eV, decelerated to the desired energy (1 to 100 eV) and charge neutralized by a gas in a collision cell interposed in the ion flight path. Preliminary tests were conducted with this apparatus with Ar, O_2 and CO_2 successively as source gases. The flux density of atoms impacting on a faraday cup target at the desired velocity range was only of order 10^9 atoms/cm^2-s. The ion source was hence substituted by a commerciably manufactured system designed for high current, low voltage operation. The ion extraction electrodes for the new source are a pair of parallel multi-apertured pyrolytic graphite grids. The output current density from the source is about 20 mA/cm^2 at 1 Kev ion energy. Neutralizing electrons from a hot wire electron emitter are drawn into the ion beam to provide a near-uniform ion beam potential.

The experimental set up is shown schematically in Figure 1. A mass selected beam of positive ions undergo charge transfer collisions in the gas cell resulting in the production of the neutral atoms at the same kientic energy as that of the ions. The charge exchange collisions are represented as

$$O^+_{(fast)} + Y_{(slow)} \rightarrow O_{(fast)} + Y^+_{(slow)}$$

where Y and Y^+ represent the neutralizing gas atoms and product ions. The $O_{(fast)}$ atoms impinge on a test surface interposed in the beam path while all charged particles are deflected off electrostatically.

The flux of atoms is estimated from the percentage attenuation, by neutralization, of the ion beam. The latter is monitored on a faraday collector interposed in front of the test surface. Appreciable loss of fast atoms from the beam by scattering is unlikely at the range of operating pressures for these experiments. (ref. 5)

EXPERIMENTAL APPROACH FOR SIMULATION

For the STS materials evaluation program we require an atomic beam facility capable of delivering a mass-selected pure atomic oxygen beam of up to 10^{13} oxygen atoms/cm^2-s. In order to compensate for the relatively low flux (compared to low earth orbits) we propose using a highly sensitive quartz microbalance (QMB) to measure extremely small sample weight changes (sensiti-

vity 10^{-9} grams). Since reaction probability depends sensitively on collision velocity but should be independent of flux density, the only disadvantage of having a flux density lower than that of the real system of interest is that longer times will be required to effect the same degradation. The advantage of the QMB is that extremely small effects are detectable and the rate of these changes can be continuously monitored. For example at a flux rate of 10^{13} O-atoms/cm^2-s, assuming a reaction probability of 0.2 a weight change of 1×10^{-9} grams will occur in approximately 3 minutes. This weight loss estimate may be conservative since we are assuming that the reacting O-atom removes two hydrogen atoms to form a water molecule. In actual tests, a weight change of 10^{-9} grams could occur in a few seconds.

THE EXPERIMENTAL TEST OBJECTIVES ARE

1. To establish a relationship between mass change on a bombarded surface and the integrated projectile flux on it.

2. To explore the dependence of mass change on the kinetic energy of the incident species.

3. To look for effects other than mass change such as etching, pitting, and optical changes on the irradiated surfaces.

PROGRESS TO DATE

Beam control devices such as einzel lenses and quadrupole lenses used previously (ref. 3) for a much lower ion current density showed space charge limitation characteristics when used with the present configuration. Appropriate modifications such as substitution of thin aperture lenses for cylinders have been made. The aspect ratio of the magnetic sector of a 45° mass spectrometer used for mass selection of primary ions from the ion source has been increased to minimize wall losses.

The diagnostic tests with the apparatus are conducted with argon as the test gas to avoid the need for frequent replacement of the heater elements in the source and pressure gauges in the vacuum system. The primary mass spectrometer for mass selection of ions from the ion source was moved out of the beam path in the first phase of the program to estimate the flux density of argon atoms. When the source is run with argon, the ion current is predominantly A^+. The test results obtained so far indicate that a flux density of about 5×10^{13} Ar atoms/cm^2-s in the desired velocity range from 3 km/s and up is attainable. The lower velocity limit is equivalent to a kinetic energy of about 2 eV for the A atoms.

Performance evaluation tests are now in progress with the primary mass spectrometer interposed between the ion source and beam neutralization chamber. As a first test, we propose to study the loss of material from a carbon coated QMB crystal exposed to a known fluence of O-atoms. Results from this experiment would provide a direct comparison with flight data where similar monitoring instruments were used (ref. 6).

In summary, the velocity range for atoms (8 km/s) desired for this program is definitely achievable. It is reasonable to expect the desired flux range of 10^{13} to 10^{14} O-atoms/cm^2-s will be reached with appropriate optimization techniques.

*This work was conducted under U.S. Air Force Space Division (AFSD) Contract F04701-84-C-0085.

REFERENCES

1. A. Whitaker, LEO effects on spacecraft materials, AIAA paper #83-2632-CP 1983.

2. Peters, P. N., Linton, R. C., and Miller, E. R., "Results of Apparent Atomic Oxygen Reactions on Ag, C, and Os Exposed During the Shuttle STS-4 Orbits," Geophysical Research Letters, Vol. 10, July, 1983, pp. 569-571.

3. Low energy (1-100 eV) charge transfer cross section measurements for noble gas ion collisions with gases. P. Mahadevan and G. D. Magnuson, Phys. Rev. 717, pp. 103-109, 1968.

4. High efficiency source for metal ions, G. D. Magnuson, C. E. Carlston, P. Mahadevan and A. R. Comeaux, Rev. of Sc. Instr. 36, 136-142, 1965.

5. Effect of scattering on charge transfer efficiency measurement. P. Mahadevan and R. Marriott, J. Appl. Phys. 36, pp. 863-864, 1965.

6. Roy McIntosh, Goddard space flight center atomic oxygen monitor, private communication, June 1984.

Fig. 1 Schematic representation of atomic beam apparatus.

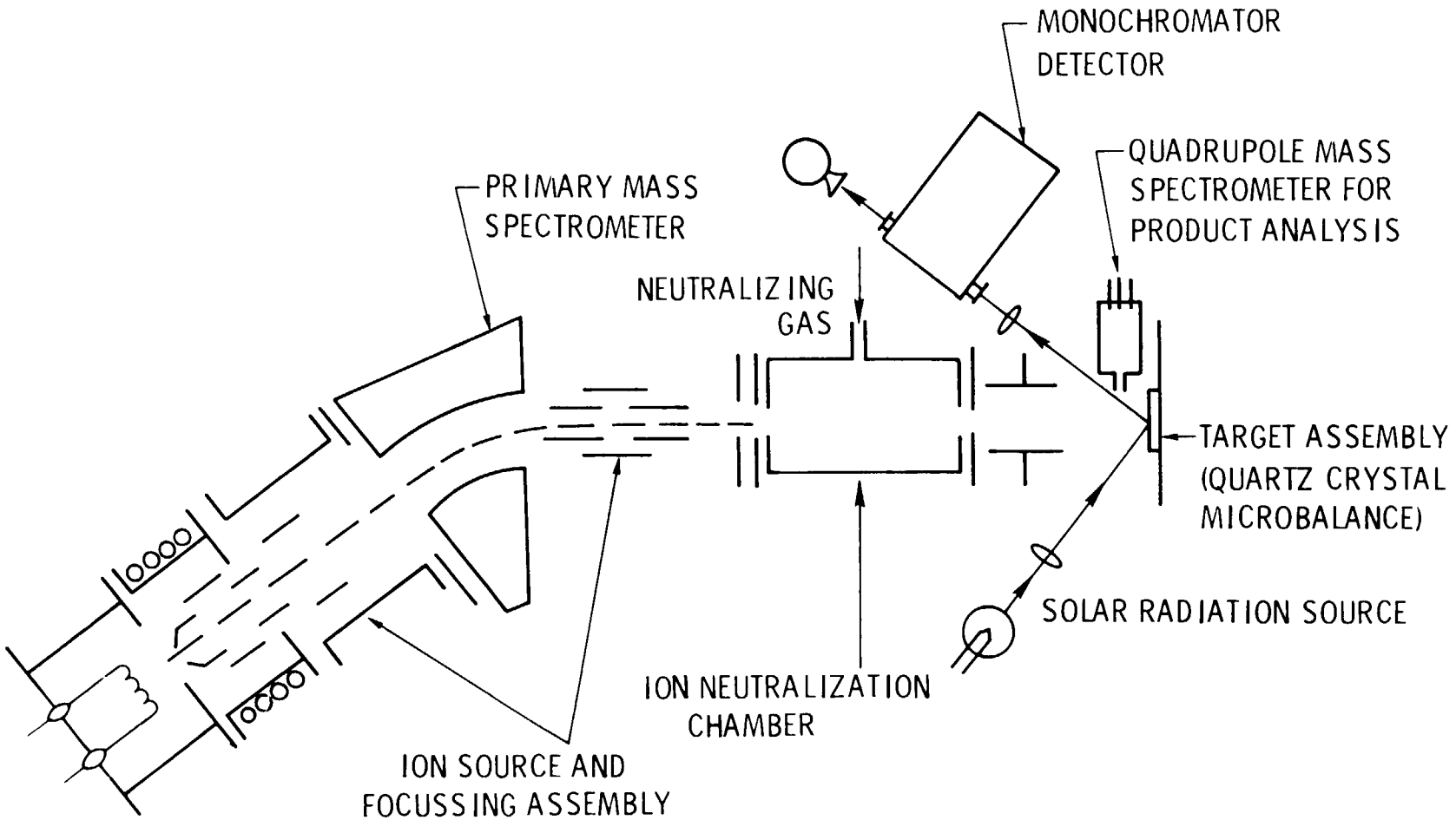

Figure 1 - Schematic representation of atomic beam apparatus.

LEAK DETECTOR FOR SPACECRAFT TESTING WITH HIGH ACCURACY

G. Sänger and A.K. Franz

European Space Agency / ESTEC
Noordwijk/NL

ABSTRACT

It proved to be very convenient to measure the leak rate of Spacecraft when the Spacecraft is kept in its container and the increment of tracer gas - mostly noble gases - in the container air is measured as function of time.
In order to meet the specification of the new voluminous Spacecraft, a leak detector with high accuracy is required. This is made difficult, because of the natural abundance of noble gases in air, which mean a considerable background exists. A leak detector is described which allows to measure an increment of the concentration of a few % using reference gas.

INTRODUCTION:

The so called "Tent-method" is still preferred for leak detection of spacecrafts and specially for the cold gas system for attitude control when the integral leak rate must be determined:

> The test object is kept in its container - the tent - and the increase of the concentration of the tracer gas in the container is measured as function of time. For this a sample of the container air is sucked into the leak detector and analysed for its content of tracer gas (fig. 1).

For the first test the well known He-leak detector was used on the T.D. Satellite (Ref. 1). The detecting head of this leak detector is adapted for the atomic mass unit (a.m.u.) 4, that of He. For later projects such as ISEE-B it seemed desirable to replace this He-leak detector by one with mass spectrometer allowing the use of other tracer gases; for the ISEE-B the propulsion gas itself could be used. Furthermore it is possible to test different subsystems simultaneously when different tracer gases are used.

Though the mass spectrometer is a very sensitive and flexible equipment the shortcoming is the dynamic range; that is the ratio of

$$\frac{\text{minimum detectable partial pressure}}{\text{total pressure}}$$

which is of the order 10^{-5} - 10^{-6}, and this means a concentration of the order of some ppm (parts per million) may just be measured, or, in a container of $\sim 5m^3$ volume a few cm^3 of tracer gas. This was just sufficient

to detect whether the specified values were met or not, there was no factor of safety.

By installing a Titamium Sublimation Pump (T.S.P.), however, the total pressure may be reduced whilst the partial pressure of the tracer gas remains unchanged since a T.S.P. has no - or at least a very little - pumping effect for these gases. In this way the effective sensitivity could be increased by two orders of magnitude. On the ISEE B spacecraft tests was demonstrated that leak rates of 0.02 cm^3/h NTP of freon 14 (CF_4) could be measured.

With this standard leak detector of the Testing Division at ESTEC, four Spacecraft projects have been tested and four others are planned in the future. However, Spacecrafts became in the mean time not only more expensive but also more sophisticated and bigger with narrower tolerance requirements. Since for obvious reasons often noble gases are used for tracer gases this means that the content of noble gases in a big container is also higher because all noble gases are present in natural air. The consequences can be illustrated in the example of EXOSAT:

> The EXOSAT container had a volume of $\sim 30 m^3$; the natural abundance of He in air is 4.66 ppm; hence the content of He in the container is approximately 140 cm^3 NTP. Considering the specified leak rate of 5 cm^3/h this means that within one hour the He-concentration will increase only by 3.6% above the background. Of course one could wait instead of 1 hour about 10 hours, giving a higher concentration. On the other hand one has to consider that the actual leak rates are often about one order of magnitude smaller than specified. The mass spectrometer is a highly flexible instrument offering a wide measuring range, its absolute accuracy, however, is not very high, only a few %, which means we are at the limit for the above mentioned leak rates. In order to overcome this problem one has either:
>
> . to flush the container with, say, pure GN_2 till nearly all air is blown out, or
>
> . to use no noble gas as tracer gas but only inert gases e.g. freons.

Flushing the container with pure GN_2 is time consuming; in case the content of air shall be reduced to $\sim 10\%$, an amount of GN_2 is required which is ~ 10 times the volume of the container; and to blow this huge amount of gas through the container several hours are needed; one has to keep in mind that no high overpressure and gas streaming is tolerated.

The use of inert gases like freons is from the leak detectional point of view very convenient because the background in air would be zero; it is, however, not always possible, and e.g. for a hydrazine system only He is tolerated as tracer gas: the use of other gases than noble gases might poison the catalyser and a heavier noble gas might cause bubble forming in the expansion area in case the system is not carefully cleaned.

Thus there is a demand for a leak detector in the near future which allows the measurement of an increment of only a few % of the concentration above the natural abundance of noble gases in air.

BOUNDARY CONDITIONS AND PROBLEM AREAS

When a sample of the container is sucked into the leak detector for analysis, the partial pressure of the tracer gas indicated by the mass spectrometer depends on the adjusted in-leak rate and the pumping speed, accordingly:

$$\dot{Q} = \overline{P}_{tracer} \cdot S$$

$\dot{Q}$ → in leak rate
S → pumping speed
$\overline{P}_{tracer}$ → partial pressure of tracer gas

When using a turbomolecular pump the pumping speed remains constant and is furthermore nearly independent of the molecular velocity - or weight of the gases. The in-leak rate of the leak valve should be kept constant within ± 0.1% (or at least be known so that a correction is possible) in order to achieve the envisaged accuracy of ~1%. The commercially available leak valves did not show the required stability or reproducibility; better experience made with capillaries, although variations, of ± 5% were observed over long periods.

The best solution found so far is a combination of both:

. a capillary leak for coarse adjustment and in parallel

. a variable leak valve for fine adjustment and/or correction.

The sensitivity and reproducibility of the mass spectrometer itself is difficult to assess with the accuracy required above. This is because it has always to be operated in a vacuum system and it cannot easily be distinguished whether the gas composition changed due to absorbing or degassing effects of the chamber or that the sensitivity of the mass spectrometer changed. Besides amplification variations in the mass spectrometer supply unit the emission current may vary because of contamination of the filament.

In general, however, all this may be considered to vary the sensitivity over longer periods (several hours). For short periods, in the range of seconds, the mass spectrometer may be assumed reproducible and furthermore that its indicated signal is proportional to the partial pressure. (The same things may be said of the ionisation gage).

The above considerations should be sufficient to allow the design of a leak detector which measures small increases in concentration even in the ppm range.

The data for the implementation are then as follows:

container volume	30 m^3
content of He in container (4.66 ppm in natural air)	140 cm^3
increment due to leak rate of Spacecraft in container (leak rate assumed 1cm^3/h	1 cm^3/h 0.7%
adjusted in-leak-rate into leak detector	2.10^{-3} mbar l/sec
pumping speed of turbomolecular pump	200 l/sec
p.total pressure in leak detector (without T.S.P.)	$1 \cdot 10^{-5}$ mbar
partial pressure of He ($\overline{P}_{He}$)	$4{,}7 \cdot 10^{-11}$ mbar
increment of partial pressure of He ($\overline{\Delta P}_{He}$) within one hour	$3.3 \cdot 10^{-13}$ mbar
In addition a T.S.P. of 2000 ℓ/sec pumping speed may be installed the total pressure would then be reduced to	$2 \cdot 10^{-7}$ mbar

GENERAL APPROACH

In order to control the obviously unavoidable instabilities and long term variations of the mass spectrometer, the following procedure is foreseen (Fig. 2):

At the beginning of the test a certain amount of container gas shall be stored which is then used as reference for the leak rate measurements later. When this reference gas and gas from the container (called test gas) are alternately led into the leak detector, the sensitivity variations can be assessed; or when the measurements are performed with a chopper and lock-in-amplifier the reference gas acts as zero indicator and so the increment of the concentration of the test gas is measured directly.

This required of course that the vacuum system is pumped down fast enough so that no interference of reference gas and test gas occurs. If one considers the following:

$$t = \frac{2.3.V}{S} \log \frac{P_1}{P_2}$$

where:

t = pump down time (sec)
v = volume (liters)
S = pumping speed (liters/sec)
$\frac{P_1}{P_2}$ = ratio of pressures at the beginning and at the end

this should be easily possible.

IMPLEMENTATION OF THE LEAK DETECTOR

To meet the above mentioned requirements, two mechanically different solutions are considered:

1. Leak detector with chopper and lock-in-amplifier

The first model was based on a chopper with a lock-in-amplifier. (Ref. 2 ; Fig.3). It was possible to measure an increment of the tracer gas of 0.5% for relatively high concentrations. It was, however, obvious that the accuracy decreased when the concentration of the tracer gas decreases (fig. 4). Though several deficiencies of the model were indentified and could have been improved, preference was given for a model where the chopper was replaced by valves. This was because the chopper mechanism is expensive and offers little flexibility. Its only advantage being to allow the use of higher frequency , is of minor importance for this application.

2. Leak detector with controlled valves for reference gas and test gas.

Considerably greater flexibility may be expected when the reference gas and test gas are led into the vacuum system by valves which may be easily controlled, say by a frequency or timing generator. Furthermore, it is easily possible to make use of a computer to control the equipment and evaluate the measurements. The lay out is shown in fig.2, 5. The valves were normally operated in the following sequence:

time	reference gas valve	test gas valve
1. sec.	open	closed
2. sec.	closed	closed
2. sec.	closed	open
4. sec.	closed	closed

In order to have a relatively flat pressure profile instead of a sharp pressure peak during the opening periode of the valves, buffer volumes were installed (see fig. 5).

Because low partial pressures were to be measured, a T.S.P. was installed. The noise level of the mass spectrometer signal was, however, still high so that integration circuits for both reference gas and test gas had to be added. A time constant of ~1 min was chosen so that integration of several cycles took place. The consequence was of course a long response time (~5 min). This is not significant because several hours have to be envisaged for the leak detection when a measurable increase of the tracer gas concentration in the spacecraft container shall be obtained.

RESULTS.

This leak detector must measure a small increment of the concentration of noble gases above their natural abundance in air. Some characteristics of the noble gases are:

Helium (4.66 ppm) : He is the standard tracer gas for leak detection; it is relatively cheap and there are no other gases on the a.m.u. 4, that of He (D_2 may be disregarded). Its disadvantages are that it diffuses easily through plastics and its ionisation probability is low.

Neon (16 ppm) : Neon has two isotopes 20 (90%) and 22 (10%). The isotope 20 cannot be used because double ionised Argon has the same m/e ratio , and the argon content in air is nearly 1% (approximately 600 times more than Ne)

Krypton (1.08 ppm) : Kr exists in several isotopes, the most important ones are

Kr_{86}	17.4%	(0.19 ppm)
Kr_{84}	60%	(0.61 ppm)
Kr_{83}	11.6%	(0.125 ppm)
Kr_{82}	11.6%	(0.125 ppm)
Kr_{80}	2.3%	(25 ppb)

The abundance is low. The disadvantages are that it is rather expensive and that the a.m.u. of Kr are within those of a hydrocarbon group often found in the residual gas.

Xenon : Xenon was not investigated, but the same results should be expected as for Krypton

Air was used as reference gas. For preparing the test gas with the desired higher concentration of He and Ne, a 200 l vessel was pumped down. Into this volume the required amount of cm^3 of a rarified gas

mixture of He or Ne and air (ratio 1:1000) was introduced, the vessel was then vented to atmospheric pressure by air.

For Kr a similar procedure was followed but employing rubber bludders.

The accuracy of the increased concentration of the prepared tracer gas is expected to be ± 0.1%.

The results for He and Ne are shown in figs. 6, 7, 8, 9. The lower peaks are from the reference gas, the higher ones from the test gas. The proportionality is always obvious. For He a concentration increment above the natural abundance of 0.9% could be measured with an experimental scatter of the value of ±15%. The difference of the partial pressure of 0.9% is equivalent to a pressure of $3.8 \cdot 10^{-13}$ mbar in the vacuum system. For Ne the achieved accuracy was lower. At an increment of 2.7% the experimental scatter was already ± 15%; the value at 3.8% is ~ 0.4% too high because the reference gas in leak was lower (fig. 8).

For both, He and Ne the ratio of the peak heights of testgas and reference gas agrees with the increment of the concentration which proves that the effect of background in the vacuum system can be neglected at this a.m.u.

In fig. 10 and 11 the results are shown for the Kr isotopes. The best agreement is obtained with Kr 86 where the background is lowest (fig. 10, 11), even though the abundance of Kr 84 is higher. The ratio of test- and ref gas peak was for the 16% increment not 1.16 but only 1.12. This discrepancy is due to the hydrocarbon background at this a.m.u. (fig. 12). For the same reason Kr 82 shows a bad agreement. For Kr 80 the experimental scatter is higher than the signal for the 3% value. On the other hand one should keep in mind that the difference of the partial pressure is already in the middle 10^{-15} mbar range, which approaches the sensitivity limit of the mass spectrometer. For Kr 80, 82, 84 only the final results are given (Fig 11)

In order to check the detectibility of hydrocarbons a test was performed with propane, a gas which may also be used as propulsion gas for attitude control. Unfortunately most pronounced peaks of the crack product pattern are in the same range where not negligible peaks are found in the residual gas of the system. The best a.m.u. was found to be 37 giving a peak height of propane of only 3% of the maximum peak on a.m.u. 44. The result is given in fig. 13, 14. For the lowest value we approach the 10^{-14} mbar range. A concentration of 0.5 ppm is however detectable.

DISCUSSION AND OUTLOOK

The measurement of a small increase of the concentration of the tracer gas required more effort than the measurement of a very low concentration. The latter could be solved simply with the aid of the T.S.P. Concentrations of 10 ÷ 50 ppb, depending on the gas, could be measured - and in a GN_2 atmosphere even far below the ppb level. (Ref. 3.)

The described leak detector should however allow to measure a concentration increase of 50ppb for He and this is sufficient to detect leak rates below 1 cm^3/h. When sampling times of ~15 h, say overnight,are employed, leak rates down to 0.2 cm^3/h are detectable in Spacecraft containers with a volume of ~30m^3. The content of hydrocarbons in the residual gas was relatively high.

This is due to prior measurements and careful bake would very likely achieve better results. This would also result in higher sensitivity for hydrocarbons.

The price for the high sensitivity is the long response time, which, however, is considered acceptable for the conditions given for leak detection.

REFERENCES:

1. P. Erichsen, private communication 1972.

2. G. Sänger, A.K. Franz
   Über die Lecksuche bei Raumfahrtzeuger, Vakuumtechnik März 1984.

3. First Flight Testing Cenference Las Vegas Nov. 1981; Paper 81-2463

4. P.C.M.N. Bruijs: Detectie en meting van lekken met Krypton 85. 14 (1976) 1-9 Nederlands Tijdschrift voor vacuumtechniek.

5. R.W. Odom, D.L. Smith and J.H. Futrell
   A study of electron attachment to SF_6 and auto-detechment and stabilization on SF_6. J. Phys. Atom Molec. phys. Vol 8 No.88 1975

6. C.A. Hofmann Quadrupole mass spectrometer of various performance groups Vacuum Vol. 24 number 2.

7. W.Becker Erhöhung der Empfindlichkeit des Heliumleckzuchers durch Verwendung einer Turbo Molekular-Pumpe. Vakuumtechnik Heft 8/1968 203 - 205

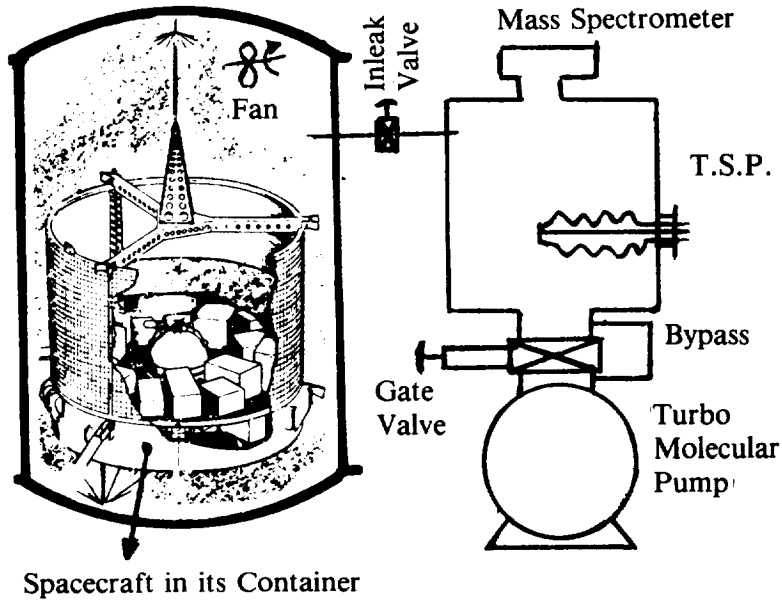

Fig. 1: Principle of the leak detection according to the tent method using a selective

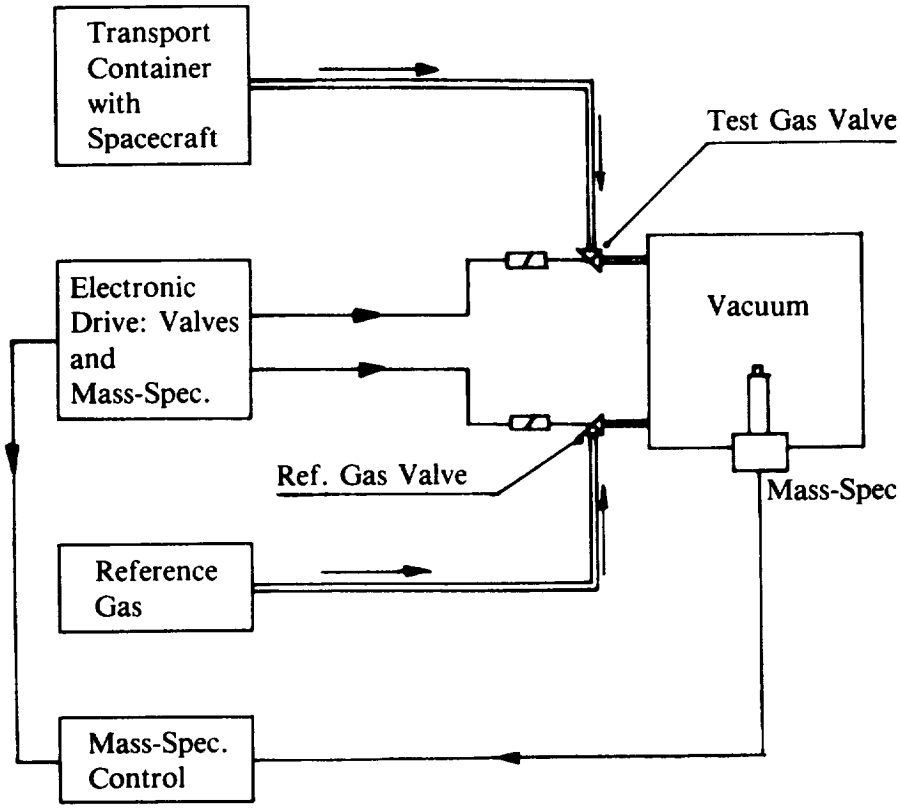

Fig. 2: Schematic diagram for the leak detection using ref.gas

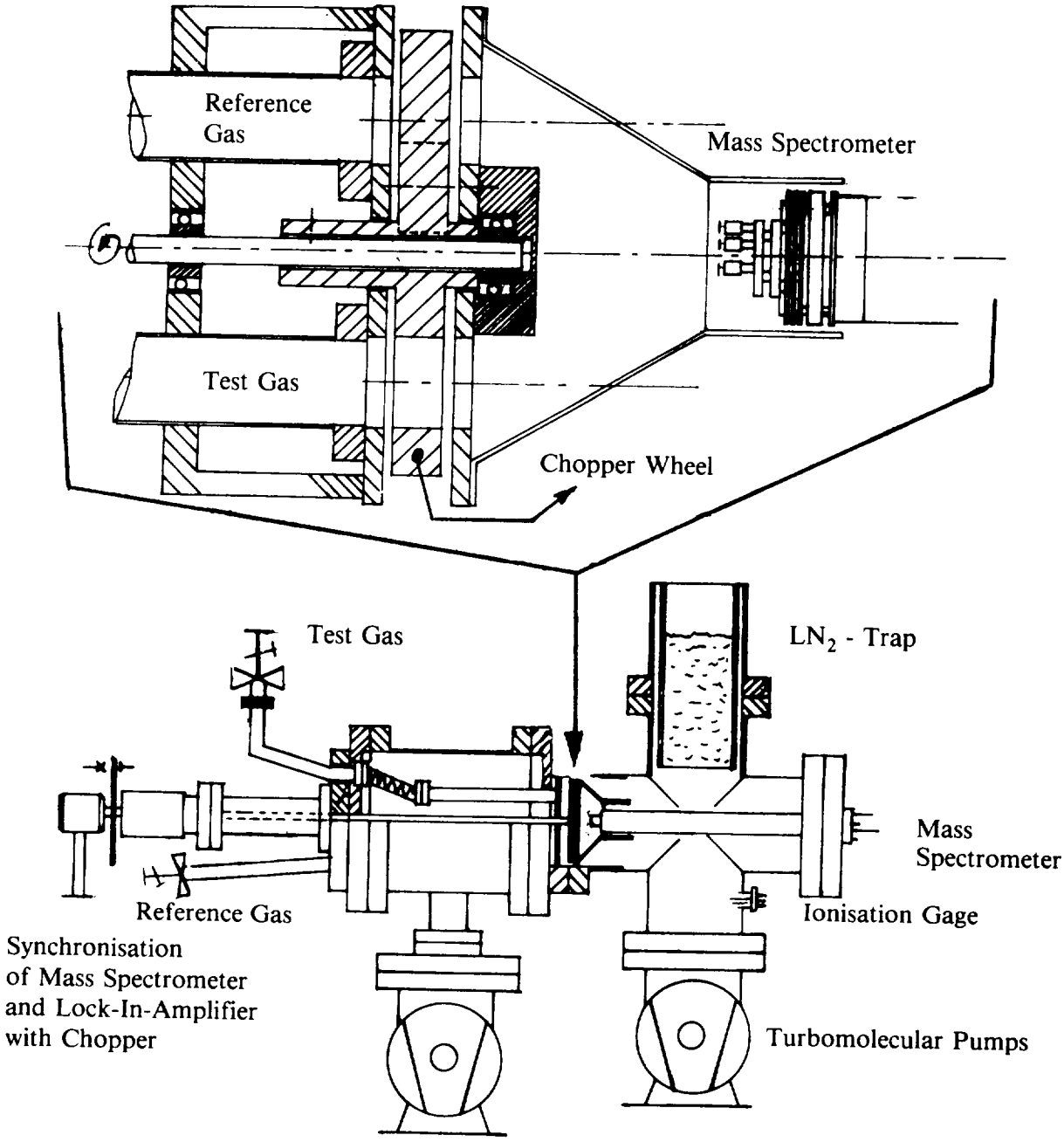

Fig. 3 : First design of leak detector based on chopper and lock - in - amplifier arrangement. The turbomolecular pump on the gasinle part was installed to remove the escaping gas on the chopper wheel.

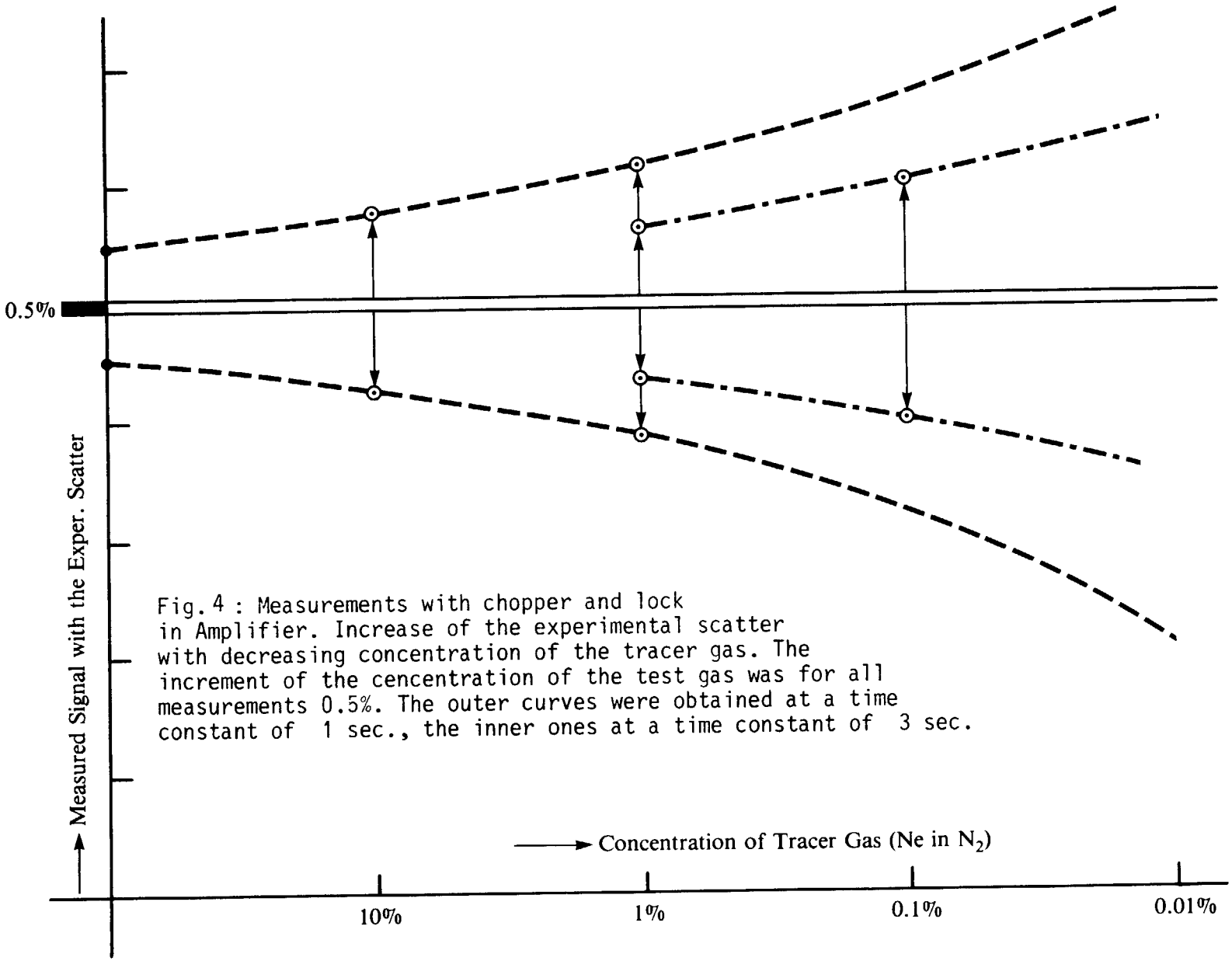

Fig. 4 : Measurements with chopper and lock in Amplifier. Increase of the experimental scatter with decreasing concentration of the tracer gas. The increment of the cencentration of the test gas was for all measurements 0.5%. The outer curves were obtained at a time constant of 1 sec., the inner ones at a time constant of 3 sec.

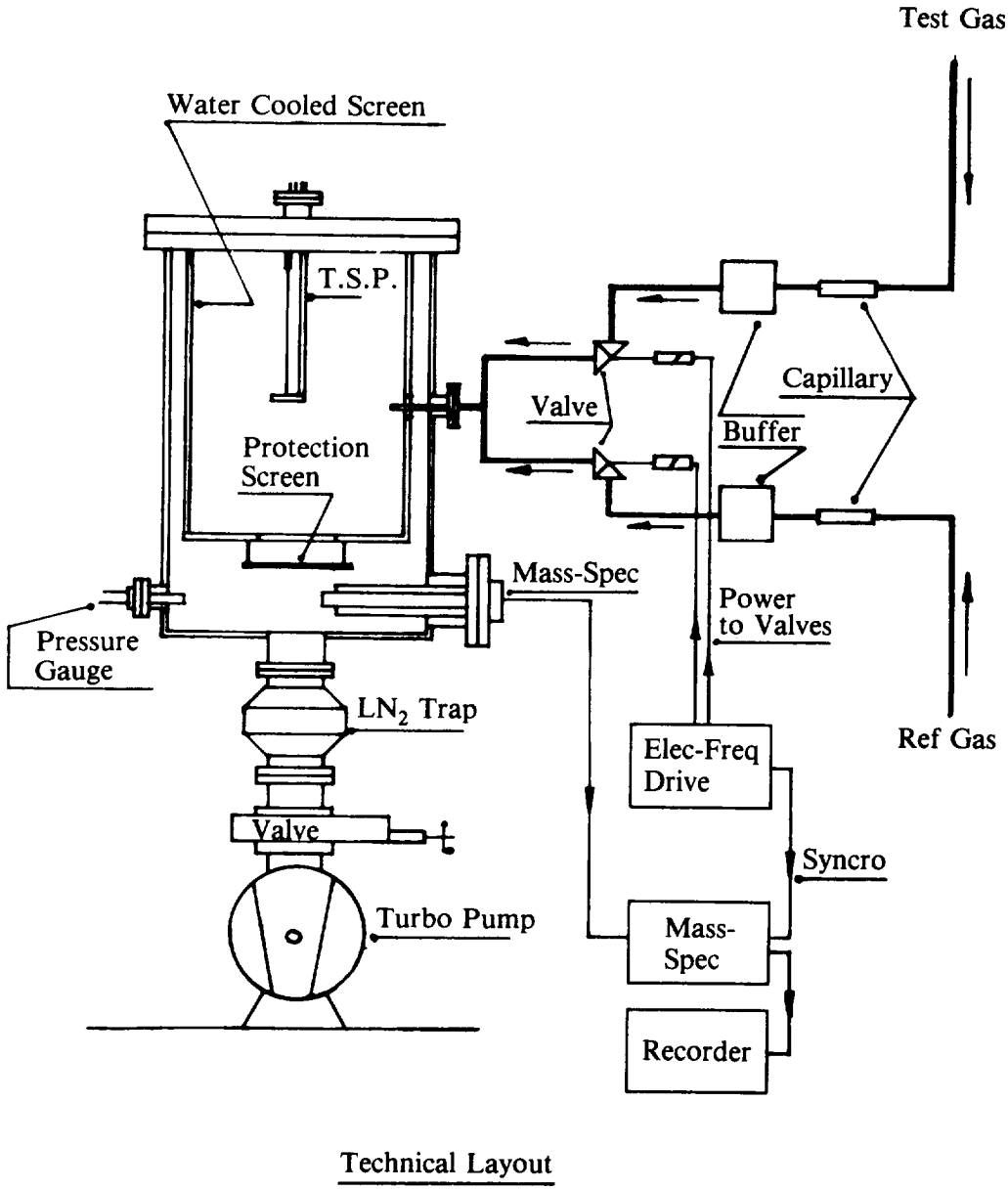

Fig. 5 : Design of leak detector with controlled valves for reference gas and test gas. On both capillaries were leak valves installed in parallel for adjustment (not shown in this drawing)

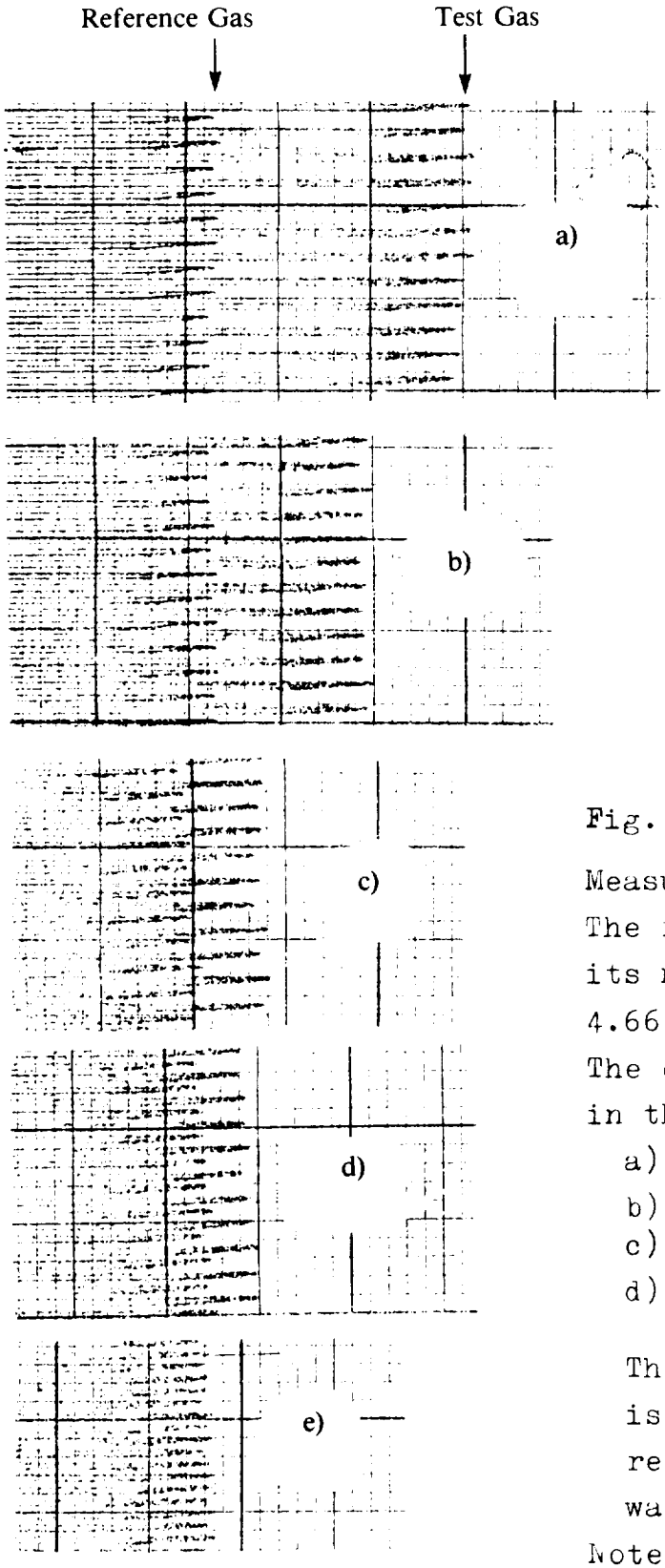

Fig. 6 :

Measurements with He
The reference gas was air with its natural abundance of 4.66 ppm He.
The content of He was increased in the test gas for :

a) by 7 % total 5 ppm
b) by 4 % " 4.85 ppm
c) by 2 % " 4.75 ppm
d) by 0.9 % " 4.70 ppm

The comparison of both signals is shown in e) where for reference and test gas air was used.

Note: All fig. with zero suppression.

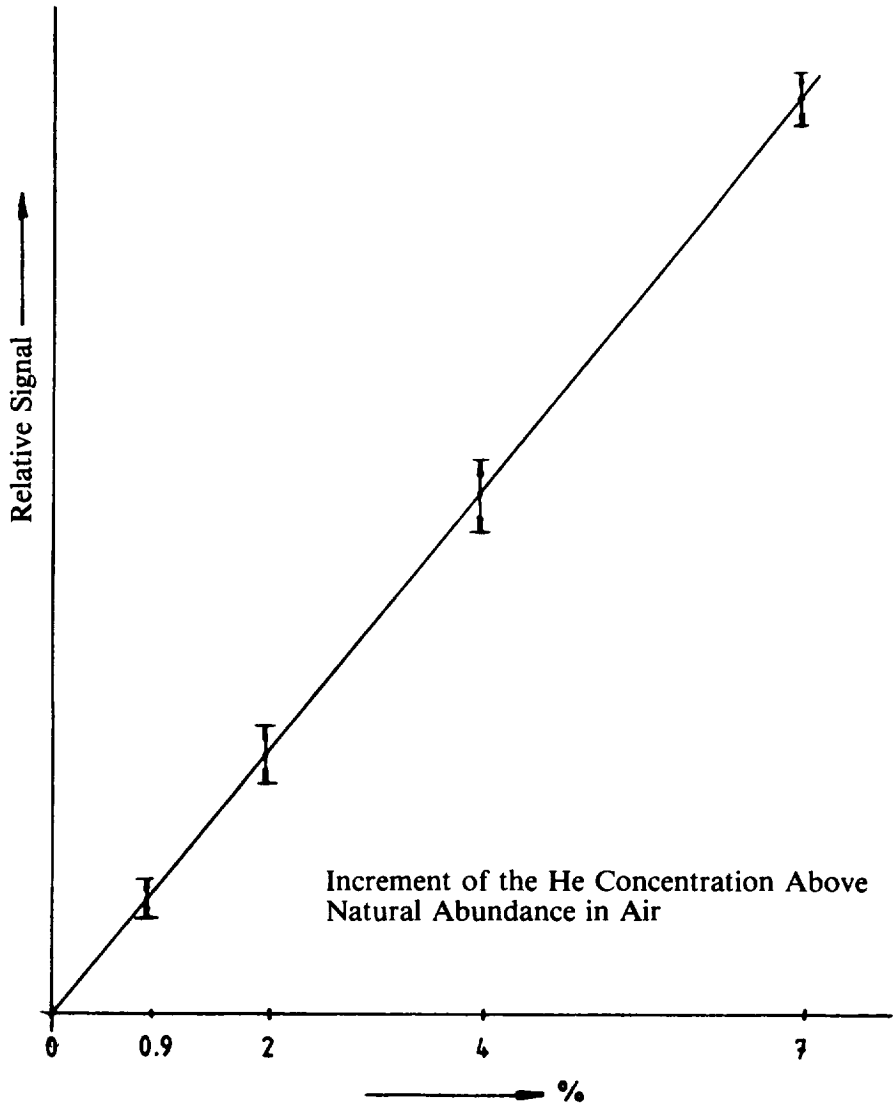

Fig. 7 : Evaluation of the measurements with He (Fig. 6) The difference of the partial pressure of He $\left(\overline{\Delta P_{He}}\right)$ for test gas and reference gas agrees within the experimental scatter with the increment of He concentration above the natural abundance in air; the arrows indicate the experimental scatter.

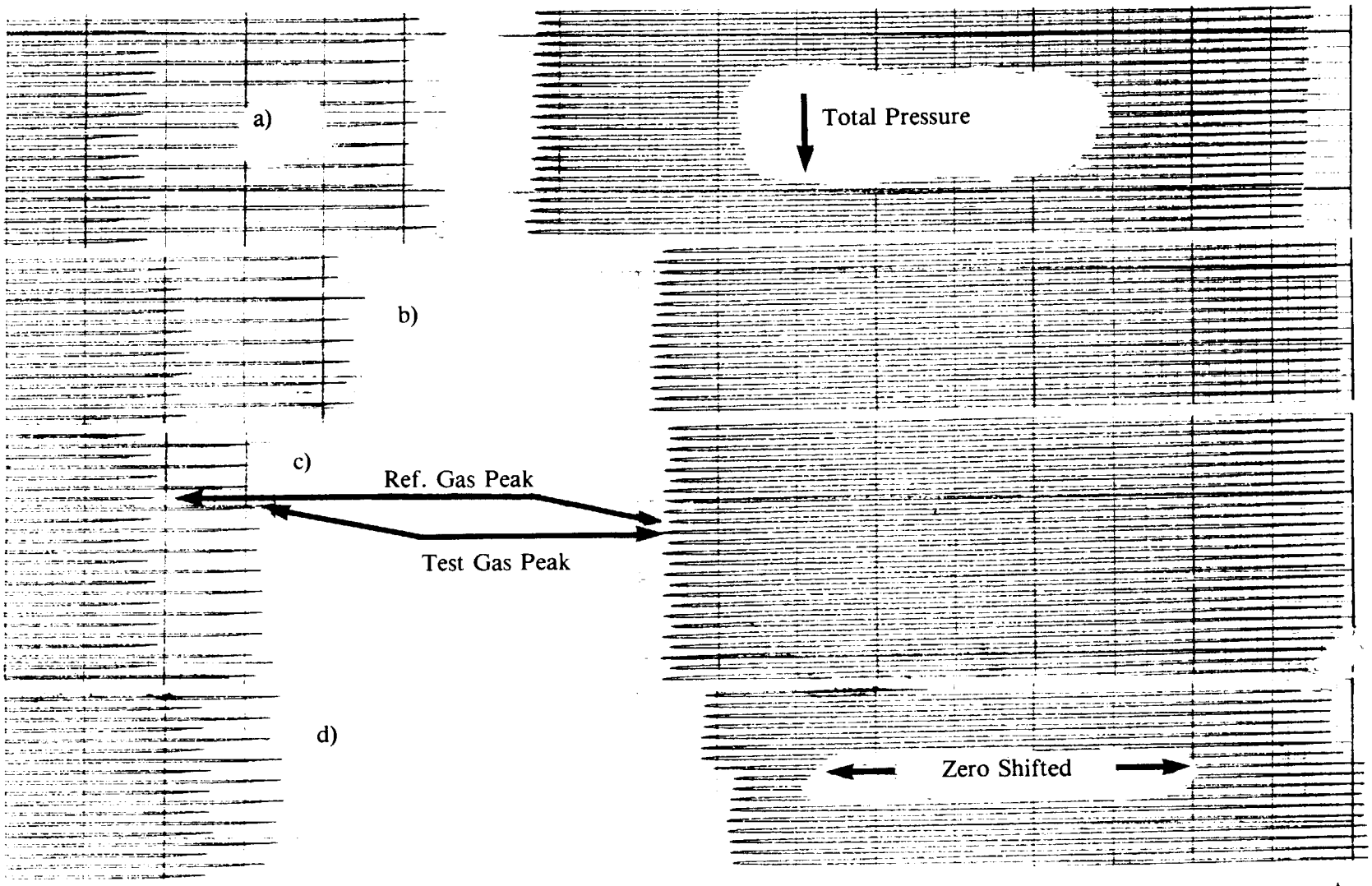

Fig. 8: Measurements with Ne on a.m.u. 22. For comparison also the total pressure is shown, without zero suppression. It was not always possible to adjust the reference in leak rate for full agreement with the test gas in leak rate, (highest deviation was for c) at 3.8%).

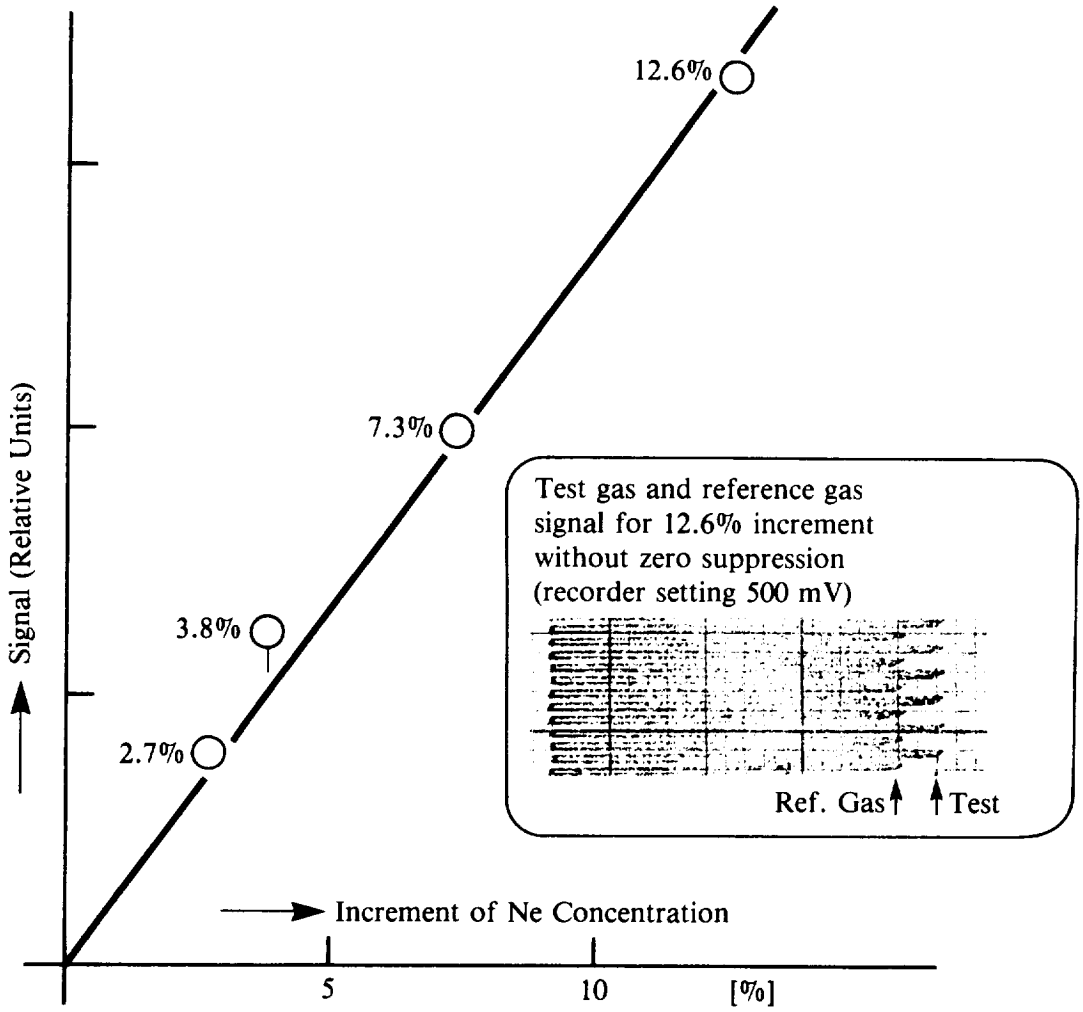

Fig. 9 : Evaluation of the measurements with Neon a.m.u. 22 (Fig. 8). Also here the signal obtained is proportional to the increment of the Ne concentration above natural aoundance in air. In Fig. 8 also the total pressure is given, and specially for c) (3.8%) the reference pressure was noticably lower. The decreasing total pressure from a to d is due to the increased filament power ot the T.S.P., it has no effect on the partial pressure of Ne. Inset shows Fig. 8a without zero suppression.

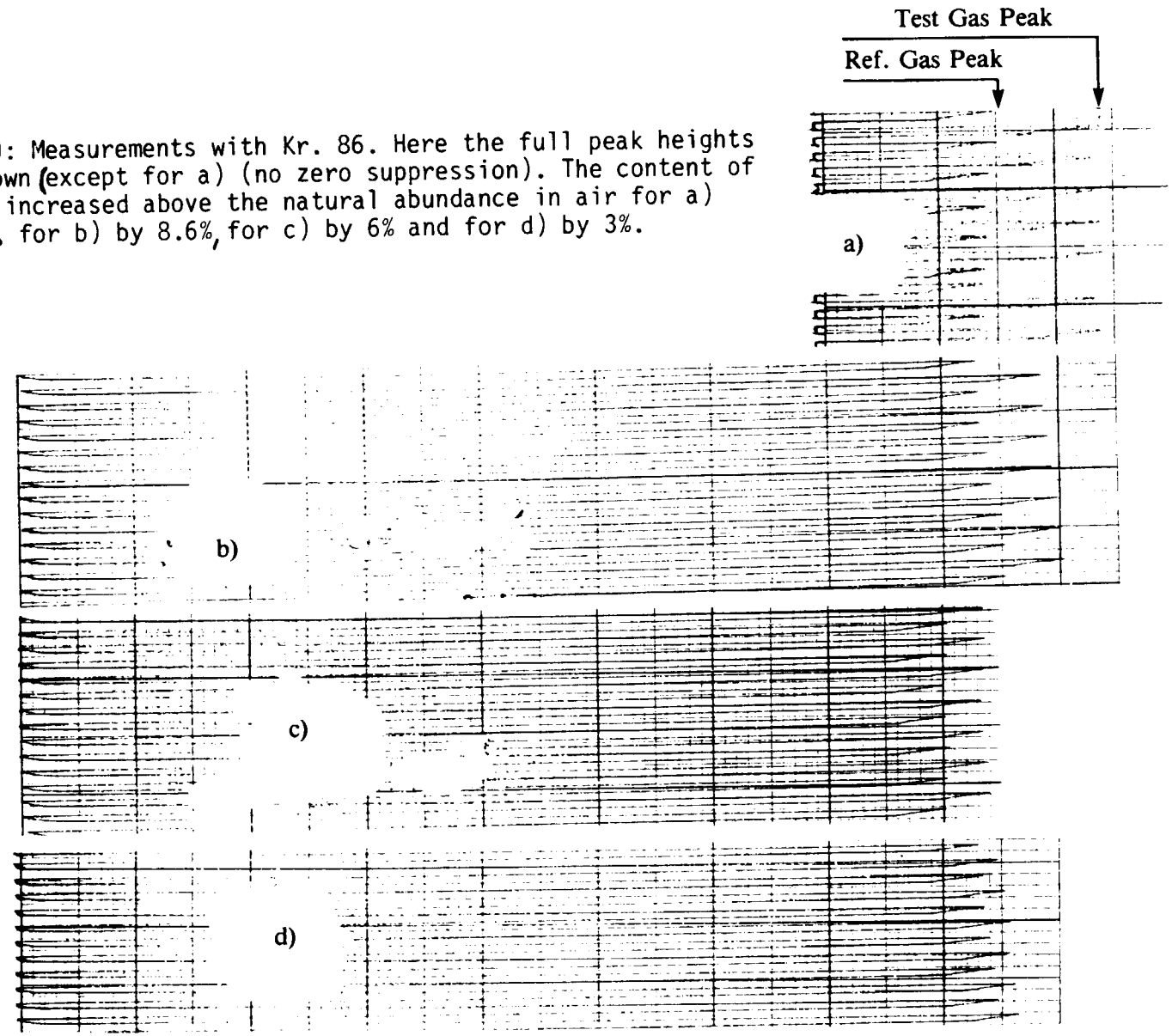

Fig. 10: Measurements with Kr. 86. Here the full peak heights are shown (except for a) (no zero suppression). The content of Kr was increased above the natural abundance in air for a) by 16%, for b) by 8.6%, for c) by 6% and for d) by 3%.

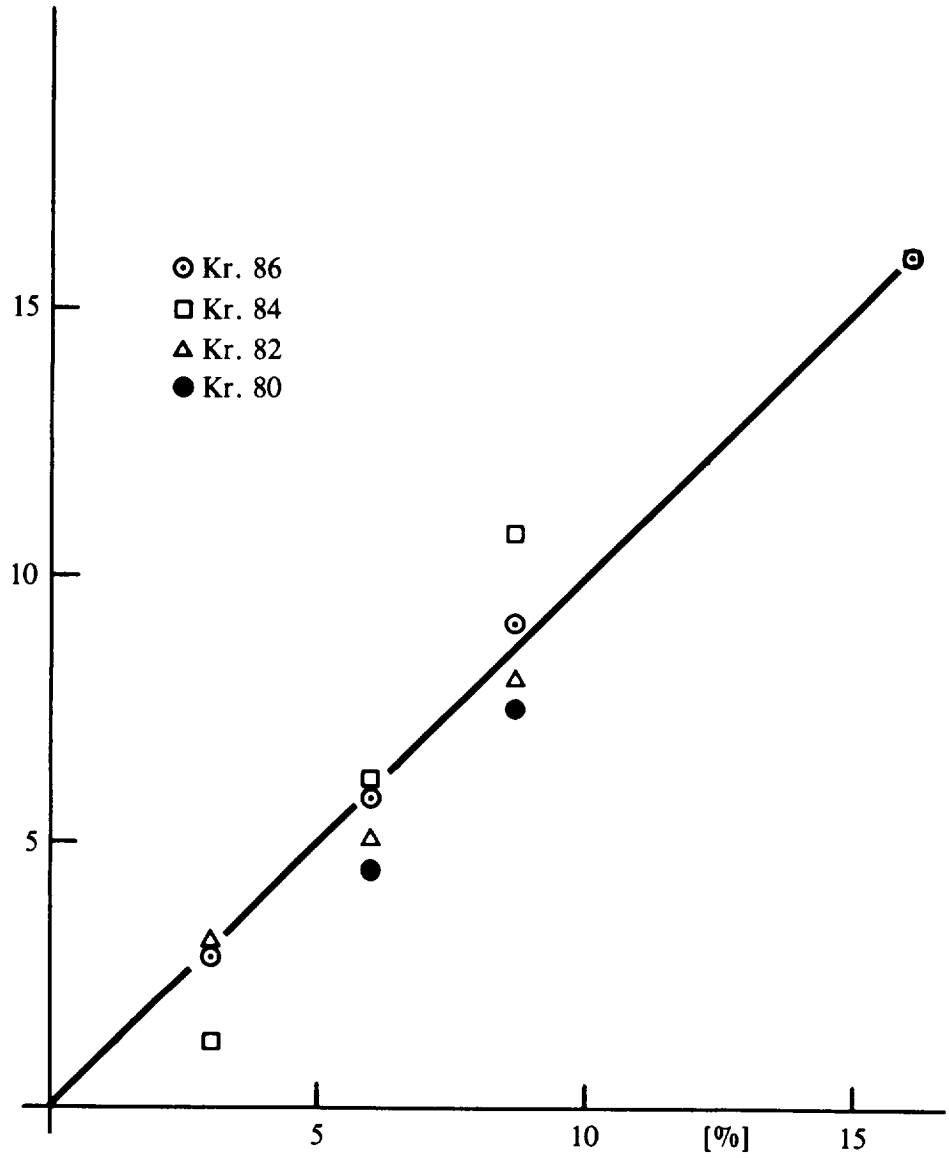

Fig. 11 : Evaluation of the measurements with Kr. The difference of the partial pressures of test gas and reference gas for Kr 80 at the 6 % - value is in the low 10^{-14} mbar range; it is equivalent to a concentration of 1.5 ppb in air.

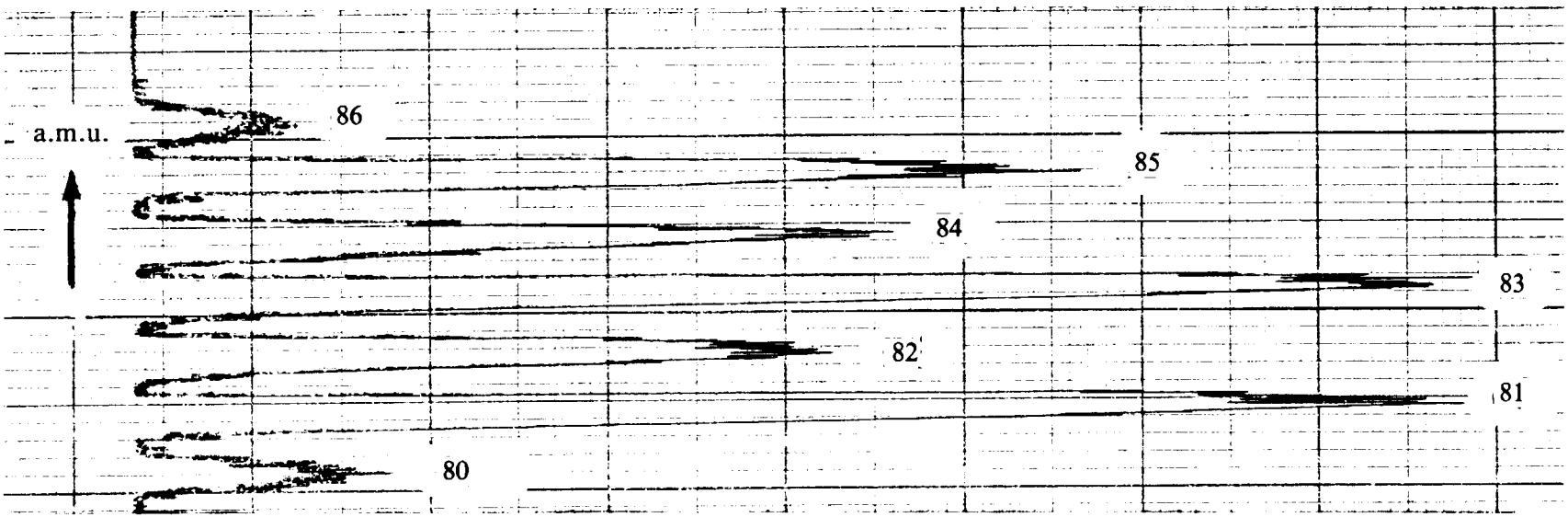

Fig. 12: Mass spectrum of the residual gas in the empty chamber for the a.m.u. from 80 to 86, no gas inlet. The ultimate pressure was $8_9 10^{-10}$ mbar, when the T.S.P. was switched on the pressure increased; (here to $4.4.10^{-9}$ mbar). Due to the high peak on a.m.u. 83 no measurements were performed for Mr. 83.

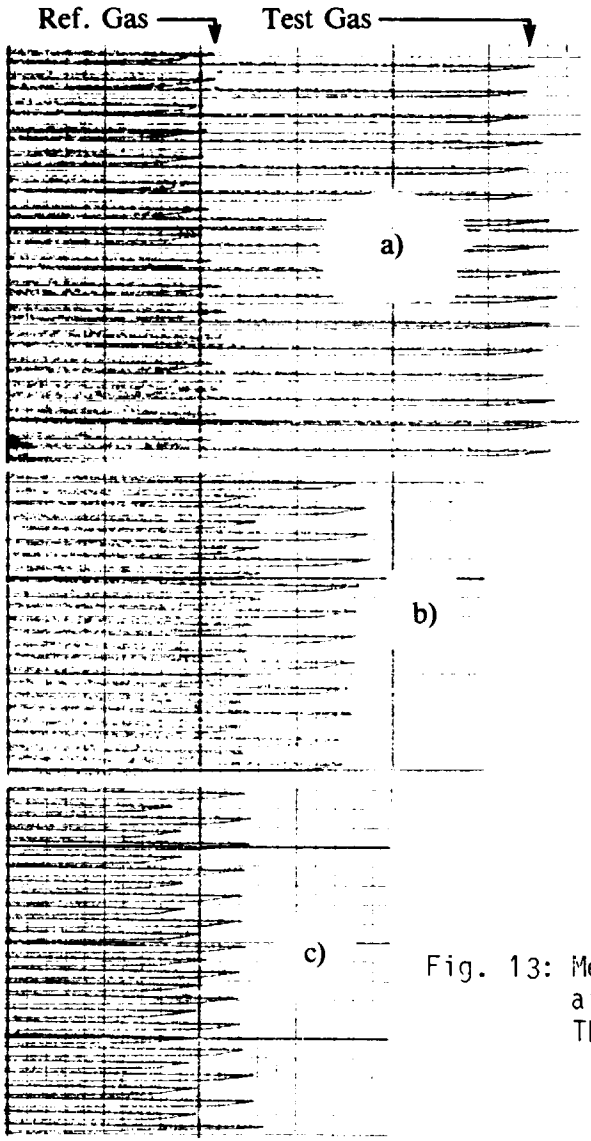

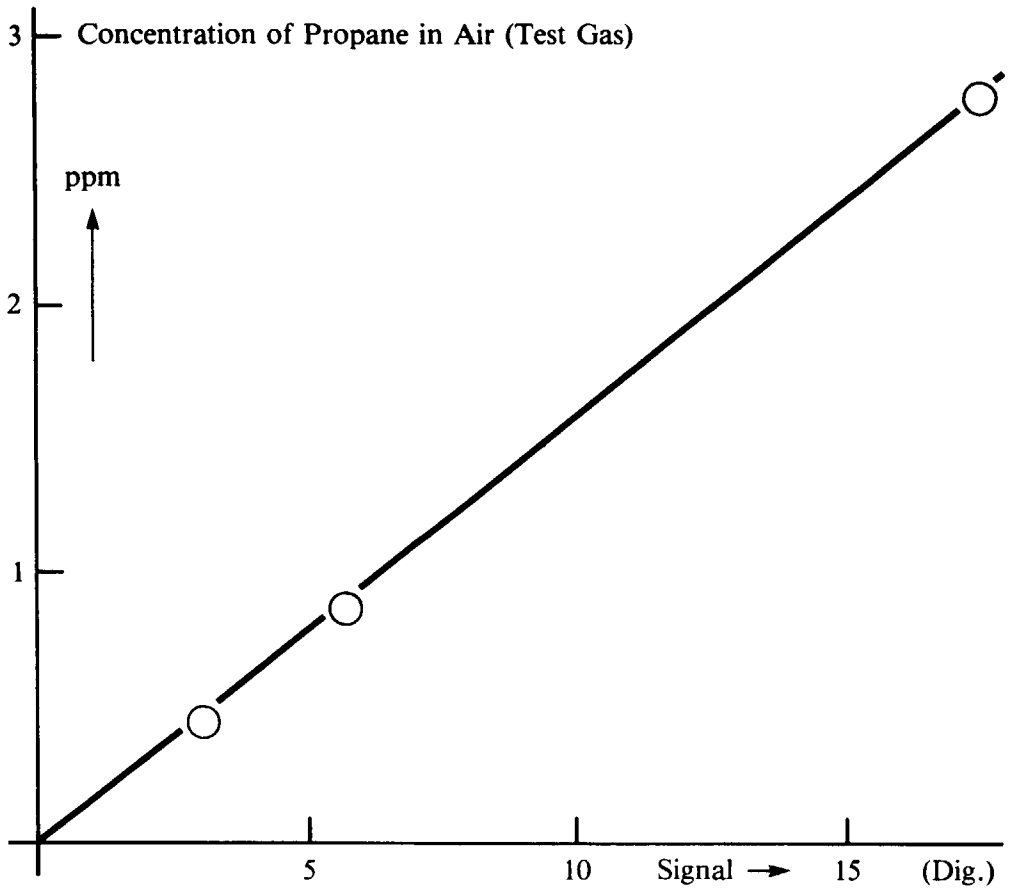

Fig. 13: Measurements with propane on a.m.u. 37; concentration of propane in air for the test gas was for: a) 2.8 ppm, b) 0,38 ppm, c) 0.45 ppm). The reference gas was air, without propane.

DESIGN OF AN ORBITAL HEATING SIMULATOR USING IR TECHNIQUES*

M. Donato, G. Bush, A. Harris

Spar Aerospace Limited, Ste. Anne de Bellevue, Quebec, Canada

and B. Muir

David Florida Laboratory, Ottawa, Ontario, Canada

INTRODUCTION

The present work reports on the design and setup of an orbital thermal simulator capability using infrared simulation at the David Florida Laboratory (DFL). This system is to be used for off-line testing of the OLYMPUS thermal model. The results will be correlated with the solar simulation tests that are being done at the Jet Propulsion Laboratory (JPL) and eventually with flight data. The aim of the infrared tests is to verify the test technique as a viable and cost effective alternative to solar simulation for thermal math model verification.

The use of infrared fluxes for the thermal simulation of orbital conditions has become increasingly popular in recent years. With the advent of large spacecraft, the cost of performing solar simulation tests has escalated significantly. Infrared simulation techniques require a lower capital investment and operating costs (1), and generally encounter fewer operational problems (2). The IR technique can also be used to reproduce albedo and planetshine radiation (3), and the end of life conditions where the degradation of second surface mirrors (SSM) can double or triple their surface absorptivities (4). In addition, the IR technique provides for a greater test flexibility on spacecraft whose orientation and movement are limited by heat pipes and/or rigid RF test connections.

In order to simulate orbital conditions, the spacecraft surfaces are partitioned into isoflux zones each receiving an equivalent radiative solar flux corresponding to a specified orbital position. The solar fluxes are obtained by zone controlled infrared radiation in DFL's 7m by 10m thermal vacuum chamber. The resulting test data are used for the verification and calibration of the thermal math model.

* This work was partially supported by the Canadian federal government's Department of Communications.

The IR fluxes are generated by tungsten filament "Quartz-lined" General Electric lamps and by rod shaped heaters, "Calrods", manufactured by Chromalox. The lamps are mounted in a gold plated Research Inc. reflector to increase flux uniformity and maximize the power efficiency. They offer low blockage area to the shroud enabling simulation of eclipse transients. Calrods are used on the SSM faces which are not subject to an eclipse and where the power requirements are low. In this situation, their long slender shape produces uniform flux patterns that are amenable to analytical description.

BACKGROUND

OLYMPUS is a three axis stabilized spacecraft with a large communications payload. The shape of the spacecraft is rectangular with approximate dimensions of 1.8m x 2.1m x 3.5m. A schematic of the spacecraft in the thermal vacuum chamber is shown in Figure 1.

In orbit the smallest surface is oriented towards the earth at all times and is referred to as the earth-facing panel. It is the +Z face based on the co-ordinate system used in the analysis of the spacecraft. Except for two reflectors, all of the antennas are located on this panel. The +Z face consists of 5 reflectors of various sizes, a tower and a number of horns resulting in a complicated geometry.

The two faces of the spacecraft that align principally with the earth's north and south poles are known as the +Y and -Y faces based on the spacecraft co-ordinate system. The solar arrays are connected to the spacecraft through these panels. These surfaces are mostly oriented toward space and are used for heat rejection. Thus the majority of the Y faces are covered with SSM. Because most of the heat rejection of the spacecraft is through these faces, they have a dominant influence on the operating temperature of the spacecraft.

The two remaining sides of the spacecraft are known as the +X and -X faces. With each orbit, these faces see both space and sun over most of their surfaces. These surfaces are blanketed to reduce the effects of large changes in incident flux. There is a large reflector supported by each X face. These reflectors shadow the X faces producing a non-uniform incident flux distribution.

Excluding pumpdown and recovery, there are five infrared test phases corresponding to the SS phases that will be performed at JPL. The first condition tested in steady state thermal balance is equinox. The equivalent solar radiation is input perpendicular to the east panel (+X face). The spacecraft

is then subjected to a 72 minute eclipse from steady state. In orbit the sharp eclipse only occurs when the full sun is on the earth facing panel (+Z face). However this cannot be done in the JPL solar simulator because of the horizontality requirement of the heat pipes. The third condition is an extended sun "OFF" full power calibration case. Following this, both solstice conditions are simulated with steady state thermal balance tests. An additional test phase on flux sensitivity is to be performed with the IR rig. The flux input on the SSM is to be increased by a factor of 2.5 in order to simulate the end-of-life condition. The additional heat input to the uninsulated surfaces will provide a wider range of data for the verification of the thermal math model.

SOFTWARE

Software was developed to calculate the absorbed flux in a zone resulting from IR lamps or Calrods, with or without baffles. The program can treat zones separately resulting in increased flexibility and reduced execution time. The program inputs can be from a file or through interactive prompts. The normal mode of operation is for the user to specify the lamp arrangements, geometry, baffles and S/C surface properties. The program then calculates the flux intensities for the region of interest. The position, intensity and quantity of heating elements can be optimized for a particular flux distribution over a surface.

The program was initially set up to calculate the radiation intensity at a point from an IR lamp using the equation developed and calibrated for the program IRSIM (5). Subsequently, a new equation was derived (6) taking into account the finite lamp length in order to improve predictions when the IR lamp is located near the surface. This same equation was modified to give the exact analytical form for the view factor of a Calrod. The total radiation intensity received at a point on the S/C surface from an IR lamp or Calrod array is obtained by superposition.

The program can treat specular baffles by creating images of the lamps or Calrods at the proper locations. When four specular baffles are used to surround the zone an infinite symetrical array will result. The default criterion in the program is that images whose rays intercept the surface at an angle greater than 85 degrees with respect to the normal are ignored. The maximum error associated with a lost image is less than 0.1% which is considered adequate for most calculations. This criterion may be modified by the user.

The program allows for different baffle relectivities. In such cases, the intensity of a ray is reduced proportionally to the number of reflections it undergoes. However, this calculation is valid only if the baffles are kept cold and do not radiate to the surface. The net effect of baffles that heat up was analysed in detail using results from Monte-Carlo calculations for imperfect specular reflections (7) and the TMG finite difference thermal code. It was found that for high reflectivity surfaces the flux distribution and the total flux were almost identical to calculations that treated the baffles as perfectly specular.

RADIOMETERS

The total radiation input to the spacecraft surfaces arises from many sources (lamps, Calrods, other S/C surfaces, and the IR rig). Calculation of the infrared radiation absorbed by a particular surface from a measured incident flux distribution can be subject to significant errors arising from differences in angular and spectral absorptivities between the sensor's surface material and the spacecraft surfaces. For this reason the sensors are coated with spacecraft surface material before calibration and thus provide a direct measurement of the total radiation absorbed by a particular surface.

A sketch of the sensor is shown in Figure 2. Each sensor consists of a thin copper disc backed by multi-layer insulation (MLI). The upper face of the sensor, which is exposed to the infrared radiation, is coated in the appropriate spacecraft surface material. A 30 gauge copper-constantan thermocouple is soldered to the back face underneath the MLI blanket.

The equilibrium temperature of the sensor, measured by the thermocouple, is a function of the total absorbed flux. At equilibrium the radiation absorbed by the front face of the sensor is equal to the radiation emitted by that face plus the losses, which include those along the thermocouple wire, through the MLI blanket and from the edge of the disc. To minimize these losses, the thermocouple wires are blanketed, ten layers of MLI are used on the rear face and the edge of the disc is tapered to 0.005 cm.

The sensors are calibrated using a procedure similar to that developed at TRW for their isothermal body sensor. The calibration is absolute and its accuracy is not dependent on a knowledge of the optical properties of the spacecraft material or the losses cited above. An etched foil resistance element is bonded to the back face of the copper disc, such that the power absorbed from the element accurately simulates the heating

effect of absorbed radiation. The sensors are calibrated in a vacuum cold wall environment similar to the test environment. A calibration curve is generated for each sensor of equivalent absorbed flux density versus sensor temperature. The accuracy of the calibration procedure, which is a function of the measurement error in the applied power, the disc temperature, and the disc area, is within 2%.

S/C ZONES

Based on the geometry of the surfaces and orientation of the spacecraft with respect to the sun, Spar was provided with zones of constant incident flux for equinox, summer solstice and winter solstice (Table 1). A uniformity requirement was specified for each zone based on the relative effect the zone had on the thermal balance of the spacecraft. The case examined considers the sun to be in the -X direction during equinox. The spacecraft is rotated ±23.5 degrees about the Z-axis to simulate summer solstice and winter solstice respectively. During summer solstice the north panel (-Y face) is irradiated. Similarly during winter solstice the south panel (+Y face) is irradiated.

In order to verify the thermal mathematical model the most important criterion in irradiating a zone is to produce an input which can be accurately quantified. In addition it is desirable to approach expected operating conditions. These objectives are most easily accomplished by applying a uniform flux of specified intensity to individual zones. This simplifies placement of the radiometers within the zone and reduces the need for extensive mapping. If spacecraft couplings affect flux uniformity or there is significant flux spillover from adjacent zones then additional analysis, mapping and monitoring is required.

Baffles are well suited to produce a uniform flux distribution with a minimum number of IR lamps/Calrods. They reduce spillover resulting in decoupled zones each receiving radiation equivalent to an infinite array of IR lamps/Calrods. For cases where baffles are not feasible, a compromise must usually be made between uniformity, spillover, and blockage. For zones where uniformity requirements have been dropped, a maximum incident flux of 1 solar constant is specified.

-X Face

The -X face has a total of 11 zones including 5 zones for the large TVB2 reflector and its associated support structure (Figure 3). As a result of shadowing from the reflector the flux variations are large over the surface of the -X face. The 5 reflector zones are irradiated using IR lamps without baffles.

The lamps are close to the surface so that spillover is low and the inputs are well known. The remaining -X face zones are irradiated using IR lamps and are baffled producing high uniformity (±1%). Variations in intensity are obtained by adjusting IR lamp voltage.

±Y Faces

The +Y and -Y faces are similar in construction, function, and environment. The surfaces are made up of sections of MLI and SSM (Figure 4). Because MLI and SSM have extremely irregular shapes on both Y faces, the Y faces are treated as single zones. Each zone is surrounded at the perimeter using baffles. The zones are uniformly irradiated at the intensity required for the SSM. The lower than required energy input to the spacecraft through the thermal blankets has little effect on the overall spacecraft thermal balance. All sensors are placed on the MLI sections of the zones so as not to affect the properties of the radiators.

The specified absorbed solar flux is achieved using 16 Calrods. Calrods were selected for the Y faces because SSM absorptivities vary substantially with small changes in intensity at low IR lamp powers. Additionally fewer Calrods were required simplifying rig design.

Both the Y faces have a shadow because of the Solar Array Drive Arm. This is simulated using an LN_2 cooled plate formed to the shape specified and suspended 5 cm above the surface.

The Solar Array Pallets are parallel to the Y faces but not in place during testing. These pallets heat up due to the heat rejected by the SSM and due to direct solar radiation during solstice. Once warmed, these pallets radiate heat towards the Y faces. This effect is simulated by increasing the power to the Calrods such that the additional flux from the Calrods matches that which would be supplied if the pallet were in its actual position.

+Z Face

The +Z face consists of a number of zones, each with complex geometry (Figure 5). The objective for the +Z face was to obtain the required average absorbed solar flux for each zone without irradiating nearby surfaces. IR lamps were chosen over Calrods because their reflectors focus the emitted radiation. IR lamps also have a faster response to eclipse conditions which occur on this face. In all cases the IR lamps were placed close to the surface to reduce the number of lamps required and minimize spillover.

RIG HARDWARE DESIGN AND ANALYSIS

A rig was designed whose purpose was to support the OLYMPUS spacecraft dryweight, maintain its horizontality within 2mm/m, and to hold the baffles, lamps, and Calrods in their required position while minimizing blockage between the spacecraft and the shroud. Figure 6 shows the top view of the rig and spacecraft in the thermal vacuum chamber.

The support structure has two parallel I-beams that traverse the chamber, resting on wall hard points. The I-beams have interconnecting cross members which are bolted together to form a rigid structure. At each end of the I-beams an additional member is mounted to form a triangle. Shims are provided to ensure that the support structure is level in the chamber and that the four feet are all correctly seated on their respective points. A layer of teflon is used between the support structure and the hard points of the chamber to reduce friction. Two leveling devices (jactuators), supported by the I-beams, are attached to the +Z end of the spacecraft using cables. A third jactuator is located in the centre of the cross-member at the -Z end. The baffles, IR lamps, and Calrods are supported from the I-beam structure using aluminum tubing. The baffles are constructed using aluminized kapton bonded to thin aluminum sheets. The support structure allows spacial adjustment of the IR lamps and Calrods.

A thermal analysis was performed on the rig to determine blockage between the support structure and the spacecraft, equilibrium temperatures of the rig components, and the magnitude of displacements of lamps and baffles as a result of thermal distortions.

With the support structure painted black, the equilibrium temperature of the I-beams was calculated to be -60 °C. To further reduce this temperature specular V-shape foils, attached to the large support structure members, are used to deflect radiation leaving the spacecraft to the shroud.

To reduce the effect of the support structure during eclipse, all circular members parallel to the spacecraft surfaces are painted black only on the shroud facing surface. Since the surface facing the spacecraft is aluminum, the radiation from the structure to the spacecraft surface during eclipse is reduced to acceptable levels.

The jactuators must be maintained at approximately ambient temperature to ensure proper operation. This is accomplished using film heaters which are supplemented by a GN_2 purge capability. The jactuators are isolated from the environment using

MLI on all surfaces and kevlar shims at all mounting points.

Thermal distortions are controlled to planar motions parallel to the spacecraft surfaces by design. Teflon inserts in moving junctions allow for motion as a result of thermal expansions or contractions.

THERMAL CONTROL AND DATA PROCESSING SYSTEMS

The thermal control system consists of 256 microprocessor controlled D.C. power supplies, each capable of delivering up to 2 kW of regulated and monitored output power to a resistor load. The system is based on a modular design for user versatility and to minimize the consequences of hardware failure. A switch mode, or pulse width power control technique is used to reduce system equipment size and significantly increase power efficiency over that achieved with linear control technology. All channels are voltage controlled with power as an output variable. As the lamps are wired in parallel circuits this permits failure identification and prevents burnout of the second lamp.

Parameters for output voltage value and corresponding limit level specification, both prior to and during testing, are set through the console controller. The console, which is also responsible for current channel status and alarm displays is connected to eight node controllers, which in turn, control 32 power supplies each. The power supplies operate on a closed loop system to provide, regulate and monitor the desired output voltage. The measured load current is used to calculate the output power level. The operating limits of the system are as follows:

- Maximum number of channels: 256
- Maximum load current per channel: 10 A.D.C.
- Maximum output voltage per channel: 240 V.D.C.
- Power input: 208 V.A.C. three phase 25 KVA
- Voltage control range: 0 to 100%
- Programmable voltage level resolution: 1 volt
- System control accuracy: less than 1% of set value

Alarm and protection facilities provided by the system include open or short circuited load detection and shutdown, open or short circuited load sense line alarms, channel set point level versus monitored level compliance and out-of-limit alarms. In the event of a power failure, emergency power to the system is provided by a diesel generator.

The data processing system consists of a PDP 11/60 main computer, with a PDP 11/34 which is either used as backup or configured for real time operation to augment the number of avilable channels. The system handles up to a maximum of 1568 channels in any combination of thermocouple, voltage or current input.

All spacecraft temperatures are measured using copper constantan thermocouples. To achieve the specified test accuracy requirements of $\pm 0.2^{\circ}C$, the thermocouple flying leads are attached to a floating uniform temperature reference located inside the thermal vacuum chamber. Copper-copper leads may therefore be used to connect to the dataloggers external to the chamber, avoiding the errors normally associated with vacuum wall feedthrough junctions.

SUMMARY

An IR rig has been designed to supply and monitor radiation fluxes in order to verify a thermal math model. The design incorporates IR lamps, Calrods and baffles to best suit the requirements of the specific zones. The required fluxes are calculated from the IR lamp/Calrod configuration software which can account for the effect of specular baffles and surface absorptivities. Radiation intensities are measured using the absorbed flux technique. Sensors, with surface properties matched to the appropriate spacecraft zone, are calibrated under conditions identical to test. The rig itself is capable of reproducing all test conditions and is versatile enough to handle other spacecraft.

REFERENCES

1) Brinkman, P.W., Shickle, W.A. and Walker, J.B., "Economic Use of Facilities for Testing of Large Satellites and Subsystems", ESA SP-198, 1978

2) Nuss, H.E., "Thermal Vacuum Testing of Solarpanels by Solar Simulation and Infrared Simulation", Proc. of Ins. of Environmental Science, Washington, 1979

3) Sweet, G.E., Taylor, J.T., Abbot, I.H.A., "The Design and Operation of a Planet Emitted and Albedo Radiation Simulator", I.H.A. Abbot, NASA SP-299, 1972

4) Wise, P., "Solar Simulation vs IR Thermal Design Verification of Spacecraft", Intelsat Colloquium Testing of Large Spacecraft, November, 1983.

5) Rogers, P., "Calculation of Infrared Flux in a Test Chamber Environment", Program IRSIM, E.W.P. 1325, ESTEC, 1982

6) Donato, M., Ruel, C., Harris, A. and Muir, B. "Absorbed Flux Predictions for Spacecraft IR Testing", SAE Technical Paper No. 840978, presented at the 14th Intersociety Conference on Environmental Systems, San Diego, 1984

7) Edwards, D.K. and Bertak, I.V., "Imperfect Reflections in Thermal Radiation Transfer", Paper 70-860, AIAA 5th Thermophysics Conference, Los Angeles, CA

TABLE 1

REQUIRED ABSORBED SOLAR FLUX FOR SELECTED ZONES

Control Zone Number	Control Zone Description	Surface Type	Unif. Req't	Absorbed Solar Flux (W/m^2)		
				Equin	S.S.	W.S.
1	20/30 GHz "A" Back	Blanket (ITO Kapton)	L	164	159	120
4A	TVB1 Refl.	White Paint	L	151	92	112
9	Tower	Blanket (ITO Kapton)	L	360	469	137
14	CM/SM -X Plane	Blanket (B.P. Kapton)	H	1318	1162	1240
17A	CM/SM -X Plane	Blanket (B.P. Kapton)	H	522	579	615
24	TVB2	White Paint	L	13	12	13
25	North Radiator	Blanket (B.P. Kapton)	H	-	504	-
26	North Radiator	ITO SSM's	H	-	58	-
27	North Radiator	Shadow	H	-	-	-
31	South Radiator	Blanket (B.P. Kapton)	H	-	-	538
32	South Radiator	ITO SSM's	H	-	-	62
33	South Radiator	Shadow	H	-	-	-

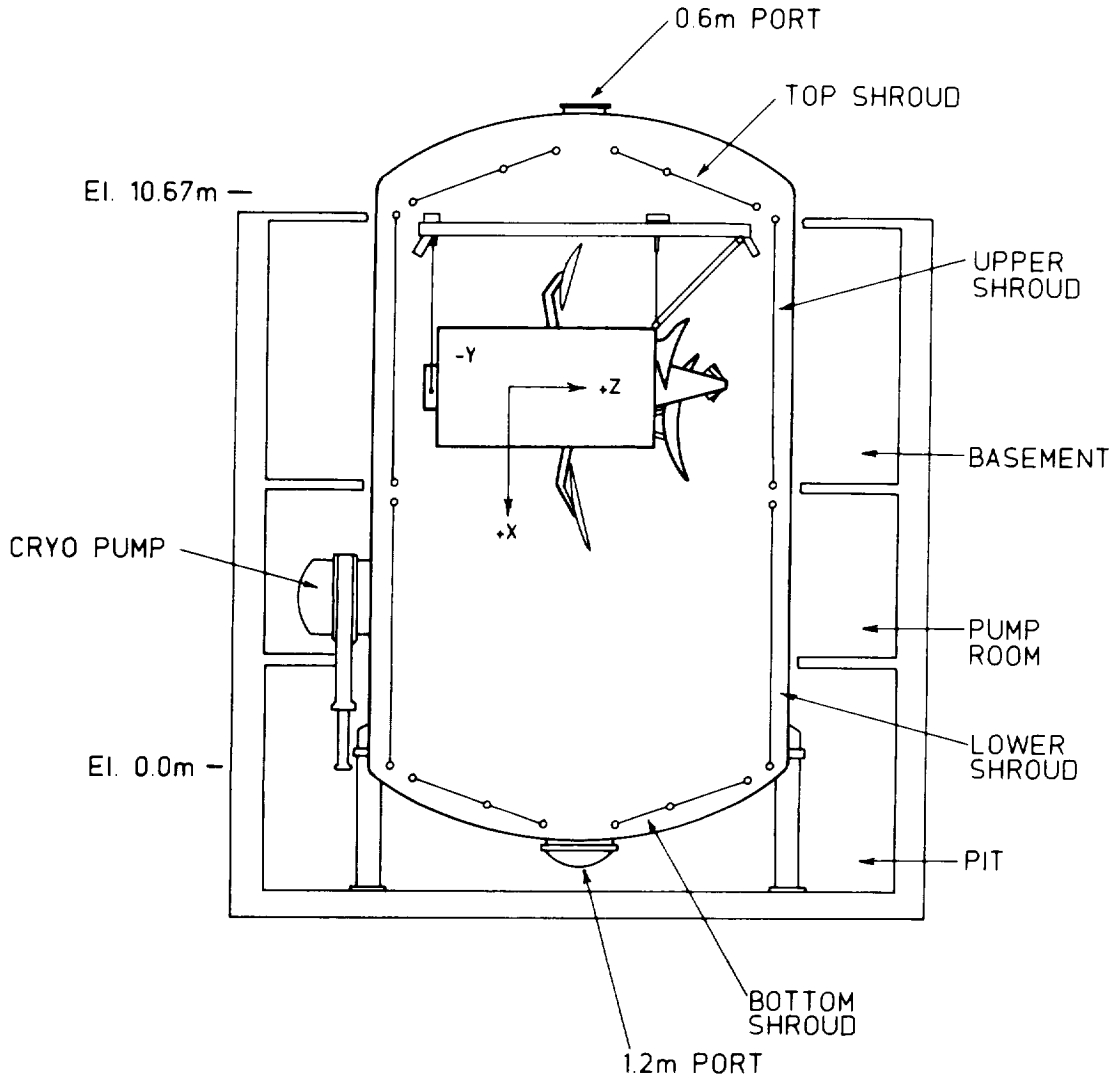

FIGURE 1 SCHEMATIC OF CHAMBER AND SPACECRAFT

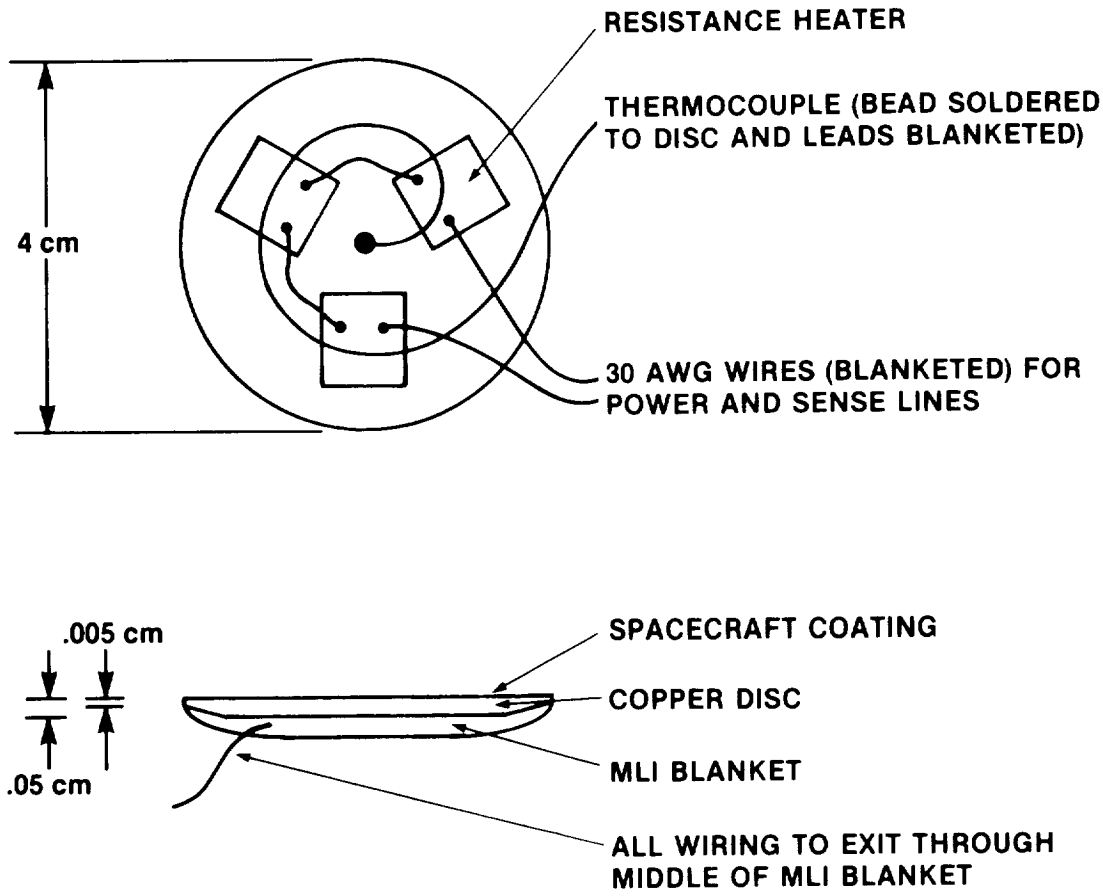

FIGURE 2 ABSORBED HEAT FLUX SENSOR

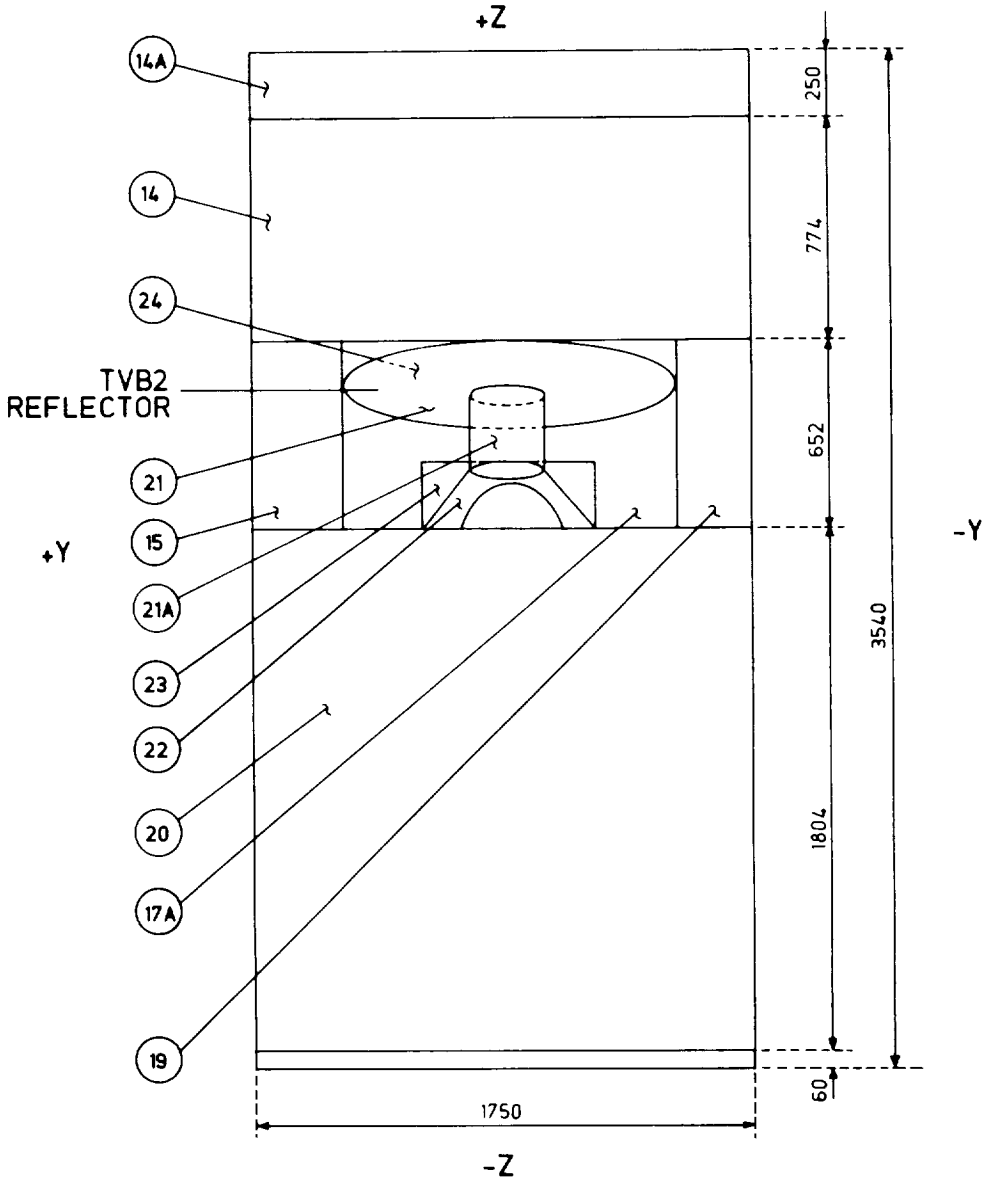

NOTE:- ALL DIMENSIONS ARE IN mm

FIGURE 3 -X FACE ZONES

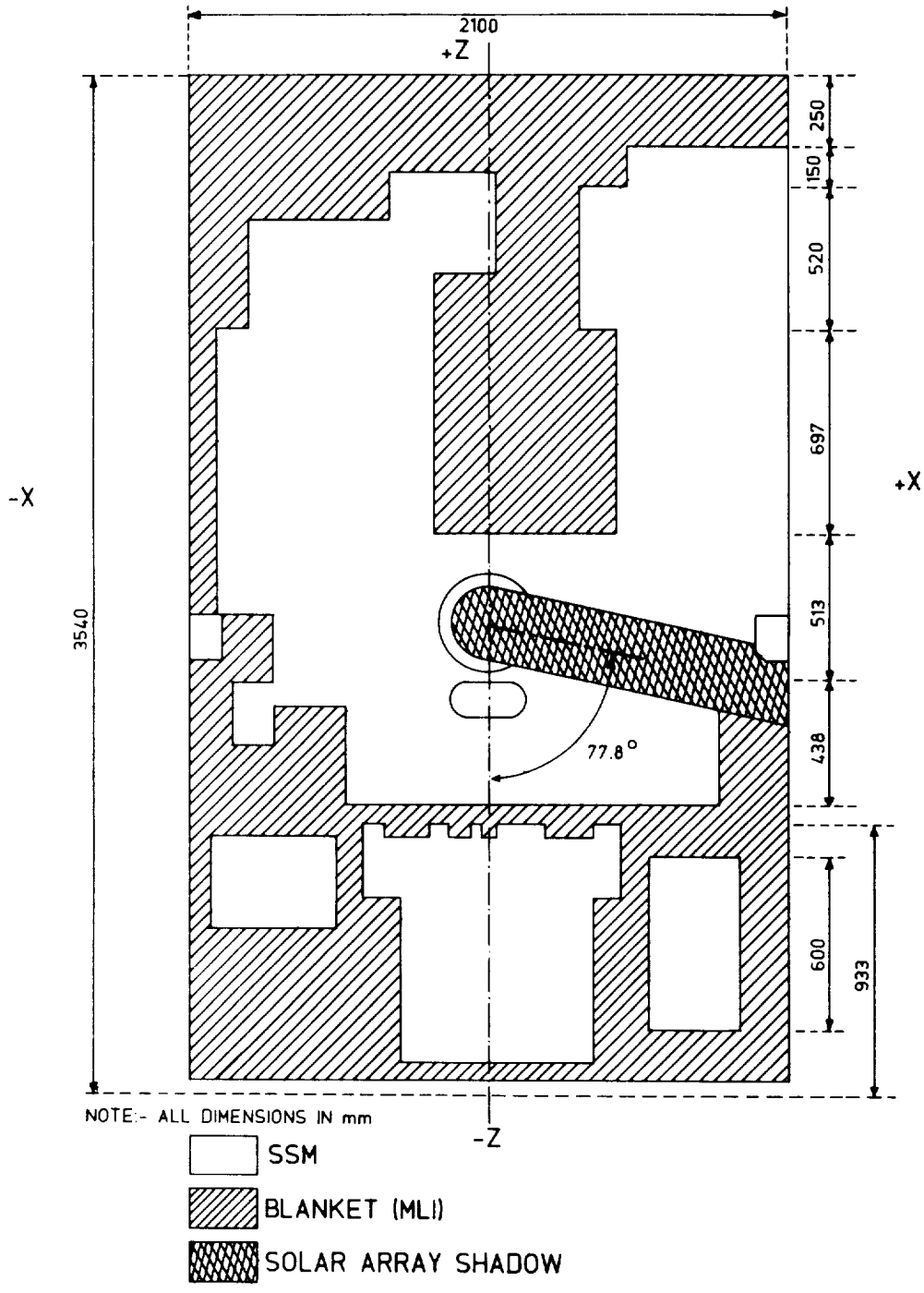

FIGURE 4 -Y FACE ZONES

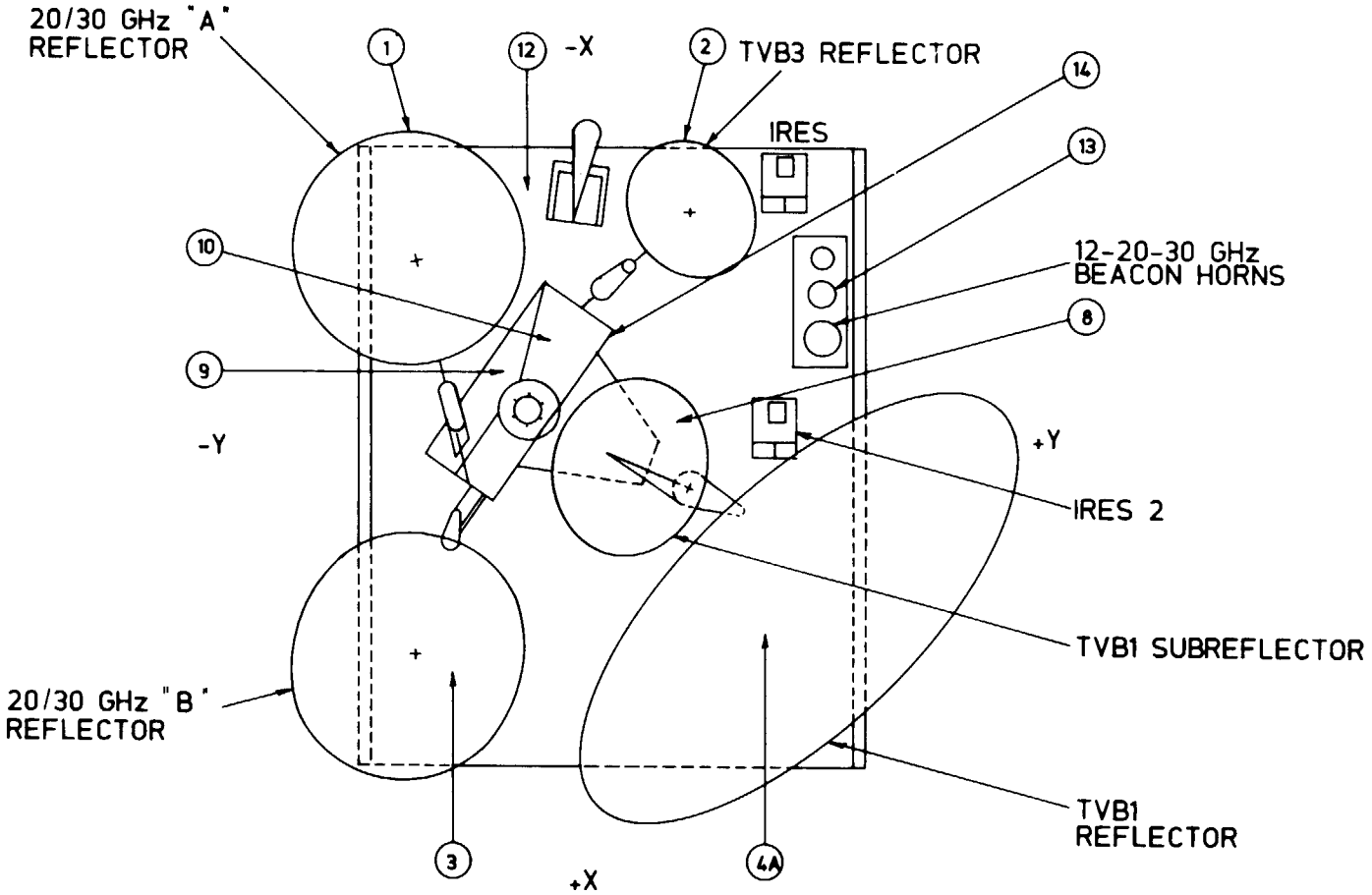

FIGURE 5 +Z FACE ZONES

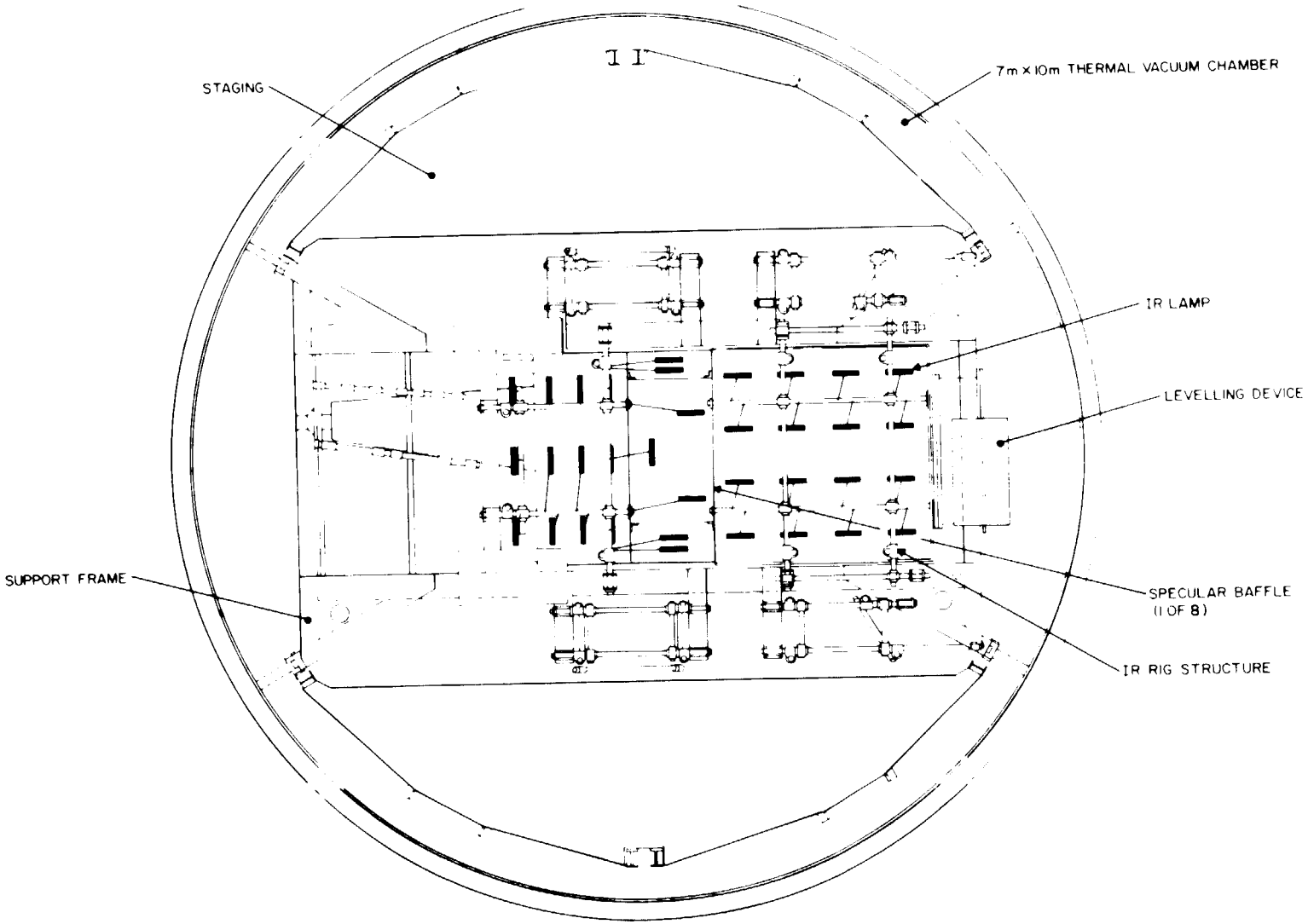

FIGURE 6 TOPVIEW OF RIG ASSEMBLY IN THERMAL VACUUM CHAMBER

TAPE HEATING METHOD FOR SPACE SIMULATION TESTING

H. W. Presley and R. P. Clifford
Members Of Technical Staff

TRW Space & Technology Group

ABSTRACT

An ohmic heating technique for simulating the solar heat input to a spacecraft during space environment testing was developed. Tests of spacecraft radiator sample panels were used to evaluate the heating method for its potential hazard to sensitive surfaces and for its application accuracy prior to use in full-scale thermal vacuum tests of flight spacecraft and thermal models.

INTRODUCTION

Spacecraft thermal vacuum test philosophy has undergone a change since the days when arc projection systems were used in an effort to duplicate the solar radiation in our test facility. The development of the analytical tools that can now be brought to bear on the process has shifted the emphasis in thermal testing toward establishment of an accurately defined set of boundary conditions at the spacecraft interface to provide a basis for verification of its thermal control design and for fine tuning the analytical thermal model.

This trend has allowed flexibility in the selection of means for applying the solar input to the test article so that in many cases more manageable sources of thermal energy can be used to simulate solar heating.

Electrical ohmic heating of the solar exposed surfaces of a spacecraft has long been an attractive test heating method. However, earlier attempts to utilize this approach on thermal models were not entirely satisfactory since in these cases the heaters were installed on the inner surfaces of spacecraft panels in areas not otherwise occuppied by electronic components. The necessarily non-uniform heating resulted in unrealistic temperature gradients.

Recently at TRW, we had the opportunity to put into practice a different approach to ohmic heating wherein the heaters were applied to the external surfaces of the spacecraft panels. Since the outer surfaces are normally unobstructed, heating elements can be physically arranged to produce uniform heat distribution, and where lightweight honeycomb panels are concerned, solar heating can be simulated on the exterior surfaces of enclosure panels where it actually occurs.

For a spacecraft whose configuration is amenable to this heating technique, a host of test advantages can be realized. Some of these are:

- accurate heat input measurement
- uniform heat distribution
- wide intensity control range
- unlimited test article size
- elimination of spacecraft rotating fixtures
- elimination of heat source support fixtures
- unobstructed test article view of the cold shroud
- adaptability to automated control
- test-to-test repeatability
- less instrumentation, data reduction, and post-test analyses
- less in-chamber set-up time
- less power consumption
- less capital investment

The candidate for the initial application of this test method at TRW was a spacecraft equipment compartment whose enclosing sides consisted almost entirely of radiating panels covered by second-surface glass mirrors (see Figure 1). The project test program included a thermal/vacuum test of a full-scale detailed thermal model and thermal/vacuum acceptance tests of the flight spacecraft. To preserve correspondence between these tests, it was desired that the heating method employed be equally applicable to the flight units and the thermal model. This meant that if the external surface ohmic heating method were to be employed, heaters would have to be applied to the sensitive mirror covered surface of the flight radiators.

Of obvious concern in this case was the potential for mechanical damage to the flight surfaces by heater operation as well as by the physical installation and removal of the heaters. Concerns were raised about contamination of the flight mirrors by the heater adhesive and the potential for accelerated space degradation of the radiators by nonremoved contaminants. Additional concerns were expressed about the efficiency of heaters installed on glass surfaces, as well as about the radiant emittance mismatch between the two.

SAMPLE PANEL TESTS

In an effort to answer these and other questions, a number of exploratory tests were conducted with sample panels ranging in size from about 0.09 to 0.18 m^2 (1-2 ft^2). These were constructed of either 0.31 cm (.125 in.) thick solid aluminum sheet or 2.5 cm (1 in.) thick lightweight aluminum honeycomb with thin aluminum facesheets on which 4 x 4.3 x 0.015 cm (1.6 x 1.7 x .006 in.) fused quartz second-surface mirror slips were bonded to one surface. Four filament, self-adhesive, 1.27 cm (0.5 in.) wide commercially available heating tape was applied over the center of each row of mirrors across the panel in a serpentine arrangement as shown in Figure 2. After being instrumented with thermocouples, the panels were insulated with a multi-layer insulation blanket which covered the rear surface and the edges of the panel.

A total of eight such test panels were eventually assembled and these were subjected to about two dozen different tests or test conditions in a vacuum cold wall environment to evaluate various aspects of the proposed heating method.

Our findings and conclusions from these tests are briefly summarized and discussed under the various topics which dealt with our principal concerns about the test heating method.

SAMPLE PANEL TEST RESULTS

MECHANICAL DAMAGE TO MIRRORS

With but one exception, none of the mirrors on our various test panels suffered any form of cracking, chipping, or debonding as a consequence of the tape application or removal. Panels were driven by means of their heaters to temperatures ranging from -34°C to 66°C (-30°F to 150°F) and at applied power densities of 140 to 538 w/m^2 (13 to 50 w/ft^2) without detrimental effect. Some test panels underwent tape installation and removal several times without being damaged.

The one exception occurred when a panel was over driven to 86°C (188°F); in this case, 9 of the 70 mirrors on the panel exhibited small hairline cracks. This inadvertently confirmed predictions that mirror cracking could be expected at panel temperatures in excess of 66°C to 71°C (150°F to 160°F) due to differential expansion for mirrors bonded to aluminum substrates.

The silicone pressure-sensitive adhesive with which the tape is normally supplied was found to have the desired degree of agressiveness to produce a bond firm enough to hold the tape in place, but yet permit the heater to be stripped from the test surface with ease. There was no evidence that the adhesive either cured or softened during extended use at the temperatures with which we were concerned.

TAPE ADHESIVE RESIDUES AND MIRROR CONTAMINATION

Examination of test panel mirror surfaces after exposure to tape heating in vacuum disclosed no visible residues. Spectral reflectance measurements of exposed samples indicated that the post-test reflectances of uncleaned mirrors were generally within 1% of new clean reference specimens. The conclusion was that any residues left by the tape application could not be effectively detected by spectral reflectance measurements.

Additional panels which had also undergone tape heating exposure in vacuum were examined to determine the amount and species of non-visible mirror contaminants. Here, the measurements were made prior to and after solvent cleaning and it was found in many cases that the contamination was actually increased by the cleaning attempt. At that time, the recommended cleaning procedure involved wiping the radiator surface first with toluene then with isopropyl alcohol. It was determined that toluene from the first wiping entered the gaps between mirror slips where it dissolved some of the mirror bonding RTV so that the succeeding alcohol wipe simply smeared this solution over the mirror surface where the contaminants remained. This was solved by first applying a wet alcohol wipe to permit the alcohol to fill the mirror gaps and thereby buffer the RTV from the subsequent toluene wiping. The idea was to immediately follow the alcohol first wipe with the toluene wipe before the alcohol evaporated. This procedure was thereafter followed with consistently good results. For example, where contaminants prior to solvent cleaning amounted to 13.34 milligrams/m^2 (1.24 mg/ft^2), the post-cleaning amount was 1.29 mg/m^2 (0.12 mg/ft^2). Infra-red analyses indicated in all cases that the surface contaminant was methyl phenyl silicone.

SPACE STABILITY OF EXPOSED MIRRORS

Single mirror witness samples which had experienced tape heating exposure at 66°C (150°F) for 360 ks (100 hours) in vacuum were subjected to accelerated far ultraviolet (FUV) radiation exposure in both uncleaned and solvent cleaned conditions. The purpose was to determine to what extent, if any, nonremoved mirror contaminants would affect in-space degradation of the flight radiators. It was found that the increase in solar absorptance for an uncleaned specimen was 0.04 after FUV irradiation equivalent to 31 x 10^6 sec (6.4 years) of solar exposure, while for a solvent cleaned specimen, the increase was 0.02 in solar abosrptance for the same exposure. It was concluded that changes in solar absorptance of 0.02 were not significant in view of the predicted change of 0.10 over the normal lifetime of mirrors in space.

TAPE HEATING EFFICIENCY

It was feared that if the heater tape temperature were significantly higher than that of the surrounding radiator surface, radiative losses from the tape surface would reduce the accuracy of the determination of the heat input to the test article surface. In other words, if the tape heating efficiency were low, measurement of the power applied to the heater would not accurately reflect the power applied to the test surface. The effective efficiency of the tape was determined by comparing measured input power (i^2R) with panel radiated power ($\varepsilon\sigma T^4$) determined from its surface temperature at thermal balance. Over a range of input power densities from 147 to 525 w/m^2 (13.7 to 48.8 w/ft^2) it was found that at least 98% of the applied heater power could be accounted for by the temperature of the test panel at thermal equilibrium. This meant that determination of the heat input to the test spacecraft surface within ±1% could be made by simply measuring the power dissipation of the surface heater.

PANEL TEMPERATURE GRADIENTS

Initial tests of sample radiator panels consisting of 0.31 cm (.125 in.) thick solid aluminum substrates showed that maximum temperature differences across the panels did not exceed 2°C for applied heating rates of up to 540 w/m^2 (50 w/ft^2). However, it was expected that worst case temperature gradients would occur for tape heated mirrors mounted on the thin facesheets of typical flight type honeycomb panels. To evaluate this, sample radiator panels were constructed of 2.5 cm (1 in.) thick aluminum honeycomb cores with 0.038 cm (0.015 in.) thick aluminum facesheets. Fine wire thermocouples measured the temperature of the heating tape and of the mirror surfaces adjacent to the tape and midway between tape strips. The rear surfaces of these test panels were equipped with heaters to simulate electronic component heat addition at the interior surface of the radiator.

With solar heating only, at a power density of 237 w/m^2 (22 w/ft^2), equivalent to 1 solar constant at end-of-life mirror properties, the average temperature difference across the mirror surface was 1°C and the average tape temperature exceeded the mirror surface temperature by 2°C (3.6°F). For the more realistic case of solar input to the front surface, again at 237 w/m^2 (22 w/ft^2), and an electronic component heat input of 335 w/m^2 (33 w/ft^2) to the rear surface, the average temperature difference across the mirrors was 0.5°C (0.9°F) while the average tape to mirror difference was 1.4°C (2.6°F).

These results provided the basis for further evaluation of the heating efficiency of the heater tape installation. For example, at a panel average temperature of 52°C (125.6°F), which resulted from the two surface heat addition previously mentioned, the tape radiated energy at a rate 1.5% higher than did the surrounding mirror surface due to its 1.4°C (2.6°F) higher temperature. But since the tape typically occuppied 31% of the total radiating area, the unaccounted for loss from the radiator amounted to only 31% x 1.5% or 0.46% of the total power applied. Thus, the heating efficiency of the tape at maximum power dissipation for simulating the solar input to an earth orbiting spacecraft was determined to be at least 99%.

On the basis of the positive results from the exploratory test program, it was concluded that the proposed heating method would provide a realistic and accurate test means for simulating the solar input to the spacecraft and that the condition of the flight models would not be compromised by its use. A decision was, therefore, made to utilize the heating method for the full-scale spacecraft tests.

SPACECRAFT THERMAL MODEL INSTALLATION

The environmental heating system for the full-sized test article consisted of tape heaters on ten spacecraft radiators as well as heaters on several attachment interface boundaries. On nine of the ten radiators of the thermal model, the mirrors were simulated by other materials. The tenth radiator (Figure 3) consisted of a mirror-surfaced flight quality panel supplied for further evaluation of the heating tape applied to mirror surfaces under actual test conditions.

To improve the operational reliability of the system, the panel heaters were provided with redundant counterparts. This was accomplished by utilizing two of the four filaments of the tape for the primary heater set and the remaining two for the redundant set. Since both heaters, therefore, had the same resistance and occuppied the same area, no adjustment to the control system would be necessary in the event that a switchover were required.

As normally supplied, the heater tape has an aluminum foil outer surface with an emittance of 0.15. In our early developmental tests, this foil was removed to expose a fiberglass fabric insulating layer with an emittance of 0.88 to better match the 0.79 emittance of the mirrors. The effective emittance of the test panel radiators with tape applied was then determined on the basis of the fraction of the total area occuppied by the tape and by the mirrors. The prospect, however, of having to eventaully remove the aluminum foil from long lengths of tape prompted arrangements with the manufacturer to supply the tape with a surface emittance better suited for our application. This was provided by the application of a 2 mil thick aluminized Kapton outer layer to the standard heater tape which produced a tape emittance of .77 - .78 closely matching the emittance of the flight radiator fused quartz second-surface mirrors.

Approximately 250 m (820 ft) of tape was required to heat the exposed areas of the spacecraft. This required completing approximately 130 individual heater filament wire electrical terminations to connect the system.

In over 1300 ks (360 hours) of continuous operation, at hard vacuum during the thermal model environmental test, no difficulty of any sort was experienced with the heating system nor were the redundant heaters called into operation.

Careful post-test inspection of the entire heater installation disclosed no tape debonding and no mirror damage on the flight quality radiator panel.

SPACECRAFT FLIGHT MODEL INSTALLATION

The flight model spacecraft was identical to the thermal model except of course that all radiating areas were covered with mirrors. For the flight model test, a slight change was made in the taping configuration to improve its solar heating simulation and better adapt the installation to the requirements of the flight spacecraft. Where previously the folded-over sections of the heater tape between mirror rows were located just outside of the radiating area under the insulation blanket, they were now located just inboard of the insulation cutout within the exposed area of the radiator as shown in Figure 2. This modification improved the correspondence between the tape and solar heated areas of the radiator and required lifting only a small section of the flight insulation blanket for post-test removal of the heater installation.

As a precaution against possible outgassing, the heater tape, prior to its application on the flight hardware was conditioned by self-heating the tape rolls at 80°C (176°F) for 86 ks (24 hrs) in vacuum.

Again for 1300 ks (360 hours), as it had for the thermal model test, the tape heating system functioned without incident or use of its redundant heaters during the flight model thermal vacuum acceptance test.

Post-test inspection of the tape installation disclosed no damaged mirrors and no visible deposition on the radiator surfaces.

HEATER CONTROL

One of the advantages of the ohmic heating method is its ready adaptability to automated test control. Control parameters can be either surface temperature or applied power, both of which can be simply and accurately measured by direct means. For our full-scale spacecraft thermal vacuum tests, the environmental heaters were operated by means of a computer-automated system which controlled power to the individual panel heaters as a function of either constant or time varying panel temperature or applied power. Software was developed which permitted the heaters to be programmed to operate in accordance with any desired power application profile so that the same on-orbit diurnal solar heating curves used by the thermal designers could be precisely duplicated by the environmental heaters during the test.

Briefly described, the control system consisted of a desktop computer and multiprogrammer to control resistance-programmed DC power supplies. Feedback control data from either thermocouples mounted on the radiator panels or current shunts in the heater power circuits were handled by a scanner and digital voltmeter. Switchgear was incorporated in the system to permit the heaters to be manually controlled, if necessary.

RECOMMENDATION FOR THE FUTURE

The heating tape used in implementing this test method is a readily available commercial product not specifically designed for this application. In further development of the heating technique for spacecraft test applications, some attention might be directed toward developing heating tape with lower outgassing characteristics, especially for applications involving test articles with exposed optical elements. Such a heating tape might conceivably consist of filament wires encapsulated between two Kapton film strips bonded with acrylic based adhesives. This would result in a somewhat more pliable tape construction. A further improvement would be to have the tape supplied with unvarnished filament wires which would preclude having to painstakingly scrape off the tenacious polyimide varnish with which the present material is supplied. It is estimated that this feature alone could reduce tape heater installation labor by 25 to 30%.

CONCLUDING REMARKS

The tape heating method has proven to be an accurate, controllable, and cost effective means for simulating solar heating in spacecraft environmental testing. Its reliability has been demonstrated in at least two major spacecraft long duration thermal vacuum tests. It is and will continue to be a practical alternative to radiant heating methods in space simulation testing.

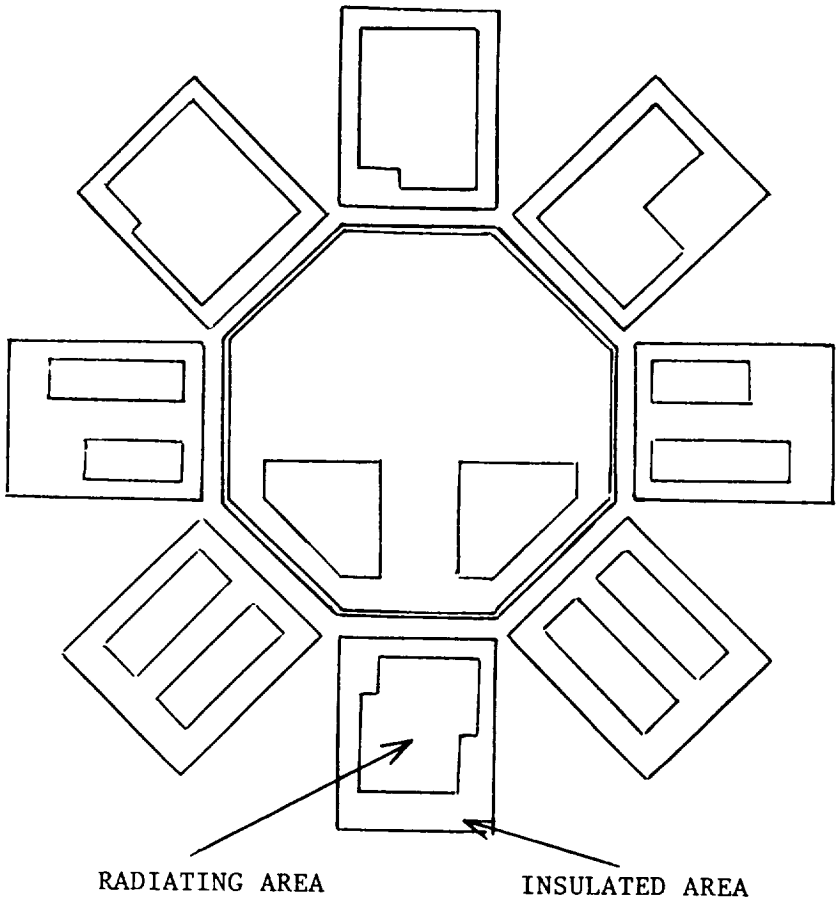

Figure 1 - Top View of Spacecraft Equipment Compartment with Side Panels Folded up to Show Radiators

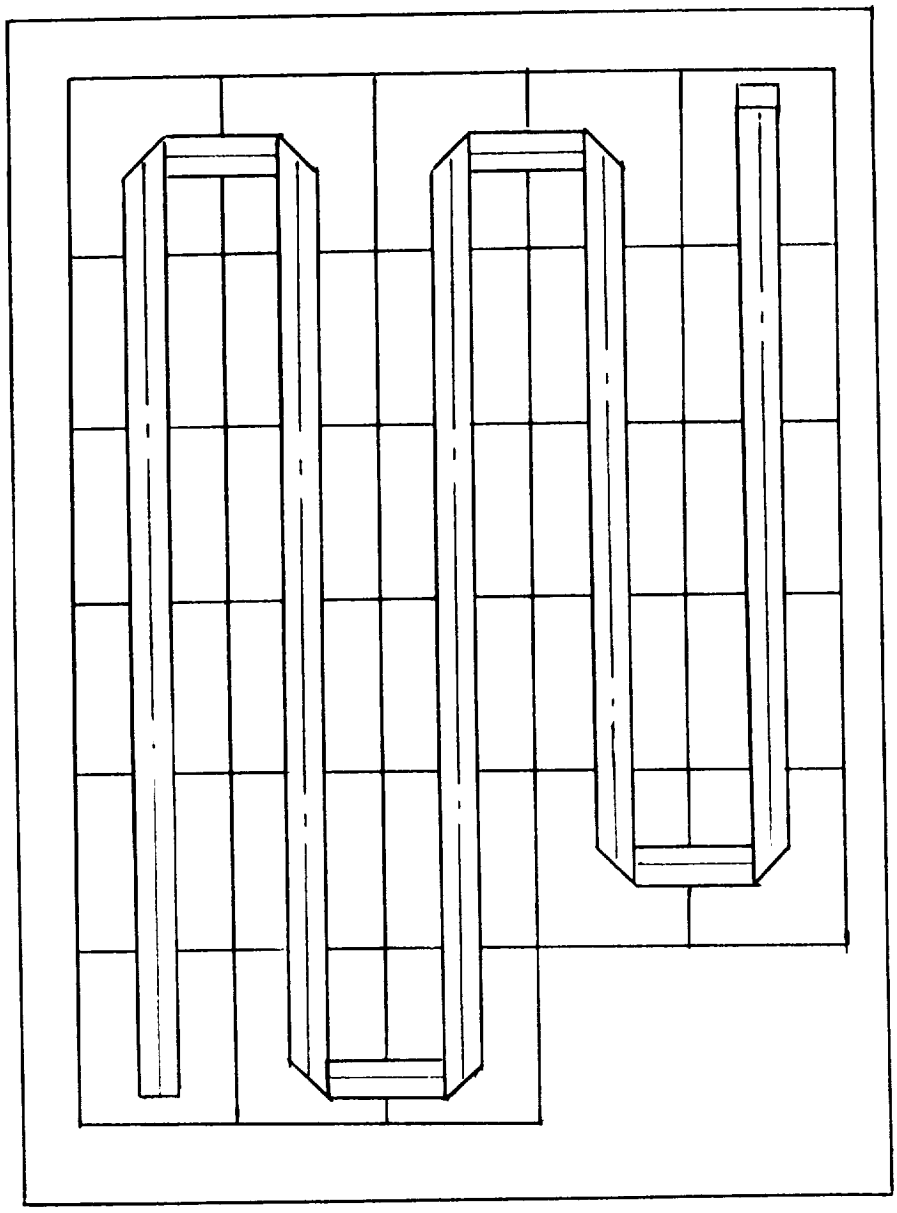

Figure 2 - Radiator Panel with Typical Tape Heater Arrangement

Figure 3 - Flight Spacecraft Radiator Panel with Heater Tape Applied Over Mirror Surface

THE ROLE OF THE SHUTTLE ENGINEERING SIMULATOR IN THE SOLAR MAX RESCUE MISSION

Robert H. St. John
NASA Johnson Space Center

Bernd Strassner
Lockheed Engineering and Management Services Co., Inc.

ABSTRACT

The Shuttle Engineering Simulator (SES) is a real-time, man-in-the-loop simulation of the Space Shuttle ascent, on-orbit and entry mission phases. It is a fixed base simulator with instrumented forward and aft flight decks which include computer generated representation of the out-the-window visuals and CCTV system. The simulation contains high fidelity math models of the Shuttle guidance, navigation and control (GN&C) sensor and effector subsystems, vehicle dynamics and flight environment, and a functional representation of the Orbiter GN&C flight software and CRT displays. The SES was used in the Shuttle Program as a development tool for the man/machine related design evaluation activities and has more recently been used to develop flight techniques and mission unique flight procedures. It has also been used as a part task crew training facility for rendezvous, proximity operations, Remote Manipulator System (RMS) operations and Manned Maneuvering Unit (MMU) operations.

The Solar Max repair mission (STS 41-C) presented several unique challenges which are firsts for the Shuttle program. STS 41-C exercised for the first time the complex Shuttle GN&C flight software to perform a rendezvous with the Solar Max satellite. The MMU activities on flight day 3 represented the first real use of the MMU as a tool of the Shuttle program. Finally, the STS 41-C mission marked the first time the Shuttle was used as a satellite service vehicle.

The SES played a significant role in the preparations for this mission. The SES on-orbit simulation provided the capability to perform continuous end-to-end operations of the flight day 3 activities including rendezvous, proximity operations, MMU operations and RMS capture of the satellite. The three-body capability (Orbiter, MMU, free-flying target) provided by the SES is unique to the Shuttle Program, allowing the Orbiter and MMU to operate independently but in full view and voice contact of one another while performing the complex satellite retrieval.

This paper will present background information concerning the makeup of the SES, the role it traditionally plays in support of the Shuttle Program, its capabilities and the specific work performed on the simulator during the sixteen months preceeding the Solar Max repair mission.

SES ROLE IN THE SHUTTLE PROGRAM

Engineering simulation, specifically real-time man-in-the-loop simulation, provides an important tool for the development of manned spacecraft. It provides the environment in which the designers can evaluate the man/machine interfaces during each step of the development process. The Shuttle Engineering Simulator, located at the NASA Johnson Space Center in Houston, Texas, grew out of an engineering simulation facility which was built in the early 1960's to support the Mercury, Gemini and Apollo programs. Shuttle work on the simulator was initiated in the fall of 1969 to perform conceptual evaluation studies associated with the landing of the unpowered Orbiter. Subsequently, many conceptual level design studies were performed which looked at the various proposed Orbiter and launch vehicle configurations. As the design concept solidified, the SES evolved into a three mission phase simulation facility to support the ongoing design process. Simulations were developed for powered flight phases (ascent and powered aborts), unpowered flight phases (entry, landing and the unpowered portion of aborts) and on-orbit operations. The simulator was used throughout the design phase and continues to be used as a design evaluation tool to support postflight design changes and mission unique requirements.

A natural and expected evolution in the role of the SES has taken place as the Shuttle program has transitioned from development to operations. The design evaluation workload has been replaced to a large extent by flight techniques design and mission specific flight procedures development activities. Ascent/abort work has virtually disappeared although the capability is maintained on the simulator, and the entry workload is gearing down. The on-orbit simulation workload has increased more than enough, primarily in support of Shuttle operations, to keep the facility busy ten shifts per week.

SES DESCRIPTION

The SES is a fixed base simulator which is comprised of a large, dedicated computing facility, instrumented Orbiter forward and aft flight decks and a Manned Maneuvering Unit (MMU) crew station. Computer-generated visuals are mounted at the windows of the Orbiter flight decks and at the MMU crew station to provide realistic in-flight visual cues. A functional block diagram showing the laboratory configuration is shown in Figure 1. The Orbiter forward and aft flight decks are physically separated and the computer facility is partitioned such that on-orbit simulations (aft flight deck/MMU) can be run in parallel with either entry or ascent simulations (forward flight deck). The STS 41-C mission support provided in the SES consisted entirely of on-orbit simulation activities; therefore, only that simulation configuration is addressed in detail.

ON-ORBIT SIMULATION DESCRIPTION

The SES on-orbit simulation configuration is pictured in Figure 2. It is a high fidelity math model simulation of the Orbiter, a free-flying payload or target and the MMU. The math model simulation is limited to functions directly related to the dynamics of flight. In other words, no attention is given to Orbiter systems management functions or subsystems not related to the guidance, navigation or flight control onboard systems. Table 1 lists all Orbiter, target, MMU and flight environment related math models contained in the simulation.

The onboard flight software is functionally represented on the SES laboratory computing system. This is unlike other JSC facilities, specifically the Shuttle Mission Simulator training facility and the Shuttle Avionics Integration Laboratory, which use flight computers with flight software loads as part of their flight simulation configuration. The use of functional onboard software allows the SES to simulate a specific mission configuration well in advance of the flight software release for that mission. It also facilitates the ongoing design evaluation tasks involved with proposed changes to the flight software. Similarly, the onboard CRT displays are functionally represented in the SES. The CRT displays available in the SES crew stations are limited to those related to the dynamics of flight.

The SES aft flight deck and MMU crew station are fully instrumented and accurately driven by the simulation. The Orbiter flight deck, pictured in Figure 3, consists of an Orbiter pilot station on the left and an RMS station on the right. Visuals are located overhead of both stations, looking aft from the RMS station and on the two closed circuit television (CCTV) monitors at the RMS station. These provide a high fidelity representation of the environment outside the orbiter flight deck. The onboard camera systems located in the payload bay and on the RMS are accurately modelled, including the camera/CCTV selection available to the crew at the aft flight deck. The pan/tilt/zoom features of the cameras are modelled. All display and control functions necessary to pilot the Orbiter and operate the RMS are provided.

The MMU crew station shown in Figures 4 and 5 is, like the Orbiter flight deck, a fixed-base mockup utilizing the computer-generated visuals to provide motion cues relative to the external environment. The MMU mockup is located in a room which is darkened during operations to provide the pilot with a more realistic flight environment. During simulation operations, the pilot is situated in close proximity (approximately 18 inches) to a visual display consisting of a high resolution color monitor mounted above a columnating optics unit which projects a 37^{o} vertical by 48^{o} horizontal scene focused at infinity. The pilot's field of view is the limiting factor in the obtainable realism in the simulation of MMU operations. The real-world helmet provides the MMU pilot with a 120^{o} x 135^{o} field of view, approximately nine times greater than that achievable in the SES. To partially compensate for this deficiency, a field of view select box (Figure 6) was developed for the simulation which allows the pilot to select in real

time any 37^{o} x 48^{o} window which would normally be available through the helmet. This is accomplished on the visual by rotating the computed eyepoint (but not the display) for presentation at the mockup.

An electronic scene generation system provides the computer-generated visuals at the Orbiter aft flight deck and MMU crew station. The system is limited in both the number of eyepoints (channels) available at any time and by the amount of detail which can be represented in the visuals.

Only two scene channels are available simultaneously. Real-time selection of driven eyepoints is available at the two crew stations so that the MMU visual and the five eyepoints in the aft flight deck (two overhead windows, one aft window and two CCTV monitors) effectively share the two channels on demand during simulation operations. The nominal configuration used during combined MMU/Orbiter operations would be one channel dedicated to the MMU and the other to the Orbiter.

The scene model developed for the Solar Max repair mission includes the Orbiter, the Solar Max satellite, the MMU and the earth. Because of the system limitations on the amount of modelling detail available for any scene load, high levels of detail were given to critical areas such as the MMU/Solar Max docking interface, the RMS and the Solar Max RMS grapple fixture. Less detail was provided on the Orbiter and the MMU. Pictures of the visuals are shown in Figures 7, 8 and 9.

ON-ORBIT SIMULATION CAPABILITIES

Prior to December 1982, the SES on-orbit simulation capabilities consisted of Orbiter/target proximity operations and RMS operations. In the spring of 1982, a requirement was introduced to develop rendezvous capability on the simulation in preparation for the Solar Max repair mission. The rendezvous capability was incorporated into the on-orbit simulation by December 1982, in time to support engineering analysis, flight techniques and procedures development activities associated with the rendezvous phase of the mission. In June 1983, the JSC training community requested that the MMU capability be added to the on-orbit simulation specifically to support the Solar Max repair mission activities. The MMU capability buildup was completed in December 1983, in time to provide training support for both the STS 41-B and the STS 41-C crews.

SES UNIQUE CAPABILITIES

The SES on-orbit simulation contains several unique features available nowhere else in the Suttle program. These features, in conjunction with the basic on-orbit capabilities proved invaluable during Solar Max mission preparations and during actual mission support. The SES provides the only comprehensive, three-body simulation available to the program. Continuous simulation capability exists to fly the full rendezvous profile, transition to proximity operations, fly the MMU from the Orbiter payload bay to a

docked configuration with the Solar Max and then fly the Orbiter to the MMU stabilized satellite to perform the RMS track and capture sequence. This three-body feature is unique to the program. MMU operations around the Orbiter and the satellite are performed in full view and voice contact of the simulated Orbiter. During the simulation runs, the Orbiter crew can practice the integrated activities associated with retrieving the satellite, including the MMU rescue maneuers in the event the MMU becomes disabled.

Another feature provided only in the SES is the dynamic effect of the Orbiter Reaction Control System (RCS) plume impingement on the satellite or on the MMU. This effect is very important and was required for both the proximity operations procedures development and crew training.

Other unique simulation features are the flexible dynamics RMS model and the high fidelity KU band radar model. The fidelity in the RMS model allowed realistic assessment of the Solar Max grapple task and the high fidelity radar model was required for both the rendezvous and proximity operations.

SOLAR MAX REPAIR MISSION OVERVIEW

The planned Solar Max repair mission activities which were simulated on the SES were to take place on flight day 3. A practice satellite rendezvous with a Shuttle deployed Integrated Rendezvous Test (IRT) satellite was aborted on STS 41-B when the IRT failed to inflate after deployment. Thus, the flight day 3 activities on STS 41-C were to begin with the first Shuttle rendezvous with a satellite. After the completion of the rendezvous maneuvers, the Orbiter was to stationkeep with the Solar Max at a range of 200 feet while the MMU flew over to the rotating satellite, matched rotational rates and docked to an existing trunnion pin using a specially built Trunnion Pin Attachment Device (TPAD) mounted on the MMU. In a docked configuration with a still rotating Solar Max, the MMU pilot would engage the MMU attitude control at the point when the RMS grapple fixture located on the Solar Max was in view of the Orbiter. The MMU attitude control would stabilize the Solar Max, halting all rotational rates. The Orbiter would then maneuver to the Solar Max to within the 30-foot reach envelop of the RMS. The RMS would then be used to capture the Solar Max and berth it in the cargo bay for repair. After repair and system checkout, the RMS would again be used (flight day 5) to deploy the satellite.

SES SUPPORT ACTIVITIES

Simulations on the SES supported every task described in the Solar Max repair overview. The activities for which the simulation was used included engineering analysis, flight techniques and procedures development and crew training.

The engineering analysis activities included work in the areas of rendezvous, RMS track and capture contingencies and fuel budget for mission

planning. Because this was the first rendezvous mission, a great deal of attention was given to insuring that the rendezvous would be successful, even under failure conditions. This activity was started in December 1983 when the rendezvous capability became available on the simulation and continued all the way until flight. The RMS analysis work was concerned with the contingency situation where the arm might be called upon to grapple a rotating Solar Max satellite. Integrated Orbiter/RMS activities looked at the achievability of this task including capture envelop constraints, maximum acceptable rates on the satellite and structural loading limits. Finally, a simulation product of the procedures development activity is the expected Orbiter propellant usage involved in nominal and dispersed mission scenarios. The data derived from the simulation activities was used to establish the Orbiter propellant budget and similarly mission rules regarding contingency procedures.

The flight techniques and procedures development activities were, in fact, an extension of work performed on the simulator and in flight for previous missions. Preparations began with the STS 7 flight in which the RMS deployed the SPAS-01 satellite, the Orbiter maneuvered around it and then retrieved it with the RMS. The STS 41-B mission was also a preparatory mission for the Solar Max repair mission as well as future satellite servicing missions. The MMU activities on STS 41-B were designed to preview the MMU/Solar Max activities and the aborted rendezvous test was also planned in preparation for the STS 41-C mission. Flight techniques and mission specific procedures were developed for all of the Orbiter/free-flying target activities using the SES. Techniques and procedures used to fly the MMU were developed at the Martin Marietta Space Operations Simulator facility in Denver, Colorado.

Techniques and procedures developed on the SES specifically for the Solar Max repair mission included rendezvous with and without sensor failures or navigation errors, final approach to the target under both nominal and failure conditions, MMU rescue procedures, RMS track and capture procedures under nominal and off-nominal conditions, RMS berthing and the Orbiter/MMU/Solar Max integrated procedures.

Crew training was performed on the SES for virtually all of the flight day 3 activities. The SES was used because of the capabilities which are unique in the facility; namely, the three-body capability, high fidelity RMS and radar math models and plume impingement math models.

MISSION SUPPORT ACTIVITIES

On Sunday, April 8, 1984, the Orbiter completed a successful rendezvous with the Solar Max satellite. With the Orbiter stationkeeping at approximately 200 feet from the Solar Max, the MMU pilot maneuvered from the Orbiter to the satellite, matched the nominal one degree per second spin rate at the target trunnion pin and proceeded to attempt to dock with the satellite. Docking attempts failed and the resulting situation left the satellite in a tumbling configuration and the Orbiter low on forward RCS propellant.

The SES had been in an on-line mission support role beginning at 2:00 a.m. on flight day 3. At noon, JSC personnel began using the simulation to develop a method of retrieving the Solar Max in light of all that had happened. Specific problems which were addressed beginning Sunday noon and running almost continuously until the retrieval was accomplished on Tuesday morning included:

a. The profile for the second rendezvous given the forward fuel problem.

b. Procedures to approach the satellite to reduce plume impingement effects as well as conserve forward fuel.

c. Assessment of the capability to capture a tumbling Solar Max satellite with the solar arrays left intact or jettisoned.

The Sunday problem became critical as the Goddard team was attempting to stabilize the satellite before the onboard batteries went dead. With the batteries dead, any rotatinal rates left on the satellite would remain for the attempt to capture the satellite with the RMS. The solar arrays being attached caused problems in the RMS capture scenario because they limited the reach envelop for the RMS. Furthermore, one array was situated in an area directly over the RMS grapple fixture, making the grapple task more difficult. The solar arrays could be jettisoned but only as long as battery power was available. A direct line was kept open between Mission Control and the SES on Sunday evening as Goddard slowly stabilized the Solar Max while the batteries continued to fail. Solar Max rotational rates were relayed to the SES where the simulation was initialized with the rates while flight crew attempted to fly the Orbiter to the satellite and capture it with the RMS. A parallel activity was performed by lab personnel to modify the simulation to remove the solar arrays. This involved removing the arrays from the visuals and changing the Orbiter/Solar Max plume impingement model. Tests were flown in this configuration with satellite rotational rates which included the effects of jettisoning the solar arrays. Fortunately, the satellite was stabilized completely before the batteries were lost and all systems returned to normal on the Solar Max prior to the actual retrieval.

With the satellite stabilized and the fuel problem critical but workable, the second rendezvous and retrieval with the RMS became a reasonable task. The satellite was spun up to the nominal one degree per second for the retrieval in order to insure that the satellite would place the RMS grapple fixture in a reachable orientation without unnecessary maneuvering of the Orbiter. The flight crew was able to maneuver the Orbiter to the Solar Max without perturbing it with the Orbiter plume and then capture the rotating Solar Max with the RMS. The crew had been trained on the SES to perform this scenario.

CONCLUDING REMARKS

The SES played a significant role in the preparations for the STS 41-C Solar Max repair mission and during the mission in the development of the plan and procedures to retrieve the satellite after the MMU docking attempts failed. The development of the on-orbit simulation capabilities required to support this mission was to a very large extent simply an expansion of the capabilities designed into the SES to support previous engineering simulation requirements for the Space Shuttle program. Generic capabilities which were implemented specifically to support this mission; namely, the Shuttle rendezvous capability and the Manned Maneuvering Unit, will be used to support other Shuttle missions which include similar operational requirements. A design goal in the SES is that the simulator be easily adaptable to any Shuttle mission configuration. This goal has apparently been achieved.

TABLE 1

ON-ORBIT MATH MODELS

Orbiter System
- 6 DOF earth centered equation of motion.
- Orbiter mass properties
- Atmospheric effects (drag, pitching moment)
- RCS plume impingement
- RCS and OMS propulsion systems
- Gravity and gravity gradient

Remote Manipulator
- Flexible arm dynamics
- Flexible arm geometry
- Joint servo models
- End effector models for capture transition
- Stow/deploy mdel
- Malfunction
- Joint loads

Sensors
- Rendezvous radar
- Inertial measurement unit (IMU)
- Star tracker
- Crew Optical Alignment Sight (COAS)

Target
- Physical characteristics and mass properties
- 6 DOF earth centered equations of motion
- Target plume impingement
- Atmospheric effects
- Payload control system

Manned Maneuvering Unit (MMU)
- MMU subsystems
  - control system
  - propulsion system
  - electrical system
- MMU dynamics (6 DOF relative equations of motion)
- Physical characteristics and mass properties
- Malfunctions

Relative State
- Coordinate transformation
- Orbiter/Target/MMU relative motion

TABLE 1

ON-ORBIT MATH MODELS

(continued)

Displays and Controls

- Aft crew station mockup
- MMU crew station
- Out-the-window displays
- Closed circuit TV
- Multifunction CRT display system

Orbiter Flight Software

- Flight software executive
- Orbit rendezvous/navigation
- Universal pointing
- Orbit targeting
- Orbit flight control
- Sequencers
- Interface software for displays, controls and sensors
- Keyboard processors
- RMS control systems

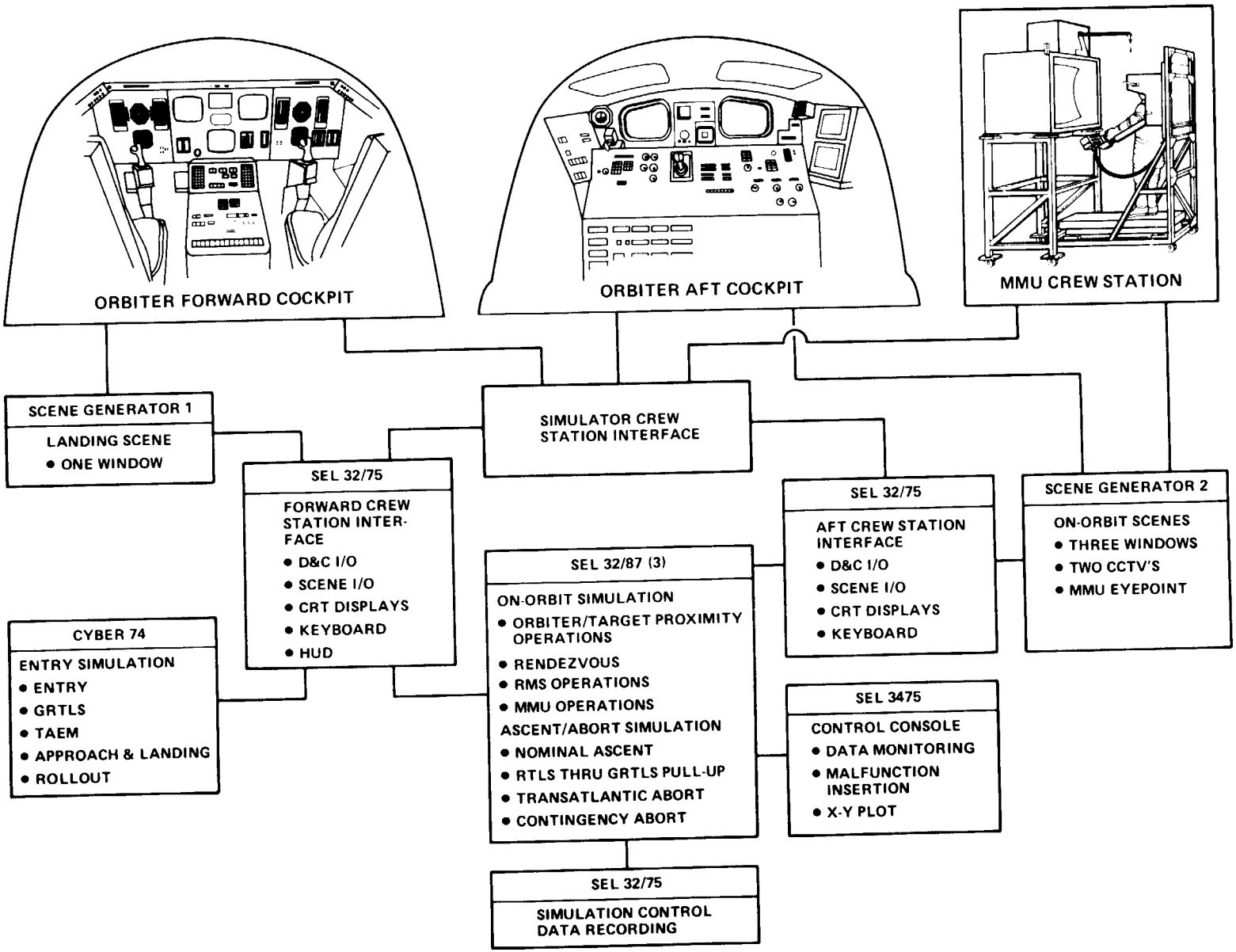

Figure 1 - SES Functional Block Diagram

SHUTTLE ENGINEERING SIMULATOR - ON-ORBIT

SES ON-ORBIT FEATURES

- THREE-BODY SIMULATION OF:
  - ORBITER
  - FREE-FLYING PAYLOAD
  - MANNED MANEUVERING UNIT
- ON-ORBIT OPERATIONS CAN INCLUDE ANY OR ALL OF THE FOLLOWING:
  - RENDEZVOUS
  - PROXIMITY OPERATIONS
  - PAYLOAD DEPLOYMENT AND RETRIEVAL WITH RMS
  - MMU OPERATIONS
- PAYLOAD MODELS DEVELOPED AS REQUIRED:
  - VISUALS
  - MASS PROPERTIES
  - PLUME IMPINGEMENT
  - AERO DRAG
  - RADAR SCATTER CHARACTERISTICS
  - CONTROL SYSTEM

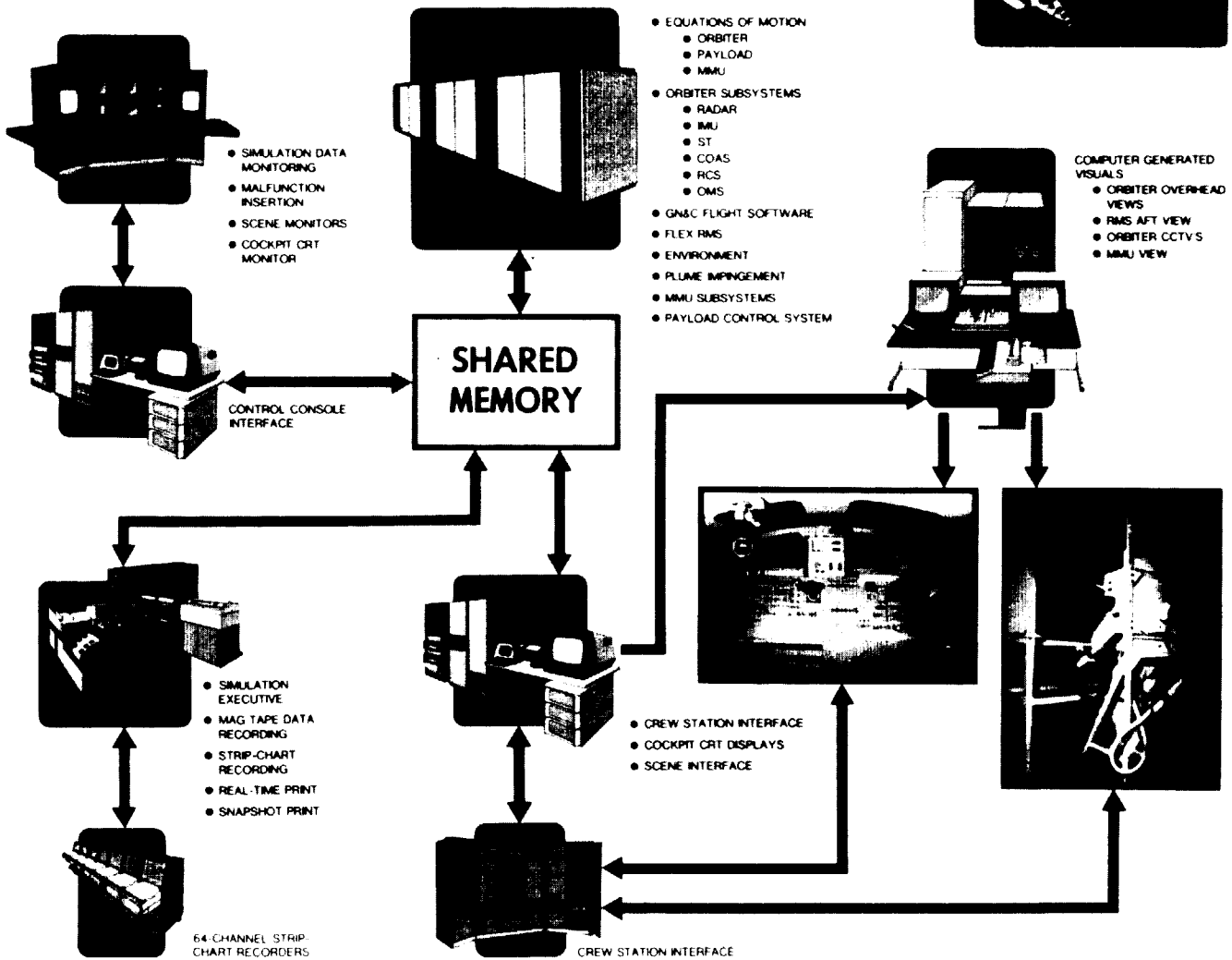

Figure 2 - SES On-Orbit Simulation Configuration

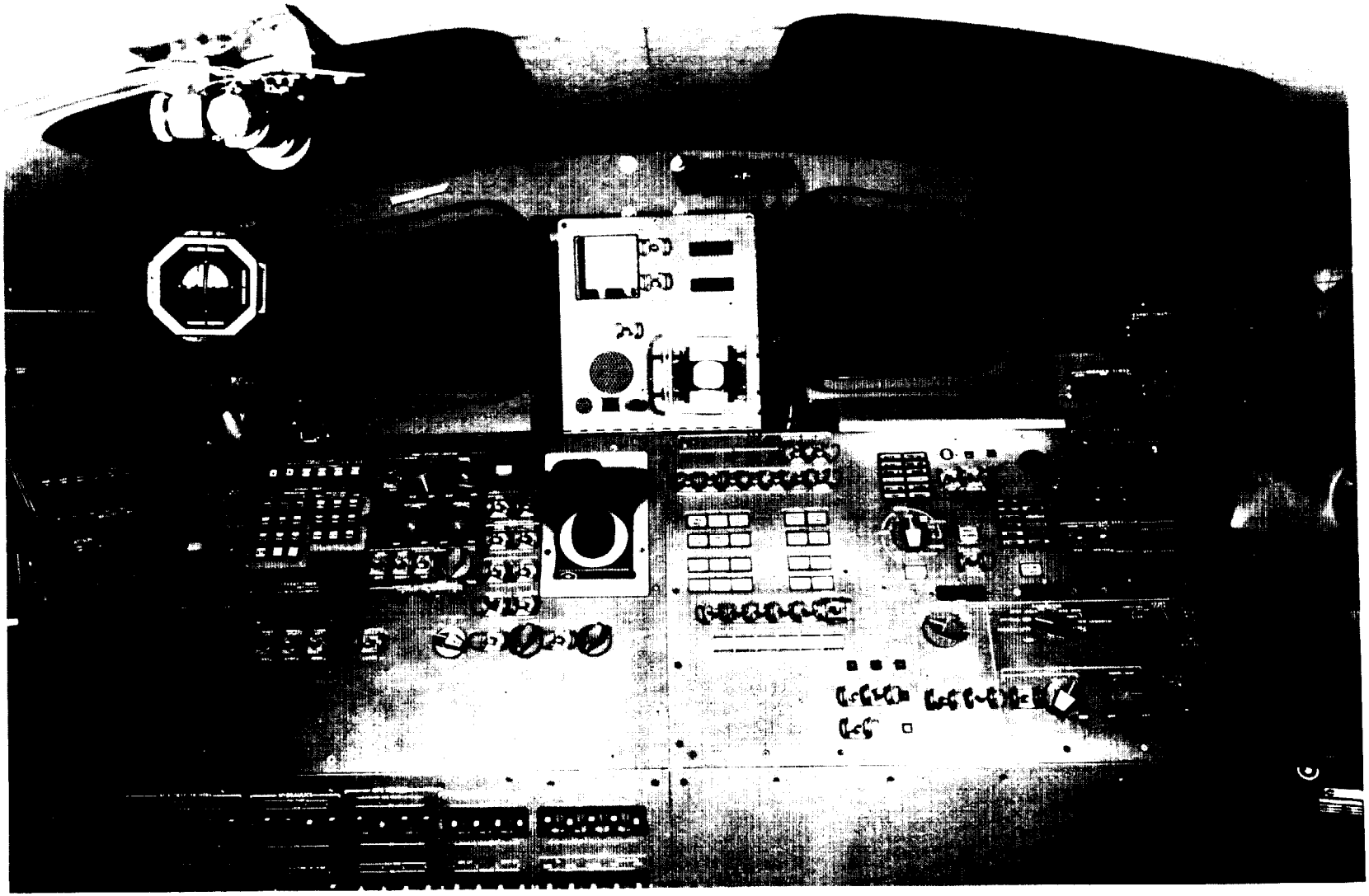

Figure 3 - SES AFT Orbiter Flight Deck

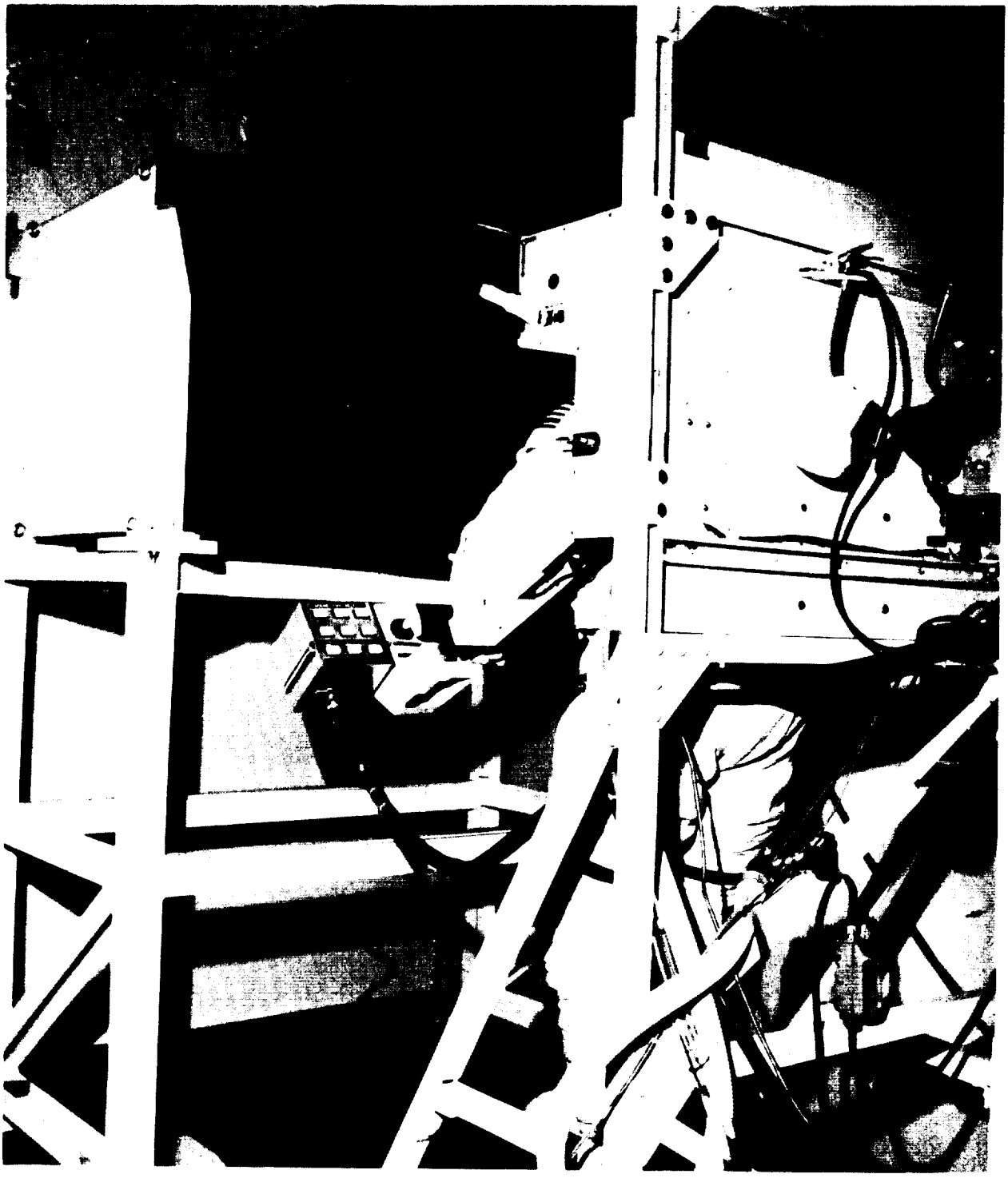

Figure 4 - SES MMU Crew Station

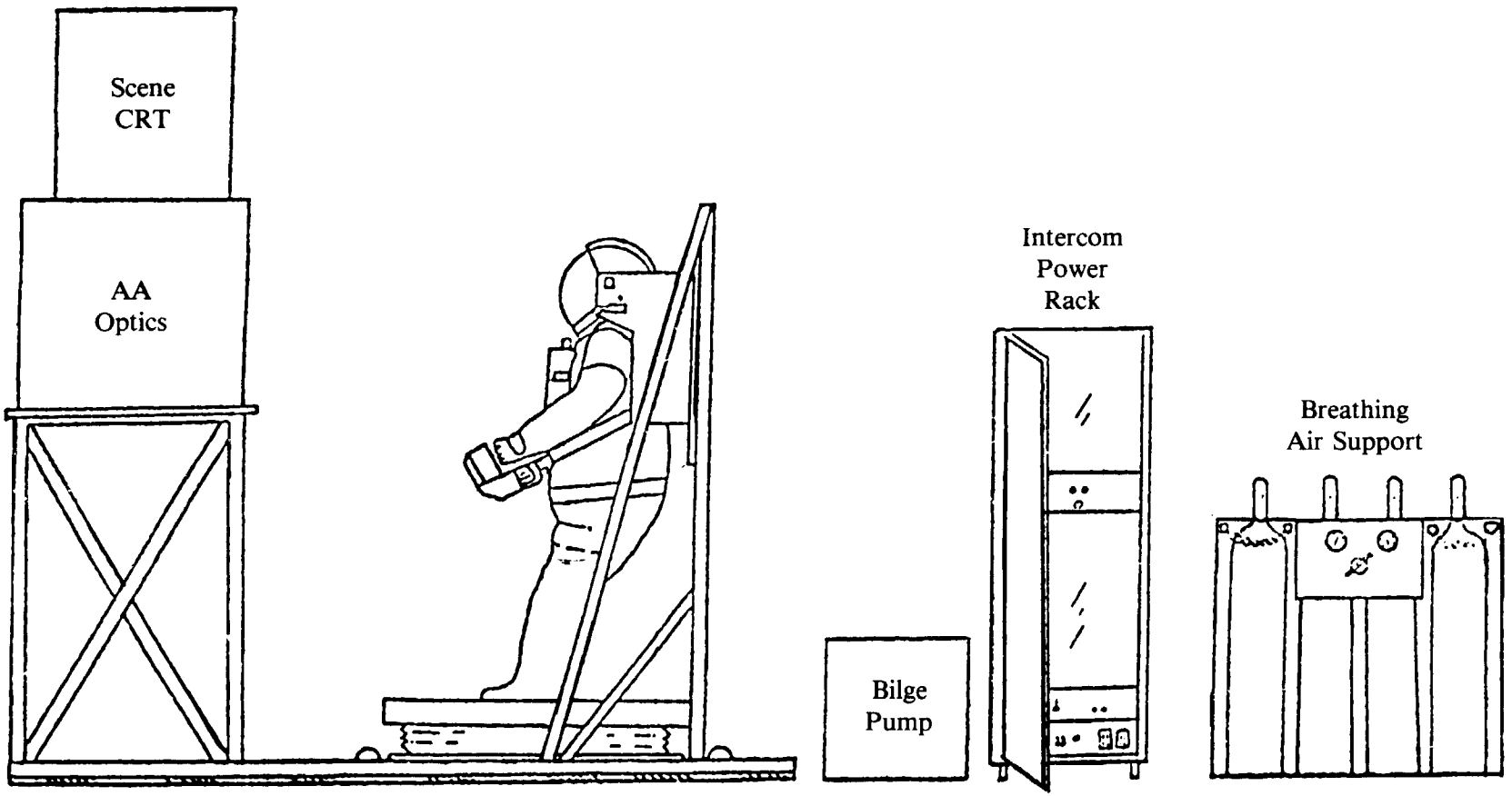

Figure 5 - SES Man-Maneuvering-Unit Mockup

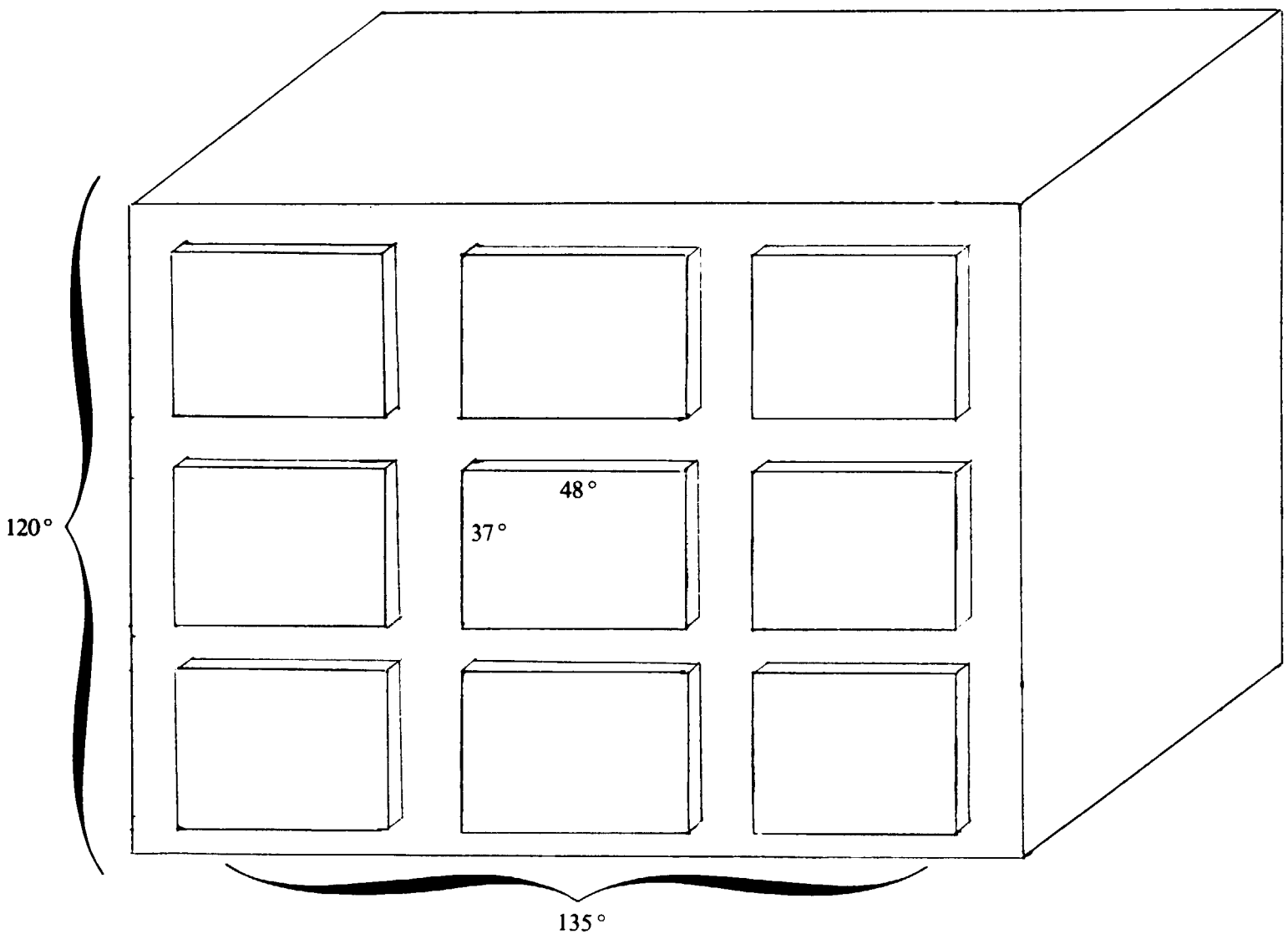

Figure 6 - Field of View Select Box

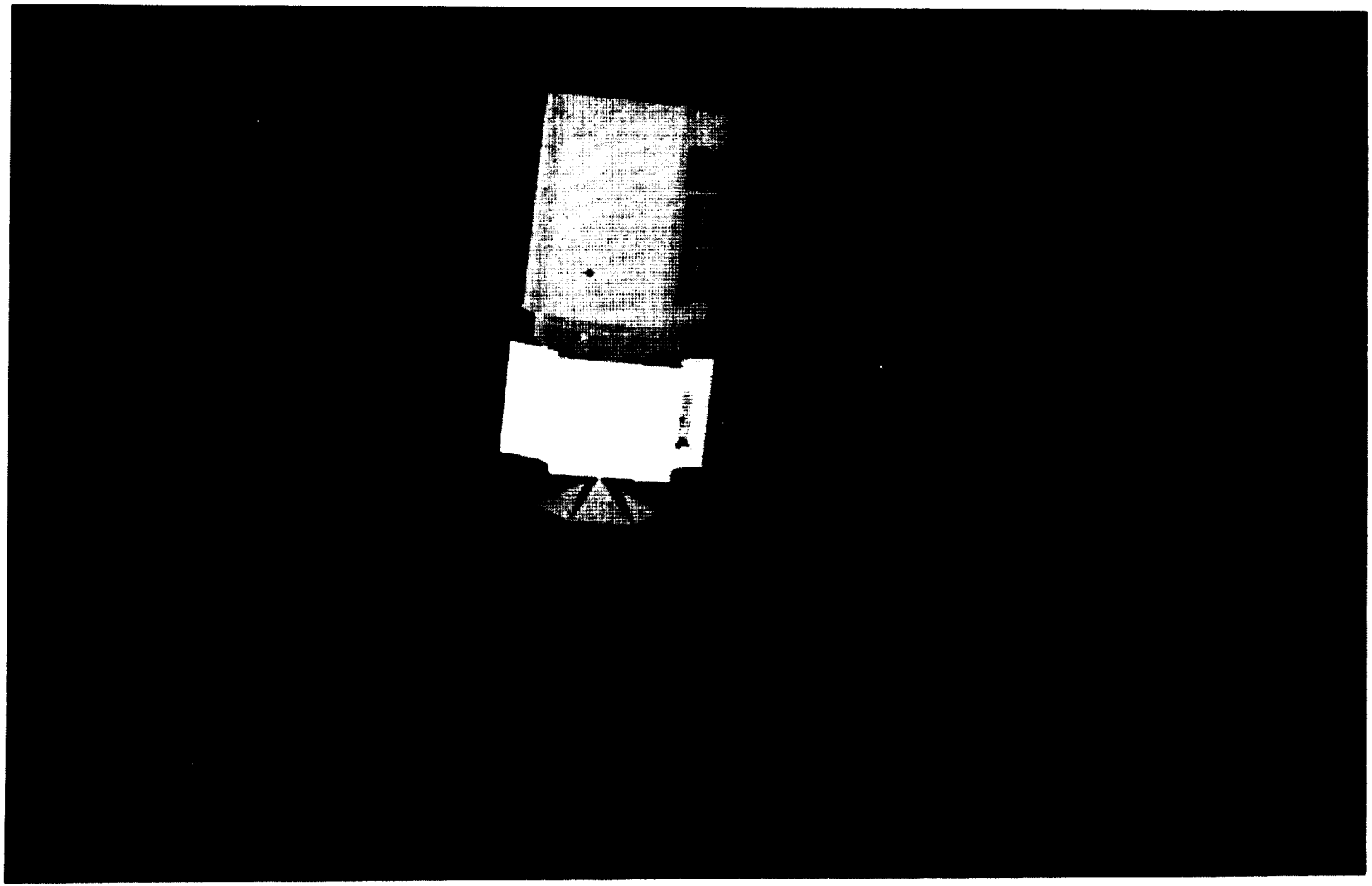

Figure 7 - MMU View of Solar Max

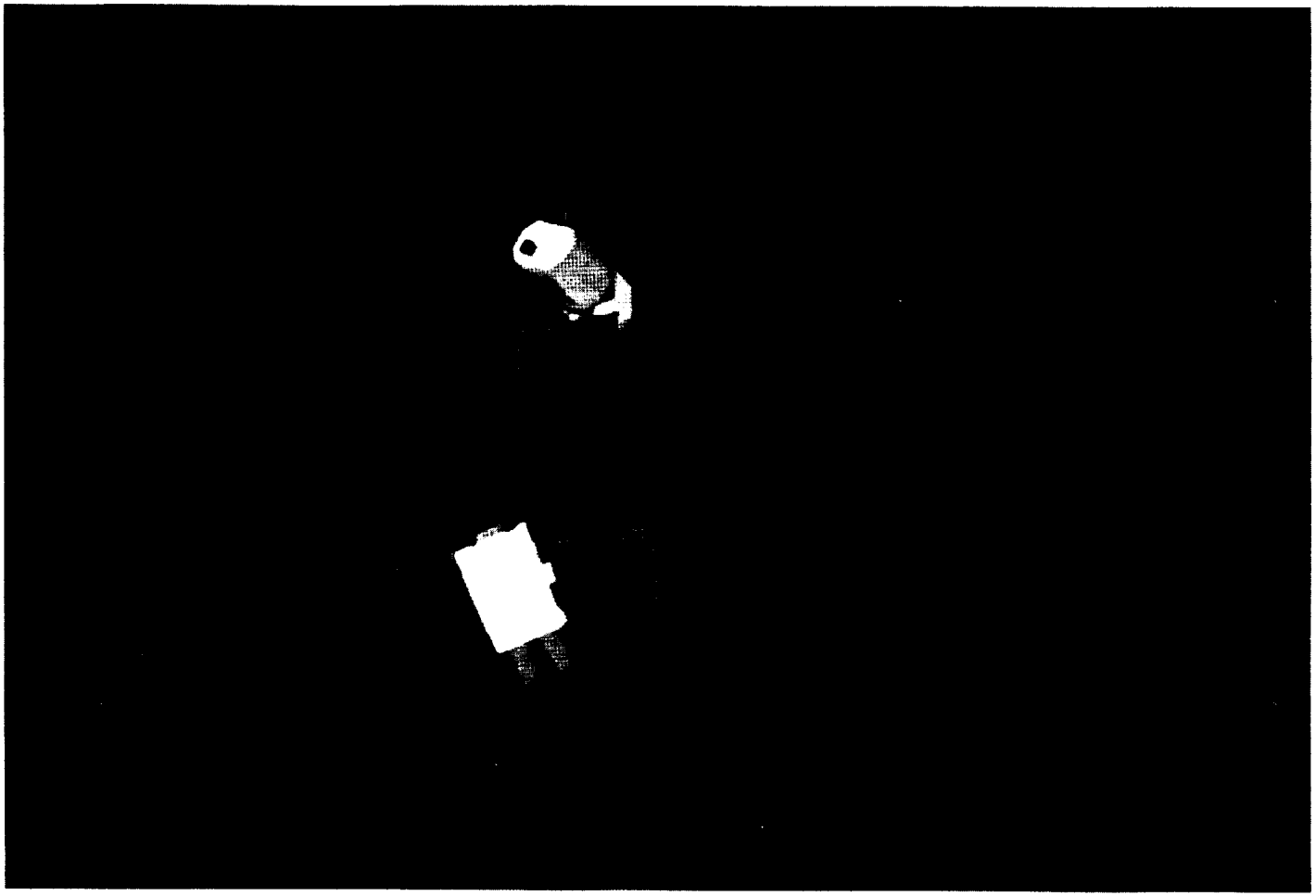

Figure 8 - Orbiter View of Solar Max and MMU

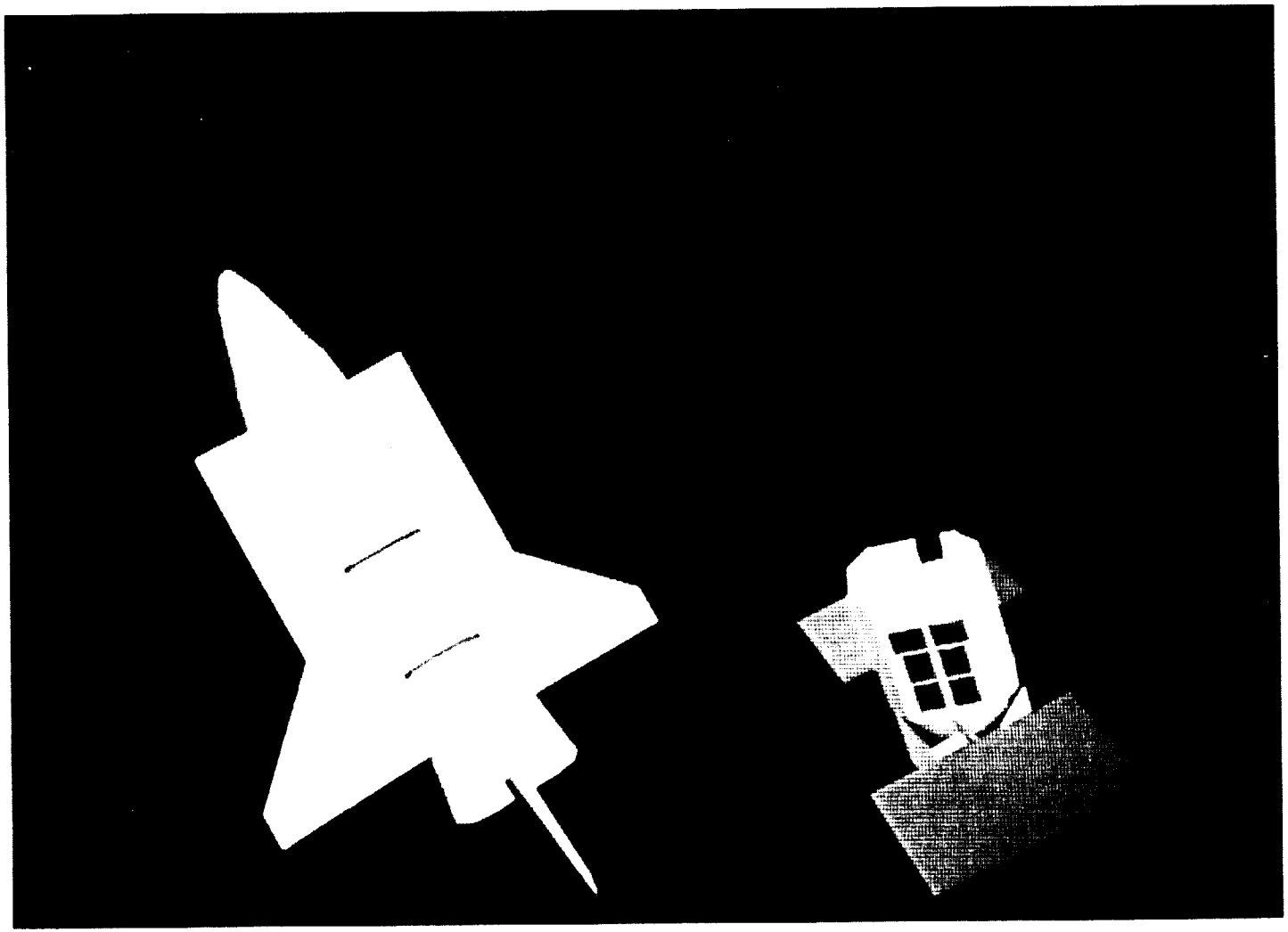

Figure 9 - MMU View of Orbiter and Solar Max

MANNED MANEUVERING UNIT SIMULATIONS ON THE SPACE OPERATIONS SIMULATOR

Craig Hartley, Dave Cwynar, and Lex Ray
Martin Marietta Aerospace
Denver, Colorado

ABSTRACT

The Manned Maneuvering Unit (MMU) built by the Martin Marietta Company is a self-contained, propulsive backpack that provides space-suited astronauts with six degree-of-freedom precision maneuvering capability to at least 150 meters (500 feet) from the Shuttle Orbiter. Martin Marietta trains astronauts to use the MMU in its Space Operations Simulator (SOS). MMU simulations in the SOS use two major devices. The first is a six-degree-of-freedom moving base carriage that allows the trainee freedom to fly the MMU in a large room and to match rates and dock with full-scale targets. The second device is a large-screen television display that provides the trainee with accurate views of tumbling targets from any point in a surrounding sphere up to 300 meters (1000 feet) in diameter. Astronauts used the SOS to train for the Solar Max repair mission and are now using it to train for a mission to recover the Palapa-B communications satellite. Subjective comparisons by astronauts of on-orbit MMU performance to simulated MMU performance in the SOS indicate that the simulations are very realistic. Data from the Solar Max mission have resulted in two software upgrades that increase SOS fidelity for the next MMU mission: a model of contact dynamics between the MMU and a target spacecraft, and a model of MMU plume impingement forces during docking. Success of recent MMU flights and NASA commitment to use the unit for the Palapa-B recovery suggest a busy future for MMU missions and simulations.

INTRODUCTION

In 1963 the Denver Aerospace Division of the Martin Marietta Company built a Space Operations Simulator (SOS) to conduct studies of rendezvous and docking for the Gemini program. The simulator was based on a large Moving Base Carriage (MBC) having six degrees of freedom (roll, pitch, yaw, up-down, left-right, and forward-backward). The carriage was subsequently man-rated in 1966 to enable simulations of Gemini astronaut Extra Vehicular Activity (EVA) using various experimental maneuvering systems. Since these early studies, the simulator laboratory has served as an important element in the systems development efforts for a succession of manned EVA devices including the Skylab M-509, T-020, and T-013 experiments and the current Manned Maneuvering Unit (MMU). For example, MMU design improvements made as a result of SOS simulations included reversed hand controller polarity for pitch and yaw, improved attitude hold circuitry, redesigned propellant isolation valve circuitry, relocation of power switches, addition of new control modes, and several modifications to thruster select logic. Most recently, procedures

development and training for NASA astronaut crews have been conducted in the SOS Lab to support the Solar Max Repair Mission (41-C) and a future mission to recover the Palapa-B communications satellite (51-A). This paper describes the features of the MMU, the Space Operations Simulator facility, how simulation is used to prove mission concepts and to train EVA astronauts to perform their tasks safely, how on-orbit data compare with simulation, and the future outlook for MMU missions and simulations.

MANNED MANEUVERING UNIT

The Manned Maneuvering Unit (MMU) is a self-contained, propulsive backpack that provides six-degree-of-freedom precision maneuvering capability to the shuttle astronaut. An astronaut equipped with a space suit, portable life support system, and the present version of the MMU can operate independently more than 150 meters (500 feet) from the orbiter. Future enhancements could allow the MMU to travel more than 1000 meters (3000 feet) from the orbiter. This improved capability could enable the MMU to support operations such as space telescope optics maintenance, which cannot be performed in close proximity to the orbiter because of potential contamination of satellite sensors by orbiter thruster plumes.

The MMU (Figure 1) uses clean, compressed gaseous nitrogen expelled from small (0.77 kg. (1.7 lb.)) thrusters to provide forces and moments for translational and rotational motions. The pilot commands these motions through two hand controllers, one for each type. The hand controllers generate electrical signals that are processed by two independent, redundant control electronics modules. When hand controller switch closures are detected, the control electronics refer to a table containing thruster select logic for that combination of switch closures. The control electronics then sends thruster firing commands to the appropriate thrusters. Table 1 lists the MMU performance characteristics for large and small space-suited astronauts. These values do not include any additional equipment that may be carried by the MMU to support a particular mission.

The MMU is comprised of four subsystems: electrical, propulsion, thermal control, and structures and mechanisms. The electrical subsystem includes switches to enable different control modes, propellant isolation valves, locator lights, power conditioning circuits, gyros, and the control electronics. Each of the MMU redundant electronic systems is powered internally by a dedicated silver zinc battery controlled by a main power switch.

Six-degree-of-freedom control authority is provided by the Control Electronics Assemblies (CEA) that process inputs from hand controllers and gyros. The control electronics module contains gyros, thruster select logic, valve and thruster drive amplifiers, and power supplies. The control electronics has two redundant circuits that are normally operated simultaneously. MMU flight is possible with only one operational circuit, although in this mode the translational control authority is halved in all three directions.

The MMU is also equipped with an inertial attitude hold function that is activated by a push button on the rotational hand controller. When activated, the attitude hold establishes and maintains all rotational MMU rates at a near zero value. When the rates have been nulled, the system enters a phase plane that maintains pointing to + or - 1.25 degrees in any axis in attitude hold. Attitude hold can be disengaged by either switching off gyro power or inputting a rotational command.

Two pilot selectable control modes were added to the MMU control system specifically to support the Solar Max repair mission. When the first mode, Axis Inhibit, is selected, the attitude hold function in one preselected axis is disabled. This allows the MMU pilot to use attitude hold in two rotational axes without disturbing a previously attained rotation rate in the third axis. For the Solar Max repair mission, the yaw axis was selected as the attitude hold inhibited axis so the MMU astronaut could set up a yaw rate to match the Solar Max rotation as he approached the target. This feature reduced the pilot workload by making rotational control constant thus allowing him to concentrate on translational control. The second mode, Satellite Stabilization, uses an alternate set of thruster select logic tables. This mode was designed to fire additional thrusters to compensate for the large mass of the Solar Max Satellite attached to the front of the MMU.

The MMU propulsion subsystem is divided into two redundant sides, each controlling twelve thrusters. Each side is fueled by a separate propellant tank capable of holding 5.3 kg. (11.6 lbs.) of gaseous nitrogen at 204 atm. (3000 psi) pressure. The two tanks are connected by manually operated crossfeed valves used to equalize the pressure in each tank. Isolation valves located downstream from each tank may be closed by the pilot to conserve propellant in the event of a leak in one system. The propulsion system is also equipped with two quick-disconnect fittings for recharging the propellant tanks from the orbiter systems. Illuminated analog gauges display tank pressures to the pilot.

A regulator reduces the pressure to the thrusters to approximately 13.6 atm. (200 psi), and a relief valve protects the thrusters from damage in the event of a regulator failure. The low pressure nitrogen is manifolded to four sets of three orthogonal thrusters for each redundant side. The twelve thrusters per side are physically placed so that thrust is balanced even if only one system is being used. Thruster firing for each side is indicated by a separate cue light mounted on an adjustable fiber optic rod extending from the MMU structure to a point in front of the astronaut's visor. The thrusters are solenoid operated by drive signals coming from the control electronics.

Finally, the thermal control subsystem consists of thermal coatings, multilayered insulation, thermal isolators, thermostats, and heaters for temperature control within the MMU. The lightweight aluminum structure gives the MMU a dry weight of approximately 150 kg. (330 lbs.). Special mechanisms include control arms that can be adjusted in length and also rotated downward from the flight position to a stowed position. The stowed position provides the pilot with a large reach envelope to facilitate manual tasks.

SPACE OPERATIONS SIMULATOR

The Space Operations Simulator (SOS) is the only Martin Marietta facility used to train astronauts to fly the MMU. The heart of the simulator is the six-degree-of-freedom moving base carriage (Figure 2a) that moves on rails and gimbals in a large room. In the MMU configuration, the astronaut is placed in the carriage gimbal ring equipped with a partial full-scale mockup of the MMU. The astronaut pilots the MMU as he would on orbit and, in effect, can "fly" freely in the room. A PRIME 750 computer contains the equations of motion for both the MMU and a target satellite (if any) as well as models for MMU electrical, propulsion, and control systems. Astronaut hand control commands cause the carriage MMU to translate and rotate relative to the target vehicle in real time as if both were on orbit.

Because of the physical constraints imposed by the room dimensions, carriage travel is limited to no more than 15 meters (50 feet) from the target. Therefore, scale models are used for simulations greater than 15 meters. In these simulations, a camera is mounted in the carriage gimbal ring and a scale model is placed nearby in a three-axis gimbal (Figure 2b) that is under computer control. In a separate room, the astronaut stands in a mockup of the MMU that is mounted 3 meters (10 feet) in front of a 2 x 3 meter (6 x 9 foot) large-screen television display (Figure 2c). Use of scale models in the three axis target gimbal makes it possible to simulate much greater viewing distances than would be possible in full scale. For example, use of a 1/10 scale model yields 10 times 15 or 150 meters (500 feet) simulated distance. Similarly, 1/20 scale yields 300 meters (1000 feet) of travel. Also, the three axis gimbal motion makes it possible for the camera to view the model from any point in a sphere surrounding the target in space.

All SOS simulations are controlled from a Test Conductor/Run Coordinator (TC/RC) console. Console operators can set initial conditions for the MMU and target and can also input malfunctions anytime during the simulation. During each simulation run, approximately 200 variables are recorded on tape every second. Data plotting can also be done real-time so the astronaut can receive feedback regarding his performance immediately after his training session.

ASTRONAUT TRAINING FOR SOLAR MAX RENDEZVOUS AND DOCKING

For the Solar Max training, a full-scale high fidelity mockup of the Solar Max satellite was placed on a single axis gimbal at one end of the simulator room. The suited astronaut stood in a partial full-scale MMU mockup mounted in the moving base carriage gimbal ring. The MMU mockup was fitted with all switches, controls, and displays; and a high fidelity mockup of the Trunnion Pin Attachment Device (TPAD) was attached to the MMU arms (Figure 3). The astronaut was given random starting points approximately 10 meters (35

feet) from the target and flew the MMU and attached TPAD over to the spinning Solar Max; matched rotational rates with it; and then docked the TPAD over a trunnion pin mounted on the target. This procedure was repeated for a variety of possible Solar Max rotational rates until the astronaut developed proficiency at the piloting task.

When a target mockup is mounted at one end of the room, it is not physically possible for the astronaut to fly the simulated MMU completely around the target. To compensate for this limitation, special "wash-out" software was developed to provide the relative motion of the satellite with respect to the astronaut. Thus, if the astronaut matched rates with Solar Max, both he and the Solar Max mockup would stop rotating in the room as seen by an observer. Alternately, if the astronaut attempted to fly around Solar Max in the opposite direction, the satellite would rotate faster in the room than its nominal spin rate. Therefore, the target and moving base carriage movement software provided the astronaut with proper relative motion cues to fly completely around Solar Max.

Another simulation element used to train MMU astronauts for the Solar Max mission was a full-scale mockup of the forward end of the orbiter cargo bay. This mockup was rolled into the simulation room and used to train for mission phases such as Flight Support Station (FSS) ingress and egress. The FSS, a stowage, recharge, and don/doff station for the MMU, was mounted in the cargo bay mockup. The astronauts used it to practice performing their MMU check-out maneuvers and for training to fly back into the cargo bay and to the FSS.

For distances greater than 15 meters (50 feet) between the MMU and the target spacecraft, training simulations were performed that were similar to those in the Shuttle Engineering Simulator (SES) at the Johnson Space Center. The large screen display was used for simulations of long range (90 meter) translations between Solar Max and the orbiter. A 1/10 scale Solar Max or a 1/20 orbiter were mounted in a large three-axis gimbal for these training sessions. The large screen display did not make it possible for the astronaut to feel realistic acceleration cues or touch the real target, but it did provide adequate visual cues to fly the MMU anywhere within a 150 meter (500 ft.) radius sphere about the target. Simulation of final approach and docking was completed using the full scale mockups with the astronaut on the carriage.

During training, the SOS run coordinator has the option of inserting simulated MMU malfunctions while the astronaut is performing his task. The 200 selectable malfunctions include stuck on/off thrusters, failed switches, failed gyros, and dead batteries. MMU astronauts are trained to sense each malfunction and take the appropriate action to compensate for it. Interestingly, it is this requirement for the pilots to sense malfunctions that establishes SOS fidelity requirements. MMU simulator fidelity is critical because the only way the pilot can detect most malfunctions is through subtle changes in unit performance. The SOS fidelity is such that the effect of changing the size of a single capacitor in the MMU control electronics is accurately represented to the pilot as a change in moving base carriage performance. Malfunction recognition and correction was a significant part of the training regimen for the Solar Max repair mission crew.

MISSION SUPPORT

The SOS Lab provided mission support for the Solar Max flight by conducting special ground simulations to answer two questions that arose during the mission. The first related to satellite motion. When the astronaut George (Pinky) Nelson attempted to dock with the Solar Max, he was unable to do so because of a mechanical problem with the trunnion pin. The failed docking attempt imparted motions to the Solar Max satellite and left it in a slow tumbling state. NASA operations managers wanted to know if MMU docking with the satellite would be possible given it's new rotational rates. To answer this question, SOS pilots flew ground simulations with the full-scale Solar Max mockup rotating at the observed rates. They concluded that the MMU had sufficient control authority and that another docking attempt by the flight crew could succeed.

The second mission question pertained to alternative MMU rescue techniques. Mission activities related to the failed Solar Max docking attempt resulted in more expenditure of forward Reaction Control System (RCS) fuel on the orbiter than was expected. Consequently, the standard rescue technique of using the orbiter to retrieve a disabled MMU was no longer feasible. Mission controllers wanted to know if a disabled MMU could be retrieved by another fully functional MMU. SOS personnel evaluated five different rescue configurations that used one MMU to rescue another. From these simulations they concluded that four of the five provided sufficient controllability to be practical.

COMPARISON OF ON-ORBIT DATA WITH SIMULATION

A series of MMU on-orbit engineering tests was performed during the Solar Max mission to evaluate MMU performance and the mass properties of the MMU/-astronaut system. These tests consisted of +X (forward) translations and various attitude maneuvers. For instance, the simulations on the SOS during crew training predicted that a two second +X command would result in a specific delta-velocity increment as well as some pitch motion (when not in attitude hold) because of the system center of gravity (c.g.) displacement from the center of thrust. Similarly, coupling between the rotational axes was expected because of products of inertia.

Unfortunately, the television and motion picture images taken during these tests lack sufficient detail to thoroughly evaluate the results because the crew switched from an orbiter camera to a helmet camera during the test. This made evaluation of the MMU response difficult. Since the MMU is an operational system and not an experiment, it carries no instrumentation to record events. The video record and the subjective evaluation by the pilots provide the only on-orbit performance data. From what could be seen on the video, the pitch rate obtained from the +X translation was in good agreement

with the expected value. Therefore, the c.g. location (up/down) appears to be what was calculated on the ground and used in the simulator. Additionally, the pitch, roll, and yaw response of the MMU appeared to be similar to that expected.

Subjective comments from the mission astronauts were encouraging. Both commented that the MMU flew just like the simulator. James (Ox) Van Hoften felt his MMU mass properties were identical to those in the SOS; hence, the MMU response was nominal. Nelson also cited overall good performance and noted that there appeared to be less cross coupling on orbit than in the simulator.

Propellant consumption is another area of performance comparison between the on-orbit MMU and the simulator. Unfortunately, pilot read-outs of the pressure gauges at certain times during the mission and tank temperature readings several hours after the flight constituted the only recorded data of fuel consumption. No specific on-orbit maneuvers were planned for propellant consumption evaluation. From the mission profile the astronauts flew, it appears that the propellant consumption on orbit and in the simulator compare favorably. However, detailed evaluation is not possible because of inherent gauge inaccuracies, the difficulty in reading the gauges, and because there were no identical maneuvers on the ground and on orbit to form a basis for comparison.

The transfer from the orbiter to the vicinity of the Solar Max appeared nominal compared to the training exercises, but the time it took for Nelson to make the first docking attempt appeared longer. In the SOS, both pilots translated toward Solar Max, matched rates, and immediately docked. On orbit, the time between matching rates and performing the final dock was considerably longer. In Nelson's opinion, this discrepancy occurred not because the task was harder, but because he took more time trying to execute a perfect dock.

ON-ORBIT DATA IMPACT ON FUTURE SIMULATIONS

Astronauts are currently being trained at the SOS for the mission to retrieve the Hughes 376 satellites (Palapa-B and Westar) lost during the 41-B flight. This mission is much more ambitious than Solar Max because rotation rates of the Hughes vehicles may be ten times faster than those of the Solar Max. The current concept is for the MMU to fly a two meter (six foot) stinger rod into the nozzle of the apogee kick motor on the Hughes satellite and then to mechaniçally attach the MMU and a grapple fixture to four points on a structural ring just outside the exterior of the nozzle (Figure 4).

From Solar Max attitude rate data received by Goddard during the retrieval, it can be seen that the MMU thruster plumes imparted some momentum to the target satellite. In fact, a change in the attitude motion of Solar Max was perceived even while the MMU was approximately 6 to 9 meters (20 to 30 feet) from the satellite. Since the Solar Max to MMU mass ratio was approximately 7 to 1 and the Hughes 376 to MMU mass ratio is only 1.5 to 1, some modification

of the Hughes satellite motion due to MMU plume impingement can be expected. This motion may be significant depending upon the approach path to the satellite. As a result, a plume impingement model was added to the SOS software to provide a more reasonable representation of the Hughes 376 motion and, thus, a higher fidelity simulation. Any initial rate on the Hughes satellite may be modified if a thruster plume were to hit it. This can change the astronaut's task from one of docking to a satellite with a simple spinning motion to docking to a satellite with a severe tumble.

Similarly, contact dynamics software was added to the SOS to model MMU stinger rod contact with the Hughes nozzle and contact pad impact with the structural ring. It is quite evident from the orbiter video records and Goddard strip charts that the motion of Solar Max was significantly modified each time Nelson attempted to dock. As a result, his docking task became more difficult with each attempt. The addition of such features as plume impingement models and contact dynamics should give the astronaut realistic practice in dealing with the worst case conditions he might encounter during the actual Palapa-B recovery mission.

FUTURE SIMULATIONS

Only 16 months were allowed to develop and deliver the current MMU model. To meet this schedule and to minimize qualification requirements, existing space-qualified hardware and a conservative design were used. As a result, the present unit is relatively large and heavy and has minimal pilot displays. An MMU having enhancements over the current version has been on the drawing boards at Martin Marietta since 1976. One enhanced MMU feature includes a microprocessor control assembly that would reduce pilot workload and allow more flexibility in task performance. This would be accomplished by automatically altering thruster selection logic when the MMU is transporting payloads such as beams for large space structures. The microprocessor would also provide a caution and warning system and improved instrumentation. Physically, the MMU can be made smaller, lighter, and easier to maintain. Increased propellant tank size and pressure would provide a larger delta velocity capability that would enable longer and more complicated missions.

Plans call for the SOS to be upgraded in order to support additional utilization of the MMU for both Shuttle and future space station applications. These upgrades may include:

* direct communication links between the SOS and NASA installations to facilitate real time mission support and integrated mission simulations;

* capability to integrate actual flight hardware and software into SOS system architecture;

* a higher resolution servo system that will greatly enhance the resolution, reliability, safety, and smoothness of the moving base carriage motion;

* a load cell array that will be able to sense the forces and moments of the MMU pilot and integrate these into the simulation equations of motion;

* a computer graphics system that will superimpose the earth, sun, moon, stars, and other spacecraft over the video image on the large screen display;

* a helmet mounted display integrated with moving base carriage motion for use in simulating full missions by an EVA crewman; and

* an improved computer architecture that will allow multiple MMUs or space station elements to fly in the same realtime simulation.

Many future roles are currently envisioned for the MMU. The Solar Max and Palapa-B missions illustrate the satellite servicing role. The MMU can also be used to service the space telescope and assemble space station components. The NASA decision to use the MMU for the Palapa-B recovery flight is indicative of their confidence in the safety, reliability, and effectiveness of the unit. Thus, it appears there will be many MMU missions and simulations in the future.

Table 1

MMU PERFORMANCE CHARACTERISTICS FOR
LARGE AND SMALL SPACE-SUITED ASTRONAUTS

Limits for Small Astronauts		Limits For Large Astronauts	
5% Female	47 kg	95% Male	98 kg
Spec EMU (4.5 kg H_2O Used)	90 kg	EMU (CEI Spec)	95 kg
Spec MMU (10.5 kg GN_2 Used)	143 kg	MMU (0.0 kg GN_2 Used)	153 kg
TOTAL	280 kg	TOTAL	346 kg
Nominal Thrust = 0.77 kg		Nominal Thrust = 0.77 kg	
Translational Acceleration = 0.109 M/S^2		Translational Acceleration = 0.088 M/S^2	
Delta Velocity * = 24.9 M/S		Delta Velocity * = 20.2 M/S	
Pitch Acceleration = 9.7 DPS^2		Pitch Accleration = 6.8 DPS^2	
Yaw Acceleration = 10.4 DPS^2		Yaw Acceleration = 7.9 DPS^2	
Roll Acceleration = 9.7 DPS^2		Roll Acceleration = 7.1 DPS^2	
*SPECIFIC IMPULSE = 66 seconds.			

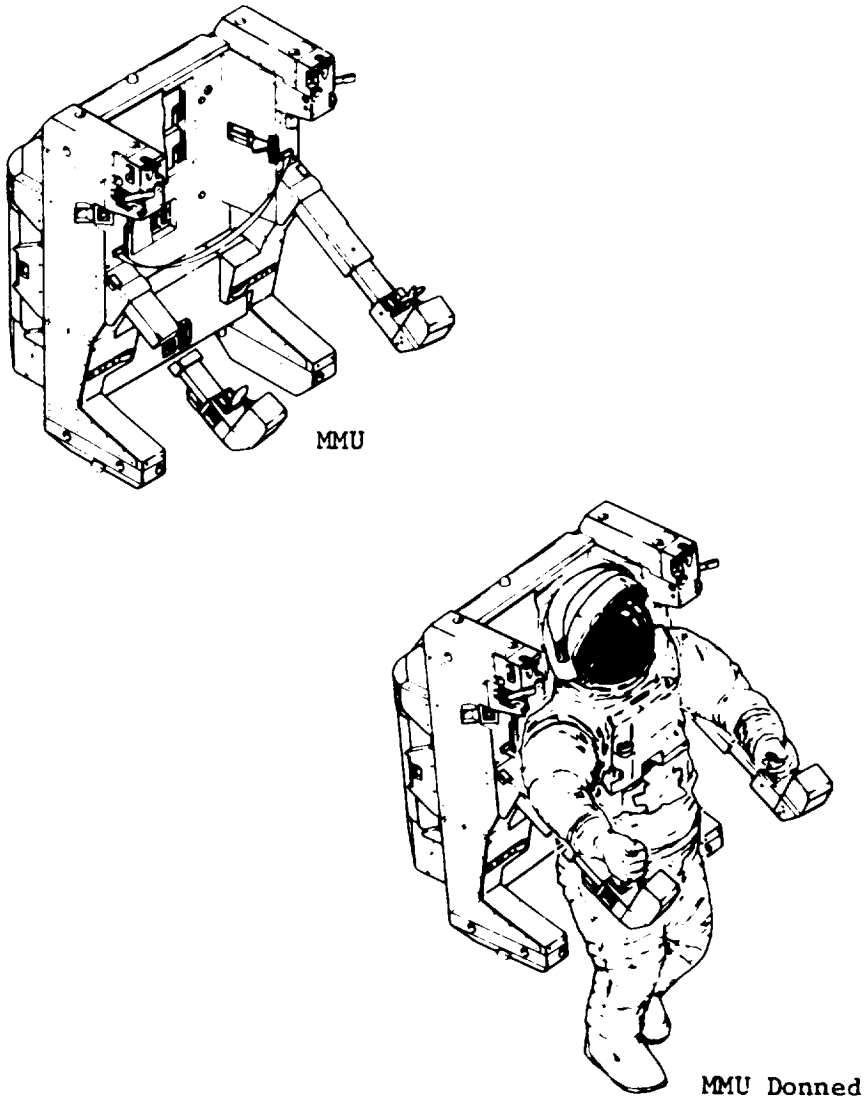

Figure 1 - Manned Maneuvering Unit (MMU)

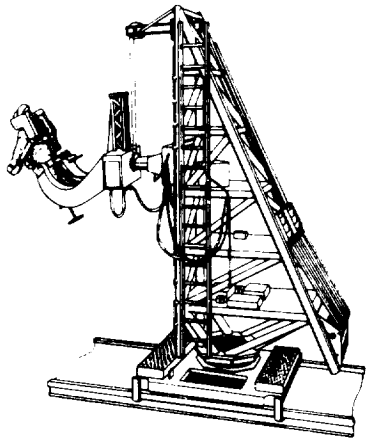

Figure 2A - Moving Base Carriage (MBC)

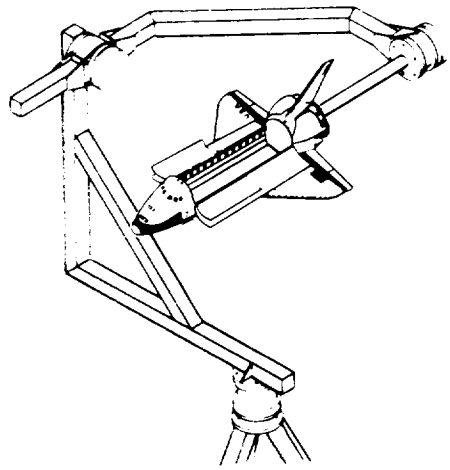

Figure 2B - Three-Axis Target Gimbal

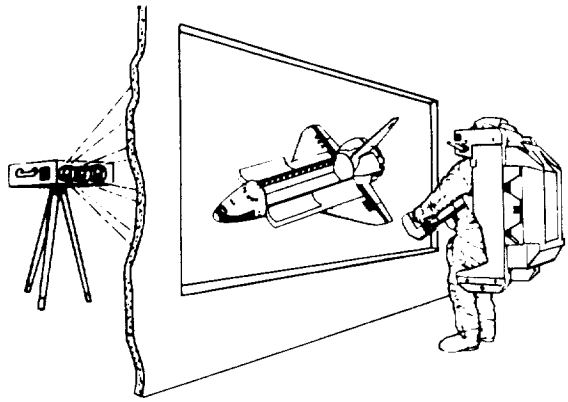

Figure 2C - Large Screen Television Display

Figure 2 - Space Operations Simulator (SOS) Components

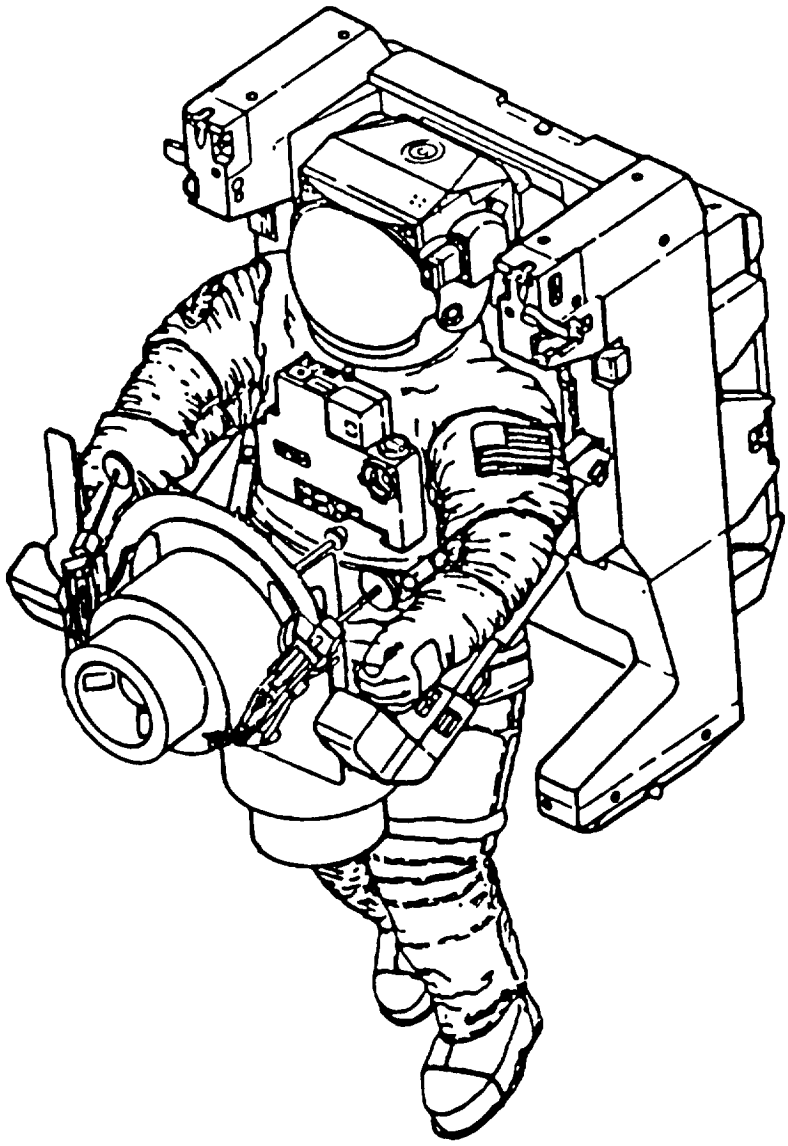

Figure 3 - Trunnion Pin Attachment Device (TPAD) Mounted on MMU

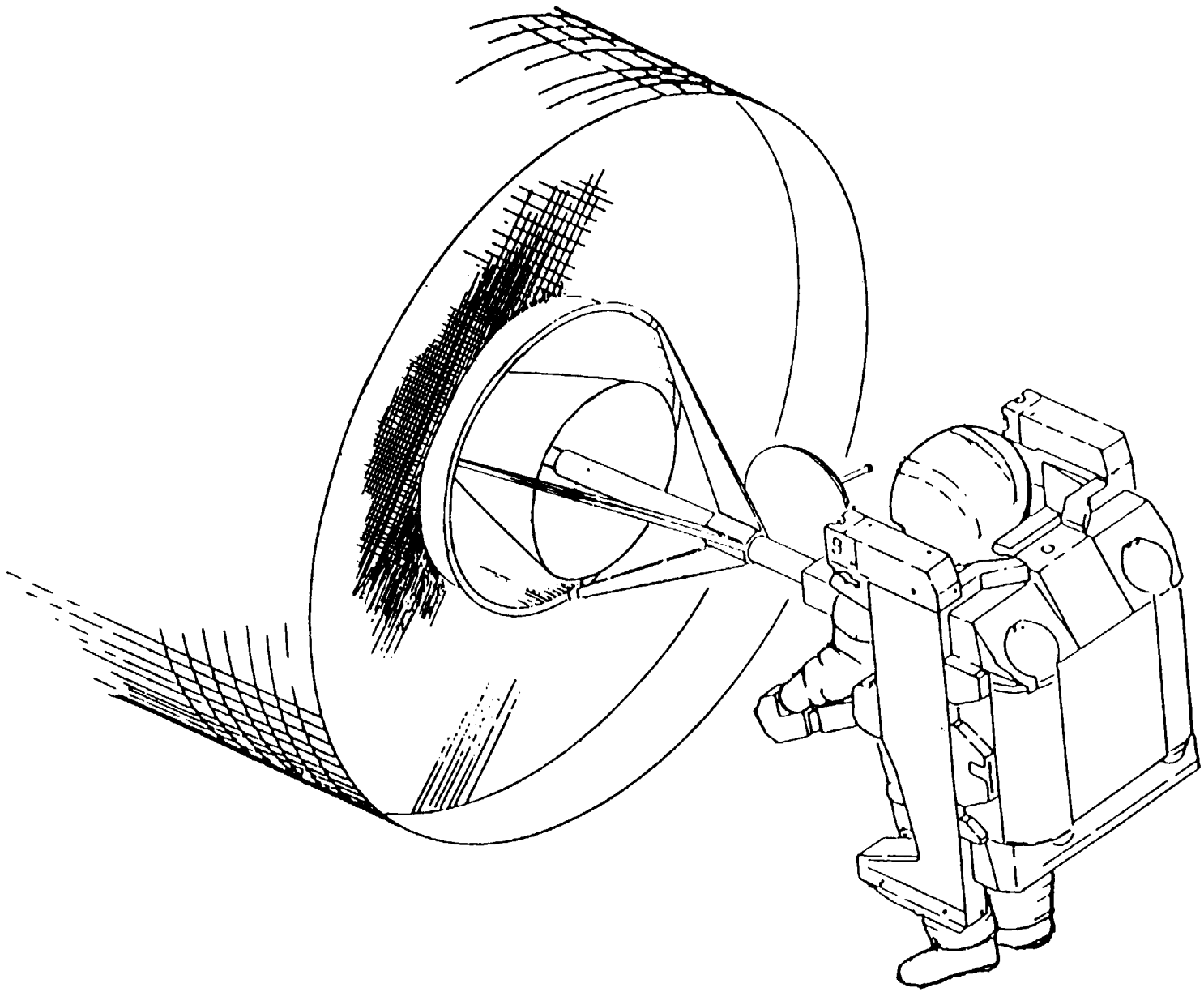

Figure 4 - MMU with Stinger Attached to Apogee Kick Motor of Hughes 376 Satellite

DISTORTION MEASUREMENT OF ANTENNAS UNDER SPACE SIMULATION CONDITIONS WITH HIGH ACCURACY AND HIGH RESOLUTION BY MEANS OF HOLOGRAPHY

Holm U. Frey
Industrieanlagen-Betriebsgesellschaft mbH (IABG)
Ottobrunn, W. Germany

ABSTRACT

The use of Laser Holography for measuring the distortion of antennas under space simulation conditions is described.

The subject is the so-called double exposure procedure which allows to measure the distortion in the order of 1 to 30/um ±0.5 per hologramme of an area of 4 m diameter max. If the total distortion is larger, it must be measured in single steps e.g. during the cool down phase. The hologramme shows the distortion in the interference fringe pattern like contour lines on a map.

The method of holography takes into account the constraints of the space simulation facility; the development achieved so far permitted the successful completion of several tests, as

- Antenna of MBB, Development Model, 1.2m dia.
- K-Band West Spot Beam Reflector, 1.2m dia.
- C-Band Receive Reflector, Development Model, 3.6m dia.

In this report the test method, the test set up and the constraints by the space simulation facility are described. The results of the performed tests are presented and compared with the theoretical predictions. The test on the K-Band Antenna e.g. showed a distortion of ≈ 140/um ±5/um measured during the cool down from -10 °C to - 120 °C.

INTRODUCTION

Since the photogrammetric method to measure the distortion of satellite antennas under space simulation conditions has unsatisfactory resolution and accuracy and since measuring by means of theodolites is not practical during space simulation tests, some experiments with holography were made at IABG in Ottobrunn, W-Germany.

In many applications the method of the double exposed hologrammes is successfully used for the determination of the distortion [1 to 7]. Until now the procedure was scarcely used for the determination of the distortion of antennas under simulated space conditions. The most serious difficulty is caused by the high sensitivity of the measurement.

APPLICABILITY OF THE HOLOGRAPHY FOR DISTORTION MEASUREMENT ON SATELLITE ANTENNAS

The hologrammes of a double exposure show the distortion in the interference fringe pattern like the altitude contour lines on a map (Figs. 4, 5). If a point P of the test article (1. exposure) moves to a point P' (2. exposure) during a temperature change, the distortion DS can be determinated as follows:

$$DS = \frac{\lambda \cdot n}{2 \cos \frac{\alpha}{2}}$$

Herein is:

$\lambda = 0.694$ µm: Wave length of the laser

n: Order of interference lines in the measuring point

α: Angle between direction of illumination and direction of observation

DS: Displacement

Direction of DS: Half angle between direction of illumination and direction of observation.

Depending on the quality of the hologramme, 0.1 to 1 order of interferences have to be resolved or 10 - 100 lines have to be counted. Therefore the range of the distortion which is covered by one hologramme, is 3.5 - 35 µm ±1 %.

Usually the mounting support of the antenna for a space simulation test originates a wide spectrum of vibrations in the antenna and stimulates an oscillation with eigenfrequencies. Without adequate precaution the amplitudes of these oscillations are much higher than the thermal distortions that can be detected by one hologramme. Therefore, the decoupling of the antenna by means of suitable filters is the basis of a successful distortion measurement by holography. Laser, optical system and photographic plate also must not perform any motions larger than 0.1 µ.

Since the distortion of an antenna, beginning with the hot thermal equilibrium (e.g. frontal sun 1 SC) to the cold equilibrium, is in the range of 0.1 to 1 mm, the total distortion can not be determinated by one hologramme only. It must be determined usually in about 20 partial steps; the distortion is then measured by one hologramme each for a small temperature range (ca. 2 °C). The hologrammes are taken along the cool down curve

at intervals of 5 - 10 °C. In order to obtain the total distortion over the whole temperature range, a linear interpolation between the several measurements is carried out. This is no disadventage, apart from the evaluation work, since the distortion can thus be determined as a function of the temperature. Thus when the direction of the distortion changes due to the temperature, more detailed information about the behaviour of the antenna can be obtained than with a single total measurement. Besides the mentioned characteristics of the holographic method, some additional constraints, which usually do not influence the measurement, must be described:

- Since the information is stored on a photographic plate, the test object may be illuminated in the moment of exposure by the laser only, i.e. the solar simulator must be switched off during the exposure.

- The surface of the test object must reflect the light in a diffused way; (it should be painted white or grey).

- The distortion is measured in the direction of the angle bisector between the direction of the observation and of the illumination. In order to obtain the true three-dimensional distortion, three hologrammes in three different directions have to be evaluated.

For the verification of mathematical models usually the measurement of one distortion component is sufficient:

- Additional constraints for the test set up may be caused by the geometry of the space simulation facility, the position of the windows, the direction of the solar radiation and the characteristics of the laser.

- Qualitative results are available immediately after the photograph plates are developed, i.e. during the test run. The quantitative evaluation is time consuming due to the selected range (number of the measuring points to be evaluated).

TEST SET UP

The antenna is decoupled via a mechanical filter and suspended in the middle of the space simulation facility (Fig. 1). The ray trace is shown in Fig. 2. For the illumination of the antenna a pulse laser of the following characteristics is used:

Power:	10 Joule (200 MW · 50 ns)
Wave length:	694 nm
Coherence length:	≈ 2 m

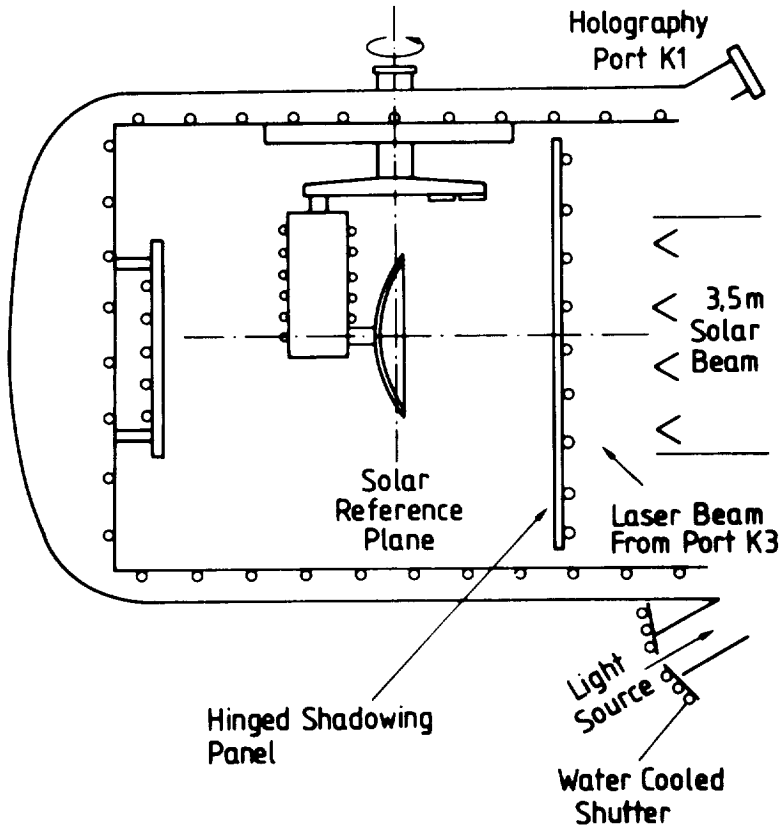

Figure 1: Test Configuration in the Chamber (Front Sun)

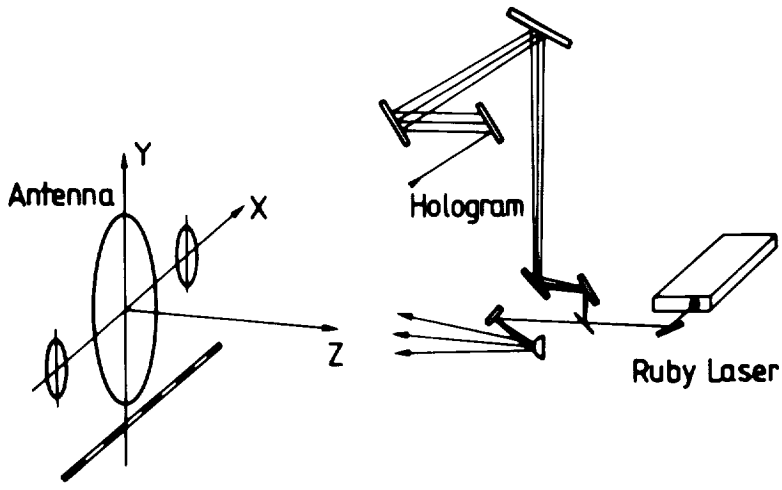

Figure 2: Holographic Test Configuration. Ray Trace Schematic

TEST RESULT

The procedure was developed and tested at IABG; test object was a MBB shell antenna (development model) of 1.2 m diameter. Fig. 3 shows the distortion along a cool down curve from -35 to -119 °C, and the achieved accuracy.

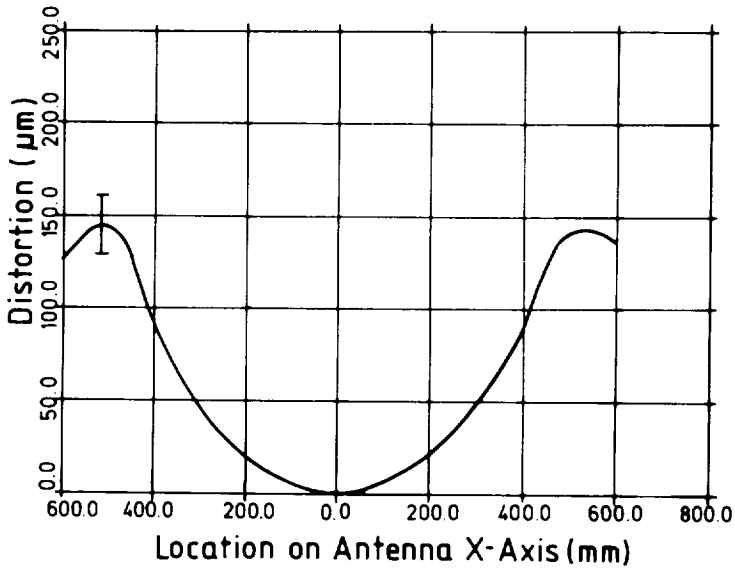

Figure 3: MBB Development Shell Antenna 1.2 m dia.
Thermal Distortion of the Antenna during
Cool Down from -35.6 °C to -119 °C

For the first time the procedure was used for the acceptance tests on a reflector of a communication satellite*. Figs. 4 and 5 show typical holographmes. They were taken during the cool down phase once after a full illumination with the solar simulator and once after a half illumination of the antenna. Contrary to the photogrammetry or measurements by theodolite, which provide a pointwise information only, the holographmes show the total distortion behaviour of the whole antenna surface.

Foldings, discontinuities, rear structure and inclosures are recognizable.

*The antenna was designed and manufactured by British Aerospace.
The holographmes were taken by Dr. Steinbichler,
Labor für kohärente Optik

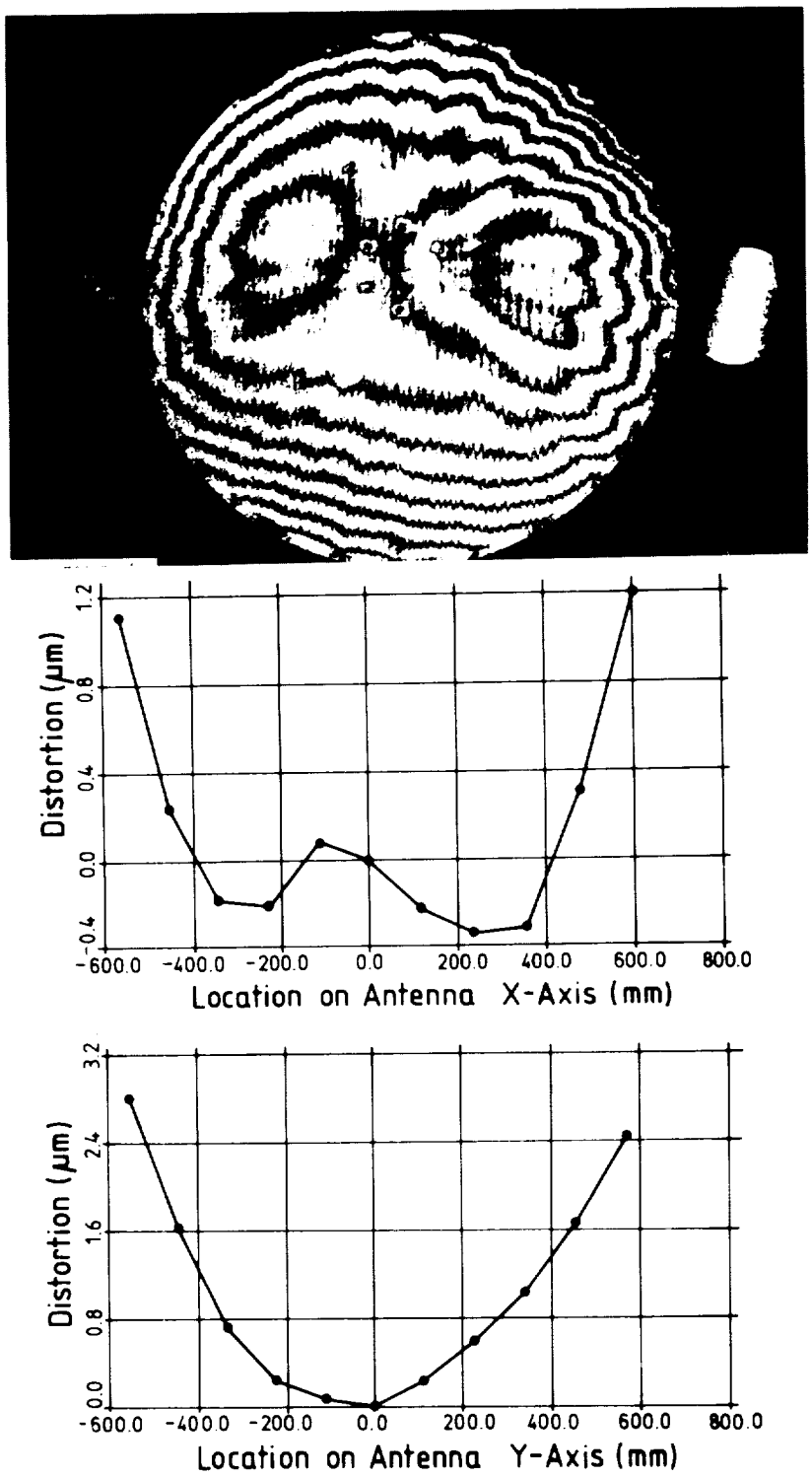

Fig. 4: Example for a Double Exposed Hologramme and its Evaluation along Cuts on the x- and y-Axis for a K-Band Reflector 1.2 m dia. Test phase: Cool Down after Front Sun 1 SC. Hologramme No. 59: First Flash at T = 70.48 ^{o}C, DT = 1.91 ^{o}C.

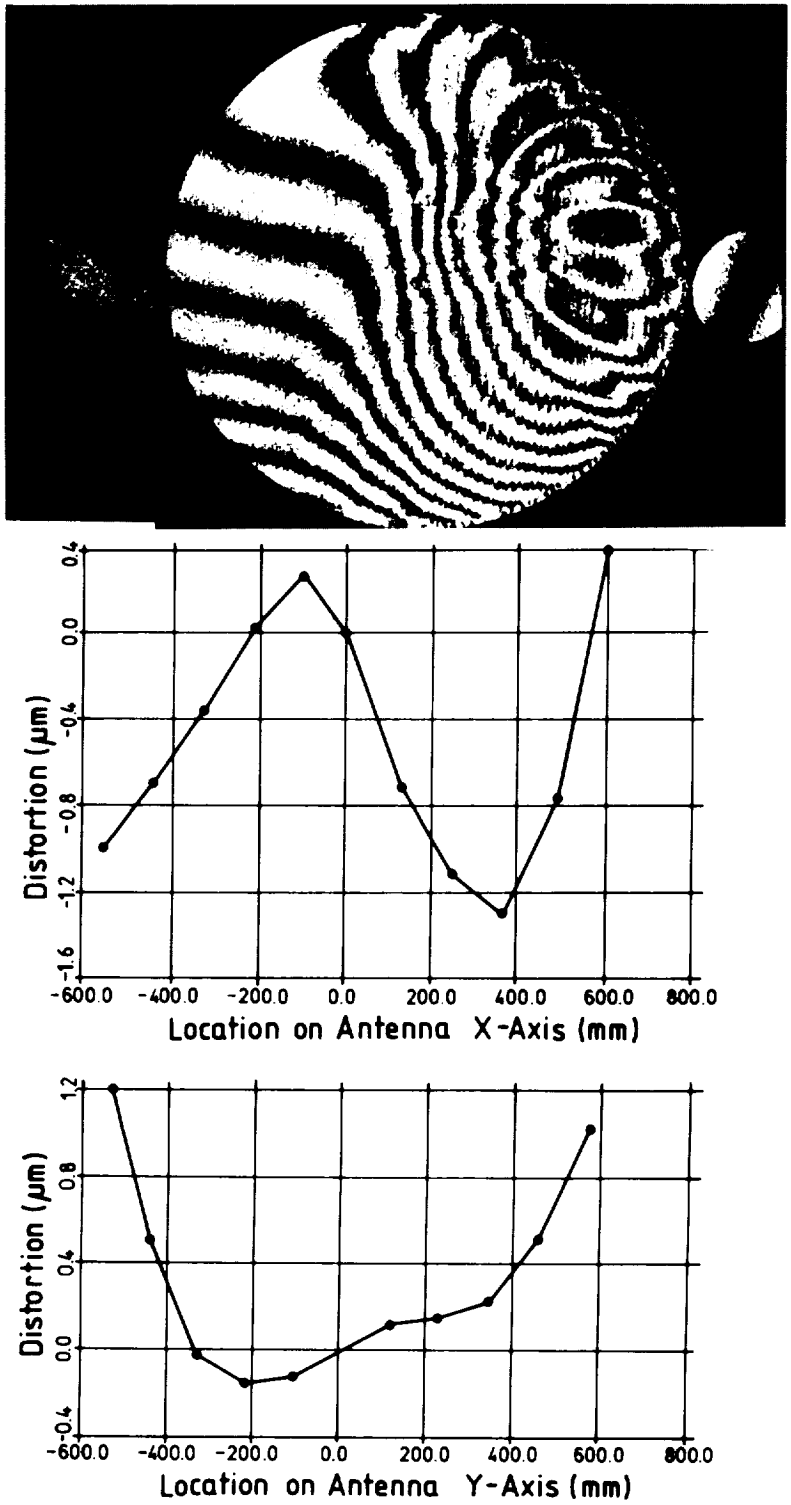

Fig. 5: Example for a Double Exposed Hologramme and its Evaluation along Cuts on the x- and y-Axis for a K-Band Reflector 1.2 m dia. Test Phase: Cool Down after half Shadow Front Sun 1 SC. Hologramme No. 222: First Flash at T =-27.64 ^{o}C, DT = -2.17 ^{o}C.

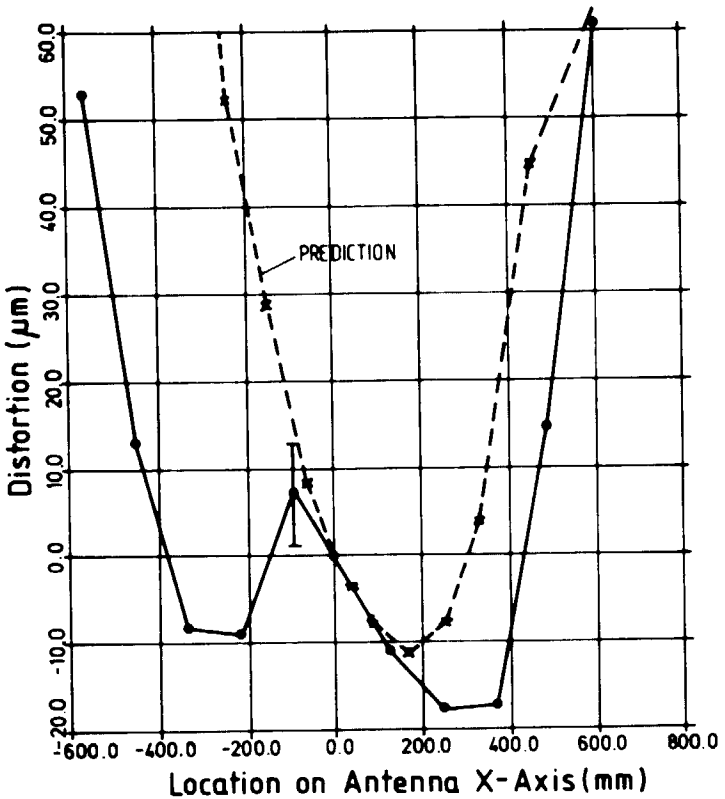

Figure 6: Cumulated Distortion along the x-Axis of the Temperature Range -16.1 °C to -110.5 °C.

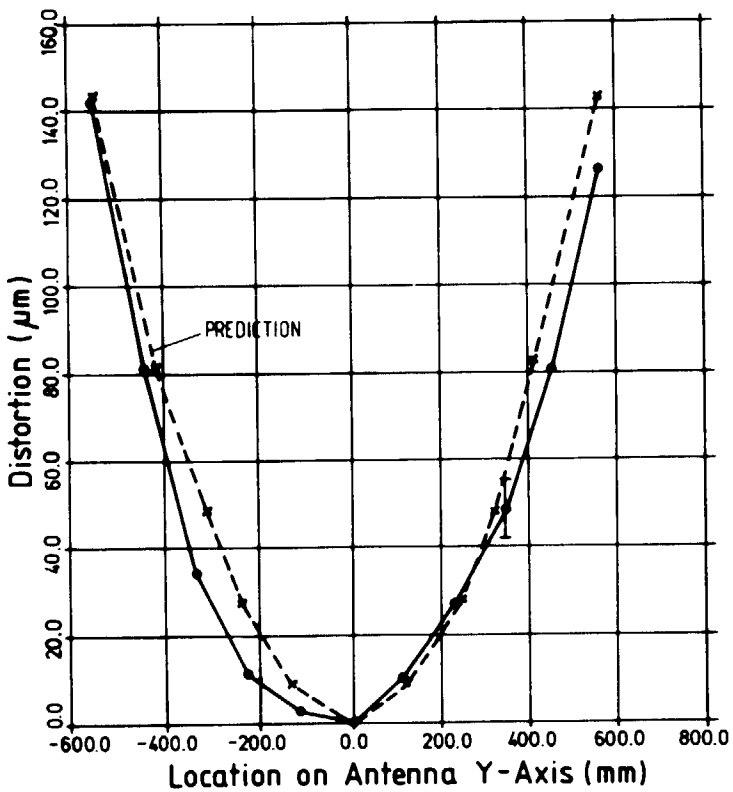

Figure 7: Cumulated Distortion along the y-Axis of the Temperature Range -16.1 °C to -110.5 °C.

Measured on a Telecommunication Satellite K-Band Reflector 1.2 m dia. Test Phase: Cool Down after max. Temperature Front Sun 1 SC

Figs. 6 and 7 show the total distortion in the range from -16 to -110 °C along the x- and y-axis.

Fig. 8 shows the cumulated distortion of a point on the antenna. All single measurements and corresponding interpolations lead to a continuously formed curve. The evaluation method proves to be usable and gives reasonable results.

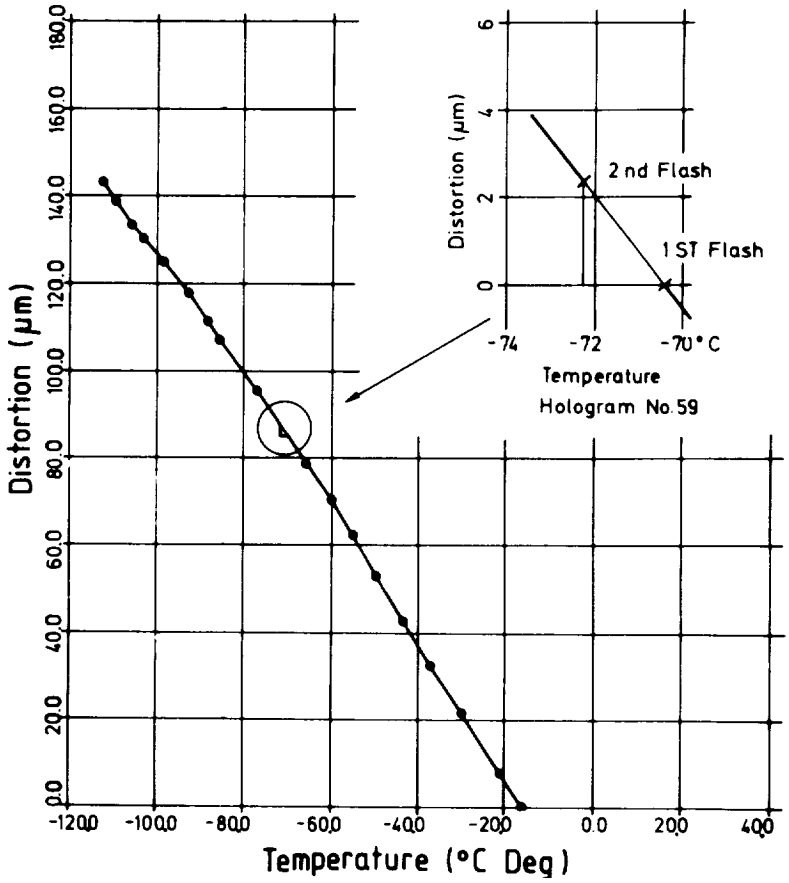

Figure 8: Distortion Cumulated for a Point on the Antenna on y-Axis at -560mm. Temperature Range -16.1 °C to 110.5 °C for a Telecommunication Satellite K-Band Reflector 1.2 m dia.
Test Phase: Cool Down after max. Temperature Front Sun 1 SC

Also on the development model of a C-band receive reflector* of a communication satellite of 3.6 m diameter holographic measurements were performed. Fig. 9 shows a hologramme. In this hologramme the rear structure is clearly recognizable.

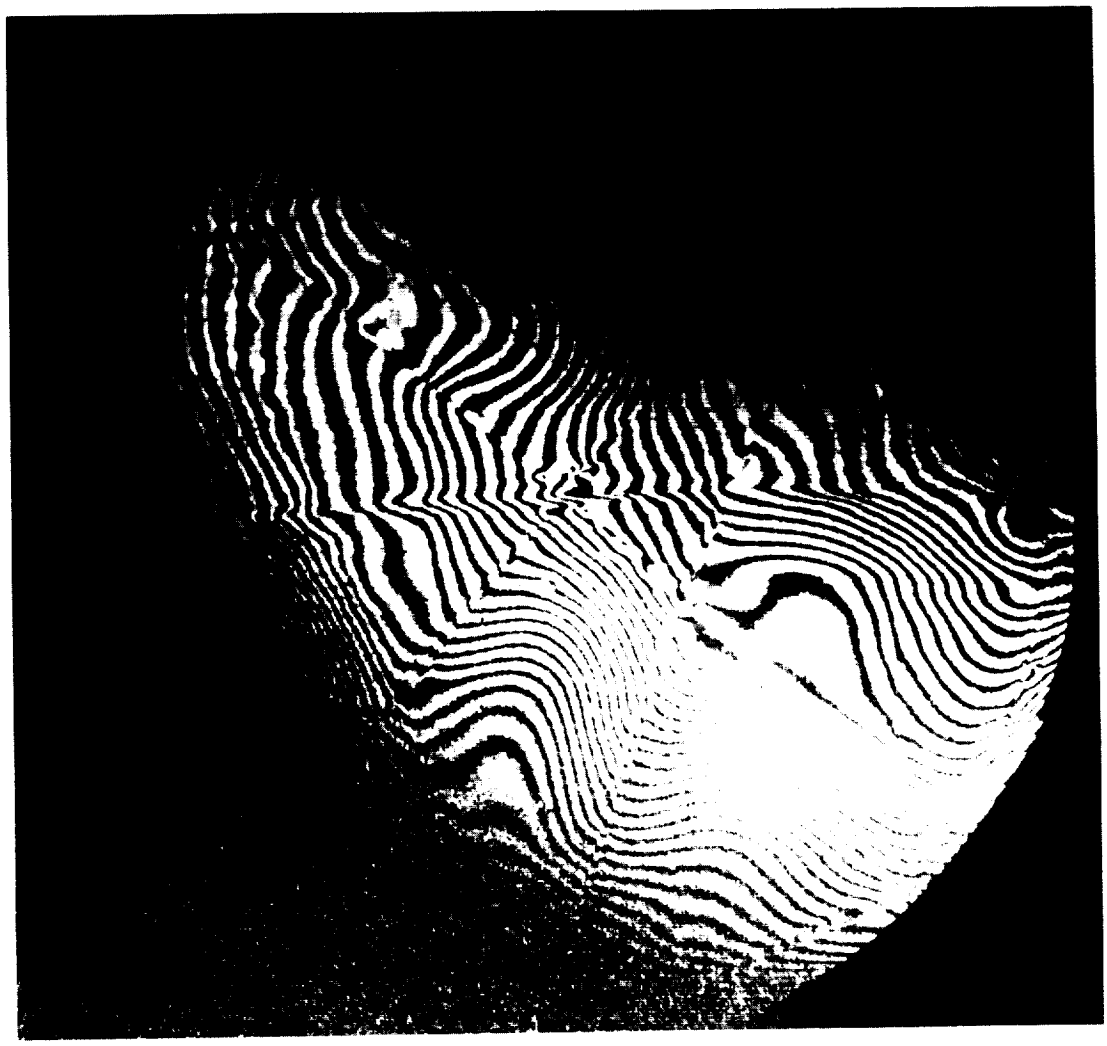

Figure 9: Example for a Double Exposed Hologramme of a 3.6 m dia Dish of a Telecommunication Satellite C-Band Receive Reflector Composed of KEVLAR Honeycomb Skinned by KFRP and CFRP Materials.
Test Phase: Cool Down after Front Sun 1 SC
Hologramme No. 331: First Flash at T = -93.78 ^{o}C, DT = -0.53 ^{o}C.

The Influence of the Backing Structure and of the Inserts is visible in this Distortion Patterns.

COMPARISON WITH THEORETICAL PREDICTIONS

The theoretical predictions are for the y-axis in a good agreement with the measurements. For the y-axis especially on the left side (-X) prediction and measurement are only in the same order of magnitude (Fig. 4, 5). The differences in magnitude and shape between test and prediction for the x-axis has been attributed to the relaxation of internal stresses induced during the manufacturing process: the use of a single sheet of honeycomb for the antenna

core leads to a slight saddling of the manufactured antenna which is reflected in the observed distortions but not represented in the mathematical model.

CONCLUSION

The study showed that holography can be successfully used for the determination of the distortion of antennas even for tests under space simulation conditions. Herewith a highly accurate measuring method is available, in order to verify theoretical predictions during the development phase by an actual test.

REFERENCES

1. Francon, M.: Holographie (1972) Springer Verlag Berlin

2. Robertson, E.: Harvey, J.M.: The Engineering Uses of Holography, Proceedings of a conference held at Strathclyde, Sept. 1968, Cambridge, University Press 1970

3. Vest, Ch.M.: Holographic Interferometry. New York, Chichester, Brisbane, Toronto: John Wiley & Sons 1979.

4. Aleksandrov, E.B. and Bronch - Bruevich, A.M.: Investigation of Surface Strains by the Hologramme Technique, Soviet Physics-Technical Physics Vol. 12 (1967) No. 2/258

5. Abramson, N.: The Holo-Diagram: A Practical Device for Making and Evaluating Hologramms, Appl. Opt. 8 (1969) 1235; Appl. Opt. 9 (1970) 97,2311, Appl. Opt. 10 (1971), 2155/2161; Appl. Opt. 11 (1972), 1143/1147

6. Steinbichler, H: Beitrag zur quantitativen Auswertung von holografischen Interferogrammen, Dissertation an der T.U. München vom 13.10.1972

7. Dändliker, R., Marom, E., Mottier, F.M.: Two Reference-Beam-Holographic Interferometry, J. Opt. Soc. Am., Vol. 66 No. 1, Jan. 1976.

VIBRATION ISOLATION SYSTEM FOR TESTING IN A VACUUM

Jack Dankowski
Barry Controls, a Unit of Barry Wright Corp.
Burbank, California

ABSTRACT

The scope of this paper deals with the design, manufacture and testing of an isolation system placed under a bench which simulates a space platform during testing in a hard vacuum. A low natural frequency isolation system is used to decouple ground vibrations from the bench. The materials used are vacuum compatible and do not introduce unwanted matter which would contaminate the payload optics and/or the testing environment. The system accommodates payloads of varying weights and envelopes.

INTRODUCTION

Evolution of the Optical and Electronic industries towards greater measurement precision requirements has created a need for low vibration environments. In addition, development of space applications for such systems requires ground based simulation of space environments. It became more and more evident that ground vibrations played a significant role in these system performance degradations, as measurement precision increased.

This creates the need for equipment which produces a vibration free environment and functions in a hard vacuum. This paper presents a brief overview of the analysis, design considerations and test results of a vacuum compatible, soft vibration isolation system that would be subjected to various inputs caused by the ever present normal ground vibrations and typical industrial vibrational sources.

One such requirement was established for the Thematic Mapper Environmental Test Bench for Hughes Aircraft Company at El Segundo, California. This test bench was supported by a servo controlled, soft pneumatic isolation system which decoupled the bench from the ground allowing the bench to simulate a free-free mode. The isolation system natural frequencies (vertical and horizontal) needed to be much lower than the lowest mode of the bench while the payloads were of varying weights, sizes and centers of gravity. The system had to be capable of attitude and balancing adjustments accomplished automatically while maintaining a constant natural frequency through wide variations in load.

The isolation system was constructed from low outgassing materials to minimize possible contamination problems. The system design also incorporated a flexible diaphragm. To meet the outgassing specification, a search was conducted to select an appropriate elastomer for this diaphragm.

The system was designed, built and then subjected to extensive functional and environmental testing, culminating in test results which met or exceeded the predicted performance. Test data included system natural frequencies, damping, transmissibility, returnability and leak rate criteria.

SYMBOLS

A	Area cm^2 (in^2)
d	Pendulum rod effective diameter cm (in)
D_{eff}	Effective diameter of the diaphragm cm (in)
D_v	Diameter of the spring and damping chamber when integral as shown cm (in.)
E	Modulus of Elasticity MN/m^2 (lb/in^2)
f_{nv}	Natural frequency, vertical, Hz
f_{nh}	Natural frequency, horizontal, Hz
g	Gravity 9.80 m/s^2 (386 in/sec^2)
I	Area moment of inertia cm^4 (in^4)
k_h	Horizontal spring rate N/cm (lb/in)
k_r	Apparent pendulum rod stiffness N/cm (lb/in)
k_v	Vertical spring rate N/cm (lb/in)
ℓ	Length of pendulum cm (in)
n	Ratio of specific heats, 1.40 for Air or GN_2, 1.30 Methane, 1.67 Argon
n	Number of cycles
P	Pressure MN/m^2 (psig)
Q	Output to input ratio

SYMBOLS (continued)

V	Volume, cm^3 (in^3)
V_d	Volume damping chamber, cm^3 (in^3)
V_s	Volume spring chamber, cm^3 (in^3)
W	Weight N (lb)

SYSTEM THEORY AND DESIGN CONSIDERATIONS

An idealized schematic model of a pneumatic isolator is shown in Figure 1 and consists of a weightless piston having a cross sectional area supporting a weight, moving without friction in a sealed cylinder containing a gas at some pressure and volume.

Under static conditions, equilibrium constraints require that:

$$PA = W \tag{1}$$

Assuming a polytropic adiabatic process (Reference 1), when the weight is increased, the pressure in the cylinder must increase resulting in a volume decrease,

$$P_1 V_1^{\,n} = P_2 V_2^{\,n} \tag{2}$$

where n is the ratio of the specific heat at constant pressure to the specific heat at constant volume of a gas. Since the decrease in volume due to the increased weight requires a displacement of the piston, the action is similar to that of a conventional coil spring. Therefore, the vertical stiffness of the air spring is characterized by its spring rate, k_v. If the change in volume due to an increase in the weight is small compared to the volume of the cylinder supporting the initial weight, it can be shown that the spring rate of the air spring is given by (Reference 5),

$$k_v = \frac{nPA^2}{V} \tag{3}$$

The vertical natural frequency of such an ideal air spring supporting a weight would then be given by,

$$f_{nv} = \frac{1}{2\pi}\sqrt{\frac{kg}{W}} = \frac{1}{2\pi}\sqrt{\frac{nPA^2 g}{VW}} \tag{4}$$

For such an air spring, the damping would essentially be zero. When subjected to forced vibrations, the amplification at the natural frequency of such an isolator would then theoretically go to infinity if the forcing frequency coincided with the natural frequency. It would, therefore, be desirable to add some damping mechanism to the pneumatic isolator. This

was accomplished through the addition of a damping chamber which is integral with the isolator assembly.

A schematic representation of an air spring isolator is shown in Figure 2. The piston action is provided by a diaphragm clamped to a circular cylinder. The diaphragm is also attached to a circular piston which supports the weight to be isolated since the spring chamber is pressurized. A structural separation containing a flow restriction separates the spring chamber from the damping chamber. The type and size of the restriction is primarily a function of the linearity and amount of damping desired in the isolator.

When finding the vertical natural frequency of a typical pneumatic isolator such as in Figure 2, an assumption[1] must be made to modify Equation 4. Since the isolator uses an integral plate which separates the spring chamber from the damping chamber, the restriction(s) must be of small open area so that the damping chamber volume does not become part of the isolator stiffness equation. Therefore, an effective spring chamber volume is used, and then the vertical natural frequency may be expressed as (see Figure 3),

$$f_{nv} = \frac{1}{2\pi} \sqrt{\frac{nPA^2 g}{V_{eff}\, W}} \tag{5}$$

Where $$k_v = \frac{nPA^2}{V_{eff}} \tag{6}$$

Moreover, it appears that for very small displacements, the spring chamber and damping chamber act as a similar volume since little gas flows through the holes and, therefore, provides little or no resistance.

Therefore, it may be concluded that for large displacements of the piston, V_{eff} is approximately equal to the spring chamber volume, but for very small displacements V_{eff} is approximately equal to the sum volume of both chambers.

The effective isolator volume has been established empirically by extensive testing of various configurations. The results reveal that,

$$V_{eff} = \frac{V_d + V_s}{2} \tag{7}$$

Where $$4V_s > V_d > V_s \tag{8}$$

---

1 Dankowski, J. C.; "A Trade-Off Study and Math Model Development of a Pneumatic Vibration Isolation System", Barry Controls Report No. WD93589-1-002, 6 December 1979, Burbank, CA.

and $$D_v \approx D_{eff} \tag{9}$$

The use of these constraints have rendered an effective vertical natural frequency accuracy of ±10%.

Since this isolator used a restriction between the damping chamber and spring chamber, the gas was displaced by piston movement forcing the gas from the spring chamber into the damping chamber. The restriction may have one or more holes of discrete diameters or a series of baffles resulting in laminar flow which yields constant damping with frequency. This system required low to moderate damping in the vertical direction, so a three hole pattern was used as the restriction. This approach tends to be partially amplitude sensitive, but since the change in damping is usually small, it did not have a significant effect on system performance. During loading and unloading of the test bench the pistons experienced large displacements and, therefore, produced greater vertical damping which is desired during this procedure.

Considering damping in the vertical direction, it would appear that for micro-inch amplitudes the damping should be essentially zero. However, this does not mean that damping provided by the entire isolator will be negligible. Even at micro-inch amplitudes, the diaphragm has flex and/or strain. Elastomers retain their damping characteristics even at micro-inch amplitudes. The damping ratio for the diaphragm material (Viton) is about .03 to .05. It should be noted that there is no vertical damping directly between the ground and the test bench, since this would result in coupling the ground motion to the test bench through a velocity dependent force.

The horizontal natural frequency is determined much more simply and is accomplished by using a dual pendulum approach, two pendulums in series (see Figure 4). Developing this approach it is known that (Reference 4),

$$f_{nh} = \frac{1}{2\pi}\sqrt{\frac{k_h g}{W}} \tag{10}$$

and $$f_{nh} = \frac{1}{2\pi}\sqrt{\frac{g}{\ell}} \tag{11}$$

Combining equation 10 and 11,

$$k_h = \frac{W}{\ell} \tag{12}$$

is the horizontal stiffness per rod. However, since the rods are used in series the following applies,

$$\frac{1}{k_{ht}} = \frac{1}{k_{h_1}} + \frac{1}{k_{h_2}} \tag{13}$$

The weight on the inner rod is slightly less than that of the outer rod since it does not support the connecting structure. However, compared to the payload the weight difference is negligible.

The remaining consideration is the tuned pendulum (or rod) apparent stiffness. This may be shown by,

$$k_r = \frac{3EI}{\ell^3} \tag{14}$$

Where, $$I = \frac{\pi d^4}{64} \tag{15}$$

Since the rod to be selected should be as thin as possible to minimize stiffness, a rod material of high tensile strength should be used. This system uses a tuned rod which has large threaded ends for fastening by means of lock nuts with spherical washers. A tuned rod is a rod which has a modified shape to reduce bending stiffness. When considering the horizontal stiffness of a rod the following applies,

$$\frac{1}{k_{rt}} = \frac{1}{k_{r1}} + \frac{1}{k_{r2}} \tag{16}$$

When comparing equation 13 to the overall stiffness (equation 13 plus 16), it is found that the rod stiffness is much less for moderate to heavy loads, but should be considered in most cases. When considering the light loadcase, the rod stiffness becomes significant and must be used to establish the total horizontal stiffness.

Horizontal damping is accomplished by using a Met-L-Flex® (Reference 6) pad which is of a doughnut shape. This pad contacts the midstructure which is connected by the pendulum rods to the isolator outer housing and the inner tank which is sometimes called the spring and damping chamber assembly. The pad provides slight friction damping for the midstructure. However, the inner diameter of the doughnut is slightly larger than a protruding member at the tank bottom. This provides slight to moderate damping for the inner structure and virtually no damping for the tank for small horizontal inputs. When larger displacements occur, such as during test set up or loading and unloading, the Met-L-Flex® damper provides damping up to 10 percent of critical.

The pad material is a formed wire fabric made of corrosion resistent steel and cleaned after forming to preserve non-contamination compatibility with the system.

The diaphragm is a preconvoluted design which produces a small spring gradient or centering effect that tends to return the diaphragm to its neutral radial position. The effective area does not change regardless of the stroke position as long as the diaphragm remains in its convoluted state. The rolling action of the diaphragm eliminates sliding contact and break away friction. The diaphragm composite is made up of a layer of

specially woven dacron fabric, impregnated with a thin layer of elastomer. The total thickness of the convolute is .1 cm. The dacron fabric which gives high tensile strength to the diaphragm, permits free rolling action while preventing axial distortion and thereby eliminating diaphragm stretching or ballooning. A thin diaphragm was selected to minimize any hysteresis effect, since thicker or multi-ply diaphragms, bladders and air bags do transmit vibrations of low amplitude.

A search for the optimum diaphragm material was conducted. The criteria for elastomer selection was based on the following: A proven material with adequate data for proper evaluation; low durometers available; material which could be compounded for optimum qualities; low out-gassing; operating temperature range of 10°C to 40°C (50°F to 104°F); and low permeability. As a result Viton (Reference 2) was selected and subsequently approved by the NASA Materials Group for this application.

This fluoroelastomer is a fluorine compound containing hydrocarbon which makes it relatively impermeable to air and other gases (see Figure 5, Reference 3). Elastomeric sealing materials outgas and suffer weight loss in a hard vacuum. This loss may result in changes of the mechanical properties of the material. One consideration of the program was the condensation of volatile outgassing constituents on the payload optical surfaces.

The diaphragms were baked at 250°C (482°F) for 20 hours to accomplish the required postcure. This procedure removes virtually all volatiles which would eventually outgas and cause contamination to be introduced in the vacuum chamber.

Under hard vacuum conditions, this material which is a Viton impregnated dacron fabric, exhibits a Total Mass Loss (TML) of only .85 percent and a Collected Volatile Condensable Material (CVCM) of .09 percent indicating that it is virtually immune to outgassing (Reference 7).

Each isolator incorporates an integral pneumatic servo valve which is mounted to the bottom of the piston. The valve lever arm extends into the tank adjustment access area. Three small sealed ports house three valve arm adjustment screws which control the valve gain and system floating height. Vacuum sealing screws are removed from each port for adjustment access. The flexible valve supply and exhaust lines feed through the lower portion of the tank. External corrosion resistant flex lines attach to the tank and terminate at the upper portion of the outer housing for ease of connection to the vacuum chamber bulkhead by means of supplied rigid lines.

The exposed portions of the isolators are made of corrosion resistant materials or were electroless nickel plated to resist corrosion for maintaining non-contaminating surfaces.

Each isolator base is bolted to a common frame for a fixed orientation. The test bench rests on the isolator tapered surfaces for registration. The isolator piston does not contact the table when non-pressurized at the rest condition. The loading and unloading of the bench payload is accomplished when the system is at rest.

When the system is pressurized in the vacuum chamber, each isolator piston engages the table and within minutes raises the table one centimeter which is the preadjusted floating height. Depressurization occurs in a reverse fashion but at a slower rate.

The system is controlled and monitored from a control panel external to the vacuum chamber. The panel houses the pressurization and depressurization valves, gas filter, pressure regulator and pressure gages which indicate each isolator pressure and the regulated supply pressure.

TESTING AND RESULTS

The isolation system (Figure 6) was set-up on an equally spaced 152 centimeter (60-inch) diameter and each isolator was levelled with the other isolators within one millimeter. The height of the isolators was 82 centimeters from their base. A dial indicator was attached to each unit. At the rest position of the isolators, the indicators read 0.000 floating height.

The bench (2250 kilograms/4960 pounds) and the payload (1590 kilograms/3505 pounds) was installed on top of the isolation system (Figure 7). When the system was pressurized with GN_2 to float, the pressure in each isolator was 0.612 MN/m^2 (74 psig), 0.681 MN/m^2 (84 psig) and 0.591 MN/m^2 (71 psig) the differences being due to eccentric payload loading. The floating height of each isolator was set at one centimeter.

The isolation system, while floating, was depressesd at a point over one isolator, until that isolator bottomed out, then the force was released. After 23 minutes, the system came back to its original position within ± 1 millimeter. After repeating the test several times, the results were the same.

The system was then deflated until all gages read zero pressure. The isolators were then inflated and the time required to obtain a floating position was 40 minutes.

Each isolator was measured from the outer isolator structure to the pressure chamber as a reference. The chamber was displaced in a radial direction and recorded; then it was displaced in a reverse direction and recorded. The test was repeated twice on each isolator in 2 different horizontal directions which were 90 degrees apart. The results of the test revealed that the movement of the pressure chamber in the test direction was equal to or greater than 9.5 mm.

DYNAMIC TESTS

Vertical dynamic testing required a vertical velocity meter (geophone) to be secured on the payload. The test was accomplished by depressing the payload and releasing it. The results were recorded on an oscilloscope to measure natural frequency and damping.

The vertical natural frequency of the system was .625 Hz. The vertical damping (percent of critical) was calculated according to the equation (Reference 5),

$$\zeta = \frac{1}{2\pi n'} \ln \frac{Xo}{Xn'} \qquad (17)$$

$$\zeta = .08$$

The vertical transmissibility test used only natural ground vibration inputs. A second velocity meter was set on the ground. The following is a sample of the data,

Hz	Q
3.5	.107
4.0	.077
5.0	.036
7.0	.018

This data demonstrates an isolation roll-off of 8 db/octave which is greater than the theoretical 12 db/octave due to diaphragm influence.

The horizontal dynamic tests were set up in similar fashion, however horizontal velocity meters were used. The horizontal natural frequency of the system was recorded as .50 Hz. The horizontal damping was approximately 5% of critical.

A sample of the horizontal transmissibility test data was as follows,

Hz	Q
3.5	.071
5.0	.039
8.0	.025
9.0	.022

The data demonstrates an isolation roll-off of 6.5 db/octave which is greater than the 12 db/octave due to the Met-L-Flex® coulomb damping.

GAS LEAK RATE TESTING

A leak rate test was performed on each isolator to determine the maximum gas loss per isolator. The technique used to determine the leakage flow rate is called the accumulation method. The test sample was charged with a trace gas (dichlorodifluoromethane) and placed inside a chamber.

The chamber atmosphere was then sampled to determine the concentration of trace gas. These readings were compared to readings taken when a leak standard was placed in the chamber.

The test criteria for a grouping of three isolators was 7.3×10^{-3} Standard ATM cc/sec. The worst case was found to be 1.31×10^{-3} Standard ATM cc/sec. The system gas loss was less than 4×10^{-2} Standard ATM cc/sec due to the many fittings required in the vacuum chamber (Figure 8).

SUMMARY

This vacuum compatible vibration isolation system was designed to support a round seismic mass which would be the platform for the Thematic Mapper System tests requiring a space simulated environment.

The vibration isolated mass and isolators are made from low-outgassing materials so that they can be used in vacuum. The system was developed for precise optical equipment that must not pick up contamination from the outgassing of nearby objects. A scaled-down version would have wider applications in optics, electron beam lightography or other similar equipment.

The bench is a vacuum compatible, epoxy coated mounting table 2.29 m (7.51 ft) in diameter, with a mass of 3,000 kg (6614 lb). The table is supported by three vibration isolators. The bench is designed for a maximum load of 1,590 kg (3505 lb).

Each pneumatic vibration isolator attenuates vertical and horizontal vibrations. The Servo-Valve controls the gas pressure to maintain a steady state level position by sensing vertical position.

These isolators allow the system to produce zero deflection under load as compared to conventional spring systems.

The pressure chamber that houses the spring and damping chambers is supported at its base by three inner pendulum rods. These rods are supported at their upper ends by a supporting cylinder that is, in turn, supported by three outer pendulum rods. This double pendulum support system is used because it provides the required low horizontal natural frequency for vibration equation while requiring less height than would be needed for a single pendulum or other type of suspension. The metalic tubing that runs from the system to the gas supply and exhaust lines is flexible to minimize any horizontal vibration coupling or isolation short-out.

The isolator components are all hermetically sealed within the pressure chamber to prevent leakage into the vacuum chamber. All materials and finishes are selected for low outgassing qualities and compatibility with equipment sensitive to contamination in a vacuum.

The vertical natural frequency is less than 0.7 Hz while the horizontal natural frequency is 0.5 Hz. The system provides 85 percent or greater isolation for both the vertical and horizontal direction at frequencies above 5 Hz. The gas leakage rate is less than 4×10^{-2} atm-cm^3/sec (4×10^{-3} Pa-m^3/s). A summary of the system major features is given in Figure 9.

This program took 1-1/2 years to design, develop, and manufacture with subsequent extensive testing.

These systems are currently in use in several parts of the country.

REFERENCES

1. Hirtreiter, A.B.; "Air Springs" Machine Design, 37, 104 (1965)

2. E. I. DuPont de Nemours & Co., Inc., Elastomer Chemicals Department, Wilmington 98 D.E.

3. Military Standardization Handbook; "Rubber and Rubber-Like Materials"; MIL-HDBK-149A, 30 June 1965

4. Thomson, W. T., Vibration Theory and Applications, Prentice Hall Inc., Englewood Cliffs, N.J., 1965.

5. Shock and Vibration Handbook, Chapter 33, Richard D. Cavanaugh, Vol. 2, McGraw Hill Co. (1961).

6. Trademark of Barry Controls, a Unit of Barry Wright Corp.

7. Outgassing Data for Spacecraft Materials, Report No. NASA-RP-1061, August, 1980 (National Technical Information Service Ref. N80-30441).

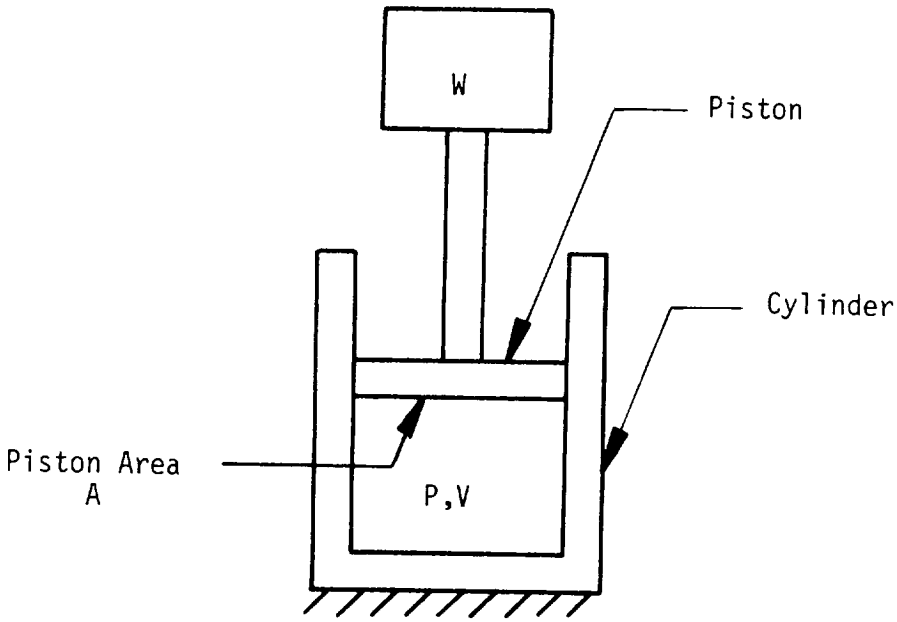

Figure 1 - Idealized Air Spring Model

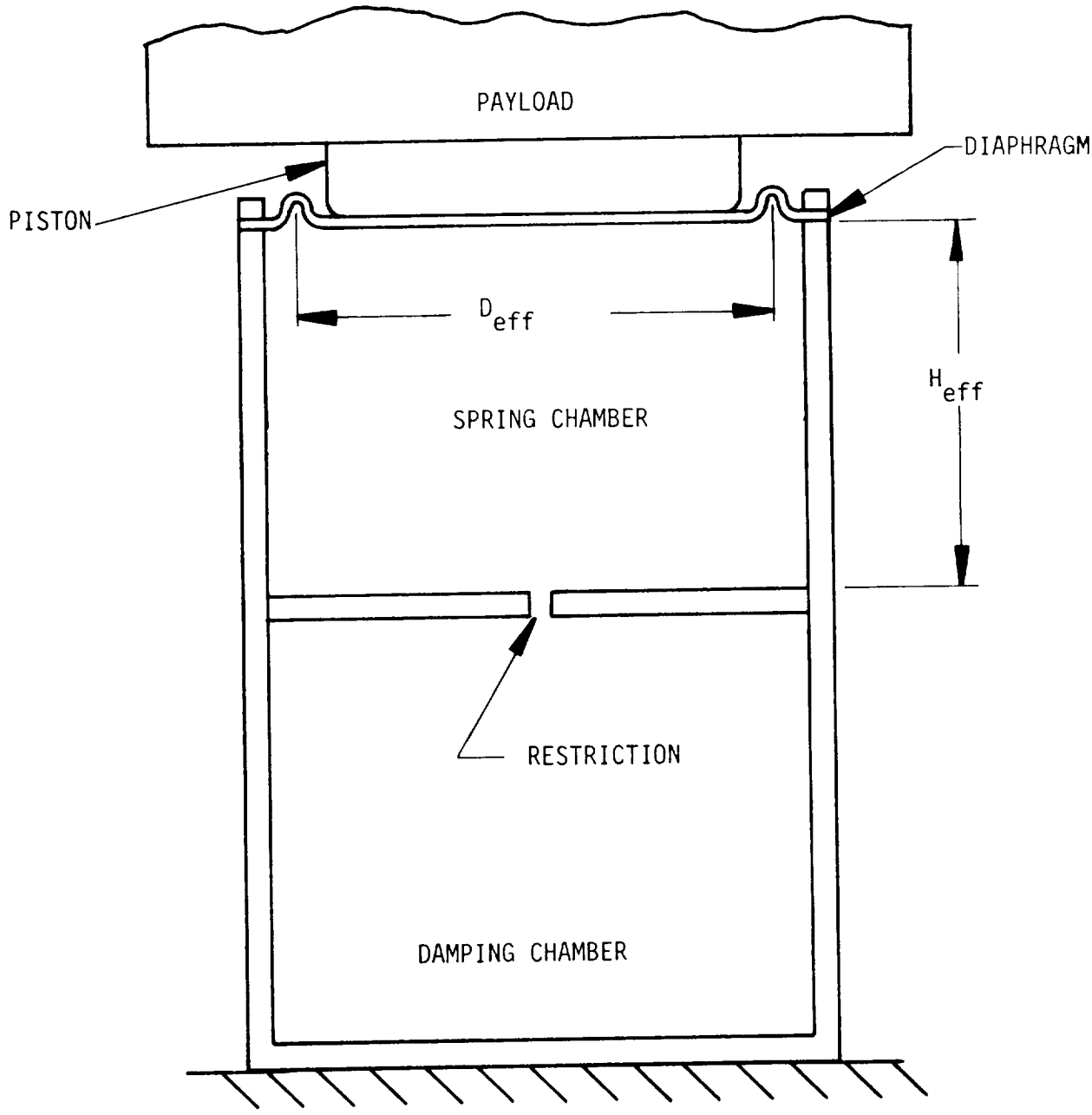

Figure 2 - Pneumatic Isolator Schematic

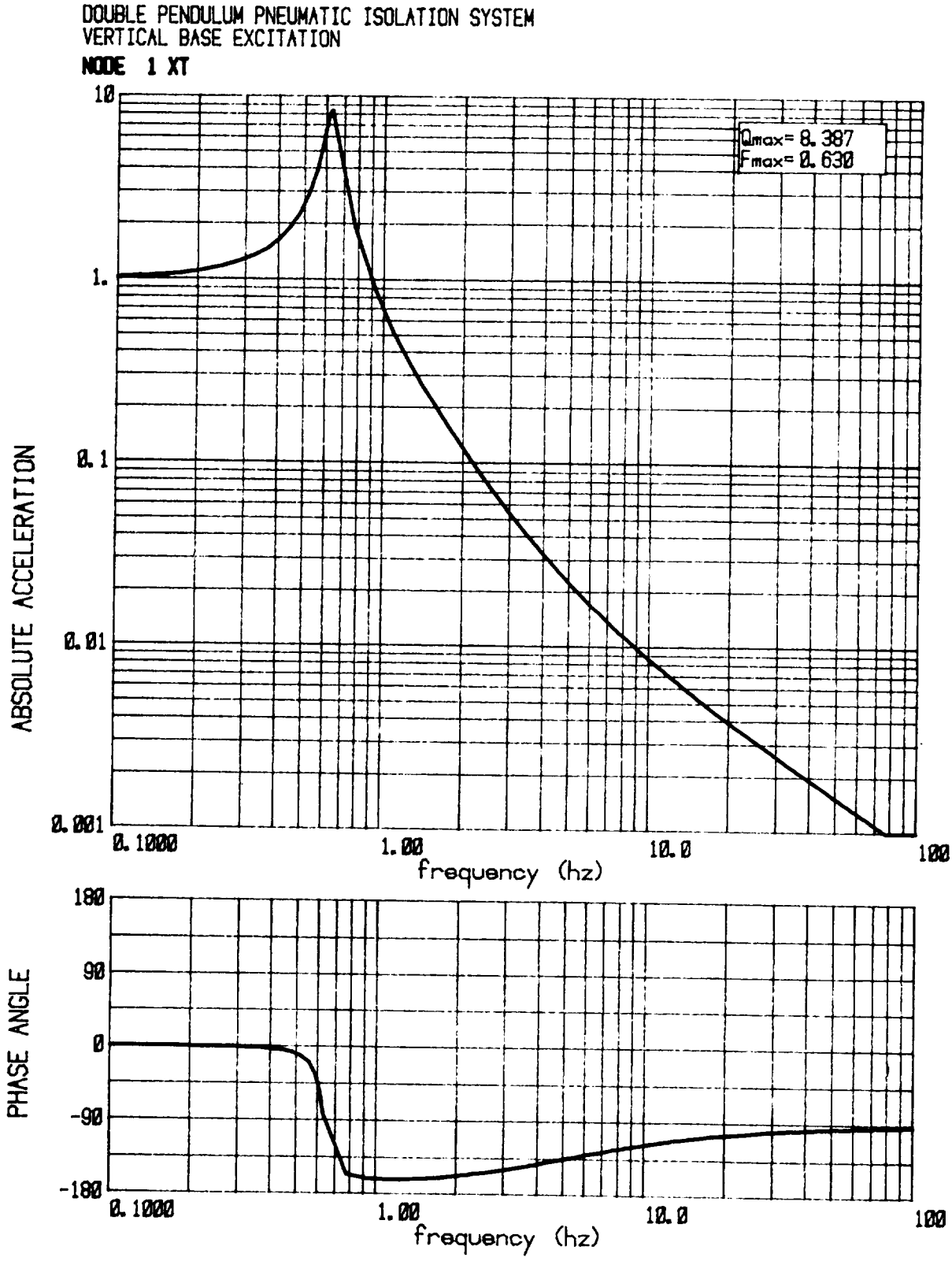

Figure 3 - Double Pendulum Pneumatic Isolation System Vertical Base Excitation

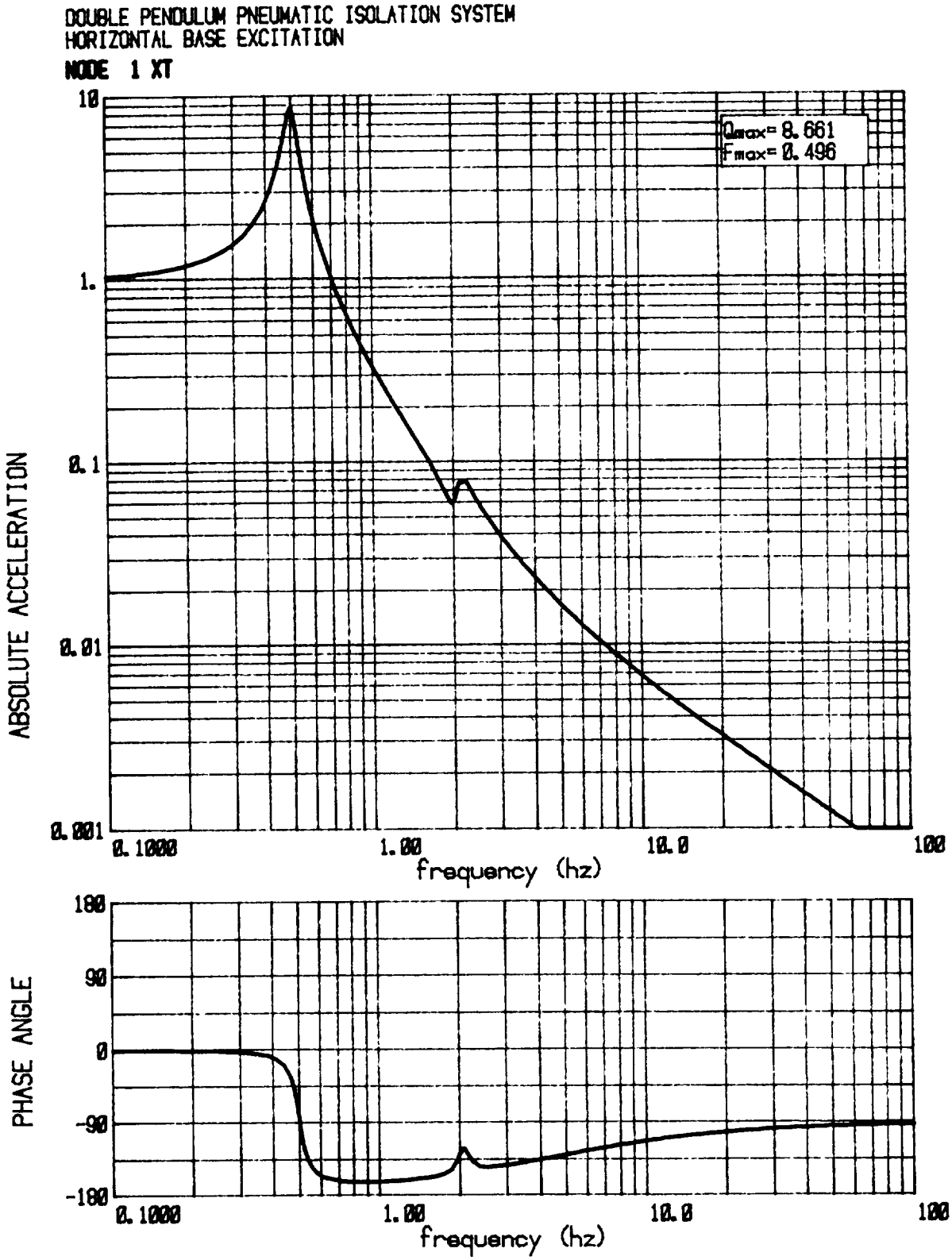

Figure 4 - Double Pendulum Pneumatic Isolation System Horizontal Base Excitation

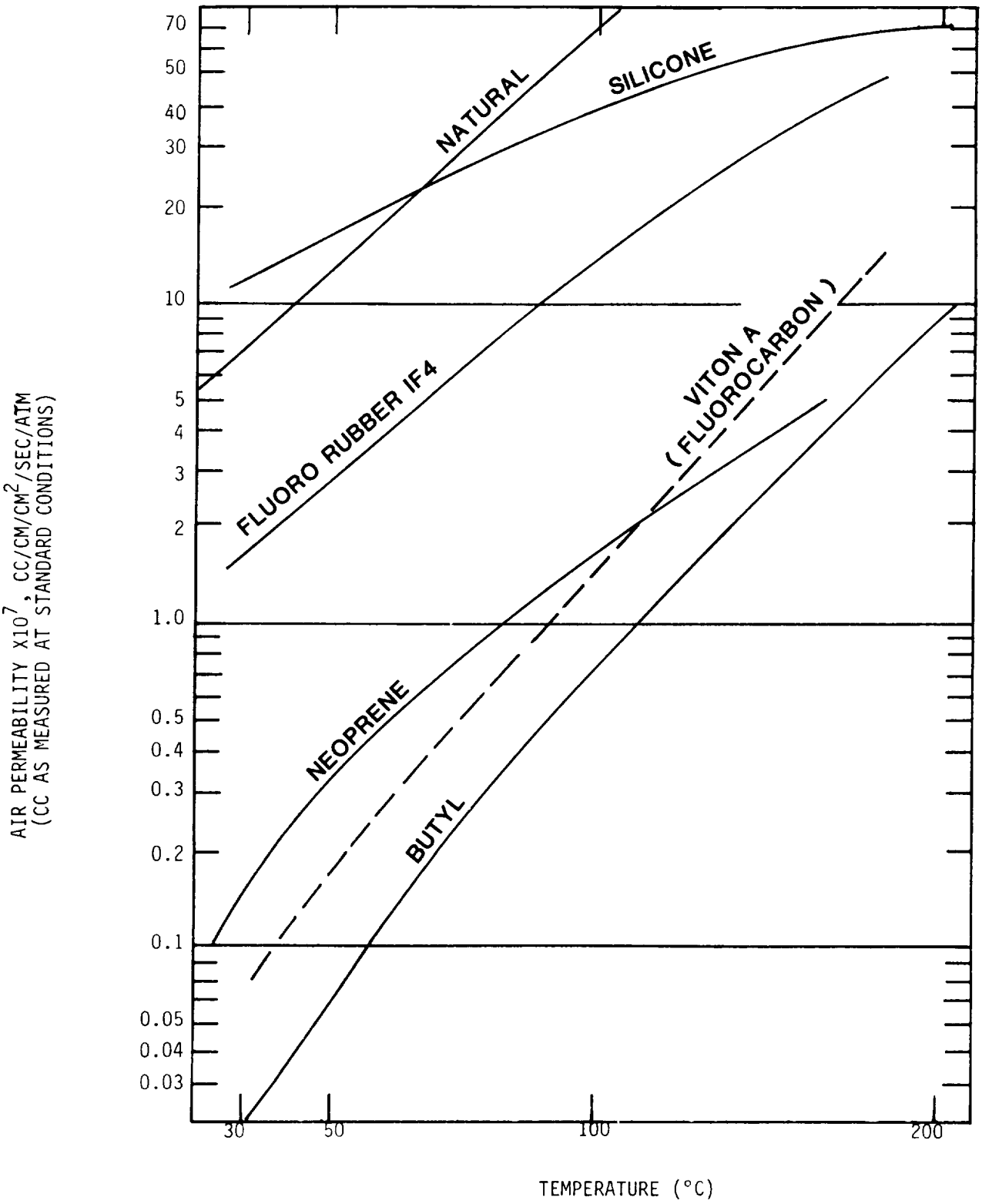
AIR PERMEABILITY X10^7, CC/CM/CM^2/SEC/ATM
(CC AS MEASURED AT STANDARD CONDITIONS)
70
50
40
30
20
10
5
4
3
2
1.0
0.5
0.4
0.3
0.2
0.1
0.05
0.04
0.03
NATURAL
SILICONE
FLUORO RUBBER IF4
VITON A
(FLUOROCARBON)
NEOPRENE
BUTYL
30
50
100
200
TEMPERATURE (°C)

Figure 5

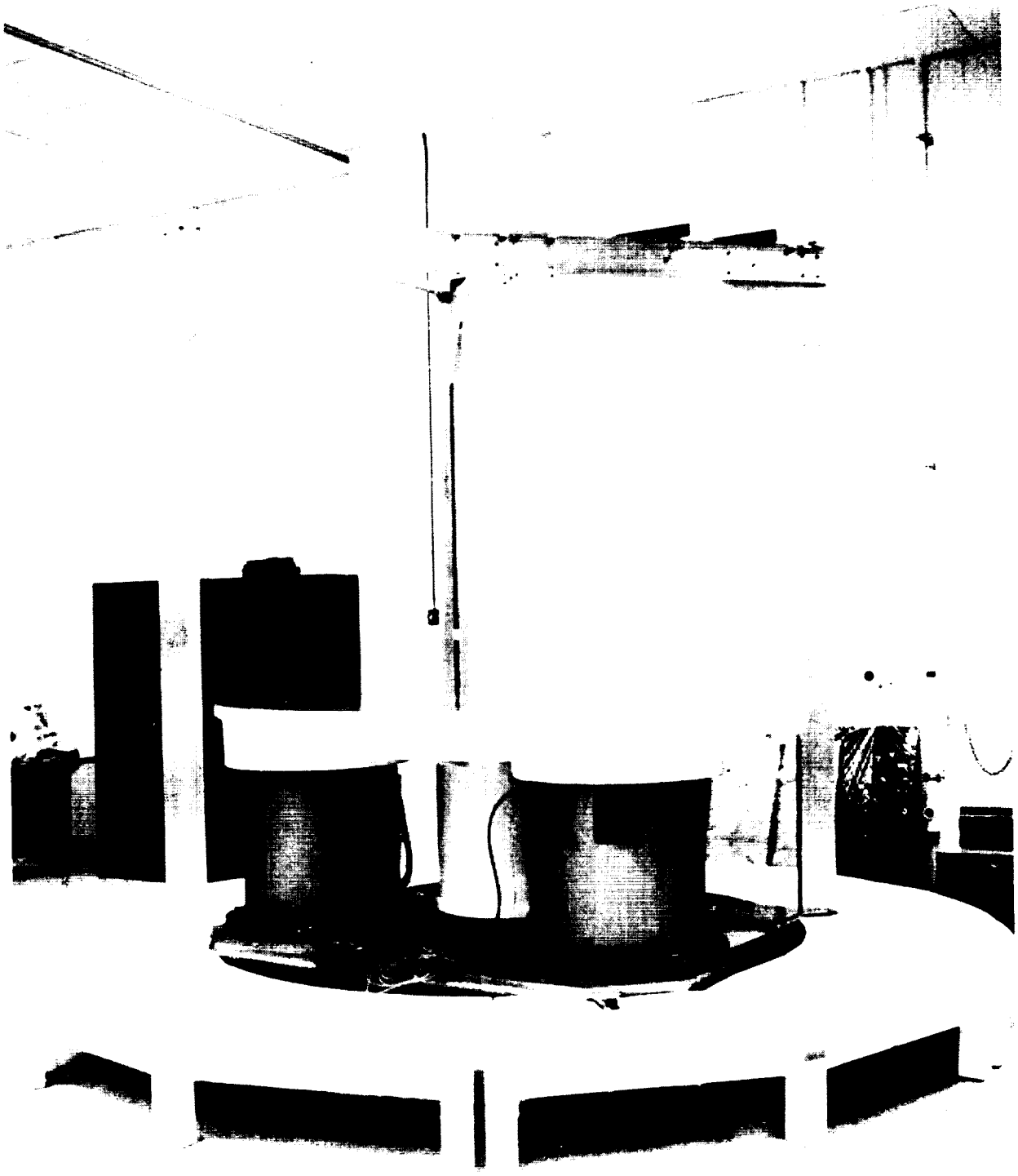

Figure 6

Figure 7

Figure 8

SUMMARY OF SYSTEM MAJOR FEATURES

Vertical Characteristics	
Type of Isolation	Active Pneumatic
Natural Frequency	0.7 Hz maxmimum
Damping	4 - 10% of critical
Isolation Rate (theoretical roll-off)	12 dB/octave
Horizontal Characteristics	
Type of isolation	Passive Pendulus
Natural Frequency	0.5 Hz nominal
Damping	4 - 6% of critical
Isolation rate (theoretical roll-off)	12 dB/octave
Vertical Control	Pneumatic Servo Valves
System Returnability	± .025 cm
Pneumatic Supply	GN_2
Source pressure	1.14 MN/m^2 (150 psig) minimum
Air Filter Size (control panel)	5 micron
Environment	
Operating	
Temperature	0°C to 60°C (32°F to 140°F)
Humidity	2% - 100%
Storage	
Temperature	-40°C to 80°C (-40°F to 176°F)
Humidity	2% to 100%
Expected Life	10 years minimum

Figure 9

PREDICTIVE THERMAL-VACUUM MODELING BY VARIABLE COEFFICIENTS

John T. Chuvala
Perkin-Elmer Corporation
Danbury, Connecticut

ABSTRACT

In computer-assisted thermal-vacuum testing an accurate mathematical thermal model is necessary. This model can indicate what effect a given change in control temperature will produce on the test article. This paper illustrates, with the use of a three-node thermal model, some numerical methods used to increase the accuracy by generating more accurate coefficients for the model.

ABSTRACT

IMPROVED MATERIALS CHARACTERIZATION FOR SPACECRAFT APPLICATIONS

Lt. R. Cull, USAF
Wright-Patterson AFB, OH

Future space missions are going to stress spacecraft designs and materials. The missions will entail higher power levels, longer space life (7-10 years), and larger, more sensitive optics than are currently being employed. The effects of contamination from outgassing materials are going to become more critical on these future spacecraft, since the contamination can degrade solar cell efficiency, degrade optics, and decrease the efficiency of thermal control materials. The Air Force Materials Laboratory has a long history of research in spacecraft contamination prediction, and materials characterization. The current efforts include developing improved materials and developing outgassing and condensation tests. Future efforts include determining the effects of contaminates on optical surfaces. The goal of these programs is to provide the necessary data to accurately predict the degradation of critical surfaces from contamination.

The current test to determine a material's outgassing potential is the ASTM-E595 test. In this test a material is heated to 125 °C in a vacuum of 5×10^{-6} torr for 24 hours. Afterwards the material is weighed to determine the total mass loss. A 25 °C witness plate is used to determine how much of the outgassing material will condense. This test is effective as a material screening tool; but, it does not provide the kinetic rate data required in contamination modeling. A contract was awarded to Lockheed Missile and Space Company, Palo Alto, California to develop improved material outgassing and condensation tests. The principal investigator at Lockheed is Dr. Peter Glassford.

The purpose of this program is to develop standard tests the aerospace community will adopt; therefore, industry participation in the test development was essential. An industry survey was conducted to determine what data are needed in the contamination models, as well as determine what equipment and expertise was available in industry. Once the tests were designed, a workshop was held to obtain industry's input.

The material outgassing test that has been designed consists of an effusion cell, mass spectrometer, and thermally controlled quartz crystal microbalance (TQCM). The material sample is placed in the effusion cell at a predetermined temperature, and the sample is outgassed in a vacuum of 10^{-6} torr range. The total outgassing mass as a function of time is determined with the TQCM which is cooled to LN_2 temperatures. Based on the view factor of the TQCM, the total outgassed mass can be determined. The technique will be verified by comparing the results to the actual mass loss of the sample which is determined by hanging the diffusion cell from a Cohn Microbalance. The mass spectrometer can be used to determine if there are any low molecular weight components outgassing, such as nitrogen which does not condense on the TQCM.

After the material has outgassed to a point of saturation, the effusion cell will be closed off, and the TQCM will be slowly heated. This will allow the condensed film to be broken down into its components. As the temperature is increased, the components will evaporate from the surface at a different rate. They can then be detected with the mass spectrometer. The relative amount of

each component can be found by the change in frequency of the TQCM as the component evaporates. Hence, from this test, not only is isothermal kinetic data obtained, but the primary components can also be identified in terms of their molecular weight. This is beneficial in both contamination modeling, as well as reducing the outgassing of a material during material development.

The condensation test will consist of TQCMs (one or several), and again an effusion cell and mass spectrometer. The sample will be placed in the effusion cell at a constant temperature, and the condensible materials of the outgassing sample will be determined for a wide range of temperatures, by either varying the temperature of the TQCM, or using several TQCM, all at different temperatures to cover a wide temperature spectrum.

Phase I of the program has been completed, which encompasses the workshop, survey, test design, and an extensive literature search. Phase II has begun which consists of developing and assembling the test apparatus, verifying the test techniques, and establishing standard procedures. The preliminary testing should begin in April, 1984.

Future plans of the Air Force Materials Laboratory include developing a test, and screening materials to determine the effects of contamination on optical windows and thermal control surfaces.

PREPARATION AND CLEANLINESS VERIFICATION OF A SPACE SIMULATION CHAMBER FOR CONTAMINATION SENSITIVE TEST SPECIMENS

W. R. Koch and M. J. Moseley
McDonnell Aircraft Company
McDonnell Douglas Corporation

ABSTRACT

Contamination sensitive optical devices were to be evaluated under thermal vacuum conditions. Test specifications called for an extremely clean chamber environment, ambient temperature chamber walls, and optical surface temperatures at approximately -30°C.

Chamber preparation included the replacement of diffusion pumps with cryopumps and the cleaning of the chamber walls to reduce contamination levels. Chamber cleaning using vacuum bake was tried and abandoned as time consuming and ineffective. Chemical cleaning and cleanliness verification methods were developed. Gas chromatograph analysis techniques were used extensively throughout the cleaning process to verify cleanliness levels prior to evacuating the chamber.

A chamber cleanliness verification test using a thermoelectric quartz crystal microbalance (TQCM) and witness samples was performed as a final demonstration to prove an appropriate cleanliness level had been achieved.

INTRODUCTION

Thermal vacuum testing of contamination sensitive optical devices requires the vacuum chamber environment be extremely clean. Molecular contaminates depositing on cold optical assemblies can severely degrade the optical performance and irrecoverably damage the optical assembly. The sources of contamination must be removed to prevent this from occurring. A major source of contamination can be the vacuum chamber itself. The test article is usually shielded from the vacuum chamber by the use of a liquid nitrogen cooled shroud. In this case, the test conditions prevented the use of such a shroud by requiring the test article be exposed to ambient temperature chamber walls. Complete refurbishment of the vacuum chamber was necessary to meet the cleanliness requirements.

FACILITY DESCRIPTION AND HISTORY

The vacuum chamber is a stainless steel horizontal cylinder 2.45 m (8 feet) in diameter and 4.9 m (16 feet) in length with one end removable. The chamber walls were polished to a #4 finish. The chamber was equipped with two 89-cm (35-inch) diameter oil diffusion pumps and a mechanical backing pump for vacuum operation down to 1×10^{-8} torr. A liquid nitrogen cooled shroud lined the chamber. The chamber was also equipped with bake-out heaters sufficient to raise the chamber wall temperature to 290°C.

The chamber was heavily contaminated by recent operations. Graphite epoxy wing skins had been baked in the chamber using the bake-out heaters and the mechanical pumping system. The vacuum chamber walls were covered with epoxy resins. These resins had to be removed in order to meet the test cleanliness requirements.

TEST REQUIREMENTS

The test requirements specified that the test article be exposed to ambient temperature chamber walls. Chamber pressure was to be maintained below 1×10^{-5} torr. The total contamination deposited on a -55°C surface over 100 hours of testing was not to exceed 0.1 $\mu g/cm^2$.

CHAMBER MODIFICATIONS

Extensive modifications were performed on the vacuum chamber. The diffusion pumps were replaced by 120-cm (48-in.) diameter cryopumps. Each cryopump was separated from the chamber by an 89-cm (35-in.) diameter high vacuum gate valve. The mechanical pump was replaced by a trapped Roots blower/mechanical pump combination. A new 2.45-m (8-foot) diameter liquid nitrogen shroud and shroud elbows for the pump ports were purchased. Only the pump port shrouds were installed for the test. An interlocked control system and a computer-based data acquisition system were installed to facilitate chamber operations. Figure 1 illustrates the modified chamber configuration.

CHAMBER BAKE-OUT

Chamber bake-out was performed in an effort to clean the vacuum chamber. Four bake-out cycles were performed. Each bake-out cycle consisted of wiping the chamber walls with 2-propanol, evacuating the chamber to 1×10^{-3} torr, and elevating the chamber walls to 290°C for eight hours. A liquid nitrogen cooled collection plate was installed to trap contamination. Epoxy resin was found in extensive quantities on the collection plate and on the chamber walls after each bake-out cycle. It was apparent that adequate chamber cleanliness could not be achieved in any reasonable amount of time using the chamber bake-out method.

CHEMICAL CLEANING

Chemical cleaning of the chamber was performed as an alternative to bake-out. The chamber was divided into sections approximately one square meter in area. Each chamber section was individually cleaned and checked to an appropriate cleanliness level.

MATERIALS USED

Material selection was an important consideration. All solvents used were ACS Certified Pure. This insured that the solvents were assayed by lot and had a nonvolatile residue less than 5 ppm. Solvent selection was made on the basis of contaminate solubility, availability, and safety considerations. Trichloroethylene, acetone, and 2-propanol were all used as cleaning solvents. Trichloroethylene was used because the epoxy resins were very soluble in it, but was abandoned as a cleaning solvent due to safety considerations. Acetone and 2-propanol proved to be effective general purpose cleaning solvents.

Materials which were to come into contact with the solvents and the chamber walls were chosen based on their availability and solvent compatibility. Solvent compatibility was determined by immersing pieces of candidate materials in each of the solvents for at least 12 hours. The residual solvents were analyzed using a gas chromatograph/mass spectrometer (GC/MS), chosen because of its high sensitivity for detection and identification of type of contaminates expected. The candidate material was accepted or rejected based on the contaminates found.

Cheesecloth was chosen as a primary cleaning material, because it was readily available and had remarkably good solvent compatibility. Nonsterile cotton swabs were used to clean corners and penetrations. The cotton swabs had a low solvent compatibility due to contaminates leaching out of the wooden shaft. This problem was mitagated by minimizing the exposure time of the swab to the solvent and the chamber.

Chamber cleaning personnel wore special clothing to prevent contamination of the chamber during the cleaning process. They wore Dacron polyester coveralls and hoods, tennis shoes, two layers of polyethylene gloves, and two layers of polyethylene boots. Polyethylene plastic was the only glove/boot material found to be solvent compatible. A forced air respirator system was used to protect personnel from solvent fumes while cleaning inside the chamber.

WIPE SAMPLING

The method used for checking contamination levels during cleaning is an adaptation of the wipe sampling method described in Reference 1. GC/MS was used instead of infrared spectroscopy to maximize sensitivity. A Hewlett Packard 5730A gas chromatograph and a 5987A gas chromatograph/mass spectroscopy system were used for sample analysis. The wipe sampling method used consisted of:

a. Preclean 10-ml glass vials and cotton swabs with acetone, hexane, or methylene chloride using an ultrasonic Soxhlet extractor. Check swabs and vials for cleanliness using GC/MS.

b. Add 5 ml of chromatographic grade 2-propanol or hexane to the glass vials. Seal each vial with aluminum foil under the vial cap.

c. Sample the chamber location by opening the vial and immersing the swab tip in the solvent. Wipe 1 square foot of the area with the swab, repeatedly wetting the swab tip with solvent.

d. Break off the swab tip into the glass vial and replace the cap.

e. In the chemistry laboratory, transfer the solvent in the glass vial to a 5-ml graduated conical tube.

f. Using nitrogen, slowly and gently evaporate the solvent in a water bath evaporator to a final volume of 0.05 ml.

g. Inject a 2-µliter aliquot of the residual solvent into the gas chromatograph, set at the following parameters:

Column	1.5 m (5 ft) Dexsil 300 (3.175 mm ss tube)
Oven Temp.	200°C - programmed to 320°C at 10°C/min. Hold for 2 min. at 320°C
Injector Temp.	250°C
Detector Temp.	350°C
Detector Type	Flame ionization

The Hewlett Packard 5730A gas chromatograph was used extensively for the routine examination of the wipe samples. The 5987A gas chromatograph/mass spectroscopy system was an invaluable tool for identifying unknown contaminates and in increasing sensitivity because of its powerful computer analysis system and its selective ion monitoring capabilities. Sensitivity was found to be extremely dependent on both wipe sampling and analysis techniques. Cleaning and prechecking of swabs and sampling containers is essential to obtaining meaningful data. Personnel must be cognizant of the proper techniques that must be developed and maintained. Large variations in sensitivity have been observed and traced to minor variations in operator techniques.

In an effort to determine the effectiveness of the wipe sampling technique, known concentrations of DC-704 diffusion pump oil in hexane were coated on a chamber section of known surface area. Concentrations varying from 0.16 µg/sq cm to 0.006 µg/sq cm were applied to the chamber section. The chamber section was cleaned between each application. Recovery efficiencies of 40-50 percent were obtained, indicating that low levels of contamination can be detected with this technique. Sensitivity could be further increased by using selective ion monitoring and increased wipe sample surface area.

CLEANING PROCEDURE

The chamber was divided into cleaning sections approximately one square meter in area. Each section was individually wiped clean and its cleanliness level checked using the technique described above. Wipe cleaning a section consisted of pouring the desired solvent onto cheesecloth, repeatedly scrubbing the section, and discarding the cheesecloth. The chamber section

was then checked for cleanliness using the GC/MS wipe sampling method. If a section was found to be contaminated, it was recleaned and rechecked until an acceptable cleanliness level was attained.

A study was made to determine the minimum number of times a section should be wiped to obtain a clean surface. Different sections of the chamber surface were cleaned using different numbers of wipes. Each area was then checked for cleanliness using the wipe sampling technique. The results, shown in Figure 2, were normalized to a wipe sample taken from an uncleaned chamber section. On the basis of these results, each chamber section was cleaned using 16 cleaning wipes of cheesecloth and solvents. Different solvent combinations were also examined. Eight wipes with acetone followed by eight wipes with 2-propanol was selected.

CLEANLINESS VERIFICATION TESTS

CONTAMINATION MONITORING SYSTEM

The contamination monitoring system consisted of a TQCM, a Goddard LN2 cooled cold finger, and two LN2 cooled witness samples. The witness samples were made of 2.54-cm (1-in.) diameter quartz discs plated with nickel and gold. The film thicknesses on the post test witness samples were measured using a helium-neon laser ellipsometer. The laser ellipsometer requires the index of refraction and density of the film material in order to determine film thickness. Since the film composition was unknown, the values for DC-704 diffusion pump oil were used. The TQCM was operated at -55°C and continuously monitored throughout the test. The contamination monitoring system was mounted on the chamber door, as shown in Figure 3.

CLEANLINESS TESTS

Two cleanliness tests were performed, the first after bake-out cleaning and the second test after chemical cleaning. The chamber pump-down sequence to working pressure consisted of a pure GN2 sweep at 5 torr for two hours while the pump port shrouds were cooled to LN2 temperature, followed by rough pumping to 1×10^{-2} torr, and then cryopumping to working pressure. Each cleanliness test was conducted at a working chamber pressure of less than 1×10^{-6} torr.

The bake-out cleanliness test revealed large amounts of contamination present. The TQCM recorded a deposition of 12 $\mu g/cm^2$, as shown in Figure 4. Each witness sample had a visible film, more than 6 $\mu g/cm^2$, which is the upper measurement limit of the laser ellipsometer. The chemically cleaned chamber displayed great improvement over the bake-out cleaned chamber. The TQCM recorded a deposition of 0.63 $\mu g/cm^2$, as shown in Figure 4. The witness samples had approximately 1 $\mu g/cm^2$.

SUMMARY

The results of the cleanliness verification tests demonstrate that a space simulation chamber can be prepared for contamination sensitive testing by chemical cleaning. Proper attention must be given to material selection and in developing cleaning techniques. The wipe sampling method combined with GC/MS analysis capabilities is a powerful technique for the identification of contaminates and in assessing chamber cleanliness level before testing. Chemical cleaning can be a viable alternative to bake-out in situations where a space simulation chamber must be cleaned in a short amount of time.

REFERENCES

1. Wolff, C. M.: Some New Techniques in Passive Contaminant Analysis of Space Environment Simulation Chambers, Sixth Space Simulation Symposium, May 1972, pp. 151-165.

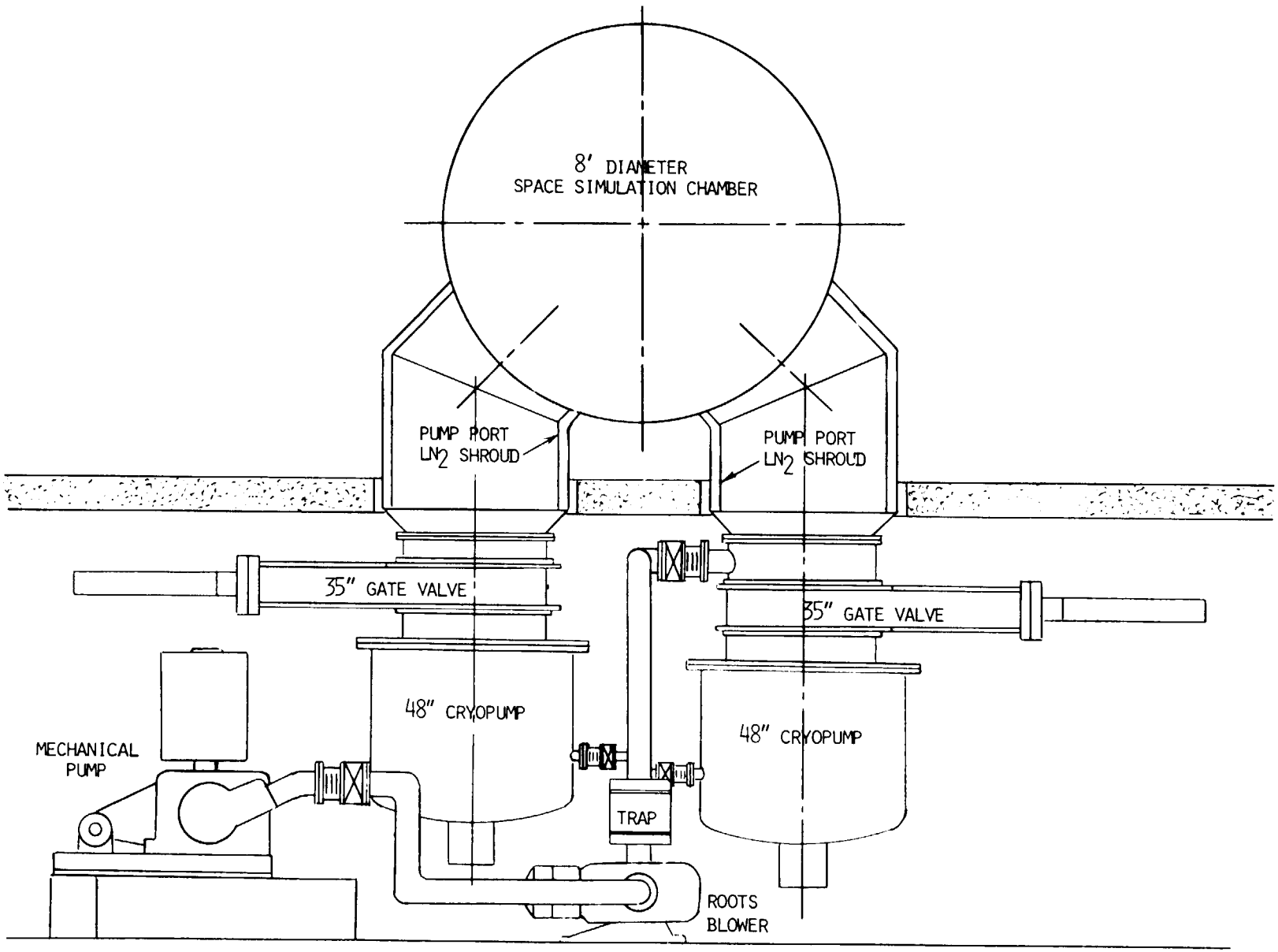

Figure 1 - Modified Space Simulation Chamber

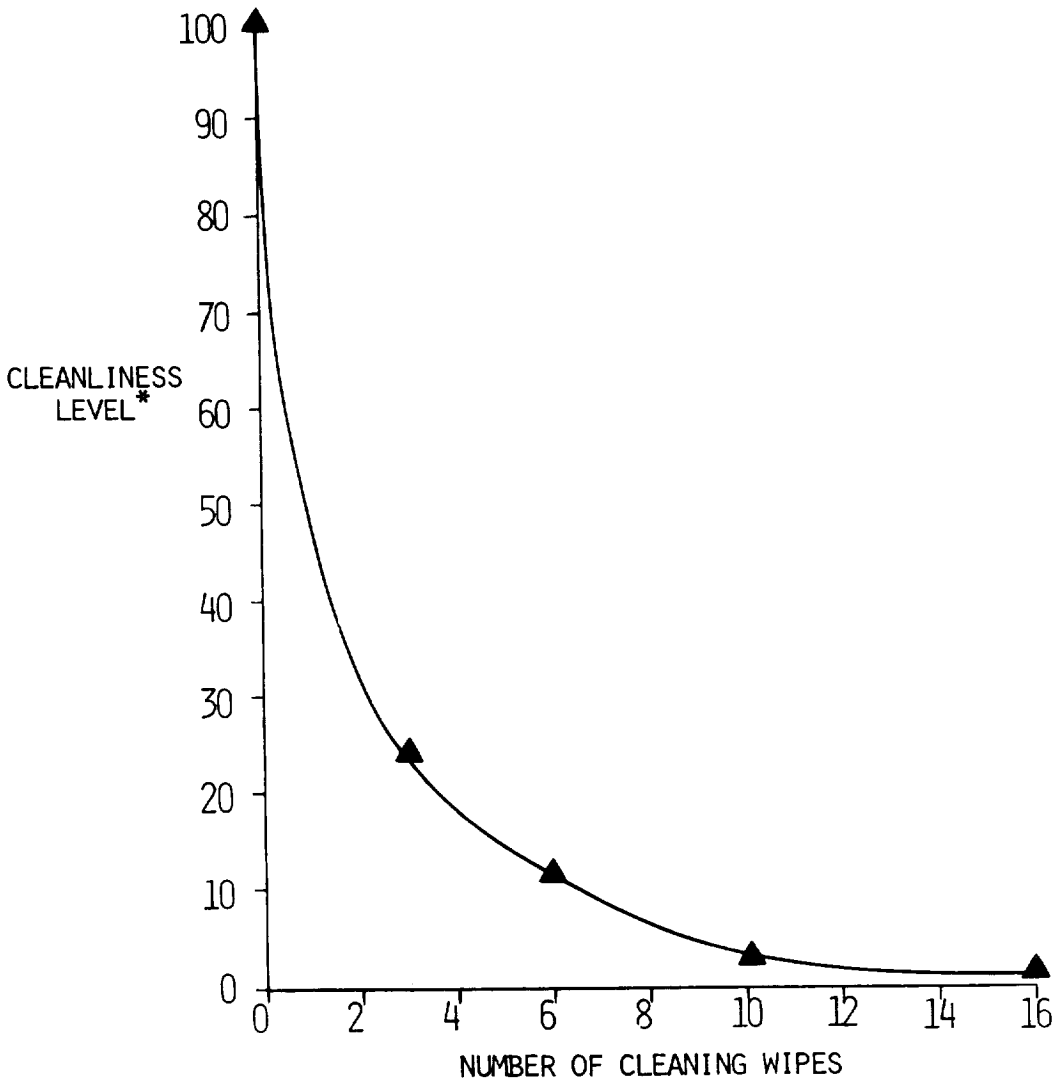

*NORMALIZED TO AN UNCLEANED SURFACE

Figure 2 - Chamber Wall Solvent Cleaning

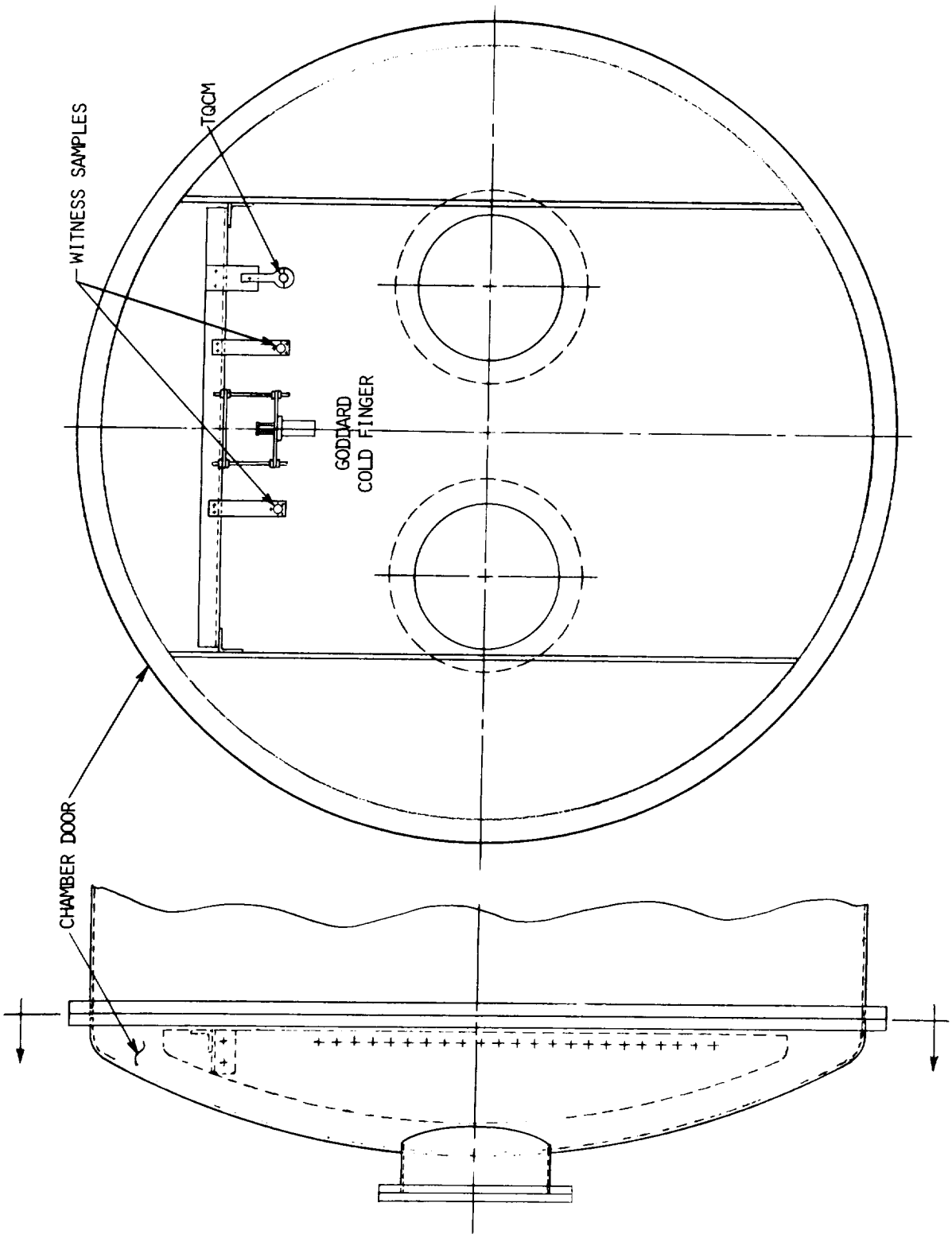

Figure 3 - Contamination Monitoring System

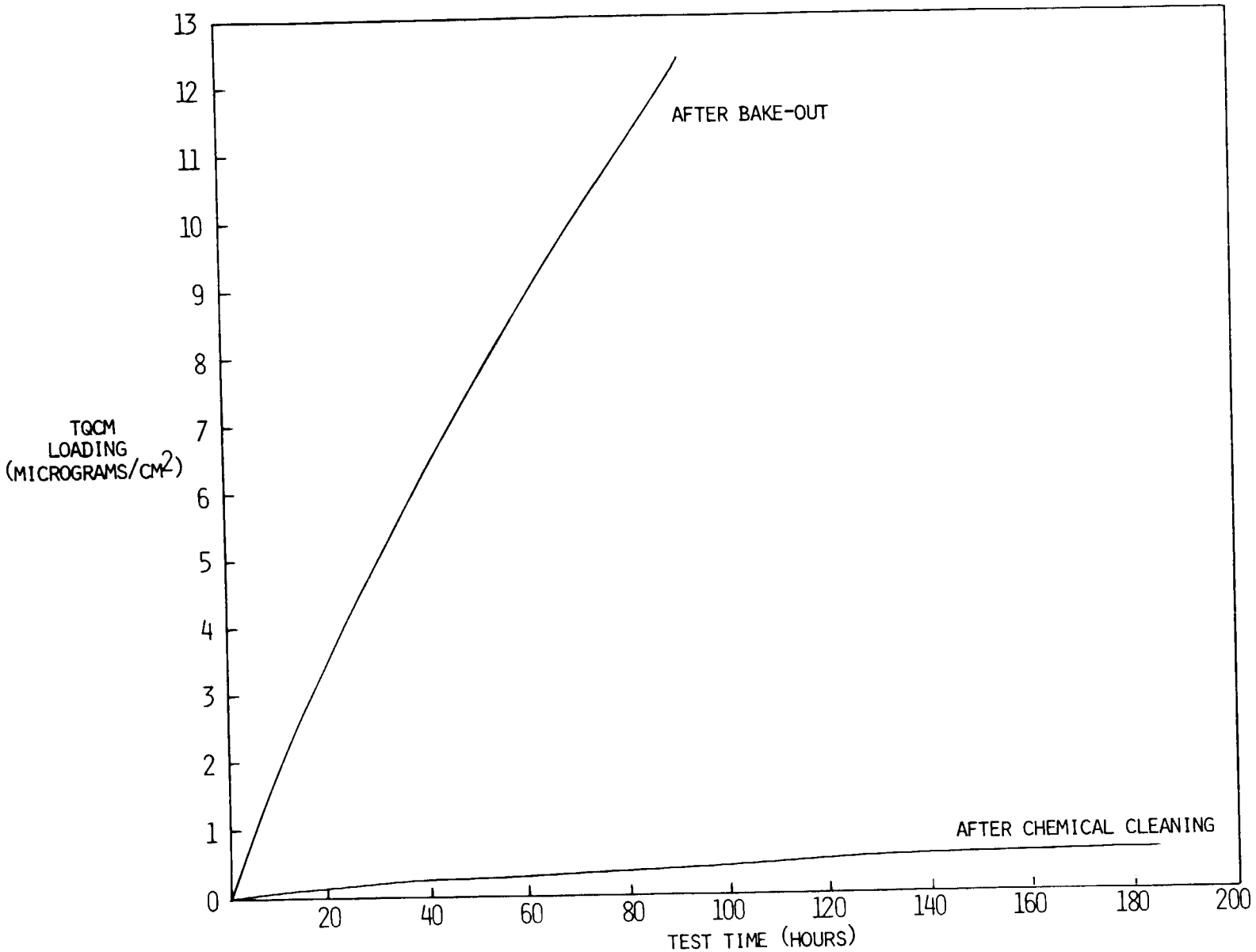

Figure 4 - Cleanliness Verification Test Results

CONTAMINATION MEASUREMENTS DURING IUS THERMAL VACUUM TESTS IN A LARGE SPACE CHAMBER[1]

C. R. Mullen and C. G. Shaw
Boeing Aerospace Company

ABSTRACT

Contamination measurements which are made during thermal vacuum tests have been very valuable in understanding the contamination potential from vented electronics compartments. These measurements can be used directly to predict in-flight contamination potential of an upper stage booster and spacecraft.

The Boeing Aerospace Company, over the last four years, has conducted qualification and acceptance thermal vacuum tests on a number of Inertial Upper Stage (IUS) vehicles as a part of the development and verification of the upper stage booster. Because of concerns about IUS materials outgassing condensing on sensitive surfaces of IUS-borne spacecraft, contamination measurements have been made during these tests to quantify the levels of contamination that originate from inside the equipment support section (ESS) due to outgassing from electronics components and wiring operating at elevated temperatures (80-160°F).

In the latest of these tests (IUS-5), the contamination measurements consisted of pressure measurements inside and outside the ESS and mass deposition measurements made with quartz crystal microbalances (QCM) facing into and away from ESS vents. The OCM's were operated at -50°C and -180°C using thermoelectrically and cryogenically cooled QCM's. Gaseous nitrogen flow inside the ESS was used to obtain the effective molecular-flow vent area of the ESS, which was evaluated to be 359 cm^2 (56 in^2) compared to the 978 cm^2 (150 in^2) estimated by an earlier atmosphere-pressure billowing test. The total outgassing rate of the ESS materials at a temperature of 60°C (140°F) decays with a time constant of 11.5 hours based on pressure measurements during the hot cycle. A time constant of 22 hours was estimated for the fraction of the outgassing which will condense on a -50°C surface. In contrast, the time constant is only 10.1 hours for the outgassing material which will condense on a surface at -180°C. A surface at -180°C will collect approximately one-half of the material vented form the ESS which impinges on it. Pressure measurements show very good correlation with the mass deposition measurements. Additional thermal vacuum contamination measurements are required to establish consistency and repeatability of the data.

INTRODUCTION

The IUS equipment support section (ESS) contains approximately 44 kg of miscellaneous organic materials. Outgassing rates of these materials in vacuum have been determined by laboratory tests of small samples. Predictions of total outgassing rates in the ESS have been based on the sample test data and material masses. Limitations of the sample data base and temperature variations of the materials cause uncertainty in outgassing and contamination predictions.

[1]This work was accomplished under Air Force Contract 04701-83-C-002

The purposes of the ESS vacuum outgassing test were to confirm prediction methods and establish full scale outgassing rates under realistic operating conditions from the electronics and wiring in the ESS. Very little of the deposition measured in this test would be deposited on a spacecraft. Additional analyses would be required to make this prediction.

TEST DESCRIPTION

The contamination tests were run as an add-on to the standard thermal vacuum acceptance test for the IUS-5 vehicle. Testing began on March 19, 1983, and was completed by March 24, 1983. The vehicle was equipped with most of its flight equipment, with the notable exception of the solid rocket motors. A metal dummy motor case was used in the vehicle's ESS. The vehicle was positioned in BAC's large space chamber with the roll axis vertical and the fore end uppermost. A cylindrical array of quartz-tungsten infrared lamps surrounded the IUS. The chamber was evacuated and the shroud which lines the chamber cooled by liquid nitrogen. In this simulated space environment, the vehicle was heated and cooled to the extremes of its acceptance temperature range. As a result of the vacuum and thermal conditions, the vehicle outgassed a significant amount of material, most of which was expected to exhaust from the main vents from the ESS. Special equipment to characterize this outgassing and its condensation onto cold surfaces was installed in the vehicle and chamber. Descriptions of this equipment and its operation are given in the following paragraphs.

CONTAMINATION MEASUREMENT EQUIPMENT

In addition to the standard cold fingers and witness plates, four UHV Bayard-Alpert nude ion gages, four Hastings-type DV-6 thermocouple gages, and five quartz-crystal microbalances (QCM) were used as contamination monitors. The eight ion and thermocouple gages were mounted inside the ESS at the locations shown in figure 1, with one gage of each type at each of the four locations. The thermocouple gages, for measuring ambient gas pressures from 10^{-3} to 1 Torr, were wrapped with Kapton insulation and small heaters used to maintain their environment at 142°F (at which temperature these gages had been calibrated). The ion gages were used to measure ESS pressures below about 10^{-3} Torr. Flight insulation was used to close the top of the ESS after the gages were installed. In addition to the internal ESS gages, two ion gages were mounted in the vacuum chamber well above the vehicle to measure external pressures below 10^{-3} Torr.

The QCM's measure the deposition of contaminants on quartz crystals held at a predetermined temperature level. AS outgassing material impinges on the crystal, some fraction of the material condenses and causes the piezoelectric vibration of the crystal to slow down. The difference between the frequency of this crystal and that of an identical crystal hidden behind the first (and therefore shilded from molecular impingement) thus increases, serving as a measure of the total mass deposited. Two types of QCM's were used: a cryogenic or CQCM for measurements at -180°C and a thermoelectrically cooled or TQCM for measurements at -50°C. The CQCM will collect water and most outgassed products except for hydrogen, helium, and common atmospheric gases. The TQCM will only collect those materials liable to contaminate shaded spacecraft surfaces at temperatures in the vicinity of -50°C.

One CQCM and one TQCM were mounted just outside the vent over one of the IUS computers, looking radially inward (see figs. 2 and 3). Above each of these, but looking radially outward (toward the chamber shroud), was an identical instrument used to establish a base deposition rate from any ambient condensible gas background. Since a primary source of contamination for IUS-borne spacecraft is reflection of vented outgassing off the top of the computers, a third TQCM was mounted looking down at the top of the second computer from the interstage plane (see fig. 4).

TEST PROCEDURE

The general thermal-vacuum acceptance test procedure (fig. 5) involved allowing the vehicle to cool until certain components had reached their acceptance minima (typically near $-24°C$), holding for 8 hours, turning on all equipment and the lamp array to reach certain component acceptance maxima (near 71°C), holding for 8 hours, and then repeating. For this test, the vehicle was turned off and allowed to cool following its second hot soak, the chamber was backfilled and the shroud warmed to ambient, then the chamber was pumped down again for a nitrogen bleed test.

All thermocouple gages and their heaters were energized prior to the start of pumping and run throughout the test. The ion gages were energized at roughly 10^{-3} Torr. During the course of the thermal-vacuum test, some of the ion gages were turned off whenever it was suspected that heating from the hot ion gage filaments might have an adverse effect on the acceptance test. The QCM's were energized prior to pumpdown at temperatures near 25°C. The TQCM temperatures were lowered to $-50°C$ when the chamber pressure dropped below 10^{-4} Torr. When the chamber walls had been cooled, the CQCM temperatures were set to $-180°C$. Whenever a QCM overloaded with condensed material, its temperature was raised and held until the major portion of the deposit was burned off, then lowered as soon as possible back to the operating temperature. At the end of the thermal-vacuum test, the QCM's were warmed in 20°C steps, holding at each step for 30 minutes to allow for determination of the desorption rates for the deposited material. The QCM's were turned off during the nitrogen bleed test, in which pressures were measured inside and outside the ESS as various rates of nitrogen gas flow were introduced into the ESS via a metal tube.

DATA ANALYSIS

NITROGEN BLEED TEST

The nitrogen bleed test was conducted after completion of the vehicle thermal cycling test. The purpose of this phase was to determine effective vent areas from the ESS.

Controlled flow rates of nitrogen were introduced into the ESS cavity to establish the pressure flow rate relationship. Two ion gages, one inside and one outside the ESS were used for vent area calculations for flow rates of 0 to 0.005 g/s. The thermocouple type pressure gages (DV-6 gages) were used for ESS pressures with the higher nitrogen flow rates. Table 1 summarizes the pressure and flow rate data which were used for calculating vent area.

The effective vent area was calculated from the free molecular flow equation:

$$A_e = \frac{F\left(\frac{T}{M}\right)^{1/2}}{0.058\ \text{DELTA P}}$$

where:

F is the nitrogen flow rate in g/s
T is temperature in °K
M is molecular weight in g/mol
DELTAP is vent pressure drop in torr (ESS internal pressure minus chamber pressure).

A straight line least squares fit to the six pressure versus flow rate points (fig. 6) results in 328 cm^2 (51 in^2) effective vent area. Using only the four lowest flow points (ion gage range) results in 359 cm^2 (56 in^2) effective vent area. The data from a previous nitrogen-flow test with the IUS-6 vehicle produced 374 cm^2 (58 in^2) vent area using the same analysis method. The good agreement between the two test results provides confidence in both results. The 359 cm^2 vent area was used for subsequent ESS outgassing flow analyses because all pressures were in the ion gage range.

ESS PRESSURES AND MASS OUTGASSED

Figures 7 and 8 compare pressures inside the ESS (UHV #1 and #4) with the vacuum chamber pressures (UHV #6). The UHV #5 chamber pressure data are not shown since UHV #5 agreed well with UHV #6 and chamber pressures were much lower than ESS pressures.

The slope of the ESS pressures during the hot soak cycles matches the 11.5-hour time constant lines shown on figures 7 and 8. The time constant lines shift approximately 0.7 days between the two hot cycles. The initial ESS pressure is approximately 2.3×10^{-4} Torr. The initial outgassing rate equivalent to the initial pressure is 0.0014 g/s based on 359 cm^2 vent area and an assumed molecular weight of 30. The equivalent 24-hour mass loss is 52g based on the initial rate and an 11.5-hour time constant. This observed 24-hour loss is 61% of the expected loss derived from material test data (table 2) at 65°C (149°F).

The effect of temperature on outgassing rate was derived from the pressure change between hot and cold cycles, for which average ESS interior temperatures are roughly 140°F and 0°F respectively. Assuming an exponential temperature relationship, the outgassing rate is:

$$R_T = R_{140°F}\, e^{(140-T)/37}$$

where:
R_T is the outgassing rate at temperature T,
$R_{140°F}$ is the rate at 140°F, and
T is the desired temperature.

The temperature relationship was derived from ratio of the pressure at the midpoint of the cold cycle to the time constant line midway between the two hot cycles.

The temperature relationship predicts the 149°F outgassing rate to be 27.5% greater than the 140°F rate. Increasing the 52g 24-hour 140°F mass loss by 27.5% results in 66.3g/24-hours at 149°F. This result is 78% of the predicted 85.4g from table 2. The discrepancy between the test and predicted value is not large considering error sources such as:

1. Pressure gage accuracy is probably not better than 20%.

2. A molecular weight of 30 was assumed.

3. The prediction is based on small test samples instead of actual flight hardware.

Approximate ESS vent pressure drop data for the complete test were developed from the ESS and other chamber pressure data of figures 7 and 8. Flow rates determined from the pressure drop data were integrated to produce the test outgassing mass history of figure 9 where again a molecular weight of 30 was assumed.

QUARTZ-CRYSTAL MICROBALANCE (QCM) DEPOSITION

A plot of the frequency versus time has the general appearance of a series of sawtooths, with a rise due to mass deposition followed by a sharp decrease as the QCM overloads, is heated to evaporate the deposit, then is cooled to its operating temperature and begins to pick up mass again. These "sawtooth" plots were used to generate smooth deposition curves by extrapolating the positive slope prior to each overload across the "burn-off" gap and lifting the next sawtooth so that it starts on the extrapolated line. The smooth deposition curves plotted in this fashion represent the deposition which would be seen if the QCM's never overloaded (see Fig. 10).

Comparisons among the results of the QCM data can best be made by calculating the maximum rate of deposition from each of the curves. The maximum slopes during the hot cycles are listed in table 3 in units of kHz/day.

The most obvious result is that the deposition on the outward-looking QCM's is small compared to their inward-looking counterparts (0.49% at T = −50°C and 2.14% at T = −180°C, based on the first hot cycle). This indicates that deposition from the ambient chamber environment can be safely ignored in predicting ESS outgassing from the inward-looking QCM results. The similarity of the inward- and outward-looking curves indicates that the ambient background of condensible material is just rebound of ESS outgassing from the cold chamber shroud. The more volatile materials collected at −180°C but not at −50°C will not be as efficiently trapped by the LN2-cooled shroud, so that the ratio of outward- to inward-looking depositions should be larger at the lower temperatures, as is confirmed by the above percentages.

The ratio of outward to inward depositions hardly changes at all (from 0.49% to 0.48%) in the second cycle for the TQCM's. This probably indicates that the composition of outgassed material condensible at −50°C did not change significantly over the duration of the test, since the "sticking" to the cryoshroud seems relatively unaffected. For the CQCM's, however, the ratio

falls from 2.14% to 1.67%, which indicates that the more volatile materials tend to be released earlier in the test.

Flux factors from the computer vents to the QCM's were calculated by modeling the vents as networks of planar sources of molecular flux with a cosine distribution about the normal IUS radius vectors through their centers. Both direct impingement and reflection of molecules off the exterior top surface of the computers were taken into account. The flux factors represent the ratio of the molecular flux arriving at the QCM to that leaving the vent. They have the values 0.0879, 0.1701, and 0.1742 for the down-facing TQCM, inward-facing TQCM, and inward-facing CQCM, respectively. With these numbers, the down-facing TQCM should get about 52% of the deposition received by the in-facing TQCM. The ratio of the measured deposition rates in table 3 is 34%. Although the vent seen by the down-facing TQCM may be passing a smaller flux than the vent where the other QCM's are located (due to a different local outgassing geometry just inside the vent), it is more likely that the assumption of a cosine distribution from the vent is in error. Since the computer top surface extends into the vent, it probably tends to make the vent operate slightly less like an orifice and slightly more like a tube, causing more of the flux to be directed in a forward direction at the expense of the higher angles. This error is probably more pronounced at the higher angles than in the forward direction where the inward-looking QCM's are located.

Using the flux factors, the QCM mass sensitivity of 1.56 $\mu g/cm^2$-kHz, and the data in table 3, the maximum condensible mass flux out of the vents is calculated to be:

0.0796 $\mu g/cm^2$-sec for a $-50°C$ surface

1.173 $\mu g/cm^2$-sec for a $-180°C$ surface

With a total vent area of about 359 cm^2, the total mass of condensible outgassed material from the ESS is 0.10g ($-50°C$) or 1.52g ($-180°C$) maximum for every hour that the IUS is at its acceptance temperature maxima in space.

CORRELATION OF QCM DEPOSITION WITH ESS PRESSURE

The curve derived from integration of the ESS pressure (fig. 9) bears a strong resemblance to the QCM deposition curves. Between time points 321.1 and 322.0, the inward-looking CQCM recorded a frequency increase of 4000 kHz, which corresponds to a total emission of about 0.036g from every cm^2 of vent area. With a total vent area of 359 cm^2, this represents a total of 12.9g of outgassed material (condensible at $-180°C$) escaping from the ESS. Between the same limits, the pressure-integration curve gives an ESS mass loss of approximately 30g, where a mean molecular weight of 30 atomic mass units was assumed. Since the CQCM surface at $-180°C$ would not be expected to collect the lighter molecules which may make up a substantial portion of the outgassing, the difference between the CQCM and pressure-integration results is reasonable.

The deposition curves from the inward-looking QCM's were fitted with exponential-decay curves, yielding decay constants of 22 hours for TQCM #3 at $-50°C$ and 10.1 hours for CQCM #4 at $-180°C$. As stated above, the time constant for ESS pressure decay is 11.5 hours. The higher volatiles that stick at $-180°C$ but not at $-50°C$ should be depleted faster than the less volatile material that will condense at $-50°C$, so the difference in QCM time constants is to be

expected. Also, since the CQCM deposition rates are over one order of magnitude larger than those for the TQCM, it is quite reasonable that the overall pressure decay time constant (which contains contributions from all outgassing species) is dominated by that of the high volatiles.

Without in-situ mass spectroscopy to provide the masses of the outgassed molecules in the ESS, no further correlation between the QCM and pressure measurements can be made.

CONCLUSIONS

1. The IUS-5 vehicle has an effective ESS vent area for molecular flow of 359 cm^2 (56 in^2) based on the internal to external ESS pressure differences measured for various rates of nitrogen flow into the internal volume of the ESS.

2. The total outgassing rate of the ESS materials at a temperature of 60°C (140°F) near their acceptance temperature maxima decays with a time constant of 11.5 hours. For that fraction of the outgassing which will condense on a −50°C surface, the time constant is 22 hours. In contrast, for the outgassing material which will condense at −180°C, the time constant is only 10.1 hours.

3. The total mass of outgassing in 24 hours from a 60°C ESS, as measured by ESS pressure, is approximately 78% of that predicted from standard total mass loss test data on the ESS materials.

4. Rebound of vented ESS outgassing from the cryoshroud walls creates an ambient background of condensible gas that is negligible compared to the flux out of the vents but which may have serious effects on QCM's pointed at other vehicle areas in the space chamber. The background accounts for the majority of the contamination measured by some QCM's in previous IUS thermal vacuum tests.

5. The maximum flux of outgassing from the ESS vents which is condensible on a −50°C surface is 0.0796 $\mu g/cm^2$-sec.

6. The −50°C condensible outgassing flux from the ESS computer vents is somewhat more in the radially outward direction than a cosine distribution would predict. Thus, predictions of the flux from the vents to an IUS-borne spacecraft are conservative in their use of a cosine model for the venting.

7. The maximum flux of outgassing from the ESS vents which is condensible on a −180°C surface is 1.173 $\mu g/cm^2$-sec.

8. Under the assumption of a mean molecular weight for outgassing molecules of 30 atomic mass units, a surface at −180°C will collect approximately half of the material vented from the ESS at its acceptance temperature maxima.

9. The maximum increase in ESS pressure caused by outgassing of materials near acceptance temperature maxima is under $3x10^{-4}$ Torr, too low to be of concern for corona discharge in any unsealed RF switches. Note that this pressure does not include any outgassing caused by solid rocket motor materials or heat-soak effects.

RECOMMENDATIONS FOR SUBSEQUENT TESTS

1. Check all QCM circuitry prior to testing with a wave generator that simulates the full frequency and amplitude range of the QCM as input to the QCM controller. Identify and remove all electronic interference and noise from the QCM signal as measured at the data acquisition equipment.

2. Install a residual gas analyzer either within the ESS or at the end of a baked-out, heated tube positioned to catch the outgassing flux from one of the computer vents. This should provide information on the molecular weights of the outgassed material.

3. Operate internal ESS ion gages on duty cycles of no more than 1 minute of operation out of every 30 minutes, to minimize contamination effects on the gage. Post-calibrate the gages with the same duty cycle to minimize the removal of contamination the calibration.

4. Flush the chamber with dry nitrogen prior to pumping, cool one of the cold fingers to liquid nitrogen temperature, then cool the QCM's to their minimum operating temperatures before starting the pump-down. This will allow a measurement of the amount of outgassing released between 760 and 10^{-4} Torr.

Table 1 - Nitrogen Flow Test Data Summary

Pressure Gage Type	Nitrogen Flow Rate g/sec	Pressure Inside ESS Torr	Vacuum Chamber Pressure Torr	Vent Pressure Drop Test
Ion	0	9.73×10^{-5}	7.96×10^{-5}	1.77×10^{-5}
	0.0005	2.72×10^{-4}	1.30×10^{-4}	1.42×10^{-4}
	0.001	4.5×10^{-4}	2.01×10^{-4}	2.49×10^{-4}
	0.005	1.64×10^{-3}	8.18×10^{-4}	8.22×10^{-4}
Thermocouple	0.016	5.09×10^{-3}	1.19×10^{-3}	3.90×10^{-3}
	0.04	9.01×10^{-3}	2.41×10^{-3}	6.60×10^{-3}

Table 2 - IUS-5 Equipment Support Section Outgassing Materials

Material	Total Mass, kg	24-Hour Mass Loss at 65°C	
		Percent	Grams
Epoxy Primer	0.454	2.16	9.81
Silicone rubber clamps	1.710	0.20	3.42
Silicone fiberglass air ducts	1.542	0.08	1.23
Black paint on avionics	0.136	0.27	0.37
Wire harness insulation	5.443	1.10	59.87
Conformal coated circuit boards and misc. organics in avionics	30.127	0.02*	6.03
Multilayer insulation	4.64	0.10	4.64
Total			85.37

*Taken as 1/2 the measured 24-hour rate for a cured board with acceptance test thermal vacuum bakeout.

Table 3 - Maximum QCM Deposition Rates

Instrument	First Hot Cycle Rate (kHz/day)	Second Hot Cycle Rate (kHz/day)
TQCM #1 looking down	258.06	--
TQCM #2 looking out	3.64	1.60
TQCM #3 looking in	750.00	333.33
CQCM #4 looking in	11,320.75	3,680.98
CQCM #5 looking out	242.42	61.54

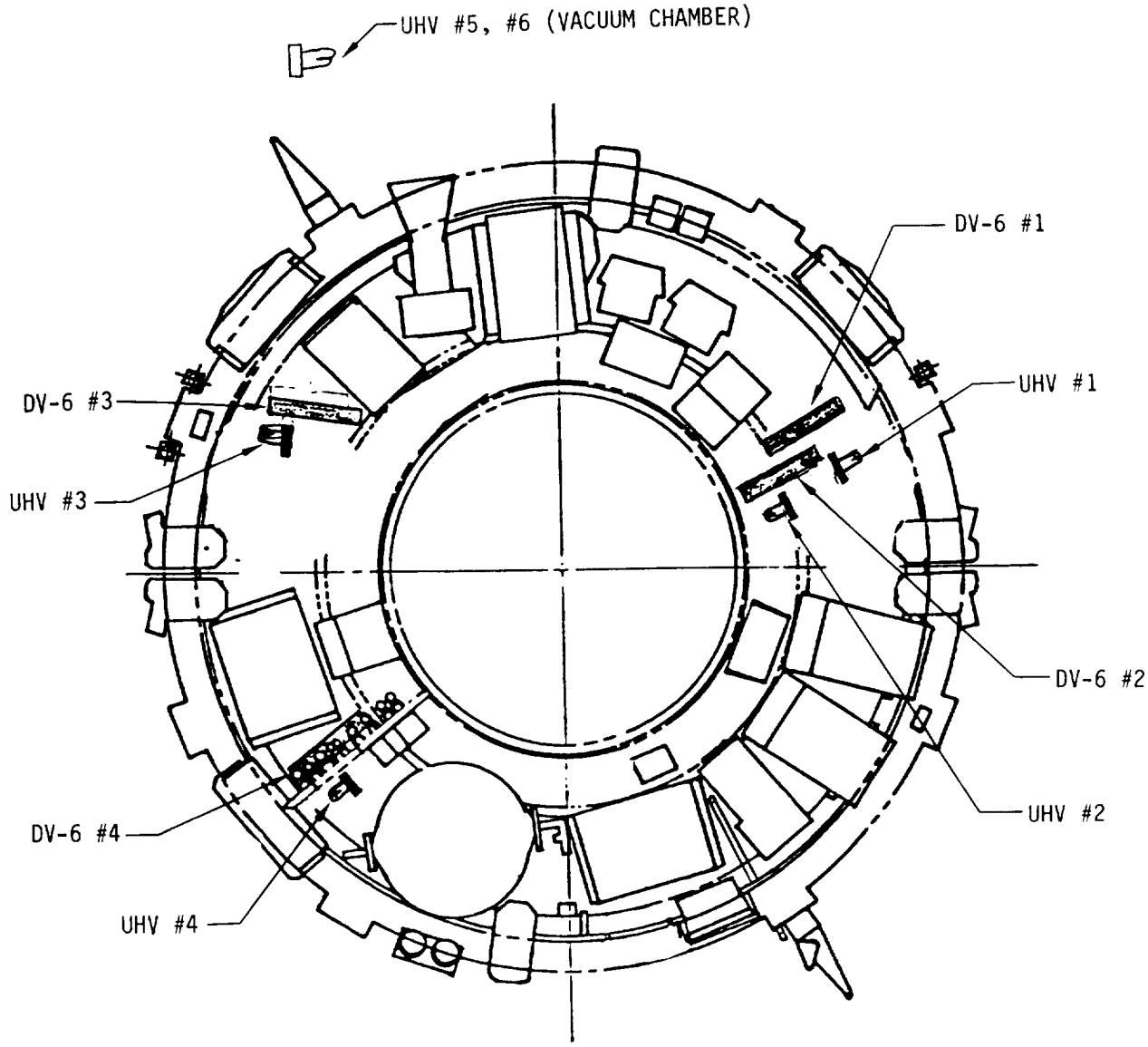

Figure 1 - Pressure Gauge Locations in ESS

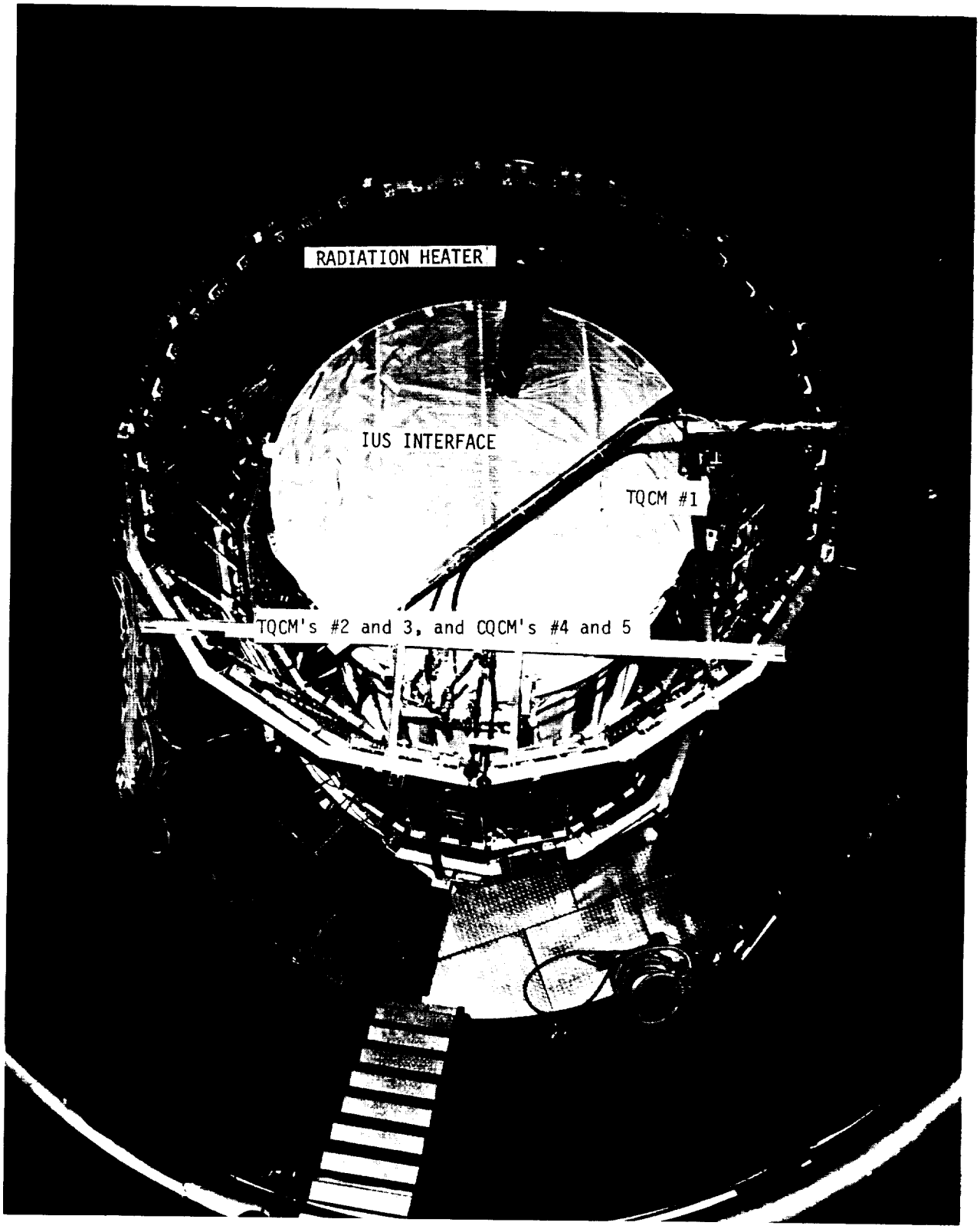

Figure 2 - Top View of IUS, Showing General Location of QCM's

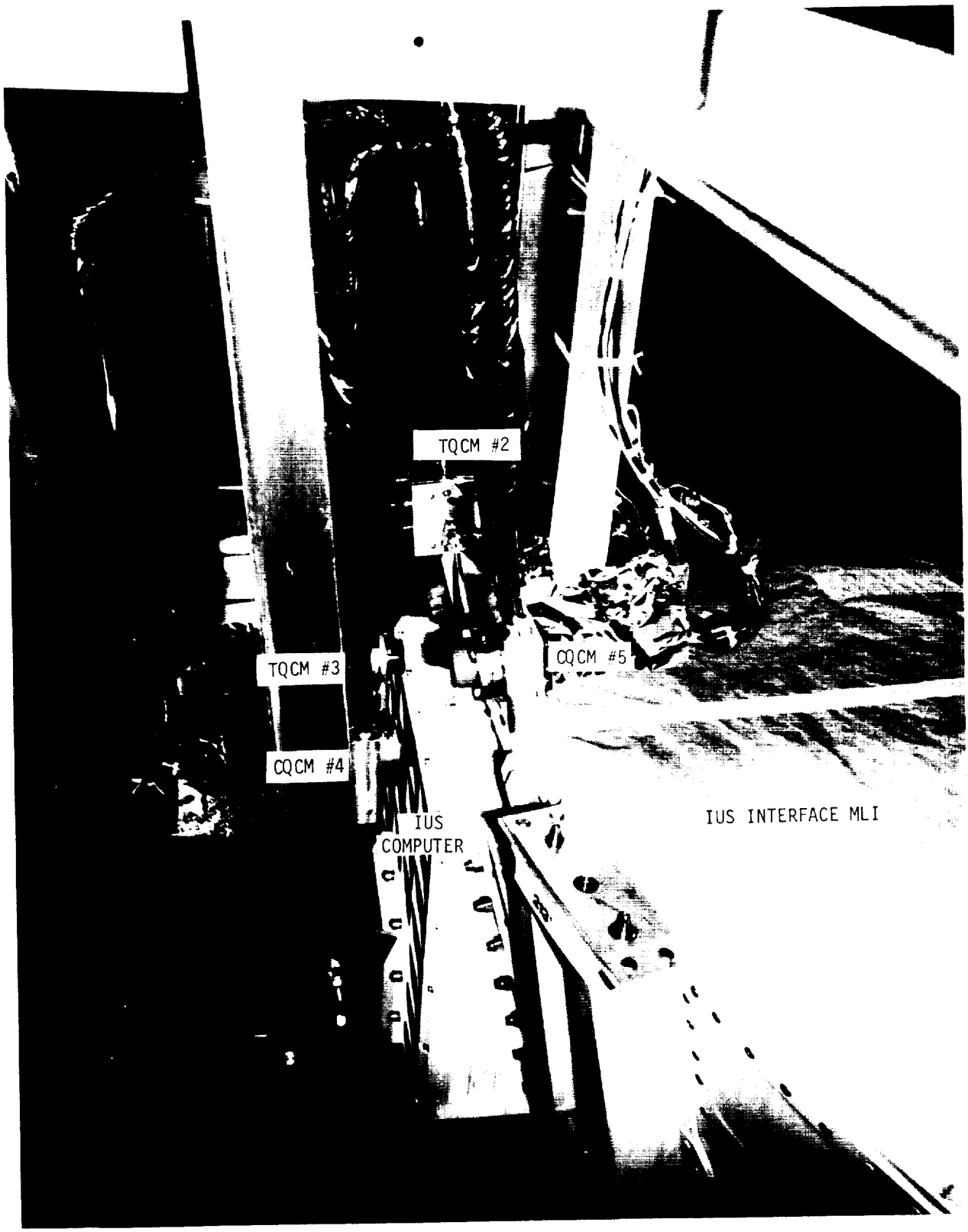

Figure 3 - Side View of TQCM's #2 and 3, and CQCM's #4 and 5

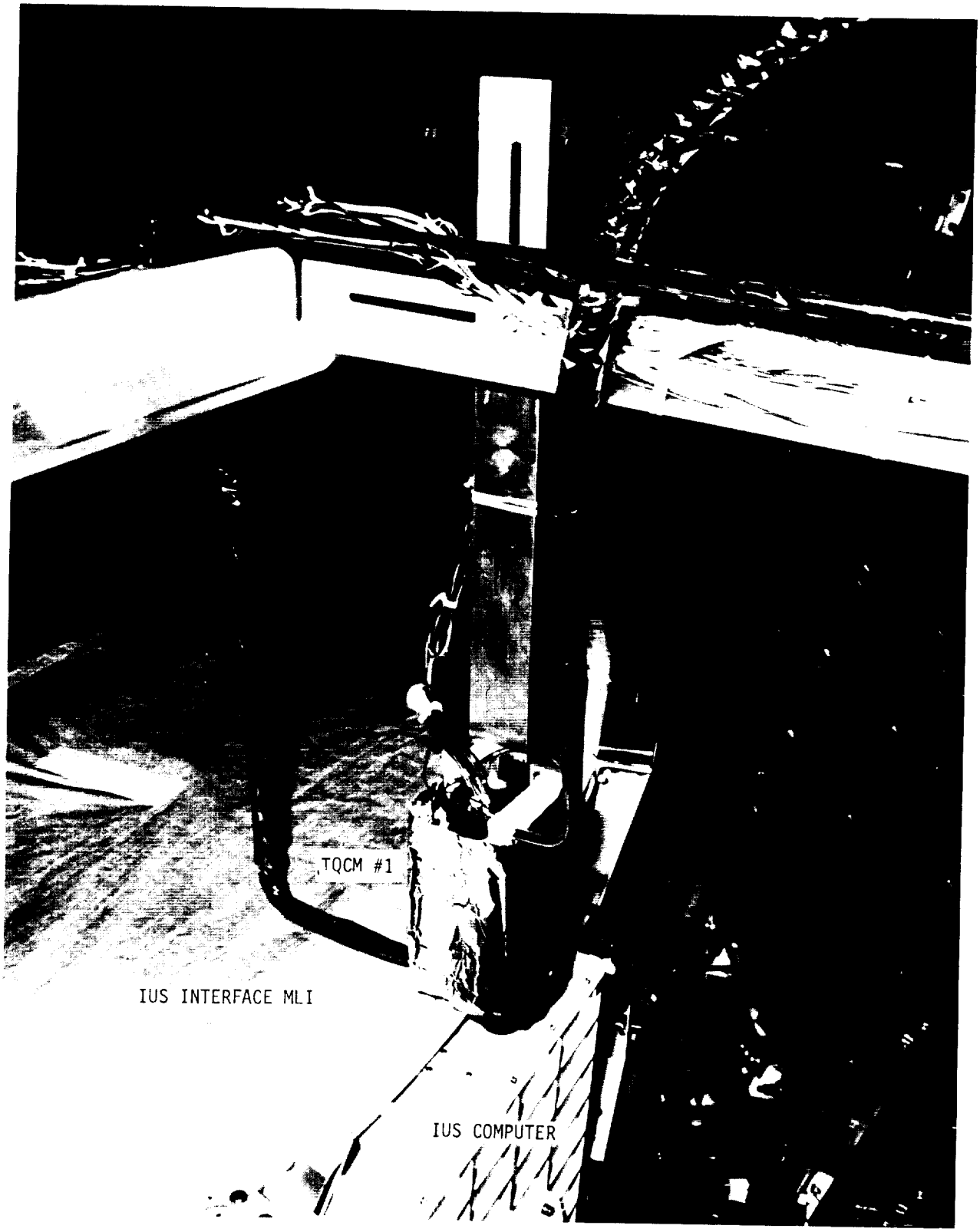

Figure 4 - View of TQCM #1

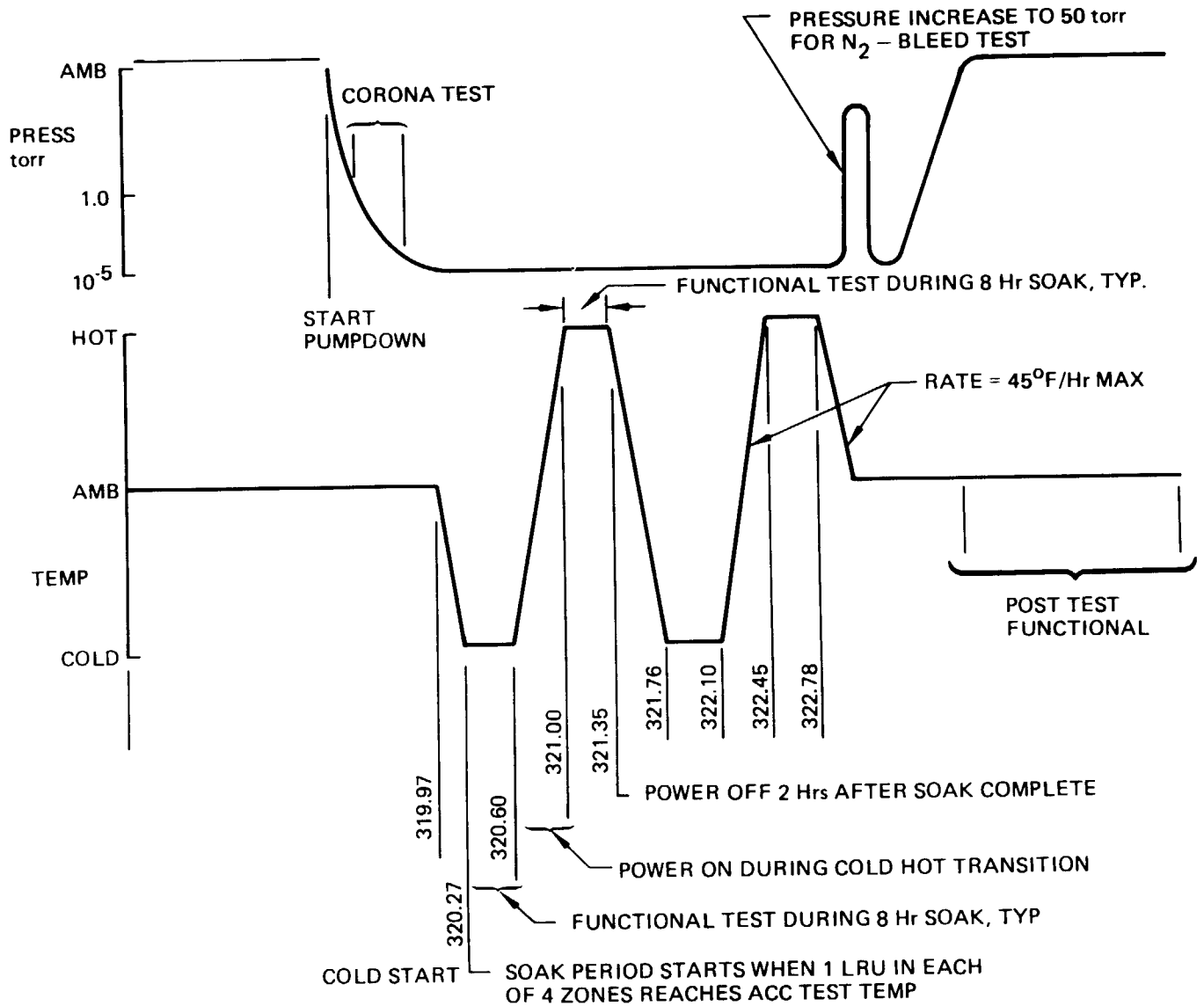

Figure 5 - IUS-5 Thermal/Vacuum Acceptance Test Thermal Cycle

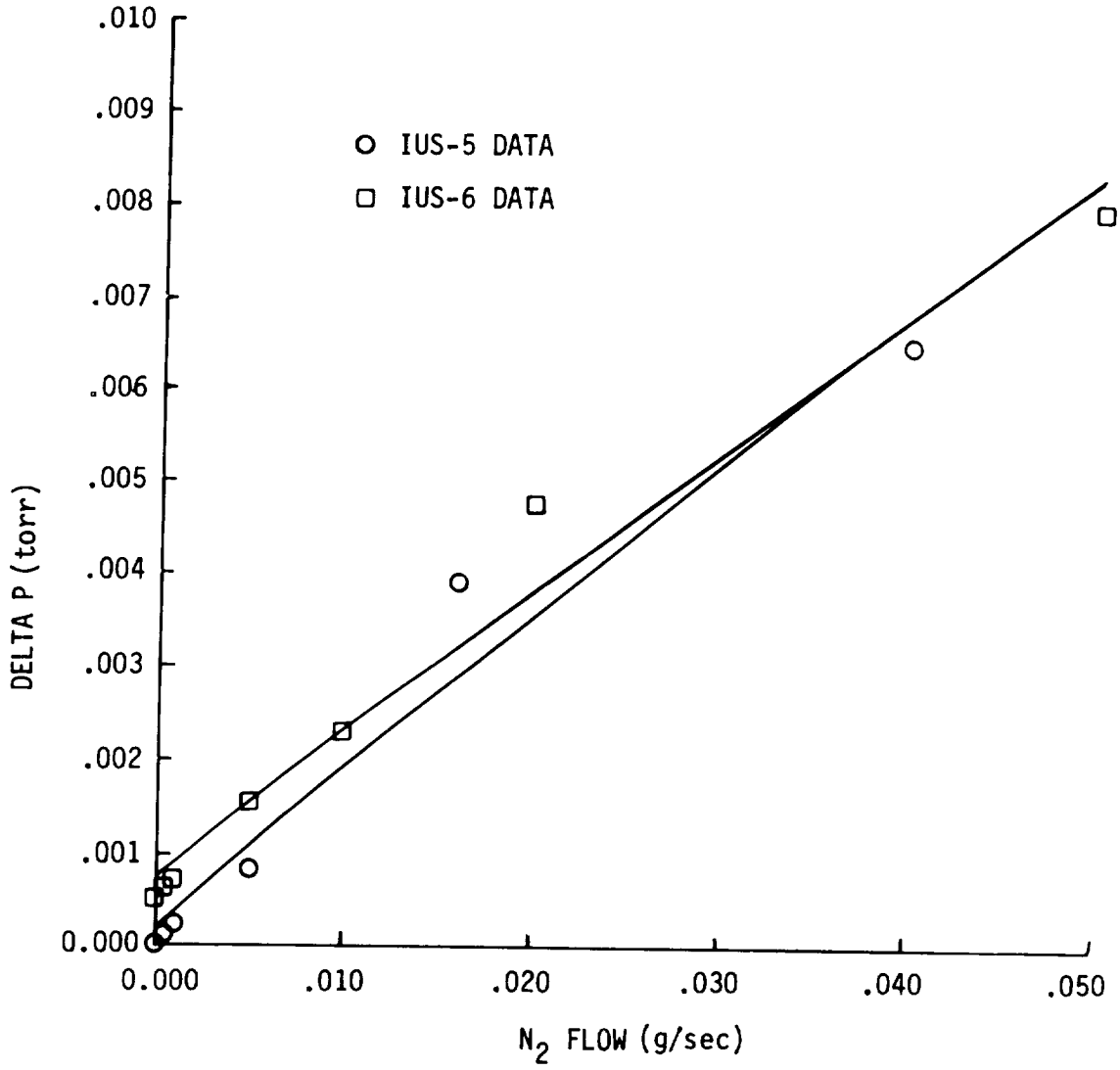

Figure 6 - Nitrogen Bleed Test Data

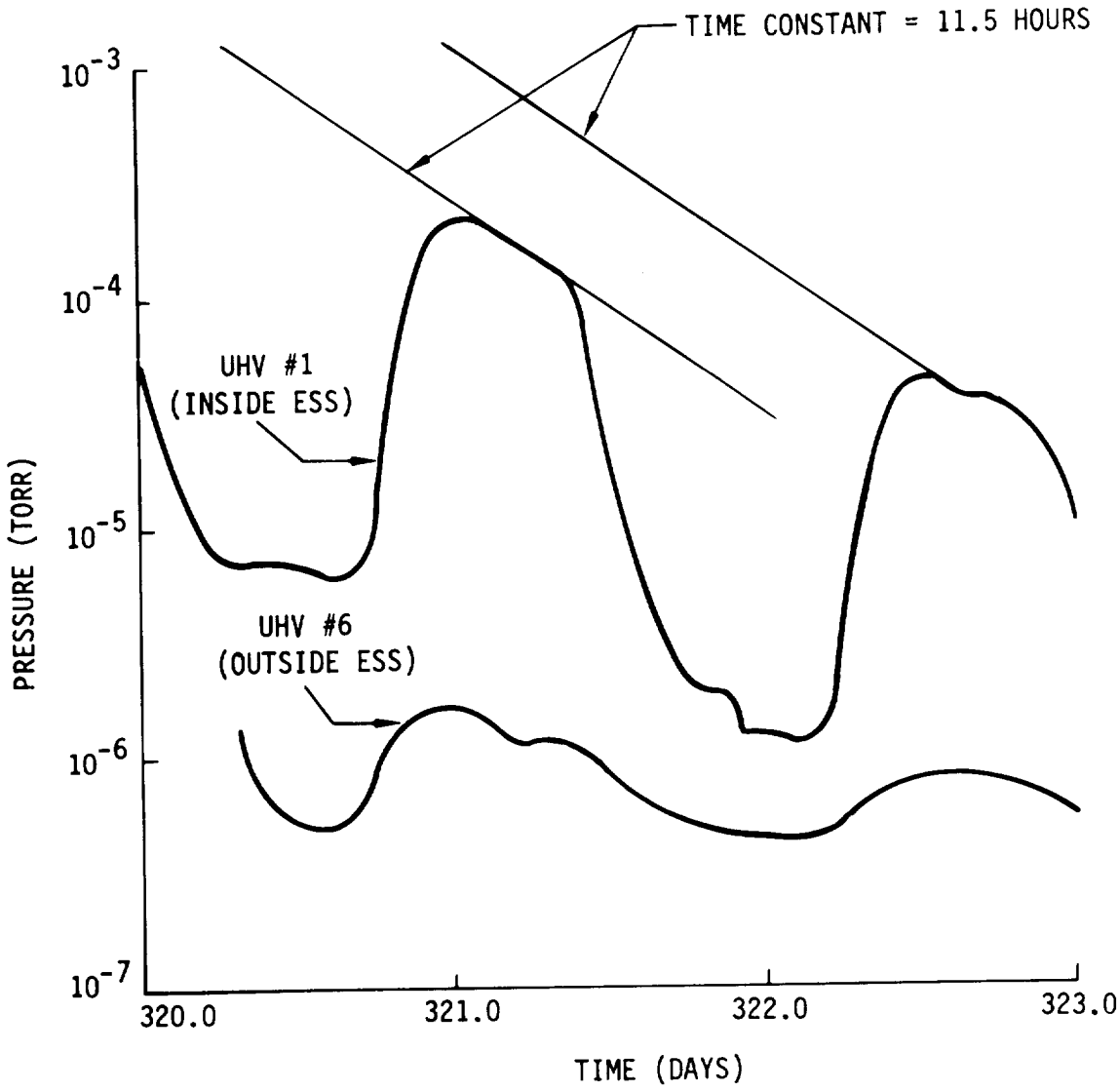

Figure 7 - ESS and Chamber Pressure vs Time

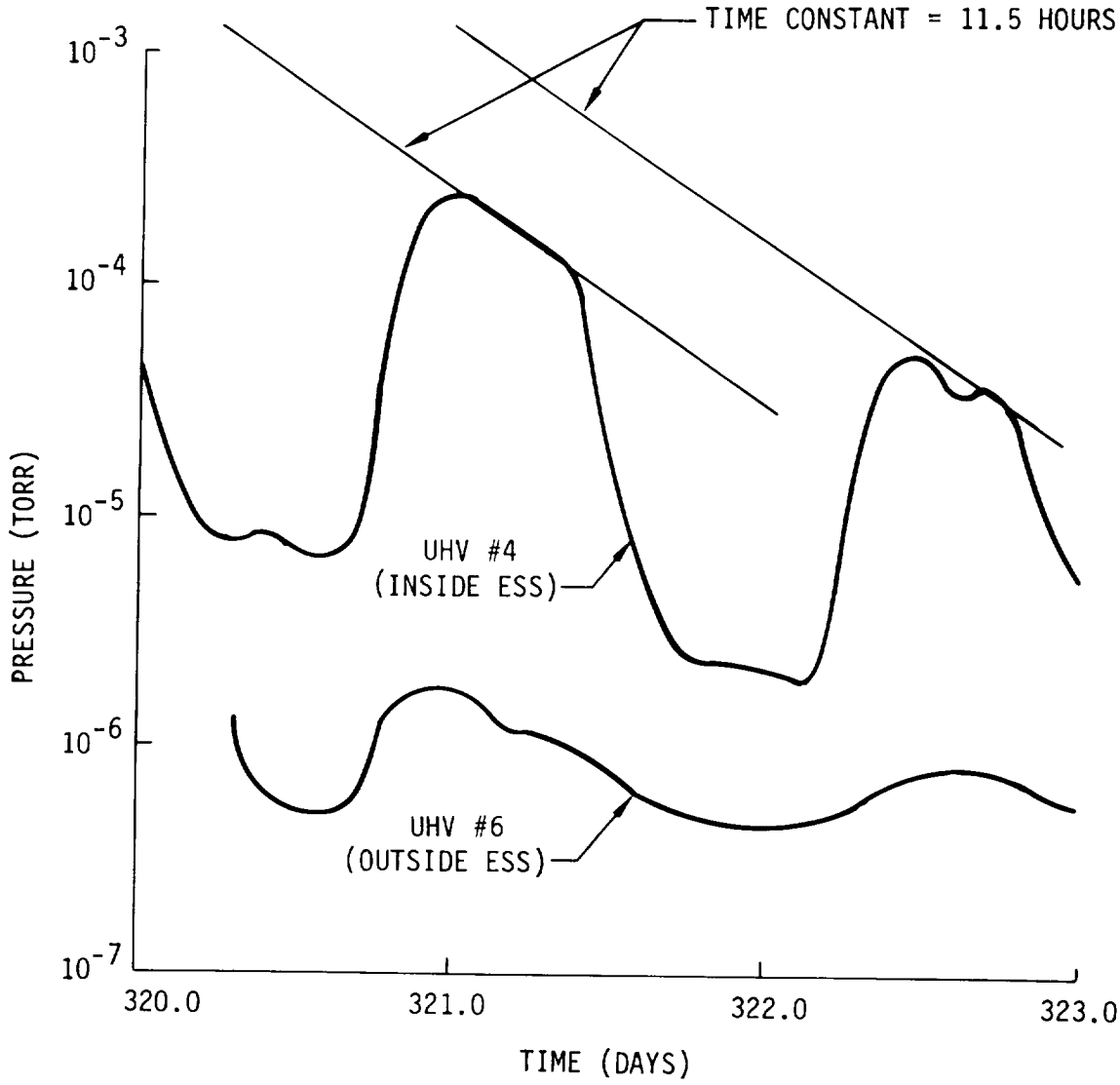

Figure 8 - ESS and Chamber Pressure vs Time

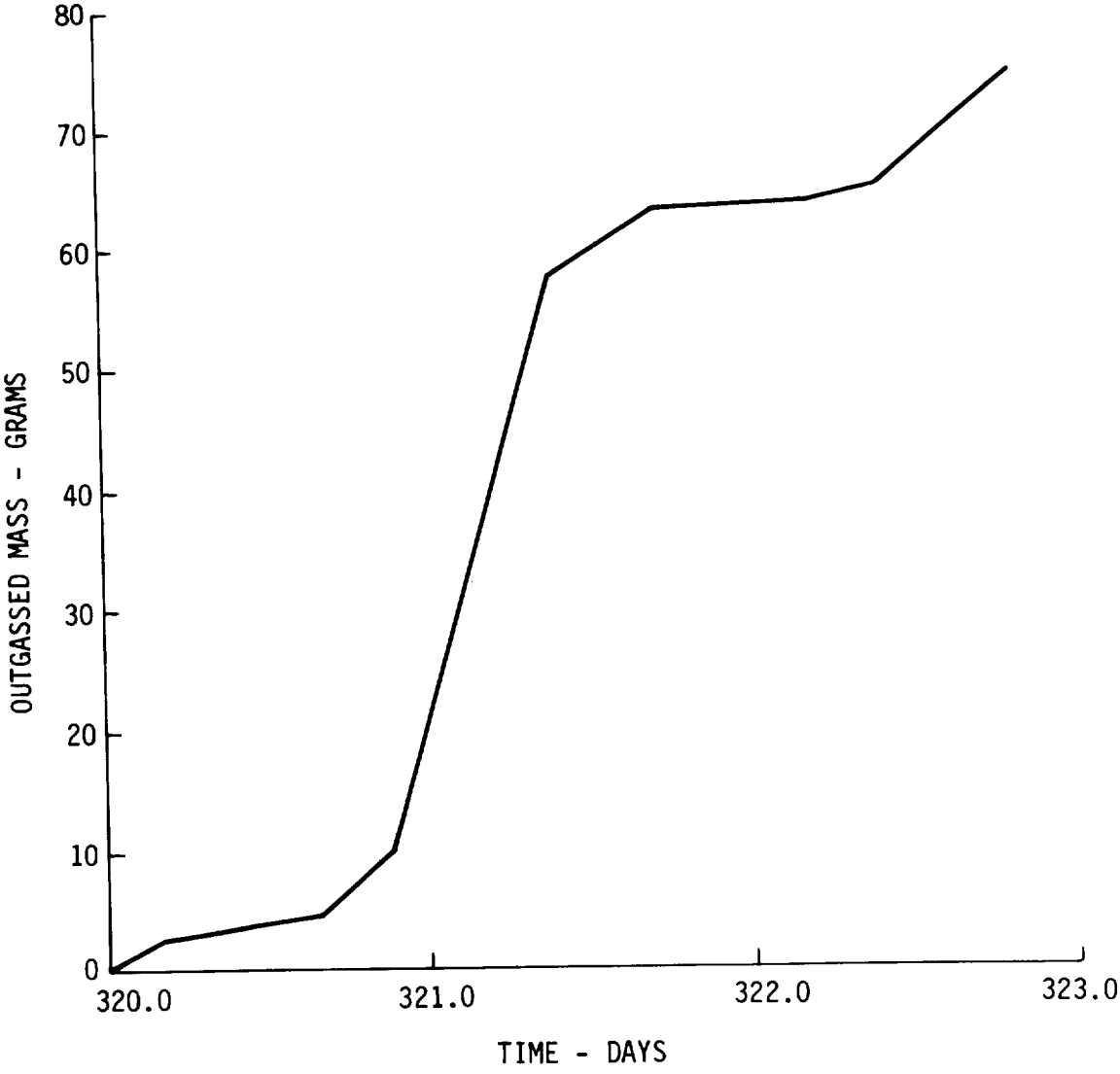

Figure 9 - ESS Outgassing Mass History

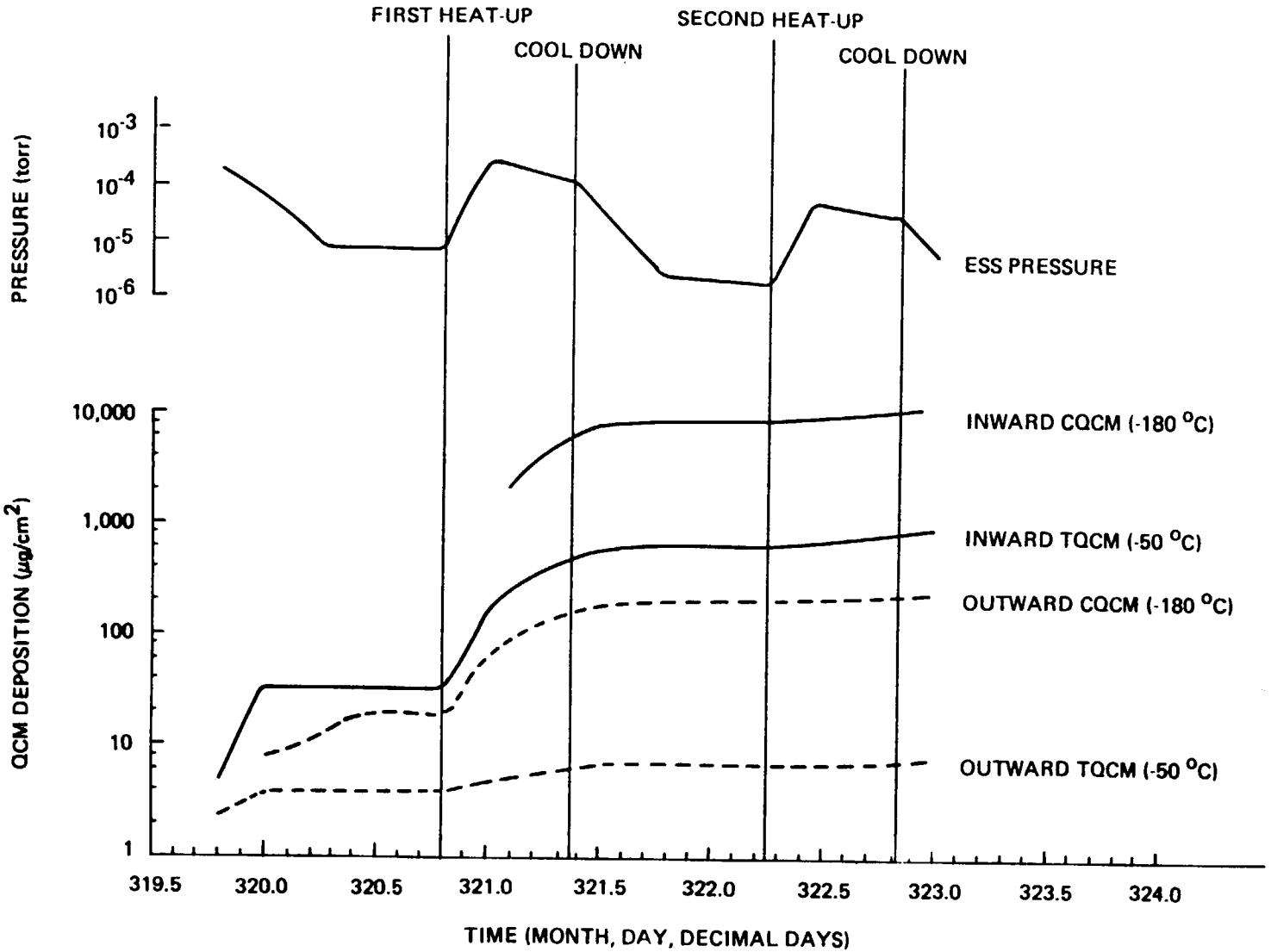

Figure 10 - IUS-05 Thermal Vacuum Test Contamination Measurement Results

HUBBLE SPACE TELESCOPE

COMPONENT QUALIFICATION UTILIZING

A RESIDUAL GAS ANALYZER

Alvin H. Westfall
Perkin-Elmer Corp.

ABSTRACT

Optical devices require a contamination free system to acquire a distinct, optically clear image. Thermal vacuum outgassing prior to component assembly into the spacecraft helps to achieve this goal by reducing contamination at its source. Thermal vacuum outgassing facilities have been in operation at Perkin-Elmer's System Operation Division for two years as the final component cleaning operation at the manufacture of the Hubble Space Telescope.

This paper describes our approach to integrating an automated Residual Gas Analyzer (RGA) into the thermal vacuum outgas process. The RGA has the capability of detailed analysis over a 200-amu range with monitoring of each peak as the test progresses. The NASA criterion of either a 50% reduction of each peak over 44 amu or less than an 0.1% amplitude of the 28 amu base peak for all amu's above 44 amu has been satisfied. A computer sorts, reports which peaks have not satisfied the criterion, and reports test completion. The computer plots amplitudes of all the peaks from 1 amu through 200 amu for each scan.

This RGA real time approach is unique in that it provides sufficient detail to highlight a problem as it occurs. By comparison, a quartz crystal microbalance (QCM) or a thermoelectric quartz crystal microbalance (TQCM) indicates to the operator when changes occur, but not what has happened. Optical-witness samples indicate whether a test was satisfactory within a few days after the test was completed.

ABSTRACT

CONTAMINATION CONTROL AND CLEANLINESS LEVEL INTEGRITY FOR THE SPACE SHUTTLE ORBITER PLB, PAYLOADS AND FACILITIES AT KSC

D. Bartelson, Lockheed, Kennedy Space Center, FL

The Space Shuttle Orbiter Payload Bay is a unique and highly specialized compartment for transporting commercial, scientific, and military payloads into space.

This paper will introduce and develop the evolving technology and science of contamination control as it relates to ground operations at Kennedy Space Center/Eastern Launch Site for the Orbiter PLB and its interfacing facilities.

The payload bay environment is a major concern during cargo processing and a determining factor for the success or failure of a shuttle mission. In an effort to achieve an environment in the PLB compatible with its mission cargo, NASA has levied several cleanliness requirements for the payload bay/cargo/payload canister and interfacing facilities.

The PLB, its cargo, and payload canister must satisfy the cleanliness requirements of visual clean (VC) level 1, 2, 3, or special as stated in NASA document SN-C-0005A. The specific level of cleanliness is chosen by the payload bay customer for their mission.

During orbiter turnaround processing at KSC, the payload bay is exposed to the environments of the Orbiter Processing Facility (OPF) and the Payload Changeout Room (PCR). In supportive response to the orbiter payload bay/facility interface, it is necessary that the facility environment be controlled and monitored to protect the cleanliness/environmental integrity of the payload bay and its cargo.

Both the OPF and PCR are "clean work areas" (CWA) with an air cleanliness of class 100,000 per federal standard 209B. Although the OPF and PCR are not classical clean rooms, the resulting benefits of air filtration/flow direction techniques, restric debris-producing material, contamination control-oriented hardware, special procedures and CWA operational rules have collectively presented the Orbiter PLB facilities as a successfully accomodating counterpart.

As mentioned earlier, there are several different cleanliness levels available to the cargo community, e.g., VC level 1, 2, 3, and special. Visual clean level 1 is an STS baseline requirement and is performed and verified for every mission at no additional cost to PLB customers. Although if a payload is contamination sensitive, "higher" cleanliness levels are available to the cargo community at additional cost considerations.

For each mission, the PLB is inspected and certified to the specification of the chosen VC level during orbiter processing and as a final "look-see" prior to closing the payload bay doors for flight. For critical contamination-sensitive cargo, additional precautions may be implemented. These added assurances include debris covers, curtains, air/gas purges, and stricter operation/personnel control procedures.

With the special attention to cleanliness integrity in the PLB, successful and satisfactory final results would not be realized if the open PLB surrounding environment was not a compatible counterpart.

To support the PLB, orbiter facilities also have program environmental requirements to be satisfied and maintained during an orbiter processing flow. Along with personnel/operational rules and procedures, an array of environmental parameters are constantly monitored. These parameters include air quality (airborne particulate count), particle fallout, non-volatile residue (NVR), hydrocarbon concentration, salt, static pressure, temperature, and relative humidity. Each parameter has been assigned an acceptable range or max/min limit values for normal system monitoring. Facility environmental requirements and "normal" operating environmental data (STS-6 thru STS-13) are presented in the main body of the paper.

The NASA and SPC are committed to presenting the cargo community a payload bay which satisfies the program cleanliness requirements, thereby ensuring a cargo/orbiter compatibility interface. This commitment is exemplified by the development of an entire spectrum of contamination control procedures, practices, and orientation information for payload bay customer familiarity.

These documents are available to the cargo community and their content familiarity by the community is highly encouraged. Successful cargo processing in association with maintaining the mission cleanliness requirements if further supported by the dedication of manhours, materials, and mission schedule time necessary to achieve the program goals as each mission becomes reality.

BIBLIOGRAPHIC DATA SHEET

1. Report No.	2. Government Accession No.	3. Recipient's Catalog No.
CP 2340		

4. Title and Subtitle	5. Report Date
THIRTEENTH SPACE SIMULATION CONFERENCE: THE PAYLOAD – TESTING FOR SUCCESS	6. Performing Organization Code 750
7. Author(s) Joseph Stecher, Editor	8. Performing Organization Report No.
9. Performing Organization Name and Address NASA Goddard Space Flight Center Greenbelt, Maryland 20771	10. Work Unit No. 11. Contract or Grant No.
12. Sponsoring Agency Name and Address National Aeronautics and Space Administration Washington, D.C. 20546	13. Type of Report and Period Covered Conference Publication October 8 - 11, 1984 14. Sponsoring Agency Code
15. Supplementary Notes	

16. Abstract

The Institute of Environmental Sciences Thirteenth Space Simulation Conference "The Payload – Testing for Success" provided participants a forum to acquire and exchange information on the state-of-the-art in space simulation, test technology, thermal simulation and protection, contamination, and test measurements and techniques. A panel discussion of "Simulation of Upper Atmosphere Oxygen" was held and should be the basis for future studies. The papers presented at this conference and the resulting discussions carried out the conference theme of "The Payload – Testing for Success."

17. Key Words (Selected by Author(s))	18. Distribution Statement
Space Simulation Thermal Simulation Contamination Control Dynamic Testing	Unclassified - Unlimited STAR 18

19. Security Classif. (of this report)	20. Security Classif. (of this page)	21. No. of Pages	22. Price*
Unclassified	Unclassified	382	

*For sale by the National Technical Information Service, Springfield, Virginia

GSFC 25-44 (10/77)